

ÉCOLE DOCTORALE ED548 MER ET SCIENCE

Laboratoire MEMOCS

Università degli Studi dell'Aquila

THÈSE

présentée par :

Minh Tuan VU

soutenue le : **28 February 2017**

pour obtenir le grade de Docteur en Ingénierie côtière

Spécialité : Modélisation numérique

Une approche numérique pour la conception d'ouvrages de protection côtière au tombolo oriental de la presqu'île de Giens

THÈSE dirigée par :

Mr Yves Lacroix Professeur, SEATECH, Toulon/U. dell'Aquila

JURY :

Mr Charles-François Boudouresque Professeur, Aix-Marseille Universités

Mr Sylvain Guillou Professeur, ESIX, Université de Caen

Mr Didier Léandri Professeur, SEATECH, Toulon

Mr Kim Dan Nguyen Professeur, Université de Paris Est

Mr Jacques Piazzola Professeur, SEATECH, Toulon

ACKNOWLEDGEMENTS

Accomplishing this PhD thesis would not have been possible without the help and support of the kind people around me and some good organizations, to only some of whom it is possible to give particular mention herein.

First of all, I would like to express my sincere gratitude to Vietnam Ministry of Education and the staff members of the Project 911 for letting me fulfill my dream of researching in France by financially supporting for this PhD study. This was a great opportunity to increase my knowledge, and to discover an amazing world far beyond the borders of my country. I am equally thankful to Campus France, especially to Madam Abokatma. With their supports of accommodation, insurance and registration, my life in France became more comfortable.

I want to express my deepest appreciation to my supervisor Prof. Yves Lacroix, who offered me the chance to undertake this interesting research. Thanks to his guidance, patience, understanding and encouragement during three years. It has been an honour to learn from his experience and discuss ideas with him. In addition, the stories of life from him are useful and meaningful to me. I am truly grateful to the referees, Prof. Sylvain Guillou and Prof. Kim Dan Nguyen, for their contribution to reading this thesis as well as their precious constructive comments. I would also like to recognize the always-valuable support and critical review provided by my examiners, Prof. Didier Léandri, Prof. Jacques Piazzola, and Prof. Charles François Boudouresque. I would like to thank them for not only all the time they have spent reading my work, but also for the beneficial comments and advices. I should here acknowledge Prof. Yves Blache and Madam Casanova for their supports in registration of Ecole doctorale and giving me an opportunity to attend the international conference.

This thesis work is also a result of teamwork and cooperation. Therefore, I would like to recognize collaboration of all co-authors of appended papers: Than Van Van and Nguyen Viet Thanh. Mr Van also transferred all what he had and knew about the study area to me. With his data, my research could be carried out easily and more precisely. With Mr Thanh, I would like to acknowledge him particularly for his ideas, his explanations and all the time I discussed with him. If without their support, it was very difficult for me to do this project.

This research benefited from a large variety of data that were made available by different institutions, and I would like to acknowledge their representatives. Firstly, I would like to thank Dr. Samuel Meulé for sharing the wave data at La Capte beach in 2009. Without this dataset, the numerical model could not be verified and calibrated fully. Both Mr Alain Le Berre (Cerema) for providing the wave data of Buoy of 08301 and 08302 available and Mr Xavier Kergadallan (CETMEF) for making the ANEMOC dataset

available, are also sincerely acknowledged. I should also mention the authorities of Hyères city for providing me with the helpful reports and materials as well as the powerful computer. I am grateful to EOL, SHOM, and REFMAR for providing the other in situ measurement data and to DHI for allowing a free license for using MIKE software.

A special thanks goes to my Vietnamese and French friends in Toulon. They made me feel like one family in three years. We supported and overcame many difficulties together with heart-warming consolations. The new-year parties, picnics and football matches abated the nostalgia. I would like to acknowledge Nguyen Thanh Phuong for being my close friend. We had good time to sharing the same hobbies and interests, stories about job, science, and even life. In addition, his ideas as well as his knowledge about MatLab help me to open my vision. I will never forget them in the rest of my life.

I would like to thank Prof. Nguyen Viet Trung and all my colleagues at the Division of Urban Transport and Coastal Engineering, University of Transport and Communications for their support. They helped me to complete some educational tasks when I absent.

I also express my heartfelt gratitude to my parents and my younger brother for their unconditional love, support, and for always providing a pleasant atmosphere in a happy family. It is really a big mistake if I do not acknowledge my parents in law. With their support, I could focus on my research without worries about my house and my son. Especially, my mother in law, she gave my son with huge love and took care of him when I absent. Based on what they gave me, no words can express my gratitude to them.

Last but not least, I would like to express a great thanks and recognition go to my dear wife, Trang, for her eternal love, support and perseverance during all my PhD study. She took my place to take care of my big family during three year without complains. I understood that it was so difficult for her to look after our son during my three-year absence. I really respect your great sacrifice, my beloved.

ABSTRACT

The double tombolo of Giens, located in the town of Hyères, South East of France, is a unique and rare geomorphological formation in the world, which links Giens Island to the continent. It was mainly formed due to the wave diffraction and refraction by the islands. It consists of two parts: the western branch (Almanarre beach) directly facing the Gulf of Giens and the eastern branch lying on the western coast of Hyères bay. These parts are distinctly separated by the salt pond of Pesquiers. The eastern part of Giens tombolo extends over more than ten kilometers from the mouth of Gapeau river in the north to La Badine beach in the south. The beaches along the eastern tombolo, especially Ceinturon and Bona beaches are subject to beach erosion and beach narrowing due to both natural causes and human interference, but anthropogenic interventions are still dominant. In order to mitigate or prevent coastal erosion, various coastal structures have been used along the eastern Giens tombolo. They can only solve local erosion in some cases, but may also trigger some undesirable effects as well as disadvantages. Even the shore-normal structures that interfere with longshore sediment transport, not only result in the deficit of sediment and erosion in the downstream drift, but also blot out surrounding landscape of the beaches.

The main objectives of this study was to better understand the physical processes underlying the morphodynamics, and also anticipate future evolution of the eastern Giens tombolo in response to different actions and interventions taking place along the coast. Thereof, the submerged breakwater (SBW) was proposed to not only protect the Ceinturon and Bona beaches and stabilize the shoreline in the long term, but also maintain beach amenity or aesthetics. DHI's MIKE 21 and LITPACK numerical models are used in order to achieve these above-mentioned objectives. Additionally, the historical and future medium-term shoreline evolution along the eastern Giens tombolo is also evaluated and predicted by using the combination of remote sensing, geographic information system (GIS) techniques coupled with the Digital Shoreline Analysis System (DSAS) along with linear regression method. These numerical models were satisfactorily tested available historical data, as they could reproduce the observed hydrodynamics and coastal evolution. Especially, a novel approach suggested to simulate the presence of *Posidonia* seagrass and various types of seabed is presented in this work. The numerical results interpret the role as well as impact of wind change, seasonal variation, extreme events, *Posidonia* seagrass, sea level rise, and beach nourishment on the morphological evolution of the eastern Giens tombolo. Moreover, the results obtained strongly demonstrate that the SBWs play a very important in protecting Ceinturon and Bona beaches to a certain degree, viz. effectively reducing the nearshore wave heights, current speed and sediment transport as well as counteracting the retreat of the shoreline under the wave conditions apart from the semi-centennial and centennial storms.

RÉSUMÉ

Le double tombolo de Giens, situé dans la ville de Hyères, dans le sud-est de la France, est une formation géomorphologique unique et rare dans le monde, qui relie l'île de Giens au continent. Il a été principalement formé en raison de la diffraction d'onde et de la réfraction par les îles. Il se compose de deux parties : la branche ouest (plage de l'Almanarre) directement en face du golfe de Giens et la branche orientale située sur la côte ouest de la baie d'Hyères. Ces parties sont séparées par l'étang salé des Pesquiers. La partie orientale du tombolo de Giens s'étend sur plus de dix kilomètres de l'embouchure de la rivière Gapeau au nord jusqu'à la plage de La Badine au sud. Les plages le long du tombolo oriental, en particulier les plages de Ceinturon et de Bona, sont sujettes à l'érosion et au rétrécissement en raison de causes naturelles et d'interférences humaines, mais les interventions anthropiques dominent.

Afin d'atténuer ou d'empêcher l'érosion côtière, diverses structures côtières ont été utilisées le long du tombolo oriental de Giens. Elles ne peuvent résoudre l'érosion locale que dans certains cas, mais peuvent aussi engendrer des effets indésirables. Les structures côtières qui interfèrent avec le transport des sédiments le long des côtes, non seulement entraînent un déficit de sédiments et l'érosion dans la dérive en aval, mais aussi effacent le paysage environnant des plages.

Les principaux objectifs de cette thèse étaient de mieux comprendre les processus physiques sous-jacents à la morpho-dynamique et d'anticiper l'évolution future du tombolo oriental de Giens en réponse aux différentes actions et interventions le long de la côte. La mesure structurelle la plus appropriée a été proposée non seulement pour protéger les plages de Ceinturon et Bona et pour stabiliser le rivage à long terme, mais aussi pour maintenir l'accessibilité ou l'esthétique des plages. Les modèles numériques MIKE 21 et LITPACK de DHI sont utilisés pour atteindre ces objectifs. L'évolution historique et future à long terme du rivage est également évaluée et prédite en utilisant la combinaison de techniques de télédétection, de système d'information géographique (SIG) et de régression linéaire. Ces modèles numériques ont été testés de manière satisfaisante sur des données historiques disponibles, car ils pouvaient reproduire l'hydrodynamique observée et l'évolution côtière.

En particulier, une nouvelle approche suggérée pour simuler la présence de posidonies et divers types de fonds marins est présentée dans ce travail. Les résultats numériques interprètent le rôle ainsi que l'impact du changement de vent, la variation saisonnière, les événements extrêmes, les herbiers de posidonies, l'élévation du niveau de la mer et le ré-ensablement de la plage sur l'évolution morphologique du tombolo oriental de Giens. De plus, les résultats obtenus démontrent que les digues sous-marines jouent un rôle très important dans la protection des plages de Ceinturon et Bona, elles permettent de réduire efficacement la hauteur des vagues, la vitesse du courant et le transport des sédiments ainsi que contrecarrer le retrait du rivage dans toutes les conditions des vagues, à l'exception des tempêtes semi-centenaires et centennales pour lesquelles une certaine érosion persiste. Combinées à des ré-ensemblés périodiques mais limités en espace et en temps, elles semblent constituer le meilleur compromis de protection à moyen et long terme.

TABLE OF CONTENTS

ACKNOWLEDGEMENTS	i
ABSTRACT	iii
RÉSUMÉ	iv
TABLE OF CONTENTS	v
LIST OF FIGURES.....	ix
LIST OF TABLES	xxii
LIST OF MAIN SYMBOLS	xxvi
LIST OF MAIN ABBREVIATIONS	xxx
CHAPTER 1. GENERAL INTRODUCTION	1
1.1. Background	1
1.2. Research objectives.....	4
1.3. Thesis structure.....	4
CHAPTER 2. STUDY AREA AND THE DRIVING FACTORS	5
2.1. Site description	5
2.2. Typical characteristics of the study area	6
2.2.1. Bathymetry	6
2.2.2. Water level and tides	8
2.2.3. Typhoons and storm surges.....	11
2.2.4. River flow and sea currents.....	14
2.2.5. Waves.....	19
2.2.6. Wind	32
2.2.7. Sediment.....	38
2.2.8. Posidonia and seabed characteristics	41
2.3. Key factors affecting the morphological evolution in Giens tombolo	48
2.3.1. Wind condition.....	48
2.3.2. Wave condition	49
2.3.3. Current condition	49
2.3.4. Biological factors	50
2.3.5. SLR due to global climate change.....	51
2.3.6. Human actions.....	52
2.4. Conclusion	61
CHAPTER 3. METHODOLOGY.....	62
3.1. Introduction.....	62

3.2. Coastal morphodynamics	63
3.2.1. Coastal hydrodynamics.....	63
3.2.2. Sediment transport.....	75
3.3. Morphological evolution analysis.....	81
3.3.1. The cross-shore coastal evolution	81
3.3.2. The long-shore morphodynamic change	86
3.4. Conclusion	93
CHAPTER 4. MORPHOLOGICAL EVOLUTION	94
4.1. Introduction.....	94
4.2. Shoreline changes.....	94
4.2.1. Consideration of littoral zones.....	94
4.2.2. Results of historical shoreline changes and discussion	95
4.2.3. Results of future shoreline changes and discussion.....	102
4.3. Beach profile evolution.....	107
4.3.1. Division of study area	107
4.3.2. Beach evolution.....	109
4.3.3. Equilibrium Parameters of EBP Functions.....	125
4.4. Conclusion	135
CHAPTER 5. MODELING OF HYDRODYNAMIC AND SEDIMENT TRANSPORT.....	136
5.1. Introduction.....	136
5.2. Study scenarios.....	137
5.2.1. No SLR conditions	137
5.2.2. SLR conditions	138
5.3. Determination of the most appropriate mesh.....	139
5.3.1. Model performance statistics	139
5.3.2. Grid sensitivity analysis.....	141
5.4. Model calibration.....	154
5.4.1. Regional area-Grand Var	155
5.4.2. Local area-The eastern Giens tombolo	160
5.5. Results of Regional area-Grand Var and discussion.....	164
5.5.1. Wind variations.....	164
5.5.2. Seasonal variations.....	167
5.5.3. Extreme events.....	170
5.6. Results of Local area-the eastern Giens tombolo and discussion.....	175

5.6.1. Effect of wind on hydrodynamics and sediment transport	176
5.6.2. Effect of seasonal changes on hydrodynamics and sediment transport.....	181
5.6.3. Effect of extreme events on hydrodynamics and sediment transport	185
5.6.4. Effect of Posidonia seagrass on hydrodynamics and sediment transport	191
5.6.5. Effect of SLR on hydrodynamics and sediment transport.....	206
5.6.6. Effect of beach nourishment on hydrodynamics and sediment transport	217
5.7. Conclusion	242
CHAPTER 6. PRELIMINARY STUDY OF COASTAL PROTECTION MEASURES.....	245
6.1. Introduction.....	245
6.2. Proposed some suitable structures for coastal protection.....	247
6.3. Design of SBWs	248
6.3.1. Considerations of SBW design parameters.....	250
6.3.2. Stability of SBW.....	258
6.4. Sensitivity analysis of design parameters.....	261
6.4.1. Salient predictions for the Ceinturon and Bona beaches.....	261
6.4.2. Determination of rational crest width	263
6.5. Results and discussion.....	266
6.5.1. Effects to wave fields	266
6.5.2. Effects to current fields.....	276
6.5.3. Effects to sediment transport.....	287
6.5.4. Effects to bathymetry evolution	293
6.5.5. Effects to shoreline change.....	309
6.6. Conclusion	324
CHAPTER 7. CONCLUSIONS AND FUTURE WORK.....	326
7.1. Conclusions	326
7.2. Future work	329
APPENDICES.....	330
Appendix A - Data sources of bathymetry.....	330
A.1. EMODnet database.....	330
A.2. Litto3D database.....	330
A.3. EOL database.....	331
Appendix B - Data treatment of water level	332
B.1. Observation data.....	332
B.2. Simulation data.....	332

Appendix C - Data sources of wave	335
C.1. Data collection.....	335
C.2. Data treatment.....	338
Appendix D-MATLAB codes	349
D.1. Extraction and prediction of the shoreline.....	349
D.2. Wave statistics.....	350
Appendix E - Numerical results of SBWs	352
E.1. Ceinturon beach	352
E.2. Bona beach	365
BIBLIOGRAPHY.....	382

LIST OF FIGURES

Figure 1. General location of Giens double tombolo.	3
Figure 2. The study area and marine meteorological stations.....	6
Figure 3. The bathymetry in nearshore of the eastern Giens tombolo in 2010.	7
Figure 4. Comparison of daily sea levels between Toulon and Port Ferreol from 29 th March 2012 to 27 th October 2015.	9
Figure 5. Monthly sea level distribution at Port Ferreol station from 2012 to 2015.....	11
Figure 6. Monthly sea level distribution at Toulon station from 1961 to 2015.	11
Figure 7. River system in the study area.	15
Figure 8. Average monthly discharges over the period from 1961 to 2014. (Source: Banque Hydro).....	16
Figure 9. Nearshore current data of SCAPT4 at La Capte beach in 2009.....	17
Figure 10. Nearshore current at Almanarre beach in 2000.	18
Figure 11. The currents in Hyères bay (Jeudy De Grissac (1975), Courtaud (2000), modified).....	18
Figure 12. Location of wave buoys in situ.....	19
Figure 13. Rose of nearshore wave in November 2000 (OPHIURE III).....	20
Figure 14. Direction and height of the waves recorded in November 2000.....	20
Figure 15. Height and period of waves recorded in November 2000.	20
Figure 16. Height and period of waves recorded in the rough sea in November 2000.....	21
Figure 17. Height and period of waves recorded at SCAPT1 in La Capte in 2009.....	21
Figure 18. Height and period of waves recorded at SCAPT2 in La Capte in 2009.....	22
Figure 19. Height and period of waves recorded at SCAPT3 in La Capte in 2009.....	22
Figure 20. Height and period of waves recorded at SCAPT4 in La Capte in 2009.....	23
Figure 21. Height and period of waves recorded at SCAPT5 in La Capte in 2009.....	23
Figure 22. Wave rose in Porquerolles Island from 1992 to 2015.....	24
Figure 23. Monthly wave height distribution over 24 years.....	27
Figure 24. Directional wave height distribution over 24 years.....	27
Figure 25. Plans of northeast, east and southeast waves ($T = 7s$) and refraction coefficients (Blanc (1971), as modified by Courtaud (2000)).	30
Figure 26. Rose of winds in B.A.N. Hyères station for the period 1999-2015.....	32
Figure 27. Wind rose in Le Levant station for the period 2000-2015.	35
Figure 28. Longitudinal distribution of sediment in the swash zone in Hyères bay (Courtaud (2000), Capanni (2011), modified).....	40

Figure 29. Distribution of sediment in the seabed of Hyères bay (Source: SHOM).	41
Figure 30. Distribution of <i>Posidonia Oceanica</i> (red line) along the coast of the Mediterranean Sea (Vacchi et al., 2016).	42
Figure 31. Structure of <i>Posidonia oceanica</i> (Manca, 2010).	43
Figure 32. Distribution of <i>Posidonia</i> seagrass in Hyères bay.	45
Figure 33. Distribution of median grain size D_{50} in Hyères bay.	47
Figure 34. Distribution of Nikuradse roughness height k_s in Hyères bay.	47
Figure 35. Distribution of Manning's number M in Hyères bay.	48
Figure 36. Wood fences.	53
Figure 37. Ceinturon beach before and after nourishment in 2008 (Capanni, 2011).	55
Figure 38. Seawalls along the eastern tombolo.	57
Figure 39. Other revetments along the eastern tombolo.	58
Figure 40. The groynes in the eastern tombolo.	59
Figure 41. The port facilities in the eastern Giens tombolo.	60
Figure 42. General flow diagram for the simulation of morphological changes in the eastern Giens tombolo.	63
Figure 43. Actual shoreline position (2015) and predicted shoreline position (2015) along Zone 2 in the eastern Giens tombolo.	89
Figure 44. Longshore discretization.	92
Figure 45. Definition of baseline orientation.	92
Figure 46. The studied zones in the eastern Giens tombolo.	95
Figure 47. Positions of shorelines, transect lines and shoreline change rates using EPR method in the zone 1 of the eastern Giens tombolo over a period of 1973-2015.	96
Figure 48. The variation of shoreline change rates using LRR method in the zone 1 of the eastern Giens tombolo over a period of 1973-2015.	96
Figure 49. Positions of shorelines, transect lines and shoreline change rates using EPR method in the zone 2 of the eastern Giens tombolo over a period of 1973-2015.	97
Figure 50. The variation of shoreline change rates using LRR method in the zone 2 of the eastern Giens tombolo over a period of 1973-2015.	97
Figure 51. Positions of shorelines, transect lines and shoreline change rates using EPR method in the zone 3 of the eastern Giens tombolo over a period of 1973-2015.	98
Figure 52. The variation of shoreline change rates using LRR method in the zone 3 of the eastern Giens tombolo over a period of 1973-2015.	99
Figure 53. Positions of shorelines, transect lines and shoreline change rates using EPR method in the zone 4 of the eastern Giens tombolo over a period of 1973-2015.	100

Figure 54. The variation of shoreline change rates using LRR method in the zone 4 of the eastern Giens tombolo over a period of 1973-2015.	100
Figure 55. Positions of shorelines, transect lines and shoreline change rates using EPR method in the zone 5 of the eastern Giens tombolo over a period of 1973-2015.....	101
Figure 56. The variation of shoreline change rates using LRR method in the Zone 5 of the eastern Giens tombolo over a period of 1973-2015.	101
Figure 57. Positions of shorelines and transect lines as well as shoreline change rates using EPR method in the zone 1 of the eastern Giens tombolo over a period of 2015-2050.	103
Figure 58. Positions of shorelines and transect lines as well as shoreline change rates using EPR method in the zone 2 of the eastern Giens tombolo over a period of 2015-2050.	103
Figure 59. Positions of shorelines and transect lines as well as shoreline change rates using EPR method in the zone 3 of the eastern Giens tombolo over a period of 2015-2050.	104
Figure 60. Positions of shorelines and transect lines as well as shoreline change rates using EPR method in the zone 4 of the eastern Giens tombolo over a period of 2015-2050.	105
Figure 61. Positions of shorelines and transect lines as well as shoreline change rates using EPR method in the zone 5 of the eastern Giens tombolo over a period of 2015-2050.	106
Figure 62. Location of the studied zones and beach profiles along the eastern branch of Giens tombolo, Hyères.	108
Figure 63. Beach profiles measured by E.O.L at Gapeau beach from 2001 to 2010.	111
Figure 64. A comparison of an average measured beach profile and the predicted EBPs at Gapeau beach.....	111
Figure 65. Beach profiles measured by E.O.L at Ayguade beach from 2001 to 2010.....	112
Figure 66. A comparison of an average measured beach profile and the predicted EBPs at Ayguade beach.	113
Figure 67. Beach profiles measured by E.O.L at La Marquise beach from 2001 to 2010.	113
Figure 68. A comparison of an average measured beach profile and the predicted EBPs at La Marquise beach.....	114
Figure 69. Beach profiles measured by E.O.L at Plein Sud beach from 2001 to 2010. ...	115
Figure 70. A comparison of an average measured beach profile and the predicted EBPs at Plein Sud beach.....	116
Figure 71. Beach profiles measured by E.O.L at Aéroport beach from 2001 to 2010.....	116

Figure 72. A comparison of an average measured beach profile and the predicted EBPs at Aéroport beach.	117
Figure 73. Beach profiles measured by E.O.L at Amont beach from 2001 to 2010.....	118
Figure 74. A comparison of an average measured beach profile and the predicted EBPs at Amont beach.....	118
Figure 75. Beach profiles measured by E.O.L at Bona beach from 2001 to 2010.....	119
Figure 76. A comparison of an average measured beach profile and the predicted EBPs at Bona beach.	120
Figure 77. Beach profiles measured by E.O.L at Hyères beach from 2001 to 2010.....	121
Figure 78. A comparison of an average measured beach profile and the predicted EBPs at Hyères beach.	121
Figure 79. Beach profiles measured by E.O.L at Pesquiers beach from 2001 to 2010. ..	122
Figure 80. A comparison of an average measured beach profile and the predicted EBPs at Pesquiers beach.....	122
Figure 81. Beach profiles measured by E.O.L at La Capte beach from 2000 to 2010.....	123
Figure 82. A comparison of an average measured beach profile and the predicted EBPs at La Capte beach.	124
Figure 83. Beach profiles measured by E.O.L at La Badine beach from 2000 to 2010. ..	124
Figure 84. A comparison of an average measured beach profile and the predicted EBPs at La Badine beach.....	125
Figure 85. A comparison of Dean (1977)'s EBPs with variation of the A parameter at La Badine beach.....	126
Figure 86. A comparison of Vellinga (1987)'s EBPs with variation of H_{os} and w at Plein Sud beach.	127
Figure 87. A comparison of Lee (1994)'s EBPs with variation of C and D parameters at La Capte beach.	128
Figure 88. A comparison of Bodge (1992)'s EBPs with variation of B and k parameters at Bona beach.	129
Figure 89. A comparison of Bodge (1992)'s EBPs with variation of B and k parameters at Hyères beach.	129
Figure 90. A comparison of Bodge (1992)'s EBPs with variation of B and k parameters at Pesquiers beach.....	130
Figure 91. A comparison of Komar et al. (1994)'s EBPs with variation of S_o at Gapeau beach.....	131
Figure 92. A comparison of Komar et al. (1994)'s EBPs with variation of S_o at Aeroport beach.....	131

Figure 93. A comparison of Sierra et al. (1994)'s EBPs with variation of F , G and x_0 parameters at Ayguade beach.....	132
Figure 94. A comparison of Sierra et al. (1994)'s EBPs with variation of F , G and x_0 parameters at La Marquise beach.	133
Figure 95. A comparison of Sierra et al. (1994)'s EBPs with variation of F , G and x_0 parameters at Amont beach.....	133
Figure 96. Summary of simulation runs.....	136
Figure 97. The study domain of regional scale-Type I.	142
Figure 98. The study domain of regional scale-Type II.....	142
Figure 99. The study domain of regional scale-Type III.	143
Figure 100. An example of computational mesh and bathymetry of regional scale-Type I.	144
Figure 101. An example of computational mesh and bathymetry of regional scale-Type II.....	144
Figure 102. An example of computational mesh and bathymetry of regional scale-Type III.	145
Figure 103. Boundary conditions of regional domain-Type I.	146
Figure 104. Boundary conditions of regional domain-Type II.....	146
Figure 105. Boundary conditions of regional domain-Type III.	147
Figure 106. Time series of OBS and SIM wave height in the case of IIIi_v3.	147
Figure 107. The study domain of local scale.	152
Figure 108. An example of computational mesh and bathymetry of local scale.....	152
Figure 109. Boundary conditions of local domain.....	153
Figure 110. Time series of OBS and SIM wave height in the case of E11.....	154
Figure 111. The computational mesh of the regional scale for calibration.....	155
Figure 112. Calibration of current speed at Almanarre beach.....	157
Figure 113. Comparison between the OBS and SIM current speed with $Mn = 20$ at Almanarre beach in November 2000.....	157
Figure 114. Calibration of wave height at Almanarre beach.	158
Figure 115. Comparison between the OBS and SIM wave height with $k_s = 0.04$ at Almanarre beach in November 2000.....	159
Figure 116. Comparison between the OBS and SIM wave height with $k_s = 0.04$ at La Capte beach in March 2009.....	160
Figure 117. Comparison between the OBS and SIM current speed with $Mn = 20$ at La Capte beach in March 2009.....	160

Figure 118. The computational mesh of the local scale for calibration.....	161
Figure 119. Comparison between the OBS and SIM wave heights of SCAPT3 station at La Capte beach in March 2009.....	163
Figure 120. Comparison between the OBS and SIM wave heights of SCAPT4 station at La Capte beach in March 2009.....	163
Figure 121. Comparison between the OBS and SIM current speeds of SCAPT4 station at La Capte beach in March 2009.....	163
Figure 122. Comparison of OBS and SIM profile at Aéroport beach for the period from November 2007 to November 2008.....	164
Figure 123. Current speed of the regional model under the impact of northeast wind.	165
Figure 124. Significant wave height of the regional model under the impact of northeast wind.	165
Figure 125. Current speed of the regional model under the impact of east wind.....	166
Figure 126. Significant wave height of the regional model under the impact of east wind.	166
Figure 127. Current speed of the regional model under the impact of southeast wind.	167
Figure 128. Significant wave height of the regional model under the impact of southeast wind.	167
Figure 129. Current speed of the regional model in February 2007.....	168
Figure 130. Significant wave height of the regional model in February 2007.....	169
Figure 131. Current speed of the regional model in July 2007.....	169
Figure 132. Significant wave height of the regional model in July 2007.....	170
Figure 133. Current speed of the regional model under the decadal storm.....	171
Figure 134. Significant wave height of the regional model under the decadal storm. ...	171
Figure 135. Current speed of the regional model under the tri-decadal storm.	172
Figure 136. Significant wave height of the regional model under the tri-decadal storm.	173
Figure 137. Current speed of the regional model under the semi-centennial storm.....	173
Figure 138. Significant wave height of the regional model under the semi-centennial storm.....	174
Figure 139. Current speed of the regional model under the centennial storm.	175
Figure 140. Significant wave height of the regional model under the centennial storm.	175
Figure 141. Current speed in the study area under the impact of variation of wind direction with Posidonia.....	177

Figure 142. Significant wave height in the study area under the impact of variation of wind direction with Posidonia.....	177
Figure 143. Sediment transport rates (total load) in the study area under the impact of variation of wind direction with Posidonia.....	178
Figure 144. Bed level change in the study area under the impact of variation of wind direction with Posidonia.....	179
Figure 145. Beach profile evolution at Central Ceinturon beach under the impact of variation of wind direction with Posidonia.....	179
Figure 146. Beach profile evolution at Bona beach under the impact of variation of wind direction with Posidonia.....	179
Figure 147. Current speed in the study area under the impact of seasonal variation with Posidonia.....	181
Figure 148. Significant wave height in the study area under the impact of seasonal variation with Posidonia.....	182
Figure 149. Sediment transport rates (total load) in the study area under the impact of seasonal variation with Posidonia.	183
Figure 150. Bed level change in the study area under the impact of seasonal variation with Posidonia.	183
Figure 151. Beach profile evolution at Central Ceinturon beach under the impact of seasonal variation with Posidonia.	184
Figure 152. Beach profile evolution at Bona beach under the impact of seasonal variation with Posidonia.	184
Figure 153. Current speed in the study area under the impact of variation of storm scale with Posidonia.	186
Figure 154. Significant wave height in the study area under the impact of variation of storm scale with Posidonia.....	187
Figure 155. Sediment transport rates (total load) in the study area under the impact of variation of storm scale with Posidonia.....	188
Figure 156. Bed level change in the study area under the impact of variation of storm scale with Posidonia.	189
Figure 157. Beach profile evolution at Central Ceinturon beach under the impact of variation of storm scale with Posidonia.....	190
Figure 158. Beach profile evolution at Bona beach under the impact of variation of storm scale with Posidonia.	190
Figure 159. Significant wave height in the study area under the impact of variation of wind direction without Posidonia.....	192

Figure 160. Significant wave height in the study area under the impact of seasonal variation without Posidonia.....	192
Figure 161. Significant wave height in the study area under the impact of variation of storm scale without Posidonia.....	193
Figure 162. Current speed in the study area under the impact of variation of wind direction without Posidonia.....	195
Figure 163. Current speed in the study area under the impact of seasonal variation without Posidonia.....	195
Figure 164. Current speed in the study area under the impact of variation of storm scale without Posidonia.....	196
Figure 165. Sediment transport rates (total load) in the study area under the impact of variation of wind direction without Posidonia.....	197
Figure 166. Sediment transport rates (total load) in the study area under the impact of seasonal variation without Posidonia.....	198
Figure 167. Sediment transport rates (total load) in the study area under the impact of variation of storm scale without Posidonia.....	199
Figure 168. Bed level change in the study area under the impact of variation of wind direction without Posidonia.....	201
Figure 169. Beach profile evolution at Central Ceinturon beach under the impact of variation of wind direction without Posidonia.....	201
Figure 170. Beach profile evolution at Bona beach under the impact of variation of wind direction without Posidonia.....	201
Figure 171. Bed level change in the study area under the impact of seasonal variation without Posidonia.....	202
Figure 172. Beach profile evolution at Central Ceinturon beach under the impact of seasonal variation without Posidonia.....	203
Figure 173. Beach profile evolution at Bona beach under the impact of seasonal variation without Posidonia.....	203
Figure 174. Bed level change in the study area under the impact of variation of storm scale without Posidonia.....	204
Figure 175. Beach profile evolution at Central Ceinturon beach under the impact of variation of storm scale without Posidonia.....	205
Figure 176. Beach profile evolution at Bona beach under the impact of variation of storm scale without Posidonia.....	205
Figure 177. Modeled cross-shore variations in wave heights under the impact of SLR and variation of wind direction at Bona beach.....	207

Figure 178. Modeled cross-shore variations in wave heights under the impact of SLR and variation of wind direction at Ceinturon beach.....	207
Figure 179. Modeled cross-shore variations in wave heights under the impact of SLR and variation of storm scale at Bona beach.....	208
Figure 180. Modeled cross-shore variations in wave heights under the impact of SLR and variation of storm scale at Ceinturon beach.....	208
Figure 181. Modeled cross-shore variations in current speed under the impact of SLR and variation of wind direction at Bona beach.	211
Figure 182. Modeled cross-shore variations in current speed under the impact of SLR and variation of wind direction at Ceinturon beach.	211
Figure 183. Modeled cross-shore variations in current speed under the impact of SLR and variation of storm scale at Bona beach.....	212
Figure 184. Modeled cross-shore variations in current speed under the impact of SLR and variation of storm scale at Ceinturon beach.....	212
Figure 185. Modeled cross-shore variations in sediment transport rates under the impact of SLR and variation of wind direction at Bona beach.	213
Figure 186. Modeled cross-shore variations in sediment transport rates under the impact of SLR and variation of wind direction at Ceinturon beach.	214
Figure 187. Modeled cross-shore variations in sediment transport rates under the impact of SLR and variation of storm scale at Bona beach.....	214
Figure 188. Modeled cross-shore variations in sediment transport rates under the impact of SLR and variation of storm scale at Ceinturon beach.....	215
Figure 189. Beach profile evolution at the central Ceinturon beach under the impact of SLR and variation of wind direction.....	215
Figure 190. Beach profile evolution at Bona beach under the impact of SLR and variation of wind direction.....	216
Figure 191. Beach profile evolution at the central Ceinturon beach under the impact of SLR and variation of storm scale.	216
Figure 192. Beach profile evolution at Bona beach under the impact of SLR and variation of storm scale.....	217
Figure 193. Three basic types of nourishment profiles (Dean, 1991).	220
Figure 194. The typical design profile of Ceinturon beach.....	221
Figure 195. The typical design profile of Bona beach.....	221
Figure 196. Rectangular beach fill (t=0).....	224
Figure 197. The relationship between the wave height and the half-life of beach nourishment in Ceinturon.	226

Figure 198. The relationship between the wave height and the half-life of beach nourishment in Bona.....	226
Figure 199. Modeled cross-shore variations in wave heights under the impact of beach nourishment and changes of wind direction at Ceinturon beach.....	227
Figure 200. Modeled cross-shore variations in wave heights under the impact of beach nourishment and seasonal changes at Ceinturon beach.	228
Figure 201. Modeled cross-shore variations in wave heights under the impact of beach nourishment and change of storm scale at Ceinturon beach.....	228
Figure 202. Modeled cross-shore variations in current speed under the impact of beach nourishment and changes of wind direction at Ceinturon beach.....	229
Figure 203. Modeled cross-shore variations in current speed under the impact of beach nourishment and seasonal changes at Ceinturon beach.	229
Figure 204. Modeled cross-shore variations in current speed under the impact of beach nourishment and changes of storm scale at Ceinturon beach.....	230
Figure 205. Modeled cross-shore variations in sediment transport rates under the impact of beach nourishment and changes of wind direction at Ceinturon beach.....	231
Figure 206. Modeled cross-shore variations in sediment transport rates under the impact of beach nourishment and seasonal changes at Ceinturon beach.	231
Figure 207. Modeled cross-shore variations in sediment transport rates under the impact of beach nourishment and changes of storm scale at Ceinturon beach.	232
Figure 208. Beach profile evolution at the central Ceinturon beach under the impact of beach nourishment and changes of wind direction.	232
Figure 209. Beach profile evolution at Ceinturon beach under the impact of beach nourishment and seasonal changes.....	233
Figure 210. Beach profile evolution at the central Ceinturon beach under the impact of beach nourishment and changes of storm scale.....	233
Figure 211. Modeled cross-shore variations in wave heights under the impact of beach nourishment and changes of wind direction at Bona beach.....	235
Figure 212. Modeled cross-shore variations in wave heights under the impact of beach nourishment and seasonal changes at Bona beach.	235
Figure 213. Modeled cross-shore variations in wave heights under the impact of beach nourishment and changes of storm scale at Bona beach.	236
Figure 214. Modeled cross-shore variations in current speed under the impact of beach nourishment and changes of wind direction at Bona beach.....	237
Figure 215. Modeled cross-shore variations in current speed under the impact of beach nourishment and seasonal changes at Bona beach.	237

Figure 216. Modeled cross-shore variations in current speed under the impact of beach nourishment and changes of storm scale at Bona beach.	238
Figure 217. Modeled cross-shore variations in sediment transport rates under the impact of beach nourishment and changes of wind direction at Bona beach.....	238
Figure 218. Modeled cross-shore variations in sediment transport rates under the impact of beach nourishment and seasonal changes at Bona beach.	239
Figure 219. Modeled cross-shore variations in sediment transport rates under the impact of beach nourishment and changes of storm scale at Bona beach.	240
Figure 220. Beach profile evolution at Bona beach under the impact of beach nourishment and changes of wind direction.	240
Figure 221. Beach profile evolution at Bona beach under the impact of beach nourishment and seasonal changes.....	241
Figure 222. Beach profile evolution at Bona beach under the impact of beach nourishment and changes of storm scale.	241
Figure 223. The main dimensions of SBW.	249
Figure 224. Relation between H_b and d_b of annual condition in Ceinturon beach.	251
Figure 225. Relation between H_b and d_b of annual condition in Bona beach.	252
Figure 226. Relation between H_b and d_b of annual condition in Pesquiers beach.	253
Figure 227. Key beach and breakwater parameters in the Silvester et al. (1997) method.	256
Figure 228. Wave transmission design curves (Tanaka, 1976).....	258
Figure 229. Design curve of stability number (N_s) and depth ratio for the submerged reefs (Gadre et al., 1992).....	259
Figure 230. The arrangement of the SBWs for Ceinturon and Bona beaches.	260
Figure 231. Prediction of salient amplitude in Ceinturon beach.....	261
Figure 232. Prediction of salient length in Ceinturon beach.	262
Figure 233. Prediction of salient amplitude in Bona beach.	262
Figure 234. Prediction of salient length in Bona beach.	263
Figure 235. The location of observation points.	264
Figure 236. Significant wave height distribution induced by annual winds in Ceinturon beach.....	267
Figure 237. Significant wave height distribution induced by seasonal variation in Ceinturon beach.	268
Figure 238. Significant wave height distribution induced by storms in Ceinturon beach.	270

Figure 239. Significant wave height distribution induced by annual winds in Bona beach.	273
Figure 240. Significant wave height distribution induced by seasonal variation in Bona beach.	274
Figure 241. Significant wave height distribution induced by storms in Bona beach.	275
Figure 242. Current velocity distribution induced by annual winds in Ceinturon beach.	277
Figure 243. Current velocity distribution induced by seasonal variation in Ceinturon beach.	278
Figure 244. Current velocity distribution induced by storms in Ceinturon beach.	279
Figure 245. Current velocity distribution induced by annual winds in Bona beach.	283
Figure 246. Current velocity distribution induced by seasonal variation in Bona beach.	285
Figure 247. Current velocity distribution induced by storms in Bona beach.	286
Figure 248. Location of cross-shore beach profiles.	293
Figure 249. Bed level change of Ceinturon beach induced by annual winds.	294
Figure 250. Cross-shore changes of beach profile 2 due to different wind directions.	295
Figure 251. Cross-shore changes of beach profile 3 due to different wind directions.	295
Figure 252. Bed level change of Ceinturon beach induced by seasonal variation.	296
Figure 253. Cross-shore changes of beach profile 2 due to seasonal variation.	297
Figure 254. Cross-shore changes of beach profile 3 due to seasonal variation.	297
Figure 255. Bed level change of Ceinturon beach induced by storms.	299
Figure 256. Cross-shore changes of beach profile 2 due to different storms.	301
Figure 257. Cross-shore changes of beach profile 3 due to different storms.	301
Figure 258. Bed level change of Bona beach induced by annual winds.	302
Figure 259. Cross-shore changes of beach profile 10 due to different wind directions.	303
Figure 260. Cross-shore changes of beach profile 11 due to different wind directions.	303
Figure 261. Bed level change of Bona beach induced by seasonal variation.	304
Figure 262. Cross-shore changes of beach profile 10 due to seasonal variation.	305
Figure 263. Cross-shore changes of beach profile 11 due to seasonal variation.	305
Figure 264. Bed level change of Bona beach induced by storms.	306
Figure 265. Cross-shore changes of beach profile 10 due to different storms.	307
Figure 266. Cross-shore changes of beach profile 11 due to different storms.	307
Figure 267. Bathymetry and cross section profiles along Ceinturon beach.	309
Figure 268. Bathymetry and cross section profiles along Bona beach.	310

Figure 269. Comparison of OBS and SIM shorelines of Ceinturon beach for the period from November 2007 to November 2008.....	311
Figure 270. Comparison of OBS and SIM shorelines of Bona beach for the period from November 2007 to November 2008.....	311
Figure 271. The Ceinturon shoreline changes before and after the construction of SBWs in the winter.....	313
Figure 272. The Ceinturon shoreline changes before and after the construction of SBWs in the summer.	314
Figure 273. The Ceinturon shoreline changes before and after the construction of SBWs in the decadal storm.	315
Figure 274. The Ceinturon shoreline changes before and after the construction of SBWs in the tri-decadal storm.....	316
Figure 275. The Ceinturon shoreline changes before and after the construction of SBWs in the semi-centennial storm.	317
Figure 276. The Ceinturon shoreline changes before and after the construction of SBWs in the centennial storm.....	318
Figure 277. The Bona shoreline changes before and after the construction of SBWs in the winter.	320
Figure 278. The Bona shoreline changes before and after the construction of SBWs in the summer.....	320
Figure 279. The Bona shoreline changes before and after the construction of SBWs in the decadal storm.....	321
Figure 280. The Bona shoreline changes before and after the construction of SBWs in the tri-decadal storm.	322
Figure 281. The Bona shoreline changes before and after the construction of SBWs in the semi-centennial storm.....	323
Figure 282. The Bona shoreline changes before and after the construction of SBWs in the centennial storm.	324

LIST OF TABLES

Table 1. Statistical results of monthly sea level changes in Port Ferreol station.....	10
Table 2. Statistical results of monthly sea level changes in Toulon station.....	10
Table 3. Characteristics of storm wave at Porquerolles Island in the period of 1999-2015.....	12
Table 4. The strongest wave measured during rough seas at Toulon in the period of 1992-1999.....	12
Table 5. Total storm surges observed at the port of Toulon from 1982 to 2015.....	13
Table 6. Total storm surges observed at the port of Toulon from 1982 to 2015 (continued).....	14
Table 7. Estimated sea levels in the study area.....	14
Table 8. The distance and origin of fetches in the study area.....	24
Table 9. The statistical characteristics of offshore waves in Porquerolles from 1992 to 2015.....	25
Table 10. The general statistical characteristics of seasonal offshore waves in Porquerolles over the period 1992-2015.....	26
Table 11. Return periods of significant wave heights (CEREMA, 2014).....	28
Table 12. Return periods of maximum significant wave height $H_{1/3max}$	28
Table 13. Estimated extreme wave heights in the study area.....	28
Table 14. The general statistical characteristics of winds at B.A.N. Hyères station for the period 1999-2015.....	33
Table 15. Frequency (in %) of wind at B.A.N. Hyères station for the period 1999-2015 classified by Beaufort scale.....	34
Table 16. The general statistical characteristics of seasonal winds at B.A.N. Hyères station for the period 1999-2015.....	35
Table 17. The general statistical characteristics of winds at Le Levant station for the period 2000-2015.....	36
Table 18. Frequency (in %) of wind at Le Levant station for the period 2000-2015 classified by Beaufort scale.....	37
Table 19. The general statistical characteristics of seasonal winds at Le Levant station for the period 2000-2015.....	37
Table 20. The dimensional characteristics of Posidonia seagrass (Paquier, 2009).....	46
Table 21. Nourishment Chronology in the eastern Giens tombolo (OCEANIDE, 2010)....	56
Table 22. Wentworth grain size scale.....	76
Table 23. Porosity of natural sand beds (Soulsby, 1997).....	77

Table 24. List of satellite imagery used for the study.....	87
Table 25. Estimated errors for each shoreline data source.	91
Table 26. Statistical summary of shoreline change rate for the eastern Giens tombolo over a period of 1973-2015.....	102
Table 27. Statistical summary of shoreline change rate for the eastern Giens tombolo over a period of 2015-2050.....	106
Table 28. Beach-face slope and sediment characteristics in Hyères bay (Capanni, 2011; Courtaud, 2000; E.O.L, 2010).	108
Table 29. Comparison of R-square among EBP functions at beaches along the eastern Giens tombolo.	109
Table 30. Comparison of RMSE among EBP functions at beaches along the eastern Giens tombolo.....	110
Table 31. The best-fit parameters of EBPs function for beaches along the Eastern tombolo.....	134
Table 32. A summary of study scenarios in no SLR conditions.	138
Table 33. A summary of study scenarios in SLR conditions.....	139
Table 34. Qualification of error ranges (Van-Rijn et al., 2003).....	141
Table 35. Statistical results of regional model comparison between the OBS and SIM waves at Almanarre beach in 2000.....	148
Table 36. Statistical results of regional model comparison between the OBS and SIM waves at Almanarre beach in 2000 (continued).	149
Table 37. Statistical results of regional model comparison between the OBS and SIM waves at Almanarre beach in 2000 (continued).	150
Table 38. Statistical results of regional model comparison between the OBS and SIM waves at Almanarre beach in 2000 (finished).	151
Table 39. Statistical results of local model comparison between the OBS and SIM waves at La Capte beach in 2009.....	154
Table 40. Parameters for the regional MIKE 21 HD model.	155
Table 41. Calibration of current speed for regional scale (from 9 th to 11 st , November, 2000).	156
Table 42. Parameters for the regional MIKE 21 SW model.....	158
Table 43. Calibration of wave height for regional scale (from 31 st October to 12 nd November, 2000).....	159
Table 44. Validation of wave height and current speed for regional scale (from 24 th to 29 th March, 2009).	160
Table 45. Parameters for the local MIKE 21/3 Coupled FM model.....	162

Table 46. Calibration of wave height and current speed for local scale (March, April, 2009).	163
Table 47. Effect of wind direction and Posidonia on the hydrodynamics and sediment transport.	180
Table 48. Effect of Posidonia and seasonal change on the hydrodynamics and sediment transport.	185
Table 49. Effect of Posidonia and storm scale on the hydrodynamics and sediment transport.	191
Table 50. Effect of Posidonia on wave field.	194
Table 51. Effect of Posidonia on hydrodynamics and sediment transport.	200
Table 52. Effect of SLR on hydrodynamic fields and sediment transport.	209
Table 53. Average percentage frequency of occurrence of significant wave height-direction offshore Ceinturon beach.....	217
Table 54. Average percentage frequency of occurrence of significant wave height-direction offshore Bona beach.....	218
Table 55. Sediment characteristics of receiving beach.	218
Table 56. The values of berm slopes according to the grain size (U.S.A.C.E, 2012).	219
Table 57. Summary of the results of the fill sand volume.....	222
Table 58. A summary of results of beach nourishment longevity corresponding to wave height and frequency in Ceinturon beach.	225
Table 59. A summary of results of beach nourishment longevity corresponding to wave height and frequency in Bona beach.	225
Table 60. Effect of beach nourishment on hydrodynamic field and sediment transport in Ceinturon.	234
Table 61. Effect of beach nourishment on hydrodynamic field and sediment transport in Bona.	242
Table 62. Alternative Solutions for coastal Erosion Protection (U.S.A.C.E, 2002).	246
Table 63. The calculation of breaking depth and breaking height for annual wave condition (1/1 year) in Ceinturon beach.....	251
Table 64. The calculation of breaking depth and breaking height for annual wave condition (1/1 year) in Bona beach.....	252
Table 65. The calculation of breaking depth and breaking height for annual wave condition (1/1 year) in Pesquiers beach.....	252
Table 66. Summary of breaking conditions.....	253
Table 67. Parameters of designed armour layer.	259
Table 68. Parameters of designed SBWs.	260

Table 69. Dissipation coefficient for SBWs in the winter scenario.....	264
Table 70. Dissipation coefficient for SBWs in the semi-centennial storm scenario.	265
Table 71. Comparison of wave height at representative points under different winds and seasons.....	271
Table 72. Comparison of wave height at representative points under storms.	272
Table 73. Comparison of current speed at representative points under different winds and seasons.	281
Table 74. Comparison of current speed at representative points under storms.....	282
Table 75. Comparison of sediment transport rate at representative points under different winds.....	288
Table 76. Comparison of sediment transport rate at representative points under seasonal changes.....	289
Table 77. Comparison of sediment transport rate at representative points under storms.	291
Table 78. Erosive area of beach profiles in Ceinturon beach with and without SBWs (m ²).	300
Table 79. Erosive area of beach profiles in Bona beach with and without SBWs (m ²). .	308
Table 80. Calibration of the shoreline (November 2007- November 2008).	310
Table 81. The accretion and erosion area in Ceinturon beach for the different scenarios.	314
Table 82. The accretion and erosion area in Bona beach for the different scenarios.....	324

LIST OF MAIN SYMBOLS

Roman symbols

A	A scale parameter depending on sediment characteristics
A_F	The A parameter for fill sands
A_N	The A parameter for native sands
a	The projected Posidonia area per unit volume
B	The leading coefficient defining the offshore water depth, which the Profile reaches asymptotically
B_b	Beach berm height above still-water level
B_c	Breakwater crest width
B_t	Breakwater bottom width
B_o	Distance between two adjacent wave orthogonals in deep water
B_1	Distance between two adjacent wave orthogonals in shallow water
C	Extension factor which relates to the bottom sediment diameter
C_B	Skin friction drag coefficient
C_D	Drag coefficient
C_f	Friction coefficient
C_l	Empirical coefficient
$\overline{C_D}$	Bulk drag coefficient for seagrass
c	Wave phase velocity
c_g	Wave group velocity
D_C	Depth of closure
D_f	Wave energy dissipation due to bottom friction
D_ω	Wave energy dissipation due to wave breaking
D_{50}	Median grain size
D_{50}^F	Median grain size of fill material
D_{50}^N	Median grain size of native material
d	Water depth measured relative to MSL
$d(x)$	EBP function
d_b	Breaking water depth
d_n	The grain diameter for $n\%$ of the grains by mass is finer
d_p	The width of Posidonia leaf
E_d	Digitizing error
E_p	Pixel error
E_r	Rectification error
E_s	Seasonal error

E_{td}	Tidal fluctuation error
F	Freeboard of breakwater measured relative to MSL and crest level
f_c	Friction coefficient for the current
g	The acceleration due to gravity
G	Gap distance between adjacent breakwaters measured as the gap distance between the breakwater crests
H_b	Wave height at breaking
H_c	Wave height at the same location with no breakwater
H_e	Non-breaking significant wave height that is exceeded only 12 hours out of a single year (or the greatest 0.137% waves in a year)
H_i	Height of the incident wave on the seaward side of the structure
H_m	Mean wave height
H_{max}	Limiting wave height
H_{os}	Deep water significant wave height
H_{rms}	Root-mean-square wave height
H_s	Significant wave height
H_t	Height of the transmitted wave on the landward side of the structure
H'_o	Unrefracted wave height in deep water
H_o	Wave height in deep water
H_{os}	Significant wave height in deep water
H_1	Wave height in shallow water
$h_{act}(x)$	Height of the active cross-shore profile
h_c	Height of breakwater from seabed
h_p	Canopy height of seagrass
K_r	Refraction coefficient
K_t	Transmission coefficient
k	Wave number
	Exponential term describing the profile curvature
	Empirical coefficient related to the depth and the closure depth of the horizontal distance to the beach
k_s	Nikuradse roughness height
k_{Δ}	layer coefficient
L_{max}	Limiting wavelength
L_S	Length of the breakwater measured along the breakwater crest
L_o	Wavelength in deep water
L_1	Wavelength in shallow water

$l_{1/2}$	One-half the length of the rectangular project
M	Manning's number
N_s	Stability number
n	Ratio of wave group to phase celerity
n_p	Density of seagrass per unit area
p_{wave}	Hydrostatic pressure component of the wave
Q	Total load of sediment transport
$Q(x)$	Longshore transport of sediment expressed in volumes
$Q_{sou}(x)$	Source/sink term expressed in volume/ Δx
q_b	Bed load transport
q_s	Sediment transport in suspension
q_t	Total sediment transport
S_o	Beach face slope at the shore which varies with grain size and wave conditions
S_r	Specific gravity of the armor unit
S_{xx} and S_{yy}	Normal stresses that include the hydrostatic pressure in the water column
S_{xy} and S_{yx}	Shear stress components of the wave
s	Specific gravity
T	Wave period
	Water temperature
T_e	Associated significant wave period
T_m	Mean wave period
T_o	Mean zero-crossing period
T_p	Peak wave period
t_a	Average thickness of armor stone layer
$t_{50\%}$	Half-life of the specified beach fill
U_a	Annualized error
U_t	Total positional uncertainty
u	Current velocity
u_x and u_y	Water particle velocities in x and y direction
V_c	Current speed
W	Design berm width
W_r	Stable weight of armor unit
w	Fall velocity
w_r	Unit weight of the armor unit

w_w	Unit weight of water
X	Cross-shore distance of the breakwater relative to a characteristic initial shoreline
X_{off}	Distance from the tip of the salient and the breakwater
x_c	Distance from the closure depth to the shoreline
x_{CB}	Cross-shore distance from the shoreline to the offshore end point of beach nourishment
$y_c(x)$	Distance from the baseline to the shoreline
z	Bed level
z_o	Bed roughness length

Greek symbols

α_o	Deep water incidence angle
γ	Breaking index
Δx	Longshore discretization step
Δz	Bed level change
ε	Shoreline diffusivity parameter
η	Surface elevation
θ	Wave direction
θ_c	Critical Shields parameter
κ	Von Karman constant
ν	Fluid kinematic viscosity
ρ_s	Sediment density
ρ	Fluid density
ρ_a	Density of air
σ	Angular frequency
φ	Sorting index
ω_j	Radian frequency

LIST OF MAIN ABBREVIATIONS

ANEMOC	Atlas Numérique d'Etats de mer Océanique et Côtier
BSS	Brier Skill Score
CANDHIS	Centre d'Archivage National de Données de Houle In Situ
CEREMA	Centre d'Etudes et d'expertise sur les Risques, l'Environnement, la Mobilité et l'Aménagement
CETMEF	Centre d'Etudes Techniques Maritimes Et Fluviales
CFSR	Climate Forecast System Reanalysis
CM	Cartes Marine
DGPS	Differential Global Positioning System
DHI	Danish Hydraulic Institute
DREAL	Direction Regionale de l'Environnement de l'Amenagement et du Logement
DSAS	Digital Shoreline Analysis System
DSD	Directional Standard Deviation
EBP	Equilibrium beach profile
ECMWF	European Centre for Medium-Range Weather Forecasts
EDF	Laboratoire National d'Hydraulique et d'Environnement
EGB	European Marine Observation and Data Network Gridded Bathymetry
EMODnet	European Marine Observation and Data Network
EOL	Etude et Observation du Littoral
EPR	End Point Rate
ERAMM	Etude Recherche Aménagement en Milieu Marin
ETM	Enhanced ThematicMapper
FM	Flow Model
GENESIS	GENERALized model for Simulating Shoreline change
GIS	Geographic information system
HD	Hydrodynamics
HWL	High Water Level
IAHR	International Association of Hydraulics Research
IGN	Institut national de l'information géographique et forestière
IPCC	Intergovernmental Panel on Climate Change
JONSWAP	Joint North Sea Wave Project
LAT	Lowest Astronomical Tide
LITPACK	Littoral processes and coastline kinetics

LITTO3D	A precise, continuous land-sea digital elevation model jointly produced by SHOM and IGN
LNHE	Laboratoire National d'Hydraulique et Environnement
LRR	Linear Regression Rate-of-change
MARS3D-MENOR1200	3D hydrodynamic model of North West Mediterranean Sea of PREVIMER with a spatial resolution of 1.2 km
MEDNORD	Wave model of North West Mediterranean Sea of PREVIMER
MLW	Mean Low Water
MLLW	Mean Lower Low Water
MSL	Mean sea level
MSS	Multispectral Scanner
MWD	Mean wave direction
NCEP	National Centers for Environmental Prediction
NGF	Nivellement Général de la France
NOAA	National Oceanic and Atmospheric Administration
NRC	National Research Council
NTF	Nouvelle triangulation de la France
OBS	Observation
OGIMET	a Weather Information Service
OLI	Operational Land Imager
OPHIURE III	Un houlographe-courantographe
P.E.P	Prefabricated Erosion Prevention
PREVIMER	The project is coordinated by Ifremer and SHOM
RMSE	Root Mean Square Error
RTK	Real-Time Kinematic
SBW	Submerged breakwater
SHOM	Service Hydrographique et Océanographique de la Marine
SIM	Simulation
SLR	Sea level rise
ST	Sediment Transport
SW	Spectral Waves
TM	Thematic Mapper
UNIBEST	UNIform BEach Sediment Transport
WW3-MENOR-2MIN	Wave model of North West Mediterranean Sea of PREVIMER with a spatial resolution of 3.7 km

CHAPTER 1. GENERAL INTRODUCTION

1.1. Background

The coastal zone is commonly defined as the interface between land and sea. It is highly dynamic environment with many physical processes, such as tidal inundation, sea level rise and coastal geomorphology (Dewidar, 2011). The horizontal position of the land-water interface, as namely shoreline, is one of the most important linear features on the earth's surface which is also one indicator for coastal process (Winarso et al., 2001). Its shape and position change continuously and extend over time due to both natural factors and human activities. The shoreline change normally induces coastal erosion or accretion, depending on the dominant processes acting on the shoreline. The effects of waves, tides, winds, currents, storms, sea-level change, river discharge, the geomorphological processes such as erosion and accretion are primary natural factors that influence the coast, whereas anthropogenic intervention through construction of artificial structures, mining of beach sand, offshore dredging or building of dams on rivers causes beach erosion. The erosion and accretion processes, especially erosion, greatly affect human life, cultivation and aquaculture, natural resources, and waterway transport activities along the coastal zone.

Coastal areas are very important for human beings since antiquity because of the ease of water-based transportation. Today about 50% of the world's population lives in these areas in which much of this population resides in 13 of the world's 20 largest cities (Vellinga et al., 1989). In addition, anthropogenic activities have also developed along coasts for multiple purposes including fishing, aquaculture, coastal agriculture, forestry, hydro-technical engineering and coastal construction, mining, shipbuilding, oil extraction, transfer and transportation, electric power generation, coastal navigation, seaport operation, naval operations, tourism and recreation. In Provence, southern France, the economic stakes of the coastal fringe are considerable and mainly related to the tourism industry. Indeed, seaside tourism in this area accounts for an annual turnover of 4.6 billion euros, corresponding to a fifth of the total turnover of the French tourism industry. Therefore, the beaches in Provence, particularly in Hyères bay, represent an extremely important economic stake (Brunel et al., 2007).

Along with the rapid increase of population, various developmental projects are made along the coastal areas, placing great pressure on it, leading to various coastal hazards like coastal erosion, seawater intrusion, shoreline change, etc (Sheik et al., 2011). Now, coastal erosion is a global and topical problem; at least 70% of the world's beaches are experiencing coastal erosion (Bird, 2005), whereas all of 23 investigated sandy beaches in Provence underwent erosion between 1896 to 1998 (Brunel et al., 2007). The shoreline along the eastern Giens tombolo located on the western coast of Hyères bay,

has suffered both accretion and erosion processes due to natural causes such as waves, winds and storms, or even due to human interference (Figure 1). Several authors have studied the sedimentology as well as the shoreline evolution of the eastern Giens tombolo. Based on the study on the coastal and submarine sedimentology, Blanc (1958) uncovered that the sediment transport was done mostly under the east wind, from east to west coast and from north to south along the eastern tombolo. Jeudy De Grissac (1975) presented the research about dynamic sedimentology of Giens and Hyères bay. Through the in-situ granulometric experiments as well as the analysis of wind and wave fields, he established the map of current. In the bay of Hyères, the waves and swells induce the longshore current first directed from east to west and from north to south. This drift and notable fluvial Gapeau formed the eastern tombolo of Giens. In addition, from the visual comparison of aerial photographs from 1955 to 1972, he highlighted that the eastern branch was threatened in some places and more particularly between the mouth of Gapeau and La Capte (Figure 1). This erosive phenomenon was resulted in the implementation of transverse structures (port, jetty, groynes) stopping the longshore drifts from east to west and from north to south. GEOMER (1996) conducted a diachronic study of the shoreline by photo-interpretation at the right of Les Cabanes du Gapeau for the period of 1954-1993 and also noted an almost continuous decline of the shoreline from the mouth of Gapeau river to approximately 800m south with the average erosion rate of -1.5 m/year, especially a remarkable decline of -40 m between 1969 and 1975. Capanni (2011) investigated the shoreline evolution of the eastern Giens tombolo with the aid of aerial photographs and some field surveys, using digital processing of imageries. During the period from 1972 to 2003, the southern part of Gapeau river mouth, Ceinturon beach and Pesquiers beach experienced the retreat with an average erosion rate of -0.68 m/year, -0.35 m/year, and -0.1 m/year, respectively; whereas the remainders along the eastern tombolo were accreted with an average advance rate of +0.26 m/year. In the near future, the coastal erosion in these areas can be intensified more seriously by sea level rise due to the global warming and the regression of *Posidonia* seagrass meadow.

In order to mitigate or prevent coastal erosion along the coast of the eastern Giens tombolo, various coastal structures have been implemented to protect sandy beaches and stabilize the shoreline. In 1960, two groynes were first installed at Pesquiers and Hyères beaches. From 1978 to 1982, four groynes with the total length of 4x50 m were constructed to protect the northern Ceinturon beach. Moreover, armor stone revetments were installed in the central Ceinturon beach, the southern parts of Hyères port and Gapeau river mouth (1995), whilst seawalls were established along La Capte beach (2008) and Pesquiers beach. Recently, two submerged geotube breakwaters were implemented at La Capte beach in March 2008. Some of these coastal protection methods described can solve local erosion in some cases, but may also trigger some

undesirable effects as well as disadvantages (Kliucininkaite et al., 2011). Especially, the shore-normal structures, viz. groynes and jetties, not only cause the deficit of sediment and erosion in the downstream of these structures (Capanni, 2011), but also interfere with visual beach amenity and aesthetics which are essential for maintaining the tourist value of many beaches (Ranasinghe et al., 2006). OCEANIDE (2010) conducted the study for the protection of the beaches from port of La Capte to Port de L'Aiguade in the eastern branch of Giens tombolo. They utilized the package of TELEMAC to simulate the current, wave, and sediment transport with the different scenarios for all the study area and then proposed the protection structures such as the submerged geotube breakwater, groynes, and revetments for each detail beach. The preliminary dimensions and position of these structures were also determined specifically. Nevertheless, the effect of these structures in the proximity of the study area as well as in future was not still analyzed and considered in their work.

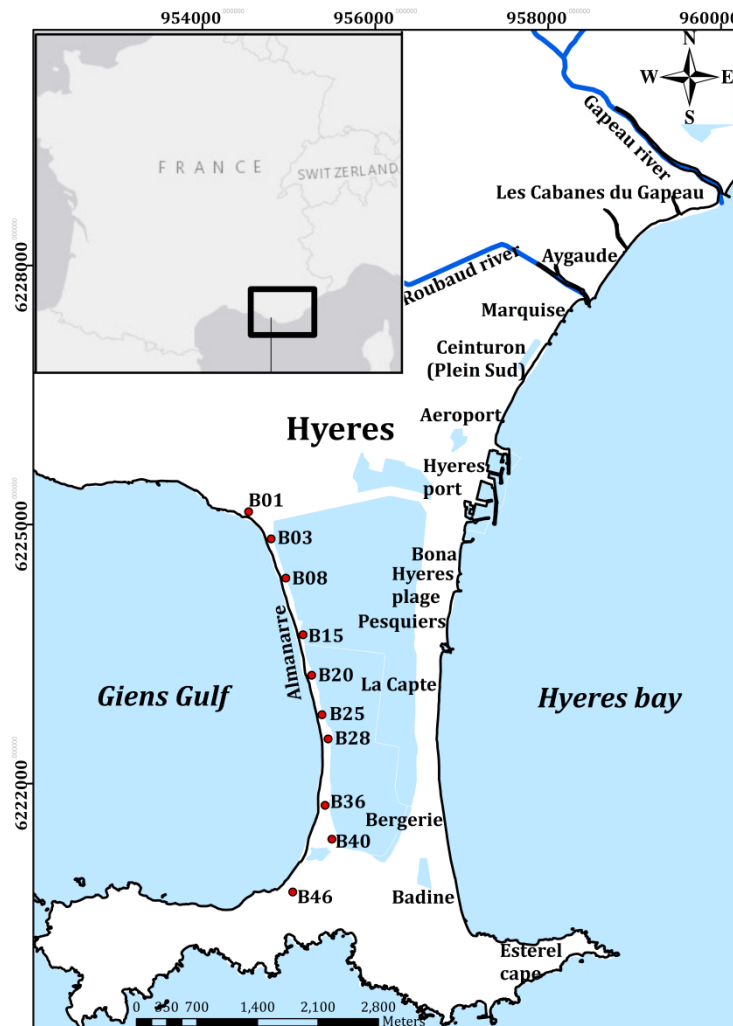


Figure 1. General location of Giens double tombolo.

Therefore, the comprehensive understanding of the hydrodynamic and sediment transport pattern in the area under the impact of different scenarios including the effects of Posidonia and sea level rise is essentially necessary for protection and maintenance of sandy beaches along the eastern Giens tombolo.

1.2. Research objectives

The main aim of this thesis is (1) to investigate the changes in coastal hydrodynamic and sediment transport conditions induced by seasonal variation, extreme events, Posidonia seagrass, the existing coastal structures, beach nourishment and sea level rise, (2) to design the most suitable coastal engineering alternatives for the eastern Giens tombolo, and particularly for the central Ceinturon and Bona beaches, to protect these beaches from losing sand during stormy periods in the winter, and (3) to estimate the effects of these alternatives on shoreline evolution. The provision of coastal protection during the summer along with tourism amenity enhancement is other important objectives, which have to be obtained. DHI's MIKE 21 and LITPACK numerical models are employed in order to achieve these above-mentioned objectives. Additionally, the historical and future medium-term shoreline evolution along the eastern Giens tombolo is also evaluated and predicted by using the combination of remote sensing, GIS techniques coupled with DSAS along with linear regression method.

1.3. Thesis structure

The thesis is composed of seven main chapters. The first chapter gives the general introduction on the coastal problems. The second chapter synthesizes an overview of the study area, viz. hydraulic and meteorological conditions, bathymetry, marine biocenosis, and concludes key factors affecting the morphological evolution. The third chapter describes briefly the theories of hydrodynamics and sediment transport applied in the numerical simulation and introduces the research methodology. The historical shoreline changes and predicted future shorelines as well as beach profile evolution along the eastern Giens tombolo are discussed in the fourth chapter. The fifth presents the model setups and results for the simulations carried out for the natural conditions without the implementation of structures. This chapter is divided into two main parts, viz. Calibration runs and Main runs. In the calibrations, the regional model was run for the time period of one month from 31st October to 30th November 2000, and the local model was run for the period of one month from 12th March to 12th April 2009. Then, the model results are compared with field measurements at that time to obtain the best-fit hydrodynamic parameter set. In the main runs, the study area is simulated with the different scenarios to arrive at an understanding of the hydrodynamic and sediment transport conditions present on the eastern Giens tombolo of the Hyères bay. Before conducting both the calibration and main runs, a sensitivity analysis is carried out to determine the most suitable meshes for the regional and local models. The sixth chapter presents the design of the most suitable coastal structures for Ceinturon, Bona, and Pesquiers beaches and their effects on hydrodynamics, sediment transport and shoreline change along the eastern Giens tombolo. Finally, the seventh chapter concludes the report with brief interpretation of the results and includes open questions for future research. The literature list is presented in the end of the report.

CHAPTER 2. STUDY AREA AND THE DRIVING FACTORS

2.1. Site description

The double tombolo of Giens is located in the town of Hyères, South East of France (Figure 2) at the coordinates: 6°05'28" to 6°10'23" East longitude and 43°01'34" to 43°04'55" North latitude. It lies on the French Mediterranean coast, between the Gulf of Giens and Hyères bay. It consists of two parts: the western branch (Almanarre beach) and the eastern branch. These parts are distinctly separated by the salt pond of Pesquiers. The eastern part of Giens tombolo with the width of about 250 m extends over more than ten kilometers from the mouth of Gapeau in the north to la Badine beach in the south. On the other hand, the Almanarre beach with the width of approximately 30 m spans nearly 4 km, along the Salt Road, and consists of sand and small gravel.

The double tombolo of Giens is a unique and rare geomorphological formation in the world, which links Giens Island to the continent. It results from the combination of several factors, but was mainly formed due to the wave diffraction and refraction by the islands. Waves approach the flanks of Giens Island at different angles of incidence and are then slowed by the shallow water surrounding it (Blanc, 1958). These waves bend around the island to the opposite side as they approach. The wave pattern created by this water movement causes a convergence of longshore drift on the opposite of the island. The sediments from Gapeau and Pansard - Maravenne rivers that are moving by lateral transport on the lee side of the island will accumulate there. Moreover, the presence of *Posidonia* seagrass also facilitates the deposition of sediment. Nowadays, this tombolo has been the subject of some previous studies, presents a lot of challenges for policy makers because it is extremely fragile to the action of storm waves from the Mediterranean Sea, and has suffered from coastal erosion, especially Ceinturon, Bona and Pesquiers beaches in the eastern Giens tombolo.

The wind data of Hyères and Levant station are used in this work because their wind data are measured in the continuous and longer duration as well as are the closest stations to the site (Figure 2). The tidal data recorded at Toulon tide gauge and at Port Ferreol were used to estimate the tidal range, surge elevations and sea level rise. The off-shore wave data is measured and recorded by the buoys 08301 and 08302 located about 1.8 km south of Porquerolles island at 90 m depth (Figure 2), whereas the near-shore wave data comes from the in-situ measurements carried out at La Capte beach by Meulé (2010) and at Almanarre beach in 2000. The more important fluvial sediment supplies in Hyères bay come from Gapeau river 6 km north and Pansard-Maravenne river 11 km north-east. The discharge data of Gapeau river is recorded by Sainte Eulalie station which is located about 6 km from the river mouth in Hyères bay. All input data is acquired, preprocessed and presented more details in Annexes.

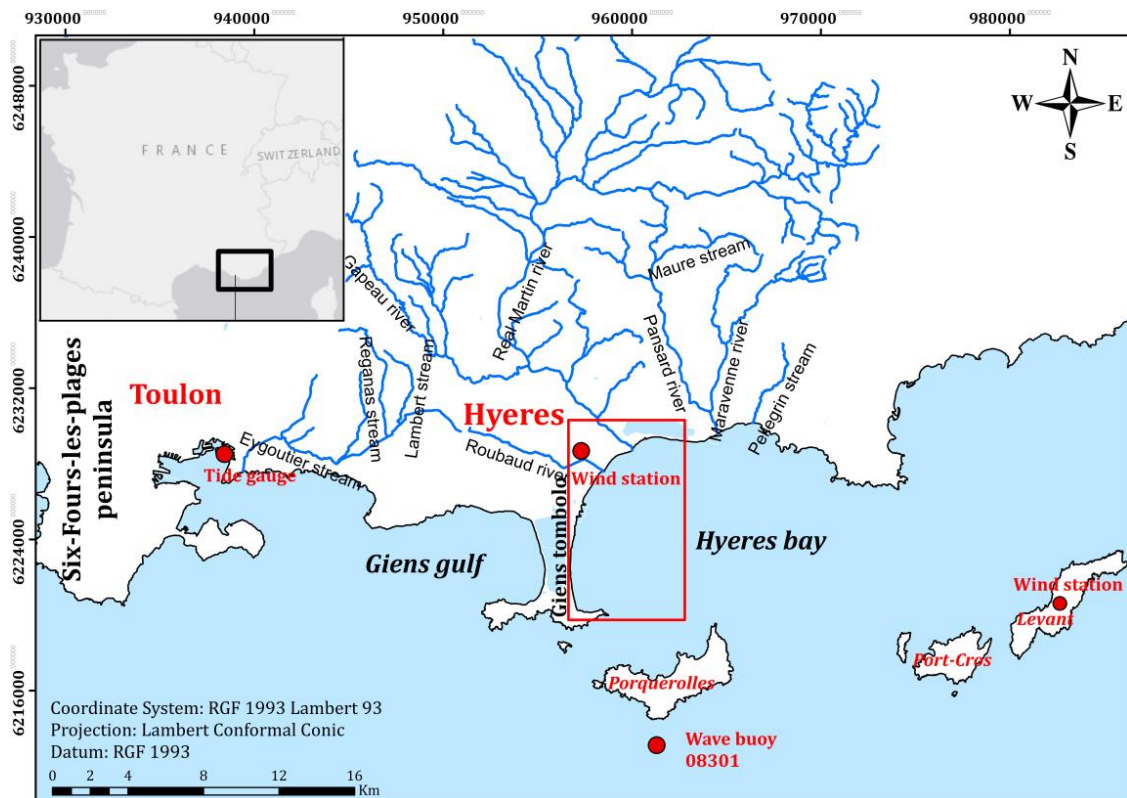


Figure 2. The study area and marine meteorological stations.

2.2. Typical characteristics of the study area

2.2.1. Bathymetry

In this study, the bathymetric data of the offshore area obtained from EGB and Litto3D, whereas the nearshore bathymetric data of the study area was measured from 1999 to 2010 by E.O.L. More details regarding bathymetry sources can found in Appendix A. The bathymetry of the study area is depicted in Figure 3.

From the mouth of Gapeau to Ayguade beach, the submarine beach retains a concave profile. In the shallow area, there is a very light deposit of sediment. The cross-shore slope of beach remains about 4.5% over the first 35 meters and then reduced to a value of 1.6% from the depth of 50 meters to the upper limit of the Posidonia meadows. Specifically at Gapeau, the shape of beach profile still maintains the slightly downward concave, although it was eroded comparing with the data of 2002. The highest erosive area appears at the depth of 2 to 3 m and distance of about 150m from the shoreline. In contrast, the accretive area occurs in Ayguade beach profile from the shoreline to the depth of 2 m. The overall profile has the upward concave shape with many low bars and troughs at the depth of 4.5 m and far from the coast about 250 m.

In La Marquise beach, the profile over time changes not too much with a little erosion between -1 m and -2.5 m in the distance between 50 m and 150 m from the shoreline. The general slope remains approximately 1.7% in range of 200 m wide from the shoreline. Subsequently, some low bars and troughs appear continuously at the depth of 3.5 m. The Posidonia seagrass is situated about 180 m from the shore, at a depth of -4 m.

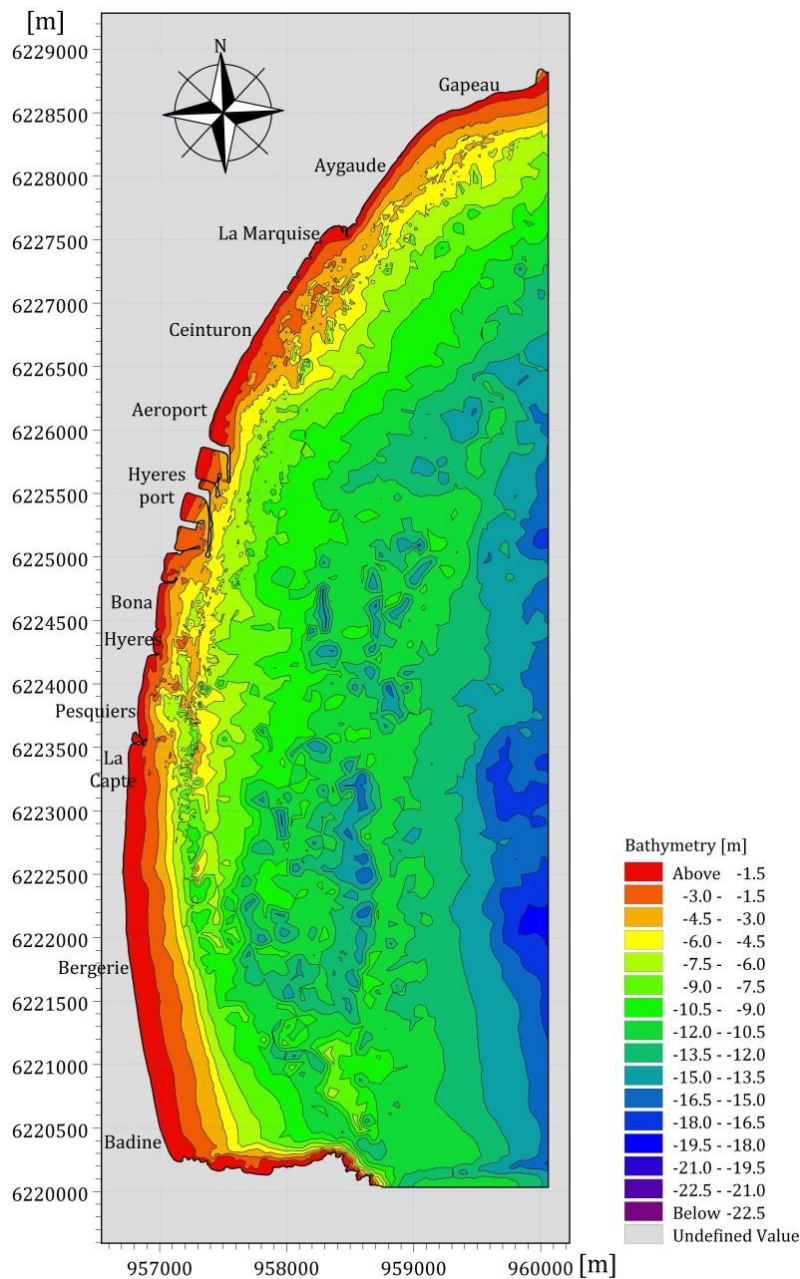


Figure 3. The bathymetry in nearshore of the eastern Giens tombolo in 2010.

The erosive phenomenon starts occurring in the central Ceinturon beach (Figure 3). The erosional hot spot happens in a distance of about 100 m from the shoreline to the depth of 3 m. Nevertheless, by performing the regular nourishment on Marquise beach and between the groynes, this part seems to be in balance after 2010. In the offshore direction, the bathymetry changes suddenly with many troughs and bars from the depth of 3 m, but the overall profile has the upward concave shape.

The Aéroport beach is in regular erosion, more or less compensated by artificial nourishments conducted annually. Additionally, the contribution of rocks to build the road has had a detrimental effect on the accelerating erosion of beach (OCEANIDE, 2010). The slope of the submarine beach is about 2.7% to the upper limit of Posidonia seagrass. Also in this beach profile, the 2m deep trough has been easily observed in the distance of about 120 m from the shoreline.

From Bona beach to Hyères beach, along the first 35 meters, the slope remains steep and reached 4.5%. In Pesquiers beach, the *Posidonia* seagrass appears in the very shallow area of the submarine beach (about -2.5 m deep). There is an active depositional band is about 60 m wide. The slope of beach remains 4.7% from the shore to the upper limit of *Posidonia* seagrass. According to the bathymetric data obtained from EOL measurement campaigns in period of 2001-2010, the submarine beach slope is 4.5% in the south and 2.5% in the north of Hyères beach. This beach seems to be stable. However, this stability can come from frequent nourishments made upstream on Bona beach and transported by the North-South longshore drift (E.O.L, 2010).

Regarding Pesquiers beach, a slight deposition is observed in 100 m of nearshore because the northern breakwater of La Capte marina hindered the sediment transport carried by the longshore drift and trapped sediment. The report of OCEANIDE (2010) indicates that the bathymetric profiles change little on that area and maintain the stable trend in the sea bottom. The foreshore area, about in the distance of 50 m from the shoreline, is quite steep. In the offshore direction, the seabed is rugged with deep troughs and high bars.

In accordance with the report of E.O.L (2010), La Capte beach profile shows the organization of the first *Posidonia* mattes located at a depth of -4.5 m around 250 m from the shore. The average slope of beach reduces to 1.7% if comparing with Pesquiers beach. Before 2008, this area was subject to the alarming erosion. However, with the implementation of geo-tube SBW, this phenomenon was stopped almost completely and this beach has been accreted gradually (Lacroix et al., 2015).

In Bergerie beach, there is an active sedimentological band exceeding 500 m wide in the offshore direction. The first slope until 250 m from the shoreline (about 1% up to the limit of 300 m) increases to reach the seagrass bed (almost 3%) at 7 m deep. Finally, at La Badine beach, the width of the active sedimentological band is up to 500 m with an upper limit of *Posidonia* seagrass situated to -7 m deep. The slope is always lower than 1% in a distance of 500 m from the shore (E.O.L, 2010).

2.2.2. Water level and tides

In the study area, the water level and tide data are incomplete and discontinuous. Therefore, the author uses various sources such as the measurement data (mainly acquired from Toulon and Port Ferreol station) and the simulation data (extracted from the coastal hydrodynamic model of PREVIMER_F2-MARS3D-MENOR1200) to obtain the water level. Then these data were solved as presented in Appendix B.

The tide patterns belong to an irregular semidiurnal tide along the coast of Var. The study area is a microtidal environment; the sea level fluctuations due to the astronomical tide is usually of around 20 cm and seldom exceeding 30 cm (SOGREAH, 1988a). However, the variations of sea level related to those pressures and wind are

greater than those of the astronomical tide. In case of storm surges, they often reach from +30 cm to +40 cm above NGF corresponding from +55.3 cm to +65.3 cm above CM. On the coast, storm surges are even more important because the raising of the MSL due to waves is approximately +0.5 m above NGF. The MSL is estimated in the same report to +1.5 m above NGF in Hyères bay during strongest stormy events.

From the recorded data at Toulon station in the period from 26th June 1981 to 27th October 2015, the daily sea level oscillates between -28 and +74 cm above NGF. On the other hand, the daily sea level at Port Ferreol ranges from -25 cm to +104 m above NGF in the period from 29th March 2012 to 31st October 2015. In addition, the sea level data at Toulon and Port Ferreol is also compared in the period of 2012-2015 as shown in Figure 4. The result of this comparison reveals that sea level in Port Ferreol is normally higher than that in Toulon with an average differential value of 6 cm. This difference may be comes from the astronomical tide. Moreover, Port Ferreol is in an exposed area to wave action, whilst Toulon station is located in the quite enclosure bay. Therefore, sea level fluctuation in Port Ferreol is strongly affected by both the astronomical tide, the sudden changes of atmospheric pressure and wind as well as wave set-up.

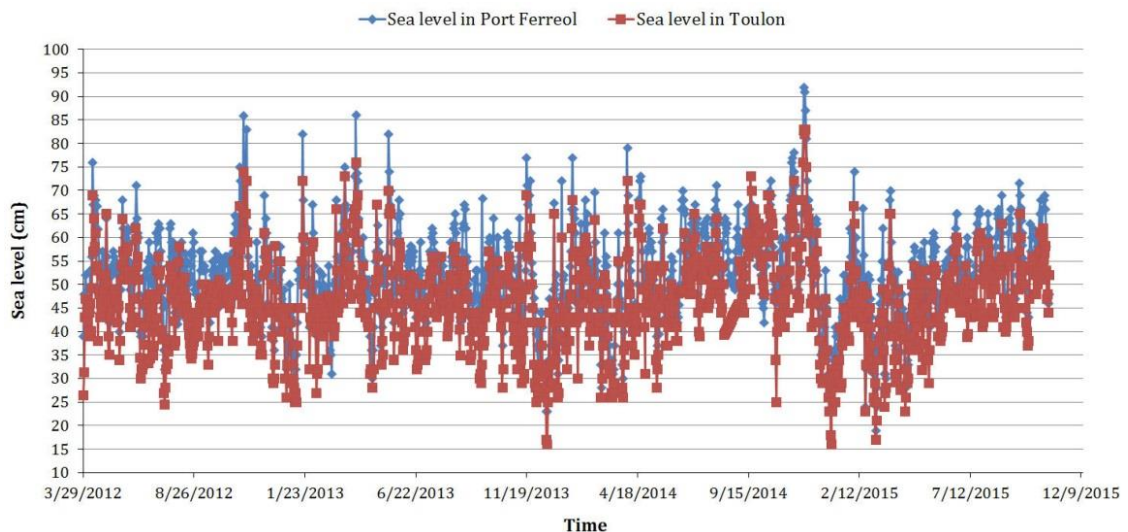


Figure 4. Comparison of daily sea levels between Toulon and Port Ferreol from 29th March 2012 to 27th October 2015.

The monthly change of sea levels is analyzed by means of statistical calculations on the recorded data in Toulon and Port Ferreol station. The results of this analysis are presented in Table 1, Table 2, Figure 5, and Figure 6. Figure 5 and Figure 6 illustrate that the highest sea levels are reached in January, February, March, October, November and December. In these months, the common decrease in atmospheric pressure causes positive tidal fluctuations. Thus, this results in the sea level rise. Furthermore, this is also the time when the storms appear with the greatest frequency in the year. In contrast, the sea levels tend to decline slightly in the period from April to August. In this time, the sea state is calmer than others. Indeed, it results in a decrease in the value of sea level. In addition, the lowest sea levels are observed in February at both Toulon and Port Ferreol.

Table 1. Statistical results of monthly sea level changes in Port Ferreol station.

	Sea level	Month											
		1	2	3	4	5	6	7	8	9	10	11	12
P%	≤0.3	3.46	4.66	5.78	5.59	7.65	7.98	7.06	4.92	4.87	2.98	2.19	2.08
	≤0.4	1.76	1.98	1.86	1.83	2.83	2.39	3.38	3.69	2.53	4.03	1.46	1.10
	≤0.5	0.87	0.80	0.90	0.74	0.46	0.45	0.60	0.78	0.57	2.07	0.95	0.25
	≤0.7	0.39	0.18	0.41	0.11	0.05	0.00	0.02	0.01	0.05	0.48	0.63	0.10
	>0.7	0.001	0.003	0.001	0	0	0	0	0	0	0.048	0.007	0.001
Average sea level	≤0.3	20.1	21.2	18.0	19.6	21.6	20.8	22.1	23.8	22.8	25.1	23.1	21.5
	≤0.4	34.6	34.7	34.6	34.5	34.1	34.1	34.5	34.6	34.5	35.0	35.0	34.5
	≤0.5	44.3	44.2	44.7	44.2	43.5	42.9	43.0	43.3	43.8	44.2	44.7	44.4
	≤0.7	55.2	55.9	53.8	55.1	54.6	50.7	51.1	50.8	52.6	55.0	56.1	56.3
	>0.7	72.1	73.5	73.7	72.0	0	0	0	0	0	78.4	75.1	71.2
Maximum sea level	≤0.3	29.7	29.7	29.7	29.7	29.7	29.7	29.7	29.7	29.7	29.7	29.7	29.7
	≤0.4	39.7	39.7	39.7	39.7	39.7	39.7	39.7	39.7	39.7	39.7	39.7	39.7
	≤0.5	49.7	49.7	49.7	49.7	49.7	49.7	49.7	49.7	49.7	49.7	49.7	49.7
	≤0.7	69.7	69.7	69.7	69.7	68.7	50.7	52.7	51.7	63.7	69.7	69.7	69.7
	>0.7	74.7	85.7	77.7	72.7	0	0	0	0	0	103.7	88.7	72.7
Minimum sea level	≤0.3	-5.3	-25.3	-14.3	-4.3	-25.3	-2.3	-2.3	5.7	5.7	6.7	4.7	-4.3
	≤0.4	30.7	30.7	30.7	30.7	30.7	30.7	30.7	30.7	30.7	30.7	30.7	30.7
	≤0.5	40.7	40.7	40.7	40.7	40.7	40.7	40.7	40.7	40.7	40.7	40.7	40.7
	≤0.7	50.7	50.7	50.7	50.7	50.7	50.7	50.7	50.7	50.7	50.7	50.7	50.7
	>0.7	70.7	70.7	70.7	70.7	0	0	0	0	0	70.7	70.7	70.7

Table 2. Statistical results of monthly sea level changes in Toulon station.

	Sea level	Month											
		1	2	3	4	5	6	7	8	9	10	11	12
P%	≤0.3	6.95	7.02	8.23	7.80	8.63	7.41	7.12	5.73	5.91	5.00	5.10	7.25
	≤0.4	1.15	0.82	0.81	0.98	0.75	0.70	0.52	0.73	1.11	2.30	2.14	1.10
	≤0.5	0.33	0.24	0.38	0.20	0.09	0.04	0.01	0.01	0.15	0.76	1.14	0.50
	≤0.7	0.07	0.05	0.02	0.02	0.004	0.001	0	0	0.01	0.15	0.35	0.20
	>0.7	0	0	0	0	0	0	0	0	0	0	0.001	0
Average sea level	≤0.3	13.6	12.3	11.4	15.9	17.1	16.6	17.3	19.2	19.3	21.3	19.4	15.5
	≤0.4	33.7	34.6	35	34.6	34	34	33.3	33.9	33.8	34.9	35.1	34.4
	≤0.5	43.8	44.3	43.7	43.2	43.1	42	41.4	41.3	43.6	43.6	44.2	44.4
	≤0.7	54.2	53.9	52.2	52.7	52	52.1	0	0	53.3	55.9	54.5	55.8
	>0.7	71.9	72.3	0	0	0	0	0	0	0	70.9	71.3	0
Maximum sea level	≤0.3	29.7	29.7	29.7	29.7	29.7	29.7	29.7	29.7	29.7	29.7	29.7	29.7
	≤0.4	39.7	39.7	39.7	39.7	39.7	39.7	39.7	39.7	39.7	39.7	39.7	39.7
	≤0.5	49.7	49.7	49.7	49.7	49.7	49.7	47.7	46.7	49.7	49.7	49.7	49.7
	≤0.7	69.7	69.7	62.7	56.7	55.7	54.7	0	0	59.7	69.7	69.7	68.7
	>0.7	73.7	74.7	0	0	0	0	0	0	0	71.7	73.7	0
Minimum sea level	≤0.3	-25.3	-25.3	-23.3	-17.3	-14.3	-11.3	-10.3	-12.3	-5.3	-8.3	-13.3	-15.3
	≤0.4	30.7	30.7	30.7	30.7	30.7	30.7	30.7	30.7	30.7	30.7	30.7	30.7
	≤0.5	40.7	40.7	40.7	40.7	40.7	40.7	40.7	40.7	40.7	40.7	40.7	40.7
	≤0.7	50.7	50.7	50.7	50.7	50.7	50.7	0	0	50.7	50.7	50.7	50.7
	>0.7	70.7	70.7	0	0	0	0	0	0	0	70.7	70.7	0

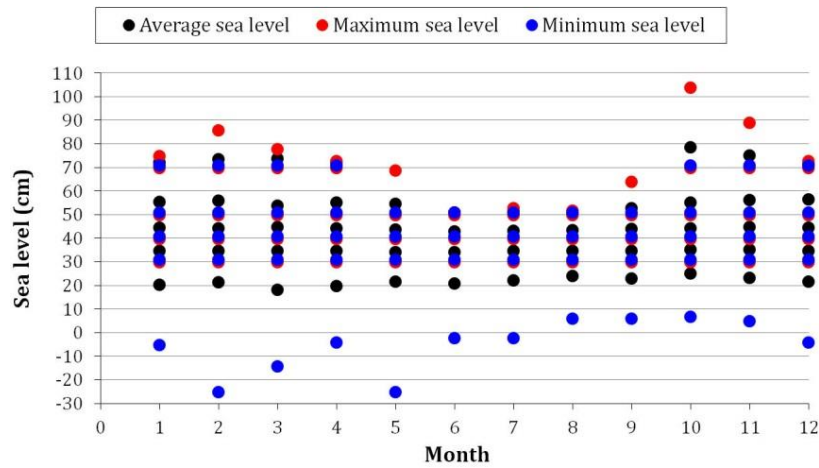


Figure 5. Monthly sea level distribution at Port Ferreol station from 2012 to 2015.

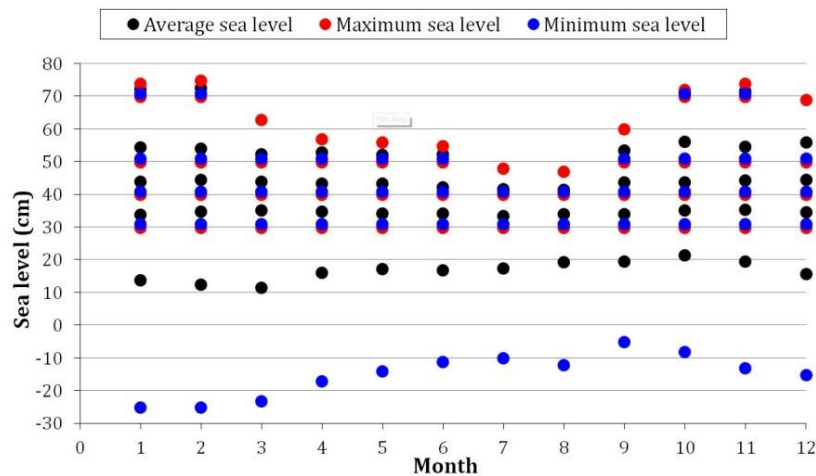


Figure 6. Monthly sea level distribution at Toulon station from 1961 to 2015.

2.2.3. Typhoons and storm surges

Typhoons play an important role in the morphological evolution of Giens tombolo. These infrequent events but high intensity can result in flooding phenomena and according to the sediment redistribution of beaches by erosion and accretion of the shoreline under the sedimentary movements. Moreover, storms cause the rise of sea level or so-called storm surge, the main risk of flooding and coastal erosion.

2.2.3.1. Rough seas and storms

In the Hyères bay, most of storms approached the coast from the east sector. According to Courtaud (2000), in the period from 14th May 1992 to 15th September 1997, there were 79 rough seas and storms observed in the study area. They come from North East (6 events), East (27 events), South East (1 event), South West (29 events), and North West (16 events). Taking into account extreme events, 15 storms cause sea level rise higher than 0.4 m above NGF. Among them, three storms come from North East, 7 events from East, 1 storm from South West and 4 events from North West. In the period from October 1997 to November 1999, no storms appeared in Hyères bay. Nevertheless, according to CEREMA (2014), Giens tombolo suffered 13 storms from December 1999 to March 2015 (Table 3) in which 5 storms occurred in 2007.

Table 3. Characteristics of storm wave at Porquerolles Island in the period of 1999-2015.

No.	Time	$H_{1/3}$ (m)	H_{max} (m)	$T_{h1/3}$ (s)	T_{hmax} (s)	H_{mo} (m)	T_e (s)
1	28 December 1999 at 03:30	5.5	8.9	9.0	10.1	6.3	9.0
2	21 January 2005 at 11:00	5.6	9.0	8.4	8.7	-	-
3	01 February 2005 at 11:30	6.4	10.2	9.9	9.2	6.8	9.2
4	13 February 2005 at 05:00	5.6	8.1	8.1	8.9	-	-
5	24 January 2007 at 00:30	6.8	12.3	9.8	8.8	6.7	9.4
6	13 February 2007 at 00:00	5.9	10.4	9.0	8.4	-	-
7	19 March 2007 at 17:00	5.8	9.2	9.2	10.9	-	-
8	28 May 2007 at 13:00	5.8	8.8	8.3	8.9	-	-
9	10 December 2007 at 04:00	5.5	9.4	7.9	8.8	-	-
10	21 March 2008 at 13:00	5.6	9.8	7.6	7.4	-	-
11	30 October 2008 at 16:30	5.8	8.6	8.5	7.7	-	-
12	26 December 2008 at 10:00	5.6	8.3	9.8	9.7	6.0	9.5
13	05 January 2014 at 08:30	4.4	7.7	8.2	9.0	4.6	8.1

In addition to storm, rough seas usually affect the evolution of Giens tombolo. The data of severe rough seas were recorded at Toulon Lighthouse during the period from 1992 to 1999 (ERAMM, 2001). The characteristics of wave in rough seas are described in Table 4. These data are an interesting information base on the duration of the events and their intensity. It is easily realized that about 8 rough seas has $H_{1/3} \geq 4m$, the peak period of agitation (between 3 and 4m) does not exceed 24 hours.

Table 4. The strongest wave measured during rough seas at Toulon in the period of 1992-1999.

No.	Date	$H_{1/3}(m)$	$H_{1/10}(m)$	$H_{Max}(m)$	$T_{1/3}(s)$	$T_{1/10}(s)$	$T_{pic}(s)$
1	05/12/92	4.03	5.36	6.88	8.4	8.4	10.2
2	28/12/92	4.4	5.36	6.8	8.7	8.8	9.4
3	10/01/95	3.88	4.9	6.62	8.2	8.2	8.8
4	11/01/95	4.02	4.99	6.27	8.7	8.5	9.4
5	11/01/95	4.94	6.27	8.8	9.7	9.7	10.2
6	13/05/95	5.55	7.42	9.79	10.2	10.5	11.1
7	20/11/96	4.09	4.8	6.03	9.4	9.5	10.2
8	09/12/96	4.07	5.18	6.25	8.3	8.5	9.4
9	04/12/98	4.17	5.51	8.07	8.6	8.8	9.4
10	27/01/99	4.01	4.88	6.37	8.6	8.6	9.4
11	28/01/99	4.35	5.48	6.71	8.8	8.7	9.4

2.2.3.2. Storm surges

The storm surge is mainly caused by a drop in barometric pressure associated with the passages of depressions. This sea level rise is independent of the astronomical tide that is very low in this region of Mediterranean (0.3 m amplitude). According to ERAMM (2001), the elevation of the sea level is proportional to the decrease in the atmospheric pressure (1cm for 1hPa); hence, a depression of 990 hPa results in the sea level rise of about 25cm.

Since 1848, many submergence and overtopping events along the sand spit of Giens tombolo were observed under not only the action of rough seas but also because of storm surges, especially in the western part of tombolo. The most memorable event is that the storm surge of 0.7 m was observed in 1958 (ERAMM, 2001). The highest storm surges are usually observed in autumn, in January and spring (April-May). Recently, the measurements of sea level recorded in Toulon since 1982 are shown in Table 5.

Table 5. Total storm surges observed at the port of Toulon from 1982 to 2015.

Year	Number of observation days in year	Day/the maximum is observed	Maximum height ⁴ (cm) (CM)	Height ⁵ above mean sea level (cm) (NGF)
1982	290	12/1	53	7
1984	51	15/11	78	32
1991	65	10/10	79	33
1992	52	17/10	81	35
1993	302	12/10	87	41
1994	319	4/11	78	32
1995	332	25/12	86	40
1996	341	10/1	92	46
1997	360	5/11	91	45
1998	292	4/10	74	28
1999	359	24/10	81	35
2000	366	1/3	94	48
2001	365	1/1	84	38
2002	363	1/1	87	41
2003	365	1/2	84	38
2004	366	2/3	81	35
2005	365	3/8	72	26

⁴ The coasts are reported to the hydrographic zero which is located 0,253 m below the zero of IGN 69 system.

⁵ NGF zero is located at 0,458 m above the hydrographic zero.

Table 6. Total storm surges observed at the port of Toulon from 1982 to 2015 (continued).

Year	Number of observation days in year	Day/the maximum is observed	Maximum height ⁶ (cm) (CM)	Height ⁷ above mean sea level (cm) (NGF)
2006	226	1/3	80	34
2007	352	1/1	90	44
2008	317	1/1	92	46
2009	365	1/1	93	47
2010	363	1/2	100	54
2011	309	1/2	92	46
2012	340	1/1	97	51
2013	350	1/3	87	41
2014	336	1/1	99	53
2015	354	2/36	77	31

Based on the observations made in Toulon, an annual storm surge elevation of sea level can be estimated about +30 cm from the NGF zero regardless of the astronomical tide. The combination of the two phenomena generated an annual sea level of +50 cm (ERAMM, 2001). From the characteristics of above-mentioned extreme events as well as the sea level data at Toulon station, some statistical scenarios of sea levels are proposed in Table 7.

Table 7. Estimated sea levels in the study area.

Return period (year)	<1	1	10	30	50	100
Sea level above CM (m)	0.5	0.65	0.95	1.0	1.15	1.5
Sea level with global warming above CM (m)	0.85	1.0	1.3	1.35	1.5	1.85

2.2.4. River flow and sea currents

2.2.4.1. River flow

Hyères bay is different from the Gulf of Giens by the presence of sources providing fluvial sedimentary supply. The two main streams flowing into Hyères bay are Gapeau and Pansard-Maravenne. Less important others are Roubaud river and small streams of Pointe de l'Argentiere - Cape Bénat although they contribute to the local sedimentation of small bays. Their typical Mediterranean flows are characterized by continuous inflows from October to May, followed by long periods of drying up in summer, all interspersed with short and violent floods.

The distribution of river network flows into Hyères bay is described in Figure 7.

⁶ The coasts are reported to the hydrographic zero which is located 0,253 m below the zero of IGN 69 system.

⁷ NGF zero is located at 0,458 m above the hydrographic zero.

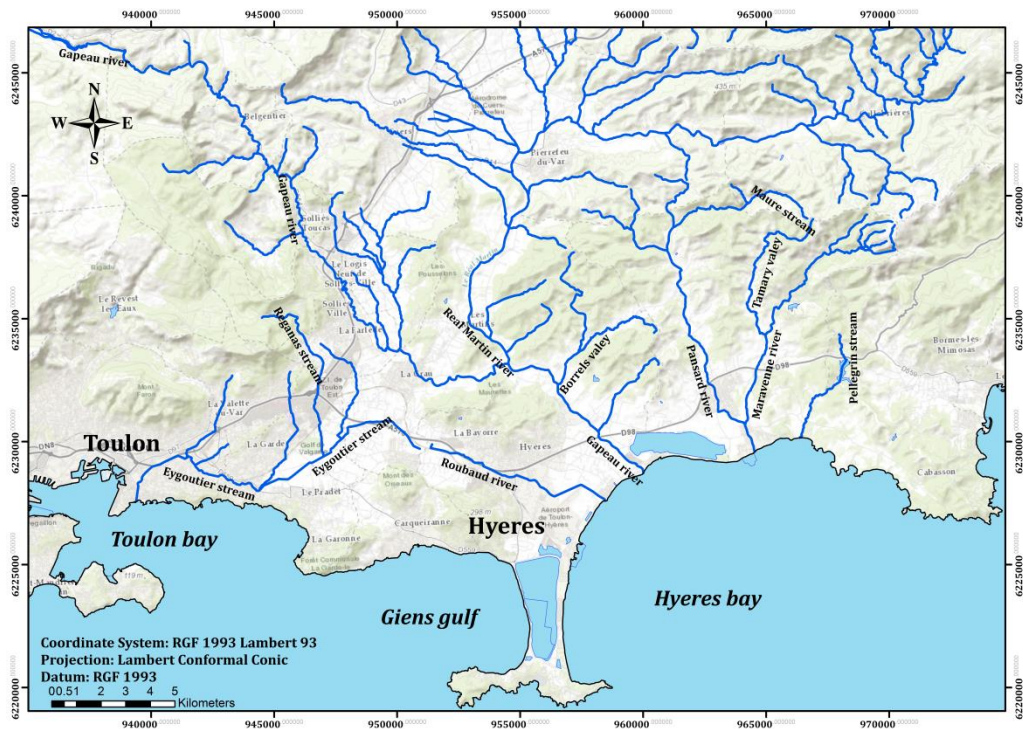


Figure 7. River system in the study area.

a. Gapeau

Total watershed of Gapeau river covers about 563 km² and has two main distinctive areas of near-symmetrical flow is that Gapeau in the west and Réal Martin in the east. Gapeau branch and its small direct tributaries such as Latay contribute a sub-watershed of 203 km², for a linear length of 42 km and an average gradient of 0.7% from the source of Latay to the mouth. On the other hand, the watershed of Réal Martin and its main tributary of Réal Collobrier are more developed to 351 km², for a linear length of 24 km and an average gradient of 0.8% from the source to the confluence with Gapeau branch. The confluence of Gapeau and Réal Martin is recognized below Mont Redon, within 7 km of the mouth (Courtaud, 2000).

The discharge data of Gapeau river is recorded by Sainte Eulalie station which is managed by DREAL. It is located about 6 km from the river mouth in Hyères bay. It was commissioned on 01st January 1961. The average daily discharge data of this station can be downloaded on the website of Banque Hydro (www.hydro.eaufrance.fr). The analysis of long-term hydrological data recorded at Sainte Eulalie station shows that between 1961 and 2014 the annual discharge of Gapeau river is approximately 4 m³/s and the discharge of dry season is about 0.5 m³/s. Furthermore, the discharges of the biannual, decadal, tri-decadal, semi-centennial and centennial floods are forecasted approximately 80 m³/s, 180 m³/s, 220 m³/s, 300 m³/s and 600 m³/s, respectively (Capanni, 2011; Courtaud, 2000). In addition, the monthly variation of flow is strong. The high values of discharge mainly occur in winter and spring and the lower values are observed in summer and autumn, as shown in Figure 8.

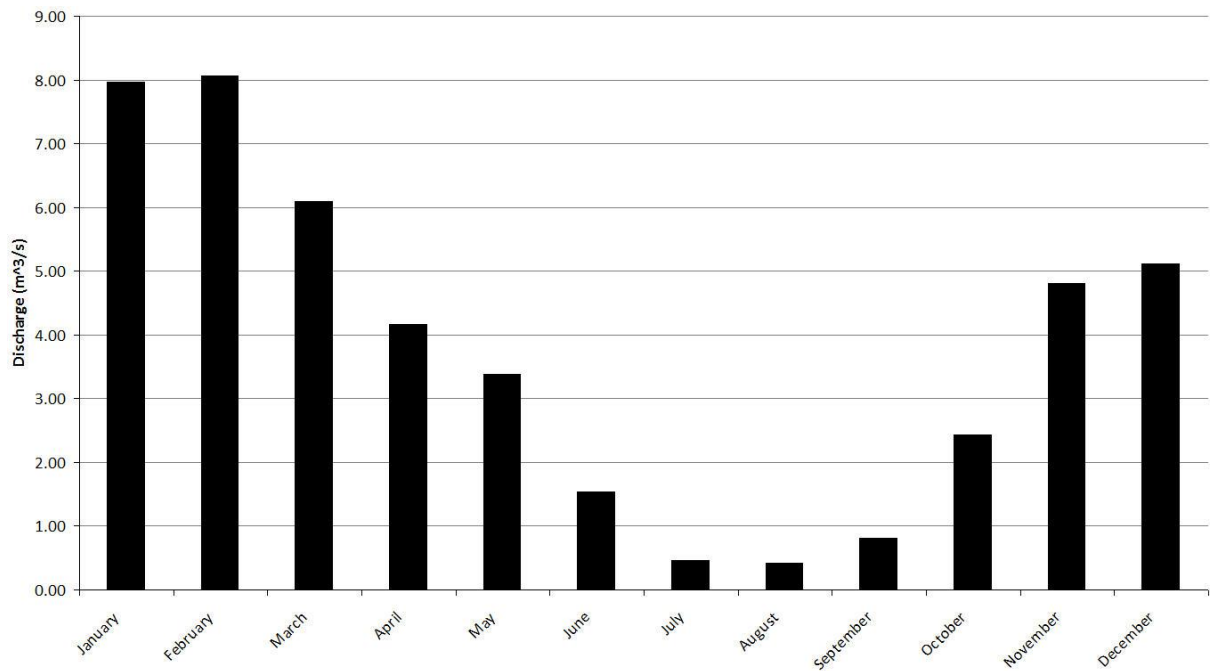


Figure 8. Average monthly discharges over the period from 1961 to 2014. (Source: Banque Hydro)

b. Maravenne-Pansard

There are two main areas of flow, Pansard and Maravenne, virtually parallel (north-south) to the confluence; from there, the river inclines from north-north-west/south-south-east to the mouth. The Pansard and Maravenne supply a watershed of 78 km². In addition, Pansard and Maravenne have a length of 14 km and 12.7 km with an average gradient of 2% and 3%, respectively. From the confluence to the mouth, the river of Pansard-Maravenne is fully calibrated and trained by the inland ports along the left bank.

The annual volumetric flow rate of Pansard - Maravenne river is estimated less than 1 m³/s. Furthermore, the decennial rate and centennial rate of this river is forecasted approximately 110 m³/s and 242 m³/s, respectively (Courtaud, 2000).

c. Roubaud

Roubaud determines a small watershed of 27 km² with 8.3 km in length. It is parallel with the downstream portion of Gapeau which is separated by the range of Maurettes at the low altitudes between 1 and 40 m within the watershed.

The annual flow rate of Roubaud is insignificant and has never been measured. In her thesis, Courtaud (2000) estimated the decadal flow rate of 28 m³/s and the centennial flow rate of 56 m³/s.

d. Other streams

Other rivers flow into the bay of Hyères between Port de Miramar and Cape Benat where small streams draining an area of approximately 20km² and at Hyères islands (watershed less than 15km²).

2.2.4.2. Sea currents

a. Nearshore currents

The nearshore current data was measured at the SCAPT4 station located 120 m seaward of the La Capte shoreline in the bay of Hyères from 13th March to 22nd April 2009. In addition, the current data was also recorded in Giens gulf at a water depth of 3.5 m, corresponding to 70 m seaward of the Almanarre shoreline in the western branch, during the period from 30th October to 28th November 2000 (Figure 12).

There are two main components of velocities including the cross-shore and longshore (Figure 9a). The cross-shore velocities are positive when they direct shoreward, conversely, they are negative when they move seaward. In general, it is noted that the currents moving towards the coast are faster than those towards the sea but only extend over a short period. Particularly, from 18th to 28th March 2009, the seaward currents are relatively weak, while the shoreward currents become stronger between 1st and 4th April, 2009. The maximum cross-shore current speed is 0.09 m/s shoreward. On the other hand, the longshore velocities are positive if they move southward; or, they are negative if they direct northward. The maximum longshore current speed is 0.14 m/s northward (Meulé, 2010). During the measurement period, both the northern and southern currents are observed mostly, but the northbound currents are still dominant and stronger than those in other directions (Figure 9b).

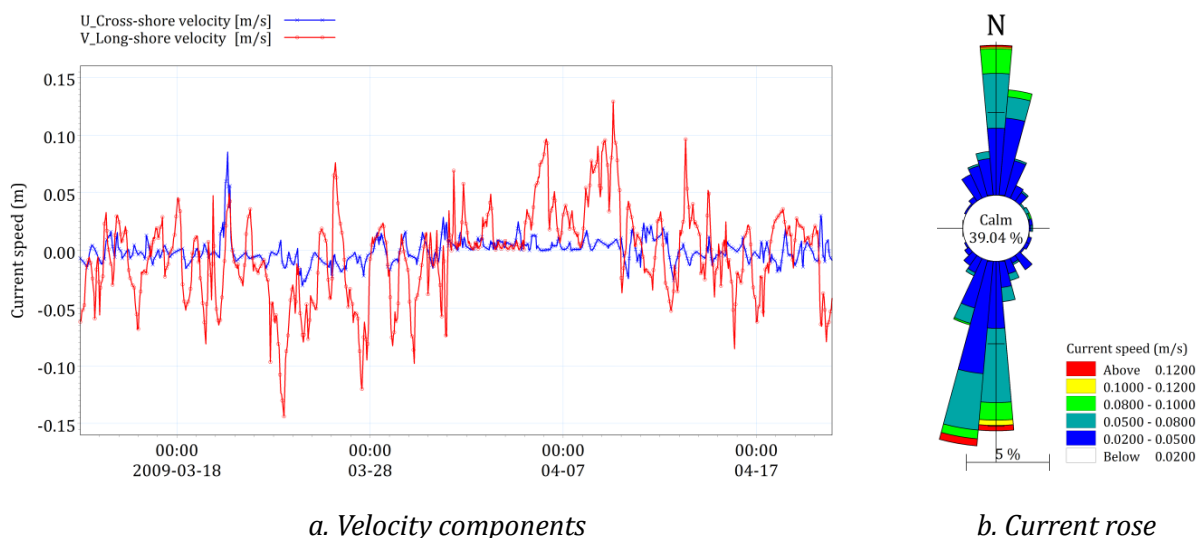


Figure 9. Nearshore current data of SCAPT4 at La Capte beach in 2009.

Regarding the nearshore currents in Giens gulf, the relationship between current speed and direction is plotted in Figure 10a. It is clearly seen that the high current speed occurred from 6th to 7th November with maximum current speed of 0.276 m/s. It was a result of rough sea state at that time. Moreover, the northwest and southeast currents dominate in the measurement period (Figure 10b), but the currents from northwest direction are the strongest. It coincides with the direction of the longshore current drift along the western Giens tombolo, which was investigated by Jeudy De Grissac (1975).

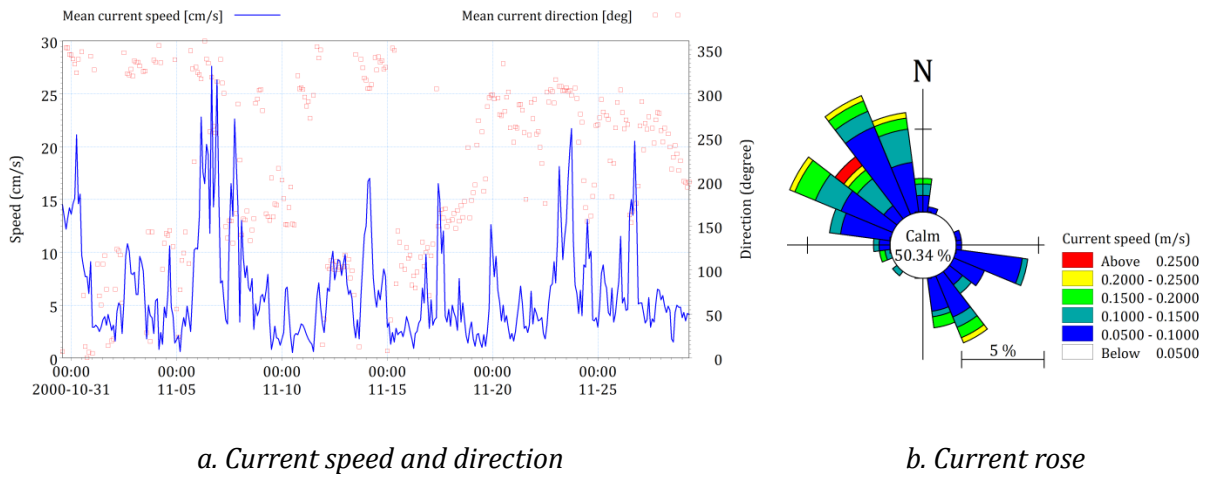


Figure 10. Nearshore current at Almanarre beach in 2000.

b. Offshore currents

By carrying out the in-situ granulometric experiments as well as the analysis of wind and wave fields, Jeudy De Grissac (1975) depicted the map of current around Giens tombolo. Then this map was continuously updated by Courtaud (2000). There are the general (Ligure) currents, the tidal currents, the wind-driven currents and the wave-induced currents, which normally occur along and near the tombolo (Figure 11).

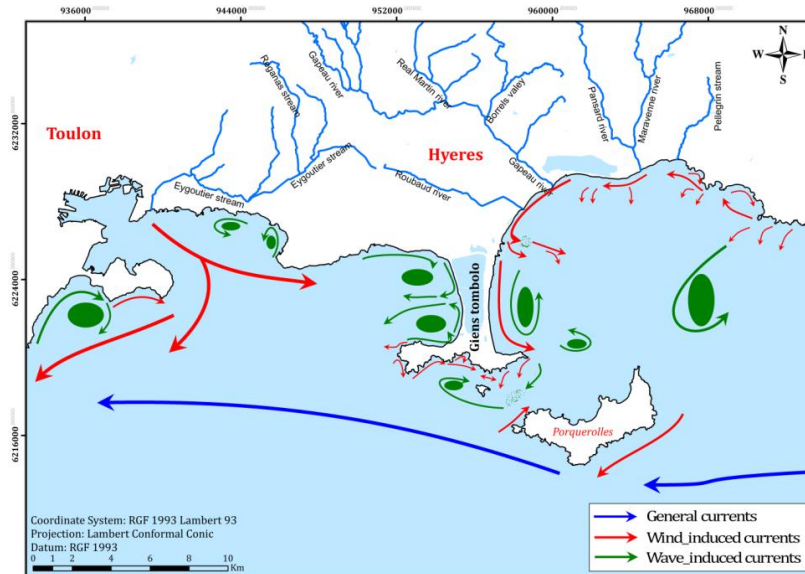


Figure 11. The currents in Hyères bay (Jeudy De Grissac (1975), Courtaud (2000), modified).

General and tidal currents are weak in Hyères bay and are unlikely to participate in sediment transport (Courtaud, 2000; SOGREAH, 1988b). In offshore of Giens peninsula, one general permanent current (blue) flows from East to West with a velocity of about 0.2 to 0.3 m/s in normal operation but can reach 0.5-1 m/s with the East wind. In the Mediterranean, the tidal currents rarely exceed 30 cm/s and are usually less than 10 to 15 cm/s. The wind-induced currents (red) are summarized in Figure 11, taken from the report of SOGREAH (1988b). According to Figure 11, the typical currents are represented by the currents due to the east wind. In the study area, there is a flow directed partly southward and partly seaward. The speed of the surface current is

estimated approximately 2 or 3% of the wind speed (IARE, 1996). During heavy storms, these speeds do not exceed 1 m/s. In the normal conditions, these currents do not exceed 0.3 m/s and are mainly involved in suspended sediment transport.

The wave-induced currents (green) play a key role in sediment transport. The swell creates two types of currents are responsible for the (re) distribution of sediments in the Gulf of Giens and Hyères bay: longshore currents related to the longitudinal component of the swell and rip currents (sagittal current) associated with the component of the swell normal to the coast. The longshore currents are induced by the oblique wave at the coast. Their intensity depends on the height, period and direction of swell and nature, roughness and slope of the seabed (Courtaud, 2000). In the normal sea condition, the longshore currents were measured in the order of 0.4 m/s on average with Southeastern wind and the maximum speed of these currents observed at 0.8 m/s. In the stormy sea condition, the flow velocities can exceed 1.3 m/s (OCEANIDE, 2010). Concerning the rip currents, their characteristics depend on the wave height and wave period that will determine the intensity and frequency of these currents. Their speed can be several tens of cm/s and are involved in the dispersion of material seaward (SOGREAH, 1988b). Blanc (1960) estimated the depth of action of rip currents between 12 and 25 meters in Hyères bay, these actions will begin appearing efficiently than from oscillations with a period greater than 4.5 s.

2.2.5. Waves

The wave data in the study area includes the data for off-shore wave and the data for near-shore wave. The offshore wave data is measured and recorded by the buoys of CANDHIS. Furthermore, it is also extracted from the numerical simulations and wave digital atlas supplied by ANEMOC, PREVIMER, and ECMWF. Near-shore wave data comes from the in-situ measurements Almanarre beach in 2000 and in La Capte beach in 2009 (Figure 12). Further information regarding the wave sources as well as the treatment of wave data can be found in Appendix C.

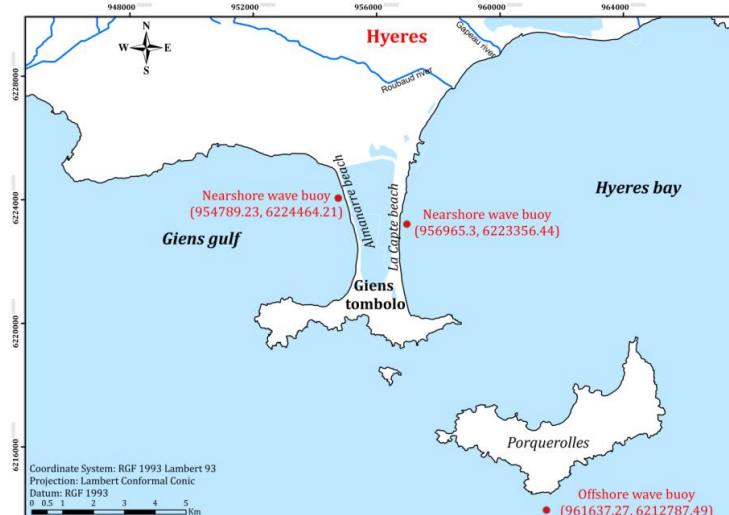


Figure 12. Location of wave buoys in situ.

2.2.5.1. Nearshore wave

From the wave data recorded at Almanarre beach by the wave recorder of OPHIURE III in period from 30th October to 28th November 2000, the rose of nearshore wave is plotted, as shown in Figure 13.

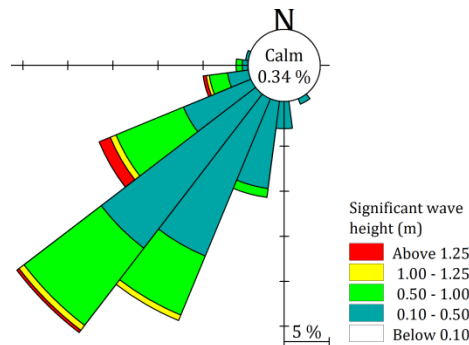


Figure 13. Rose of nearshore wave in November 2000 (OPHIURE III).

In Gulf of Giens, the dominant wave is the direction of 210°-240° (South-South-West to South-West). The significant wave height ($H_{1/3}$) varies between 20 and 80 cm. The maximum measured value during rough sea is $H_{1/3} = 1.4$ m corresponding to the period of 9.5 s.

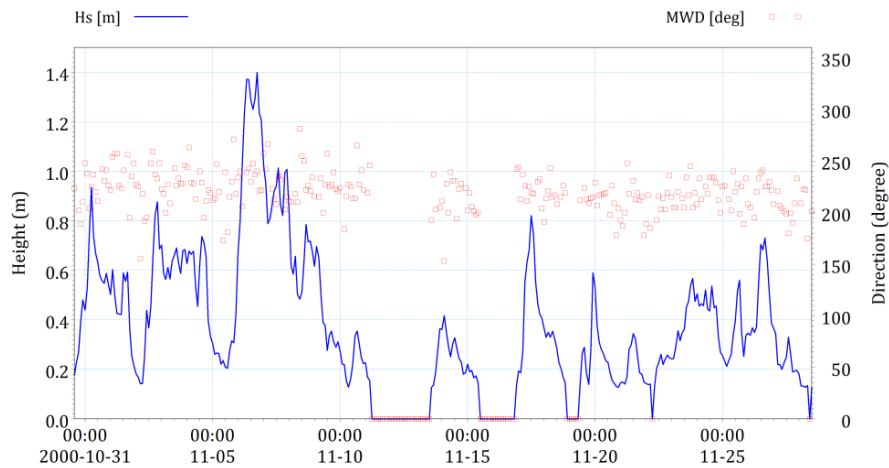


Figure 14. Direction and height of the waves recorded in November 2000.

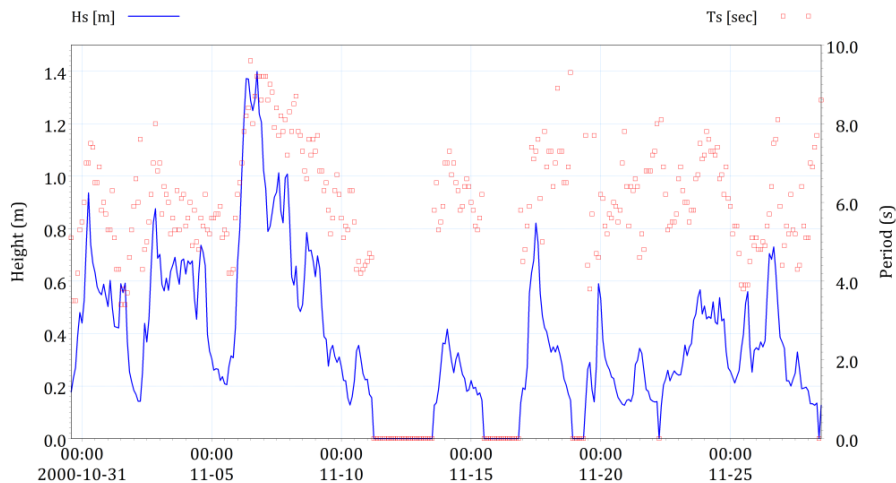


Figure 15. Height and period of waves recorded in November 2000.

During November 2000, the period of the significant wave ($T_{1/3}$) measured at site varies between 4 and 8 seconds with only 2 episodes, corresponding to rough seas (6-7 and 17-19 November) (Figure 14 and Figure 15). At that time, the highest offshore wave height in Porquerolles Island during this event reached 8.0 m with the period of 9.0 s. As a result, the significant wave height near Almanarre was considerably increased in 6 hours from 0.7 m to 1.4 m (12h to 18h) and had stabilized between 1.2 m and 1.4 m for 10 hours. This strengthening of the wave had been accompanied by an increase in the period ($T_{1/3}$). The period varied between 4 and 6 seconds in calm and reached the maximum value of 9.6 s at 12h (Figure 16).

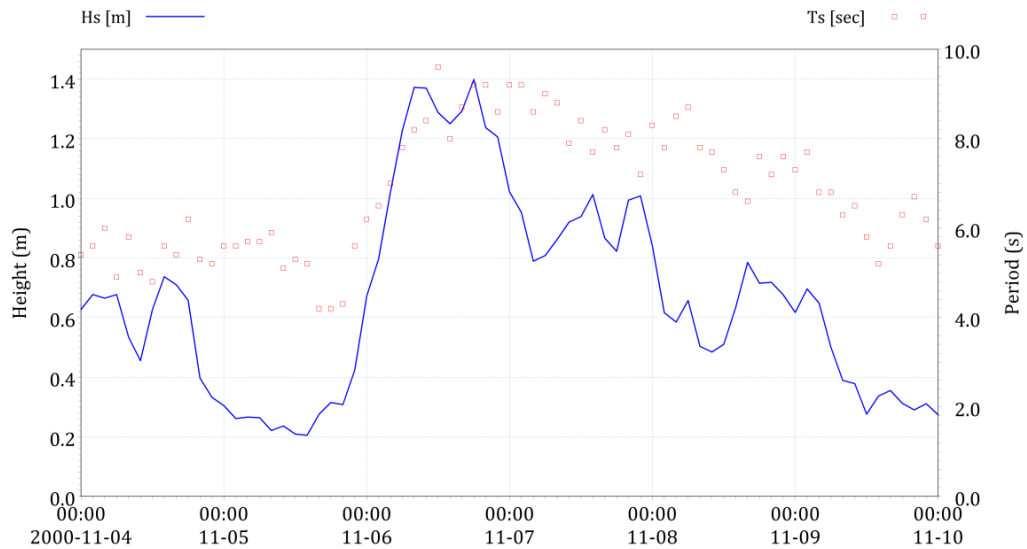


Figure 16. Height and period of waves recorded in the rough sea in November 2000.

With regard to the nearshore wave in La Capte beach, the wave data from the submerged devices was recorded over one month and a half. However, some devices experienced a failure of their batteries, not recording over a very short time (Richard, 2010). Despite this technical problem, some results can be deduced from this measurement campaign.

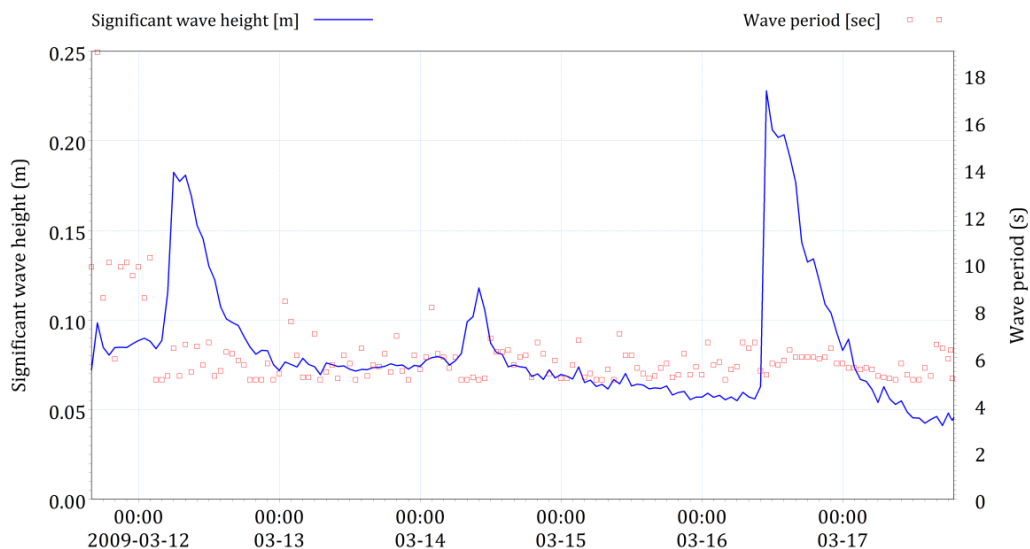


Figure 17. Height and period of waves recorded at SCAPT1 in La Capte in 2009.

Figure 17 shows the height and period of significant wave at SCAPT1 station in the period from 12th to 17th March 2009. The height of significant waves during this period is on average 0.1 m. Nevertheless, there are two peaks on 13th and 17th March in which is larger than 0.2 m. The highest wave height of about 0.23 m corresponding to the wave period of 5.3 s observed at 11h on 16th March. The average of wave period at this station is about 6 s. Moreover, the results of wave data in SCAPT1 reveal the main wave directions from the east to northeast.

At SCAPT2 station, there are also the two peaks of significant wave height corresponding to a period of bad weather when the wind is stronger than normal, as shown in Figure 18. The significant wave height in the period from 12th to 14th March 2009 varies from 0.05 to 0.2 m. The highest wave height in this period is about 0.2 m corresponding to the wave period of 5.6 s. The mean value of wave period reaches approximately 6 s.

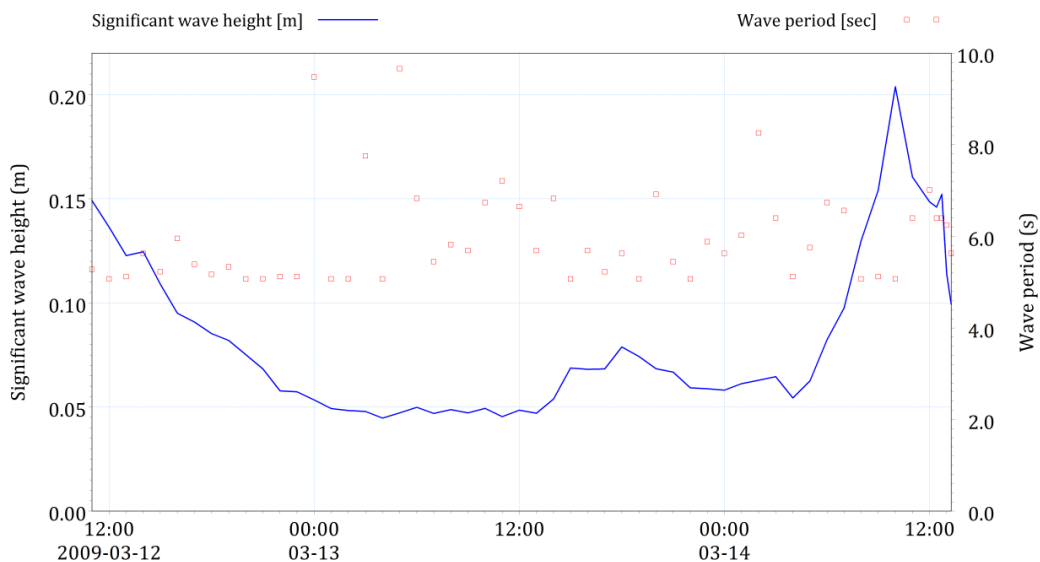


Figure 18. Height and period of waves recorded at SCAPT2 in La Capte in 2009.

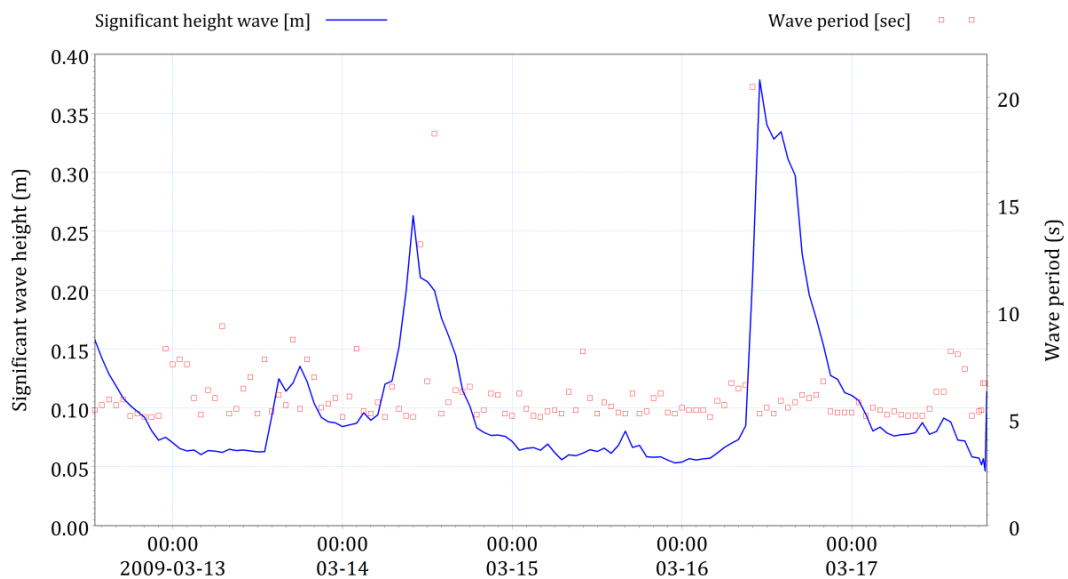


Figure 19. Height and period of waves recorded at SCAPT3 in La Capte in 2009.

Concerning SCAPT3 station, the wave directions are the same as those in SCAPT1 and SCAPT2. Nonetheless, the significant wave heights are respectively averaged about 0.2 m and 0.4 m during the two periods of bad weather (Figure 19). The highest wave height in this measurement period reaches 0.38 m corresponding to the wave period of 5.2 s at 11h on 26th March. There is an asymmetry of waves resulting from the waves which approach the coast. The average wave period at this station is about 6.2 s.

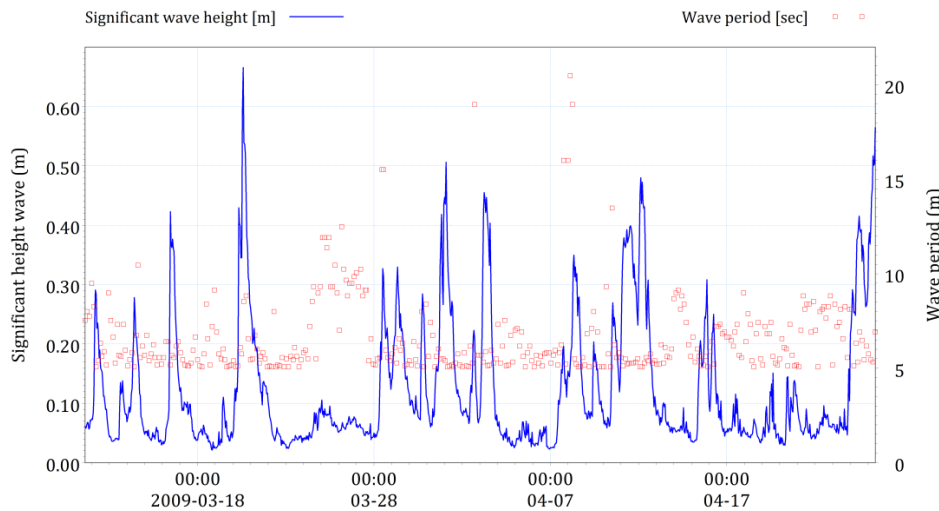


Figure 20. Height and period of waves recorded at SCAPT4 in La Capte in 2009.

The measurement of wave at SCAPT4 station was carried out in the longest period from 13th March to 22nd April. The average significant wave height is about 0.12 m but many variations are observed with the highest wave height of up to 0.67 m. Hence, during this period, the number of waves that exceeds the height threshold of 0.4 m was reached nearly 8 times, as depicted in Figure 20. The wave period at this station varies from 5 to 20 s and averaged about 6.6 s.

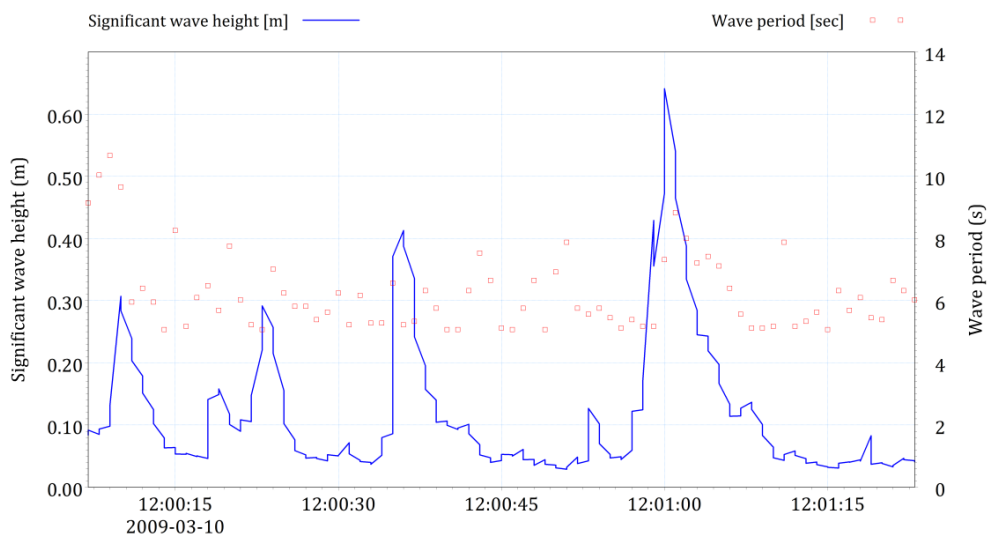


Figure 21. Height and period of waves recorded at SCAPT5 in La Capte in 2009.

Figure 21 shows the height and period of waves recorded at SCAPT5. The wave height reached the highest value of 0.64 m corresponding to the wave period of 8.1 s. The average of wave period in this station is about 6.2 s.

2.2.5.2. Offshore wave

The tombolo of Giens is very sensitive to the wave action. The western part of Giens tombolo usually suffer the attack of offshore waves which have the wave height of over 3 m with a frequency of about three or four times a year, especially in times of equinox (HYDRO-M, 1993). This part is very exposed to southwest waves. On the other hand, the eastern part of Giens tombolo is strongly affected by the southeast and east waves.

The main parameters of offshore waves considered when evaluating their impact on the coastal area are that the fetch, the direction of propagation, the wave height, and the period. The formation of the offshore waves is related to the wind field and intensity of the distance over which the wind blows (fetch) as well as their durations of influence. According to Courtaud (2000), due to the narrow width of Mediterranean Sea, the fetches associated with dominant interesting directions in Giens tombolo are not very important (Table 8).

Table 8. The distance and origin of fetches in the study area.

Direction	Origin	Distance (km)
East	Gulf of Genoa	330
North-East	Gulf of Genoa	330
South-East	Sardaigne	310
South-West	Northeast coast of Spain	350
	Baleares	400
	Gulf of Lion	230
North-West	Rhone valley	100
	Toulon bay	18

From the wave data of Buoy 08301 and 08302 near Porquerolles Island, some statistical analyses are carried out to discover the characteristics of offshore waves. Douglas sea scale is used to classify the wave height. The results are shown in Table 9. Furthermore, the wave roses in the period from 1992 to 2015 are also built, as illustrated in Figure 22.

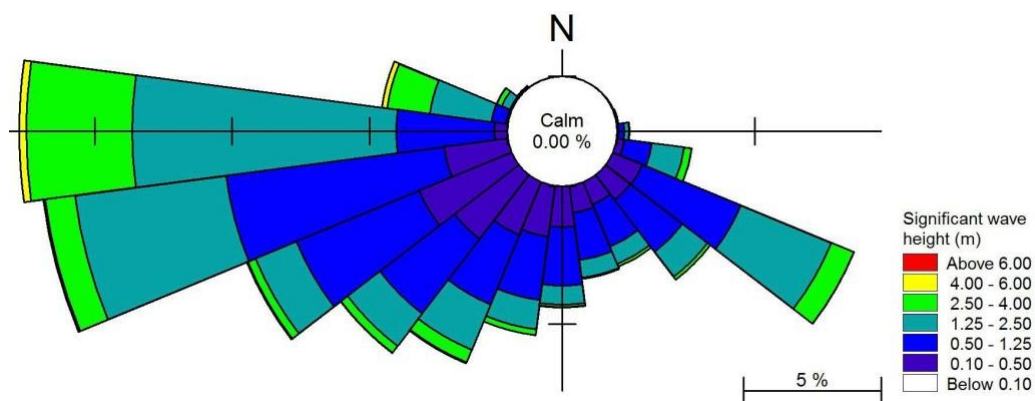


Figure 22. Wave rose in Porquerolles Island from 1992 to 2015.

Table 9. The statistical characteristics of offshore waves in Porquerolles from 1992 to 2015.

Douglas scale	Direction (degree)	N	NE	E	SEE	SE	S	SW	W	NW	N	Total (%)
		≤20	≤70	≤90	≤110	≤160	≤200	≤250	≤290	≤340	≤360	
≤0.10	Hs (m)	0	0	0	0	0	0	0	0	0	0	
	P%	0	0	0	0	0	0	0	0	0	0	0
≤0.50	Hs (m)	0.41	0.45	0.45	0.47	0.46	0.45	0.45	0.47	0.39	0.43	
	P%	0.001	0.03	0.04	0.26	3.52	4.02	9.76	2.42	0.04	0.00	20.08
≤1.25	Hs (m)	0.64	0.89	1.00	1.10	1.09	1.07	1.06	1.14	1.15	0.82	
	P%	0.001	0.01	0.10	0.85	8.45	5.36	12.39	10.96	0.08	0.00	38.20
≤2.50	Hs (m)	0	1.72	1.84	2.14	2.18	2.09	2.15	2.24	2.35	1.57	
	P%	0	0.004	0.03	0.89	5.89	2.08	5.40	16.83	0.54	0.002	31.67
≤4.00	Hs (m)	0	0	0	3.36	3.33	3.35	3.45	3.48	3.43	0	
	P%	0	0	0	0.17	1.22	0.29	1.19	6.23	0.30	0	9.40
≤5.00	Hs (m)	0	0	0	4.17	4.52	4.72	4.66	4.62	4.55	0	
	P%	0	0	0	0.001	0.021	0.009	0.098	0.430	0.02	0	0.57
≤5.34	Hs (m)	0	0	0	0	5.14	5.14	5.24	5.28	5.19	0	
	P%	0	0	0	0	0.001	0.001	0.01	0.03	0	0	0.04
≤6.00	Hs (m)	0	0	0	0	5.69	5.63	5.84	5.87	0	0	
	P%	0	0	0	0	0.001	0.001	0.004	0.02	0	0	0.02
≤6.48	Hs (m)	0	0	0	0	6.02	0	0	6.29	0	0	
	P%	0	0	0	0	0.001	0	0	0.004	0	0	0.005
≤7.03	Hs (m)	0	0	0	0	0	0	0	6.76	0	0	
	P%	0	0	0	0	0	0	0	0.002	0	0	0.002
Total (%)		<i>0.002</i>	<i>0.04</i>	<i>0.17</i>	<i>2.17</i>	<i>19.10</i>	<i>11.76</i>	<i>28.84</i>	<i>36.92</i>	<i>0.99</i>	<i>0.01</i>	<i>100</i>

Table 9 indicates that over 58% of waves have a significant height smaller than 1.25 m and that 10% of waves with H_s exceed 2.5 m. The highest significant wave height is observed up to 6.76 m corresponding to the wave period of 10.2 s and the wave direction of 283.4 degree. Moreover, this table also reveals that the waves come from three main directions. These three main directions also confirm and demonstrate in the wave rose (Figure 22). The most frequent direction is the west waves with about 36.92% of total regime. They are medium energy with heights of 0.5 to 2.5 m occupying up to 75% of cases. Nevertheless, these waves do not affect the study area so much and are quite difficult to penetrate into Hyères bay as well as most of them is reflected or changed the direction by Six-Fours-les-Plages peninsula before approaching Gulf of Giens (Figure 2). The second frequent direction is southwest with frequency of 28.84%. Although these waves generally have low energy with heights from 0.5 to 1.25 m and periods of less than 6 seconds in 77% of cases, they mainly affect the beach evolution in the western tombolo. They are generated by the combination of the north-west and

north-north-west winds (Mistral and Tramontane) (Capanni, 2011). The southeast waves play one important role to the evolution of beach profiles in the eastern part of Giens tombolo. They are less frequent (19.1% of total annual duration). However, they have heights of more than 2 m in 31% of cases, with periods of more than 6 seconds over 25% of cases. They are formed by the onshore winds from the south-south-east to south-east and are accompanied by surges of more than 1 m above MSL.

Table 10. The general statistical characteristics of seasonal offshore waves in Porquerolles over the period 1992-2015.

Direction (°)	Frequency (%)		H _s (m)		MWD (°)		T _p (s)	
	Summer	Winter	Summer	Winter	Summer	Winter	Summer	Winter
N (≤20°)	0.00	0.00	0.00	0.00	0.00	0.00	0.00	0.00
NE (≤70°)	0.05	0.08	0.51	0.57	51.99	55.15	9.09	4.83
E (≤110°)	0.93	2.52	0.70	1.55	98.16	103.96	6.14	6.39
SE (≤160°)	8.33	21.26	0.66	1.39	134.22	127.32	5.62	6.44
S (≤200°)	9.68	10.75	0.54	1.10	183.13	183.42	6.16	6.11
SW (≤250°)	35.91	26.93	0.56	1.29	231.63	225.49	5.51	6.82
W (≤290°)	44.92	36.36	1.41	1.93	263.91	267.10	5.96	7.29
NW (≤340°)	0.17	2.08	1.04	2.37	298.24	298.07	7.24	8.02
N (≤360°)	0.01	0.01	0.95	0.92	350.55	348.48	7.00	4.75

The offshore waves near Porquerolles Island also have a seasonal characteristic. The difference of wave parameters between the summer and winter is described in Table 10. It is noted that the west and southwest waves dominate in both summer and winter with the total frequency of 80.83% and 63.29%, respectively. However, these waves mainly affect the morphological evolution in the western Giens tombolo. For the eastern part, the southeast waves also have the high frequency of 8.33% and 21.26% in the summer and winter. In other words, the southeast waves play a key role in the morphological evolution in the eastern Giens tombolo. Although the east waves have the high significant height of 1.55 m, they only occur with the low frequency of 2.52% in the winter. In the year, the offshore wave climate unevenly divided between a winter gathering the strongest storms with the highest waves larger than 6.5 m, from December to February, and summer, from June to August, during which the heights are 99% below 3 m (Figure 23). March and April recorded a decline in all the wave parameters, due to the conditions of calmer weather. Waves in May experienced a further increase in significant wave height. This feature is to relate with the equinoctial storms of spring.

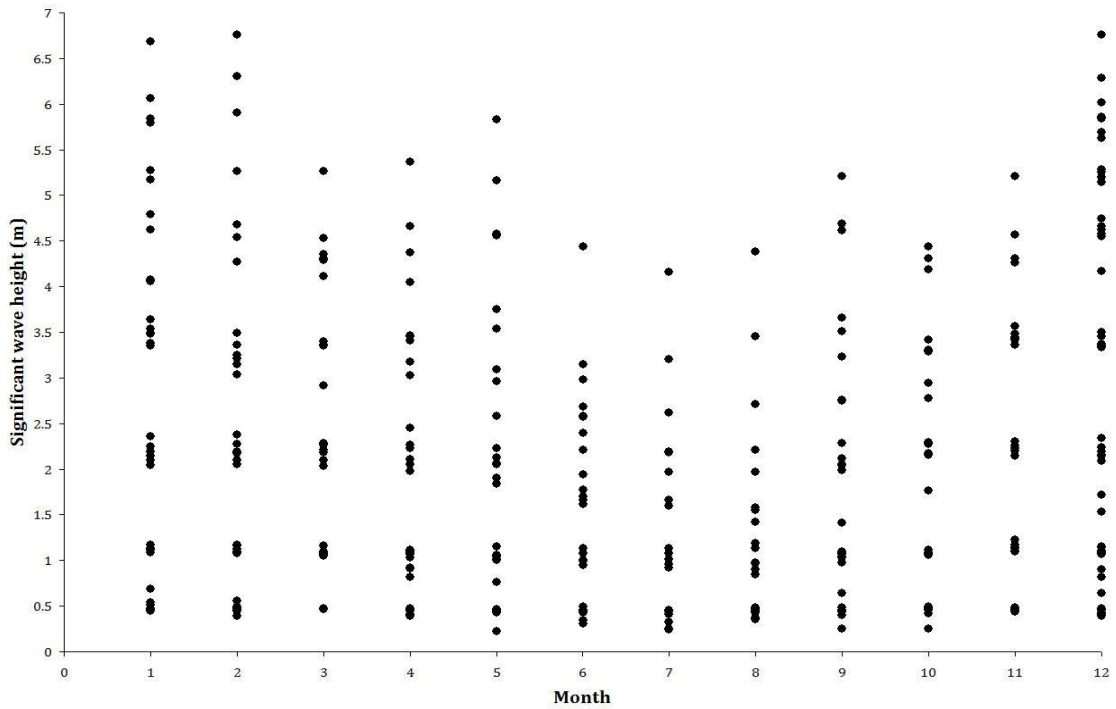


Figure 23. Monthly wave height distribution over 24 years.

The scatter plot of significant wave height for the direction in the period from 1992 to 2015 at Buoy 08301 and 08302 is presented in Figure 24. This scatter plot shows that the higher significant wave heights cover a wider band, but the waves are mostly restricted the southeast and west direction. The highest waves also come from these two directions. This comment is valid for the statistical characteristics in Table 9.

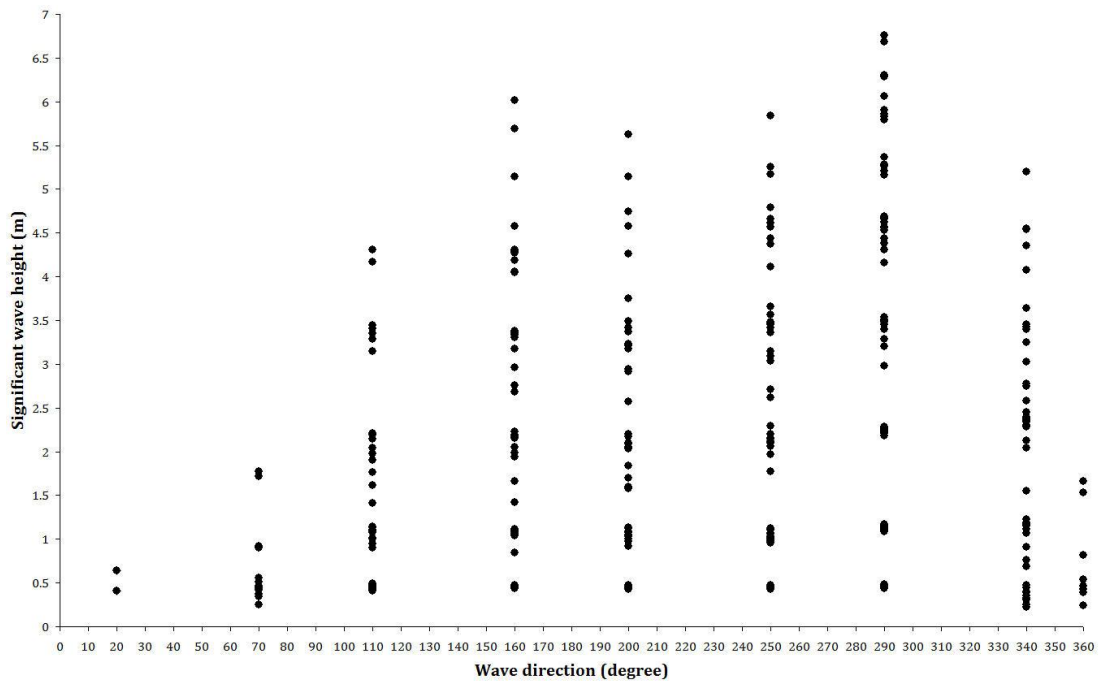


Figure 24. Directional wave height distribution over 24 years.

Also based on the wave data recorded at Buoy 08301 in the period from 1992 to 2015, CEREMA (2014) used the GPD and EXP laws to determine the return period of significant wave heights in the extreme events. The results are exhibited in Table 11.

Table 11. Return periods of significant wave heights (CEREMA, 2014).

Return period (year)	The lower bound of the confidence interval of 70% of H1/3 (m)		Estimation of H1/3 (m)		The upper bound of the confidence interval of 70% of H1/3 (m)	
	GPD	EXP	GPD	EXP	GPD	EXP
1	5.12	5.01	5.27	5.17	5.42	5.33
10	6.12	6.48	6.33	6.78	6.54	7.09
30	6.36	7.17	6.64	7.55	6.93	7.93
50	6.44	7.49	6.76	7.91	7.08	8.32

In addition, ERAMM (2001) relied on the offshore wave measured in Porquerolles Island from 1992 to 1999 as well as the offshore wave recorded from the ships to estimate the return periods of maximum significant wave height, as shown in Table 12.

Table 12. Return periods of maximum significant wave height $H_{1/3max}$.

Return period	Annual (ships)	Annual (measures)	Decadal (ship)	Decadal (measures)
$H_{1/3}$ (m)	3.5	3.3	5.0	4.4

From the characteristics of extreme events as well as the wave data in Table 11 and Table 12, some statistical scenarios of the extreme wave heights used in the present study are proposed in Table 13.

Table 13. Estimated extreme wave heights in the study area.

Return period (year)		<1	1	10	30	50	100
$H_{1/3}$ (m)	lower value	4.4	5.17	6.33	6.64	6.76	6.89
	upper value	5.0	5.27	6.78	7.55	7.91	8.39

2.2.5.3. Wave propagation

The wave determines the general equilibrium profile of the beach, thus it plays an important role in the coastal morphogenesis. Its height affects the depth from which there is no significant change in bottom elevation and no significant net sediment transport between the nearshore and offshore, so-called the depth of closure. Wave energy determines the intensity of the potential energy capable of changing the beach morphology. In theory, the offshore wave is not accompanied by any sediment transport. However, as it propagates towards the coast, the wave undergoes the change of direction, due to the geological structure and bathymetric arrangement, as well as the possible presence of Posidonia seagrass, which play an important role in setting in motion and sediment transport. These combination wave/physical parameters will define the convergence or divergence areas, in which ocean energy will be accentuated or diminished.

When the waves approach the shoreline, they undergo some different types of deformation such as refraction, diffraction, and reflection. Refraction is the bending of waves because of varying water depth underneath. The part of a wave in shallow water moves slower than the part of a wave in deeper water. So when the depth under a wave crest varies along the crest, the wave bends. A consequence of this that the wave crests tend to become aligned with the depth contours. If it is assumed that the energy transmitted between two orthogonal retains a constant value between the offshore and the coast then it is possible to calculate a refraction coefficient (K_r). Blanc (1971) introduced the wave-refraction diagrams and then was updated by Courtaud (2000) (Figure 25). For the three wave directions that penetrate in Hyères bay (Northeast, East and Southeast), a period of directions is retained. Courtaud (2000) proposed five classes of refraction coefficients to demonstrate the exposure to waves of different sectors as follows:

- The least exposed sectors to attacks swells, with a very low coefficient $K_r < 0.25$;
- Sectors with a low coefficient, with $0.25 < K_r < 0.5$;
- Moderately exposed sectors, with $0.5 < K_r < 0.75$;
- Very exposed areas, where the coefficient of refraction is strong $0.75 < K_r < 1$;
- The most exposed sectors, where $K_r > 1$.

In contrast to the refraction, the seabed plays no role in the case of the diffraction. When waves encounter surface-piercing obstacle, such as a breakwater or an island, their crests will bend bypassing this obstacle. The amplitude of wave then attenuates on entering the shelter area behind the obstacle. The diffraction phenomena are numerous in Hyères bay because of the presence of islands and rocky outcrops. Redirecting waves at the headlands of approach are shown in the wave diagrams, especially for southeast and northeast waves in the northern part of the bay (Figure 25).

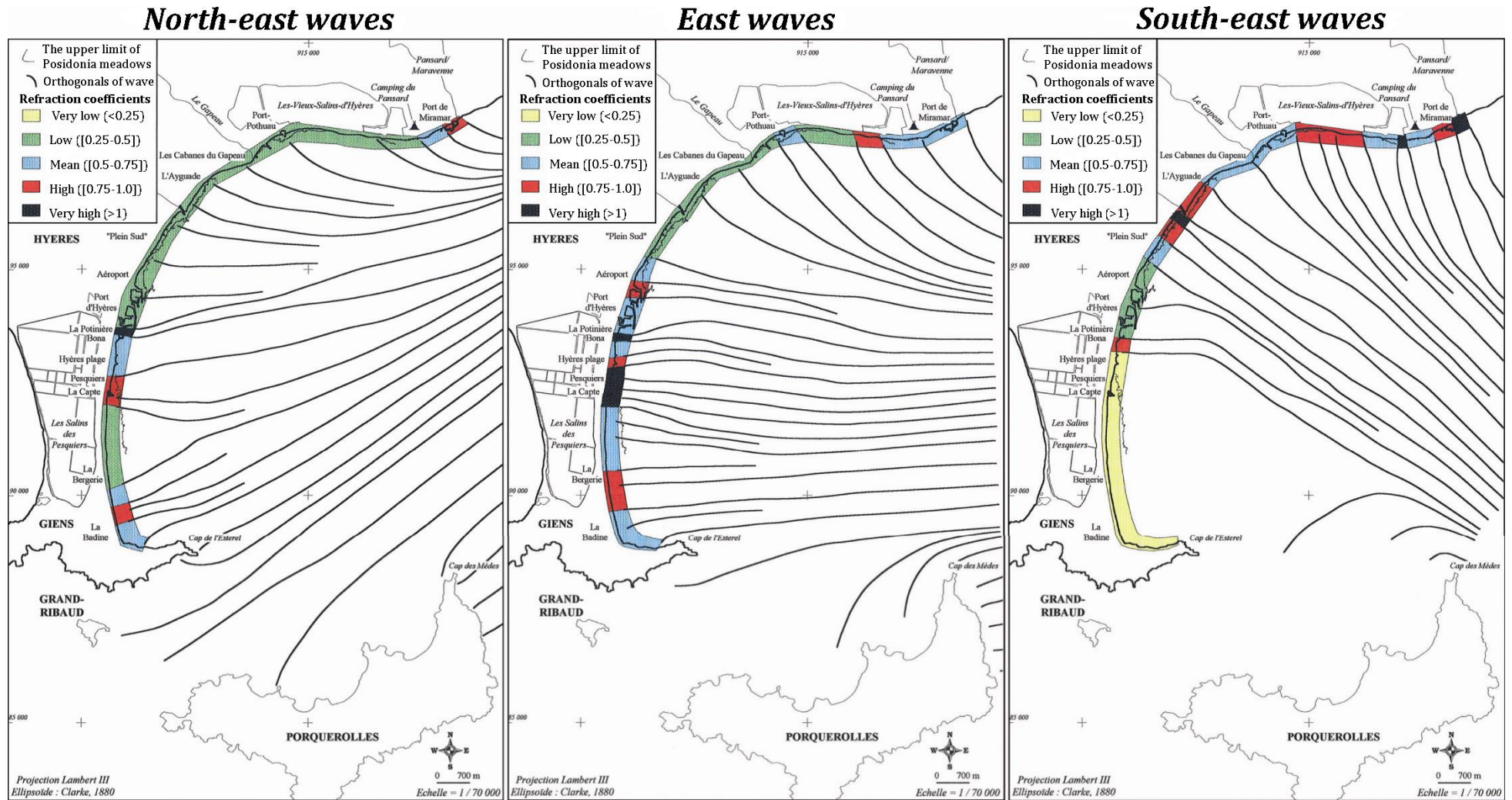


Figure 25. Plans of northeast, east and southeast waves ($T = 7s$) and refraction coefficients (Blanc (1971), as modified by Courtaud (2000)).

The wave is also subjected to the phenomenon of reflection. This occurs when the wave encounters a vertical steep obstacle (cliff, sea wall, front of breakwater...). A part of the wave energy turns back to sea, the normal orthogonal, interferes with the waves arriving and eventually absorbs.

a. The northeast waves

In northeast, waves cause alternative areas of convergence and divergence, with very few sectors with very high coefficient of refraction. The only sector with a very high coefficient is located immediately downstream from the port of Hyères ($K_r = 1.75$), while intensive areas correspond to the port of Miramar ($K_r = 0.77$), north and south of La Capte port ($K_r = 0.81$) and south of the tombolo (K_r from 0.88 to 0.94). The low coefficient occurs in numerous sectors: values range between 0.25 and 0.48 between the beach of Vieux-Salins and Hyères bay and up to 0.27 between the southern la Capte and la Bergerie. The presence of Cape Benat explains channeling northeast waves towards the area of La Capte/La Badine where orthogonal of wave concentrate according to the bathymetry. The preferential axis is located between Bergerie and la Badine where K_r varies from 0.88 to 0.94. The presence of Cape Esterel is also involved in modifying waves by focusing waves on either side of the cape.

b. The east waves

With east waves, the shoreline of Hyères bay is divided into several parts. Between the airport and la Badine, the east wave is almost frontal, which explains the strong refraction coefficients. The most sensitive areas are located at the beaches of the Potinière ($K_r = 1.36$) and Pesquiers (K_r between 1 and 1.21), where the orthogonal constrict and focus. Diffraction at Cape Benat explains the divergence of waves between the airport and Port-Pothuau and low refraction coefficients (0.38 to 0.4), and to the east of Port-Pothuau ($K_r = 0.48$). A slight convergence in Port Pothuau and west of Miramar is strengthening the coefficients up to 0.84.

c. The southeast waves

Unlike the east and northeast waves that focus on the east shoreline of the bay, the southeast waves focus on the northern part of the bay. The southeast wave is more affected by the presence of the islands; the only passage to enter the bay is located between the islands of Port-Cros and Porquerolles.

The area between Port of Miramar and the north of the airport is directly attacked by the southeast wave; the coefficients of refraction vary from 0.56 to 0.97 and beyond 1 in some places, especially at the port of Miramar ($K_r = 1.03$) at the end of Vieux-Salins-d'Hyères ($K_r = 1.29$) and in the groynes of Ceinturon ($K_r = 1.13$). However, the divergence of orthogonal induced low coefficients from the northern airport to Bona (K_r between 0.37 and 0.43) and above all between Hyères beach and la Badine where the wave is completely reoriented ($K_r = 0.16$).

2.2.6. Wind

Wind plays the key factor in coastal evolution in the study area. It directly affects the sand transport in the emerged beach and indirectly generates waves. Giens tombolo is located at the boundary of two different regimes, those of the Gulf of Lion in the west and the Gulf of Genoa in the east. The rocky outcrop of Cape Benat, Six-Fours-Les-Plages/Saint-Mandrier, and the islands of Hyères position as the physical constraints of the study site which play a key role in wind direction and therefore in the wave propagation. The prevailing winds are related to disruptions in the Gulf of Genoa (Capanni, 2011). The wind data were mainly acquired from Hyères and Levant stations. In order to understand the wind regime as well as its characteristics in the study area, Beaufort scale is used to carry out some statistical analyses such as frequency, distribution, regression, etc.

2.2.6.1. B.A.N. Hyères station

Although the wind data of B.A.N. Hyères Le Palyvestre station (Figure 2) appeared closest to the actual winds on the tombolo, its location minimizes the prevailing winds in favor of local winds. Indeed, Maurettes range in the north and together Mont des Oiseaux/Paradise in the south isolate this station from west directions (260°-280°). Moreover, it is also more or less sheltered from eastern winds (80°-100°), due to the outcrop of Cape Benat, and the south winds (180°) by the presence of Giens and Porquerolles Island, while the southwest directions (220°-260°) are not blocked by any obstacle. These directions play an important role in wave agitation in Gulf of Giens, but do not or a little affects wave agitation in Hyères bay. The wind rose in B.A.N. Hyères station clearly reflects the influence of surrounding topographic conditions on the wind direction (Figure 26).

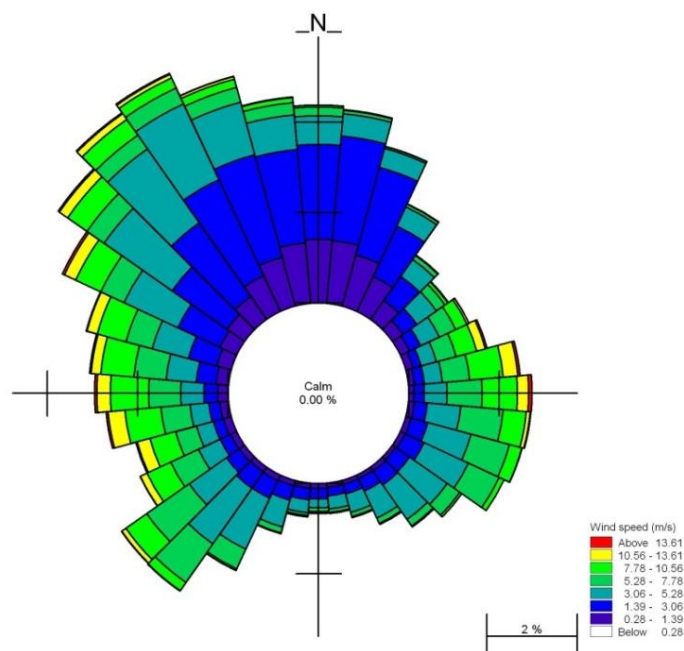


Figure 26. Rose of winds in B.A.N. Hyères station for the period 1999-2015.

Eight directions of north, northeast, east, southeast, south, southwest, west and northwest were selected for the analysis of winds. These eight directions have quite different statistical characteristics, both in terms of overall average and extreme values (Table 14) as well as frequency (Table 15).

Table 14. The general statistical characteristics of winds at B.A.N. Hyères station for the period 1999-2015.

Direction (°N)	N (≤20°)	NE (≤70°)	E (≤110°)	SE (≤160°)	S (≤200°)	SW (≤250°)	W (≤290°)	NW (≤340°)	N (≤360°)
Frequency (%)	7.98	9.42	10.58	8.07	3.31	13.56	12.10	26.00	8.98
Number of observations	10517	12414	13938	10639	4357	17869	15942	34254	11831
Mean speed (m/s)	2.09	3.92	6.22	4.11	3.55	5.48	6.24	3.87	2.48
Maximum speed (m/s)	29.59	20.31	20.31	17.99	12.19	20.31	21.47	17.99	13.35
Mean direction (°)	14.60	48.27	95.26	135.01	187.60	229.06	275.81	321.08	354.89

The morphological winds of northeast, east and southeast can cause the incident waves to the coast of Hyères bay representing 28.07% of total regime. The east winds with the maximum speed up to 20.31 m/s, a frequency of 10.58%, and an average speed of 6.22 m/s are responsible for the majority of morphological events. The northeast winds have the lower frequency of 9.42% than the east winds, but they have the same maximum speed. This means that the northeast winds may be more violent than the southeast winds, which only reached the maximum speed of 17.99 m/s. The winds little affecting the morphology of shoreline in Hyères bay represents 71.93% of cases. However, one part of them, the west and southwest winds have strong influence on the wave agitation and the coastal morphology in Giens gulf. These winds maintain the frequency of 25.66% of total observed time. They also have the high speed with the maximum value of 21.47 m/s in the west direction. The southwest has the higher frequency of 13.56 %, but the lower average speed of 5.48 m/s than those in the west speed. The remainders of winds, which only play the secondary role in the shoreline evolution of Giens tombolo, are the north and northwest winds (16.96% and 26%). They are the most violent winds, especially the north winds with the maximum speed of 29.59 m/s. Finally, the south winds cover only 3.31% of total regime and relatively low speed of 12.19 m/s.

**Table 15. Frequency (in %) of wind at B.A.N. Hyères station for the period 1999-2015
classified by Beaufort scale.**

	N (≤20°)	NE (≤70°)	E (≤110°)	SE (≤160°)	S (≤200°)	SW (≤250°)	W (≤290°)	NW (≤340°)	N (≤360°)	Total (%)
<0.28 (m/s)	0	0	0	0	0	0	0	0	0	0
≤1.39 (m/s)	2.57	2.04	0.48	0.46	0.42	0.73	1.04	3.50	2.75	13.99
≤3.06 (m/s)	4.34	2.72	1.13	1.75	1.01	1.70	1.66	9.22	4.19	27.71
≤5.28 (m/s)	0.93	2.26	2.64	4.11	1.40	4.68	2.42	8.21	1.40	28.05
≤7.78 (m/s)	0.12	1.25	3.21	1.50	0.36	3.82	2.67	2.13	0.47	15.53
≤10.56 (m/s)	0.02	0.85	2.32	0.24	0.10	1.99	3.03	2.01	0.16	10.71
≤13.61 (m/s)	0.00	0.26	0.67	0.01	0.01	0.58	1.14	0.80	0.01	3.50
≤16.94 (m/s)	0	0.04	0.13	0.00	0.00	0.04	0.14	0.13	0.00	0.48
≤20.56 (m/s)	0	0.00	0.01	0.00	0.00	0.00	0.01	0.00	0	0.02
≤24.44 (m/s)	0	0	0	0	0	0	0.001	0	0	0.00
≤28.33 (m/s)	0	0	0	0	0	0	0	0	0	0
≤32.5 (m/s)	0.001	0	0	0	0	0	0	0	0	0.001
Total (%)	7.98	9.42	10.58	8.07	3.31	13.56	12.10	26.00	8.98	100

The statistical distribution of winds in the Table 15 also provides some interesting information. The wind directions were limited into 13 classes compiled from Beaufort scale. The frequencies of the eight directions are calculated according to these classes. The weaker winds (<5.28 m/s) blow regularly, regardless of the direction and represent almost 69.75% of cases. The strongest winds with the speed larger than 10.56 m/s correspond to three dominant directions such as the west (1.29%), the northwest (0.93%), and the east (0.81%). The stormy events with the wind speed higher than 10.56 m/s that could cause the changes of shoreline in the eastern tombolo in Hyères bay occur with the low frequency of 1.12%, whilst these events only represent about 1.91% in the western tombolo in Giens gulf.

Regarding seasonal wind variation, there are two completely different wind regimes corresponding to swell seasons, viz. summer (from June to August) and winter (from December to February). The results of statistical analysis are shown in Table 16. It is clearly seen that the wind speed in the summer is mostly less than that in the winter, apart from west and southwest directions. In the summer, the morphological winds of southwest and southeast, which affect the beach evolution of Giens tombolo, are dominant with the frequency of 20.89% and 12%, respectively. However, in the winter, the prevailing winds are northwest with frequency of 36.75% and northeast with frequency of 9.32%.

Table 16. The general statistical characteristics of seasonal winds at B.A.N. Hyères station for the period 1999-2015.

Direction (°)	Frequency (%)		Mean speed (m/s)		Mean direction (°)	
	Summer	Winter	Summer	Winter	Summer	Winter
N (≤20°)	9.62	8.37	1.79	2.45	12.33	10.53
NE (≤70°)	8.1	9.32	2.04	4.61	41.88	48.97
E (≤110°)	7.98	7.68	4.66	6.86	97.93	91.81
SE (≤160°)	12	4.16	4.07	4.11	133.44	135.98
S (≤200°)	4.51	2.67	3.39	3.96	186.41	183.4
SW (≤250°)	20.89	6.06	5.72	4.56	227.19	231.42
W (≤290°)	12.4	14.02	6.23	6.12	273.16	275.69
NW (≤340°)	18.7	36.75	3.81	3.99	317.88	321.01
N (≤360°)	5.81	10.96	2.07	2.87	352.73	352.1

2.2.6.2. Le Levant station

In contrast to Hyères station, Le Levant station is located at the very high point of the Le Levant island without the effect of topographic ground such as the mountain, the high building, etc (Figure 2). The wind rose established in Le Levant station for the period from 2000 to 2015 (Figure 27) highlights the main regimes of winds affecting the study area. It is easily recognized that the west (260°-280°), Southwest (230°-260°) and Northeast (60°-80°) are three prevailing wind directions appearing at this station. Nevertheless, the Northeast direction has many the highest winds.

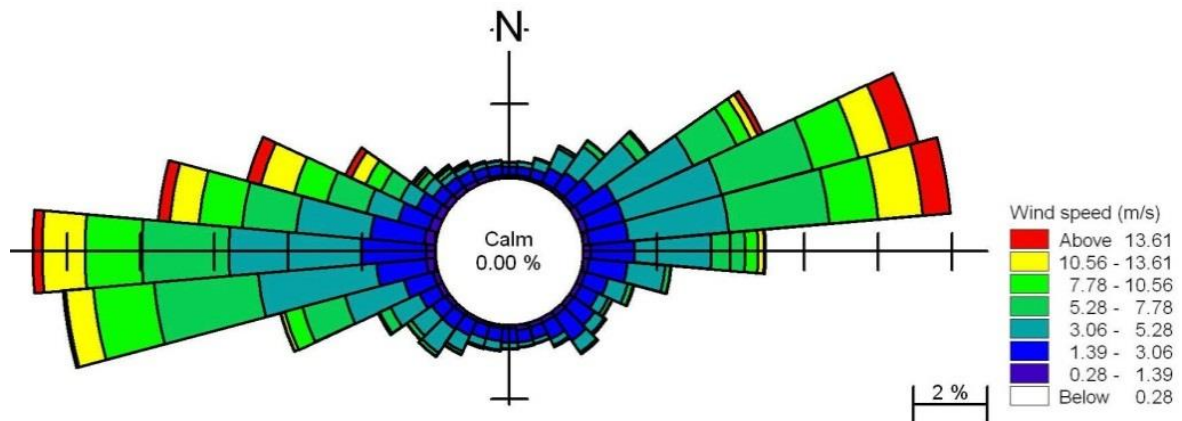


Figure 27. Wind rose in Le Levant station for the period 2000-2015.

Some statistical analyses of winds with eight directions were carried out, similarly those in Hyères station. The results are shown in Table 17 and Table 18.

Table 17. The general statistical characteristics of winds at Le Levant station for the period 2000-2015.

Direction (°N)	N (≤20°)	NE (≤70°)	E (≤110°)	SE (≤160°)	S (≤200°)	SW (≤250°)	W (≤290°)	NW (≤340°)	N (≤360°)
Frequency (%)	1.09	20.57	18.87	5.16	2.72	10.36	34.04	6.27	0.92
Number of observations	1227	23058	21156	5784	3052	11613	38160	7029	1034
Mean speed (m/s)	2.80	5.59	5.60	2.67	2.60	4.18	6.23	5.01	2.42
Maximum speed (m/s)	36.43	22.67	23.48	15.79	9.31	16.6	21.86	21.05	8.5
Mean direction (°)	15.79	59.97	87.58	137.47	185.75	236.90	272.40	311.62	354.75

The winds of northeast, east and southeast are the main factors, which might result in the change of the shoreline in Hyères bay represent approximately 44.6% of total regime with greater than or equal to maximum speed 15.79 m/s. Unlike the winds in Hyères station, the northeast winds are responsible for the majority of morphological events with a frequency of 20.57%, the maximum speed of 22.67 m/s and an average speed of 5.59 m/s. The east winds only appear with a lower frequency of 18.87% and the higher value of maximum speed 23.48 m/s. Nonetheless, they have the same average speed of 5.6 m/s as the northeast winds. On the other hand, the morphological winds, which play a vital role in the coastal evolution of the western tombolo in Gulf of Giens, are the west and southwest winds representing 44.4% of observation time. Although, blowing with the high frequency of 34.04% and the maximum speed of 21.86 m/s, the west winds have a little impact on the change of shoreline as well as on wave agitation in Gulf of Giens. The primary reason is that the rocky outcrop of Six-Fours-Les-Plages/Saint-Mandrier aligns on the same axis as Giens tombolo and isolates the western branch of Giens tombolo from waves generated by the west winds and partly the southwest winds. The rest of winds do not mostly affect the study area representing total of 11% in which the highest value of maximum speed of 36.43 m/s is repeatedly observed in the north winds and the lowest speed of 9.31 m/s occurs in the south winds.

Based on the Beaufort scale, the wind directions are divided into 13 classes, as described in Table 18. Similarly the winds in Hyères station, the winds in Le Levant station whose speeds is lower than 5.28 m/s occur with the frequency of up to 60.6 %, while the strongest winds (from 10.56 m/s) correspond to the west, east, and northeast directions with the frequency of 4.67%, 2.18 %, and 2.04%, respectively. Additionally, the winds of east, northeast, and southeast with speed larger than 10.56 m/s, which can reshape the coast of the eastern tombolo in Hyères bay merely, represent about 4.23% of total observations. Concerning the western part of Giens tombolo in Gulf of Giens, the

morphological winds of west and southwest which have the speed over 10.56 m/s appear with the lightly higher frequency of 4.81 %.

Table 18. Frequency (in %) of wind at Le Levant station for the period 2000-2015 classified by Beaufort scale.

	N (≤20°)	NE (≤70°)	E (≤110°)	SE (≤160°)	S (≤200°)	SW (≤250°)	W (≤290°)	NW (≤340°)	N (≤360°)	Total (%)
<0.28 (m/s)	0	0	0	0	0	0	0	0	0	0
≤1.39 (m/s)	0.15	0.63	0.68	0.69	0.41	0.62	1.12	0.81	0.17	5.28
≤3.06 (m/s)	0.48	3.71	3.94	2.81	1.41	2.71	5.47	1.77	0.48	22.78
≤5.28 (m/s)	0.41	7.90	6.41	1.34	0.78	4.42	9.71	1.31	0.25	32.54
≤7.78 (m/s)	0.04	4.52	3.94	0.27	0.11	1.88	7.77	1.01	0.02	19.56
≤10.56 (m/s)	0.003	1.791	1.72	0.040	0.008	0.59	5.30	0.64	0.001	10.08
≤13.61 (m/s)	0	1.11	1.39	0.010	0	0.13	3.65	0.52	0	6.79
≤16.94 (m/s)	0	0.62	0.63	0.004	0	0.01	0.93	0.18	0	2.38
≤20.56 (m/s)	0	0.26	0.13	0	0	0	0.09	0.025	0	0.51
≤24.44 (m/s)	0	0.05	0.03	0	0	0	0.003	0.001	0	0.08
≤28.33 (m/s)	0	0	0	0	0	0	0	0	0	0
≤32.5 (m/s)	0	0	0	0	0	0	0	0	0	0
≥32.78 (m/s)	0.001	0	0	0	0	0	0	0	0	0
Total (%)	1.09	20.57	18.87	5.16	2.72	10.36	34.04	6.27	0.92	100

Table 19. The general statistical characteristics of seasonal winds at Le Levant station for the period 2000-2015.

Direction (°)	Frequency (%)		Mean speed (m/s)		Mean direction (°)	
	Summer	Winter	Summer	Winter	Summer	Winter
N (≤20°)	1.48	2.01	2.92	3.26	11.2	11.9
NE (≤70°)	14.83	18.1	4.34	5.69	58.51	56.23
E (≤110°)	16.84	18.78	3.95	6.94	87.31	85.74
SE (≤160°)	6.28	4.76	2.37	3.27	135.28	136.19
S (≤200°)	3.19	4.19	2.42	3.36	183.47	183.21
SW (≤250°)	12.29	9.42	4.02	3.86	235.21	233.39
W (≤290°)	39.36	30.93	5.7	6.99	269.46	274.13
NW (≤340°)	4.67	10.37	4.22	5.95	310.92	310.19
N (≤360°)	1.06	1.44	3.11	3.36	351.41	352.07

The statistical analysis of seasonal wind data from Le Levant station was carried out to determine the predominant wind directions that affect the coastal morphology in the study area. The results of this analysis are summarized in Table 19. It is noticeable that the average wind speed in the winter is much higher than that in the summer. The strong winds normally occur in the west sector in the summer, whereas the highest wind speeds are observed in east and west sectors in the winter. In both the winter and summer, the west and east winds are dominant with a frequency of at least 31% and 17%, respectively.

2.2.7. Sediment

The sediment regime in Hyères bay is completely different from that in Gulf of Giens by the presence of organizations providing the fluvial sedimentary supply. However, this supply is subject to wide variations from two main fluvial organizations such as Gapeau and Pansard-Maravenne river. They are the typical representatives of Mediterranean flows, which have the continuous inflows from October to May, followed by long periods of drying up in summer. Nevertheless, the short and violent floods occasionally occur in these rivers. On the other side, Gulf of Giens suffers from the lack of sediment contributions in situ in long time. The small rivers in Gulf of Giens are located between the outcrop of Carqueiranne and Almanarre. Their watershed only represents 15 square kilometers with approximately 10 km of linear shoreline. The flows are negligible and have never been measured. Henceforth, it is very difficult to estimate the sediment yield of these rivers in Gulf of Giens.

2.2.7.1. Fluvial sediment contributions

Among the different rivers flowing in Hyères bay, both Gapeau and Pansard-Maravenne rivers have a significant contribution in sediment (OCEANIDE, 2010). With the watershed of 513 km² and annual volumetric flow rate of 5 m³/s, the total sediment which Gapeau would contribute is about 50,000 t/year of which 20 to 30% of sand, gravel and pebbles is still 10,000-15,000 t/year or 5,000-8,000 m³/year. On the other hand, Pansard-Maravenne rivers have a watershed of 78 km² and annual volumetric flow rate of 1 m³/s. This means that they transport the total sediment of about 6,500 t/year, including 1,500 t/year of sand, gravel, and pebbles (SOGREAH, 1988b).

In his work, Capanni (2011) estimated sediment contribution between 25,000 and 35,000 m³/year of which 20 to 30% of sand and gravel (including Gapeau river, Pansard-Maravenne river and other small streams). In addition, he also estimated the average annual suspended sediment transport from Gapeau ranging from 31,000 to 62,000 m³/year. No estimation of the average annual bed load sediment transport could be obtained from the works of Capanni (2011). Nonetheless, most researchers agree to retain the same rate of bed load compared to the total load: between 20 and 30% (Courtaud, 2000).

2.2.7.2. Longshore distribution of sediment

These observations confirm the hydro-sedimentary organization described by Blanc (1958), Blanc (1975) and Jeudy De Grissac (1975) and highlight the importance of longshore sediment transport in Hyères bay, as well as the leading role of facilities in the individualization of hydro-sedimentary systems; these facilities are causing the high erosion risk areas, particularly the south of Hyères port. In her thesis, Courtaud (2000) shows a granular-decay of sediments in the direction of longshore current and influence of facilities perpendicular to the shoreline (breakwater at the mouth of Gapeau, breakwater at the mouth of Roubaud, Hyères Port, Port of Capte) (Figure 28).

It is only from the mouth of the Gapeau appear coarse sediments, reflecting the role of fluvial contribution in the grain size of sediment in the swash zone. From the mouth of Gapeau to the port of Hyères, the sediments are refined into southbound (D_{50} of 0.65 to 0.25 mm), with a decrease in the percentage of pebbles present from the mouth of Roubaud where it seems the jetties are preventing the transport of the coarser materials. Nevertheless, pebbles present the downdrift with lower proportion (34% against 51% upstream). They could possibly come from the nourishments of coarse material along with the establishment of the groynes or later, but also the erosion of inherited sedimentary supplies, the shoreline has fallen sharply in this sector. However, it is noted that between the mouth of Gapeau and Ayguade beach, the percentage of pebbles increases (18 to 51%). However, it is highly likely that the sandy fluvial contributions took place at the time of sampling because the current size of the mouth area is very rough, except during flood events. After modification by marine dynamics, the sands are exported and remain only the pebbles (Capanni, 2011).

Between the mouth of Roubaud and the port of Hyères, the standard deviation is accompanied by a marked decrease in the percentage of pebbles (from 34% to 0%) and improved sorting (1.2 to 0.8 ϕ) in agreement with the dominant longshore drift. It also seems that the bad sorting indexes in Roubaud and Ceinturon (1.2 and 1 ϕ) result from contributions of non-native nourishment, the dismantling of structures and the destruction of embankments (Capanni, 2011).

From Hyères port to La Capte, the sediments are coarser (D_{50} is often greater than 0.5 mm), moderately sorted (0.8 to 1.2 ϕ), with a high concentration of pebbles (from 23-54%), which could here also come from inherited supplies or the dismantling of works. The presence of Hyères port causes an important phenomenon of erosion in downdrift and exports the finest materials, easily mobilized, which could generate the inherited coarse supplies. Moreover, this phenomenon is accompanied by regular nourishment, and can be pebbles, probably responsible for a poor sorting of sediments. From La Capte to La Badine, sediments are finer (0.25 mm), better sorted (0.35 to 0.4 ϕ) and the percentage of pebbles is reduced (40% at La Capte to 0% at La Badine) (Capanni, 2011).

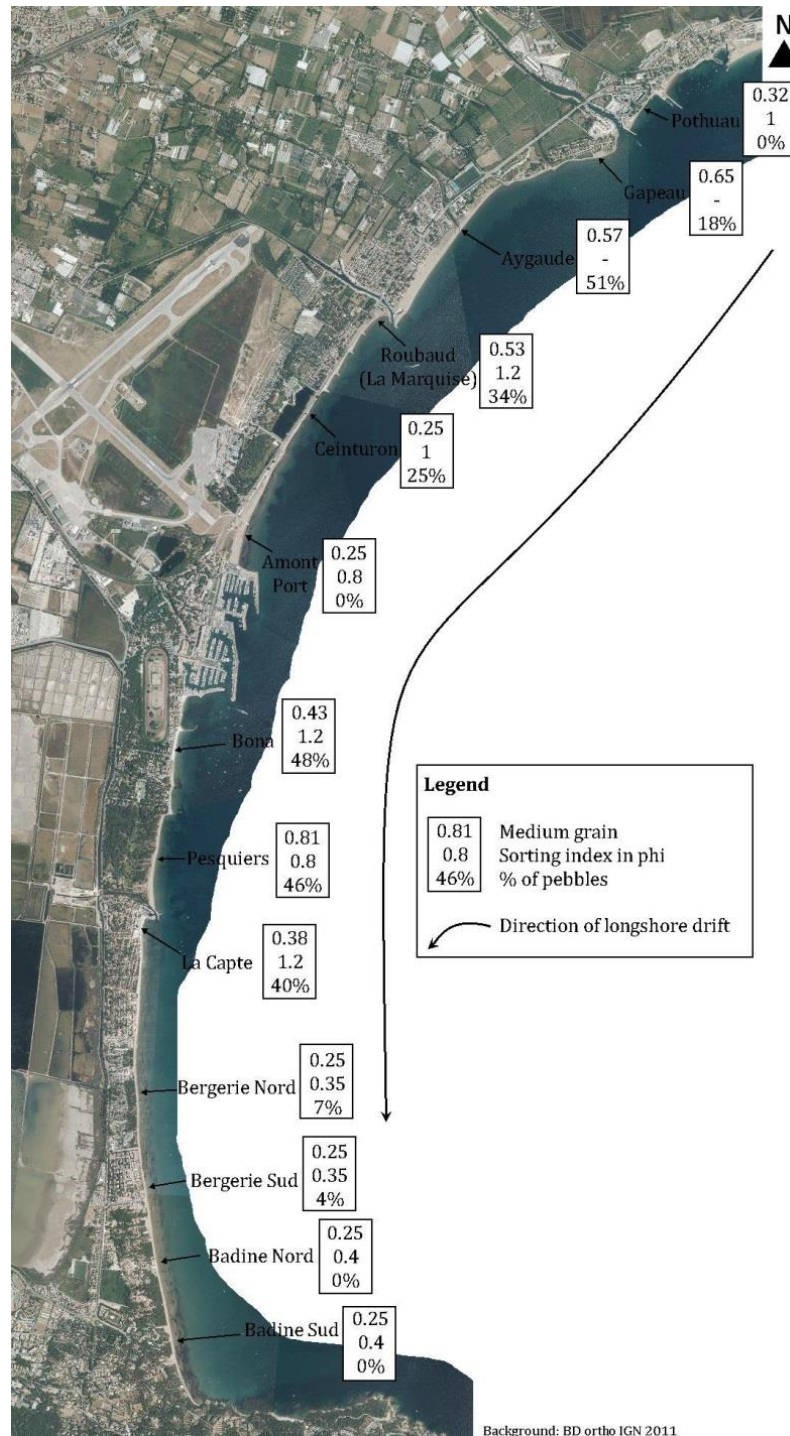


Figure 28. Longitudinal distribution of sediment in the swash zone in Hyères bay (Courtaud (2000), Capanni (2011), modified).

2.2.7.3. Spatial distribution of sediment

Most of the bay is occupied by coarse sands ($D_{50} > 2$ mm), resulting from the biological production of the *Posidonia* seagrass, particularly important in Hyères bay (Jeudy De Grissac, 1975). The proportion of sediments, which mix the calcified organisms and sand, is rarely less than 10% and varies mostly between 10 and 30%. The mobile fine sands (0.5 to 0.063 mm) are concentrated between the port of Hyères and La Badine beach. Their extent offshore corresponds to the upper limit of the *Posidonia*

meadow. The pelitic fraction (silts) occupies a very large area and is due to river flows. From the mouth of the Gapeau to the Cape of Estérel (Figure 29), the bottoms between -8 and -15 m are occupied by at least 50% of pelites, with maximums at the port of Hyères (92%). The "coastal detritic" is composed of heterometric sands, whose granulometry varies from coarse and medium sands to pelites (<10%). In the erosion channels within the posidonia meadow, the material is also very heterometric including pebbles, gravels and coarse sands from the Gapeau river as well as fragments of groynes and rip-raps (Capanni, 2011).

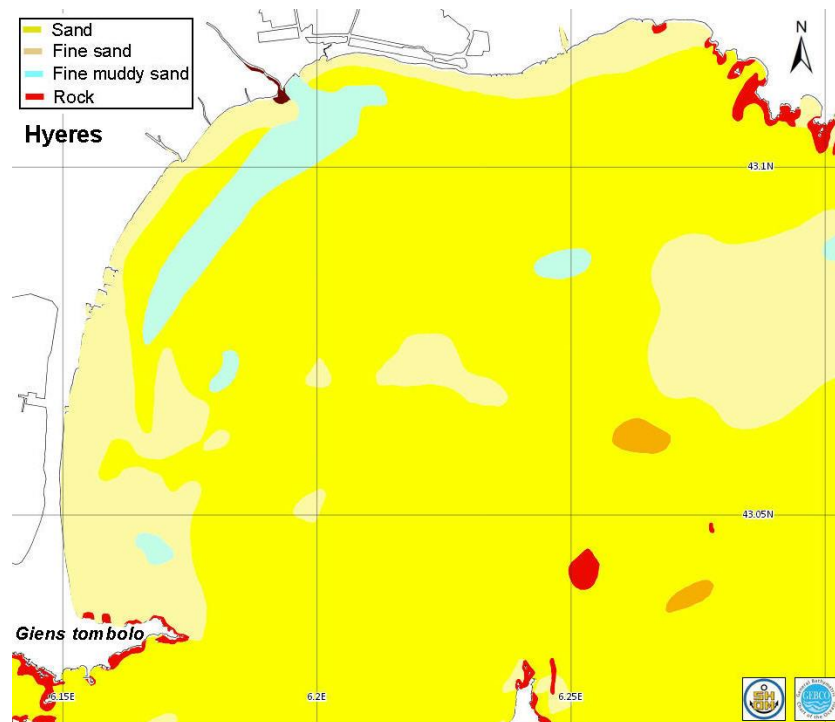


Figure 29. Distribution of sediment in the seabed of Hyères bay (Source: SHOM).

2.2.8. Posidonia and seabed characteristics

2.2.8.1. Introduction

Posidonia is one of the most important endemic seagrass species in the Mediterranean Sea. It can colonize either in soft substrates such as sand in wave-sheltered areas or rocky bottoms being exposed to relatively high wave energy and wind driven currents (Koch et al, 2006). Posidonia can form meadows or beds, which are usually distributed in shallow areas from the surface to 40-45 m depth depending closely upon water transparency. It can be seen almost throughout the Mediterranean sea except for the Middle East and along the Languedoc coast (France) between the Camargue and Port-la-Nouvelle (Boudouresque et al., 2012) (Figure 30). The total surface area of Posidonia has been estimated to be in the order of 1,224,707 ha, covering about 1.5% of the total Mediterranean Sea surface (Pasqualini et al., 1998). Along the French coast, Posidonia was found to be approximately 94,030 ha and mainly concentrated along the Var coast and around Corsica island (Telesca et al., 2015).



Figure 30. Distribution of *Posidonia Oceanica* (red line) along the coast of the Mediterranean Sea (Vacchi et al., 2016).

Posidonia oceanica is a flowered plant like all other seagrass species. The density of this plant usually varies between 500 and 1,000 plants per square meter (Koch et al., 2006). It is composed by rhizome, root, leaves, flower and fruit (Figure 31). The rhizome can grow in vertical and horizontal directions. Such a characteristic of the root allows the plant to anchor itself to the sandy bottom and to simultaneously contrast the gradual silting due to the continuous sediment storage between the long leaves. In presence of a sandy bottom, the netting of the perpendicular rhizomes creates a strong zone, called mattes (Cavallaro et al., 2010). *Posidonia oceanica* requires good quality of seawater, with high salinity, low turbidity and a sedimentary budget compatible with the growth of the matte. It dies off immediately if the salinity is below 33‰ (Ben Alaya, 1972). Therefore, it is usually restricted to the open sea and rare or absent in the vicinity of river mouths. Infantes et al. (2009) indicated that *Posidonia oceanica* is not present in areas with the threshold near-bottom orbital velocities higher than 38-42 cm/s. This velocity can be considered as a determinant of the upper depth limit of *Posidonia oceanica*. Furthermore, it does not occur shallower than the breaking depths because waves tear off shoots and some of which will then constitute cuttings. They can also erode the matte, either directly, or by leaching the sediment, which weakens the meadows (Boudouresque et al., 2012). Finally, high turbidity causes the reduction of transparency of the water and penetration of light, and can consequently induce a withdrawal of the lower limit of *Posidonia oceanica* meadows (Boudouresque et al., 2009).

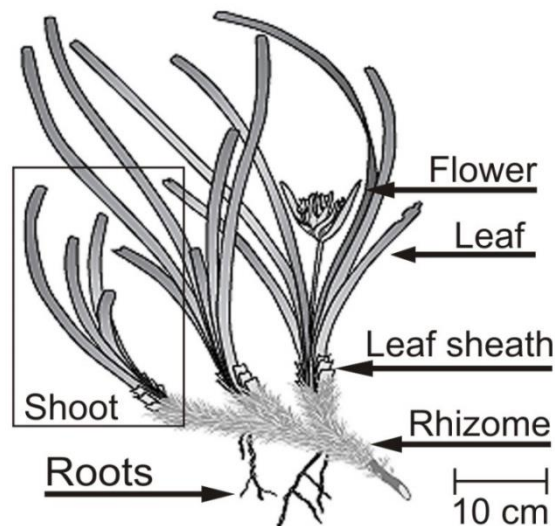


Figure 31. Structure of *Posidonia oceanica* (Manca, 2010).

The presence of *Posidonia* meadows has a strong impact on the local hydrodynamics as well as on the sediment transport, especially in the shallow water area where the length of plants is comparable with the water depth (Cavallaro et al., 2010). Up to now, the effects of seagrass have been investigated mainly by in-situ measurements (Boudouresque et al. (1983), Astier (1984), Jeudy de Grissac (1984), Jeudy de Grissac et al. (1985), Jeudy de Grissac et al. (1989), Gacia et al. (1999), Gacia et al. (2001), Bouma et al. (2005b), Temmerman et al. (2005), Simeone (2008), Infantes et al. (2009), Dijkstra (2009), Infantes et al. (2012), Gómez-Pujol et al. (2013)) and flume experiments using natural (Grizzle et al. (1996), Bouma et al. (2005a), Hendriks et al. (2008), Lefebvre et al. (2010)) or artificial vegetation (Nepf (1999), Nepf et al. (2000), López et al. (2001), Ghisalberti et al. (2002), Folkard (2005), Fonseca et al. (2006), Nepf et al. (2008), Bouma et al. (2009), Koftis et al. (2013)). According to Medina et al. (2001), the 3D structure of rhizomes creates a certain reinforcement for the sandy sediment of the submarine beach; and along with their roots and leaves, they can hinder with the sedimentary movements of the seabed, resulting in the consolidation of the sandy substratum. In addition, *Posidonia* meadows reduce current velocities within the canopy through the frictional effects of vegetation (Vu et al., 2017c). Therefore, the reduced shear stress conditions could prompt in sediment deposition and reduce re-suspension of newly deposited matter (Kombiadou et al., 2013). The foliage of the seagrass meadows increases the roughness height of the seabed boundary layer, facilitating the wave energy dissipation (Gacia et al., 1999). The wave height attenuation over the seagrass meadow ranges from 10%-35%, depending on both the seagrass characteristics and the wave parameters, as well as the fraction of the water column occupied by the vegetation (Koftis et al., 2011). The largest wave attenuation occurs when seagrasses occupy a large portion (>50 percent) of the water column (Fonseca et al., 1992).

Although *Posidonia* plays a very important role in the stabilization and protection of the coast, it has been undergoing considerable regression. An estimated loss of *Posidonia* was approximately 33.6%, corresponding to 368,837 ha in the last 50 years (Telesca et al., 2015). Boudouresque et al. (2012) indicated that anthropogenic disturbances are the dominant factor in the decline of *Posidonia* meadows. The main anthropogenic threats can be direct physical (e.g. anchoring, fishing) and chemical damages (e.g. water pollution) or indirect changes of the hydrodynamic regimes by the construction of new coastal defenses (Boudouresque et al., 2009). The building of facilities such as breakwaters, seawalls, ports, and beach nourishment represents a major threat to *Posidonia* meadows. Same as direct impacts, such constructions not only change swells and currents locally, but also cause the coastal erosion downstream due to the deficit of sediment (Astier, 1984). Either excess or deficit of sediment may have destroyed *Posidonia* meadows. If the rate of sedimentation is greater than 5–7 cm per year, the vegetative tips will die; conversely, if this rate is zero or negative, the matte rises and the rhizomes become exposed and they are then extremely easily broken off by hydrodynamics, anchors, trawling, etc (Boudouresque et al., 1983). For instance, the construction of Pointe-Rouge harbour (Marseille, southern France) directly destroyed 11 ha of *Posidonia* meadow; during the construction, the plume of turbidity from the building site caused the loss of 68 ha or more (Boudouresque et al., 2012). In the other example, the construction of artificial beaches in Le Mourillon (Toulon, France) directly caused the burial of 22 ha of *Posidonia* meadows, followed by the indirect destruction of 10 hectares due to the increased turbidity of the water and the silting up of 27 additional hectares. Even in the operational phase of a harbor, a source of turbidity is remained and the port basins are often polluted by anti-fouling paint and discharge of wastewater from boats. This pollution then spreads to the area surrounding the ports, triggering the reduction of seagrass productivity in the surviving *Posidonia* meadows (Ruiz et al., 2003). Moreover, the regression of Mediterranean seagrass meadows may be attributed to global climate change. Marbà et al. (2010) estimated that shoot mortality rates were increased by 2.2% per year for each additional degree of annual maximum temperature and by 0.1% per year for each accumulated degree of water temperature, for water remained above 26.6°C during the growing season. During the period from 1945 to 2000, the estimated contribution of human-driven warming to the SLR in the western Mediterranean Sea is between 2.75 and 5.50 cm (Calafat et al., 2009). By using Brunn's extrapolation, Boudouresque et al. (2009) predicted that this small SLR could result in a 2.75-5.5m withdrawal of the lower limit of *Posidonia* meadows in bays with gently sloping bottoms. The regression or even disappearance of *Posidonia* meadow in the future can trigger the seriously negative impacts on the coastal areas (Vu et al., 2017c). Hence, it is essential to obtain a more complete understanding of the change of coastal morphodynamics due to the reduction of *Posidonia* meadow area.

2.2.8.2. Simulating the presence of *Posidonia*

In the bay of Hyères, *Posidonia* meadows appear at very close distances from the coast (Figure 32). It ranges from the depth of 0 to the depth of 30 m covering 9200 ha in the bay of Hyères, from the south of the Giens tombolo up to Bormes-les-Mimosas (Sinnassamy et al., 1990). Unlike the Gulf of Giens, where the *Posidonia* seagrass observed by Courtaud (2000) is quite stable, the meadow of *Posidonia* in Hyères bay knew a significant change between 1924 and 2003, and has evolved differently in the different observed areas, the main cause being that of coastal constructions. For instance, at the beach of Aygaude, the construction of a jetty at the mouth of Roubaud river caused a sedimentary accretion upstream of structure. The advance of the shoreline and translation seaward of all the coastal sedimentary system resulted in the moving of the upper limits of *Posidonia* seagrass offshore, retreat average 100 m. In this area, at least 120,000 m² (or -1500m²/year) seagrass have been lost. Moreover, at the port of Hyères, the construction of various basins caused the loss of a very important seagrass area. The total loss area is estimated about 430,000 m² (or -5400m²/year) (Capanni, 2011).

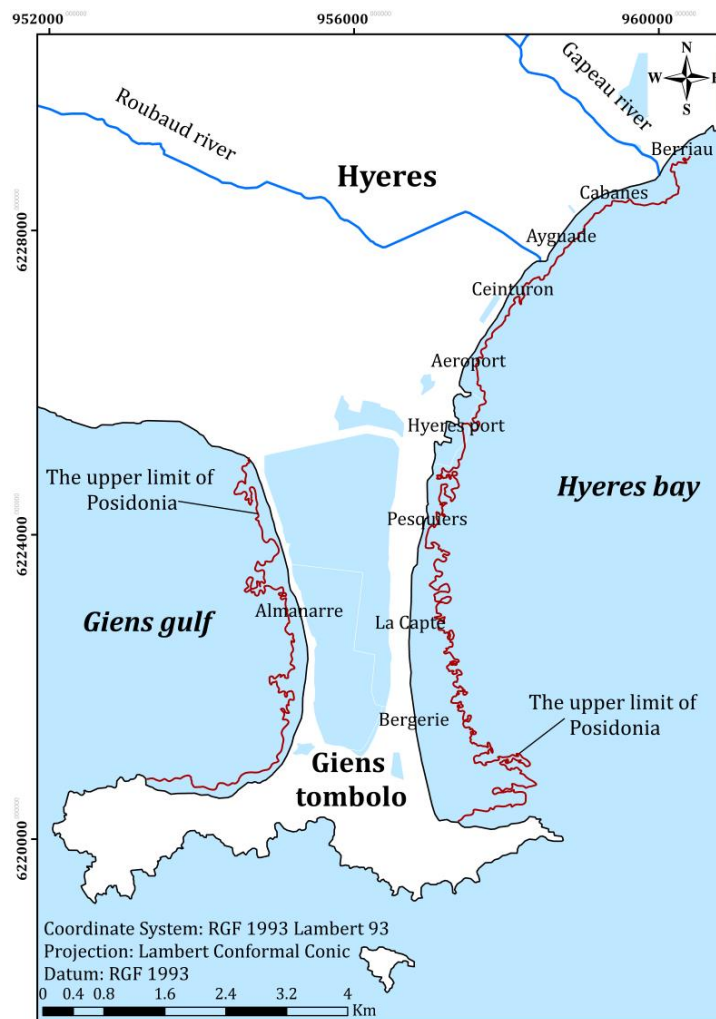


Figure 32. Distribution of *Posidonia* seagrass in Hyères bay.

(Source: Cartham-AAMP/Andromede, 2012)

The effects of Posidonia seagrass on wave attenuation, reduction of current velocities and sediment transport in Hyères bay were investigated through the adjustment of the drag coefficient and the Nikuradse roughness height. The presence of seagrass was taken into account within these parameters. However, Posidonia is commonly present at a depth deeper than the breaker zones in Hyères bay, while the remainders are only covered by sand or rock without seagrass. Therefore, the drag coefficient and the roughness height need to be estimated separately in two different areas, corresponding to the cases of Posidonia seagrass and no Posidonia seagrass.

For the seagrass areas, the vegetation issues the drag expression of Nepf (1999), which was developed based on laboratory experiments with steady flows through rigid grass mimics. The primary reason for using this expression is that it explicitly accounts for the effects of seagrass shoot density over a realistic range of densities (Koch et al., 2006). The drag coefficient is expressed as follows:

$$C_D = (1 - ad_p)C_B + 0.5\overline{C_D}ad_p \left(\frac{d}{d_p} \right) \quad (2-1)$$

Where:

a is the projected Posidonia area per unit volume (m^2);

d_p is the leaf width (m);

d is the water depth (m);

C_B is a skin friction drag coefficient (equal to constant value of 0.001) (Nepf, 2000);

$ad_p = \frac{n_p \cdot h_p \cdot d_p^2}{d}$ is the fractional volume of the water area occupied by seagrasses;

n_p is the density of seagrass per unit area (m^2);

h_p is canopy height of seagrass (m);

$\overline{C_D}$ is the bulk drag coefficient for seagrass. It is a function of ad_p approximated by Chen et al. (2007) according to Nepf (2000) as:

If $10^{-3} < ad_p < 10^{-2}$, then $\overline{C_D} = 1.17$

If $10^{-2} < ad_p < 10^{-1}$, while $\overline{C_D} = -0.255 \ln(ad_p)$

This equation takes into account the current and not wave.

The values of above-mentioned terms relating to the Posidonia characteristics come from the data provided by G.I.S Posidone (Table 20).

Table 20. The dimensional characteristics of Posidonia seagrass (Paquier, 2009).

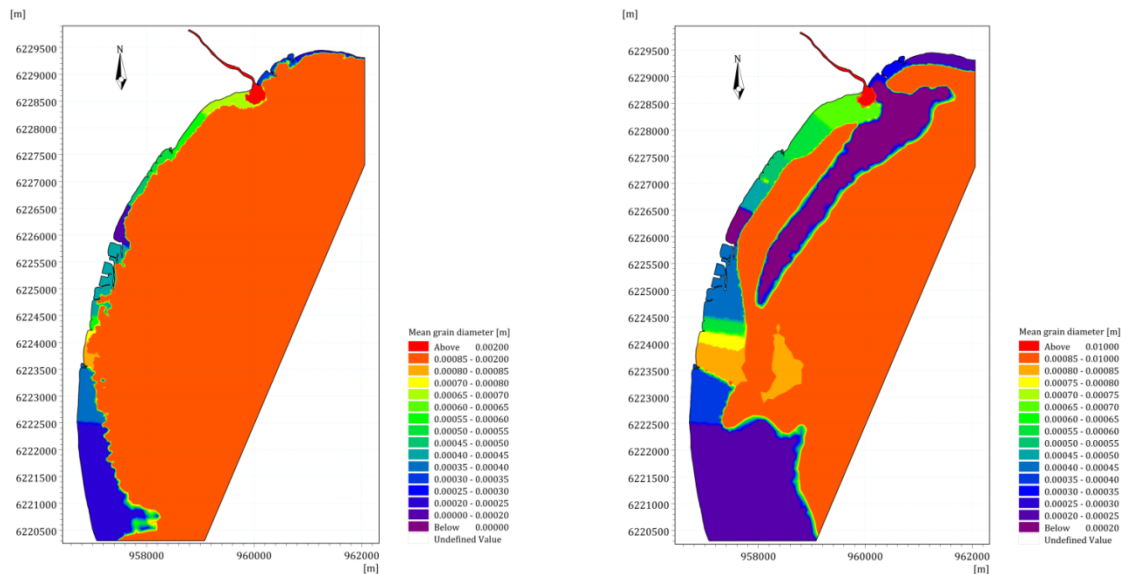
Data	Source	Value
n_p	GIS Posidone	525.9+/-197 (m^2)
h_p	Posidonium Port Cros	55 cm in average
d_p	GIS Posidone	10 mm in average

In addition to the drag coefficient, the relation between the vegetation roughness height and the deflected height of *Posidonia* seagrass has been also studied by the experimental method. Kouwen (1969) established one equation to calculate the flexible submerged vegetation roughness height in open channel. This equation is based on the experiments made in a laboratory flume.

$$k_s = h_p e^{(1-\kappa C_l) \left(1 - \frac{h_p}{d}\right)} \quad (2-2)$$

In which C_l is an empirical coefficient ($1.52 < C_l < 2.69$).

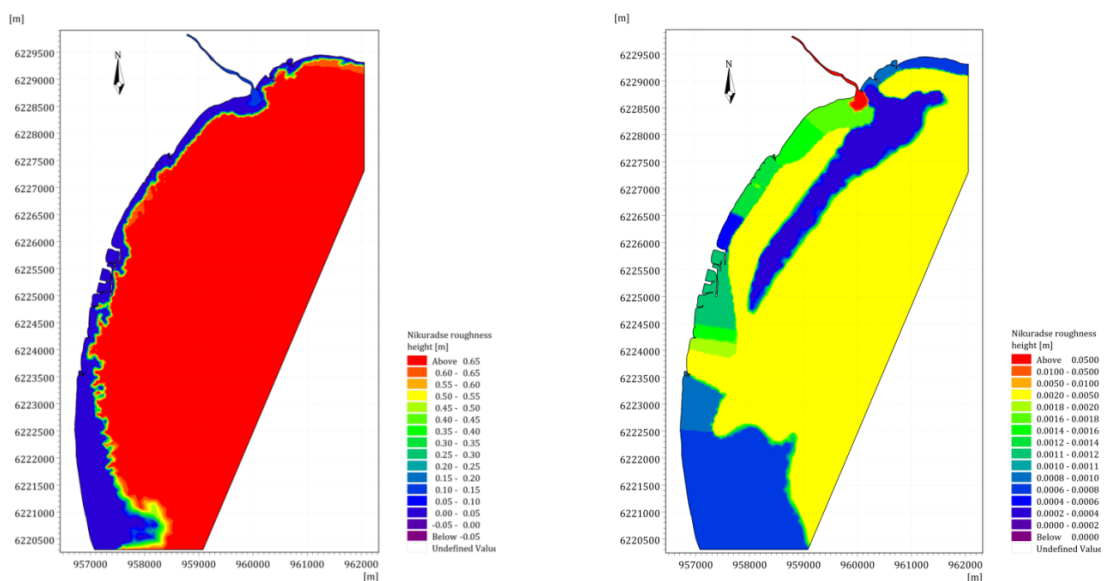
The results of estimation of the median grain diameter (D_{50}), Nikuradse roughness height (k_s) and Manning's number (M) for the entire study area are illustrated in Figure 33, Figure 34, and Figure 35, respectively.



a) With *Posidonia*

b) Without *Posidonia*

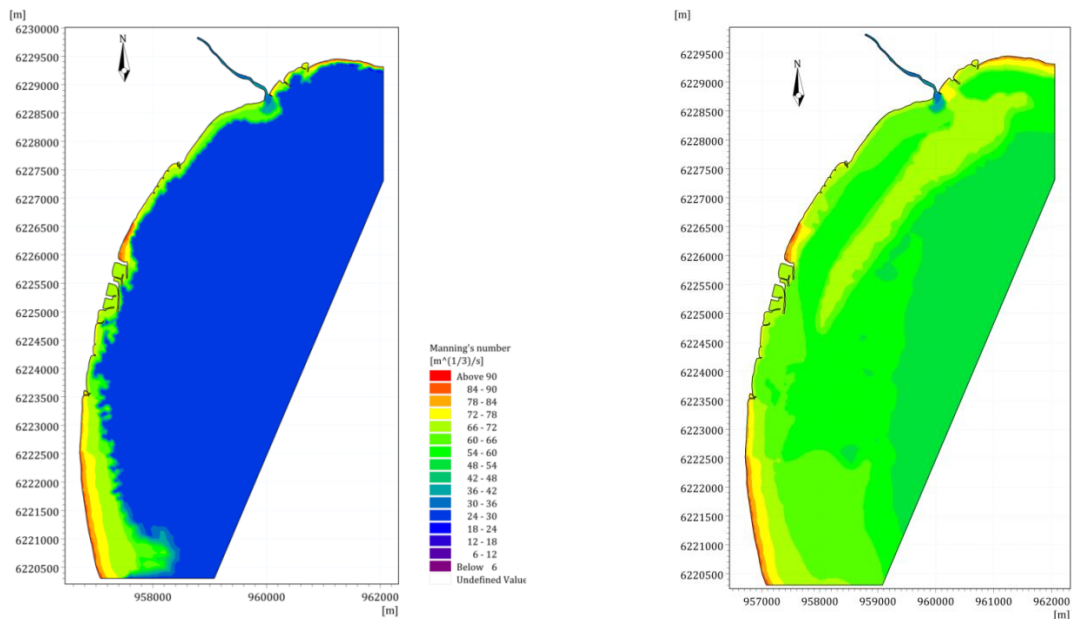
Figure 33. Distribution of median grain size D_{50} in Hyères bay.



a) With *Posidonia*

b) Without *Posidonia*

Figure 34. Distribution of Nikuradse roughness height k_s in Hyères bay.



a) With Posidonia

b) Without Posidonia

Figure 35. Distribution of Manning's number M in Hyères bay.

2.3. Key factors affecting the morphological evolution in Giens tombolo

The morphological evolution is induced by erosion and accretion which are natural processes that occur at different temporal and spatial scales. They can take place in response to smaller-scale events, such as storms, regular wave action, tides and winds, or in response to large-scale events such as glaciation. Wind, waves and currents are natural forces that easily move the unconsolidated sand and soils in the coastal area, resulting in rapid changes in the position of the shoreline as well as the bathymetry of the beach. Moreover, anthropogenic actions in river catchments and watersheds (river damming and diversion), along the coast (port facilities, groynes, jetties, land reclamation), and offshore (dredging, sand extraction) in combination with these natural forces normally exacerbate coastal erosion in many places.

The Giens tombolo is a fragile area vulnerable to the coastal erosion. There are some erosive areas along the shoreline, such as the northern and central Western tombolo (landmarks B08 and B10), the central Ceinturon beach, La Capte beach (Blanc, 1974; Capanni, 2011; Courtaud, 2000; SOGREAH, 1988c). The main causes of the erosive phenomenon are both attributed to natural factors (waves and storms) and human activities (a deficit of sediment load caused by man-made structures).

2.3.1. Wind condition

Wind is the essential factor of the littoral morphogenesis, by intervening directly on the wind transport of the emerged areas and indirectly by being the source of waves and currents. In addition, the prevailing winds accompany low-pressure situations, which can promote the storm surge phenomena during the tempestuous events. The sediment transport related to wind dynamics is estimated at between 5 and 10,000 m³/year along

the western branch and between 10 and 20,000 m³/year along the eastern branch (SOGREAH, 1988a). The winds will not have the same effects on each side of Giens tombolo. When the western branch is exposed to the southeast wind directions that generate an agitation affecting the shoreline evolution in Giens gulf, the eastern branch is in the shadow of this wind. However, it is the opposite for the eastern, northeastern, and southeastern winds. They cause the formation of swell that enters Hyères bay and participates in the coastal morphology.

2.3.2. Wave condition

Wave plays a considerable role in the morphology of Giens tombolo due to the absence of significant tide. Firstly, the two branches of the tombolo forming the bottom of bay are subject directly to dominant wave directions. Secondly, the low altitudes and the narrowness of the emerged sand spit make the shoreline facing the endangered marine dynamic attacks (Courtaud, 2000).

The western tombolo is subject to westerly wave plans. The erosive areas in this branch result of the attacks of west waves with high wave steepness, although relatively short, northwest and southwest waves, all totaling about 45 days per year (Blanc, 1973). The west direction has a strong impact on the areas between the landmarks B03-B16 and B25-B28 whereas the Southwest regime mostly affects the landmarks B04-B15 and B20-B21 (Figure 1). This direction is also the most devastating in the north of western tombolo. It promotes the wave run-up approaching the west coast. It causes the flooding of the salt road and deposition of sediment in the middle surrounding channel from landmark B08 to B10 (ERAMM, 2001). In contrast to the western tombolo, the eastern branch is attacked by the dominant wave directions of east and southeast. The most exposed sector of Hyères bay lies between the port of Hyères and la Capte beach, directly subject to attacks of the most aggressive waves of east and northeast. Accompanied with the deficit of sediment due to the presence of long breakwaters, it causes the erosion at la Capte beach. Moreover, changes in the orientation of the shoreline explicates that the area between Ceinturon beach and Port Pothuau is protected from the east and northeast waves, but exposed to the southeast waves. As a result, the downstream sides of groynes and Ceinturon beach are continuously eroded by the action of southeast waves. A significant sediment loss in this area is estimated at 50,000 m³ or -500 m³/year (Capanni, 2011).

2.3.3. Current condition

In the gulf of Giens and Hyères bay, there are some kinds of currents operating such as general currents, tidal currents, wave-induced currents, and wind-driven currents. Nevertheless, only wave and wind-driven currents have a strong impact on the shoreline changes of the tombolo. Generally, the wind-driven currents do not exceed 0.2 to 0.3 m/s and are mainly involved in suspension transport and therefore suspended material

is very thin or very light. Furthermore, they bring plant debris (*Posidonia*, *Zoostères*) that are found preferentially in calm areas: for example, the La Badine beach and port areas (SOGREAH, 1988a). In some cases, the debris banquettes on the beach play as a protective buffer layer, which can absorb one part of wave energy in the swash zone and limit the soil washing, especially in stormy durations. With winds from the east, they form a current from east to west and from north to south along the tombolo.

Regarding the wave-induced currents, they are composed of longshore current and rip current determining almost all sediment transport in the study area. The movement of longshore currents is responsible for the shoreline transit, carrying sediment between the coast and the surf zone. In the Gulf of Giens, the transport sediment volume due to these currents is approximately 5000 m³/year in the south and between 3000 and 4000 m³/year in the north. For the Hyères bay, the annual transportation varies from 3 to 5000 m³/year at La Londe-Les-Maures, and 5 to 10,000 m³/year in the area of Port-Pothuau/La Capte. Between the hippodrome and La Capte, the transit volume is estimated at about 25,600 m³/year (Courtaud, 2000). In the bay of Hyères, the dominant longshore current takes sediments of Pansard-Maravenne river and carries from east to west to Port Pothuau as a first obstacle. From there, the curvature of the shoreline forced the movement to NNE-SSW to Port of Hyères. During this trip, it will take over the contributions of Gapeau, then those of Roubaud. Beyond Port of Hyères, the current has a north-south trajectory. At La Badine beach, the current is completely blocked by the cape of Esterel. As a result, it stops the flow and therefore the transit cannot really be evacuated to the south. On the other hand, the rip current is perpendicular to the shore, carrying sediments to sea. In addition to the wave characteristics, the rip currents significantly depend on the seabed slope. The increase in the slope along some beach profiles, such as the restaurant of Le Salinas in the western branch and the campsite of la Londe in the eastern branch, promotes the departure of sediments by increasing the speed of rip currents. The existence of indentations in the *Posidonia* herbarium testify to the power of rip currents. In the Gulf of Giens, three major erosion channels are perpendicular to the shoreline while in Hyères bay, there is not very wide erosion channel through the herbarium, probably due to relatively sheltered waters. Sediment removed from the subaerial area and some sectors of the *Posidonia* seagrass will borrow the erosion channels and mainly supply the herbarium raising its offshore elevation. Sediment transport in the beach profile in the Gulf of Giens is estimated from 50 to 100 m³ per linear meter per year (SOGREAH, 1988a).

2.3.4. Biological factors

The *Posidonia* seagrass plays a fundamental role in the hydrodynamic protection of shoreline and beaches, by attenuating the power of waves and currents and stabilizing the sandy seabed. Its effect depends mainly on height, density, and width of leaf. Wave attenuation by seagrass canopies has been measured on the northeast coast of the island

of Mallorca by Infantes et al. (2012). The results of that measurement showed that root mean squared wave height (H_{rms}) is reduced by around 50% for incident waves of 1.1 m propagating over about 1000 m of a meadow of *Posidonia* with shoot density of about 600 shoots per square meter. Furthermore, the presence of a *Posidonia* in the nearshore conditions the shape of equilibrium profiles. Higher wave energy dissipated by *Posidonia* meadows could result in higher A parameters of Dean's EBP (Basterretxea et al., 2004). In addition, it also participates in trapping of sediments and reduces sediment resuspension. In other words, *Posidonia* meadow controls the beach variability and sediment exchange at annual basis (Gómez-Pujol et al., 2011). Just as a land plant, *Posidonia* seagrass lose their leaves mostly in late summer and autumn, and accumulates along shores, particularly in sheltered areas, forming banquettes whose thickness may be 2 to 3 meters. These *Posidonia* banquettes can play a certain role in the beach evolution under normal wave conditions, in particular on low energy beaches. Hence, the distribution of *Posidonia* in the Gulf of Giens and Hyères bay could affect the change of the shoreline as well as the beach evolution. More details regarding its role in hydrodynamics and sediment transport in the study area will be investigated and discussed in Part 5.6.4 of the chapter 5.

2.3.5. SLR due to global climate change

The global SLR mainly comes from mass addition from melting ice-sheets and glaciers and global steric expansion due to climate change. Within the Mediterranean Sea, a semi-enclosed basin, changes in the atmospheric forcing and in the ocean circulation mainly make that SLR. This sea has been experiencing SLR differently from the global mean (Tsimplis et al., 2008). Gomis et al. (2011) shown that Mediterranean mean sea level has been rising at a lower rate (1.1-1.3 mm/year) than global mean sea level (1.8 ± 0.5 mm/year) during the 20th century. Furthermore, Cazenave et al. (2003) confirmed that the geocentric rate of global mean SLR over the period 1993-2003 ranged around $+2.8 \pm 0.4$ mm/year, and $+2.2$ mm/year for the area from Marseille to Menton, as determined from satellite altimetry. In the 21th century, from a minimum and a maximum scenario, Galassi et al. (2014) estimated that the future sea-level variations in the Mediterranean Sea by 2040–2050 relative to 1990-2000 will be 9.8 and 25.6 cm. Particularly, based on the data of Marseille tide gauge from 1885-2012, the rate of sea level change computed by linear regression will be 1.26 ± 0.05 mm/year. On the other hand, the rate of sea level variation at Marseille by 2040-2050 can be 1.2 and 4.2 mm/year in the minimum and maximum scenarios, respectively. In addition, according to the work of Brunel (2010), the rise of MSL due to global warming is estimated about 35 cm between 2010 and 2060.

By 2100, the global SLR forecasted to be around 44 cm may have serious impacts on coastal regions (Paskoff, 2009) where about 50% of the world's population lives in these areas in which much of this population resides in 13 of the world's 20 largest cities.

Anticipated SLR will greatly amplify risks to coastal zones including increasing offshore and longshore loss of sediment, directly inundating (or submerging) marshes and other low-lying lands, increasing the salinity of estuaries and aquifers, raising coastal water tables and contaminating urban water supplies, exacerbating coastal flooding and storm damage (Vellinga et al., 1989), and displacing existing coastal animal communities and plant, especially degrading the meadows of *Posidonia* (Council et al., 2012). In addition, the SLR may also decrease the efficacy of existing coastal protection structures. For instance, a situation is when a currently emerged structure (usually placed close to the shoreline for maximum beach widening) becomes submerged due to SLR (Ranasinghe, 2016). In the study area, although the population in this area is not as large as on other coastal regions in the world, vulnerability to SLR will mainly affect industrial and tourism activities. Because the economic stakes of the coastal fringe are considerable and mainly related to the tourism industry and seaside tourism in the area accounts for an annual turnover of 4.6 billion euros, that is to say, a fifth of the total sales turnover of the French tourism industry. Thus, the beaches represent an extremely important economic stake and their disappearance due to an acceleration of SLR would be very prejudicial to the economy of the region (Brunel et al., 2009).

Now, in all negative impacts of SLR, coastal erosion is a global and topical problem. According to the investigation of Brunel et al. (2009), the beaches of Hyères bay underwent erosion with an average retreat of 12.1 (± 3.5) m corresponding to an average loss of 40 % ($\pm 10\%$) of their surface area between 1896 and 1998. Additionally, they obtained an average shoreline retreat of 5.8 (± 3.5) m due to a relative SLR of +11 cm between 1896 and 1998. By 2100, in the case of an increase in sea-level of about +44 cm, Brunel et al. (2009) also estimated an average retreat of -20 (± 2) m, with values varying between -12 (± 2) and -41 (± 2) m due to the impact of SLR. Almost one quarter of the investigated pocket-beaches may be lose at least 75 (± 10) % of their current surface-area by 2100 (Brunel et al., 2009).

The trend of global warming along with a SLR is hard to reverse and it is possible that the global climate change will not be under control in the near future. Therefore, studying on the negative impacts of climate change need to be paid more attention. The aim of this work is to present the quantitative analysis of the effects of SLR on hydrodynamics and sediment transport along the eastern Giens tombolo, especially in Ceinturon and Bona beaches (see in Part 5.6.5 of the chapter 5).

2.3.6. Human actions

Human activities are a fundamental parameter of the recent evolution of morphological Giens tombolo. The two branches have experienced very different choices of development over the last fifty years. Tourist pressure is the reason of the establishment of leisure facilities, health, infrastructure and housing ever closer to the seafront. The narrowness of the dune, aggressiveness of sea weather dynamics, and

deficit of sediment led authorities to take protective measures facing these constructions (Courtaud, 2000). Depending on the purpose of the achievements, it is possible to be categorized into five types of construction along the tombolo: port facilities, coastal protection works, rehabilitation operations of dunes, beach nourishment and calibration works of river mouths.

2.3.6.1. Rehabilitation operations of dunes

Since the late sixties of 20th century, the western branch of Giens tombolo has experienced several phases of protection and rehabilitation of the dunes. Until 1995, the wood fences were installed by CEPREL from B18 to the south (Figure 36 (a)). The presence of wood fences results into a rising of the dunes of 2 to 5 cm per year, particularly in the south. Nevertheless, it is dangerous to want us to fix the dunes mobility side whose land is already limited by the presence of salt road and Pesquiers. Wood fences were also installed along the eastern branch, at the beach of Ayguade, the beach in upstream of Hyères port, the pinewood Pesquiers, la Capte and Bergerie (Figure 36 (b)). In those areas where erosion is limited, such equipment is intended to maintain the existing sediment balance.



a. Almanarre



b. Bergerie

Figure 36. Wood fences.

The major purposes of these fences are to provide windbreaks function limiting the loss of sediment by wind transport, protect the salt road and Salins des Pesquiers against marine attacks, and protect the sand spits and the overcrowding of corresponding wildlife. The recovery rate of plants within pots is 60 to 90% providing good fixation of the sediment. Soft techniques, even when wood fences raise the morphosedimentary evolution problems of beaches. Isolation of the dunes may not be the right solution for a narrow shoreline (Courtaud, 2000).

2.3.6.2. Beach nourishment

Coastal erosion is a global and topical problem; at least 70% of the world's beaches are experiencing coastal erosion (Bird, 2005), whereas 24% of France's metropolitan shoreline is eroding, i.e. 1,723 km of coast out of a total of 7,124 km and 48% of sandy

coasts are receding, i.e. 1,153 km, representing two-thirds of all of the receding coasts (Colas, 2007). All of 23 investigated sandy beaches in Provence, southern France underwent erosion between 1896 to 1998 (Brunel et al., 2007). In addition, climate change and the associated rise in sea level are increasing the vulnerability of coastal communities and industries to flood and erosion risk globally (Nicholls et al., 2007). Sea level is estimated to rise approximately 20 cm by the year 2050 (IPCC, 1996), which could lead to translate to an average of 1 meter of shoreline erosion per year (Leatherman et al., 2000).

Two main methods of erosion control, hard and soft stabilization, have been developed and applied in an attempt to halt retreating shorelines and counteract erosional effects. Traditionally, hard stabilization, which involves the installation of permanent structures such as revetments, seawalls, offshore breakwaters, groynes and jetties, was the preferred approach in the world as well as in France. In addition to reducing flooding hazards, stabilizing the shoreline, and providing protection to upland properties, these coastal structures also trigger adverse environmental and aesthetical effects on the beach and even further away on adjacent shores (Hamm et al., 2002). Especially, the implementation of transverse structures, viz. port, jetty, and groynes, not only blocks the longshore sediment drifts, causes the deficit of sediment and erosion in the downstream of these structures (Jeudy De Grissac, 1975), but also interferes with visual beach amenity and aesthetics which are essential for maintaining the tourist value of many beaches (Ranasinghe et al., 2006). As an alternative to hard coastal structures, beach nourishment is considered worldwide to be an effective soft engineering approach to protect and restore the sandy beaches facing erosion as it often has less adverse effects on the surroundings. In France, during the period from 1962 to 1998, about 115 fills and refills have been performed in 26 sites adding to a total fill volume of about 12M m³ (Hamm et al., 2002). More specifically, thousands m³ per year has been used to nourish the sandy beaches along the eastern Giens tombolo, Hyères, from 2003 to 2010 (Table 21).

Beach nourishment comprises the placement of additional good quality sand on a beach, after sand is distributed across and along the shore by the action of waves and currents, thereby increasing the overall sediment budget. This morphological development consists of longshore spread-out of the fill sediments and cross-shore equilibrium, viz. the transformation of the construction profile to the dynamic equilibrium profile (Bodegom, 2004). Some of the main advantages associated with beach nourishment include: 1) a wider recreational beach; 2) protection to shoreline structures; 3) possible beneficial use for dredged material from nearby sources; and 4) the ability to switch to other beach management methods in the future (as long as increased coastal development does not preclude this) (NRC, 1995). However, there are some disadvantages of this method. Beach nourishment may not be cost-effective for

short stretches of beachfront, or those with high erosion rates (NRC, 1995). At Ceinturon beach in the eastern Giens tombolo, beach nourishment is carried out annually (Figure 37), but the shoreline has been experienced the retreat with an average erosion rate of -0.35 m/year (Capanni, 2011). Success rates for different replenished beaches can be highly variable and high cost overruns are not uncommon (Pilkey et al., 1996). Moreover, despite the presumption that beach nourishment is ecologically benign, it can also cause the negative impacts on marine biocenoses (Peterson et al., 2005). Beach fill usually results in excess of sediment in water, especially in rough sea conditions, which may have destroyed *Posidonia*-one of the most important endemic seagrass species in the Mediterranean Sea. For example, the construction of artificial beaches in Le Mourillon (Toulon, Var, France) directly caused the burial of 22 ha of *Posidonia*, followed by the indirect destruction of 10 hectares due to the increased turbidity of the water and the silting up of 27 additional hectares (Boudouresque et al., 2009). The efficacy and impacts of beach nourishment are likely to depend on the scale and timing of projects, as well as the source of sediment they use (Peterson et al., 2006).

Although nourishment is now widely practiced as the erosion control device of choice, there is still debate as to whether it is the best solution to the problem of beach erosion, and it can be considered a long-term solution to shoreline erosion as well as question about the efficiency of this method for the high eroded beaches (Finkl et al., 2005). In the present work, the numerical model is used to elucidate the effects of beach nourishment on hydrodynamic and sediment transport fields in Bona and Ceinturon beaches and predict the morphological behavior of these beaches after nourishment. Therefore, the effectiveness of beach nourishment method in protecting these two beaches could be uncovered and discussed more detail in Part 5.6.6 of Chapte 5.



Figure 37. Ceinturon beach before and after nourishment in 2008 (Capanni, 2011).

Table 21. Nourishment Chronology in the eastern Giens tombolo (OCEANIDE, 2010).

Date	Operation
1999-2003	- Pumping of approximately 8000 m ³ per year at the level of Jardin des mers
2003	- Renourishment of Bona beach (between 1000 and 3000 m ³)
May-June 2004	- Renourishment of the Bona beach from sediments dredged at La Capte (2500 m ³) - Reprofilng of the cord by supplying materials at the Plein-Sud beach (200 m linear) - Reprofilng of the Marquise beach cord from the dredged sediments of the port of Ayguade (3000 m ³)
December 2004	- Pumping of sand at the Jardin des Mers (11,700 m ³)
June 2005	- Renourishment of the Bona beach from the dredged sediments (1000 m ³) - Renourishment of the Potinière beach from dredged sediments (500 m ³) - Renourishment on the Plein Sud-Ceinturon area and the Northern Ceinturon from dredged sediments (4500 m ³) - Renourishment of the Marquise beach from dredged sediments (2500 m ³)
2006	- Renourishment of the beach of Bona (1000 m ³) - Renourishment of the beach of the boulevard of the waterfront from the sediments taken from the Jardin des Mers - Renourishment of the Marquise beach (1000 m ³)
2007	- Renourishment of the Marquise beach (1000 m ³)
June 2008	- Renourishment of the beach of Bona from the sediments taken from the Jardin des Mers (1200 m ³) - Renourishment of the "Plein-Sud" beach from the sediments taken from the Jardin des Mers (3000 m ³)
November 2008	- Renourishment of the sandy strand facing the "Plein-Sud": contribution of river sand (385 tonnes) and posidonia (unknown tonnage) to reconstitute the cordon
April 2009	- Renourishment of the "Plein-Sud" beach from the sediments taken from the Jardin des Mers (1500 m ³) - Renourishment with rolled, washed quarry sand on beach Bona (2935 tons)
Autumn 2010	- Renourishment of the beach of the Ceinturon from the sediments taken in the Jardin des Mers - Renourishment of Bona and La Potinière beach from rolled-washed sand (3500 T)

2.3.6.3. Coastal protection works

These works are intended to protect houses, roads, infrastructure, etc. from marine dynamic attacks whose effects are amplified in places such as La Capte beach, Ceinturon beach, by the topographical conditions related to coastal erosion. The frontal defense works and transverse structures are two types of coastal protection conducted along the eastern branch.

a. Frontal defense works

In the case of Hyères bay, the frontal defense works include a concrete retaining wall (seawall), reaches a slope of about 45° (La Capte (Figure 38a), and Pesquiers (Figure 38b), riprap revetment (e.g south of Hyères port (Figure 39a), Ceinturon beach (Figure 39b), Cabanes du Gapeau (Figure 39c)), the low walls made of wood (the area of La Badine-La Bergerie) (Figure 39d). The main objectives of these works are either form the seaward limit of a facility (walking pavement, road, etc.) or protect the shoreline and the backshore from the breaking waves. These two objectives are frequently conjunctive (SOGREAH, 1988a).



a. La Capte



b. Pesquiers

Figure 38. Seawalls along the eastern tombolo.

Unlike riprap of the eastern branch, those of the western branch were recently removed by the technical services. Indeed, the frontal structures often cause a total loss of emerged beach because the wave is reflected on the structure and produces a cross-shore current, which carries sediment seaward (Courtaud, 2000). These protection techniques are often complemented by transverse structures of groyne in order to maintain the linear beach.



a. Riprap in the south of Hyères port



b. Riprap in Ceinturon



c. Riprap in Cabanes du Gapeau



d. Wood wall in La Badine

Figure 39. Other revetments along the eastern tombolo.

b. Transverse structures

There are some types of transverse structure such as masonry, rockfill, sheet piles, wood, concrete, etc. In the case of the Hyères bay, all groynes are rockfill (Ceinturon, Ayguade, South Port of Hyères) (Figure 40) and have lengths between 30 and 50 m in most cases. They were placed perpendicular to the direction of the main longshore drift in order to trap one part of the longitudinal sediment transport and thus to promote the deposition of sediments between them. However, their effectiveness is now being challenged, particularly with regard to the observed significant erosion in downstream drift. At the beach of Ceinturon, DR 42 road, located immediately behind the beach is threatened by marine attacks because maintaining four groynes is called into question in the light of major damage observed in downstream drift (Capanni, 2011). Moreover, in Pansard beach, four groynes with the length of 30 m spaced from 70 to 80 m, their operation is limited due to the lack of sediment contributions by longshore transport and the role of the breakwater to the east that resulted in the disappearance of the beach.

Another type of transverse structures, jetty, which recalibrates the river mouth, has the same effects as the implementation of groynes. They oppose the longshore sediment transport. Consequently, a deposition zone is constituted upstream of the works while

the downstream sector is deficient. At the mouth of Roubaud, two jetties was constructed on both of two banks to facilitate south reorientation (late 1950s); then, a little perpendicular jetty (50m) has been added after the left bank jetty to solve problems of back-siltation of the mouth (1970) (Figure 41 (b)). Similarly, a jetty of 100 m long, oriented north-west/south-east, was built on the left bank of Gapeau river in the 1960s is to guide the southwest sediment transport but also to avoid the possible accumulation on the left bank of the mouth (Capanni, 2011) (Figure 41 (a)). In the 1970s, a jetty of 80 m long was also added perpendicular to the groyne of the upstream La Capte port to prevent the back-siltation in the entrance channel (Figure 41 (d)).



a. Groyne in the south of Hyères port



b. Groynes in Ceinturon beach

Figure 40. The groynes in the eastern tombolo.

2.3.6.4. The port works

Along Giens tombolo, there are several port facilities such as port of Hyères, Port of Miramar, Port of Pothuau, Aygaude port, and La Capte port (Figure 41). All these constructions port covers nearly 1,600 m, or 11% of the shoreline of the eastern branch of the tombolo (Courtaud, 2000). The successive extensions of these ports and recalibration of river mouths (Roubaud, La Capte) resulted in new coastal landscapes characterized by the advancing sea jetties and breakwaters. The advanced sea goynes and breakwaters modified the longshore current and thus disturbed the sediment transport. They force to accumulate the sediments in upstream of structures while causing the erosive areas in the downstream due to the shortage of sediment.



a. Port of Gapeau



b. Port of Aygaude (Roubaud)



c. Port of Hyères



d. Port of La Capte

Figure 41. The port facilities in the eastern Giens tombolo.

2.4. Conclusion

This chapter has described the study area with the available data for tides, storm surges, waves, winds, fluvial and sea currents, sediment characteristics, marine biocenosis, and bathymetric evolution. These data will be then used in the following chapter to model and validate the simulation procedure. It is noted that the data was acquired from many different sources, formatted in many different file types and are discontinuous over time. For instance, the wave data was not only acquired from the wave buoys of CANDHIS, but also extracted from the simulations of ANEMOC, PREVIMER, and ECMWF. Moreover, some data was not measured near the study area, viz. the water level data was taken from the Toulon tide gauge which is located up to 20 km westward to the Giens tombolo. This causes the time consuming and loss of much effort in order to treat, extract, and collect the data.

The study area is characterized by the micro tidal patterns with the maximum tidal range less than 30 cm. Hence, the waves have the largest impact on the morphological evolution of the study area. The storms usually occur in the winter along with the strong winds. The eastern part of Giens tombolo is mainly fed by the sediment of Gapeau river which is transported by the north-south and east-west longshore currents. On the other hand, the study area is mostly influenced by the southeastern and eastern waves. These waves accompanied with the presence of coastal structures, especially the shore-normal structures, has caused the erosion in Ceinturon, Bona, and Pesquiers beaches. It also is noticeable that the *Posidonia* seagrass covers almost the seabed in the study area, but its role in dissipating the wave heights, reducing the current speed, and trapping the sediment is still vague and question.

CHAPTER 3. METHODOLOGY

3.1. Introduction

Coastal morphological evolution is a complex process and affected by several factors such as environmental conditions (waves, tides, currents, wind, etc...), sediment properties, anthropogenic influence as well as their interaction. This evolution sometimes causes few unfavorable problems, typically phenomenon of coastal erosion. To avoid excessive or unwanted morphological effects on a specific area and to elucidate further about the mechanism of the coastal evolution, it is necessary to clarify the main factors controlling the morphological evolution of this area as well as their importance degree. This will support coastal engineers and researchers in finding the best protective solutions. Up to now, there are many theories and formulations uncovered and developed to predict the complex processes in the coastal area. However, only the theories of hydrodynamics, sediment transport and morphological evolution applied in the numerical simulation will be briefly described in this part.

Coastal morphodynamic changes take place at a range of time scales: millennial evolution as a result of sea level changes; long-term variability of several decades to a century related to climate change impacts; medium-term evolution of several years to a decade, associated with anthropogenic interventions and prevailing sedimentary processes; and short-term variability of days to a year induced by extreme events and seasonal changes (Karunarathna et al., 2012). In this work, only medium-term and short-term evolution is studied and discussed. Specifically, the medium-term shoreline evolution is investigated from 1973 to 2015, whereas the short term changes in beach morphology result from the storms (decadal, tri-decadal, semi-centennial and centennial) and seasonal effects (winter and summer). In addition to temporal scales, the morphological evolution of beaches along the eastern Giens tombolo is also evaluated in spatial scales. The 2D numerical models of MIKE21 are used to estimate the changes of nearshore bathymetry induced by the wave and current actions, while one line model of LITLINE is applied to predict the short-term shoreline variations. Moreover, beach profile evolution is detected by using EBP models. Separately, a combination of remote sensing, GIS techniques coupled with DSAS along with linear regression method is used to uncover and forecast the historical and future medium - term shoreline evolution along the eastern Giens tombolo. Based on beach morphological changes in both short and medium terms, the erosion and accretion areas are highlighted. This is a basis for designing the SBWs for protection of the areas threatened by coastal erosion. Finally, the MIKE21 and LITLINE models are used to estimate the efficiency and impact of these SBWs on the morphology of the eastern branch. The procedure detecting beach morphology in this work is recapped in Figure 42.

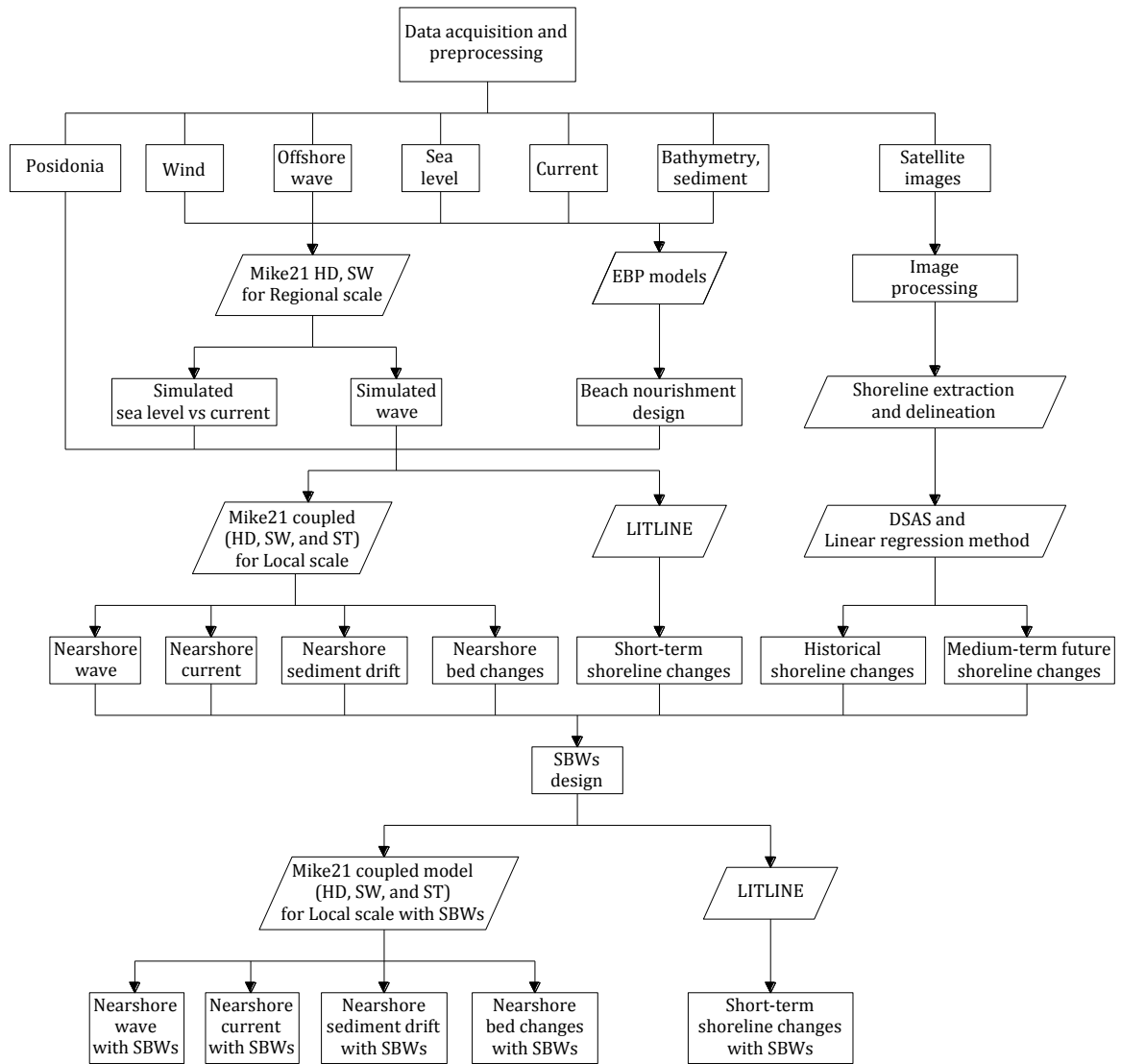


Figure 42. General flow diagram for the simulation of morphological changes in the eastern Giens tombolo.

3.2. Coastal morphodynamics

3.2.1. Coastal hydrodynamics

Coastal hydrodynamics mostly refers to some complex processes such as wave generation, wave propagation, wave transformation and dissipation, wave induced water level changes, wave-driven currents (long-shore and cross-shore currents), and wind and tidal actions (Kulkarni, 2013).

3.2.1.1. Wave transformation

When waves move into shallow water and approach a shoreline, due to influences of the seabed and various natural features or structures made by humans, they undergo a number of transformations such as refraction, diffraction, reflection, shoaling, bottom friction, wave-wave interactions, wind set-up, white-capping, and depth-induced wave breaking, etc. In addition, wave breaking can also occur at deep water when the waves are getting too steep. Many theories have been proposed taking into account these

processes in wave modeling and any combination can obtain satisfactory results based on the calibration of parameters. Airy's linear wave theory is one of the most famous researches that describes the wave transformations for simplified gravity waves (Kulkarni, 2013).

a. Wave-wave interactions

Wave-wave interactions result from nonlinear coupling of wave components and result in energy transfer from some wave component to other ones (Benassai, 2006). This process play an important role in the development of wind-driven waves in deep waters. The full expressions of these interactions have been formulated by Hasselmann (1962).

$$\begin{aligned}\vec{k}_1 + \vec{k}_2 &= \vec{k}_3 + \vec{k}_4 \\ \omega_1 + \omega_2 &= \omega_3 + \omega_4\end{aligned}\tag{3-1}$$

In which ω_j is the radian frequency and k_j is the wave number ($j = 1, 2, 3, 4$) which are related to each other through the dispersion relation ($\omega^2 = gk$).

The solution of the above-mentioned expressions is very complicated because it requires solving a 6-dimensional integral. To simulate these interactions, Hasselmann et al. (1985) proposed a simplified method, namely the discrete-interaction approximation, which considers the interactions of each wave component in the spectrum in only two quadruplets.

b. White-capping

White-capping is resulted from the limiting wave steepness, which occurs in deep water when the wave height becomes too large compared to the wavelength. It is a very complicated phenomenon which relates to highly nonlinear hydrodynamics on a wide range of scales, from gravity surface waves to capillary waves, down to turbulence (Holthuijsen, 2007). White-capping is not only important for the evolution of ocean waves; they also participate in the exchange of gas across the air-sea interface. Miche (1944) suggested this limiting steepness based on Stokes' wave theory, as follows:

$$\left[\frac{H}{L}\right]_{max} = 0.142 \tanh(kd) = 0.142 \text{ (for deep waters)} \approx \frac{1}{7}\tag{3-2}$$

Where, H_{max} and L_{max} are the limiting wave height and wave length respectively, k is the wave number and d is the water depth.

In wave models, white-capping is represented as a source term in the energy balance of the waves. This source function describing the dissipation due to white-capping is based on the theory of Hasselmann (1974). With the introduction of Janssen et al. (1989) description of wind input, it was realized that the dissipation source function needs to be adjusted in order to obtain a proper balance between the wind input and the dissipation at high frequencies. For the fully spectral formulation, the source function is given by:

$$S_{ds}(f, \theta) = -C_{ds} \left(\frac{\hat{\alpha}}{\hat{\alpha}_{PM}} \right)^m \left\{ (1-\delta) \frac{k}{k} + \delta \left(\frac{k}{k} \right)^2 \right\} \sigma E(f, \theta) \quad (3-3)$$

where, C_{ds} , δ and m are constants. Komen et al. (1996) suggested the default values of these parameters are 4.5, 0.5 and 4.0, respectively.

b. Refraction

Refraction is the phenomenon of wave direction changing due to depth-induced variations in the phase speed in the lateral direction. It usually occurs in transitional and shallow waters because waves propagate more slowly in shallow than in deep water. As a result, a bending of the wave crests so that they can approach the orientation of the bottom contours. In addition, wave orthogonal will also bend in order to converge or diverge at shore. This convergence or divergence of wave orthogonals along with the effects of wave shoaling induced local increases or decreases in wave energy as well as wave height will be defined by:

$$\frac{H_1}{H_o} = \sqrt{\frac{L_o}{2nL_1}} \sqrt{\frac{B_o}{B_1}} = \frac{H_1}{H'_o} \sqrt{\frac{B_o}{B}} \quad (3-4)$$

In which, H_o , L_o , and B_o are wave height, wave length and the distance between two adjacent wave orthogonals in deep water, respectively;

H_1 , L_1 , and B_1 are wave height, wavelength and the distance between two adjacent wave orthogonals in shallow water, respectively;

H'_o is the unrefracted wave height in deep water;

n is the ratio of wave group to phase celerity.

The ratio of the distance between two adjacent wave rays on deep water to the one on the shore defines the refraction coefficient.

$$K_r = \left(\frac{B_o}{B} \right)^{\frac{1}{2}} = \left[\frac{1 - \sin^2 \alpha_o \tanh^2 kd}{\cos^2 \alpha_o} \right]^{\frac{1}{4}} \quad (3-5)$$

Where d is the deep water depth;

k is wave number;

α_o is the deep water incidence angle.

c. Diffraction

Diffraction is caused by natural barriers (island, outcrop, headland, etc.) or man-made structures (breakwaters). In these cases, wave fronts tend to move around the barrier or structures and penetrate into the sheltered area. A qualitative understanding of this phenomenon is indispensable for evaluating the wave action behind breakwaters, in harbor basin, large offshore structures, and around islands, especially in some zones which tombolo has been formatted. It is a process by which energy transmittances laterally perpendicular to the main direction of wave propagation (Benassai, 2006).

Diffraction can be modeled using the phase-decoupled refraction-diffraction approximation proposed by Holthuijsen et al. (2003). The approximation is based on the mild-slope equation for refraction and diffraction, omitting phase information. In the presence of diffraction, the magnitude of the wave number, k , (the gradient of the phase function of a harmonic wave) is given by:

$$k^2 = \kappa^2(1 + \delta_a) \quad (3-6)$$

where κ is the separation parameter determined from linear wave theory and δ_a is a diffraction parameter defined by:

$$\delta_a = \frac{\nabla \cdot (c c_g \nabla a)}{\kappa^2 c c_g a} \quad (3-7)$$

Here c and c_g are the phase velocity and group velocity, respectively, without diffraction effects and a is the wave amplitude. Now the phase velocity, C , and the group velocity, C_g , in the presence of diffraction are given by:

$$C = \frac{\sigma}{k} = \frac{\sigma}{\kappa} \frac{\kappa}{k} = \frac{c}{\sqrt{1 + \delta_a}} \quad (3-8)$$

$$C_g = c_g \frac{\kappa}{k} = c_g \sqrt{1 + \delta_a} \quad (3-9)$$

For wave propagation over slowly varying depths and currents, the diffraction-corrected propagation velocities ($C_x, C_y, C_\sigma, C_\theta$) of a wave group in the four-dimensional phase space \vec{x}, σ and θ are given by:

$$(C_x, C_y) = \vec{C}_g + \vec{U} = \vec{c}_g(1 + \delta_a) + \vec{U} \quad (3-10)$$

$$C_\sigma = \frac{\partial \sigma}{\partial d} \left[\frac{\partial d}{\partial t} + \vec{U} \cdot \nabla_x d \right] - C_g \vec{\kappa} \cdot \frac{\partial \vec{U}}{\partial s} \quad (3-11)$$

$$C_\theta = \left[\left(\left(\frac{\sqrt{1 + \delta_a}}{\kappa} \frac{\partial \sigma}{\partial d} \frac{\partial d}{\partial m} \right) - \frac{C_g}{2(1 + \delta_a)} \frac{\partial \delta_a}{\partial m} \right) + \frac{\vec{\kappa}}{\kappa} \cdot \frac{\partial \vec{U}}{\partial m} \right] \quad (3-12)$$

Following the approach by Holthuijsen et al. (2003), the wave amplitude is replaced by the square root of the directional integrated spectral energy density:

$$A(o) = \sqrt{\int_0^{2\pi} E(\sigma, \theta) d\theta} \quad (3-13)$$

d. Shoaling

Shoaling is the deformation of waves when they travel from deep waters to shallow waters. It starts occurring if the water depth becomes less than about half the

wavelength. This phenomenon causes a reduction in the wave propagation velocity as well as shortening and steeping of the waves.

The ratio of wave height in intermediate depth H to the deep-water wave height H_0 defines the shoaling coefficient:

$$K_s = \frac{H}{H_0} = \left(\frac{2 \cosh^2 kd}{2kd + \sinh 2kd} \right)^{\frac{1}{2}} \quad (3-14)$$

e. Bottom friction

Bottom friction causes energy dissipation and thus wave height reduction as the water depth becomes shallower. It is a critical factor influencing in the coastal evolution, especially in large shallow water areas. Therefore, many different theories have been developed to predict the formulation for modeling bottom friction.

The rate of dissipation due to bottom friction is given by

$$S_{bot}(f, \theta) = -(C_f + f_c (\bar{u}, \bar{k})/k) \frac{k}{\sinh 2kd} E(f, \theta) \quad (3-15)$$

Where, C_f is a friction coefficient, k is the wave number, d is water depth, f_c is the friction coefficient for the current and u is the current velocity. The coefficient C_f is typically 0.001-0.01 m/s depending on the bed and flow conditions (Komen et al., 1996). The default value for f_c is 0 corresponding to excluding the effect of the current on the bottom friction.

Four models for determination of the possibilities for the dissipation coefficient are implemented:

- 1) A constant friction coefficient C_f , Komen et al. (1996) have shown that the mean JONSWAP value of $C_f = 2 * 0.038 / g = 0.0077$ m/s is adequate for moderate storms. The default value for C_f is 0.0077 m/s.
- 2) A constant friction factor C_f in which the friction coefficient is calculated as

$$C_f = f_w u_b \quad (3-16)$$

where u_b is the rms wave orbital velocity at the bottom given by

$$u_b = \left[2 \int_{f_1}^{f_{max}} \int_{\theta} \frac{\bar{\sigma}^2}{\sinh^2(kh)} E(f, \theta) d\theta df \right]^{1/2} \quad (3-17)$$

The default value for f_w is $0.015 * 2^{1/2} = 0.021$.

- 3) A constant geometric roughness size k_N , as suggested by Weber (1991) in which the friction coefficient is calculated by Eq.(3-16) and the friction factor is calculated using the expression of Jonsson et al. (1976)

$$f_w = e^{-5.977+5.213(a_b/k_N)^{-0.194}}; a_b/k_N \geq 2.016389 \quad (3-18)$$

$$f_w = 0.24; a_b/k_N < 2.016389$$

Here a_b is the orbital displacement at the bottom given by

$$a_b = \left[2 \int_{f_1}^{f_{\max}} \int_{\theta} \frac{1}{\sinh^2(kh)} E(f, \theta) d\theta df \right]^{1/2} \quad (3-19)$$

The default value for k_N is 0.04 m. This value was suggested by (Weber, 1991) as being compatible with the flow conditions for a range of swell and wind sea spectra.

4) A constant median sediment size D_{50} , in which the bed is modeled as a mobile bed. The empirical expressions of Nielsen (1979) is used which is based on field measurements. Thereafter, the bed roughness is calculated using the expression by Swart (1976). Finally, the friction coefficient is computed as the product of the wave friction factor (using the expression of Jonsson et al. (1966)) and the bottom orbital velocity. The default value for D_{50} is 0.00025 mm.

h. Depth-induced wave breaking

Meanwhile waves propagate into shallower water, the process of shoaling results in increasing wave heights. This process cannot continue because of energy dissipation in the surf zone and the wave height can no longer be supported by the water depth. As a result, the wave breaks. According to Miche (1944), the wave breaking will typically take place where the wave height is approximately 0.78 times the local water depth.

Breaking waves are generally divided into three main types such as spilling, plunging, and surging. Spilling occurs when steep waves propagate over flat shore faces. Spilling breaking is a gradual breaking, which takes place as foam bore on the front topside of wave over a distance of from 6 to 7 wavelengths. On the other hand, plunging is the form of breaking where the upper part of the wave breaks over its own lower part in one big splash whereby most of the energy is lost. This type of breaking normally appears in cases of moderately steep waves on moderately sloping shore faces. Regarding surging, it will take place when relatively long waves meet steep shore faces (Fredsoe et al., 1992).

The formulation of wave breaking is based on the breaking model by Battjes et al. (1978). Eldeberky et al. (1996) proposed a spectral version of the breaking model, where the spectral shape was not influenced by breaking. The source term due to depth-induced breaking can be written:

$$S_{suff}(\sigma, \theta) = -\frac{\alpha Q_b \bar{\sigma} H_m^2}{8\pi} \frac{E(\sigma, \theta)}{E_{tot}} \quad (3-20)$$

where, $\alpha = 1.0$ is a calibration constant, Q_b is the fraction of breaking wave, $\bar{\sigma}$ is the mean relative frequency, E_{tot} is total wave energy and $H_m = \gamma_d$ is the maximum wave

height. Here γ is the free breaking parameter (ratio of wave height to water depth). Recently, Ruessink et al. (2003) have presented a new empirical form for γ , where γ is determined as a function of the product of the local wave number k and the water depth d .

$$\gamma = 0.76kd + 0.2 \quad (3-21)$$

g. Wind set-up

Wind action drives onshore and offshore the surface waters and is responsible for the water level rise (wind set-up) in restricted areas subject to wind stress. While wind drives water offshore, deep waters move onshore, and vice versa. The wind stress is given by the following empirical relation:

$$\bar{\tau}_b = \rho_a c_d \overline{u_w} |\overline{u_w}| \quad (3-22)$$

where, ρ_a is the density of air; c_d is the drag coefficient of air; and $\overline{u_w} = (u_w, v_w)$ is the wind speed at 10 m above sea surface.

The friction velocity associated with the surface stress is given by:

$$U_{\tau} = \sqrt{\frac{\rho_a c_d |\overline{u_w}|^2}{\rho_o}} \quad (3-23)$$

The drag coefficient can either be a constant value or depend on the wind speed. The empirical formula proposed by (Wu, 1980, 1994) is used for the parameterization of the drag coefficient.

$$c_d = \begin{cases} c_a & w_{10} < w_a \\ c_a + \frac{c_b - c_a}{w_b - w_a} (w_{10} - w_a) & w_a \leq w < w_b \\ c_b & w_{10} \geq w_b \end{cases} \quad (3-24)$$

where, c_a , c_b , w_a and w_b are empirical factors and w_{10} is the wind velocity 10 m above the sea surface. The default values for the empirical factors are $c_a = 1.255 \times 10^{-3}$, $c_b = 2.245 \times 10^{-3}$, $w_a = 7$ m/s and $w_b = 25$ m/s. These give generally good results for open sea applications.

3.2.1.2. Wave energy balance

To determine the changes of above-mentioned wave transformations, the law of conservation of wave energy is applied to the system. When a wave propagates through a fluid, part of its energy will be transmitted throughout the fluid. The rate of energy transfer matches the group celerity C_g which is the propagation velocity of the wave packet obtained by the envelope of the group of random waves (Benassai, 2006). The total of a wave consists of two components: potential energy resulting from the displacement of the free surface and kinetic energy due to the motion of water particles throughout the fluid and can be estimated by:

$$E = \frac{1}{8} \rho g H_{rms}^2 \quad (3-25)$$

Where ρ is the density of the fluid and H_{rms} is the root-mean-square wave height.

According to Holthuijsen (2007), the evolution of the energy density of each wave can be obtained by integrating an energy evolution equation while propagating with the group velocity along a wave ray:

$$\frac{\partial E}{\partial t} + \frac{\partial}{\partial x} [E c_g \cos(\theta)] + \frac{\partial}{\partial y} [E c_g \sin(\theta)] = -D_\omega - D_f \quad (3-26)$$

Where D_ω and D_f represent wave energy dissipation due to wave breaking and bottom friction respectively. This simple equation is useful to describe the propagation and dissipation of the total wave energy for a give wave direction θ .

However, in practice, waves always present along with the currents. Therefore, the conservation of energy equation cannot describe the transfer between the waves and currents (Kulkarni, 2013). In this case, wave action density will be used instead of energy balance and be defined as follows:

$$N(\sigma, \theta) = \frac{E(\sigma, \theta)}{\sigma} \quad (3-27)$$

In which σ is the angular frequency and θ is the wave direction. The wave action density spectrum varies in time and space and can be defined by two wave phase parameters such as wave number magnitude and wave direction and angular frequency. The governing equation is the wave action balance equation formulated in either Cartesian or spherical co-ordinates (Komen et al., 1996; Young, 1999). In Cartesian coordinates the equation can be given as below:

$$\frac{\partial N}{\partial t} + \nabla \cdot (\vec{v} N) = \frac{S}{\sigma} \quad (3-28)$$

where, $N(x, y, \sigma, \theta, t)$ is the action density, t is the time, $\vec{x} = (x, y)$ is Cartesian co-ordinates, $\vec{v} = (c_x, c_y, c_\sigma, c_\theta)$ is the propagation velocity of a wave group in the four-dimensional phase space \vec{x}, σ and θ and S is the source term for the energy balance equation. ∇ is the four-dimensional differential operator in the \vec{x}, σ, θ – space. The four characteristic propagation speeds are given by:

$$(c_x, c_y) = \frac{d\vec{x}}{dt} = \vec{c}_g + \vec{U} \quad (3-29)$$

$$c_\sigma = \frac{d\sigma}{dt} = \frac{\partial \sigma}{\partial d} \left[\frac{\partial d}{\partial t} + \vec{U} \cdot \nabla_x d \right] - c_g \vec{k} \cdot \frac{\partial \vec{U}}{\partial s} \quad (3-30)$$

$$c_\theta = \frac{d\theta}{dt} = -\frac{1}{k} \left[\frac{\partial \sigma}{\partial d} \frac{\partial d}{\partial m} + \vec{k} \cdot \frac{\partial \vec{U}}{\partial m} \right] \quad (3-31)$$

Here, s is the space coordinate in wave direction θ , and m is a coordinate perpendicular to s . $\nabla_{\bar{x}}$ is the 2D differential operator in the \bar{x} -space.

3.2.1.3. Wave spectral analysis

Wind-driven ocean waves have irregular wave heights and periods, caused by the irregular nature of wind. Due to this irregular nature, the sea surface is continually varying. Therefore, a deterministic approach to describe the sea surface is not feasible. To illustrate the irregularity of the surface with many frequencies and amplitudes with different phases, wave spectral analysis is used as a statistical representation of the sea state. The wave spectral analysis method determines the distribution of wave energy and average statistics for each wave frequency by converting time series of the wave record into a wave spectrum. The transformation of the time domain is generally performed with a Fast Fourier Transform (Roelvink et al., 2012).

There are two main types of wave spectra such as directional wave spectrum and frequency spectrum. A directional wave spectrum is a plot of the energy in these component waves plotted as a function of wave frequency f and direction θ . If the wave energy is plotted as a function of only frequency, without considering wave direction, this is frequency spectrum (Sorensen, 2006). Hence, a frequency spectrum of a wave field represents the distribution of waves in frequency domain. If the spectrum is narrow, this means that the wave field is more regular. For larger and longer waves, the spectrum shifts towards the lower frequencies and contains more energy. The spectral peak is the frequency at which most of the energy is concentrated. On the other hand, a directional wave spectrum illustrates the distributions of phases over the frequency range. The wind-driven waves generate, develop, and propagate in the direction of the wind. Directional spectrum can be plotted by using some formulations, but most common of which is the cosine squared and $\cos^2 2s$ distribution. The wave spectral analysis will uncover the dominant frequencies and directions in the wave record (Kulkarni, 2013).

Measured wave spectra in the sea can be approximated by various semi-empirical forms. The two most widely used forms are the Pierson-Moskowitz spectrum, which was developed for fully developed seas in the Northern Atlantic Ocean generated by local winds, and the JONSWAP spectrum, which was developed by the Joint North Sea Wave Project for the limited fetch North Sea and is used extensively by the offshore industry. The JONSWAP spectrum is significant because it was developed taking into consideration the growth of waves over a limited fetch and wave attenuation in shallow water. Over 2,000 spectra were measured and a least squares method was used to obtain the spectral formulation assuming conditions like near uniform winds (Tchet, 2005). Both two spectra can be described by the following equation in terms of the significant wave height H_s and the radian frequency $\omega_p = 2\pi T$ at the peak of the spectrum:

$$S_{\eta}(\omega) = B \left(\frac{H_s}{4} \right)^2 \frac{\omega_p^4}{\omega^5} \exp \left[\frac{-5}{4} \left(\frac{\omega}{\omega_p} \right)^{-4} \right] \gamma \phi \left(\frac{\omega}{\omega_p} \right) \quad (3-32)$$

$$\phi \left(\frac{\omega}{\omega_p} \right) = \exp \left[-\frac{1}{2\beta^2} \left(\frac{\omega}{\omega_p} - 1 \right)^2 \right] \quad (3-33)$$

For Pierson-Moskowitz: $B = 5, \gamma = 1$; For JONSWAP: $B = 3.29, \gamma = 3.3$

$\beta = 0.07$ for $\omega \leq \omega_p$

$\beta = 0.09$ for $\omega > \omega_p$

Many flowing important characteristics of the sea state, e.g. mean wave height H_m , significant wave height H_s , root-mean-square wave height H_{rms} , mean zero-crossing period T_o , mean wave period T_m , etc... can be represented and calculated from a spectrum with the assumption that the random surface is supposed to be Gaussian.

3.2.1.4. Wave-driven set-up, set-down, and currents

When waves travel across the ocean surface, they transport not only energy, but also carry momentum. This momentum transport is equivalent to radiation stress and horizontal variations in this stress act as forces on the water column generating nearshore currents as well as changing the mean sea level, particularly in the surf zone (Holthuijsen, 2007). There are two current systems, whose flow structures are mostly horizontal, alongshore currents caused by the shear radiation stresses (S_{xy} and S_{yx}) and cell-like circulations triggered by the normal radiation stresses (S_{xx} and S_{yy}).

a. Radiation stresses, wave set-up and set-down

The presence of waves will result in an excess flow of momentum, which is defined as the radiation stresses (Longuet-Higgins et al., 1964). This flux of momentum is formed by two contributions: one due to the wave-driven velocities of the water particles and another one due to the pressure.

$$\begin{aligned} S_{xx} &= \int_{-h_0}^{\eta} (\rho u_x) u_x dz + \int_{-h_0}^{\eta} p_{wave} dz \\ S_{yy} &= \int_{-h_0}^{\eta} (\rho u_y) u_y dz + \int_{-h_0}^{\eta} p_{wave} dz \\ S_{xy} &= \int_{-h_0}^{\eta} (\rho u_x) u_y + \tau_{xy} dz = \int_{-h_0}^{\eta} (\rho u_x) u_y dz \\ S_{yx} &= \int_{-h_0}^{\eta} (\rho u_y) u_x dz \end{aligned} \quad (3-34)$$

Where, u_x and u_y are the water particle velocities in x and y direction respectively, p_{wave} is the hydrostatic pressure component of the wave and S_{xx} and S_{yy} are the normal stresses that include the hydrostatic pressure in the water column. S_{xy} and S_{yx} are the shear stress components of the wave.

The corresponding wave-induced radiation force per unit horizontal surface area in the x -direction is defined as follows (Holthuijsen, 2007):

$$F_x = -\frac{\partial S_{xx}}{\partial x} - \frac{\partial S_{xy}}{\partial y} \quad (3-35)$$

Similarly for the y -direction:

$$F_y = -\frac{\partial S_{yy}}{\partial y} - \frac{\partial S_{yx}}{\partial x} \quad (3-36)$$

These forces generally result changes in the mean water level (set-up and set-down).

b. Nearshore currents

The alongshore current, sometimes called the littoral current, is generated by the shore-parallel component of the radiation stress associated with the breaking process for obliquely incoming waves. This current, which is parallel to the shoreline, works with waves to transport large volumes of sediment along the shoreline. It greatly effects on the coastal morphology.

As above-mentioned, waves transport water when moving to the shoreline. This will result in an increase in water level at the shore called set-up. Basically, set-up is similar to storm surge, but smaller in scale and is limited to a narrow zone along the shore. In the specific conditions, the set-up produces seaward flowing currents that are quite narrow and that create circulation cells. These currents are called rip currents (Davis et al., 2009). Rip currents are concentrated within the surface layer, thus playing in main role in seaward transport of suspended sediment.

Another nearshore circulation phenomenon that is caused by landward movement of water and set-up is called cross-shore currents or undertow. When the waves are breaking, water is also transported in surface rollers towards the coast. Due to limiting of shoreline, the net flow must be zero; hence, there must be a return flow (undertow) under the wave trough level in the offshore direction to compensate for the propagating flux, which is concentrated near the bed (Benassai, 2006). This undertow current is responsible for seaward movement of sediment. It is considered as the primary factor causing coastal erosion, especially during heavy storms.

3.2.1.5. Shallow water equation

As the vertical accelerations in the shallow water can be ignored, the wave profile and its propagation can be computed with vertically integrated mass- and momentum-balance equations (Holthuijsen, 2007).

Integration of the horizontal momentum equations and the continuity equation over depth $h = \eta + d$ the following 2D shallow water equations are obtained:

* Continuity equation:

$$\frac{\partial h}{\partial t} + \frac{\partial h\bar{u}}{\partial x} + \frac{\partial h\bar{v}}{\partial y} = hS \quad (3-37)$$

* Momentum equations:

$$\begin{aligned} \frac{\partial h\bar{u}}{\partial t} + \frac{\partial h\bar{u}^2}{\partial x} + \frac{\partial h\bar{v}\bar{u}}{\partial y} = f\bar{v}h - gh\frac{\partial\eta}{\partial x} - \frac{h}{\rho_o}\frac{\partial p_a}{\partial x} - \frac{gh^2}{2\rho_o}\frac{\partial\rho}{\partial x} + \frac{\tau_{sx}}{\rho_o} - \frac{\tau_{bx}}{\rho_o} - \\ \frac{1}{\rho_o}\left(\frac{\partial s_{xx}}{\partial x} + \frac{\partial s_{xy}}{\partial y}\right) + \frac{\partial}{\partial x}(hT_{xx}) + \frac{\partial}{\partial y}(hT_{xy}) + hu_sS \end{aligned} \quad (3-38)$$

$$\begin{aligned} \frac{\partial h\bar{v}}{\partial t} + \frac{\partial h\bar{v}^2}{\partial y} + \frac{\partial h\bar{v}\bar{u}}{\partial x} = -f\bar{u}h - gh\frac{\partial\eta}{\partial y} - \frac{h}{\rho_o}\frac{\partial p_a}{\partial y} - \frac{gh^2}{2\rho_o}\frac{\partial\rho}{\partial y} + \frac{\tau_{sy}}{\rho_o} - \frac{\tau_{by}}{\rho_o} - \\ \frac{1}{\rho_o}\left(\frac{\partial s_{yx}}{\partial x} + \frac{\partial s_{yy}}{\partial y}\right) + \frac{\partial}{\partial x}(hT_{xy}) + \frac{\partial}{\partial y}(hT_{yy}) + hv_sS \end{aligned} \quad (3-39)$$

Where

t is the time and x , y and z are the Cartesian co-ordinates;

η is the surface elevation;

d is the still water depth;

$h = \eta + d$ is the total water depth;

\bar{u} and \bar{v} are the velocity components in the x and y direction;

$f = 2\Omega\sin\varphi$ is the Coriolis parameter (Ω is the angular rate of revolution and φ the geographic latitude);

g is the acceleration due to gravity;

ρ is the density of water and ρ_o is the reference density of water;

s_{xx} , s_{xy} , s_{yx} and s_{yy} are components of the radiation stress tensor;

p_a is the atmospheric pressure;

S is the magnitude of the discharge due to point sources and

(u_s, v_s) is the velocity by which the water is discharged into the ambient water.

The over bar indicates a depth average value. For example, \bar{u} and \bar{v} are the depth-averaged velocities defined by

$$h\bar{u} = \int_{-d}^{\eta} u dz, \quad h\bar{v} = \int_{-d}^{\eta} v dz \quad (3-40)$$

The lateral stresses T_{ij} include viscous friction, turbulent friction and differential advection. They are estimated using an eddy viscosity formulation based on the depth average velocity gradients.

$$T_{xx} = 2A \frac{\partial \bar{u}}{\partial x}, \quad T_{xy} = A \left(\frac{\partial \bar{u}}{\partial y} + \frac{\partial \bar{v}}{\partial x} \right), \quad T_{yy} = 2A \frac{\partial \bar{v}}{\partial y} \quad (3-41)$$

3.2.2. Sediment transport

Sediment transport is the movement of sediment particles mainly due to the action of waves and currents. It is also an essential factor causing the morphological changes. The sediment transport process usually occurs more in shallow water than in the deep sea, because surface waves can affect the seabed and currents are typically stronger than in the open ocean. This process depends not only on hydrodynamic conditions, but also on the characteristics of sediment (grain size, grain density, porosity, fall velocity, etc.) as well as the feature of seabed (bottom stress).

The interaction between hydrodynamic factors and sediment transport is very complex and more difficult to predict and simulate. It is common to divide the sediment transport modes into three main parts: bed load, suspended load and wash load. The wash load consists of very fine particles which are moved by the water and which normally are not represented in the bed. The knowledge of the material composition does not allow to estimate the rate of wash load transport (Fredsoe et al., 1992). Therefore, to reduce complexity, only bed load and suspended load are taken into account during the transport.

3.2.2.1. Sediment properties

a. Grain size diameter

Sediment grains are normally classified according to their diameter into clays, silts, sands, granules, pebbles, cobbles and boulders. Clays and silts are generally called mud, and granules, pebbles and cobbles are collectively called gravel (Soulsby, 1997). Size of sediment is determined through the phi-scale as follows:

$$\phi = -\log_2 d \quad (3-42)$$

$$d = 2^{-\phi} \quad (3-43)$$

Where d is the grain diameter in millimeters, and \log_2 is the logarithm to base 2. ϕ and d can be converted together by using the most commonly used classification of the Wentworth scale (Table 22).

Table 22. Wentworth grain size scale.

Class Name		Millimeters	Micrometers	Phi values
Gravel	Boulder	>256		<-8
	Cobble	64-256		-6
	Pebble	4-64		-2
	Granule	2-4		-1
Sand	Very coarse sand	1-2	1000-2000	0
	Coarse sand	0.5-1	500-1000	1
	Medium sand	0.25-0.5	250-500	2
	Fine sand	0.125-0.25	125-250	3
	Very fine sand	0.0625-0.125	62.5-125	4
Mud	Coarse silt	0.031-0.0625	31-62.5	5
	Medium silt	0.0156-0.031	15.6-31	6
	Fine silt	0.0078-0.0156	7.8-15.6	7
	Very fine silt	0.0039-0.0078	3.9-7.8	8
	Clay	0.00006-0.0039	0.06-3.9	14

Both grain size diameter and grading of the sediment are defined in terms of a cumulative distribution of grain sizes. The grain size distribution is usually presented as a cumulative curve showing the percentage by mass of grains smaller than d , versus d . In general, the notation d_n indicates the grain diameter for which $n\%$ of the grains by mass is finer. However, the sediment is normally characterized by its median sieve diameter d_{50} (Soulsby, 1997). Other percentiles are commonly used such as: d_{10} , d_{16} , d_{84} , d_{90} . The spread of sizes is expressed by the d_{10} and d_{90} or, alternatively, d_{16} and d_{84} . A commonly used measure of the degree of grading of a sediment is the geometric standard deviation σ_g :

$$\sigma_g = \sqrt{\frac{d_{84}}{d_{16}}} \quad (3-44)$$

Sediment is classed as well sorted if $d_{84}/d_{16} < 2$ (or $d_{90}/d_{10} < 2.4$), whereas if it has ratio of $d_{84}/d_{16} > 16$, then it is well mixed (Soulsby, 1997).

b. Grain density and porosity

The grain density, ρ_s , depends on the mineral content of the sediment and for sands it is approximately equal to $\rho_s = 2650\text{kg/m}^3$. The specific gravity is defined as the ratio of the sediment density and the fluid density, $s = \rho_s/\rho$. Apart from the grain density, the porosity (concentration) of the bed material is also an important characteristic of sediment, which is defined as the amount of pore spaces in the volume. It is often related

to the deposition history of the sediment bed and depends on the angle of internal friction (Van Rijn, 1993). Some values of porosity can be referred according to Table 23.

Table 23. Porosity of natural sand beds (Soulsby, 1997).

	Well-sorted	Average	Well-mixed
Loosely packed	0.46	0.43	0.38
Average	0.42	0.40	0.33
Densely packed	0.40	0.37	0.30

c. Fall velocity

In order to describe suspended sediment transport, it is important to understand the behavior of suspended sand grains in flow through sediment fall velocity. The fall velocity of a particle, w , depends on grain and fluid properties (i.e. grain size, grain density, fluid density, flow viscosity rate and turbulence), giving:

$$w = \sqrt{\frac{4(s-1)gd_{50}}{3C_D}} \quad (3-45)$$

Where d_{50} is grain diameter,
 s is specific gravity,
 C_D is the drag coefficient,
 g is acceleration of gravity.

The fall velocity can also be calculated as a function of the median grain size D_{50} as follows (Rubey, 1933):

$$w = \sqrt{g(s-1)d_{50}} \cdot \left(\sqrt{\frac{2}{3} + \frac{36\nu^2}{g(s-1)d_{50}^3}} - \sqrt{\frac{36\nu^2}{g(s-1)d_{50}^3}} \right) \quad (3-46)$$

Where ν is the kinematic viscosity found by:

$$\nu = (1.78 - 0.0570812T + 0.00106177T^2 - 8.27141 \cdot 10^{-6}T^3)10^{-6} \quad (3-47)$$

Where T is the water temperature in degrees Celsius.

d. Critical shear stress

Sediment particle transport will occur when a large enough force, or shear stress, from water particle movement imposes on the grains. The point which sediment initially moved will be described by the critical shear stress. The critical shear stress was investigated by Shields et al. (1936) in terms of the ratio of the submerged particle weight and the friction coefficient. The critical Shields stress, θ_{cr} , is defined as:

$$\theta_{cr} = \frac{\tau_{cr}}{g(\rho_s - \rho)d} \quad (3-48)$$

In which τ_{cr} is threshold bed shear stress. For sand positioned smoothly on a flatbed in hydraulic rough regime, θ_{cr} varies from 0.04 to 0.06 (Van Rijn, 1993).

3.2.2.2. Bottom Stress

The bottom shear stress $\bar{\tau}_b = (\tau_{bx}, \tau_{by})$ or bottom friction is an important quantity for sediment transport because it represents the flow-driven force acting on sand grains on the bed. It is related to the depth-averaged current speed $\bar{u}_b = (u_b, v_b)$ through the drag coefficient C_D and is determined by a following quadratic friction law:

$$\frac{\bar{\tau}_b}{\rho_o} = C_D \bar{u}_b |\bar{u}_b| \quad (3-49)$$

Where, ρ is the density of fluid. According to Soulsby (1997), alternative coefficients used in hydraulic and coastal engineering include the Chezy number, C , or the Manning number, M . These coefficients can be related mathematically to C_D via the relationship:

$$C_D = \frac{g}{C^2} = \frac{g}{(M \cdot d^{1/6})^2} \quad (3-50)$$

In the case of sandy or rocky bed, the drag coefficient is determined by the bed roughness length z_o and the water depth d , as follows:

$$C_D = \left[\frac{\kappa}{1 + \ln\left(\frac{z_o}{d}\right)} \right]^2 \quad (3-51)$$

Where κ is the von Karman constant and can be estimated as $\kappa = 0.4$;

z_o is the bed roughness length, $z_o = \frac{k_s}{30}$;

k_s is Nikuradse roughness height and can be determined according to the relationship with the median grain diameter of sand (D_{50}) (Soulsby, 1997) as approximately.

$$k_s = 2.5 \times D_{50} \quad (3-52)$$

According to the MIKE 21 manual, the relationship between the Nikuradse roughness height, k_s and the Manning number can be estimated using:

$$M = \frac{25.4}{k_s^{1/6}} \quad (3-53)$$

3.2.2.3. Bed load and suspended load transport

The transport of bed material particles due to a flow of water can be in the form of bed load and suspended load, depending on the size of the bed sediment and the flow conditions. The sediment transport is calculated as:

$$q_t = q_b + q_s \quad (3-54)$$

Where q_t is the total sediment transport, q_b is the bed load transport and q_s is the sediment transport in suspension.

a. Bed load transport

The bed load is defined as the part of total load that is in more or less continuous contact with the bed during the transport. It basically includes grains that roll, slide, or

jump along the bed. Therefore, the bed load must be determined almost exclusively by the effective bed shear acting directly on the sand surface (Fredsoe et al., 1992).

The dimensional bed load transport Φ_b is found by a deterministic approach of Engelund et al. (1976):

$$\Phi_b = 5p(\sqrt{\theta'} - 0,7\sqrt{\theta_c}) \quad (3-55)$$

Where p is the probability that all the particles of a layer are moving, given by:

$$p = \left[1 + \left(\frac{\frac{\pi}{6}\beta}{\theta' - \theta_c} \right)^4 \right]^{-1/4} \quad (3-56)$$

θ' is Shield's parameter determined for a plane bed and is determined as follows:

$$\theta' = \frac{U_f'^2}{(s-1)gd} \quad (3-57)$$

θ_c is the critical Shields parameter. For the general case where the flow is at an angle ψ to the slope β , it is given by:

$$\theta_c = \theta_{c,0} \left(\frac{-\cos \psi \sin \beta + \sqrt{\mu_s^2 \cos^2 \beta - \sin^2 \psi \sin^2 \beta}}{\mu_s} \right) \quad (3-58)$$

Where μ_s is a static friction coefficient ($\mu_s = \tan \phi_s$, $\phi_s =$ angle of repose) and $\theta_{c,0}$ is the critical Shields parameter for a plane bed.

From Φ_b the following time-averaged quantities are calculated:

$$\Phi_{b1} = \frac{1}{T} \int_0^T \Phi_b(t) \cos(\phi(t)) dt \quad (3-59)$$

$$\Phi_{b2} = \frac{1}{T} \int_0^T \Phi_b(t) \sin(\phi(t)) dt \quad (3-60)$$

$$q_{b1} = \Phi_{b1} \cdot \sqrt{(s-1)gd_{50}^3} \quad (3-61)$$

$$q_{b2} = \Phi_{b2} \cdot \sqrt{(s-1)gd_{50}^3} \quad (3-62)$$

Where:

$\phi(t)$ is the direction of the instantaneous flow ,

Φ_{b1} is the dimension less bed load in the mean current direction,

Φ_{b2} is the dimension less bed load normal to the mean current direction,

q_{b1} is the bed load in the mean current direction,

q_{b2} is the bed load normal to the mean current direction.

The presence of ripples does not influence the bed transport. This is the reason why Φ_b , p and λ are evaluated based on θ' .

b. Suspended load transport

When the value of the bed-shear velocity exceeds the particle fall velocity, the sediment particles can be lifted to a level at which the upward turbulent forces will be higher than the submerged particle weight (Van Rijn, 1993). As a result, these particles will move without continuous contact with the bed and the suspended load transport occurs.

The suspended sediment transport is calculated as the product of the instantaneous flow velocities and the instantaneous sediment concentration:

$$q_s = \frac{1}{T} \int_0^T \int_{z_d}^D (u \cdot c) dz dt \quad (3-63)$$

The time integration of the diffusion equation for suspended sediment is repeated until a periodic solution is obtained.

3.2.2.4. Bed level change

A morphological model is a combined hydrodynamic/sediment transport model. The hydrodynamic flow field is updated continuously according to the changes in the bed bathymetry. In case of a combined wave/current simulation, the wave field may be updated as well to reflect the changes in bed bathymetry (DHI, 2014c).

a. Sediment continuity equation

The key parameter for determination of the bed level changes is the rate of bed level change $\frac{\partial z}{\partial t}$ at the element cell centres. This parameter can be obtained in a number of ways, but in general all methods are based on the Exner equation (sediment continuity equation), which can be written (DHI, 2014c):

$$-(1 - n) \frac{\partial z}{\partial t} = \frac{\partial S_x}{\partial x} + \frac{\partial S_y}{\partial y} - \Delta S \quad (3-64)$$

Where n is bed porosity,

z is bed level,

t is time,

S_x, S_y are bed load or total load transport in the x and y directions, respectively,

x, y is horizontal Cartesian coordinate,

ΔS is sediment sink or source rate.

b. Morphological bed update

The bed is updated continuously through a morphological simulation (at every HD-time step) based on the estimated bed level change rates. New values for the bed level change rates are estimated at every N^{th} HD-time step, where N is a user defined time step factor. The new bed levels are obtained with a forward in time difference scheme stating (DHI, 2014c):

$$z_{new} = z_{old} + \frac{1}{1-n} \frac{\partial z}{\partial t} \Delta t_{HD} \quad (3-65)$$

For this reason, it is only necessary to calculate the bed load transport at the same time step as $\frac{\partial z}{\partial t}$, while the advection-dispersion equation for the concentration of the suspended sediment needs to be calculated at every time step.

3.3. Morphological evolution analysis

Coastal morphology focuses on explaining landforms in the coastal zone by examining in shoreline and in profile changes. In the study area, the coastal morphological evolution in two dimensions is a response of beach topography to the impact of natural conditions such as winds, waves, currents, and sea level changes as well as anthropogenic factor.

3.3.1. The cross-shore coastal evolution

Changes in cross-shore beach profiles are controlled by many factors including waves, currents, beach slope and sediment characteristics. These changes are commonly observed inside the depth of closure. In this work, the EBP models are used to analyze and quantify cross-shore beach profile evolution of sandy beaches along the eastern Giens tombolo during the medium-term period from 1999 to 2010, whereas the numerical model is utilized to predict the cross-shore variability of these beaches caused by storms and seasonal variation (Vu et al., 2017b).

3.3.1.1. Determining the depth of closure (D_C)

The depth of closure (D_C) for a given or characteristic time interval is the most landward depth seaward of which there is no significant change in bottom elevation and no significant net sediment transport between the nearshore and the offshore (Kraus et al., 1998). This depth can be estimated using extreme wave conditions. On basis of an analysis of available data, Hallermeier (1978) proposed the first effective method to compute the seaward limit of sediment transport. The inner limit marks the seaward extent of the littoral zone where the bed experiences extreme activity caused by waves breaking and their related currents. The outer limit denotes the limit of the shoal zone where waves will cause little sediment transport and waves have neither a strong nor negligible effect on the bed (Hallermeier, 1981b). Based on correlations with the Shields parameter and the assumption that only the highest waves cause erosion on the beach out to the D_C , Hallermeier (1978) determines the inner depth of closure as:

$$D_C = 2.28H_e - 68.5 \left(\frac{H_e^2}{g \cdot T_e^2} \right) \quad (3-66)$$

Where H_e is the non-breaking significant wave height that is exceeded only 12 hours out of a single year (or the greatest 0.137% waves in a year), and g is the acceleration due to gravity. H_e was calculated by averaging the highest 0.137% waves during each

year. T_e is the associated significant wave period which can also be defined by using the following fitted relation between T_e and H_s (see Appendix C.2.3):

$$T_e = 0.8444H_s + 3.506 \quad (3-67)$$

Using data from the USACE Field Research Facility in Duck, NC, Birkemeier (1985) evaluated Hallermeier's relationship for the D_C . From the data, he found that a better approximation for the D_C to be:

$$D_C = 1.75H_e - 57.9 \left(\frac{H_e^2}{gT_e^2} \right) \quad (3-68)$$

From the wave data measured by Buoy 08301 and 08302 from 1992 to 2015 (about 24 years), the non-breaking significant wave height is determined as $H_e = 4.28$ m, corresponding to $T_e = 7.12$ second using the equation (3-67). As a result, the depth of closure is also estimated as follows:

- According to Hallermeier (1978): $D_C = 7.23$ m.
- According to Birkemeier (1985): $D_C = 5.35$ m.

Based on the results of measurement campaign carried out by E.O.L (2010) from 1999 to 2010, it is noticeable that the changes of bathymetry along the eastern Giens tombolo are mainly observed from the shoreline to a water depth of 5 m. Therefore, the depth of closure of 5.35 m is used in the calculations in this work.

3.3.1.2. EBP models

EBP is the result of a balance between destructive forces and constructive forces acting on the beach. The EBP concept is useful for rational design of many coastal engineering projects as well as to the elucidation of near-shore processes. Particularly, it aids in the understanding of beach profiles in general and beach responses to changes of the dominant forces, viz. increases in sea level or storms. In addition, it is also very useful in predicting how beach nourishment designs will respond after they have been applied and in predicting the type of beach nourishment design that will fare best for conditions at the specified location (Özkan-Haller et al., 2007).

Dean et al. (2004) summarized three possible approaches for developing a theory for the EBP. Firstly, according to kinematic approach, the prediction of the motions of an individual sand grain (whether suspended or bed load) is based on the forces acting on them, and the form of the beach profile is calculated. On the other hand, dynamic approach shows that the balance between the constructive and destructive forces acting on the bottom will result in an EBP. Finally, this is empirical approach. This approach is a purely descriptive approximation attempting to describe the beach profile in forms that are most characteristically found in nature by through empirical coefficients to sediment size, wave characteristics, or both.

Several empirical models have been developed in an attempt to characterize EBPs. First of all, the most common beach profile expression is extracted by Bruun (1954). After analyzing beach profiles from the Danish North Sea coast and Mission Bay, California, he proposed a power law to describe the profile depth as a potential function of distance from the shoreline as followed:

$$d = A \cdot x^m \quad (3-69)$$

Where d is the still water depth at a seaward distance y from the shoreline, and A is a scale parameter depending on sediment characteristics. Moreover, Bruun also showed that a power of $2/3$ provides the best fit. To obtain the value of $2/3$, he assumed in the derivation that the bottom shear stress and wave energy dissipation were constant at equilibrium. The application of Bruun (1954)'s formula (3-69) was limited to the profile seaward of the breaker zone.

Dean (1977) extended this application through the surf zone to the shoreline by examining and analyzing approximately 500 beach profiles from Atlantic and Gulf coasts of United States. He also found that the best fit relationship describing the water depth as being proportional to the distance offshore to the two-thirds power for a given sediment grain size, but values for individual profiles ranged from about 0.2 to 1.2.

$$d = A \cdot x^{2/3} \quad (3-70)$$

Then, Dean (1987) transformed the A and D_{50} (the median grain size) relationship to the A and w (the fall velocity) relationship.

$$A = 0.067w^{0.44} \quad (3-71)$$

Where A is in $m^{1/3}$ and w is in cm/s . The value of fall velocity w can be calculated by Hallermeier (1981a) when median grain sizes are between 0.125 and 1 mm and water temperature is about 5° to 25° :

$$w = \frac{(\rho_s - \rho) \cdot g \cdot D_{50}^2}{18 \cdot \rho \cdot \nu} \quad \text{for } D_{50} < 0.13 \text{ mm}$$

$$w = \frac{\left[\frac{(\rho_s - \rho) \cdot g}{\rho} \right]^{0.7} \cdot D_{50}^{1.1}}{6 \cdot \nu^{0.4}} \quad \text{for } 0.13 < D_{50} < 0.85 \text{ mm} \quad (3-72)$$

$$w = \left[\frac{(\rho_s - \rho) \cdot g \cdot D_{50}}{0.91\rho} \right]^{1/2} \quad \text{for } D_{50} > 0.85 \text{ mm}$$

Where ρ_s is sediment density ($\rho_s = 2.65g/cm^3$ for quartz and 2.7 to 2.8 g/cm^3 for shell material), ρ is fluid density, and ν is fluid kinematic viscosity.

Kriebel et al. (1991) also found a similar correlation over a range of typical sand grain sizes from $D_{50} = 0.1$ mm to $D_{50} = 0.4$ mm where the fall velocity is between 1 and 10 cm/s :

$$A = 2.25 \left(\frac{w^2}{g} \right)^{1/3} \quad (3-73)$$

Vellinga (1987) investigated beach and dune erosion during storm surges by using wave tank tests and developed the following erosion profile which included the effect of deep water significant wave height, H_{os} , and sediment fall velocity, w :

$$\left(\frac{7.6}{H_{os}} \right) d = 0.47 \left[\left(\frac{7.6}{H_{os}} \right)^{1.28} \left(\frac{w}{0.0268} \right)^{0.56} x + 18 \right]^{0.5} - 2 \quad (3-74)$$

Where x is distance from the dune foot, in seaward direction in m, and d is the depth below storm surge level.

Romańczyk et al. (2005) proposed a three-parameter function of the equilibrium profile, consisting of two sections of the profile: the first section under mean sea level and the other above mean sea level.

$$d = A(x + x_s)^\rho \quad (3-75)$$

Where all three parameters A , ρ and x_s are to be obtained from a fitting procedure matching field data, either directly, or indirectly by relating A , ρ and x_s to other nearshore properties.

One of the first researchers used an exponential function to uncover the beach profile equilibrium shape was Bodge (1992) and he suggested the following expression:

$$d = B(1 - e^{-kx}) \quad (3-76)$$

Where k is the exponential term describing the profile curvature and B is the leading coefficient defining the offshore water depth, which the profile reaches asymptotically.

After providing EBP equation by Bodge (1992), Komar et al. (1994) tried to exert natural slope of seabed parameter and height and period of storm surge in the original equation. They considered on the behavior of the shore are linear. Their results obtained are more accurate than those of using Bodge (1992)'s equation.

$$d = \frac{S_o}{k} (1 - e^{-kx}) \quad (3-77)$$

In this equation, S_o is the beach face slope at the shore which varies with grain size and wave conditions, whereas the empirical coefficient k is related to the depth and the closure depth of the horizontal distance to the beach. The parameter k is determined approximately as follows:

$$k = \frac{1}{x_c} \left[\frac{3}{2} - \left(\frac{6D_c}{S_o x_c} - \frac{15}{4} \right)^{1/2} \right] \quad (3-78)$$

Where D_c and x_c , respectively the closure depth and distance from the closure depth to the shoreline. This depth was defined in the previous part.

Regarding the use of exponential expressions for the equilibrium profile adjustments, Sierra et al. (1994) provided the following logarithmic type best fit the Catalan coast after testing with the data of 82 beach profiles.

$$d = G.[\ln F + \ln(x + x_o)] \quad (3-79)$$

Where the coefficients of the equation, F , G and x_o are the empirical parameters determined by the site conditions.

After analyzing a series of physical equilibrium conditions in the submarine profile located between the surf zone and wave base, Lee (1994) proposed the logarithmic form to express the geometry of the submarine equilibrium profile as follows:

$$d = \frac{1}{D} \ln\left(\frac{x}{C} + 1\right) \quad (3-80)$$

Where the constant C , named extension factor which related to the bottom sediment diameter and D was estimated using the wave period T via the relation $D = 4\pi^2/gT^2$.

In addition, Bernabeu et al. (2003) validated a two-section EBP model by one or more representative beach profiles of Spain coasts. Dai et al. (2007) studied three types of EBP using 13 profiles in Lao Zuikou and 11 beach profiles in Nanwan beaches in the South China coast. Kaiser et al. (2009) used 37 beach profiles representing the accreted beaches at Abu Qir Bay and El-Burullus promontory and the eroded area at the Rosetta promontory to validate the EBP in Nile Delta Coastal Zone, Egypt. Nguyen et al. (2012) validated three types of empirical functions for the EBP by using and comparing with the field investigation dataset of 20 beach profiles at Giao Thuy and Hai Hau beaches. Recently, Aragonés et al. (2015) based on obtaining the best adjustment and least volumetric errors to develop a new methodology to increase the accuracy of the existing EBP models and apply for beaches of Valencia, Spain.

In this study, seven of the equilibrium functions: the potential forms of (3-70), (3-74) and (3-75); the exponential forms of (3-76) and (3-77); and the logarithmic forms of (3-79) and (3-80) are used to detect the EBP by means of the curve fitting toolbox in MatLab. This toolbox uses the nonlinear least squares formulation to fit a nonlinear model to the measured beach profile data through the equilibrium parameters (MathWorks, 2015). The adjustment of these parameters relies on the values directly calculated in accordance with the site conditions as well as the values recommended by the previous researchers. The goodness of fit statistics for parametric models includes R-square and RMSE. Moreover, an average beach profile was developed in each cross-section of beach to compare with the above-detected EBPs. Finally, the difference between the average beach profile and the best EBP curve, namely least surface error per profile unit (Em^2), would be determined to demonstrate the suitability of EBP model as well as the beach state. Results are presented in Part 4.3 of Chapter 4.

3.3.1.3. Numerical models

MIKE 21/3 Coupled FM including the HD, SW and ST models was used to evaluate the changes of bed level near the eastern Giens tombolo coast induced by storms and seasonal variation. The flow module MIKE21 HD (DHI, 2014d) solves the Saint-Venant equations. It can be coupled with MIKE21 SW (DHI, 2014b) to include driving forcing from wave breaking, current refraction, and flow resistance taking wave-current boundary layer interaction into account (Fredse, 1984). The transport of sand under the impact of combined waves and current computed by SW and HD models is estimated by MIKE21 ST (DHI, 2014c), which is based on a model for the vertical distribution of the turbulence with interaction between the wave and current boundary layers (Fredse, 1984) and turbulence generated by wave breaking (Deigaard et al., 1986). The bed is updated continuously at every HD-time step based on the estimated bed level change rates which are described more detail in Part 3.2 of this chapter. On the other hand, the hydrodynamic flow field and the wave field are also updated as well to reflect the changes in bed bathymetry. Subsequently, the simulated beach profile at the interest position is extracted and compared with the initial beach profile.

Before starting the main runs, the numerical model had to be calibrated and verified by the bathymetry of 2008 measured by E.O.L (2010). The median grain size, Manning's number and Nikuradse's roughness height, namely D_{50} , M and k_s , respectively, were selected as the main calibration factors. The accuracy of the simulation was evaluated using a BSS which was suggested by Van-Rijn et al. (2003). The prediction results of beach profile changes are described in detail in Chapter 5.

3.3.2. The long-shore morphodynamic change

Up to now, researchers have developed some approaches to investigate shoreline changes, which can be divided into five categories. Firstly, using historical maps are able to provide a historic record that is not available from other data sources, but there are many potential errors associated with historical coastal maps and charts. Secondly, conventional field surveying can achieve high accuracy of measurement, but is labour intensive, time consuming and high cost (Tran et al., 2009). Thirdly, aerial photographs provide sufficient pictorial information. However, the frequency of data acquisition is low, temporal coverage is limited by depending on the flight path of the fixed-wing airplane; the photogrammetric procedure is costly and time consuming. Additionally, the spectral range of these sources is minimal and may introduce errors in shoreline interpretation (Alesheikh et al., 2007). With rapid advances in computing technology, the numerical models have become increasingly popular and have been successfully used to understand and predict the shoreline evolution in the past as well as in future. They can be validated by simply observing the actual behavior of the natural systems under the influence of the wave climate, mean sea level, coastal defense works, etc. Nevertheless, a difficulty in the use of numerical models is the establishment of

boundary conditions, calibration coefficients and parameters regarding variables representing the reality of the system, that maybe induce the fail results (Pereira et al., 2013). In addition, the numerical modeling calculations are more time consuming than analytical and statistic calculations as well as the area of study domain are limited by the capacity of computer. Over the recent decades, remote sensing techniques are widely used and more attractive as they are less time consuming, inexpensive to implement, large ground coverage, and the satisfactory acquisition repetition. Therefore, this technology becomes an effective solution for monitoring shoreline changes (Winarso et al., 2001).

In this research, the methodology of remote sensing and GIS technology along with DSAS was applied to quantify shoreline changes as well as accretion and erosion in the eastern Giens tombolo over the period from 1973 to 2015, determine the main factor influencing the shoreline evolution of this area, and predict the movement trends of shoreline in the future. Furthermore, the numerical model of LITLINE are also used to estimate the longshore morphodynamic change in the study area due to the storms and seasonal variation as well as the construction of the coastal structures (Vu et al., 2017a).

3.3.2.1. Historical shoreline changes

In this study, Landsat MSS, Landsat TM, Landsat ETM+, and Landsat OLI satellite images from 1973 to 2015 were acquired for extracting the shorelines. The image selection was based on some important criteria, viz. all the images have been collected almost at the same time in summer season in good quality to eliminate the effect of sea level rise due to storms and waves; only the images with cloud cover less than 10% have been selected (Vu et al., 2017d). The details regarding satellite data are presented in Table 24.

Table 24. List of satellite imagery used for the study.

SI no.	Satellite and sensor	Acquisition date (dd/mm/yyyy)	Local time	Bands	Spatial Resolution (m)
1	Landsat 1 MSS	01/03/1973	09:51:58	4	79
2	Landsat 4 TM	27/08/1988	09:47:41	7	30
3	Landsat 7 ETM	28/08/2000	10:08:38	8	15/30
4	Landsat 7 ETM	18/08/2008	10:06:50	8	15/30
5	Landsat 8 OLI	30/08/2015	10:17:30	8	15/30

The raw satellite images usually contain many defects, like radiometric distortion, wedge-shaped gaps, geometric distortion, presence of noise, etc., due to the variations in the altitude, attitude, and velocity of the sensor platform (Lillesand et al., 2008). Therefore, they need to be preprocessed to enhance the quality of image such as radiometric calibration, atmospheric correction, gap filling, pan-sharpening, or geometric rectification, before being used as map bases.

In order to analyze shoreline extraction from optical imagery, several methods have been developed such as a single band method, the histogram thresholding method, the band ratio method, or a combination of histogram thresholding and band ratio techniques. However, the main difficulties of these methods are quite time consuming and the problem occurs in some of the coastal zones where the shoreline moves toward water (Alesheikh et al., 2007). Another approach of extraction is by automation of edge detection which is relatively simpler to implement than others (Loos et al., 2002). This technique gives an outstanding delimitation of the land-water boundary, but also time saving. In this study, the exact shoreline was obtained by using Matlab code and a nonlinear edge-enhancement technique with Canny edge detector (see in Appendix D.1). The Canny edge detection is the most common edge detection method that performs well optimizing detection localization and number of responses criteria (Canny, 1986). Due to the edge of the image corresponding to the discontinuity of the image grey value, the Canny algorithm is used to determine the pixels in the land-water boundary if their grey values have relatively large changes (Liu et al., 2004). A color composite can be used for extracting the shorelines. The best color composites for this technique are RGB (Red Green Blue) 567 (Landsat MSS images), 543 (Landsat TM and ETM+ images), and 652 (Landsat OLI images) (Vu et al., 2017d). These color composites nicely enhance the objects and distinguish clearly between soil, vegetated land, and water as well as are easily digitized. The files of digitized shorelines were in shape format for further analysis in DSAS version 4.3, which is an ArcGIS extension.

For the quantification of the shoreline changes along the eastern Giens tombolo, many methods were available in DSAS, but only the most commonly used, EPR calculations, and LRR, were used. Two different approaches are utilized to compute the coast change, viz. EPR for short term changes (1973-1988; 1988-2000; 2000-2008; 2008-2015) and LRR for long term changes (1973-2015) as well as prediction of future shoreline movement (2015, 2020, 2050). In this case, the onshore baseline was created with a position of approximately 100 m distance behind the shorelines. Based on the initial setting, a total of 347 transects in the eastern tombolo was generated for 200 meters perpendicular to the baseline for every 25 meters longshore. The intersection point coordinates between transect lines and shorelines as well as other statistical results were also computed by DSAS. Consequently, the data measured from each transect were used to estimate the shoreline change rates (m/year).

The distances between multiple historic shorelines and the baseline at each transect computed by DSAS was input into the code which the authors created to predict the position of shoreline at each transect (see in Appendix D.2). Finally, all these positions were connected together to create the future shoreline. This code uses linear regression equation and runs in Matlab. The linear regression method of determining shoreline position change rate minimizes potential random error and short term variability

through the use of a statistical approach (Douglas et al., 2000). This method is based on the assumption that the observed periodical rate of change of shoreline position is the best estimate for prediction of the future shoreline. Its main shortcoming is that the sediment transport (Michael et al., 1993) or wave interference is not taken into account because the cumulative effect of all the underlying processes are assumed to be captured in the position history (Rongxing Li, 2001). To estimate the future shoreline position, the baseline was first defined as the buffer of the shoreline in 2015. Next, transects cast perpendicular to the baseline at a user-specific spacing alongshore were generated by DSAS. Then, the intersection points between transects and multi-temporal shorelines were created to input into the linear regression equation to determine the position of future shoreline at each transect. Finally, these positions were connected together to create the future shoreline (Nguyen et al., 2010).

The predictability and model quality are defined by using cross-validation of the estimated past shoreline positions. Specifically, the positional shift in the estimated shoreline of the eastern Giens tombolo of 2015 was validated with respect to actual shoreline extracted from the satellite image of 2015. The validation was carried out through calculation of RMSE. The results of validation are shown in Figure 43. It is easily seen that the predicted shoreline is close to the actual one. The overall RMSE for the entire eastern shoreline was found approximately 6.57 m. Furthermore, the regression coefficient of R-squared is estimated about 0.981. The values of error are acceptable and reasonable; hence, this method can be applied for predicting the position of future shorelines (Vu et al., 2017a).

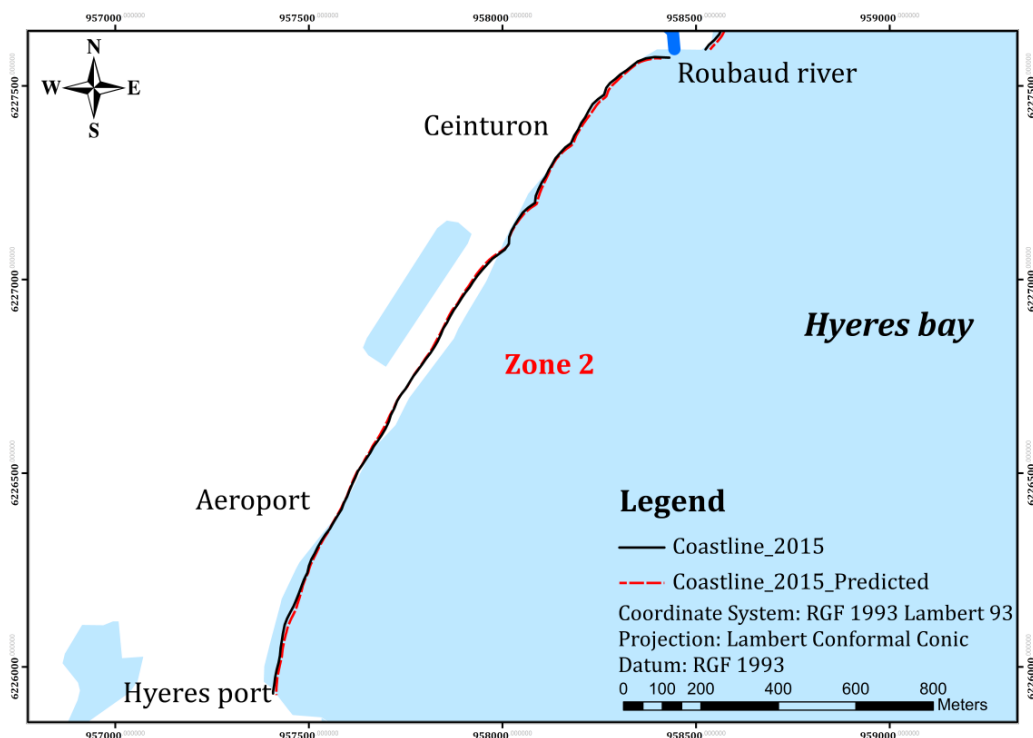


Figure 43. Actual shoreline position (2015) and predicted shoreline position (2015) along Zone 2 in the eastern Giens tombolo.

Several sources of error affect the accuracy of shoreline position and consequently shoreline change rates. There are two types of uncertainties comprising positional uncertainty and measurement uncertainty. Positional uncertainties are related to the features and phenomenon that reduce the precision and accuracy of defining a shoreline position in a given year, viz. seasonal error E_s , and tidal fluctuation error E_{td} (Fletcher et al., 2012). Seasonal error, E_s , is induced by the movements in shoreline position under the action of the waves and storms. Based on the measurement report of E.O.L (2010), seasonal shoreline position differences between the spring and fall were estimated about ± 5 m. The tidal fluctuation error, E_{td} , comes from horizontal movement in shoreline position along a beach profile due to vertical tides. The base water level used to define the shoreline is the HWL. The study area is in a micro-tidal region with the tidal range less than 0.3 m, so this error can be neglected (Rajasree et al., 2016). Regarding measurement uncertainties, they are associated with the skill and approach including digitizing error E_d , rectification error E_r and pixel error E_p (Fletcher et al., 2012). Before digitization, the satellite images of 1973 and 1988 were re-sampled from 79 m to 15 m and from 30 m to 15 m, respectively without adding any spatial information. Hence, the digitizing errors were estimated about ± 12 m for 1973, ± 6 m for 1988 and ± 3 m for remainders (Jayson-Quashigah et al., 2013). Finally, rectification error, E_r , is calculated from the orthorectification process.

According to Fletcher et al. (2012), these errors are random and uncorrelated and can be represented by a single measure calculated by summing in quadrature. The total positional uncertainty, U_t , is:

$$U_t = \pm \sqrt{E_s^2 + E_{td}^2 + E_d^2 + E_p^2 + E_r^2} \quad (3-81)$$

The annualized uncertainty of shoreline change rate at any given transect was calculated as follows (Hapke et al., 2011):

$$U_a = \pm \frac{\sqrt{U_{t1}^2 + U_{t2}^2 + U_{t3}^2 + U_{t4}^2 + U_{t5}^2}}{T} \quad (3-82)$$

Where $U_{t1}^2, U_{t2}^2, \dots, U_{t5}^2$ are the total shoreline position error for the various year and T is the 42 years period of analysis.

The maximum annualized uncertainty evaluated for individual transects is about ± 0.67 m/year (Table 25).

The results of the historical shoreline changes during the period from 1973 to 2015 and the positions of shoreline between 2015 and 2050 are described in Part 4.2 of the Chapter 4.

Table 25. Estimated errors for each shoreline data source.

Type of uncertainties	1973	1988	2000	2008	2015
Seasonal error (E_s)	5	5	5	5	5
Tidal fluctuation (E_{td})	0	0	0	0	0
Digitizing error (E_d)	12	6	3	3	3
Rectification error (E_r)	12	9.9	7.35	10.8	6.75
Pixel error (E_p)	0.5	0.5	0.5	0.5	0.5
Total error (U_t)	17.70	12.62	9.40	12.28	8.93
Annualized error (U_a)	0.67 m/year				

3.3.2.2. Estimation of shoreline changes due to the storms and seasonal variation

In the winter, some storms usually occur and approach the study area. These storms have caused the shoreline evolution along the eastern part of the Giens tombolo. Their unpredictable occurrence induces many difficulties for estimating the longshore morphodynamic change by means of GIS technology or in-situ measurements. Before installing the coastal structures, the experimental method is commonly carried to forecast the shoreline change as well as assessed the efficiency of these coastal alternatives. The experiments increase the high cost of construction. In addition, it will take the long time to observe and obtain the shoreline change after the construction of the coastal structures is completed. In such cases, numerical models for shoreline evolution provide a powerful and unique capability for establishing trends and predicting shoreline position scenarios for the short-term and long-term time scales as well as taking into account the presence of the coastal structures (Thiruvankatasamy et al., 2014). The numerical model, which is well known for studies of shoreline change phenomena is LITPACK. The main module of LITPACK including LITLINE (Shoreline evolution) is used to investigate the position of the shoreline after the impacts of the storms, seasonal variation and the construction of coastal structures in the sandy beaches along the eastern Giens tombolo.

LITLINE simulates the coastal response to gradients in the longshore sediment transport. It calculates the shoreline position based on input of the wave climate as a time series data. The model is, with minor modifications, based on a one-line theory, in which the cross-shore profile is assumed to remain unchanged during erosion/accretion. Thus, the coastal morphology is solely described by the shoreline position (cross-shore direction) and the coastal profile at a given long-shore position. LITLINE is applied in research on shoreline changes due to natural conditions, protected constructions and research on shoreline recovering measures by artificial beach nourishment (DHI, 2014a).

The main equation in LITLINE is the continuity equation for sediment volumes expressed by:

$$\frac{\partial y_c(x)}{\partial t} = -\frac{1}{h_{act}(x)} \frac{\partial Q(x)}{\partial x} + \frac{Q_{sou}(x)}{h_{act}(x)\Delta x} \quad (3-83)$$

Where:

$y_c(x)$ is distance from the baseline to the shoreline,

t is time,

$h_{act}(x)$ is height of the active cross-shore profile,

$Q(x)$ is longshore transport of sediment expressed in volumes,

x is longshore position,

Δx is longshore discretization step,

$Q_{sou}(x)$ is source/sink term expressed in volume/ Δx .

$h_{act}(x)$ and $Q_{sou}(x)$ are calculated based on user specifications, while the longshore transport rate $Q(x)$ is determined from tables relating the transport rate to the hydrodynamic conditions at breaking. Δx is user specified, while Δt is determined from stability criteria. From an initial shoreline position $y_{init}(x)$, the evolution in time is determined by solving Equation (3-83), using an implicit Crank-Nicholson scheme.

The discretization in longshore direction is sketched in Figure 44 and Figure 45, in which Q_i denotes the transport rate between x_i and x_{i+1} , while dQ_i denotes the change in the transport rate with respect to change in shoreline orientation (for values of θ close to the local orientation θ_0) (DHI, 2014a).

$$dQ(x) = \frac{\partial Q}{\partial x}(x, \theta_0) \quad (3-84)$$

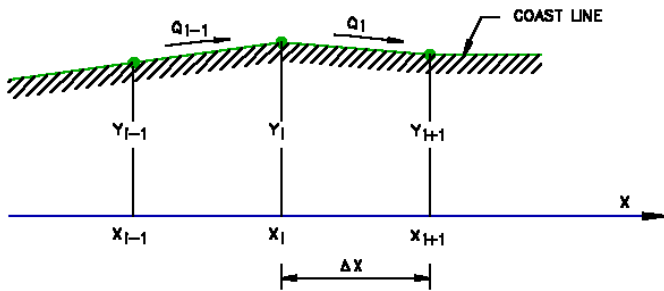


Figure 44. Longshore discretization.

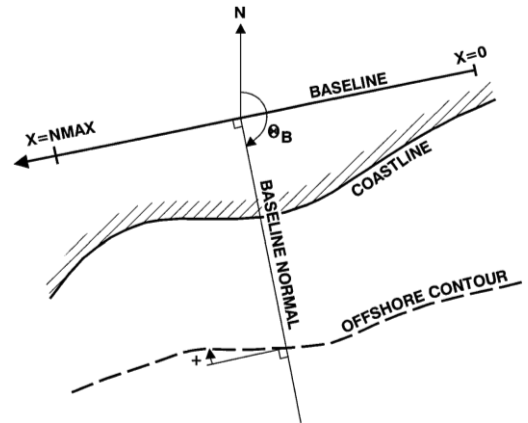


Figure 45. Definition of baseline orientation.

A subscript “ t ” denotes (known) values of the present time step, while subscript “ $t+1$ ” denotes (unknown) values of the next time step. Transport rates corresponding to time step $t+1$ are estimated through:

Based on a Crank-Nicholson scheme, the continuity equation in Equation (3-83) can be written as:

$$a_i y_{i-1,t+1} + b_i y_{i,t+1} + c_i y_{i+1,t+1} = d_i \quad (3-85)$$

In which:

$$a_i = (1 - \alpha) d Q_{i-1}$$

$$c_i = (1 - \alpha) d Q_i$$

$$b_i = \frac{\Delta x^2 \cdot h}{\Delta t} - a_i - c_i$$

$$d_i = a_i y_{i-1,t} + b_i y_{i,t} + c_i y_{i+1,t} - \Delta x \cdot (Q_{i,t} - Q_{i-1,t} - Q S_i) \quad (3-86)$$

a_i , b_i , c_i and d_i can be found for the present time step, and with two boundary conditions, the system of equations for all longshore positions can be solved by Gauss-elimination.

Input data for the LITLINE module comprise topography conditions including position of the shoreline, the dune properties, offshore contours and the appearance of the cross-shore profile along the beach, the roughness coefficient of the bed. These parameters are specified basing on a coordinate system in which x-axis is baseline quasi-parallel to the initial shoreline, and y is perpendicular to x and oriented sea (Figure 45). Another very important input data for LITINE is wave conditions (wave field depicted into 2D wave table, consisting of parameter of wave height, wave directions and periods). In this research, the statistical wave paramters of 2D wave table is solved and computed by Matlab code (see in Appendix D.2).

The results of the shoreline evolution induced by the storms, seasonal changes and the construction of coastal structures are presented in Chapter 6.

3.4. Conclusion

In this chapter, the methods used to conduct this research are introduced. The MIKE 21 software package is selected to investigate the coastal morphology along the eastern Giens tombolo. Because the morphological evolution and sediment transport are very complex processes, hence the long-shore and cross-shore morphodynamic changes are separated and investigated independently. The shoreline evolution is interpreted by using both GIS and remote sensing techniques and the numerical models. The GIS and remote sensing techniques were used to detect the historical shoreline change from 1973 to 2015 and predict the future shoreline positions between 2015 and 2050, whereas the numerical models of LITLINE estimate the impacts of the storms, seasonal variations and the coastal structures on the shoreline. Similarly, the beach profile evolution is also evaluated by using the empirical models and the numerical model.

CHAPTER 4. MORPHOLOGICAL EVOLUTION

4.1. Introduction

Morphological evolution of a beach is characterized by cross-shore and long-shore morphodynamic changes. Long-shore coastal evolution is mainly described by varying coastal forms such as changing shoreline position, beach rotation and development of rhythmic features, whilst cross-shore beach change is associated with changes to the shape of cross-shore profile in time and space. In this chapter, the combination of remote sensing, GIS techniques coupled with the DSAS along with linear regression method were applied for investigating the historical shoreline evolution as well as predicting the position of future shoreline in the eastern Giens tombolo. Regarding cross-shore beach evolution, prediction of the behavior of beach profile configuration to natural and anthropogenic changes by using the concept of the EBP could be useful in finding the most suitable measure to halt the erosion problem in some beaches along the eastern Giens tombolo. The field investigation data of 11 beach profiles along the eastern tombolo were supplied for this study. A nonlinear fitting technique was also applied to estimate the best parameter values of seven empirical formulations for EBP.

4.2. Shoreline changes

4.2.1. Consideration of littoral zones

The eastern part of Giens tombolo extends over more than ten kilometers from the mouth of Gapeau in the north to La Badine beach in the south (Lacroix et al., 2015). For analysis purposes, the eastern branch is divided into five zones. The presence of artificial structures, and river mouths, created different morphological characteristics for each zone (Figure 46).

The first zone lies between the Gapeau river and Roubaud river with total length of 1.95 km. It is accreted by the largest sediment volume from Gapeau river, especially after the upstream jetty was constructed at Roubaud river mouth from 1955 to 1960 (Courtaud, 2000). The second zone of 1.925 km in length is limited by Roubaud river and Hyères port, adjacent to the road of DR 42. Its shoreline evolution is being dominated by anthropogenic interventions such as groynes, rock-fill revetments and breakwaters. Like the second zone, the shoreline of the third zone from Hyères port to La Capte port is interrupted by some groynes which were installed to protect Pesquiers beach. This is also the shortest zone with only 1.4 km in length. The fourth zone extends the entire La Capte beach with total length of about 1.625 km. In the northern part of this zone, the concrete seawall was implemented to prevent the erosion due to waves. The last zone, 1.7 km long, covers all Bergerie and La Badine beaches.

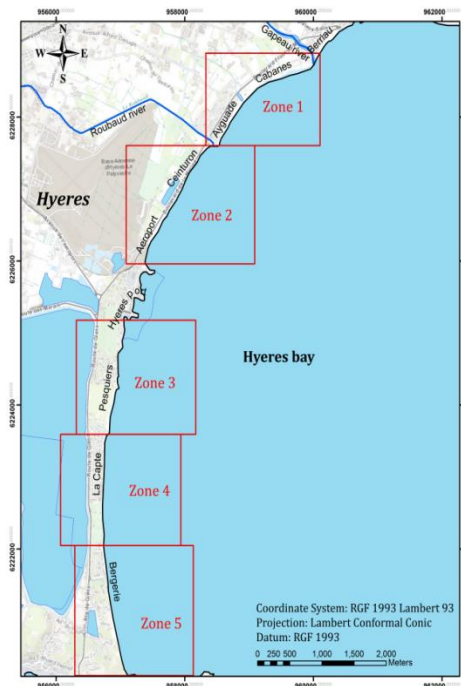


Figure 46. The studied zones in the eastern Giens tombolo.

4.2.2. Results of historical shoreline changes and discussion

For the zone 1, the rate of change was investigated over 79 transects (No. 1-79) and observed both accretion and erosion, but most of transects exhibit accretion except the period from 2008 to 2015 (Figure 47). The accreted realms are fed by Gapeau river. In the period from 1973 to 1988, the shoreline advanced at the mean rate of 1.02 m/year, but the longshore accretion pattern was transformed to erosion pattern during the second period from 1988 to 2000. In this period, the northern shoreline (Transects 1-46) was eroded at the maximum rate of -3.81 m/year (Table 26) perhaps attributed to the action of southeastern waves. To reduce the decline of shoreline, the 500 m rockfill revetment was implemented from the mouth of Gapeau river to downstream in the period from 1995 to 2000. Meanwhile, the southern part (Transect 47-79) was accumulated due to the blockage of the longshore sediment transport by the jetty of Roubaud river. The presence of revetment maintained the stable condition of shoreline for accreting during period from 2000 to 2008 period except for few transects. The maximum progradation rate of about 4.36 m/year appeared nearly Transect 5. Nevertheless, the positive trend was completely changed to the negative trend between 2008 and 2015. The entire coastal area has experienced erosion, and the shoreline is retreating at a mean rate of -1.35 m/year. The main reason of this phenomenon may be due to the shortage of sediment from Gapeau river. On the other hand, the overall shoreline changes from 1973 to 2015 are depicted in Figure 48. It is clearly showed that erosion is reported from Transects 4 to 24 (immediately downstream of revetment) with the maximum rate of -1.05 m/year, whereas accretion is observed from Transects 25 to 79 at the maximum accumulation rate of 1.35 m/year. More than 72% of transects in this zone exhibits moderate accretion.

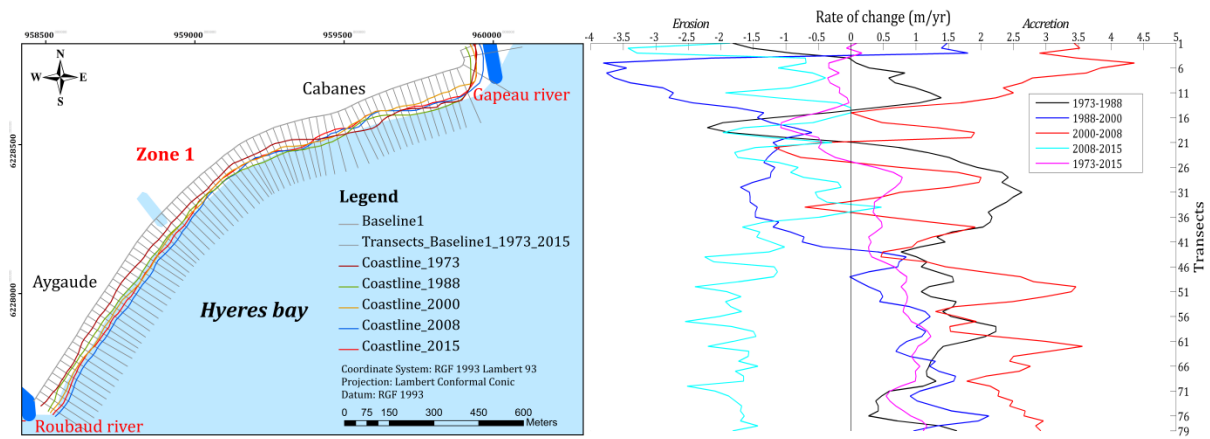


Figure 47. Positions of shorelines, transect lines and shoreline change rates using EPR method in the zone 1 of the eastern Giens tombolo over a period of 1973-2015.

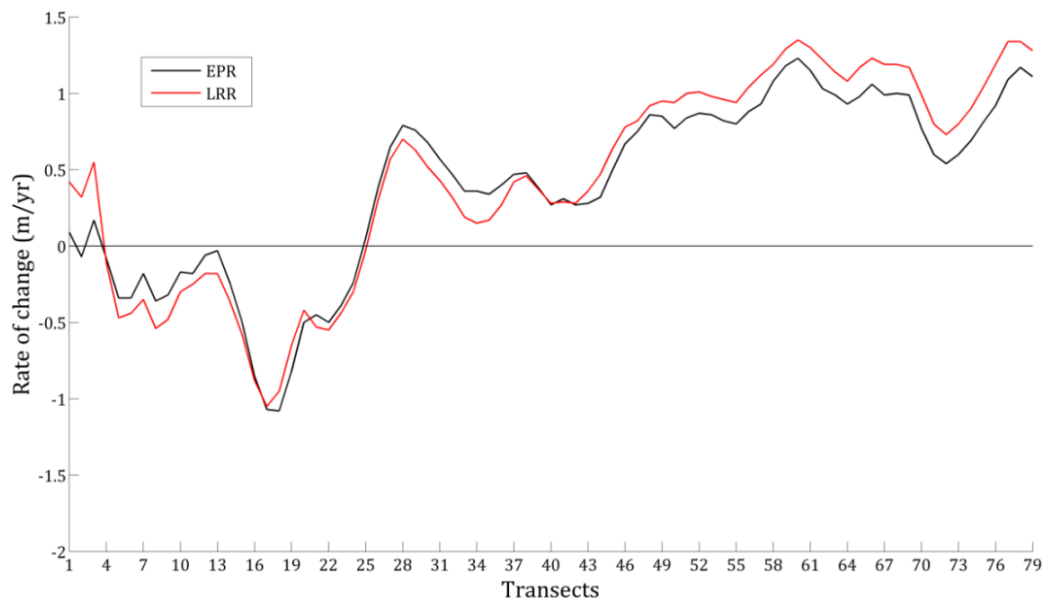


Figure 48. The variation of shoreline change rates using LRR method in the zone 1 of the eastern Giens tombolo over a period of 1973-2015.

In zone 2, the short-term analysis reveals that both accretion and erosion are observed in many places. The shoreline changes during each period were estimated for 78 transects (No. 80-157) and shown in Figure 49 as well as Table 26. In the period from 1973 to 1978, the northern part of this zone, Ceinturon beach, was subjected to severe erosion at the maximum retreat rate of -2.27 m/year due to partly the sediment deficit - due to the blockage of main longshore sediment transport by the jetty of Aygaude port, and partly to the strong impact of the southeast waves. To trap of sediment and limit erosion, four groynes were implemented in this area during period from 1978 to 1982. Conversely, the southern shoreline from Transect 128 to 157 continuously advanced seaward from 1973 to 2008, probably due to the upstream breakwater of Hyères port, which stopped the southward sediment transport. The presence of the groynes and breakwater in this realm modified the position of shoreline in the positive trend. The percentage of accretion transects was increased from 46% in the period from 1973 to 1988 to 84% in the period from 1988 to 2000. The groynes have caused localized beach

accretion and severe erosion at several places in downstream. For example, between 1988 and 2000, the shoreline advanced seaward from transect 80 to 107, but the retreat of the shoreline was observed from transect 107 to 125. After that, 92% of transects manifest accretion in 2000-2008 because of annual beach nourishment (Capanni, 2011). However, the positive trend was entirely changed to the recession mode in the period of 2008-2015. The shoreline retreated landward at the mean erosion rate of about -0.6 m/year. In addition to the above-mentioned short-term analyses, the medium-term analyses of shoreline changes in this zone were also carried out from 1973 to 2015. It is noted that both erosion and accretion occurred along shoreline (Figure 50). The maximum erosion and accretion rates are -0.77 m/year and 2.08 m/year, respectively. Erosion is observed along transect 105-135 in the south of the groynes, whilst accretion is reported in the remainders. The increase of erosion in this zone directly threatens the existence of the RD 42 road. This decay is triggered by the combination of action from southwest waves and the deficit of sediment due to the upstream groynes and jetty (Vu et al., 2017a).

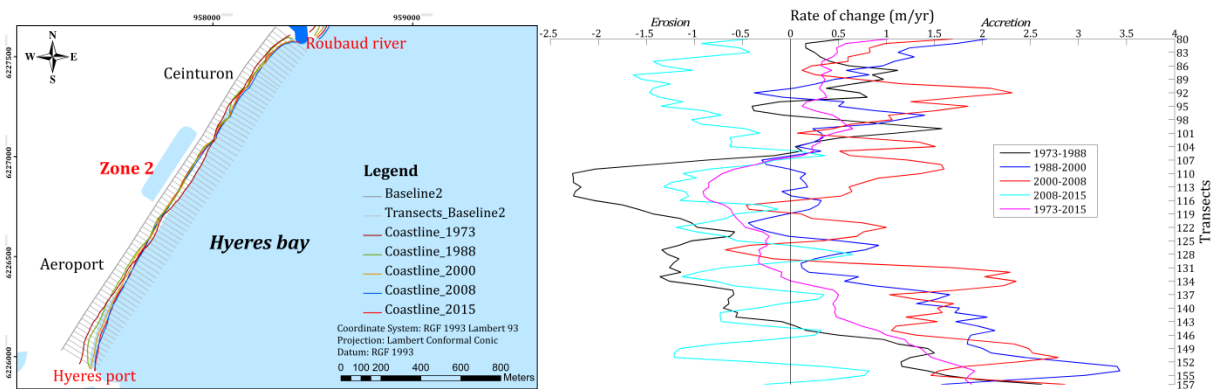


Figure 49. Positions of shorelines, transect lines and shoreline change rates using EPR method in the zone 2 of the eastern Giens tombolo over a period of 1973-2015.

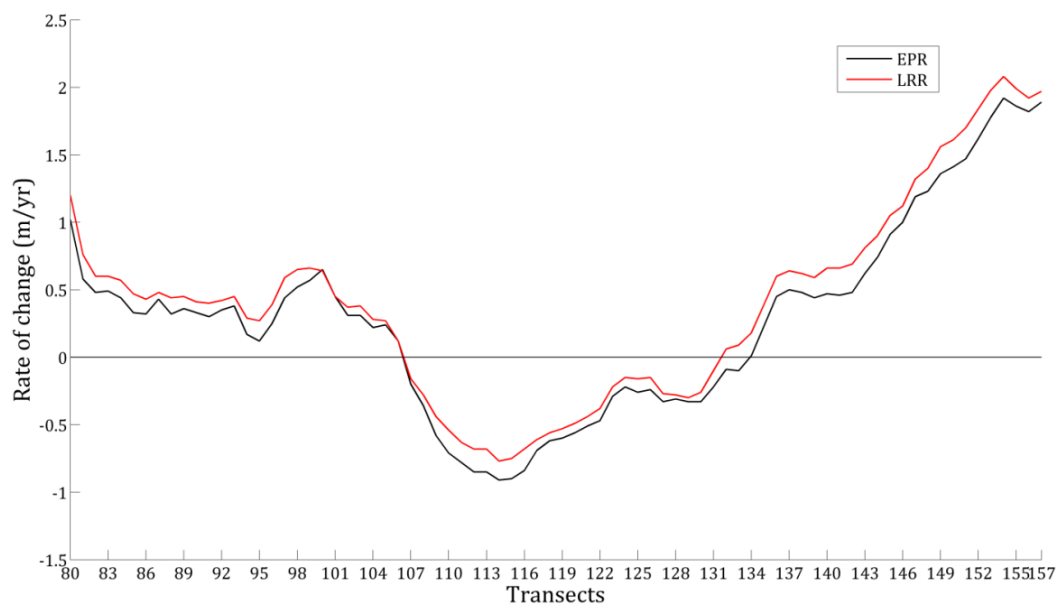


Figure 50. The variation of shoreline change rates using LRR method in the zone 2 of the eastern Giens tombolo over a period of 1973-2015.

For zone 3, from Transect 158 to 213, the short-term shoreline change analysis indicates both erosion and accretion trend, but accretion is more significant (Figure 51). Furthermore, the shoreline evolution is very complex due to the disturbance of the groynes distributed along the coast of this zone. In the period from 1973 to 1988, the erosion predominantly dominates with more than 92% of transects and the maximum erosion rate of -2.14 m/year. Subsequently, this negative trend was turned to positive in the periods from 1988 to 2000 and from 2000 to 2008 with mean advancing rates of 0.24 m/year and 0.91 m/year, respectively. The progradation trend was slightly decreased in the period from 2008 to 2015. In this duration, solely 62.5% of transects exhibit accretion. Nevertheless, the medium-term analysis demonstrates that erosion is dominant from 1973 to 2015 (Figure 52). The negative trend is resulted in not only the shortage of sediment due to the presence of the breakwaters in Hyères port but also to the wave action. This is an area of convergence of orthogonal east waves and correspondingly contributes to an increase of its energy, particularly near the vicinity of Hyères port. The 73% of eroded transects are reported in the northern part of this zone, while the 27% of deposited transects are observed in the southern part. The maximum erosion rate of about -0.44 m/year often occurs round Transect 158 and the maximum accretion rate of 0.46 m/year is recorded near Transect 210-213 (Table 26).

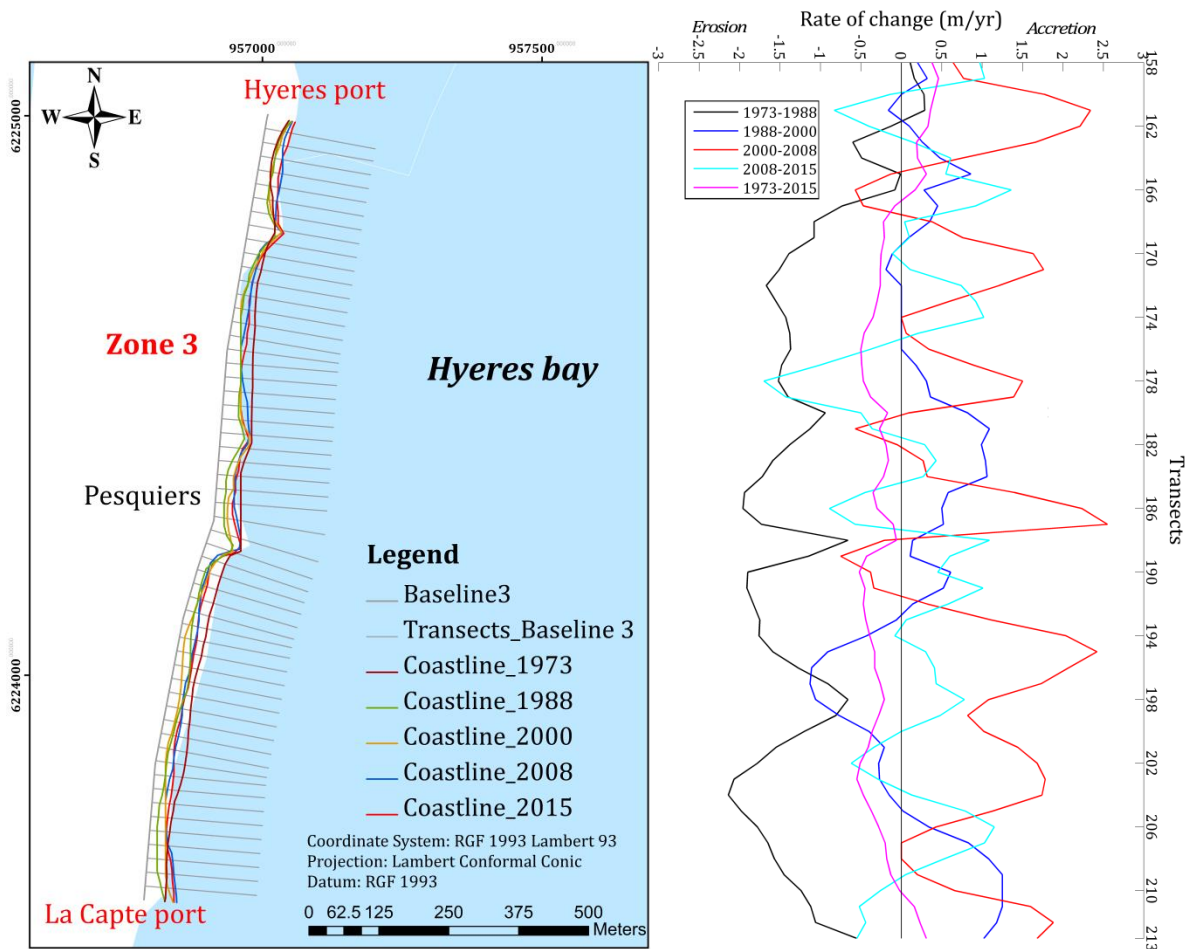


Figure 51. Positions of shorelines, transect lines and shoreline change rates using EPR method in the zone 3 of the eastern Giens tombolo over a period of 1973-2015.

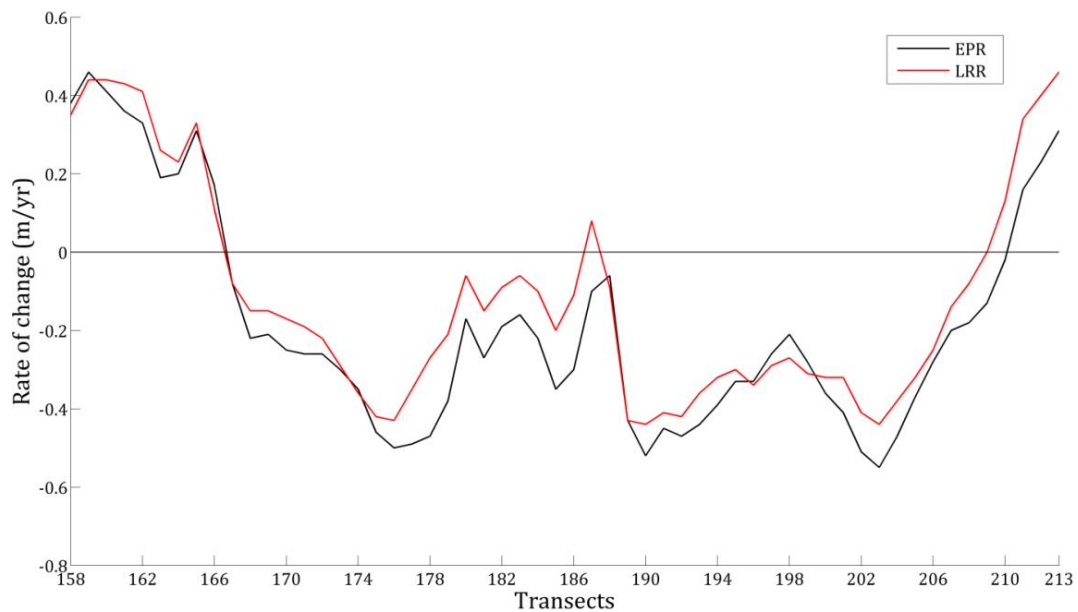


Figure 52. The variation of shoreline change rates using LRR method in the zone 3 of the eastern Giens tombolo over a period of 1973-2015.

There are 65 transects, namely from transect 214 to 278 in the zone 4. The results of the short-term analysis elucidates that the coast has undergone both accretion and erosion (Figure 53). After completing the construction of 80-m wing perpendicular to the jetty of La Capte port (Capanni, 2011), all shoreline of this zone suffered severe decline with the mean erosion rate of approximately -1.33 m/year in the period from 1973 to 1988. The maximum erosion rate of -2.71 m/year was recorded in the Transect 215, in the north of La Capte beach. This negative trend sharply decreased in the period from 1988 to 2000. Erosion was only reported in the northern part of the zone 4 with the maximum erosion rate of -0.74 m/year, whilst the southern one exhibits accretion with the maximum progradation rate of 1.25 m/year. To stabilize the shoreline as well as protect the onshore properties, two submerged geotube breakwaters were constructed in the south of La Capte port in 2007. Along with the annual beach nourishment with the large sediment volume, accretion was seen in most of transects (about 90%) in the period from 2000 to 2008. The maximum accretion rate was 4.81 m/year at transect 216. However, the alongshore accretion pattern in the north part of this zone was completely transformed into erosion pattern during the period from 2008 to 2015. The maximum erosion rate of -1.91 m/year is observed at transect 216. The main cause of this trend change may be attributed to the decline of the geotube breakwater height due to the geotube bag stretch by hydrodynamic factors, or torn by anchors and mechanical forces (Lacroix et al., 2015). Furthermore, Figure 54 describes the shoreline change rate in the medium-term period of 1973-2015. It is also noted that the southern part is accreted with the maximum deposition rate of 0.19 m/year, whereas the northern part is retreated with the maximum erosion rate of -0.29 m/year (Table 26). The numbers of accreted and eroded transects are 36 and 29 corresponding to 55.4% and 44.6%, respectively.

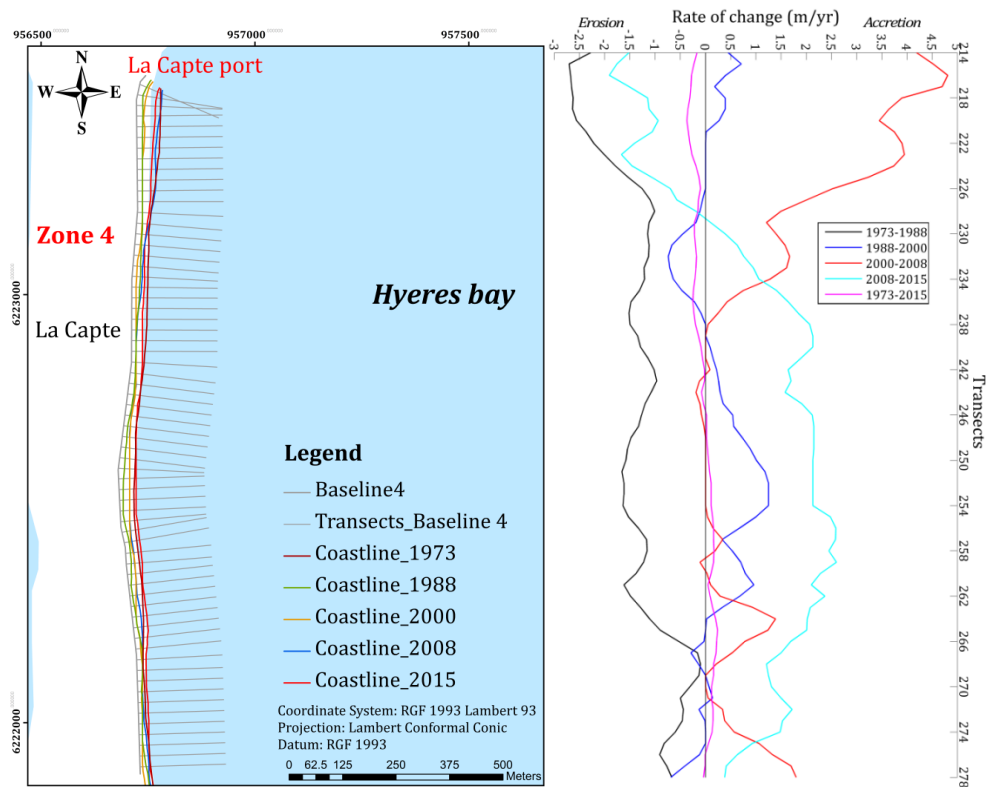


Figure 53. Positions of shorelines, transect lines and shoreline change rates using EPR method in the zone 4 of the eastern Giens tombolo over a period of 1973-2015.

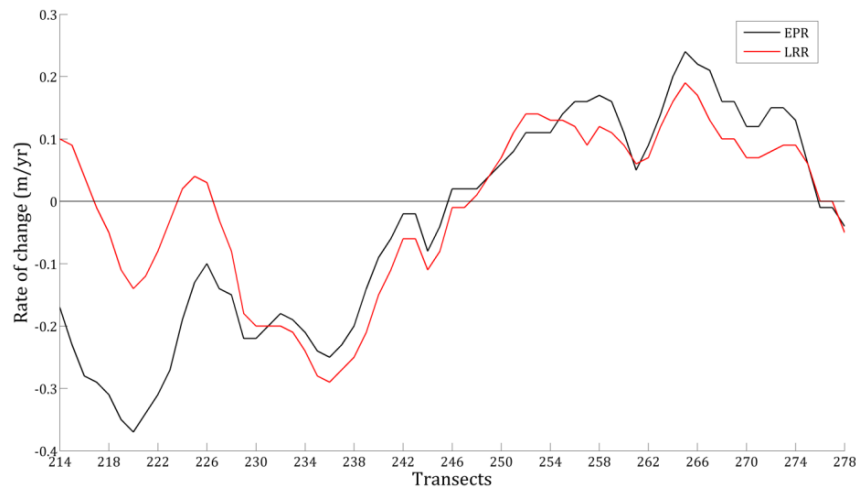


Figure 54. The variation of shoreline change rates using LRR method in the zone 4 of the eastern Giens tombolo over a period of 1973-2015.

In the last region, zone 5, the shoreline is located between transect 279 and transect 347. The shoreline changes over the short-term periods (1973-1988, 1988-2000, 2000-2008, and 2008-2015) were estimated and shown in Figure 55. It is clearly seen that during the periods from 1973 to 1988 and from 1988 to 2000, the coast experienced dominant erosion with the mean retreat rate of -0.5 m/year and -0.24 m/year, respectively (Table 26). Nonetheless, from 2000, the longshore erosion pattern totally changed to accretion pattern except few eroded transects. Over the period from 2000 to 2008, the shoreline advanced seaward at the mean deposition rate of 0.89 m/year. At that time, more than 97% of transects showed accretion. The positive trend kept

maintaining in the period of 2008-2015 with the mean accretion rate of 0.71 m/year. On the other hand, the medium-term analysis expresses that the shoreline experienced very little change from 1973 to 2015 (Figure 56). Consequently, there is certain stability or even a slight accretion with the mean progradation rate of 0.02 m/year. This accretion is due to its position sheltered by the cape of Esterel. Particularly, the divergence of orthogonal east and southeast waves in this area reduces its energy, so prompting to the accumulation of the fluvial sediment contribution from Gapeau and Roubaud river which is transported by southward longshore drift.

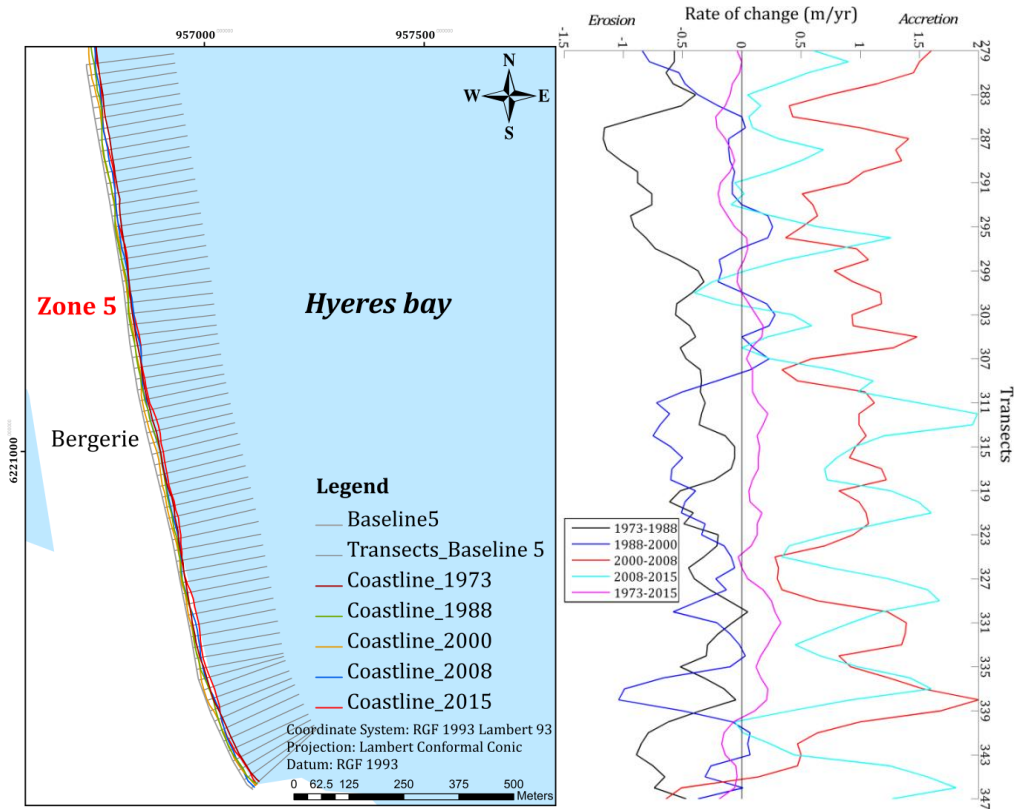


Figure 55. Positions of shorelines, transect lines and shoreline change rates using EPR method in the zone 5 of the eastern Giens tombolo over a period of 1973-2015.

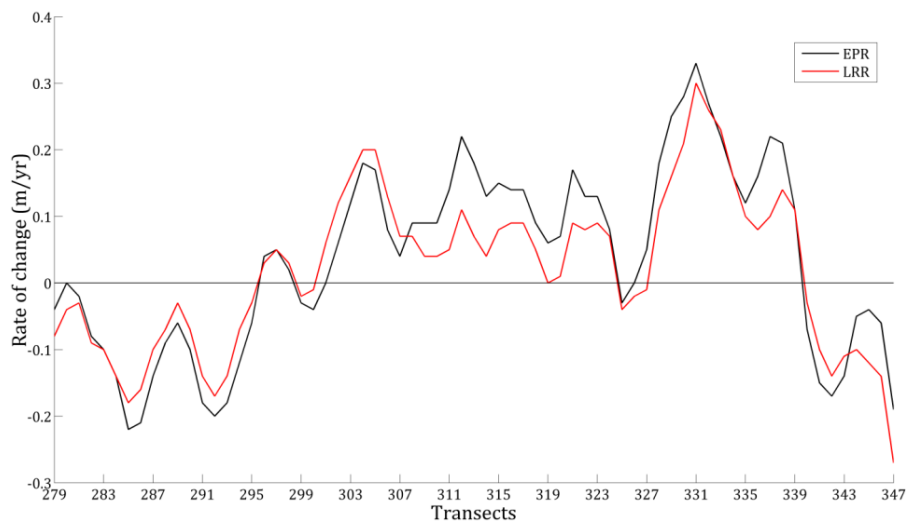


Figure 56. The variation of shoreline change rates using LRR method in the Zone 5 of the eastern Giens tombolo over a period of 1973-2015.

Table 26. Statistical summary of shoreline change rate for the eastern Giens tombolo over a period of 1973-2015.

Zone	Period	No of transect	Coast length (m)	Min rate (m/yr)	Max rate (m/yr)	Mean rate (m/yr)	No of eroded transect	No of accreted transect	% of eroded transect	% of accreted transect
1	1973-1988	79	1950	-2.21	2.63	1.02	10	69	12.66	87.34
	1988-2000			-3.81	2.12	-0.33	40	39	50.63	49.37
	2000-2008			-1.18	4.36	1.82	7	72	8.86	91.14
	2008-2015			-3.43	0.47	-1.35	76	3	96.2	3.8
	1973-2015			-1.05	1.35	0.45	22	57	27.85	72.15
2	1973-1988	78	1925	-2.27	2.62	-0.23	42	36	53.85	46.15
	1988-2000			-0.44	3.43	0.88	12	66	15.38	84.62
	2000-2008			-0.68	2.86	1.12	6	72	7.7	92.3
	2008-2015			-1.64	0.82	-0.6	65	13	83.33	16.67
	1973-2015			-0.77	2.08	0.4	25	53	32	68
3	1973-1988	56	1400	-2.14	0.29	-1.21	52	4	92.86	7.14
	1988-2000			-1.13	1.25	0.24	15	41	26.79	73.21
	2000-2008			-0.75	2.55	0.91	9	47	16	84
	2008-2015			-1.7	1.36	0.14	21	35	37.5	62.5
	1973-2015			-0.44	0.46	-0.11	41	15	73.21	26.79
4	1973-1988	65	1625	-2.71	-0.1	-1.33	65	0	100	0
	1988-2000			-0.74	1.25	0.2	19	46	29.23	70.77
	2000-2008			-0.19	4.81	1.18	6	59	9.23	90.77
	2008-2015			-1.91	2.6	1.02	15	50	23	77
	1973-2015			-0.29	0.19	-0.01	29	36	44.6	55.4
5	1973-1988	69	1700	-1.17	0.05	-0.5	68	1	98.55	1.45
	1988-2000			-1.04	0.28	-0.24	50	19	72.46	27.54
	2000-2008			-0.64	2	0.89	2	67	3	97
	2008-2015			-0.4	1.99	0.71	6	63	8.7	91.3
	1973-2015			-0.27	0.3	0.02	30	39	43.5	56.5

4.2.3. Results of future shoreline changes and discussion

The positions of shoreline in 2020 and 2050 have been forecasted for the eastern part without taking into account the disastrous impacts such as storms. For zone 1, the study of future shoreline changes indicates both erosion and accretion trend, but accretion is more significant (Figure 57). The progradation trend is dominated by the mean rates of 1.8 m/year, 0.45 m/year, and 0.62 m/year in the periods of 2015-2020, 2020-2050, and 2015-2050, respectively (Table 27). Over all periods, erosion is mainly concentrated in the area from Transect 5 to 25, whilst the remainders are accumulated by sediment supply from Gapeau river. The advance of the southern part in this zone can be resulted from the interference of Roubaud jetty in trapping the longshore sediment transport.

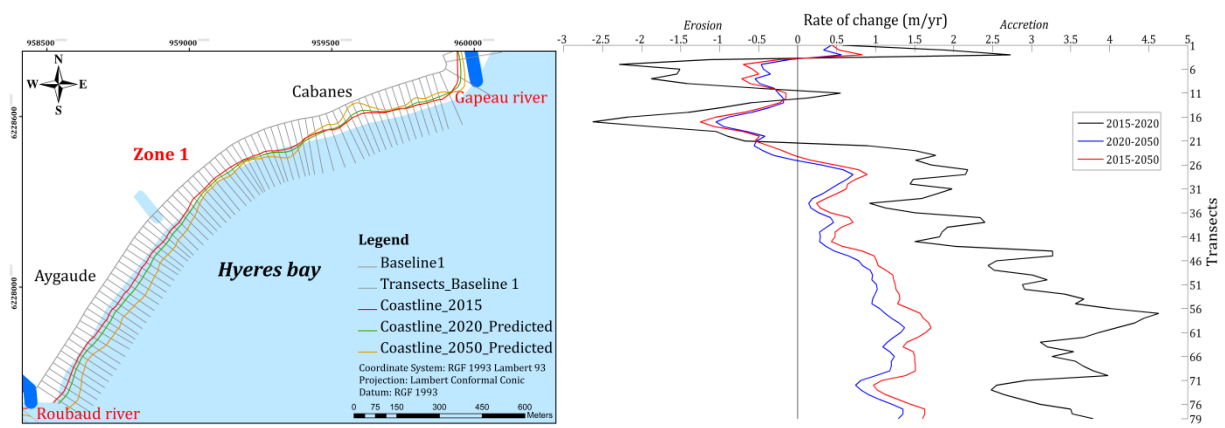


Figure 57. Positions of shorelines and transect lines as well as shoreline change rates using EPR method in the zone 1 of the eastern Giens tombolo over a period of 2015-2050.

In the zone 2, mixed erosion and accretion was exhibited. However, accretion is dominant than erosion (Figure 58). This positive trend is confirmed by the average change rates of 0.89 m/year in 2015-2020, 0.4 m/year in 2020-2050, and 0.46 m/year in 2015-2050 (Table 27). Moreover, the percentage of deposited transects is increased from 62.82% in 2015-2020 to 67.95% in the next periods. In general, Ceinturon beach will be continuously advanced seaward due to the presence of four groynes, which play the decisive role in accumulating the sediment fed by Gapeau river (Vu et al., 2017a). The maximum recession rates are often observed surrounding transect 114, immediately in the south of these groynes, whereas the maximum accretion rates mostly concentrate in the south of this zone.

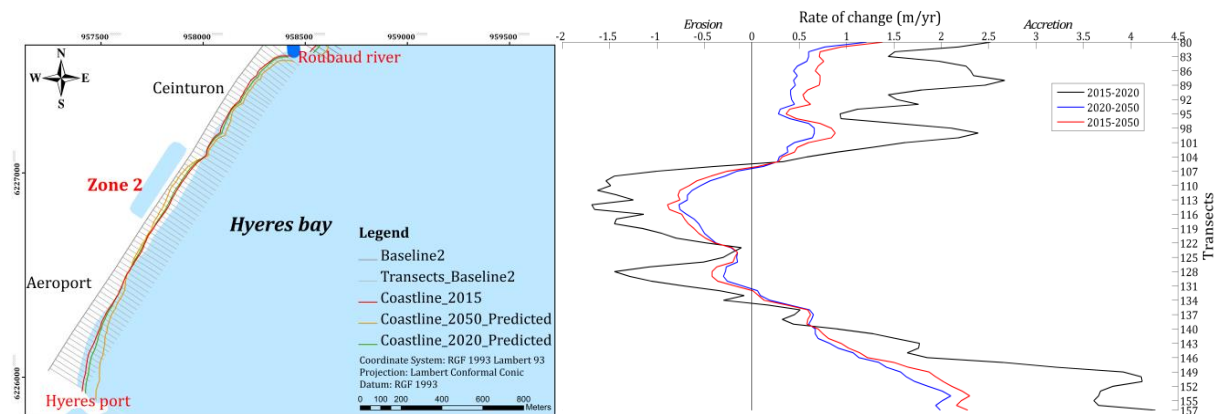


Figure 58. Positions of shorelines and transect lines as well as shoreline change rates using EPR method in the zone 2 of the eastern Giens tombolo over a period of 2015-2050.

In zone 3, most of transects manifest recession, except transect from 158 to 165 corresponding to the shoreline between Hyères port and the first groyne which are progradated (Figure 59). During the period from 2015 to 2020, the average change rate is predicted approximately -1.17 m/year, revealing an erosive trend. The maximum erosion rate of -2.59 m/year is recorded near transect 206, while the maximum accretion rate of 0.8 m/year is seen in the north of this zone. In the period from 2020 to 2050, the negative trend is maintained almost continuously from the first groyne to the jetty of La Capte port, where the maximum recession rate of -0.44 m/year is observed.

Once again, the medium-term analysis from 2015 to 2050 demonstrates the decline of shoreline with the mean change rate of -0.24m/year despite the presence of the groynes (Table 27).

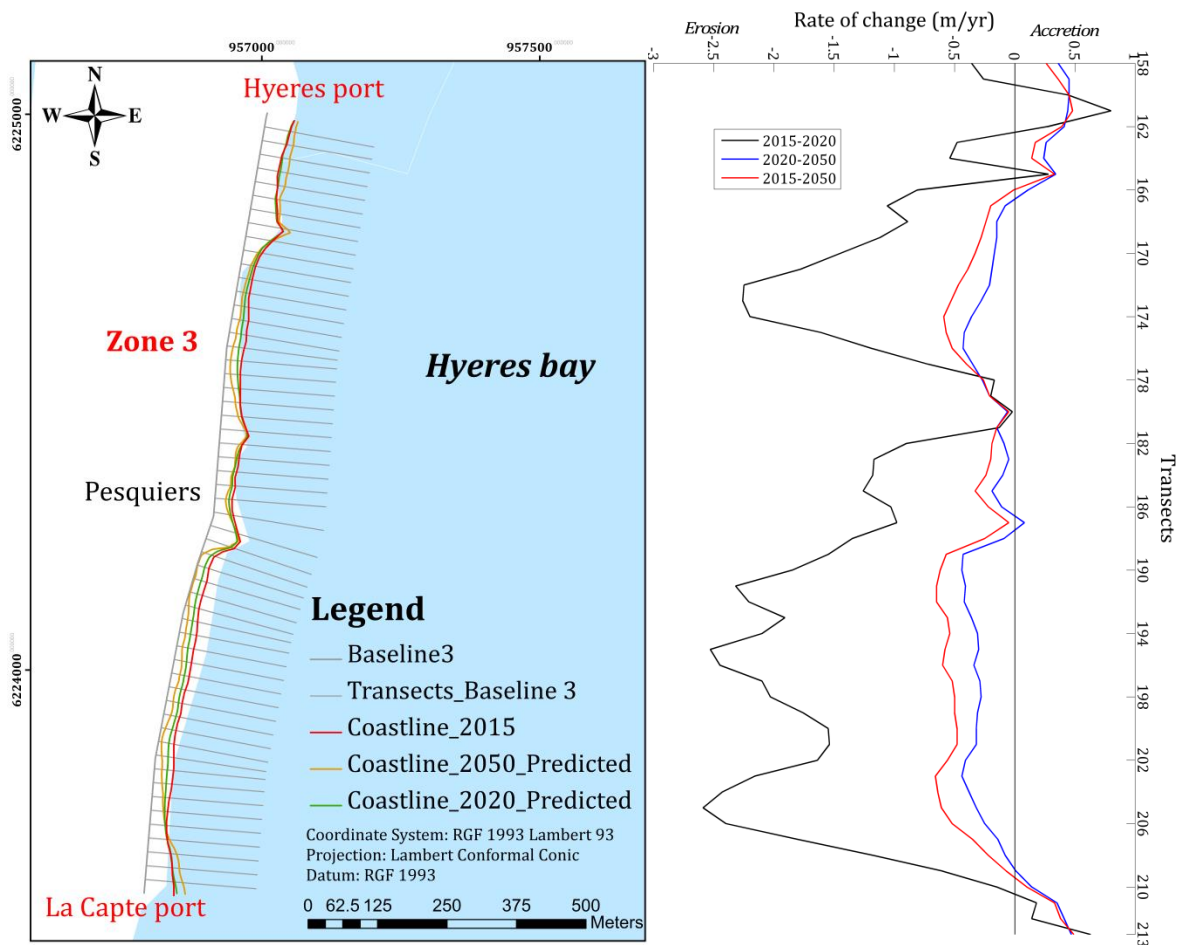


Figure 59. Positions of shorelines and transect lines as well as shoreline change rates using EPR method in the zone 3 of the eastern Giens tombolo over a period of 2015-2050.

Among of five zones along the eastern Giens tombolo, the highest erosion rate of -3 m/year is predicted for zone 4, immediately in the south of submerged geotube breakwaters. This zone is absolutely dominated by a retreating trend with 100% of eroded transects during the period from 2015 to 2020 (Figure 60). Nevertheless, this trend partly changes in the period from 2020 to 2050. The results of prediction show that the northern part of this zone has experienced erosion with the maximum rate of -0.29 m/year , whilst the southern part is subjected to sediment deposition with the maximum rate of 0.19 m/year (Table 27). Generally, the shoreline along zone 4 is forecasted to decline by the average erosion rate of -0.25 m/year over the medium-term period from 2015 to 2050, especially in the northern area of La Capte beach.

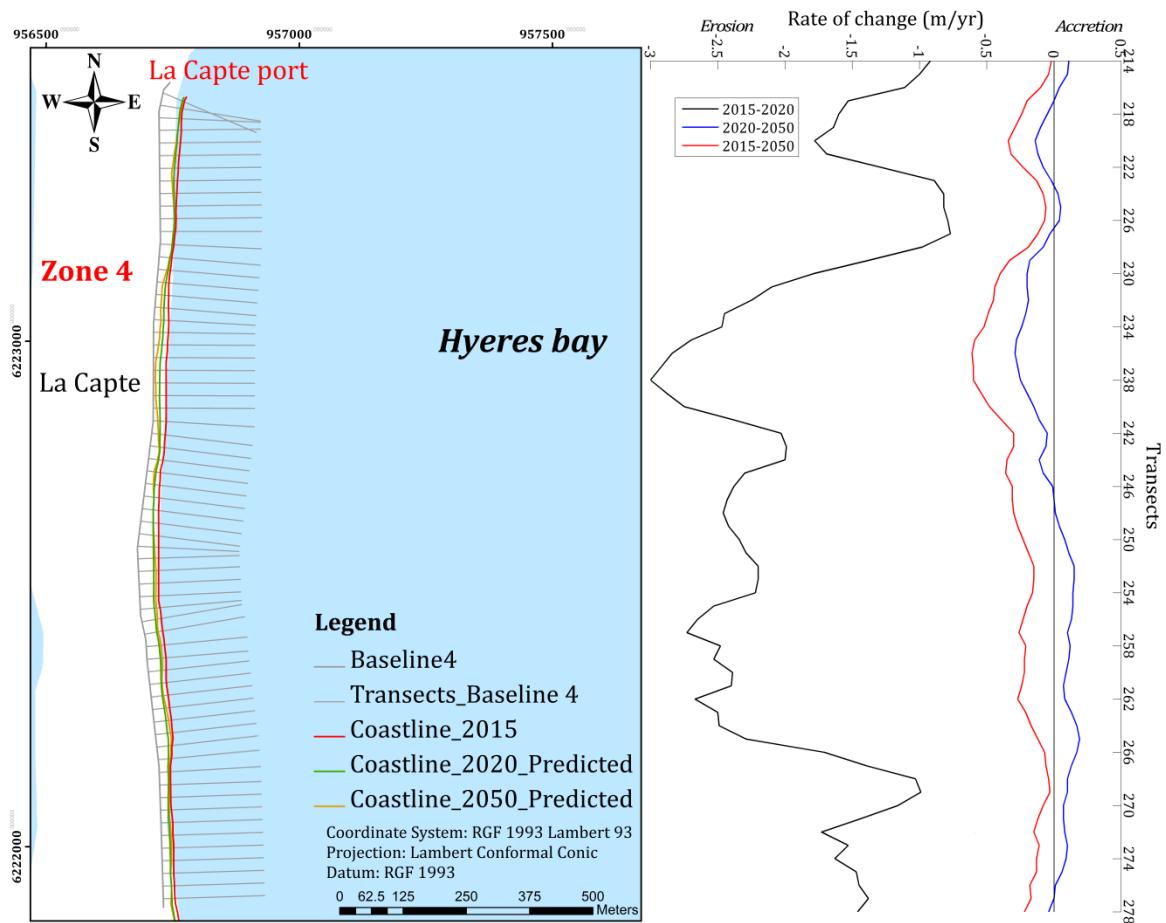


Figure 60. Positions of shorelines and transect lines as well as shoreline change rates using EPR method in the zone 4 of the eastern Giens tombolo over a period of 2015-2050.

In the last zone of the eastern branch, the variation of the shoreline over time is the lowest compared with that of other zones. Results of statistical analysis carried out for all 69 transects indicate alternating areas of erosion and accretion (Figure 61). During the period from 2015 to 2020, 100% of transects is subjected to erosion with the maximum recession rate of -2.21 m/year around transect 313. The erosive tendency decreases in the period from 2020 to 2050 with only 42% of eroded transects. Erosion is mainly concentrated in the north of Bergerie beach with the maximum recession rate of -0.28 m/year, while accretion is predicted in the south of this zone with the maximum progradation rate of 0.3 m/year. The average change rate is about 0.02 m/year, showing a little accretion trend in this period. On the other side, the medium-term analysis notices that this zone is dominated by an erosion tendency with an average retreat rate of -0.13 m/year and 82.6% of recession transects (Table 27).

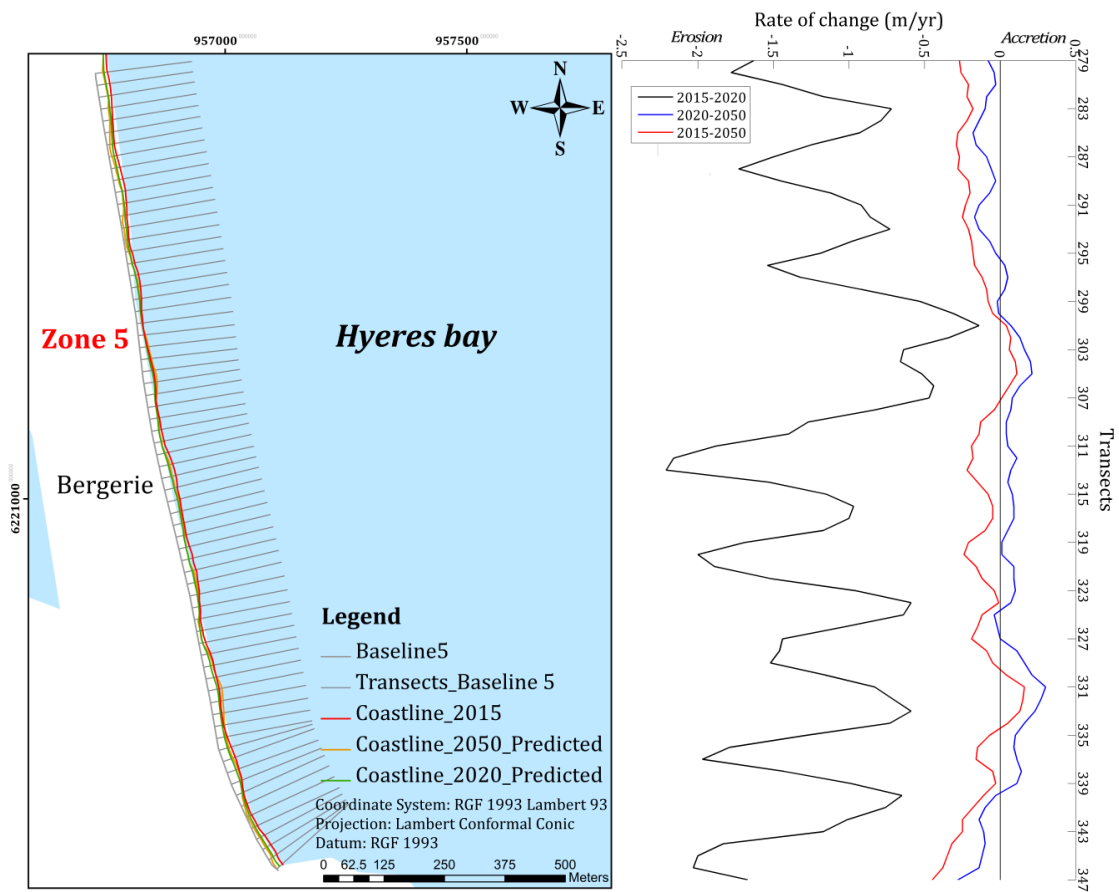


Figure 61. Positions of shorelines and transect lines as well as shoreline change rates using EPR method in the zone 5 of the eastern Giens tombolo over a period of 2015-2050.

Table 27. Statistical summary of shoreline change rate for the eastern Giens tombolo over a period of 2015-2050.

Zone	Period	No of transect	Coast length (m)	Min rate (m/yr)	Max rate (m/yr)	Mean rate (m/yr)	No of eroded transect	No of accreted transect	% of eroded transect	% of accreted transect
1	2015-2020	79	1950	-2.63	4.63	1.8	16	63	20.25	79.75
	2020-2050			-1.05	1.37	0.45	22	57	27.85	72.15
	2015-2050			-1.25	1.71	0.62	21	58	26.58	73.42
2	2015-2020	78	1925	-1.69	4.26	0.89	29	49	37.18	62.82
	2020-2050			-0.77	2.1	0.4	25	53	32.05	67.95
	2015-2050			-0.89	2.3	0.46	25	53	32.05	67.95
3	2015-2020	56	1400	-2.59	0.8	-1.17	49	7	87.5	12.5
	2020-2050			-0.44	0.47	-0.11	41	15	73.21	26.79

	2015-2050			-0.66	0.49	-0.24	44	12	78.57	21.43
	2015-2020			-3	-0.77	-1.92	65	0	100	0
4	2020-2050	65	1625	-0.29	0.19	-0.01	27	38	41.54	58.46
	2015-2050			-0.61	-0.02	-0.25	65	0	100	0
	2015-2020			-2.21	-0.14	-1.17	69	0	100	0
5	2020-2050	69	1700	-0.28	0.3	0.02	29	40	42	58
	2015-2050			-0.45	0.16	-0.13	57	12	82.6	17.4

4.3. Beach profile evolution

The beach evolution is mainly controlled by some key variables such as wave climate, sea level changes, sediment size, beach face shape, boundary conditions and interaction with coastal structures. The boundary conditions and coastal structures will be defined in each individual zone to be studied. On the other hand, due to relatively low tidal ranges, normally less than 0.3 m, sea level fluctuations at geological and intermediate time scales have not been taken into account. Accordingly, in this part, attention will be focused on the impacts of wave climate, sediment size, and beach face shape as well as their role on beach evolution.

4.3.1. Division of study area

The shoreline of the eastern Giens tombolo is from the mouth of Gapeau river to La Badine beach. The erosion or accretion rates vary depending on the position of the section that faces to the sea. In this study, the data of 11 beaches was obtained from the campaign of bathymetry measurement carried out from 2000 to 2010 along two branches of Giens tombolo by E.O.L (2010) using D-GPS technology. The selected beaches were measured once a year in mild conditions during autumn (October-November), except for measurements of 2002 and 2003, which were conducted during summer (March-April). Particularly, 2 beaches from Bona to La Badine were surveyed from 2000 to 2010, whereas 9 other beaches from Gapeau to Amont du Port (Amont) were investigated in the period of 2001-2010. The measured area extends from the shoreline to about 500-600 m seaward. These data use the horizontal coordinate reference system of NTF with the projection in Lambert III (France Sud) and the vertical reference level of LAT. Based on the characteristics of sediment and wave climate as well as the implementation of constructions, the author also propose four zones to study beach evolution in this work (Vu et al., 2017b), as shown in Figure 62.

Firstly, Zone 1 is between two mouths of Gapeau river and Roubaud river with shoreline length of 2 km. This area is mainly fed by the sediment of Gapeau river, especially in the flood season. The coarse sediments with the D_{50} of 0.65 mm occur in Gapeau mouth, reflecting the role of fluvial contribution in the grain size of sediment in the swash zone (Capanni, 2011).

Next, Zone 2 extends from Roubaud mouth to the north breakwater of Hyères port. This zone is subjected to erosion because it directly faces the southeast waves which are the most frequent direction in Hyères bay (Courtaud, 2000). Nonetheless, accretion is observed in the upstream part of Hyères port because the breakwaters of this port stop the main longshore drift from north to south. In this zone, the sediment size sorting is accompanied by a strong reduction in D_{50} (from 0.53 to 02.5 mm) (Table 28).

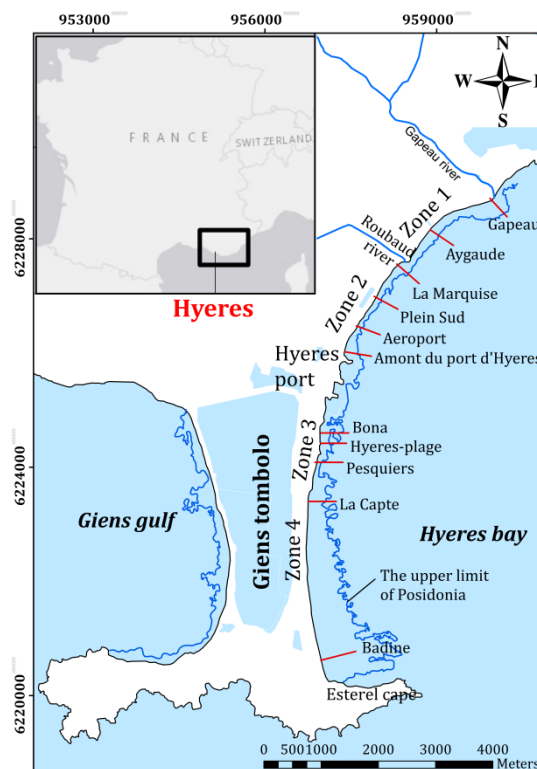


Figure 62. Location of the studied zones and beach profiles along the eastern branch of Giens tombolo, Hyères.

Zone 3 is marked by La Capte port in the south and Hyères port in the north. This zone is immediately subjected to the eastern and southeastern wave actions. From the port of Hyères to La Capte, the sediments become drastically coarser ($D_{50} \geq 0.5$ mm). The presence of Hyères port would cause a severe erosion in downstream drift and exports the finest materials, easily mobilized, which could generate the inherited coarse sediment supplies (Capanni, 2011).

Table 28. Beach-face slope and sediment characteristics in Hyères bay (Capanni, 2011; Courtaud, 2000; E.O.L, 2010).

Beach	D_{50} (mm)	w (cm/s)	A ($m^{1/3}$)	S_0 (%)
Gapeau	0.65	8.75	0.174	1.6
Aygaude	0.57	7.57	0.1633	1.9
La Marquise	0.53	6.99	0.1576	1.2
Plein Sud (Ceinturon)	0.25	3.06	0.1096	2.7
Aéroport	0.25	3.06	0.1096	1.4
Amont du Port (Amont)	0.25	3.06	0.1096	1.7
Bona	0.43	5.55	0.1424	2.0
Hyères plage	0.43	5.55	0.1424	2.4
Pesquiers	0.81	11.14	0.1935	3.3
La Capte	0.38	4.85	0.1197	1.6
La Badine	0.25	3.06	0.1096	1.0

The last area, Zone 4 has the largest shoreline length of about 3.5 km. In the north of this zone, La Capte beach is strongly suffered the impact of east and northeast waves. Hence, the erosion phenomenon usually happens in this beach. In contrast, the south of Zone 4 is quite stable due to its position sheltered by the cape of Esterel (Figure 62). The finest diameter of sediment with D_{50} of 0.25 mm (Table 28) is also found in the south of Zone 4.

4.3.2. Beach evolution

The concept of EBP is applied in many coastal engineering projects, especially in beach fill works (Dean, 1991). One hundred and ten measured beach profiles are used to validate seven EBPs at selected beaches along the eastern tombolo. The main factors controlling these EBPs are also uncovered in the present study. The detailed results are described in Table 29 and Table 30 and from Figure 63 to Figure 84.

Table 29. Comparison of R-square among EBP functions at beaches along the eastern Giens tombolo.

Name of profile	R-square						
	Bodge	Dean	Komar	Lee	Romanczyk	Sierra	Vellinga
Gapeau	0.9983	0.8523	0.9992	0.9728	0.8616	0.9894	0.8172
Aygaude	0.9589	0.9091	0.7556	0.6255	0.9141	0.9850	0.9334
La Marquise	0.9805	0.9027	0.9635	0.9806	0.9070	0.9809	0.8733
Plein Sud	0.8139	0.8526	0.8139	0.7583	0.8544	0.8503	0.9005
Aéroport	0.9696	0.8774	0.9960	0.9625	0.8689	0.9692	0.8385
Amont	0.9604	0.8759	0.9615	0.9488	0.8894	0.9743	0.8279
Bona	0.8853	0.7384	0.5971	0.5314	0.7466	0.8457	0.7826
Hyères plage	0.9720	0.8052	0.7848	0.5970	0.8112	0.8829	0.8361
Pesquiers	0.7149	0.6442	0.5944	0.4441	0.6452	0.6824	0.6505
La Capte	0.9433	0.8275	0.9433	0.9966	0.8270	0.9036	0.7669
Badine	0.9998	0.9999	0.9999	0.9936	0.9960	0.9900	0.8475

Table 30. Comparison of RMSE among EBP functions at beaches along the eastern Giens tombolo.

Name of profile	RMSE						
	Bodge	Dean	Komar	Lee	Romanczyk	Sierra	Vellinga
Gapeau	0.0816	0.7684	0.0551	0.3299	0.7439	0.2056	0.8549
Ayguade	0.2778	0.4130	0.6773	0.8385	0.4016	0.1678	0.3537
La Marquise	0.2646	0.5914	0.3623	0.2642	0.5784	0.2623	0.6750
Plein Sud	0.5016	0.4464	0.5016	0.5717	0.4437	0.4500	0.3668
Aéroport	0.2961	0.5944	0.1073	0.3289	0.6148	0.2982	0.6823
Amont	0.5102	0.9028	0.5027	0.5800	0.8521	0.4112	1.0632
Bona	0.5942	0.8974	1.1136	1.2010	0.8832	0.6893	0.8180
Hyères plage	0.2559	0.6746	0.7090	0.9703	0.6642	0.5232	0.6188
Pesquiers	0.8979	1.0031	1.0707	1.2536	1.0016	0.9478	0.9942
La Capte	0.4815	0.8396	0.4815	0.1173	0.8408	0.6278	0.9760
Badine	0.0228	0.0149	0.0196	0.1396	0.1098	0.1736	0.6794

4.3.2.1. Zone 1

In zone 1, two typical investigated cross-sections are that of Gapeau and Ayguade. At Gapeau beach, 9 beach profiles measured from 2001 to 2010 by E.O.L are supplied for this work (Figure 63). The average slope of Gapeau beach is about 1.6% from the shoreline to 450 m offshore (Table 28). It is noted that the shape of beach profile maintains slightly upward convex without bars and troughs at Gapeau beach, although it was eroded comparing with the measurement data of 2002. The highest erosive area appears at the water depth of 2 to 3 m and at position of about 150m seaward of the shoreline. Seven EBP models are fitted to the measured data of 9 beach profiles by using the nonlinear least squares formulation. Results reveal that the Dean (1977) and Romańczyk et al. (2005) EBP curves have the same R-square of 0.8514 and the same RMSE of 0.7707, but the EBP function of Komar et al. (1994) provides the best fit to the measured data with R-square of 0.9992, and RMSE of 0.0551 (Table 29 and Table 30, respectively). The average measured profile is also compared with seven EBP models (Figure 64) and it shows consistency with Komar et al. (1994)'s equation than others. The surface error between the EBP function of Komar et al. (1994) and the average beach profile is about only +3.1 m² per profile unit. This means that beach profile somewhat excesses the equilibrium profile condition. However, the beach face tends to be flattened to get the equilibrium shape without bars as these EBPs do not take into account unidirectional currents or the migration of sand bars during the storm events and flood season (Kaiser et al., 2009). The EBP expression of Komar et al. (1994) can virtually represent the trend of Gapeau beach evolution if the average predicted beach face slope S_0 could be kept around 1.56% (Table 31).

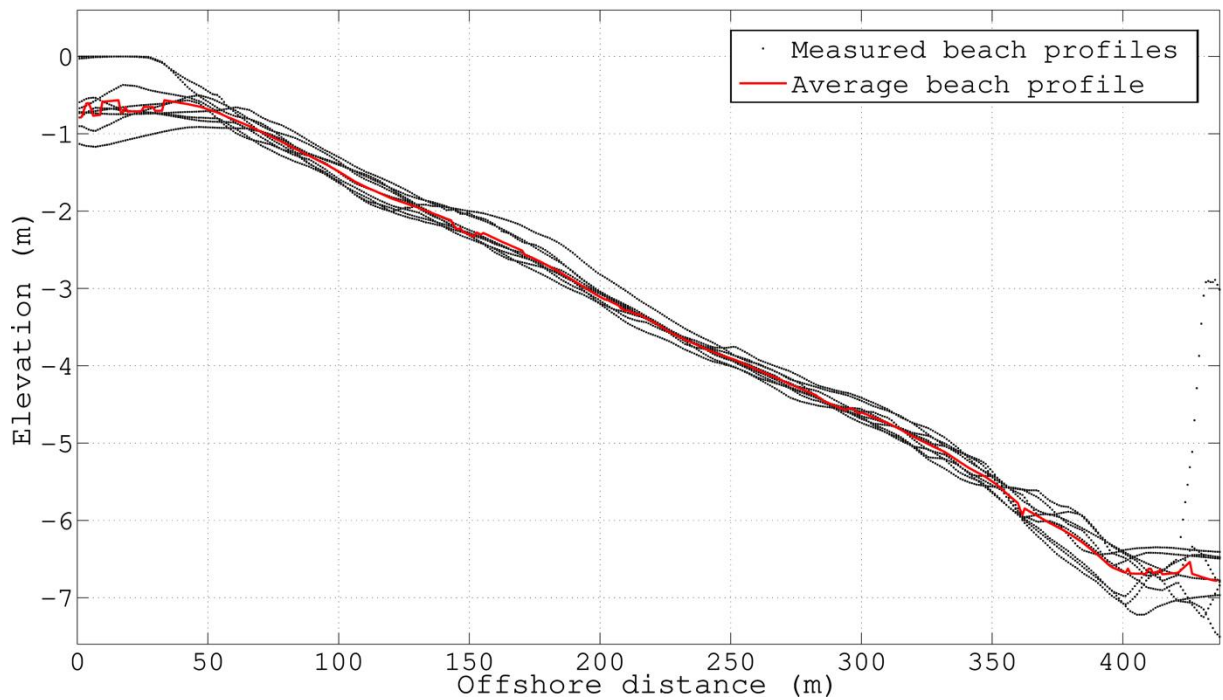


Figure 63. Beach profiles measured by E.O.L at Gapeau beach from 2001 to 2010.

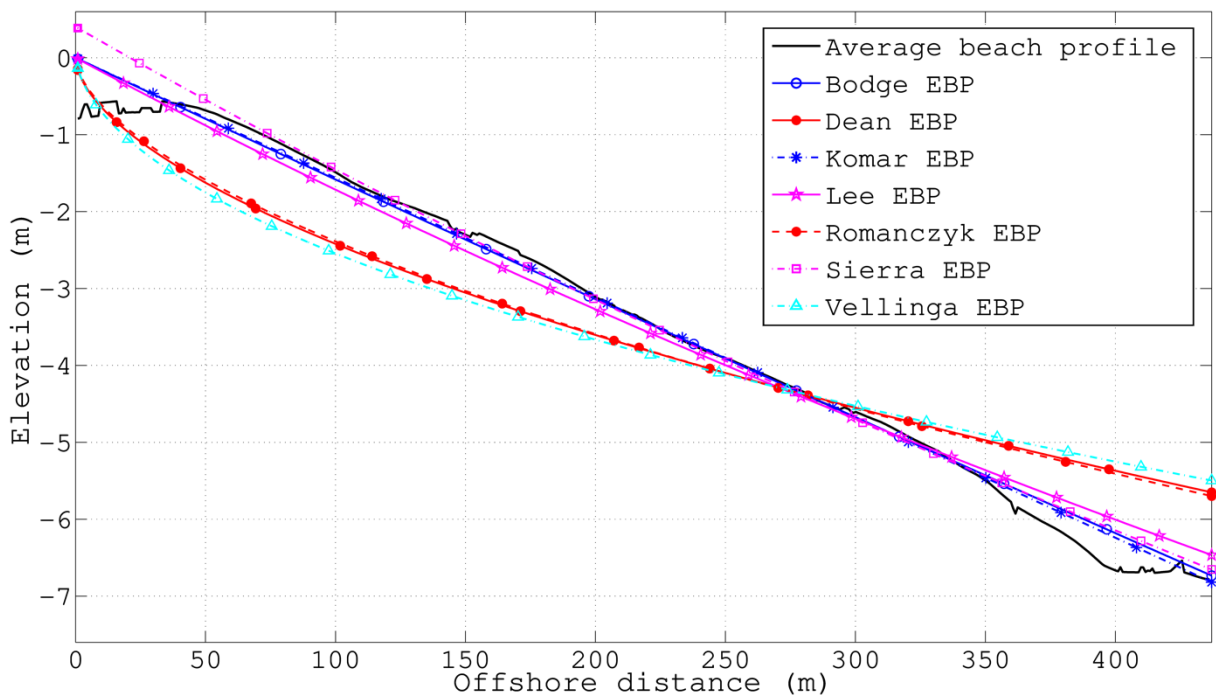


Figure 64. A comparison of an average measured beach profile and the predicted EBPs at Gapeau beach.

The Ayguade beach is located on the updrift of Roubaud jetty. As a result of the blockage of the longshore drift, an accretive area occurs in this beach from the shoreline to the depth of 2 m. Total 10 beach profiles measured by E.O.L from 2001 to 2010 were used to investigate the beach evolution as well as validate seven EBP (Figure 65). It is easily seen that the overall beach profile has the upward convex shape with many low bars and troughs at the water depth of 4.5 m and far from the coast about 250 m. This beach maintains the average slope of about 1.9% from the shoreline to 500 m seaward

of the shoreline (Table 28). All seven EBP functions describe the actual beach profile quite differently and can be distinguished (Figure 66). The average measured beach profile also reveals better match with Sierra et al. (1994)'s EBP function with R-square of 0.985 and RMSE of 0.1678 than other functions (Table 29 and Table 30, respectively). This EBP expression clings quite close to the average measured beach profile from the shoreline to 200 m seaward of the shoreline. The difference between the EBP function of Sierra et al. (1994) and the average measured beach profile results in the surface error per profile unit of -23.04 m^2 . This value also implies that the average beach profile needs to be added with moderate sediment volume in order to reach the equilibrium state, viz. in troughs from 200 m to 300 m seaward of the shoreline. This equilibrium state can be obtained, especially in flood season if accretion is continuously observed in this area with the support of Roubaud jetty. Therefore, it strongly demonstrates that the EBP function of Sierra et al. (1994) could represent the beach profile evolution of Ayguade correctly.

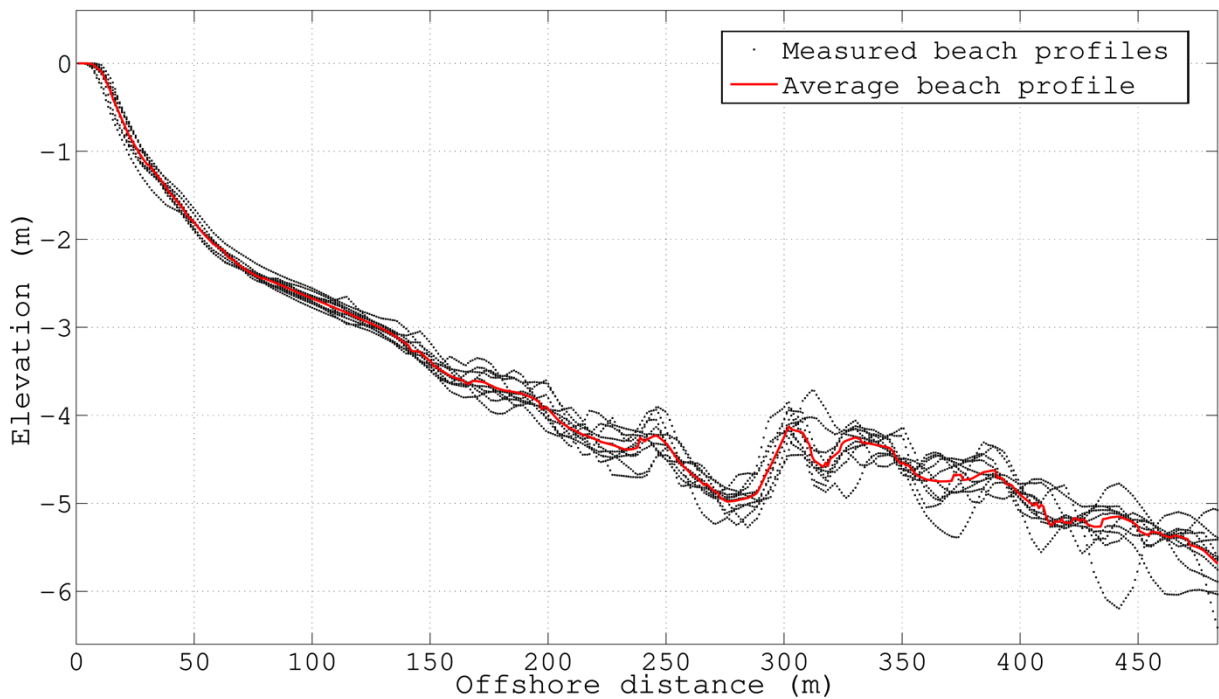


Figure 65. Beach profiles measured by E.O.L. at Ayguade beach from 2001 to 2010.

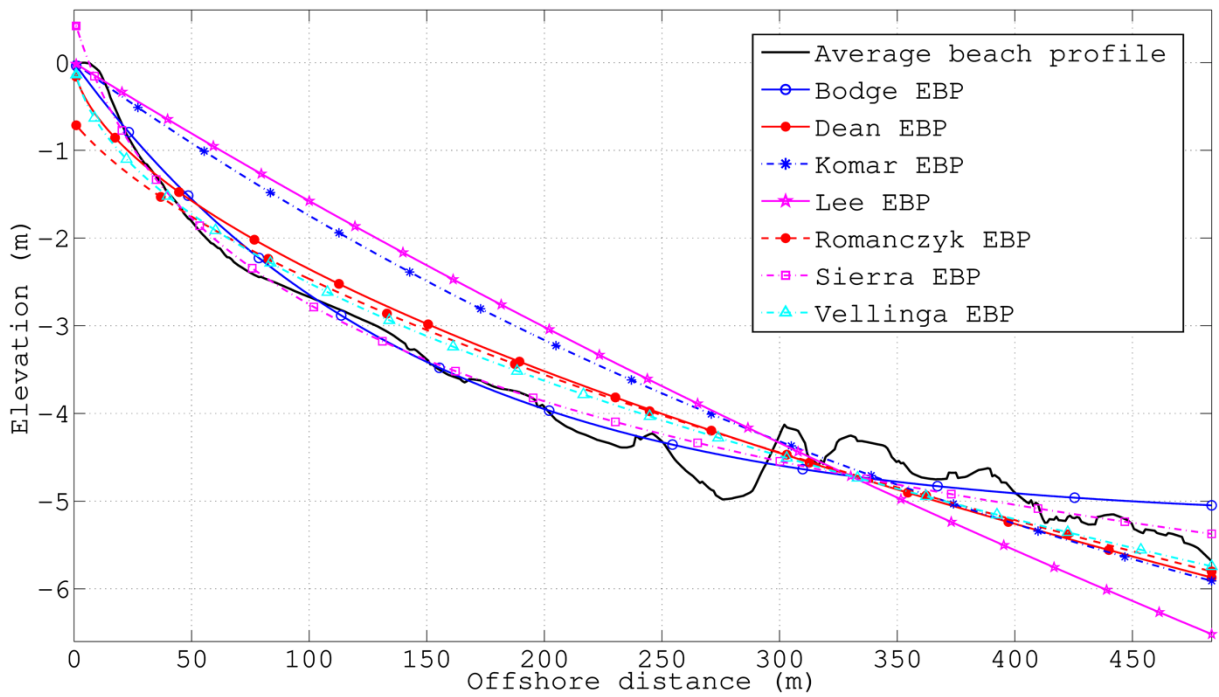


Figure 66. A comparison of an average measured beach profile and the predicted EBPs at Ayguade beach.

4.3.2.2. Zone 2

Based on the measured data of the campaigns from 2001 to 2010, it is exhibited that the bathymetry in this zone is divided into two completely different states: erosion in the north (La Marquise and Plein Sud beaches) and accretion in the south (Aéroport and Amont du Port d'Hyères beaches).

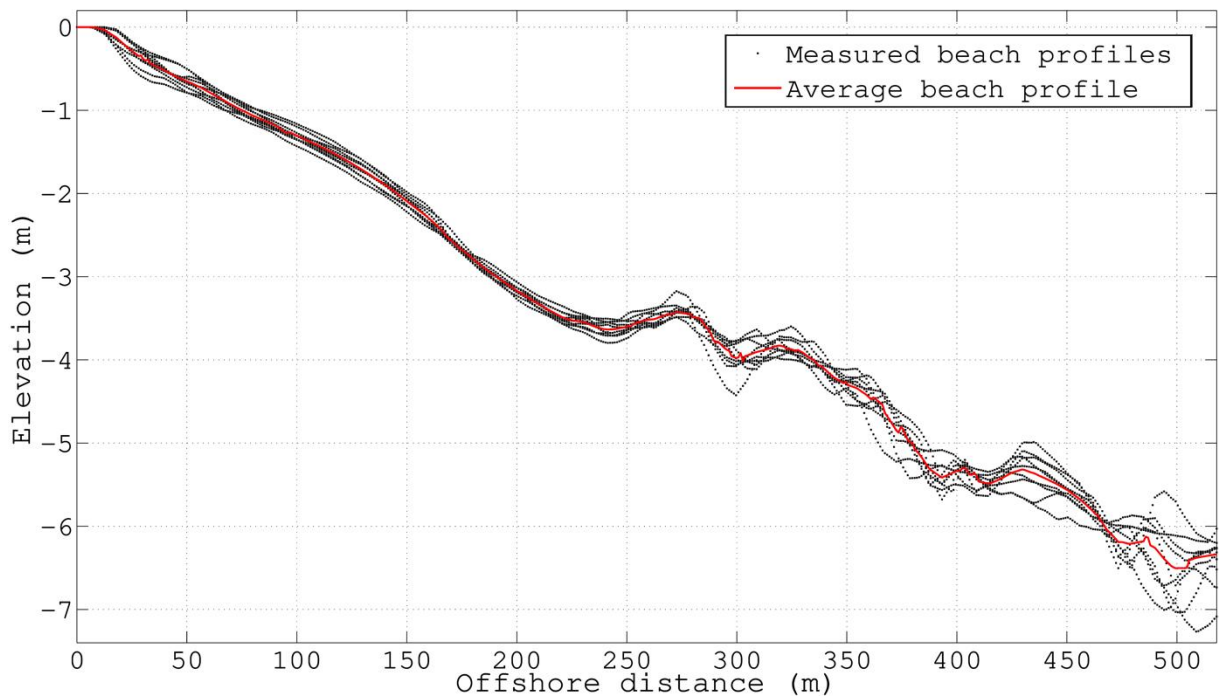


Figure 67. Beach profiles measured by E.O.L at La Marquise beach from 2001 to 2010.

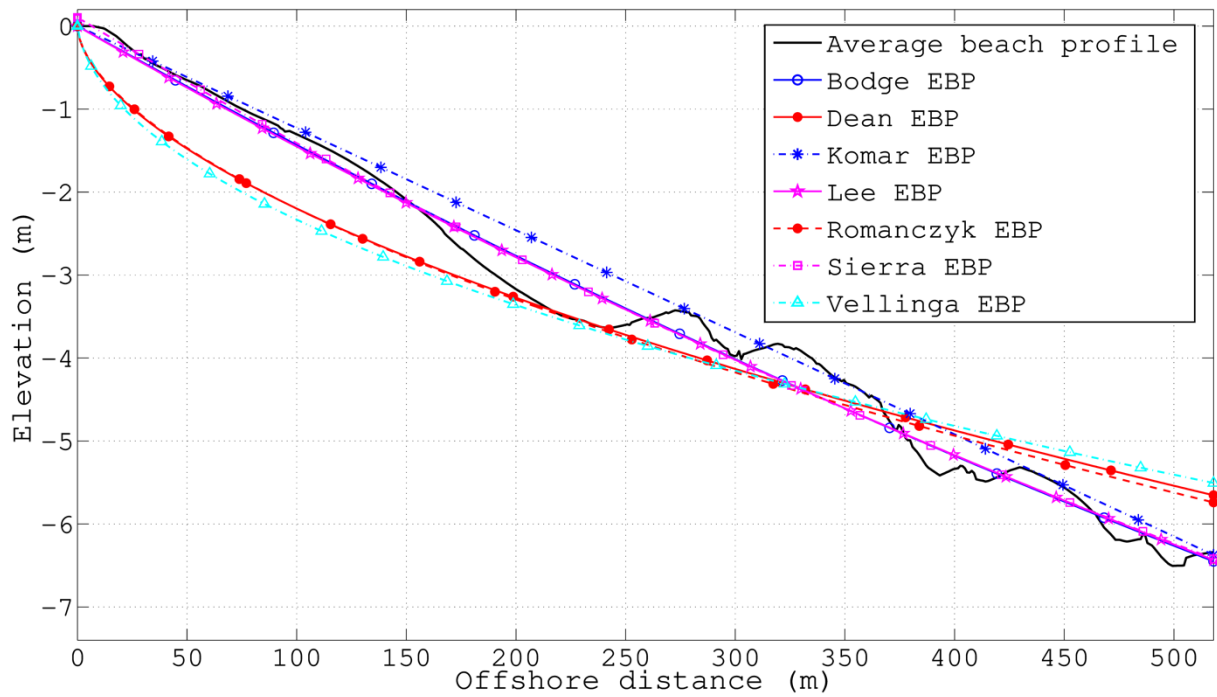


Figure 68. A comparison of an average measured beach profile and the predicted EBPs at La Marquise beach.

The current research was supplied with nine beach profiles surveyed at the downdrift of Roubaud river mouth (Figure 62). In La Marquise, the beach profile over time changes not too much with slight erosion between levels of -1 m and -2.5 m in accordance with the distance between 50 m and 150 m seaward of the shoreline. The general slope remains approximately 1.7% in range of 200 m wide from the shoreline. The average slope from the shoreline to 500 m offshore is estimated about 1.2% (Table 28). Subsequently, some low bars and troughs appeared continuously at the water depth of 3.5 m, corresponding to 250 m seaward of the shoreline (Figure 67). The shape of beach profile is slightly upward convex. Seven EBP models are fitted to the measured data of 9 beach profiles at La Marquise beach. Results indicate that Bodge (1992), Komar et al. (1994), Lee (1994), and Sierra et al. (1994) functions describe the good form of beach profile as linear and similarly coincide together. However, the EBP of Sierra et al. (1994) is the best-fit function for this actual beach profile with R-square of 0.9809 and RMSE of 0.2623 (Table 29 and Table 30, respectively). Additionally, the average measured beach profile is analyzed and compared with seven models of EBP (Figure 68) and it also presents better agreement with Sierra et al. (1994)'s function than other functions. Comparing the Sierra EBP curve with the average beach profile leads to the very small surface error per profile unit of -5.78 m^2 . If the accretion trend takes place or beach fill is carried out, the equilibrium state of this beach profile can be reached easily. Correspondingly, the EBP model of Sierra et al. (1994) exhibits the evolution trend of La Marquise beach perfectly.

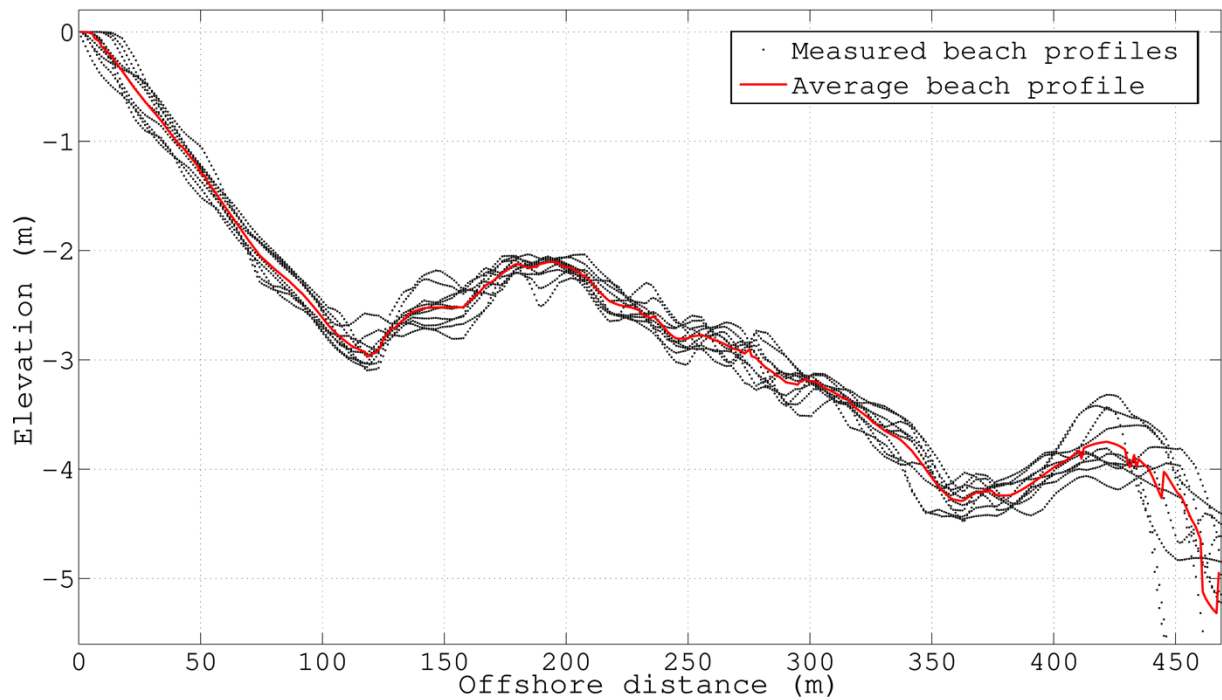


Figure 69. Beach profiles measured by E.O.L at Plein Sud beach from 2001 to 2010.

The results of the measurement campaigns by E.O.L (2010) indicate that Plein Sud beach has suffered moderate erosion which can threaten the existence of the RD 42 road. This would be explicated by the fact that the jetty of Roubaud river and four groynes in La Marquise beach block the main longshore drift and cause the sediment shortage in Plein Sud beach. Meanwhile, the strong southeast waves, which are dominant directly attack this area. The erosional hot spot happens in a distance of about 100 m from the shoreline to the depth of 3 m. The 10 beach profiles surveyed at Plein Sud from 2001 to 2010 were used in this work (Figure 69). The steep slope of about 2.7% is observed from the shoreline to 125 m seaward. The wide and shallow troughs and bars occur at a seaward distance of more than 100 m. The shape of seven EBP functions fitted to the measured beach profile data are found and depicted in Figure 70. In addition, comparing with the average beach profile uncovers that the EBP function of Vellinga (1987) also fits best with the field data. The goodness of fit statistics has R-square of 0.9005 and RMSE of 0.3668 (Table 29 and Table 30, respectively). The surface error per profile unit created by Vellinga (1987) EBP curve and the average beach profile is about -39.41 m^2 . To attain the equilibrium shape, not only a huge volume of sediment needs be placed in this beach, but also the offshore wave height of 0.66 m and the median grain size of 0.25 mm have to be maintained (Table 31). Although more than 10000 m^3 were used to nourish Plein Sud beach from 2003 to 2010 (OCEANIDE, 2010), it is still eroded and out of equilibrium.

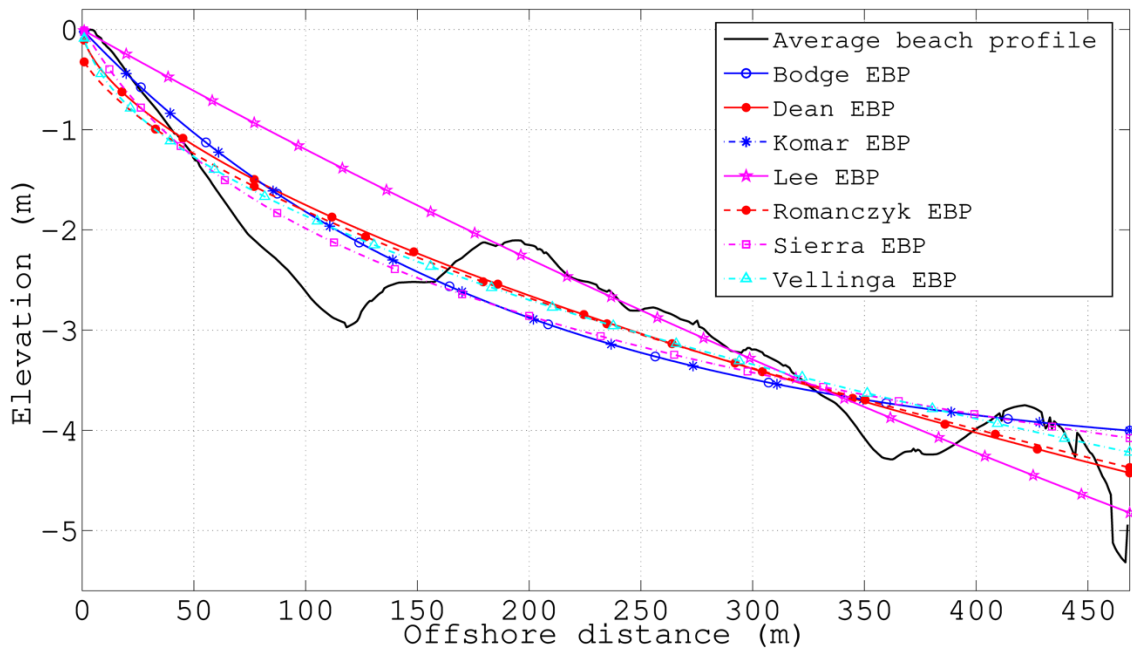


Figure 70. A comparison of an average measured beach profile and the predicted EBPs at **Plein Sud beach.**

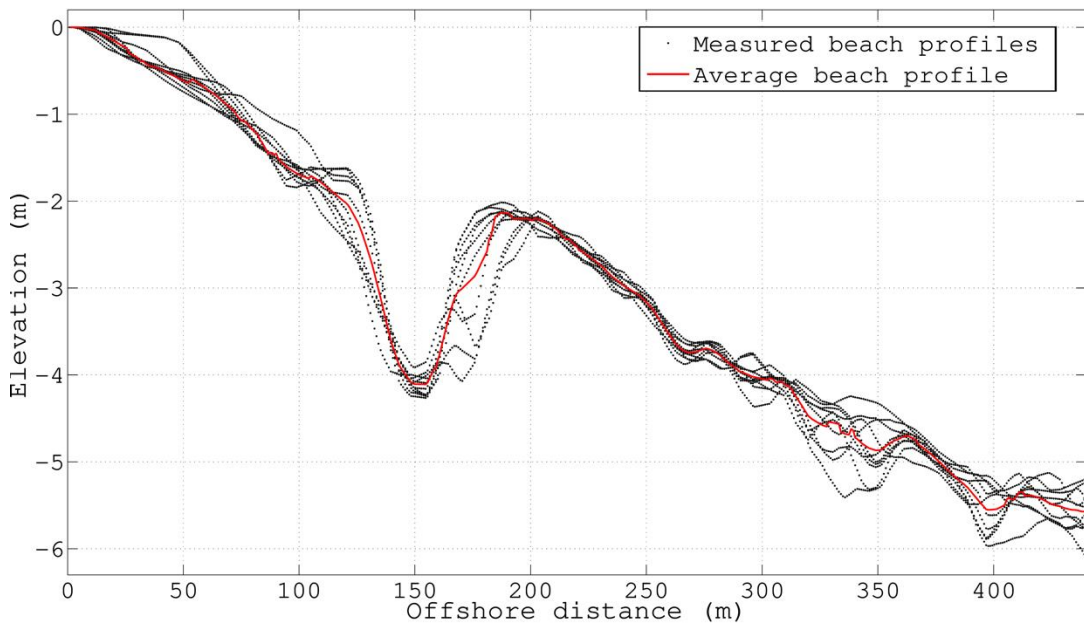


Figure 71. Beach profiles measured by E.O.L at Aéroport beach from 2001 to 2010.

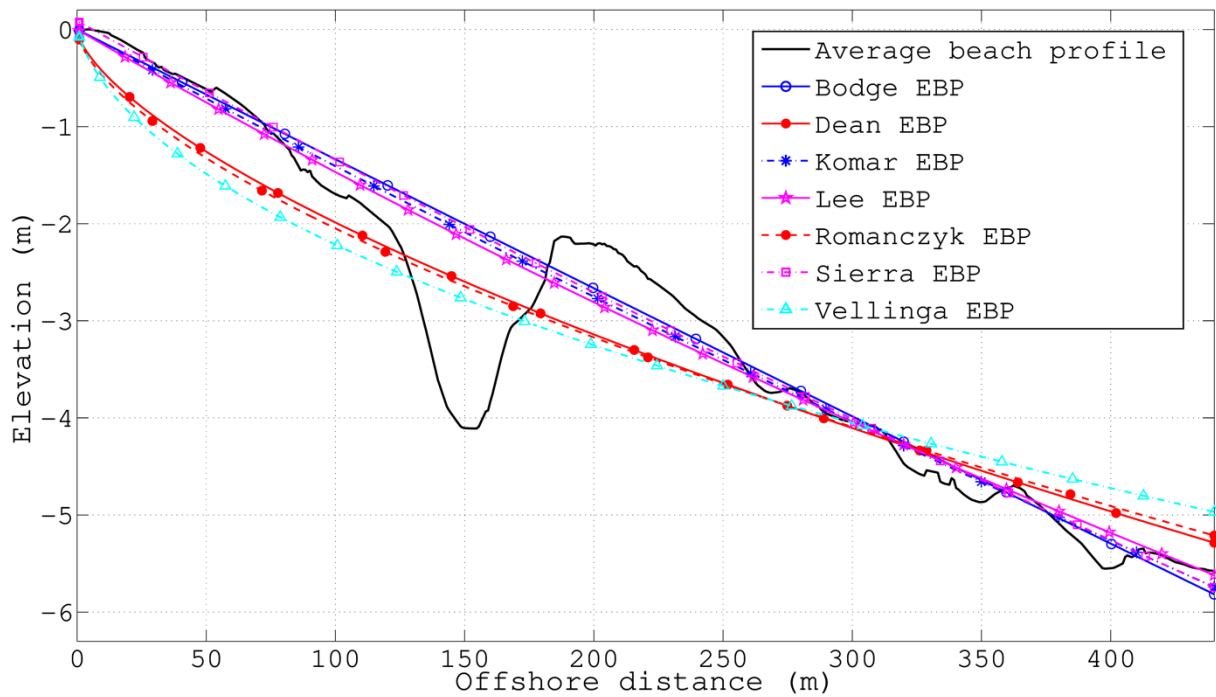


Figure 72. A comparison of an average measured beach profile and the predicted EBPs at Aéroport beach.

Similar to Plein Sud beach, ten measured beach profiles supplied by E.O.L (2010) were used to investigate the Aéroport beach evolution as well as fit EBP models. This beach is subjected to permanent erosion, more or less compensated by artificial nourishment conducted annually. Additionally, the contribution of rocks to build the road has had a detrimental effect on the accelerating erosion of the beach (OCEANIDE, 2010). The slope of the submarine beach is about 2.7‰ to the upper limit of Posidonia seagrass (Figure 62). On average, the slope from the shoreline to 500 m seaward is 1.4‰ (Table 28). Also in this beach, the 2m deep trough has been easily observed in the distance of about 120 m from the shoreline (Figure 71). Curve fitting calculations of overall profile for seven types of EBP functions were carried out. The results show that all seven EBP functions are visible distinctively (Figure 72). It confirms that the measure data is more consistent with Komar et al. (1994)'s model. Furthermore, the average profile in Figure 72 also illustrates that the EBP function of Komar et al. (1994) fits best with the measured data. The goodness of fit statistics has R-square of 0.996 and RMSE of 0.1073 (Table 29 and Table 30, respectively). Like Gapeau beach, the suitability of Komar et al. (1994) EBP curve reveals the vital influence of beach face slope on the evolution of Aéroport beach. Furthermore, the difference between the EBP of Komar et al. (1994) and the average beach profile causes the surface error per profile unit of -67.5 m². This large difference is attributed to the presence of deep trough located from 120 m to 200 m seaward of the shoreline as well as severe erosion induced by the southeast waves and sediment deficit.

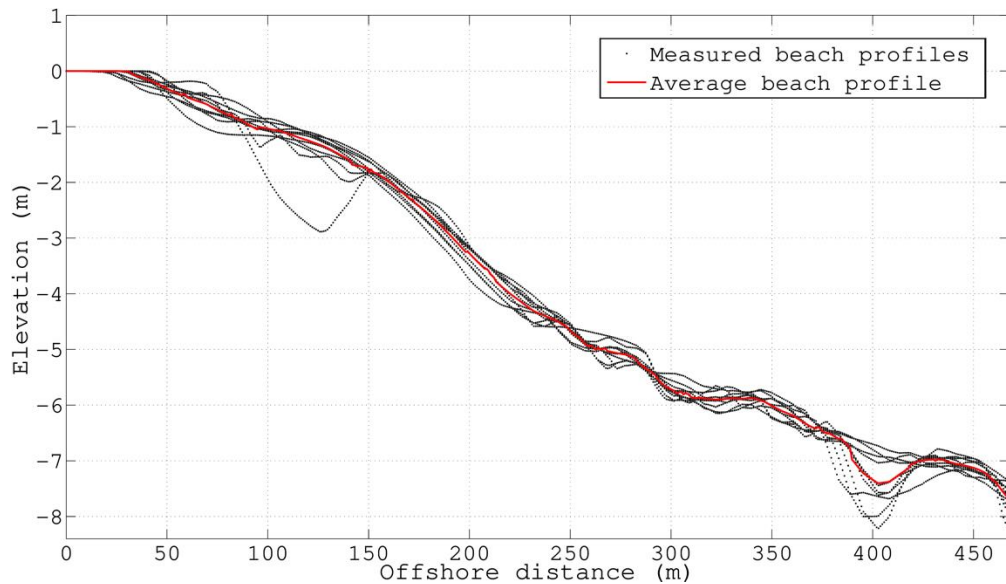


Figure 73. Beach profiles measured by E.O.L at Amont beach from 2001 to 2010.

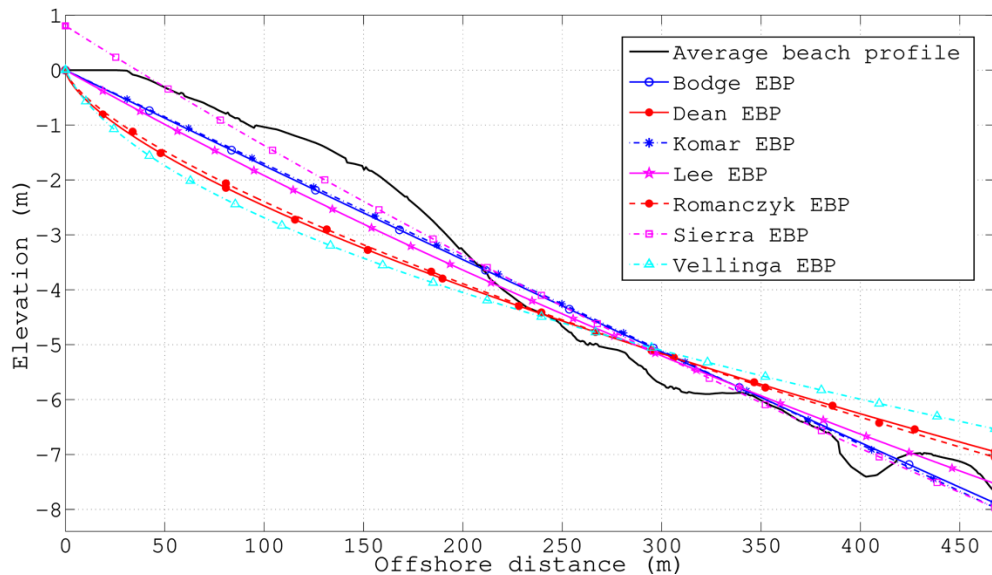


Figure 74. A comparison of an average measured beach profile and the predicted EBPs at Amont beach.

The last beach in this zone is that of Amont which is located right in the updrift of the breakwater of Hyères Port. Ten beach profiles surveyed by E.O.L from 2001 to 2010 (Figure 73) indicate that this area is a heavy deposition zone due to the blockage of alongshore sediment transport by the north breakwater of Hyères Port. It also has the gentlest slope of 1.7% and the smoothest bathymetry in this zone, but upward convex shape. Seven EBP functions were fitted to the measured beach profile data are shown in Figure 74. By means of comparing with an average beach profile, the EBP function of Sierra et al. (1994) shows more agreement with the field data than the others. The goodness of fit statistics has R-square of 0.9743 and RMSE of 0.4112 (Table 29 and Table 30, respectively). This EBP curve also makes the surface error per profile unit of +12.05 m² comparing with the average beach profile. The excess equilibrium state will continue if Gapeau river still supplies the sediment for Hyères bay.

4.3.2.3. Zone 3

This zone is divided into three discriminable sections, viz. Bona beach, Hyères beach, and Pesquiers beach, by groynes and jetty. The results of bathymetry campaigns conducted by E.O.L from 2000 to 2010 show that, from Bona beach to Hyères beach, along the first 35 m, the slope remains steep and reaches 4.5%. In Pesquiers beach, the *Posidonia* seagrass appears in the very shallow area of the submarine beach (about level of -2.5 m) (Figure 62). There is an active depositional band located from 60 m to 150 m seaward of the shoreline in the south of this beach. In general, the beach profiles in zone 3 have the upward convex shape with high bars and deep troughs.

E.O.L (2010) supplied 10 beach profiles surveyed at Bona beach. The measured beach profiles show moderate erosion occurred between the shoreline and 50 m seaward of the shoreline (Figure 75). The shoreward half of the profile tends to be downward concave with the average slope of 2.0%. The beach profile in the offshore direction is marked by the bar of about 1 m high at 180 m seaward of the shoreline. Seven EBP functions are obtained from curve fitting calculations based on the measured beach profile data. The result of these calculations is presented in Figure 76. The EBP functions of Bodge (1992) and Sierra et al. (1994) show consistency with the average beach profile from the shoreline to 150 m distance offshore, but the expression of Bodge (1992) better describes the shape of Bona beach profile with R-square of 0.8853 and RMSE of 0.5942 (Table 29 and Table 30, respectively). The wide troughs and bars have not been described by this equation. On the other hand, the surface error per profile unit between Bodge (1992)'s curve and the average beach profile is estimated approximately -34.31 m². This surface error will enlarge and the equilibrium state could not be reached if erosion takes place continuously without any protection measure.

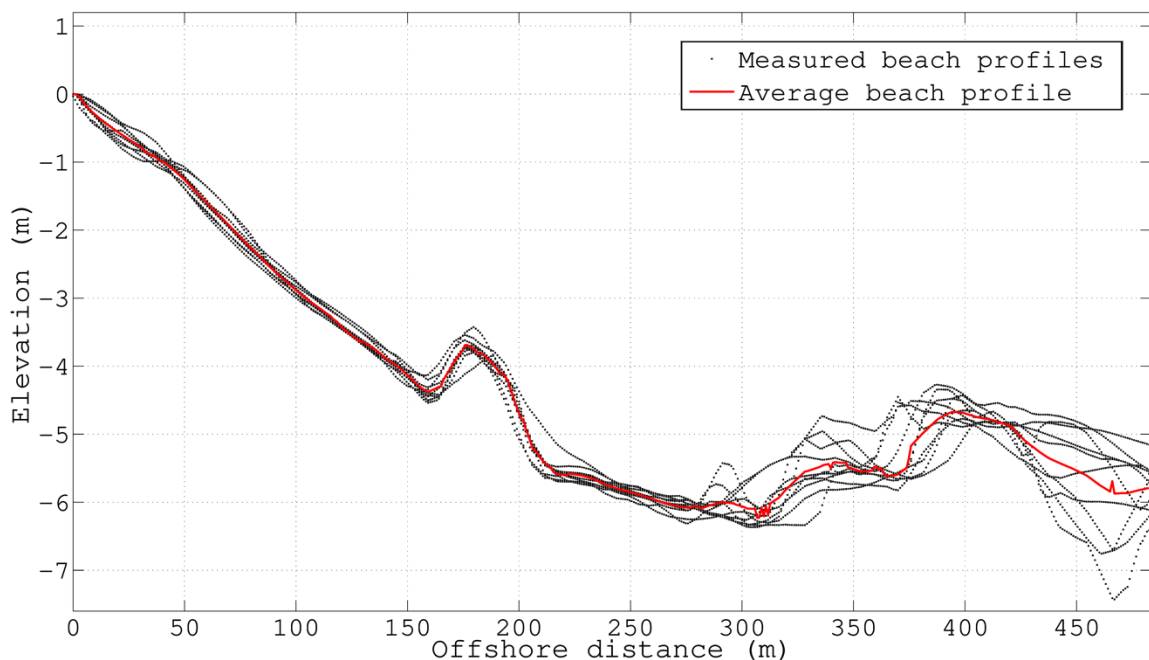


Figure 75. Beach profiles measured by E.O.L at Bona beach from 2001 to 2010.

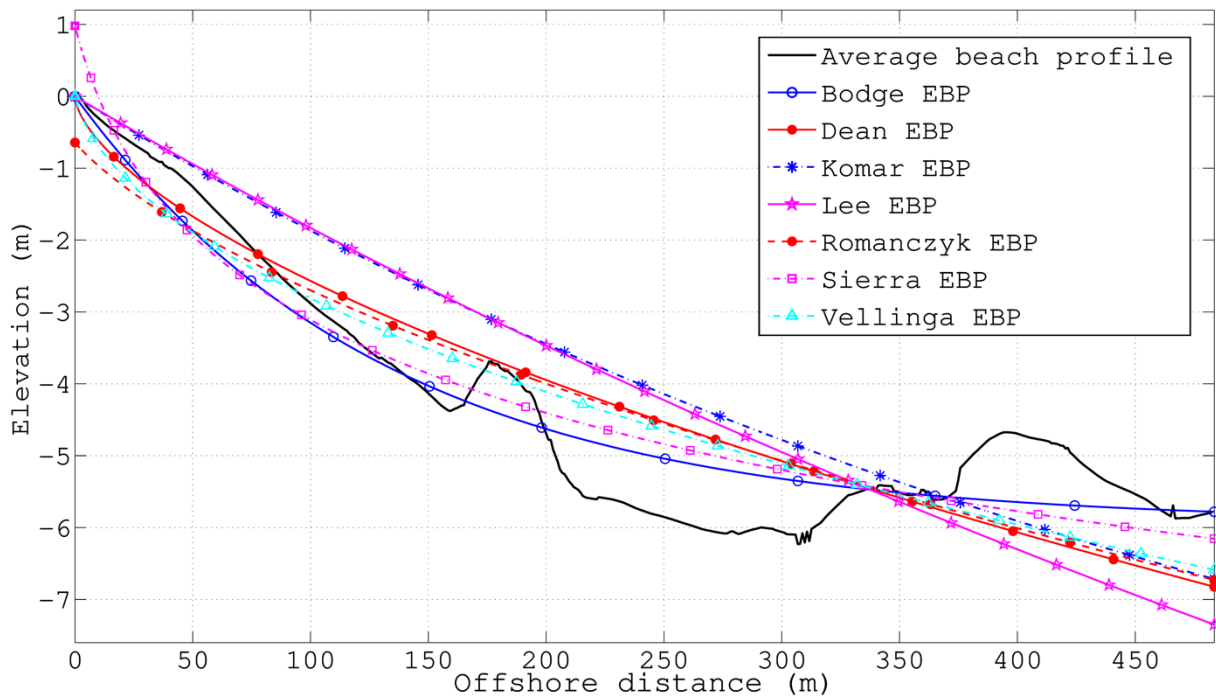


Figure 76. A comparison of an average measured beach profile and the predicted EBPs at Bona beach.

Regarding Hyères beach, ten beach profiles measured by E.O.L from 2001 to 2010 were provided for this research (Figure 77). According to the measured bathymetric data, the submarine beach slope from the shoreline to the upper limit of *Posidonia* (Figure 62) is about 2.5% and 4.5% in the north and south of Hyères beach, respectively. On average, the slope from the shore to 450 m seaward falls in around 2.4% (Table 28). As can be seen in Figure 77, the bathymetry of Hyères beach changed over time. The foreshore of 50 m is deposited by the nourishment works in 2007 and 2010. A few shallow bars and troughs are noted at distances offshore ranging from 150 to 350 m, corresponding to 3.5-5 m water depth. The measured beach profile data are also used to uncover the equilibrium parameters of seven EBP functions by curve fitting calculations. The shape of these seven EBP functions is shown in Figure 78. After that, they are still compared with an average beach profile. This comparison reveals that the EBP functions of both Bodge (1992) and Sierra et al. (1994) show consistency with the average beach profile, but, similar to Bona beach, the expression of Bodge (1992) is still the most suitable for describing the shape of beach profile in Hyères beach. The goodness of fit statistics has R-square of 0.972 and RMSE of 0.2559 (Table 29 and Table 30, respectively). Moreover, comparing Bodge (1992)'s curve with the average beach profile is carried out to determine the surface error per profile unit of -24.55 m^2 . The shortage part may be mainly due to the presence of wide trough located from 200 m to 350 m seaward along with coastal erosion caused by high east waves.

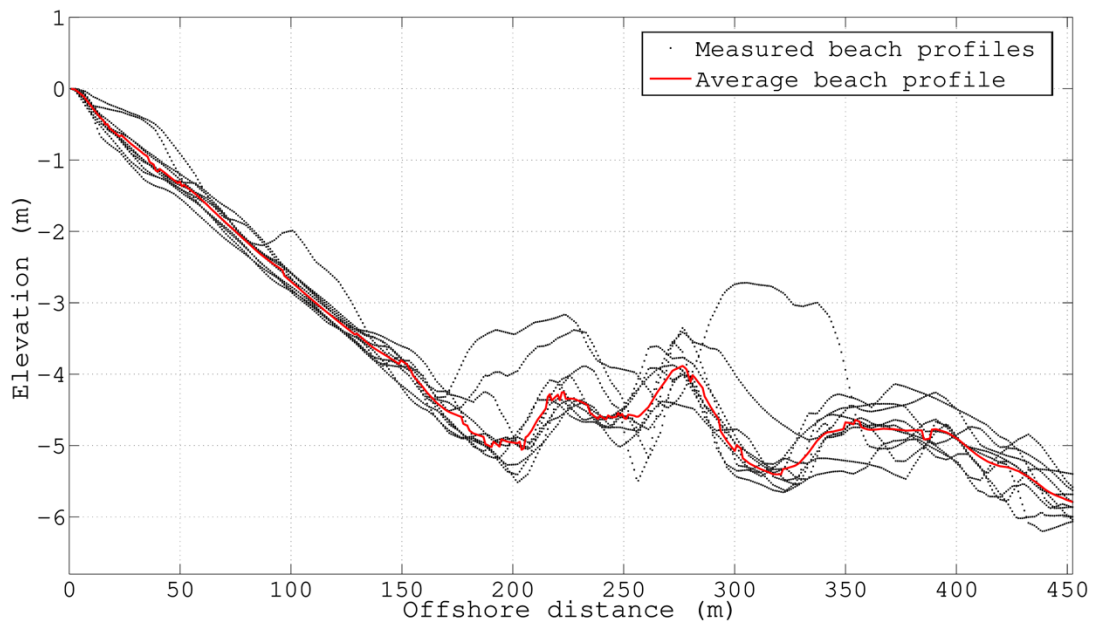


Figure 77. Beach profiles measured by E.O.L at Hyères beach from 2001 to 2010.

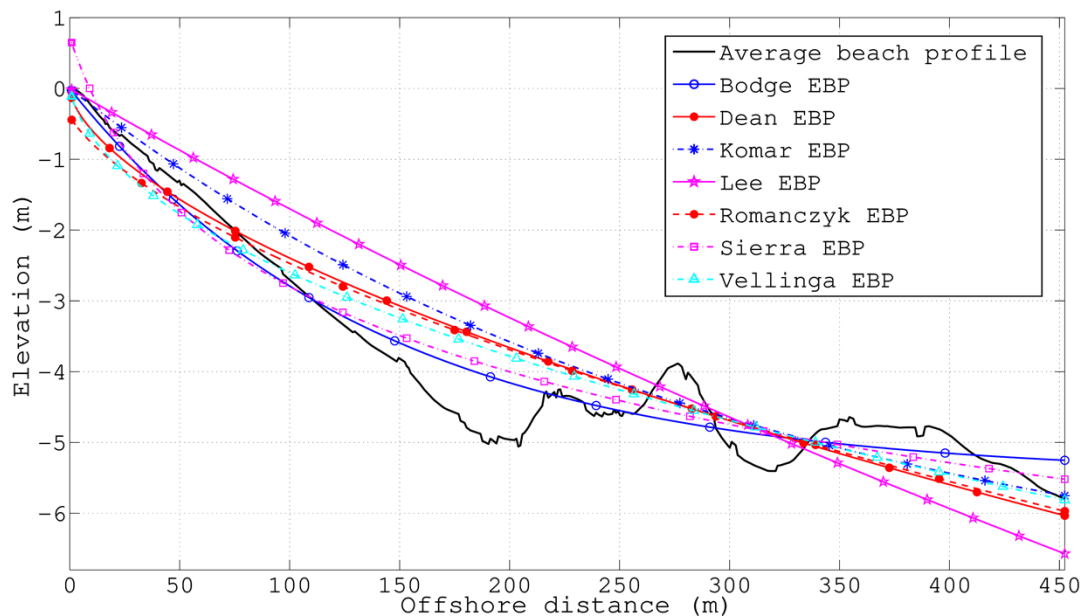


Figure 78. A comparison of an average measured beach profile and the predicted EBP's at Hyères beach.

The last beach of Zone 3, Pesquiers is located between a 70m long groyne and the jetty of La Capte marina. According the measured bathymetric data of E.O.L (2010), the north part of this beach has been subjected to moderate erosion due to the sediment shortage which the groynes and the breakwaters of Hyères port, interfering with the main longshore drift, whereas slight accretion occurs in the south part as a result of the jetty of La Capte marina. Ten beach profiles measured at the northern Pesquiers beach by E.O.L from 2001 to 2010 were used to investigate the beach evolution in this work. The shape of this beach is very complicated with the alternative presence of bars and troughs (Figure 79). It is noticeable that the highest and widest bar is located between 350 m and 450 m seaward of the shoreline. The slope of beach remains 4.7% from the

shore to the upper limit of *Posidonia*, but on average, it varies around 3.3% (Table 28). This is the steepest beach along the eastern Giens tombolo. Seven EBP functions were fitted to the measured data and compared with the average beach profile. As the complex beach shape, all EBP functions have large errors when compared with an average beach profile (Figure 80). However, the EBP function of Bodge (1992) still shows the best consistency with the beach profile shape. The goodness of fit statistics has R-square of 0.7149 and RMSE of 0.8979 (Table 29 and Table 30, respectively). The surface error per profile unit of this profile is up to -82.03 m^2 . This is the largest surface error observed in the study area. It is mainly due to the compensation for the steep slope near the shoreline as well as the deep trough located between 200 m and 380 m seaward of the shoreline.

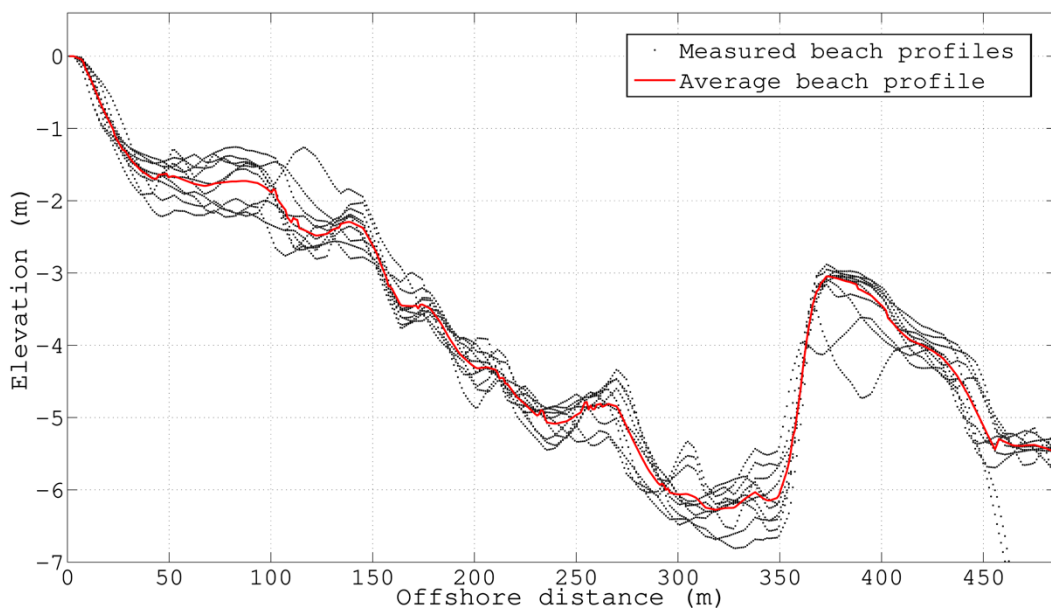


Figure 79. Beach profiles measured by E.O.L at Pesquiers beach from 2001 to 2010.

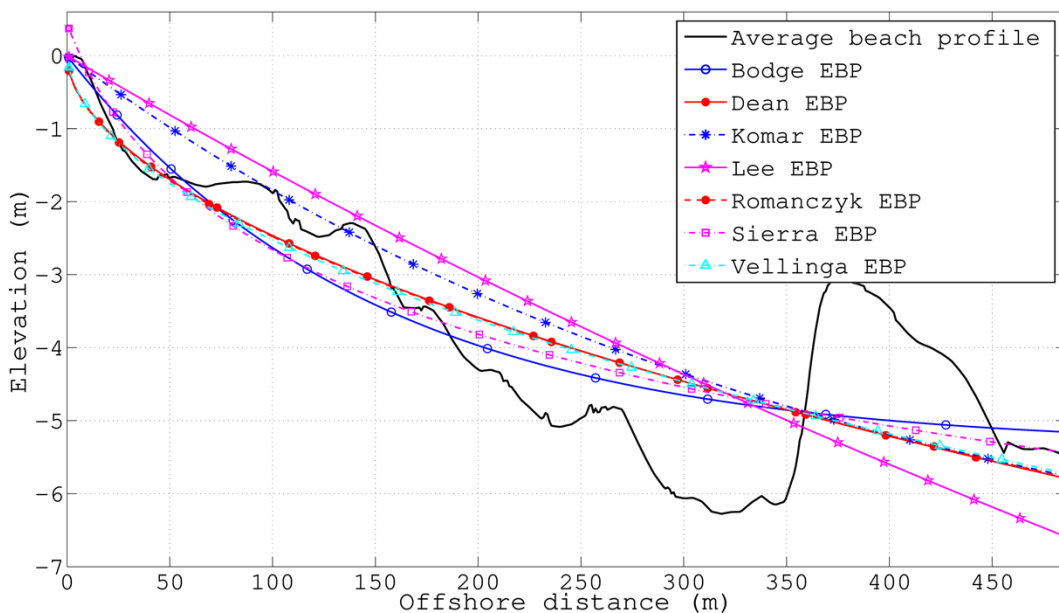


Figure 80. A comparison of an average measured beach profile and the predicted EBPs at Pesquiers beach.

4.3.2.4. Zone 4

Zone 4 is limited by the marina of La Capte in the north and the cape of Esterel in the south (Figure 62). The current work was supplied with 11 beach profiles surveyed on the downdrift of La Capte jetty from 2000 to 2010. Beach profiles have a gentle slope of 1.6% without bars and troughs until 300 m seaward of the shoreline (Figure 81). However, many bars and troughs are observed beyond 300 m distance offshore at the water depth of 4.5 m. In addition, the position of submerged geotube breakwaters can be visibly observed at the depth of -1.5 m around 125 m seaward of the shoreline. It is easily seen that the height of this breakwater in 2010 obviously decreased comparing with 2008. The reason is that the loss of sand inside the tube because the geotube bag has been stretched by hydrodynamic factors, or this bag can be torn by anchors or mechanical forces (Lacroix et al., 2015). The curve fitting calculations were made by using the measured beach profile data in order to obtain EBP functions. Results expressed in Figure 82 reveal that the EBP functions of Bodge (1992), Komar et al. (1994), and Lee (1994) are similar and even coincidental in the shoreward half of the profile. However, after comparing them with the average profile, the EBP function of Lee (1994) best describes the shape of La Capte beach profile with R-square of 0.9966 and RMSE of 0.1173 (Table 29 and Table 30, respectively). The suitability of this curve indicates the largest effects of wave climate and sediment size on the EBP expression of this beach. The surface error per profile unit is of -1.85 m^2 for the average beach profile and the curve of Lee (1994), calculated from the shoreline to 300 m seaward. This minor error reveals that Lee (1994)'s curve can fairly model the tendency of beach profile evolution and the equilibrium state can be obtained with a small sediment volume added to this beach.

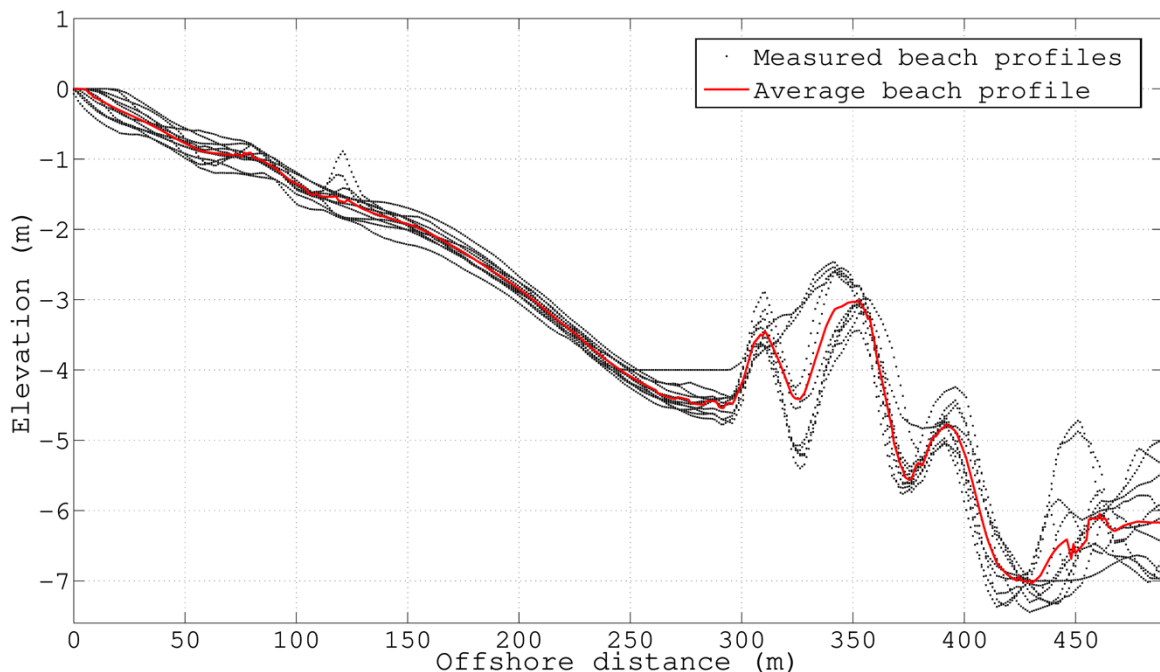


Figure 81. Beach profiles measured by E.O.L. at La Capte beach from 2000 to 2010.

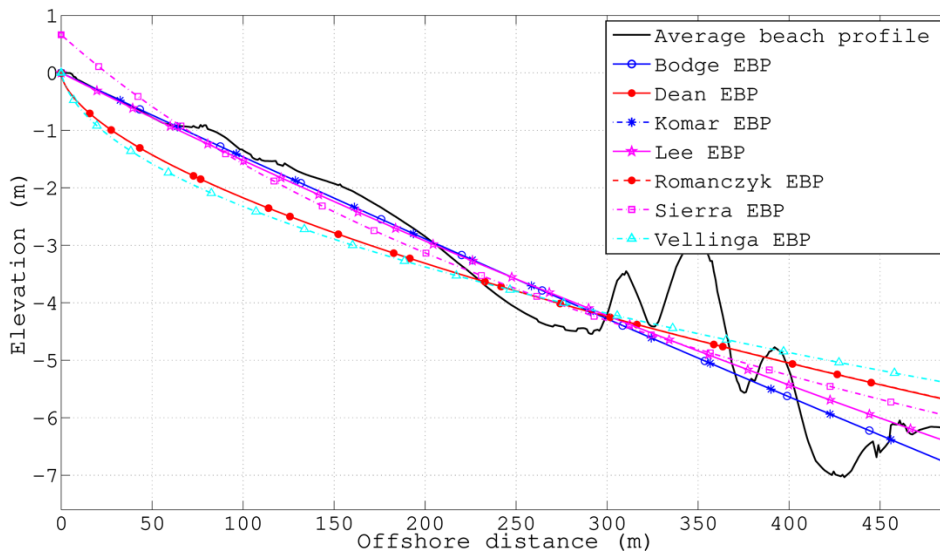


Figure 82. A comparison of an average measured beach profile and the predicted EBPs at La Capte beach.

Similar to La Capte beach, eleven beach profiles measured from 2000 to 2010 were used to investigate the evolution of La Badine beach. The beach profiles have a gentle slope of about 1% with no bars and troughs in a distance of 500 m from the shore (Figure 83). The beach profiles of this area become linear shape. The equilibrium beach configurations were calculated by curve fitting code using the measured beach profile data. The detailed results are presented in Figure 84. As can be seen in this figure, almost all EBP functions follow closely to the measured beach profile, apart from Vellinga (1987)'s function. Specifically, three curves of Bodge (1992), Komar et al. (1994), Romańczyk et al. (2005) and Dean (1977) are similarly coincident with R-square of more than 0.996 (Table 29). The worst EBP function in this case is Vellinga (1987)'s profile with R-square of 0.8475. However, when taking into account the RMSE (Table 30), the expression of Dean (1977) shows perfect consistency with the average measured beach profile. The difference between the average beach profile and the EBP equation of Dean (1977) is about 0.38 m².

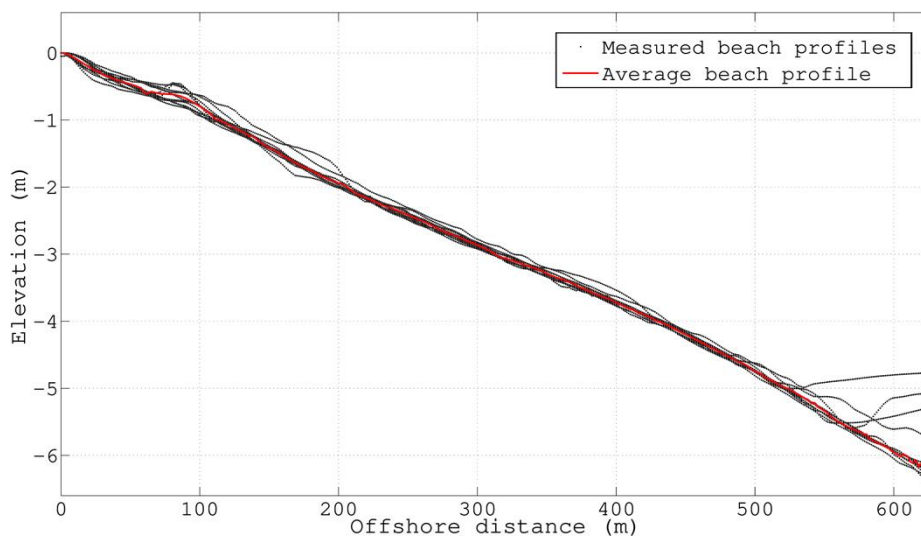


Figure 83. Beach profiles measured by E.O.L. at La Badine beach from 2000 to 2010.

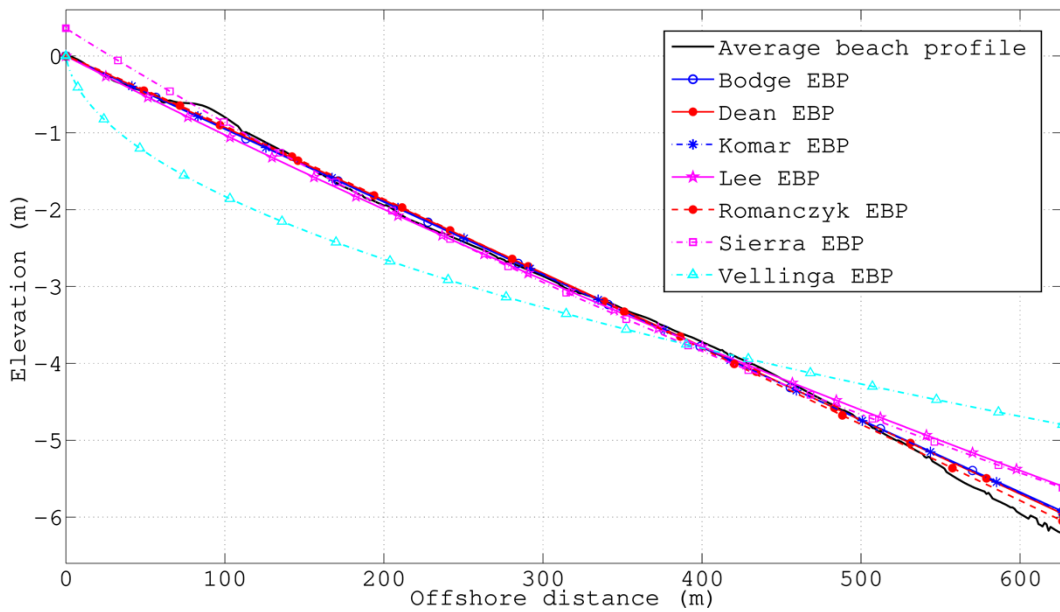


Figure 84. A comparison of an average measured beach profile and the predicted EBPs at La Badine beach.

4.3.3. Equilibrium Parameters of EBP Functions

There are three main in-situ factors, namely sediment size, wave climate, and beach profile shape, governing the EBP functions through some equilibrium parameters. Particularly, the EBP models of both Dean (1977) and Romańczyk et al. (2005) mainly depend on the sediment size data through the relationships A vs. D_{50} and A vs. w , but Romańczyk et al. (2005) further considers the difference between mean high-water level and mean low-water level in order to determine the origin of the EBP by using the parameter x_s . Meanwhile, the EBP models of Vellinga (1987) and Lee (1994) are dominantly controlled by both deep-water wave (viz. H_{os} and D , respectively) and sediment size (viz. w and C , respectively) characteristics. On the other hand, the EBP formulations of Bodge (1992) and Komar et al. (1994) take into account the effects of the beach profile shape (viz. k and S_0 , respectively) and the closure depth (viz. B and k , respectively). With the EBP model of Sierra et al. (1994), the impact of the in-situ factors is indeterminable. The values of these equilibrium parameters obtained from the regression analysis using the least squares method are shown in Table 31.

In Dean (1977)'s and Romańczyk et al. (2005)'s EBP equations, A is a scale parameter depending on sediment characteristics such as the median grain size D_{50} or the fall velocity of sediment w . This is a simple linear relationship, i.e. this parameter increases gradually with the augmentation of the median grain size. Dean et al. (2004) pointed out that 99 percent of all computed values of A were between 0.0 and 0.0914 $\text{m}^{1/3}$ with the majority of values $0.0305 < A < 0.061 \text{ m}^{1/3}$. In this work, the values of A calculated based on the site conditions vary in the range of 0.1096 and 0.1935 $\text{m}^{1/3}$ (Table 28). After adjusting and validating, its values range between 0.009 and 0.194 $\text{m}^{1/3}$ (Table 31). They are quite consistent with the observed values. The maximum value of A of 0.194 $\text{m}^{1/3}$ is

observed in Pesquiers beach where the sediment grain is the coarsest in the study area. Conversely, the minimum values of A of $0.009 \text{ m}^{1/3}$ is obtained in La Badine beach in which the sediment grain is the finest in the study area. The adjusted values of A in Table 31 also elucidate that the smaller sediment grain size could lead to the higher accuracy of the EBP functions of Romańczyk et al. (2005) and Dean (1977). In addition, a sensitivity analysis of Dean (1977)'s and Romańczyk et al. (2005)'s EBP equations to the A parameter is carried out at La Badine beach in order to quantify the impact of this parameter on the accuracy of the EBP predictions (Figure 85). The result indicates that either increasing or decreasing the A parameter around the best-fit value (Table 31) by 10%, 20%, and 30% would induce a reduction of R-squared to 4.6%, 16.2%, and 35.6%, respectively. Meanwhile, the variation of the x_s parameter is insignificant to the accuracy of Romańczyk et al. (2005)'s EBP model.

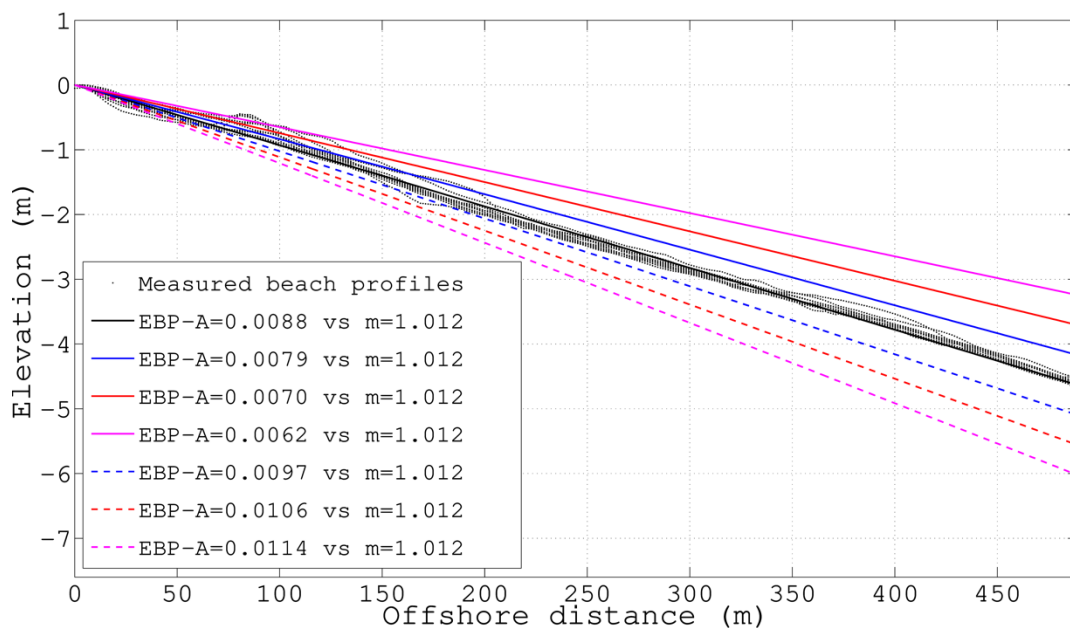


Figure 85. A comparison of Dean (1977)'s EBPs with variation of the A parameter at La Badine beach.

For the EBP equation of Vellinga (1987), the sediment size affects the prediction of beach profile through the fall velocity of sediment w . The relationship between w and D_{50} shows that the increase of D_{50} will lead to the increment of w . The values of w found by Vellinga (1987)'s tests vary from 0.78 to 2.87 cm/s. On the other side, the fall velocity w is detected typically from about 2.85 to 11.0 cm/s corresponding to the predicted median grain size $D_{50} = 0.231 \text{ mm}$ and $D_{50} = 0.8 \text{ mm}$ in this study. These values are very similar to the computed range from 3.06 to 11.14 cm/s (Table 28). In addition to the sediment characteristics, the EBP function of Vellinga (1987) is still governed by wave climate via the deep-water significant wave height H_{os} . The obtained the values of H_{os} belong from 1.5 to 2 m. In this work, its values obtained from the regression analysis of Vellinga (1987)'s model using the least squares method range from 0.52 to 2.8 m. The highest value is the deep-water wave height transmitted to the vicinity of Hyères port.

Nonetheless, it is lower than that recorded in Porquerolles station with significant wave height of 3.3m. Although both the sediment size and the wave height are attributed to act on the EBP model of Vellinga (1987), the extent of the impact of each factor on this model is still unclear. Therefore, a sensitivity analysis to the parameters of H_{os} and w is done at Plein Sud beach where Vellinga (1987)'s EBP is the best-fit prediction of beach profile (Figure 86). It is noted that either an increase or decrease of 10% around the best-fit values of both H_{os} and w would lead to the same reduction of about 15.7% in the R-squared value and about 55.5% in the RMSE. This means that the wave height and sediment size play an equivalent role in the accuracy of Vellinga (1987)'s model.

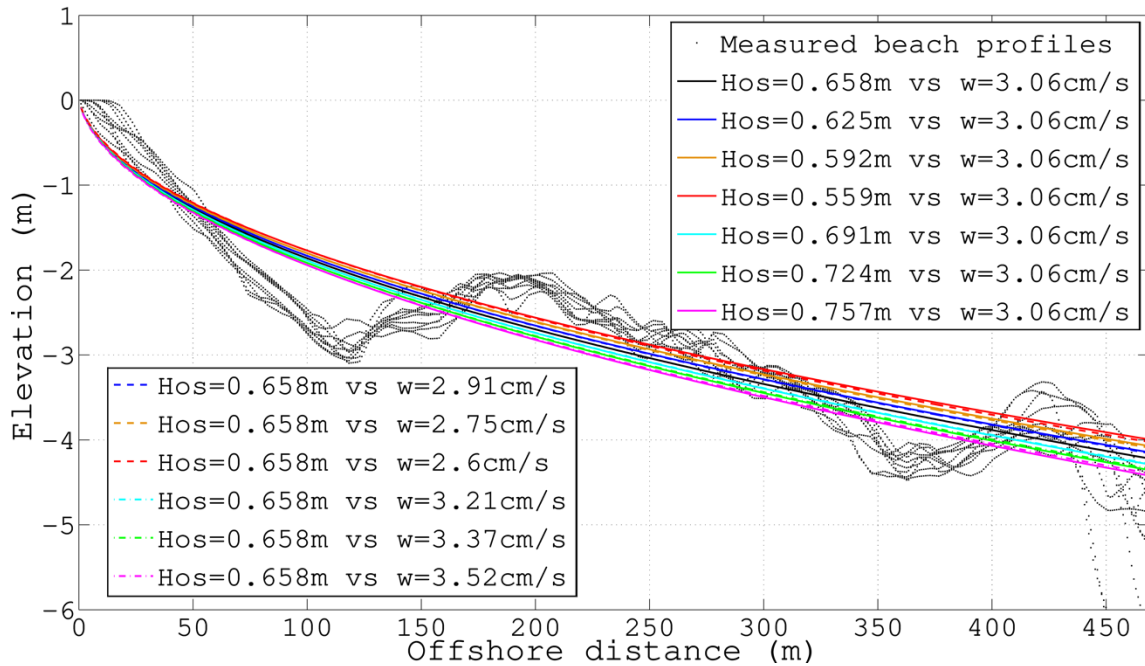


Figure 86. A comparison of Vellinga (1987)'s EBPs with variation of H_{os} and w at Plein Sud beach.

By testing in a wave tank experiment and testing and calibrating on a number of submarine profiles, Lee (1994) presented the effect of sediment size on the EBP via the extension factor C . The values of C in his work are from 1.0 to 30,000 m. However, the physical relationship between this parameter and grain size was pending further studies. In this work, the parameter C varies from 800 to 1600 m (Table 31). On the other hand, Lee (1994) also proposed to take into account the parameter of D as a function of a corresponding offshore wave period in the EBP. In his work, the values of D at different sites varied from 0.003 to 0.5 m^{-1} . As for our study, the values of the coefficient D are found about from 0.057 to 0.08 m^{-1} in proportion of $T=8.33$ s to $T=7.1$ s. These values of T are around the observed mean wave periods at the sites. In order to clarify the influence of both C and D on the predicted profile of Lee (1994), a comparison of EBPs with variation of these parameters around the best-fit values (Table 31) at La Capte beach is presented in Figure 87. As can be seen in this figure, the D parameter has the greater impact on the accuracy of Lee (1994)'s EBP than the C parameter. For

instance, a reduction of 10%, 20%, and 30% in the C parameter could cause the corresponding decrease of 0.06%, 27.34% and 58.45% in the value of R-squared, respectively, whereas decreasing the D parameter by 10%, 20%, and 30% results in a reduction of 0.3%, 33.84% and 79.5% in the value of R-squared, respectively. It also strongly proves that the wave condition at La Capte beach affects the EBP of Lee (1994) larger than the sediment size.

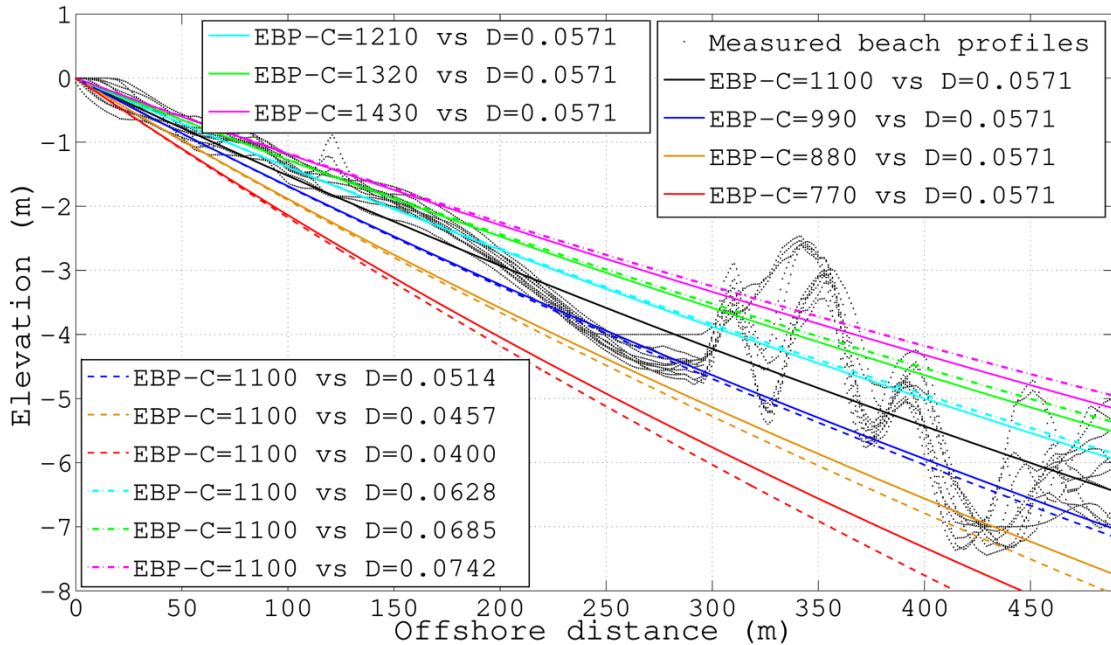


Figure 87. A comparison of Lee (1994)'s EBP models with variation of C and D parameters at La Capte beach.

In Bodge (1992)'s EBP expression, the effects of sediment characteristics and incident wave are simultaneously taken into account via the parameters k and B , respectively. Nevertheless, no attempt was made to relate these parameters to beach conditions. Based on the data from the East Coast of United States and the Gulf of Mexico, he computed the values of k ranging from $3 \times 10^{-5} \text{ m}^{-1}$ to $1.16 \times 10^{-3} \text{ m}^{-1}$ and the values of B varying from 2.6 to 60 m. In the present study, the coefficient B ranges from 4.35 m to 450 m, while the parameter of k falls in the range of $2.12 \times 10^{-5} \text{ m}^{-1}$ to $7.58 \times 10^{-3} \text{ m}^{-1}$ (Table 31). Moreover, the values of these parameters in this work reveal the notable characteristic that the gentle slope deduces the low values of k and the high values of B . The lowest values of B and the highest values of k are observed in zone 3 where the bathymetry is very complex and steep. A sensitivity analysis of Bodge (1992)'s EBP to the parameters of B and k is necessary to elucidate the effect of each parameter on this EBP at Bona (Figure 88), Hyères (Figure 89) and Pesquiers (Figure 90) beaches. The results at all three beaches highlight that a small variation of B around the best-fit value (Table 31) could lead to a significant reduction of the accuracy of the EBP model of Bodge (1992), while the same variation of k only causes a slight decrease in the accuracy of this model. For example, at Bona beach, either decreasing or increasing the B parameter by 10%, 20%, and 30%, compared with the best-fit value of this parameter

shown in Table 31, results in a reduction of R-squared to 7.8%, 31.2%, and 70.3%, respectively. On the other hand, if the k parameter is decreased or increased by 10%, 20%, and 30% around its best-fit value in Table 31, the R-squared would be only reduced to 3.1%, 10.4%, and 19.9%, respectively. It verifies that the B parameter has the greater impact on the accuracy of Bodge (1992)'s EBP than the k parameter.

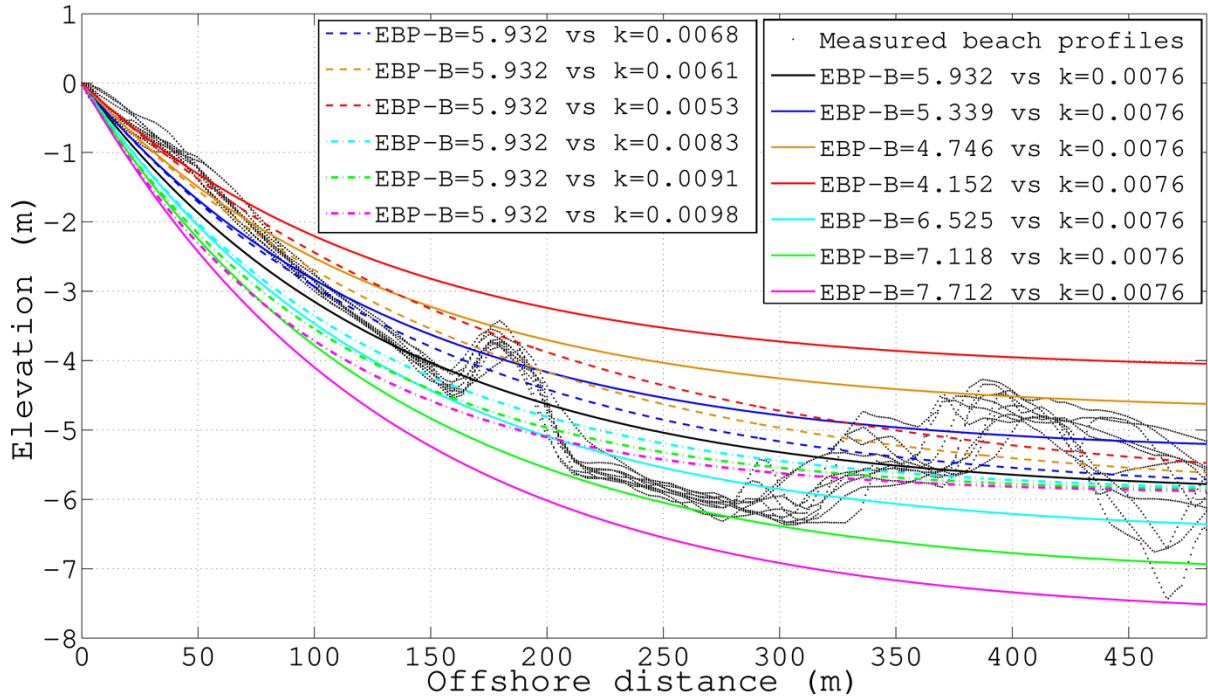


Figure 88. A comparison of Bodge (1992)'s EBPs with variation of B and k parameters at Bona beach.

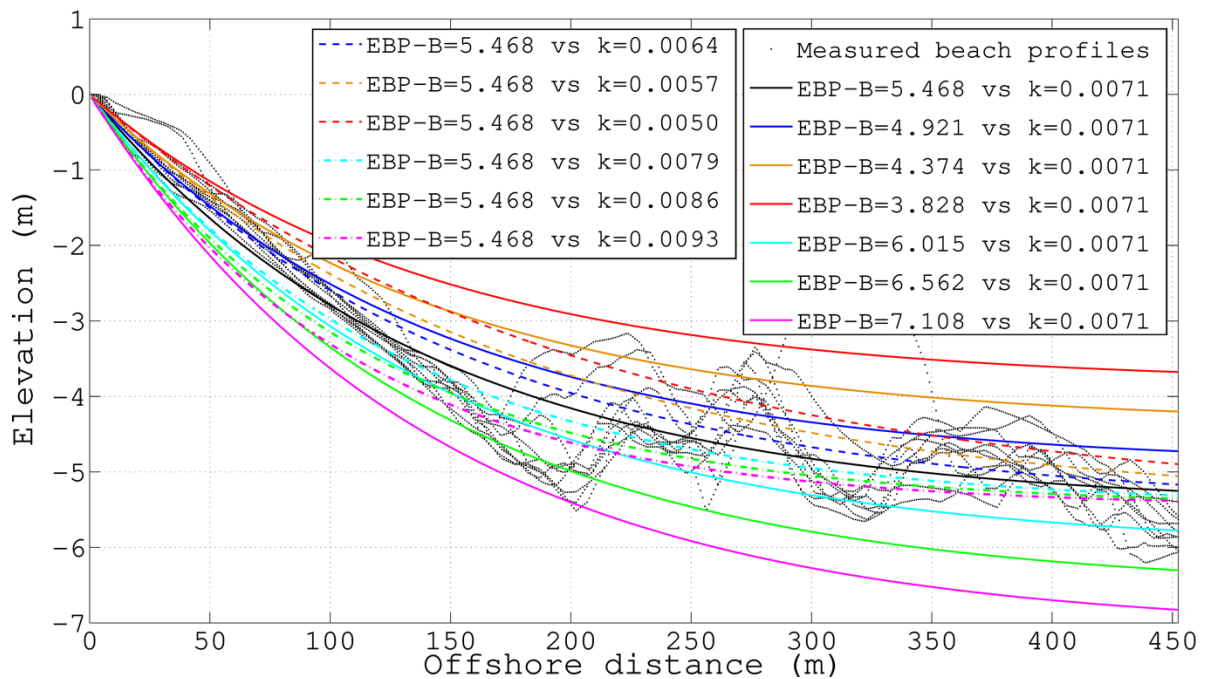


Figure 89. A comparison of Bodge (1992)'s EBPs with variation of B and k parameters at Hyères beach.

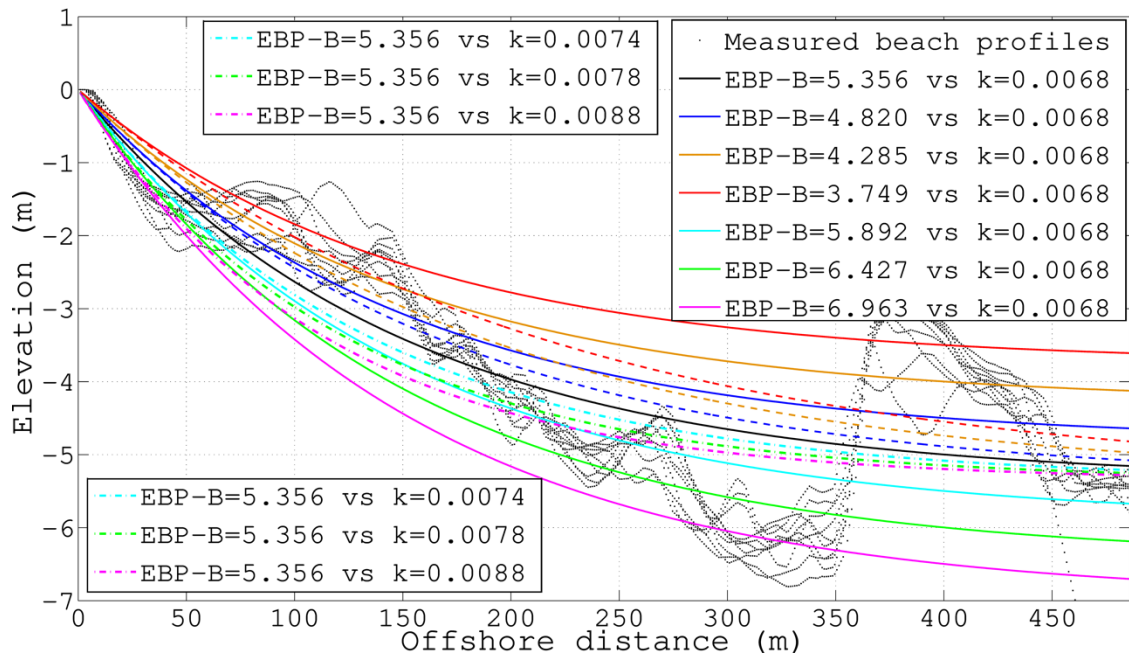


Figure 90. A comparison of Bodge (1992)'s EBP's with variation of B and k parameters at Pesquiers beach.

The beach profile shape controls the equilibrium function through the parameters of S_o and k in Komar et al. (1994)'s expression. The parameter S_o is the beach-face slope that is predictable as a function of the sediment grain size and wave parameters, whereas the empirical coefficient k which determines the concavity of beach profile. Komar et al. (1994) provided a comparison with a beach profile from the Nile Delta. The parameters of S_o and k are computed based on the best fit with measured beach profiles. The beach face slope measured alongshore is $S_o = 2.89\%$, and $k = 7.3 \times 10^{-3} \text{ m}^{-1}$ based on the offshore distance of 300 m and the water depth of 3.5 m. In the present work, the values of S_o are found on the order of 0.95% - 2.44% and the parameter k varies between 2.25×10^{-14} and $5.42 \times 10^{-3} \text{ m}^{-1}$ (Table 31). The calculated values of S_o vary around in the measured data (Table 28). Table 31 also strongly demonstrates that the smaller the value of S_o is, the more accurate Komar et al. (1994)'s EBP function is. In other words, this function best suits for the gentle beach, viz. La Badine beach. An attempt to interpret the extent of influence of the S_o and k parameters on the accuracy of the Komar et al. (1994) prediction model is made by doing a sensitivity analysis for both Gapeau (Figure 91) and Aéroport beaches (Figure 92) in which this EBP model shows more consistent with the measured data than the others. The result reveals that either increasing or decreasing the beach face slope S_o around the best-fit values in Table 31 could induce a considerable reduction in the accuracy of the Komar et al. (1994) EBP, whereas the variation of k parameter only causes the insignificant modification of this model (Figure 91). At Gapeau beach, the R-squared could be decreased by 4-5%, 9.2-10.4%, and 33.7-36.1% when variation of the S_o parameter is 10%, 20%, and 30%, respectively, around the best fit value (Table 31). Meanwhile, an increase or decrease of 10%, 20%, and 30% in the S_o parameter in Aéroport beach induces a corresponding

reduction of 13-16.7%, 23.3-30.6% and 41.6-54.1%, respectively in the R-squared. It strongly demonstrates that the beach face slope S_o plays a dominant role in the beach profile prediction of Komar et al. (1994)'s model at both Gapeau and Aéroport beaches.

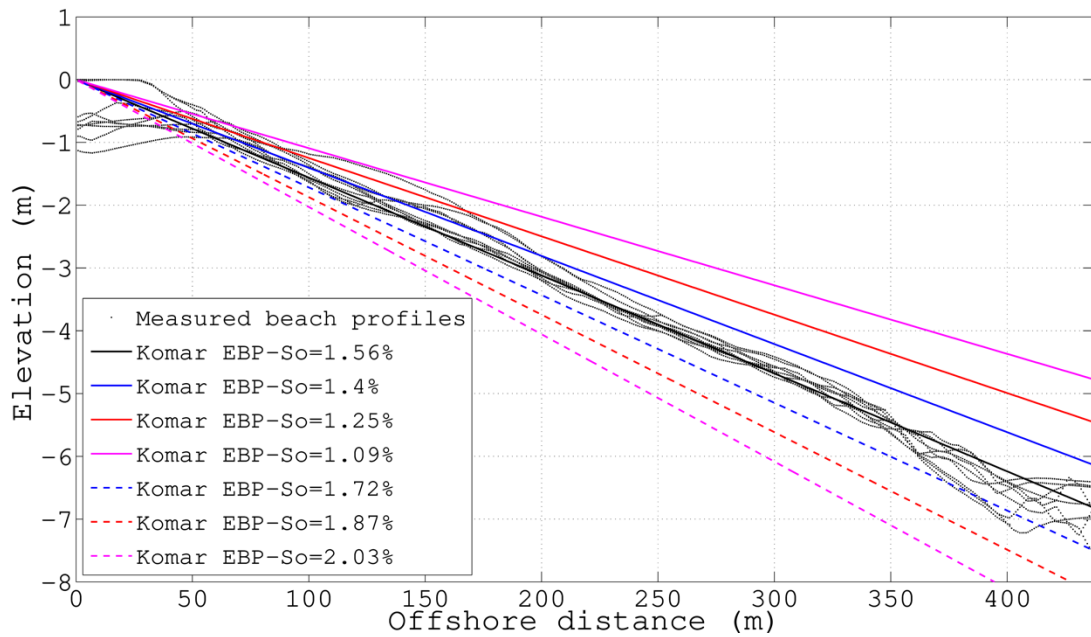


Figure 91. A comparison of Komar et al. (1994)'s EBPs with variation of S_o at Gapeau beach.

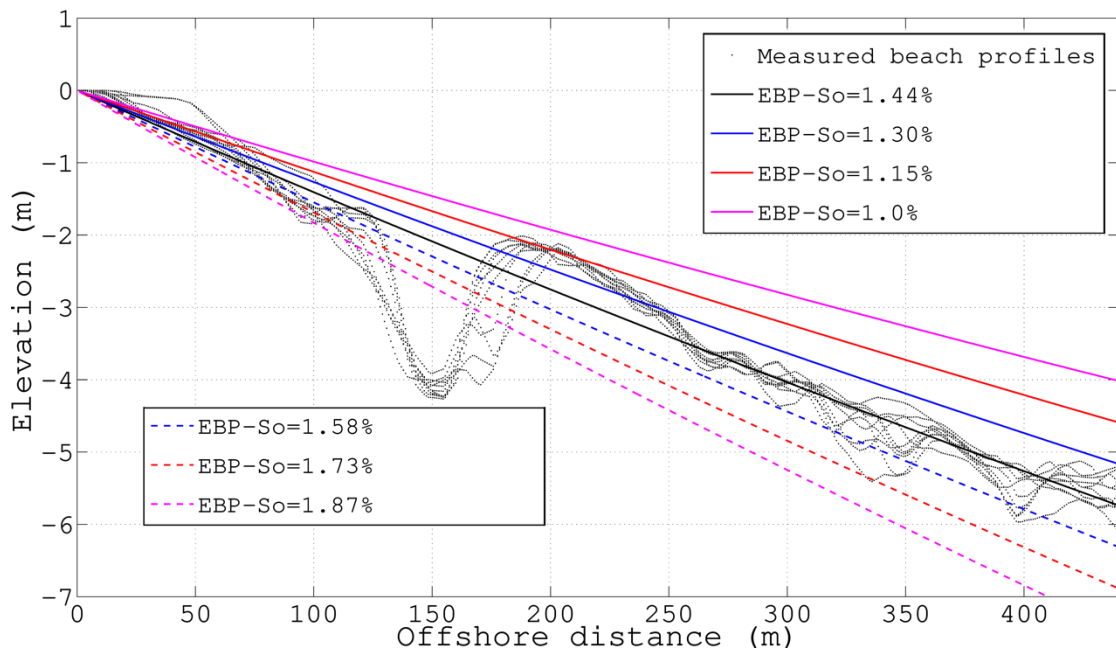


Figure 92. A comparison of Komar et al. (1994)'s EBPs with variation of S_o at Aéroport beach.

Regarding the parameters of F , G , x_0 used in the EBP equation of Sierra et al. (1994), based on the measured data of 82 beach profiles along the Catalan coast, he found that $|\ln F|$, G and x_0 fall in the range of 0-38.491, 1.171-7.642 m, and 5-155 m, respectively. Because of the characteristic of the equation and because the coefficient F takes very small values, it is preferable to work with $\ln F$. In addition, no predictive relation between these parameters and the sediment diameter was found in his work. In the

present research, the values of F , G and x_0 vary around 4.99×10^{-4} - $3.81 \times 10^{-2} \text{ m}^{-1}$, 1.627-29.33 m, and 16.43-2000 m, respectively. In addition, the authors were successful in interpreting the correlation between the equilibrium parameters and the accuracy of Sierra et al. (1994)'s EBP at Ayguade, La Marquise and Amont beaches through sensitivity analysis. The results are shown in Figure 93, Figure 94, and Figure 95. It is easily seen that the variation of the G parameter results in the largest impact on the accuracy of Sierra et al. (1994)'s model at Ayguade beach, whilst fluctuation in the x_0 parameter does not nearly change in the accuracy of this model. For instance, either increasing or decreasing the G parameter by 10%, 20%, and 30% around the best fit value in Table 31 could cause a significant reduction of 11.1%, 37.5%, and 81.3%, respectively in the R-squared; whereas variation of 10-30% in the x_0 parameter only leads to the maximum reduction of 3% in the R-squared. Moreover, the R-squared would be decreased by 4.4-25.5% if the F parameter varies between 10% and 20%. The extent of the reduction in the R-squared becomes larger seaward (Figure 93). By contrast, the F parameter affects the accuracy of Sierra et al. (1994)'s model greater than the others at both La Marquise and Amont beaches. The variation of G triggers the least impact on the accuracy of this model at these two beaches. Specifically, a decrease or increase of 5-10% in the F parameter at La Marquise beach leads to a reduction of 13.3-51.1% in the R-squared, while only a decrease of 3.7-15.8% in the R-squared is due to variation of G around 5-10% (Figure 94). Similarly, either decreasing or increasing the F and G parameters by 5-10% could induce a reduction of 19.8-74.5% and 3.4-13.5%, respectively, in the R-squared at Amont beach (Figure 95). Therefore, the value of G mainly controls the shape of Sierra et al. (1994)'s EBP at Ayguade beach, while the value of F dominates the shape of this model at La Marquise and Amont beaches.

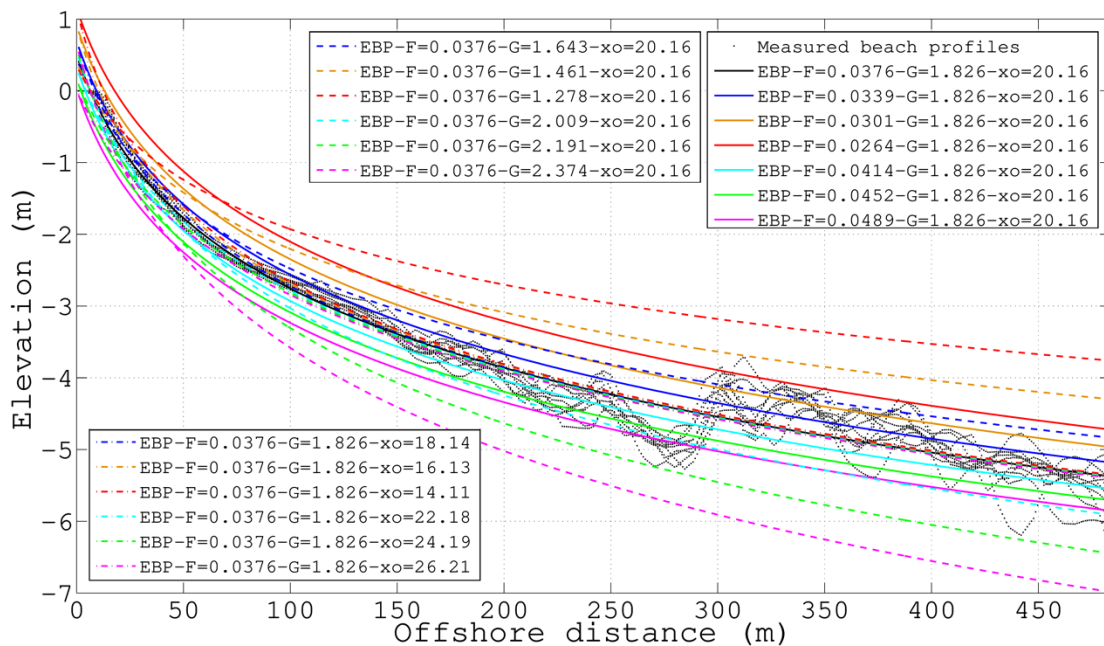


Figure 93. A comparison of Sierra et al. (1994)'s EBPs with variation of F , G and x_0 parameters at Ayguade beach.

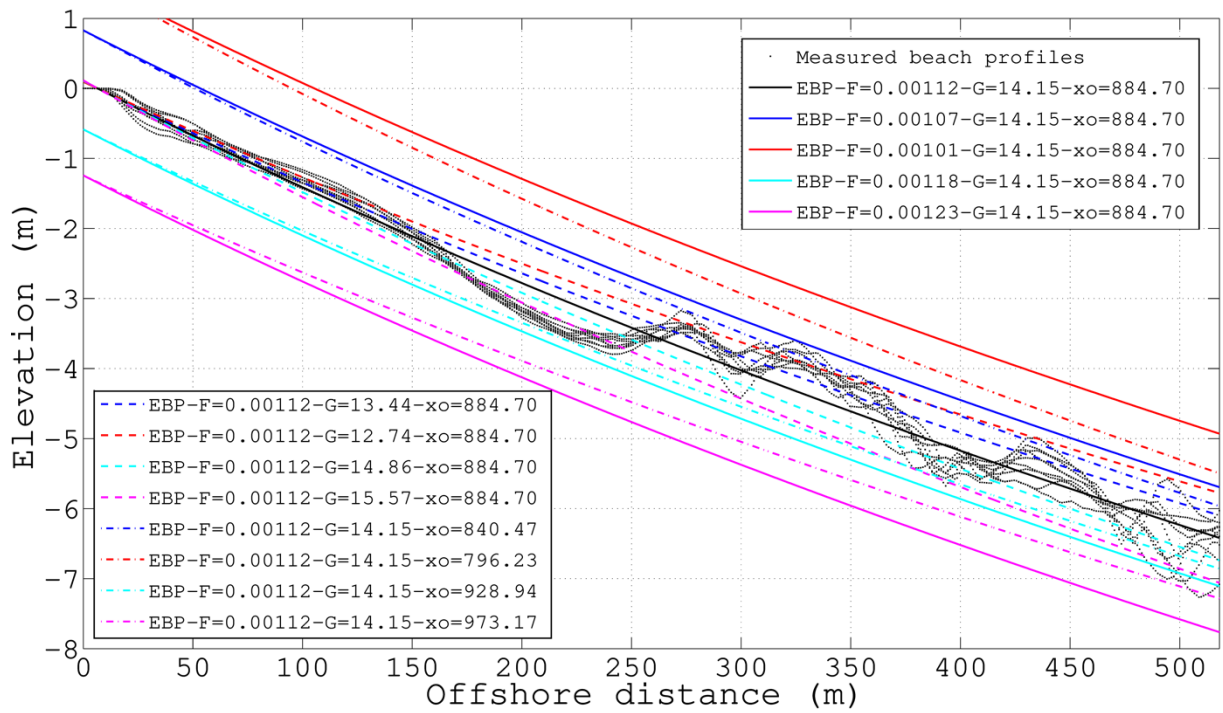


Figure 94. A comparison of Sierra et al. (1994)'s EBP with variation of F , G and x_0 parameters at La Marquise beach.

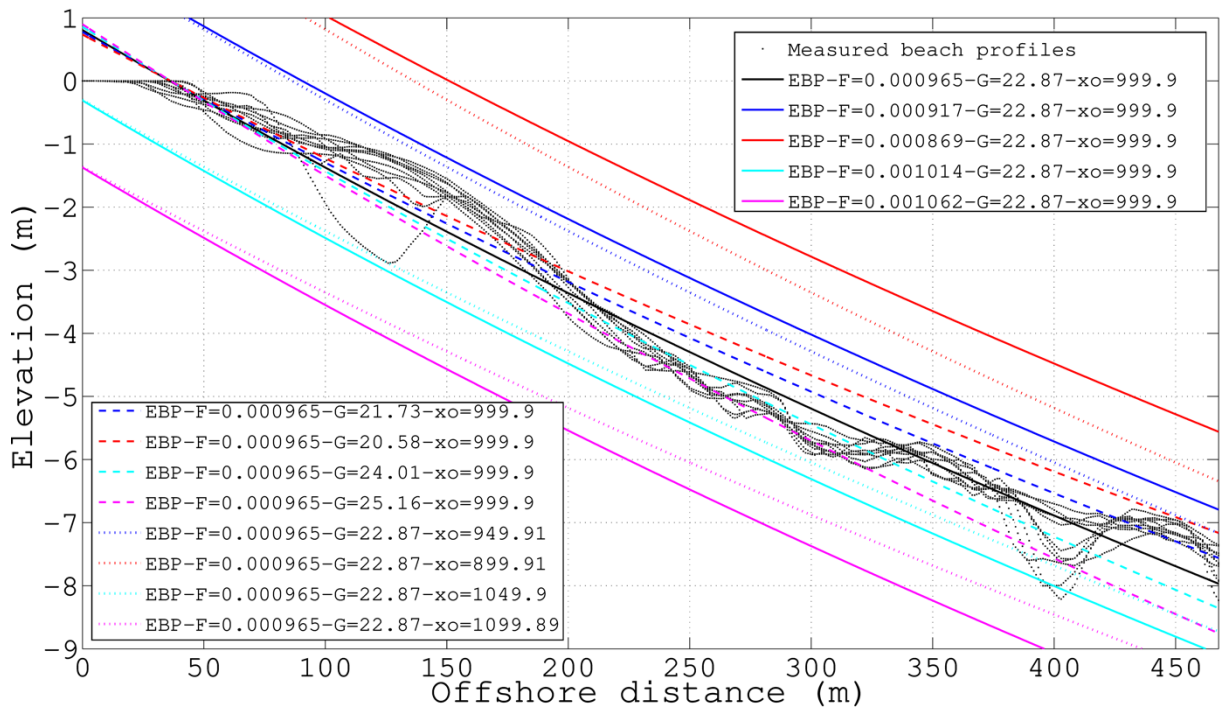


Figure 95. A comparison of Sierra et al. (1994)'s EBP with variation of F , G and x_0 parameters at Amont beach.

Table 31. The best-fit parameters of EBPs function for beaches along the Eastern tombolo.

Function	EBP Parameters	Gapeau	Ayguade	La Marquise	Plein Sud	Aéroport	Amont du Port	Bona	Hyères plage	Pesquiers	La Capte	Badine
Bodge	B	100	5.281	21.26	4.346	200	100	5.932	5.468	5.356	59.7	450
	k	1.60E-04	7.07E-03	6.98E-04	5.42E-03	6.71E-05	1.76E-04	7.58E-03	7.14E-03	6.76E-03	2.48E-04	2.12E-05
Komar	S_o	1.56	1.93	1.23	2.36	1.44	1.70	2.03	2.44	2.10	1.48	0.95
	k	2.34E-14	2.06E-03	2.25E-14	5.42E-03	4.57E-04	1.66E-12	1.68E-03	3.28E-03	2.64E-03	2.48E-04	2.30E-14
Dean	A	0.1713	0.163	0.1563	0.1105	0.09514	0.113	0.1478	0.143	0.1935	0.1322	0.008795
	m	0.575	0.5798	0.5741	0.6	0.66	0.67	0.62	0.612	0.5495	0.608	1.012
Romanczyk	A	0.1577	0.1633	0.15	0.12	0.1126	0.09534	0.153	0.1513	0.1935	0.1329	0.007856
	ρ	0.59	0.5753	0.5831	0.535	0.63	0.7	0.61	0.6	0.5495	0.607	1.032
	x_s	1.06E-12	12.03	3.92E-14	1.22E-08	7.85E-14	3.16E-14	10.52	5.084	1.10E-07	4.69E-10	1.00E-05
Vellinga	H_{os}	0.6514	0.7183	0.6121	0.658	1.23	2.8	1.41	1.01	0.5159	0.8906	0.6
	w	0.0875	0.0757	0.0699	0.0306	0.02972	0.02845	0.0561	0.06	0.11	0.04693	0.03156
Lee	C	925	990	1100	992.4	1000	820	800	900	1002	1100	1600
	D	0.05985	0.06105	0.05998	0.08021	0.06491	0.05988	0.06433	0.06198	0.06	0.05711	0.05905
Sierra	G	9.80E-04	3.76E-02	1.12E-03	2.40E-02	4.99E-04	9.65E-04	3.81E-02	3.39E-02	3.02E-02	4.98E-03	1.26E-03
	F	19.46	1.826	14.15	1.627	29.33	22.87	2.089	1.989	1.985	5	10
	x_o	1000	20.16	884.7	40.89	2000	999.9	16.43	20.38	26.49	176	766.2

Parameters' units: B (m); k (m^{-1}); S_o (%); A ($m^{1/3}$); m (-); ρ (-); x_s (m); H_{os} (m); w (cm/s); C (m); D (m^{-1}); F (m^{-1}); G (m); x_o (m).

4.4. Conclusion

The morphological evolution of Giens tombolo mostly depends on both the natural processes and anthropogenic interventions. In the western branch, the natural factors, such as the wave action and the degradation of *Posidonia* seagrass, decisively induce the change of coastal morphology, whereas combination of human activities and natural forces affect the modification of beach and shoreline in the eastern branch, but anthropogenic interventions are more dominant.

The study on the shoreline changes in Giens tombolo from 1973 to 2015 strongly confirms that the combination of remote sensing, geospatial techniques coupled with DSAS along with linear regression method is very helpful for investigating the shoreline movement over time (both short term and long term) as well as predicting the position of future shoreline with reasonable accuracy. The shoreline along the eastern Giens tombolo underwent alternating trends of erosion and accretion. Some types of protection structures such as revetments or groynes, which were implemented in some areas, solely result in localized beach accretion, even they cause severe erosion at several places, especially at Ceinturon beach and La Capte beach. Moreover, the jetties constructed in the river mouths and ports, e.g. Gapeau, Roubaud, and La Capte, have interfered in alongshore sediment transport and accumulated the sediment around their upstream areas. This is main reason provoking the shortage of sediment downstream. Similar to the western part, the beach nourishment are only the temporal method for limiting the decline of shoreline. Therefore, the proposal of some rational structures, which not only protect the shoreline, but also allow transporting sediment alongshore, should be checked and assessed in relation with neighbor areas.

Regarding the beach evolution in the eastern tombolo, the equilibrium beach profiles are governed by three main factors of wave climate, sediment size and beach profile shape. These factors affect EBP through some main parameters. Nonetheless, the role of these three factors is quite different in each profile. It depends on the position of the beach as well as the obstacles around the beach such as groynes, ports, etc. The representation of the impact of each factor on each profile will support to maintain and protect the beaches along the eastern tombolo of Giens. Furthermore, the beaches of Ayguade, La Marquise, Plein Sud, Aéroport, Pesquiers, and La Capte need to add sand volume to obtain the equilibrium shape. However, to keep the added sand volume, the the rational structural solution in Hyères bay, which does not break the landscape along the eastern tombolo as well as affect the tourists, need be required urgently.

CHAPTER 5. MODELING OF HYDRODYNAMIC AND SEDIMENT TRANSPORT

5.1. Introduction

In recent decades, numerical modeling has been developed rapidly for simulating the physical processes at coastal sites. It covers a wide range of different scales and processes, from equilibrium state predictors (Dean, 1977) to detailed numerical models incorporating a large number of physical processes (e.g., Zheng et al. (1997), Nicholson et al. (1997), Larson et al. (1998), Zyserman et al. (2002), Hanson et al. (2003), Sutherland et al. (2004a), Brøker et al. (2007), Roelvink et al. (2009), Pham et al. (2011), Nguyen (2012), Liu (2014), Than (2015), etc.). It has also elucidated to be the best method for understanding hydrodynamics and sediment transport over large spatial areas (Toorman, 2002). The predictions from each model have usually been qualitatively compared to datasets and analytical solutions of idealized cases.

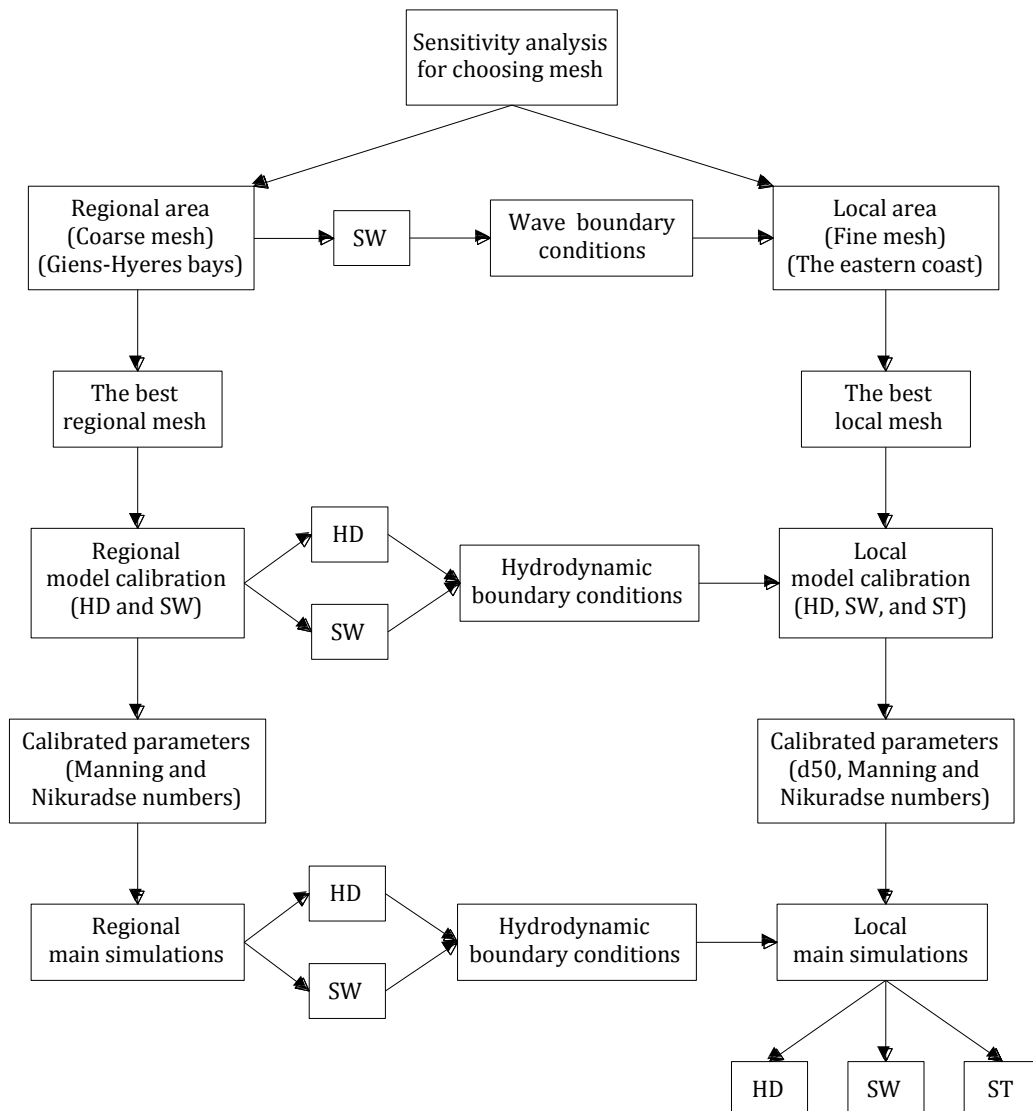


Figure 96. Summary of simulation runs.

In this chapter, the software package of MIKE 21 is used to simulate the hydrodynamic conditions and sediment transport as well as to understand the nature of these processes near the eastern Giens tombolo. To do that, two mesh types of regional and local areas were created and chosen through sensitivity analysis. A regional mesh model of the entire Giens tombolo including Giens gulf and Hyères bay was set up and run to obtain a set of boundary conditions that could be used further to estimate the conditions at the interest site. On the other hand, smaller and fine one for the eastern coast was utilized to discover the hydrodynamics and sediment transport in the interest site. After that, both of these two mesh models were calibrated according to the wave and current data recorded at Almanarre beach in November 2000 and at La Capte in March 2009. The period was selected based on the presence of most recent data available in the study area. Next, the models were officially run for difference scenarios consisting of annual, seasonal and stormy events. Finally, the results of numerical simulation were compared and analyzed. A summary of the model simulation process is presented in Figure 96.

5.2. Study scenarios

Based on the analysis purpose, the available data of waves, winds, and water levels, as well as the computational capacity, the study scenarios are classified into two main categories, viz. no SLR (normal sea level) and SLR.

5.2.1. No SLR conditions

In the no SLR conditions regardless of climate change, the annual, seasonal, and stormy scenarios are chosen and simulated. The input data of numerical simulation are described in Table 32. For annual case, the computed sea level is the average sea level (50% of frequency) recorded at Toulon station over many years. Moreover, the offshore wave parameters are extracted from Table 9 for the wave, which has the highest frequency of 5.89% approaching the eastern coast of Giens tombolo; whereas the wind parameters are the values of 70th percentile of wind data that was recorded Levant station. On the other side, the sea levels and wave parameters in the stormy cases are picked up from Table 7 and Table 13, respectively. Regarding the wind parameters in decadal and tri-decadal cases, they are the values of 95th percentile and 99.9th percentiles of wind data recorded in Levant station, respectively. Meanwhile, the wind speeds and wind directions of semi-centennial and centennial storm cases are the maximum values of Hyères and Levant stations, respectively. With seasonal cases, February of 2007 is selected to represent for winter season, while July of this year is designated as one typical of summer season. There were five heavy storms attacking the study area, especially the strongest storm occurred on 24th, January, 2007 with the wave height of 6.8 m (CEREMA, 2014). The impacts of these storms significantly changed the position of shoreline as well as nearshore bathymetry.

Table 32. A summary of study scenarios in no SLR conditions.

No.	Scenarios	Sea level (m)	Wind		Offshore wave				Discharge flow
			Speed (m/s)	Direction (°)	H _{1/3} (m)	T _p (s)	MWD (°)	DSD (°)	Q _c (m ³ /s)
1	Annual	0.39	8.5	60 (NE)	2.18	7.43	115	33	4
			6.48	90 (E)					
			5.22	120 (SE)					
2	Winter season (February, 2007)	The measured sea level data of Toulon station	The measured wind data of Hyères station		The measured wave data of Porquerolles buoy				The measured flow data at Sainte Eulalie
3	Summer season (July, 2007)								
4	Decadal storm	0.95	12.55	90	6.56	9.12	80	30	180
			12.55	120					
5	Tri-decadal storm	1	19.83	90	7.1	10.3	80	30	220
			19.83	120					
6	Semi-centennial storm	1.15	29.59	90	7.34	11	80	30	300
			29.59	120					
7	Centennial storm	1.5	36.43	90	7.64	12	80	30	600
			36.43	120					

5.2.2. SLR conditions

In the 21st century, human being is facing the climate change and global warming caused by human emissions of greenhouse gases. Global warming is projected to have a number of effects on the oceans. Ongoing effects include rising sea levels due to thermal expansion and melting of glaciers and ice sheets, warming of the ocean surface, leading to increased temperature stratification, and changing currents in the oceans as well as airflows in the atmosphere. The SLR will not only lead to coastal flooding but also modify the wave-breaking zones in nearshore. This results in the morphological change along coast. Moreover, Marbà et al. (2010) showed that seawater warming variability and increasing water depth associated with interannual variability in *Posidonia oceanica* shoot mortality, whereas *Posidonia oceanica* plays as reef-like barrier controlling sediment exchange and beach variability. In this study, only the variation of sea level due to global warming and the presence of *Posidonia oceanica* will be focused on simulating. The other effects of global warming such as change of wind speed or wave are not taken into account because of lack of data.

In SLR conditions, boundary conditions are listed in Table 33. It is clearly seen that all wave and wind data are the same as those in no SLR conditions, expect the magnitude of

sea level. For annual scenario, the sea level is about 0.5 m above CM. It was determined by sum of average sea level over many years (+0.39 m) and the minimum rate of sea level variation at Marseille by 2040-2050 (0.11 m) (Gomis et al., 2011). On the other hand, sea levels in remainders are the same values as shown in No SLR conditions but adding 35 cm caused by the phenomenon of SLR between 2010 and 2060 (Brunel, 2010).

Table 33. A summary of study scenarios in SLR conditions.

No.	Scenarios	Sea level (m)	Wind		Offshore wave				Discharge flow
			Speed (m/s)	Direction (°)	H _{1/3} (m)	T _p (s)	MWD (°)	DSD (°)	Q _c (m ³ /s)
1	Annual	0.5	8.5	60 (NE)	2.18	7.43	115	33	4
			6.48	90 (E)					
			5.22	120 (SE)					
2	Decadal storm	1.3	12.55	90	6.56	9.12	80	30	180
			12.55	120	6.56	9.12	110	35	
3	Tri-decadal storm	1.35	19.83	90	7.1	10.3	80	30	220
			19.83	120	7.1	10.3	110	35	
4	Semi-centennial storm	1.5	29.59	90	7.34	11	80	30	300
			29.59	120	7.34	11	110	35	
5	Centennial storm	1.85	36.43	90	7.64	12	80	30	600
			36.43	120	7.64	12	110	35	

5.3. Determination of the most appropriate mesh

The most appropriate meshes for regional and local areas are established by sensitivity analysis through using some statistical errors, viz. RMSE, R-squared (R²) and the BSS.

5.3.1. Model performance statistics

Evaluating the performance of numerical models in coastal morphology aims to express the goodness of fit between measurement data and the results of models by some simple and objective measures. The most common measures that several researchers used to assess the accuracy of the predictions are RMSE, a scatter index SI and the squared multiple correlation coefficient R² (Brière et al., 2007; Hsu et al., 1999; Liu et al., 2002; Liu, 2014; Mashriqui, 2003; Roelvink et al., 2009; Sutherland et al., 2004a; Sutherland et al., 2004b). Furthermore, Van Rijn et al. (2003) proposed to evaluate the performance of the models based on the BSS. All errors in the model prediction and the measurement are assumed that they are error-free. However, this cannot be achieved in practice because of inherent and random measurement errors.

5.3.1.1. RMSE

Firstly, the RMSE is the most used measure of numeric prediction quality because it contains the same scale and unit as the measured variables.

$$RMSE = \sqrt{\frac{1}{N} \sum_N (X_c - X_m)^2} \quad (5-1)$$

Where X_m are the measured values, X_c are the computed values, and N is the number of measurements. The lower values of RMSE also show better agreement of results (Table 34). RMSE is appropriate for scalar quantities (e.g. water levels, wave heights, current speed), but not for vector quantities (e.g. current velocities) (Brière et al., 2007).

On the other hand, a scatter index SI is also used to quantify the performance of numerical models:

$$SI = \frac{RMSE}{\overline{X_m}} \quad (5-2)$$

Where $\overline{X_m}$ is the average measured value.

5.3.1.2. R²

In statistics, the squared multiple correlation coefficient or the coefficient of determination (R^2) indicates the proportion of the variance in the dependent variable that is predictable from the independent variable. It is given by:

$$R^2 = \frac{(\sum_{i=1}^N (X_{m_i} - \overline{X_m})(X_{c_i} - \overline{X_c}))^2}{\sum_{i=1}^N (X_{m_i} - \overline{X_m})^2 \sum_{i=1}^N (X_{c_i} - \overline{X_c})^2} \quad (5-3)$$

The perfect agreement is achieved if R^2 is 1.0 (Table 34).

5.3.1.3. BSS

The BSS used in meteorology and has already been applied to the numerical simulation of coastal morphology by Van-Rijn et al. (2003), Roelvink et al. (2009), Pender et al. (2013), etc. The BSS is given in the following equation for comparing measured and computed profiles.

$$BSS = 1 - \left[\frac{\langle |z_{b,c} - z_{b,m}|^2 \rangle}{\langle |z_{b,0} - z_{b,m}|^2 \rangle} \right] \quad (5-4)$$

Where $z_{b,0}$ is the initial profile,

$z_{b,c}$ is the computed profile,

$z_{b,m}$ is the measured profile, and $\langle \dots \rangle$ = averaging procedure over time series.

The BSS shows the perfect agreement with measurement data if it reaches to value of 1.0 (Table 34). If the model prediction is further away from the final measured condition than the baseline prediction, the BSS is negative. The BSS is very suitable for the prediction of bed evolution (Van Rijn et al., 2003).

Table 34. Qualification of error ranges (Van-Rijn et al., 2003).

Qualification	RMAE		RMSE		BSS
	Wave height	Current speed	Wave height, Current speed	R ²	Morphology
Excellent	<0.05	<0.1	<0.1	1.0-0.8	1.0-0.8
Good	0.05-0.1	0.1-0.3	0.1-0.3	0.8-0.6	0.8-0.6
Reasonable/fair	0.1-0.2	0.3-0.5	0.3-0.5	0.6-0.3	0.6-0.3
Poor	0.2-0.3	0.5-0.7	0.5-0.7	0.3-0	0.3-0
Bad	>0.3	>0.7	>0.7	<0	<0

5.3.2. Grid sensitivity analysis

In a numerical simulation, the accuracy of numerical results and the computational time strongly depend on the mesh size used. Definitely, the smaller the mesh size is, the higher the accuracy is. However, a very fine mesh with large number of cells may be leads to require more time to solve, even exceeds the computational capacity of the computer and software. In the other hand, the coarse meshes can have considerable influence on the propagation of numerical errors and result in an imprecise solution (Karcz et al., 2012). Therefore, mesh size sensitivity analysis needs be carried out to determine the most acceptable mesh size for capturing the important features of the geometry as well as sufficient hydrodynamic details.

5.3.2.1. Regional area-Grand Var

a. Regional model domain

According to the manual 2014 of DHI, the main domain and expansion domain have to achieve some basic criteria, viz. covering all research factors; the main domain resolution is fine enough to upgrade the accuracy results and make sure the topography of particle bottom factors as well as hydraulic constructions; the boundaries must be located in which have proper distance to ensure the error is smaller; and the hydrological and oceanographic data boundaries are available for all study scenarios. Hence, three types of regional scale were proposed to carry out the sensitivity analysis, as shown in Figure 97, Figure 98 and Figure 99.

For the study domain of type I, it covers the whole of the Toulon gulf, the Giens gulf and the Hyères bay with limits approximately at Anemoc points of MEDIT-2533 and 6996 in the west, MEDIT-7312 in the south, and MEDIT-2358 and 7599 in the east (Figure 97). It extends from Bandol to Saint-Tropez, an area of about 38x76 km². The west boundary, south boundary, and east boundary are located far from Giens tombolo about 32.5 km, 18 km, and 43.5 km, respectively. The presence of all islands near Giens tombolo such as Porquerolles, Grand Ribaud, Port-Cros, and Levant are considered.



Figure 97. The study domain of regional scale-Type I.

The regional scale of type II stretches from 16 km westward to the ‘Cap Brun’, to 36 km eastward far to the ‘Cap Lardier’, and between 20 and 25 km offshore. It is limited by Anemoc points of MEDIT-2021 and 7312 in the west, MEDIT-7312 and 6975 in the south, MEDIT-6975 and 5046 in the southeast, MEDIT-2084 and 5046 in the east (Figure 98). In the type III of regional scale, the study area is reduced to 15x32 km². It includes of only two islands of Porquerolles and Grand Ribaud. The west boundary is established by MEDIT-2021, while the east boundary is set up by MEDIT-2185. The south boundary is located far from Porquerolles island about 2 km and through the wave buoy B08301 (Figure 99).

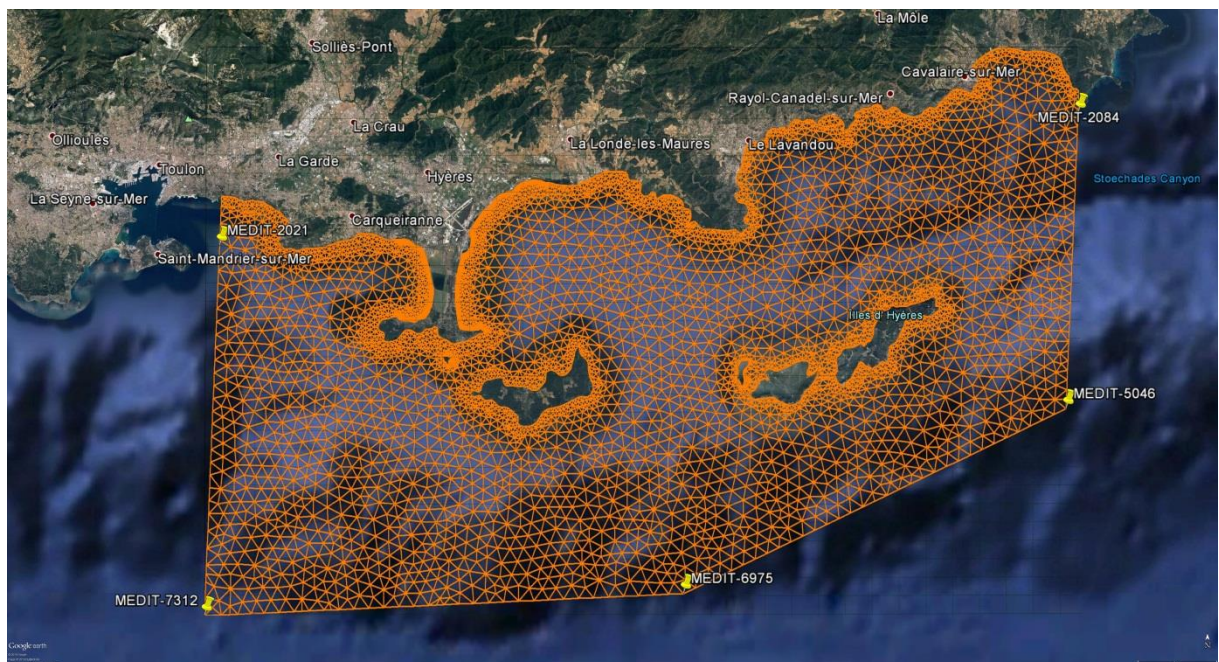


Figure 98. The study domain of regional scale-Type II.

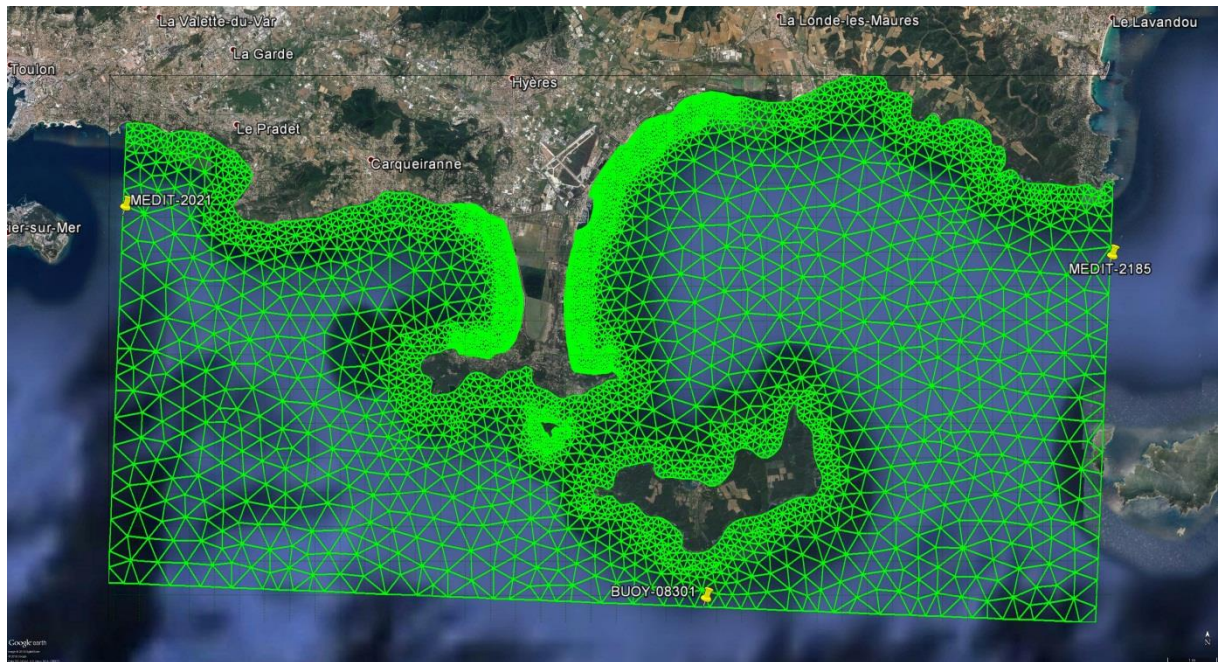


Figure 99. The study domain of regional scale-Type III.

b. Mesh and bathymetry

Totally, 103 unstructured meshes for regional scale were created by the Mesh Generator. These meshes consist of from 2770 elements to 70352 elements corresponding to from 1163 nodes to 36543 nodes. The high resolution of the mesh is concentrated along two sides of Giens tombolo for describing accurately the processes regarding the wave-energy transformation that takes place during the transition from the offshore to the coastal areas as well as calibrates the hydrodynamic parameters in this region. On the other side, the coarse mesh is distributed to offshore areas as an effective way to reduce the total number of mesh cells.

The bathymetry data of EGB is utilized to interpolate the bathymetry of offshore zones, whilst the bathymetry data of LITTO3D is used for near-shore zones along two branches of Giens tombolo. The bathymetries of study area are shown in Figure 100, Figure 101, and Figure 102. It is easily seen that most of the deepest areas are observed in the southwest of Giens gulf and outside of islands. The water depths can be deeper than 1500 meters. On the other hand, the narrowest areas are found near the coast with water depth ranging from 0 m to -10 m (CM) around islands and coast.

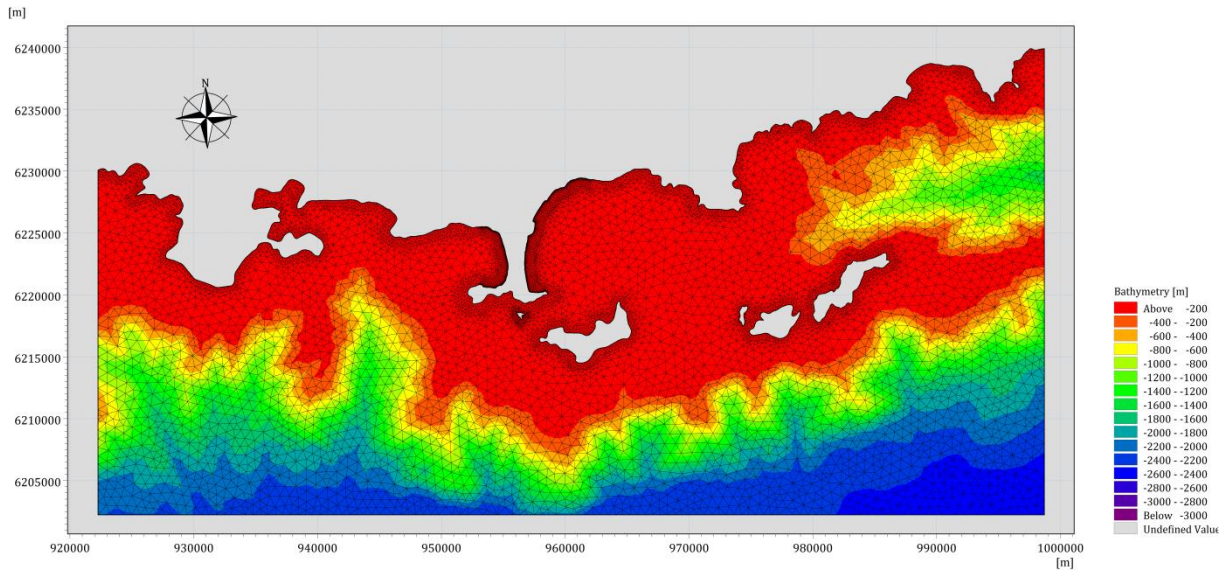


Figure 100. An example of computational mesh and bathymetry of regional scale-Type I.

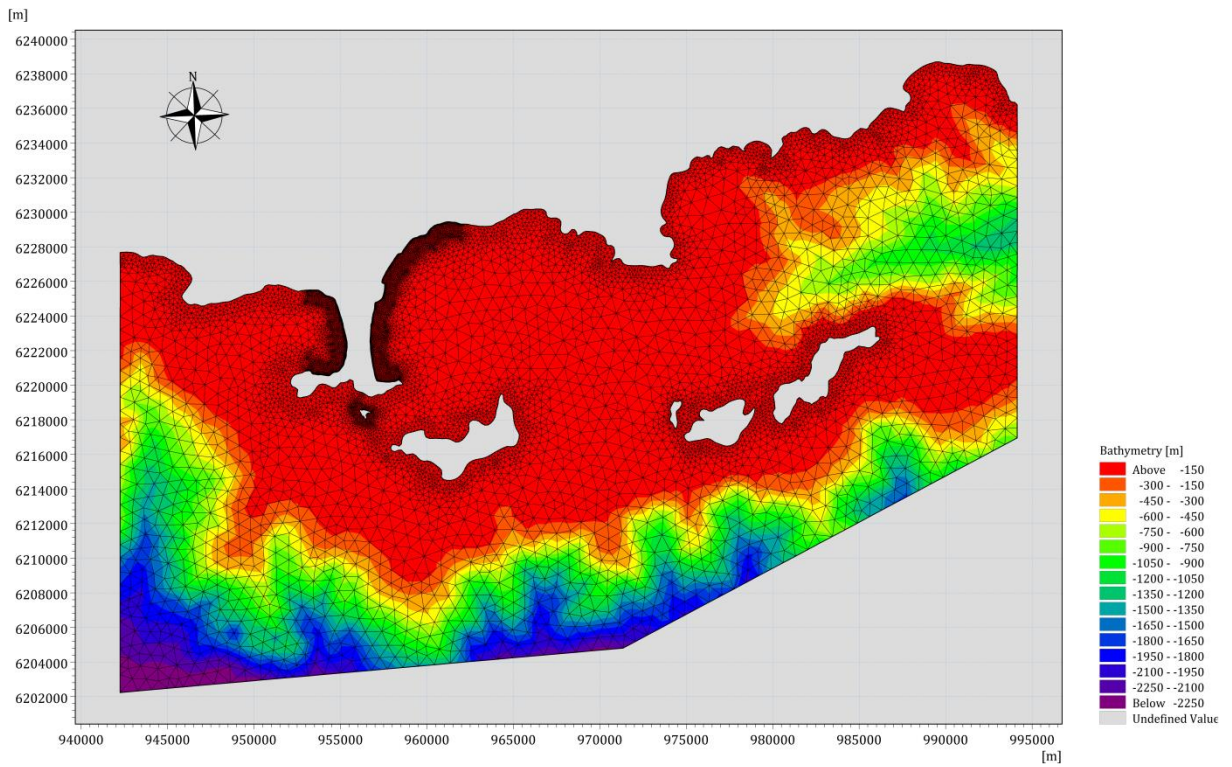


Figure 101. An example of computational mesh and bathymetry of regional scale-Type II.

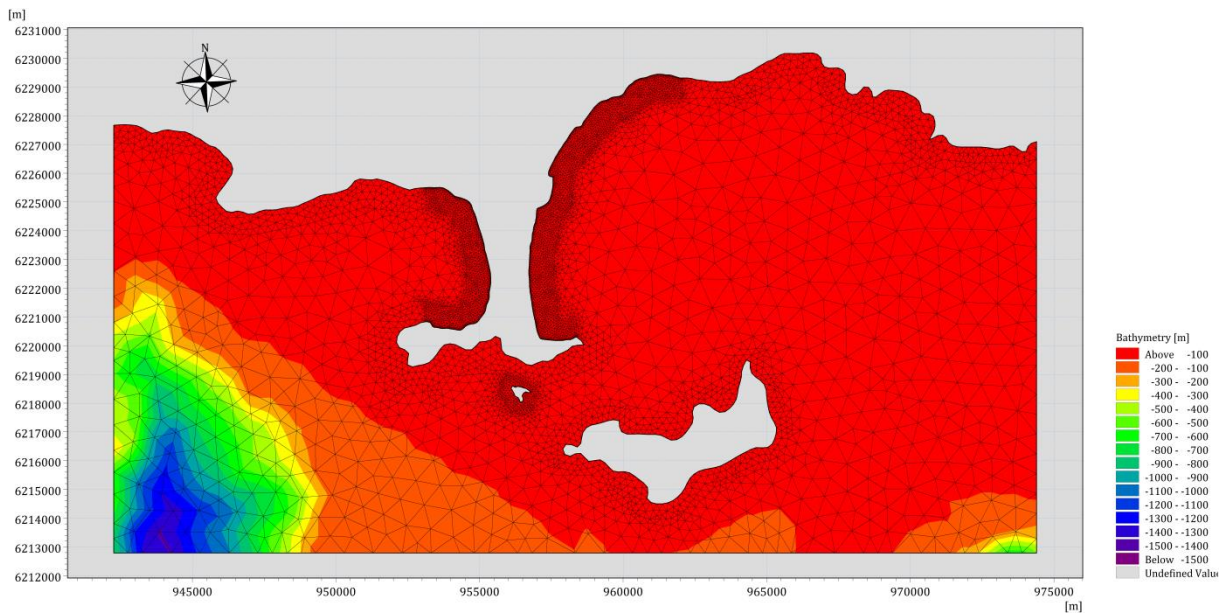


Figure 102. An example of computational mesh and bathymetry of regional scale-Type III.

c. Boundary and initial conditions

If the description of the bathymetry is the most important task in the modeling process, then the description of boundary conditions is the second most important task. Setting the appropriate boundary conditions can lead to the better numerical model results as well as fewer instability problems (DHI, 2014b).

The hourly wave data from 1979 to 2008 extracted from Anemoc models is directly assigned to boundaries. Additionally, the wave data of Buoy 08301 and 08302 recorded in every three hours from 1992 to 2015 is also used to interpolate and test for all meshes. The different effect between simulated and measured wave data on the modeling results will be interpreted.

Wind data, which includes speed and direction at 10m high, are recorded in each hour from 1993 to 2015 at Hyères meteorological station and from 2000 to 2015 on Levant Island. Using two wind data is to determine which station is the most suitable for reflecting actual situation. It is clearly seen that the wind speed at Levant station is normally higher than that at Hyères because it is not almost affected by obstacles such as high construction, high trees, etc.

For the open-sea boundary, the water level data was interpolated from the recorded data of Toulon gauge station. Moreover, the bottom friction coefficient (Nikuradse's roughness) was kept at default value of 0.04 m for all runs.

More detail regarding boundaries assigned to the study area are shown in Figure 103, Figure 104 and Figure 105.

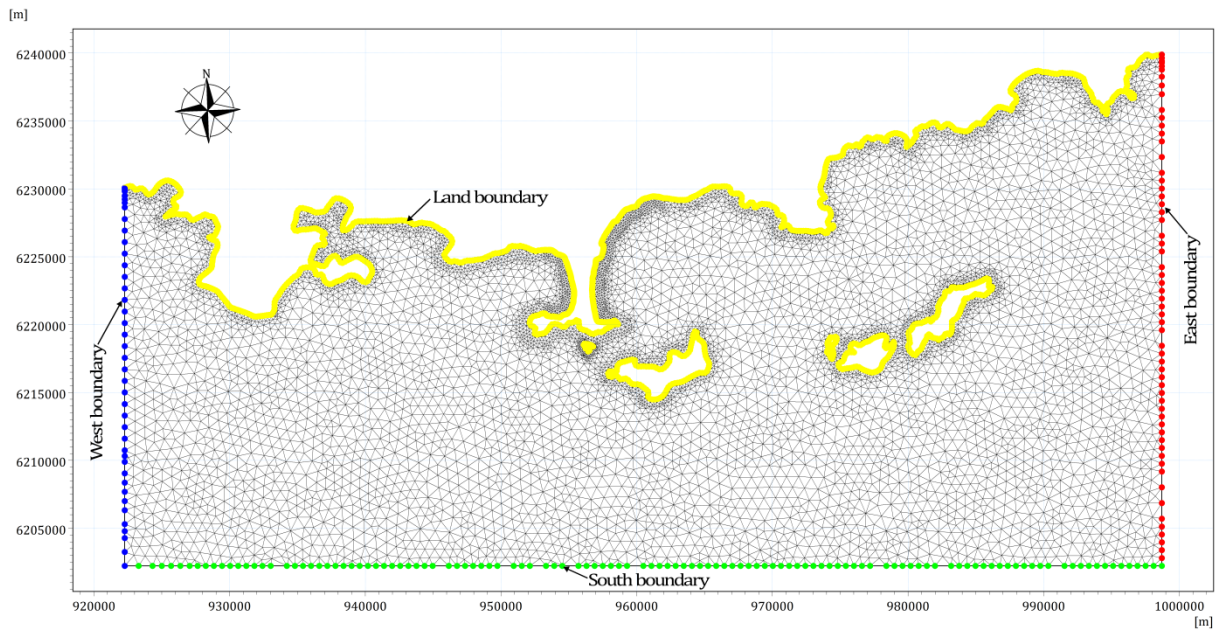


Figure 103. Boundary conditions of regional domain-Type I.

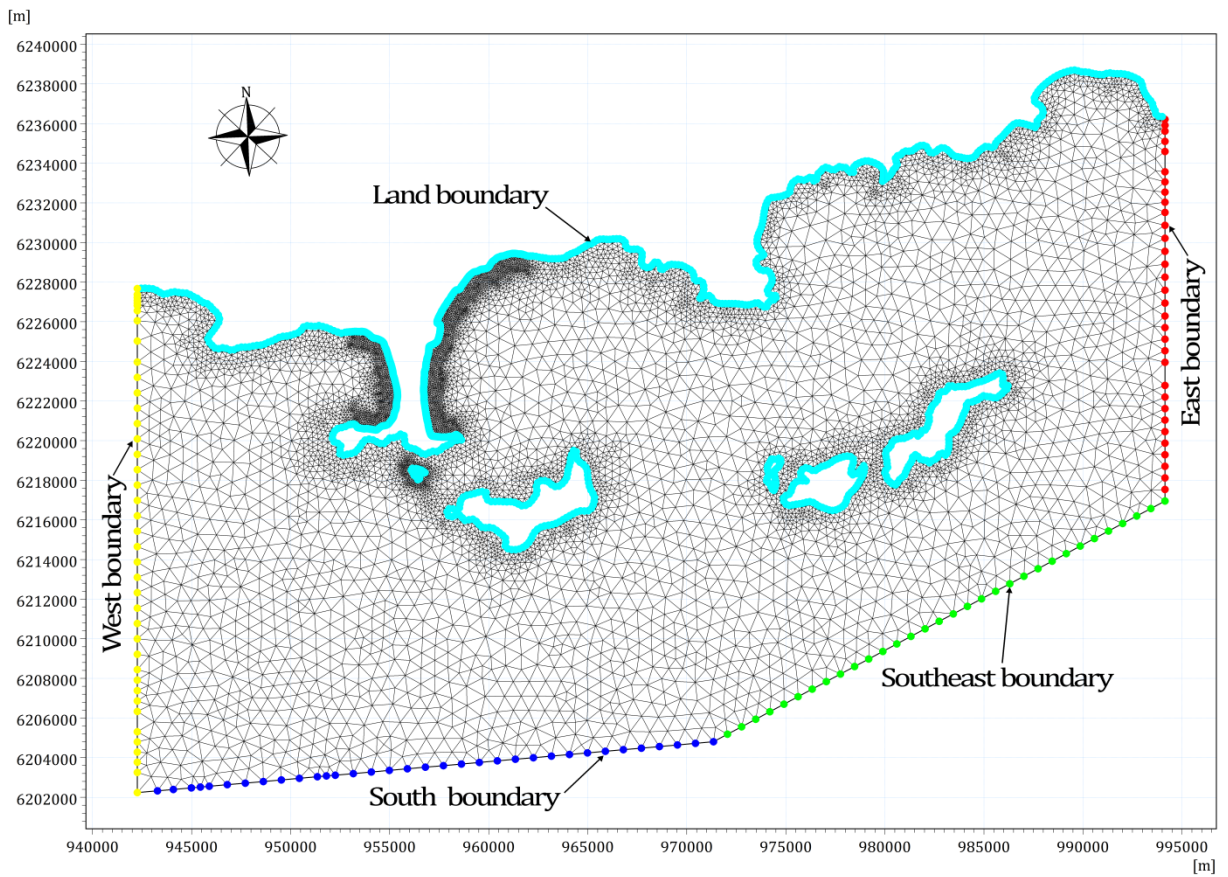


Figure 104. Boundary conditions of regional domain-Type II.

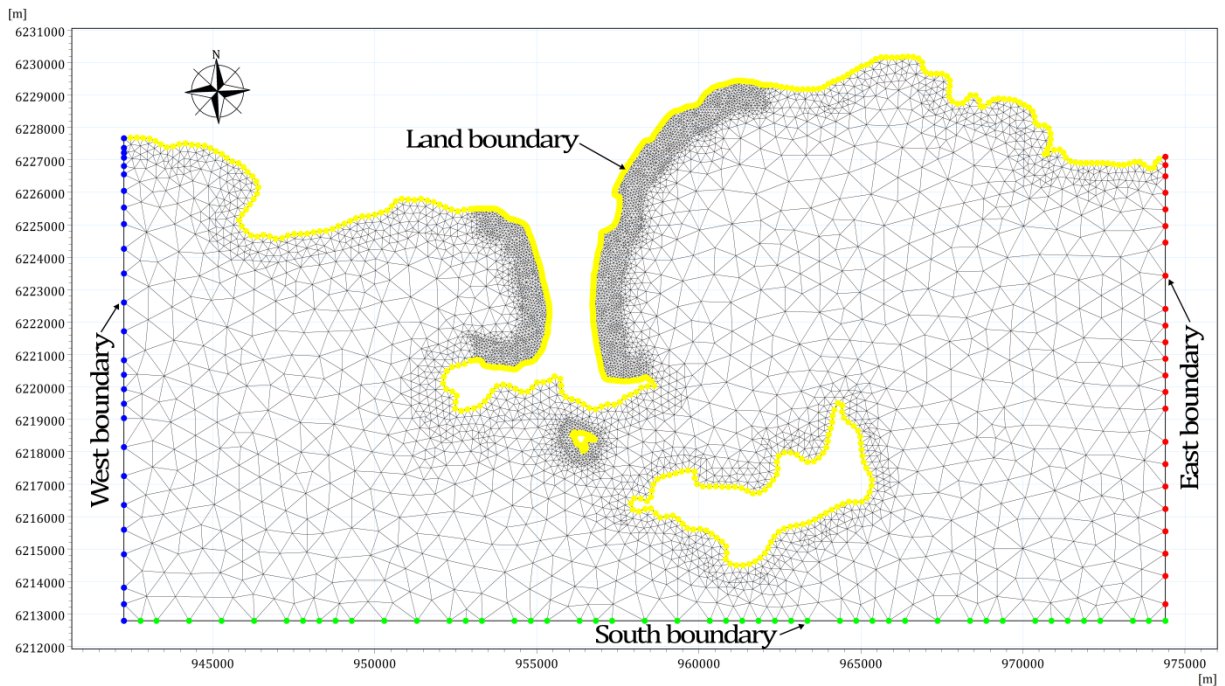


Figure 105. Boundary conditions of regional domain-Type III.

d. Results

The numerical model results are presented from Table 35 to Table 38 and Figure 106. They reveal that the regional scale of 12,053 elements is the most appropriate for describing the actual wave conditions in the study area with R-squared of 0.911 and RMSE of 0.0917. However, the most suitable mesh of 12,053 elements is not the finest mesh generated. This demonstrates that too low resolution or very high resolution does not give well goodness of fit to measured data, even using a very high-resolution mesh increases the computational time. Additionally, the boundary conditions, viz. the wind data recorded at Hyères station and the wave data interpolated from Buoys at Porquerolles island, gave more precise results than others resources. Consequently, the mesh of 12053 elements, the wind data of Hyères station as well as the wave data interpolated from Buoys 08301 and 08302 will be used for next steps.

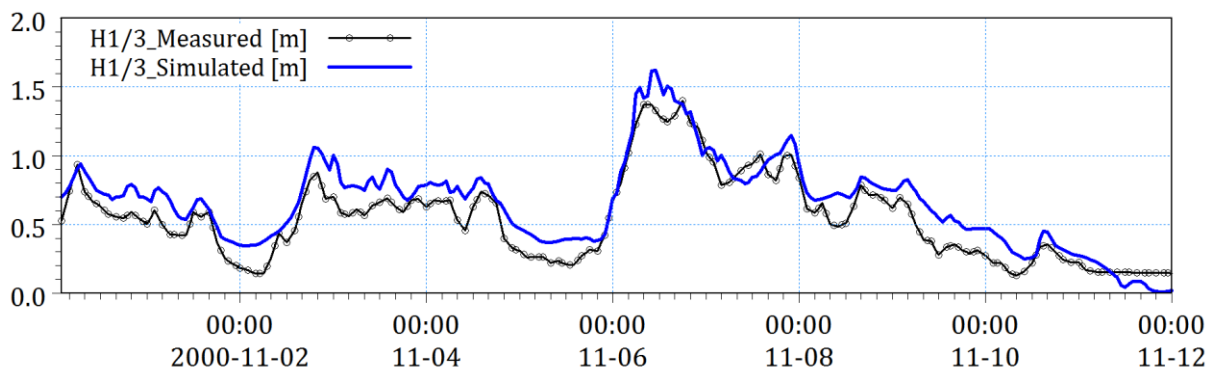


Figure 106. Time series of OBS and SIM wave height in the case of IIIi_v3.

Table 35. Statistical results of regional model comparison between the OBS and SIM waves at Almanarre beach in 2000.

Cases	No. of mesh elements	Bathymetry	Wave	Wind	R ²	RMSE	SI	
Ia_v1	8548				0.469321	0.223492	0.408279	
Ib_v1	9622				0.471717	0.222987	0.407357	
Ic_v1	10668				0.476607	0.221953	0.405468	
Id_v1	12304				0.486606	0.219822	0.401575	
Ie_v1	14000				0.477331	0.221799	0.405186	
If_v1	15488				0.477732	0.221714	0.405031	
Ig_v1	17751	EGB for offshore zone and Litto3D for near-shore zone in the eastern Giens tombolo			0.491961	0.218673	0.399476	
Ih_v1	19649				0.475893	0.222104	0.405744	
Ii_v1	21543		ANEMOC	Levant	0.481117	0.220994	0.403716	
Ik_v1	23550		points	station	0.475527	0.222181	0.405884	
Il_v1	24643				0.463715	0.224669	0.410429	
Im_v1	27514				0.474088	0.222486	0.406441	
In_v1	29301				0.465178	0.224363	0.40987	
Io_v1	34801				0.497601	0.217456	0.397252	
Ip_v1	41083				0.496613	0.217669	0.397642	
Iq_v1	53072				0.491775	0.218713	0.399549	
Ir_v1	62764				0.500551	0.216816	0.396083	
Is_v1	70352				0.486128	0.219925	0.401763	
Ia_v2	8314					0.541436	0.207752	0.379525
Ib_v2	9621					0.701873	0.167512	0.306014
Ic_v2	10680					0.7134	0.164242	0.30004
Id_v2	12203					0.722289	0.161675	0.295351
Ie_v2	14617				0.825486	0.128162	0.234129	
If_v2	15985	EGB for offshore zone and Litto3D for near-shore zone in the eastern and western Giens tombolo			0.826459	0.127805	0.233476	
Ig_v2	17817				0.831261	0.126024	0.230223	
Ih_v2	18883		Buoy 08301	Levant	0.833074	0.125345	0.228982	
Ii_v2	21400		at	station	0.833494	0.125188	0.228696	
Ik_v2	22664		Porquerolles		0.834547	0.124791	0.22797	
Il_v2	26152				0.835477	0.12444	0.227329	
Im_v2	31817				0.840328	0.122592	0.223953	
Inv2	36548				0.841278	0.122226	0.223285	
Io_v2	46494				0.843563	0.121343	0.221672	
Ip_v2	52491				0.84453	0.120968	0.220986	
Iq_v2	61671			0.848749	0.119315	0.217967		

Table 36. Statistical results of regional model comparison between the OBS and SIM waves at Almanarre beach in 2000 (continued).

Cases	No. of mesh elements	Bathymetry	Wave	Wind	R ²	RMSE	SI	
Ila_v1	5777				0.486362	0.219874	0.40167	
Ilb_v1	6634				0.483791	0.220424	0.402674	
Ilc_v1	7170				0.468709	0.223621	0.408515	
Ild_v1	8194				0.474142	0.222475	0.406421	
Ile_v1	9713				0.503275	0.216224	0.395002	
Ilf_v1	10631				0.507421	0.21532	0.39335	
Ilg_v1	12609	EGB for offshore zone and Litto3D for near-shore zone in the eastern Giens tombolo			0.517974	0.213001	0.389114	
Ilh_v1	14515				0.518859	0.212805	0.388756	
Ili_v1	17456		Anemoc points	Levant station	0.520246	0.212498	0.388195	
Ilk_v1	18529				0.505128	0.215821	0.394266	
Ill_v1	20229				0.513234	0.214046	0.391023	
IIm_v1	21680				0.511677	0.214388	0.391648	
IIn_v1	22760				0.516192	0.213394	0.389832	
Ilo_v1	26434				0.521272	0.212271	0.38778	
Ilp_v1	31300				0.51628	0.213375	0.389797	
Ilq_v1	42108				0.507027	0.215406	0.393507	
Ilr_v1	50165				0.479712	0.221293	0.404262	
Ils_v1	61544				0.524578	0.211537	0.38644	
Ila_v2	3294					0.641513	0.183689	0.335566
Ilb_v2	3771					0.698867	0.168355	0.307554
Ilc_v2	4518					0.742789	0.155593	0.28424
Ild_v2	6227					0.797909	0.137918	0.251951
Ile_v2	7105	EGB for offshore zone and Litto3D for near-shore zone in the eastern and western Giens tombolo			0.802415	0.136371	0.249125	
Ilf_v2	7630				0.810104	0.133692	0.244231	
Ilg_v2	8917		Buoy 08301 at Porquerolles	Levant station	0.814394	0.132173	0.241456	
Ilh_v2	9416				0.801919	0.136542	0.249437	
Ili_v2	9970				0.804373	0.135694	0.247888	
Ilk_v2	10839				0.806011	0.135125	0.246849	
Ill_v2	12509				0.803889	0.135862	0.248195	
IIm_v2	14245				0.80934	0.13396	0.24472	
IIn_v2	18706				0.798965	0.137557	0.251292	
Ilo_v2	23816				0.791054	0.140237	0.256187	
Ilp_v2	27054			0.78391	0.142615	0.260532		

Table 37. Statistical results of regional model comparison between the OBS and SIM waves at Almanarre beach in 2000 (continued).

Cases	No. of mesh elements	Bathymetry	Wave	Wind	R ²	RMSE	SI
IIIa_v1	2993				0.763284	0.149266	0.272682
IIIb_v1	3699				0.774118	0.14581	0.266368
IIIc_v1	4277				0.78402	0.142578	0.260464
IIId_v1	5848				0.790607	0.140387	0.256461
IIIe_v1	7738				0.791346	0.140139	0.256008
IIIf_v1	9602				0.785763	0.142002	0.259412
IIIg_v1	11839	EGB for offshore zone and Litto3D			0.78853	0.141082	0.257731
IIIh_v1	13600				0.790529	0.140413	0.256509
IIIi_v1	14337	for near-shore zone in the eastern Giens tombolo	ANEMOC points	Levant station	0.79087	0.140299	0.256301
IIIk_v1	16269				0.788755	0.141007	0.257594
IIIl_v1	17078				0.77736	0.14476	0.26445
IIIm_v1	18879				0.777434	0.144736	0.264406
III n_v1	22637				0.77576	0.145279	0.265398
IIIo_v1	32866				0.775157	0.145474	0.265754
IIIp_v1	38683				0.799727	0.137296	0.250815
IIIq_v1	41532				0.788874	0.140967	0.257521
IIIr_v1	56536				0.786076	0.141898	0.259222
IIIa_v2	2770				0.6026	0.193402	0.35331
IIIb_v2	3108				0.758022	0.150916	0.275696
IIIc_v2	3995				0.767854	0.147818	0.270037
IIId_v2	6046				0.841404	0.122178	0.223197
IIIe_v2	6515				0.855956	0.116438	0.212711
IIIf_v2	7564				0.850066	0.118795	0.217017
IIIg_v2	9319	EGB for offshore zone and Litto3D			0.847463	0.119821	0.218891
IIIh_v2	11165	for near-shore zone in the eastern and western Giens tombolo	Buoy 08301 at Porquerolles	Levant station	0.854332	0.117092	0.213906
IIIi_v2	12053				0.857295	0.115895	0.211719
IIIk_v2	13394				0.859055	0.115179	0.210411
IIIl_v2	14183				0.856602	0.116176	0.212232
IIIm_v2	15055				0.852653	0.117765	0.215135
IIIo_v2	17628				0.842692	0.121681	0.222289
IIIp_v2	25331				0.838854	0.123156	0.224984
IIIq_v2	32293				0.85109	0.118388	0.216273
IIIr_v2	35354				0.84807	0.119582	0.218455
IIIs_v2	45463				0.843607	0.121326	0.22164

Table 38. Statistical results of regional model comparison between the OBS and SIM waves at Almanarre beach in 2000 (finished).

Cases	No. of mesh elements	Bathymetry	Wave	Wind	R ²	RMSE	SI
IIIa_v3	2770				0.690588	0.170653	0.311752
IIIb_v3	3108				0.825962	0.127988	0.233811
IIIc_v3	3995				0.84363	0.121317	0.221624
IIId_v3	6046				0.903924	0.095094	0.173719
IIIe_v3	6515				0.909065	0.092515	0.169008
IIIf_v3	7564				0.907466	0.093325	0.170488
IIIg_v3	9319	EGB for offshore zone and Litto3D			0.905471	0.094326	0.172316
IIIh_v3	11165	for near-shore zone in the eastern and western Giens	Buoy 08301 at Porquerolles	Hyères station	0.907014	0.093552	0.170902
IIIi_v3	12053				0.910677	0.091691	0.167503
IIIk_v3	13394				0.907306	0.093405	0.170634
IIIl_v3	14183	tombolo			0.908092	0.093008	0.169909
IIIm_v3	15055				0.905775	0.094173	0.172037
III n_v3	17628				0.89804	0.097963	0.178961
IIIo_v3	25331				0.900353	0.096845	0.176918
IIIp_v3	32293				0.906082	0.09402	0.171757
IIIq_v3	35354				0.904353	0.094881	0.17333
IIIr_v3	45463				0.902689	0.095704	0.174834

5.3.2.2. Local area-The eastern Giens tombolo

a. Local model domain

To elucidate the mechanism of sediment transport along the eastern Giens tombolo as well as the influence of Gapeau river on the coastal morphology, the local model domain is extended from Salins beach (about 2 km in the north of Gapeau river mouth) up to La Badine beach (about 9 km in the south of Gapeau river mouth). The open-sea boundary of this domain is located at 2 km away from the eastern shoreline. Furthermore, the main flow input, namely the Gapeau river, has also been included in the study domain. The length of this river is ended at Sainte Eulalie station, which is about 6 km upstream of Gapeau river mouth. Analyses of the data show that there are no tides reaching there. Like the regional model domain, these boundaries must be located far enough to ensure that their spurious effect is kept outside the area of interest. The limitation of local domain is shown in Figure 107.



Figure 107. The study domain of local scale.

b. Mesh and bathymetry

DHI manual 2014 mentioned that it might be feasible to apply a quadrangular mesh to reflect the flow pattern more accurately in area with a pre-dominant flow direction. Accordingly, in this study, the quadrangular mesh is used for the area of Gapeau river, whereas the unstructured triangular mesh is hired for the coastal regions. Moreover, in the coastal regions, the fine triangular mesh is applied along the coast and the Gapeau river mouth, whereas the coarser triangular one is established in offshore zones (Figure 108). The fine triangular elements are concentrated in the area which stretches from the shoreline up to 5 m depth offshore (i.e. beyond the location of depth of closure) in order to describe exactly the changes of bathymetry due to action of waves and storms. All 15-mesh cases with different element numbers are generated to carry out the sensitivity analysis (Table 39).

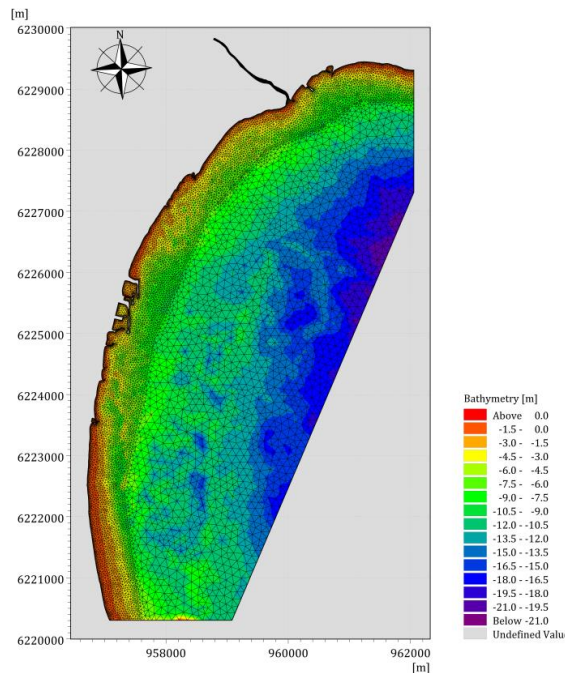


Figure 108. An example of computational mesh and bathymetry of local scale.

Regarding the bathymetry, the data of EOL measured in 2010 is utilized for near-shore zone in which is shallower than the depth closure while the simulation data of LITTO 3D is employed for deeper area. Figure 108 illustrates an example of bathymetry for local scale. It is clearly observed that the deepest area is seen in the east of computational domain with the depth beyond 20 m (CM). Moreover, the shallowest area is indicated near La Badine beach where is deposited by the blockage of the longshore sediment transport due to Cape of Esterel.

c. Boundary and initial conditions

Four boundary conditions including three offshore boundaries and one river discharge boundary were prescribed to force the local model (Figure 109). The wave data is extracted from the wave results of IIIi_v3 regional model. The wind data recorded at Hyères station and the sea level data interpolated from the data of Toulon station were still used for all simulations. The discharge data of Gapeau river measured at Sainte Eulalie station was utilized as the river flow boundary.

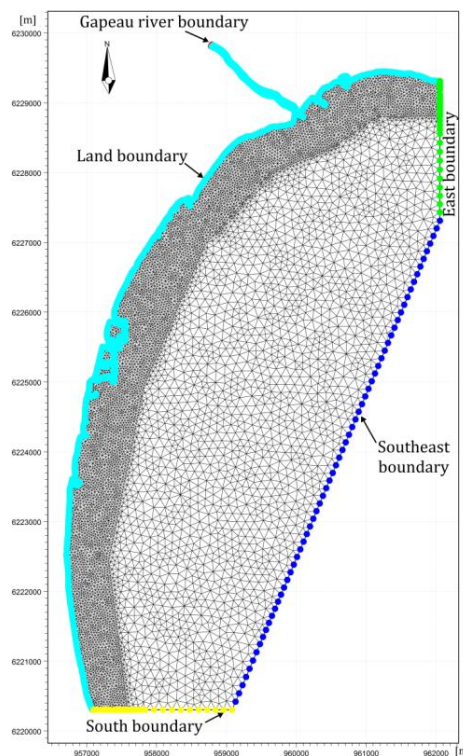


Figure 109. Boundary conditions of local domain.

d. Results

The wave data obtained from the simulations of local scale is compared and statistically analyzed with the wave data measured at La Capte beach in 2009. The results of comparison indicated that the mesh case of 22,960 elements is the most suitable for modeling the in-situ wave conditions (Figure 110). It provides the best fit to the measured data with R-square of 0.6206 and RMSE of 0.055 (Table 39). Hence, this mesh will be hired to simulate the hydrodynamics and sediment transport along the eastern Giens tombolo.

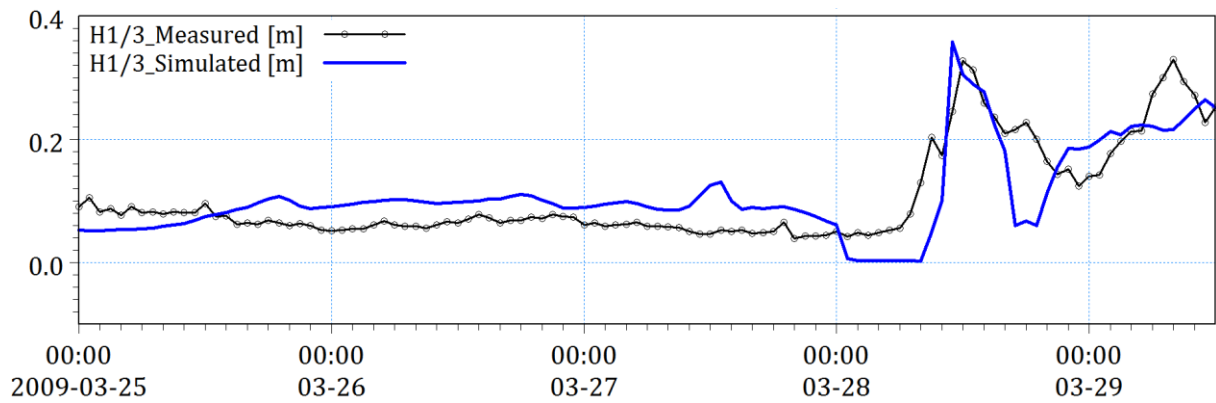


Figure 110. Time series of OBS and SIM wave height in the case of E11.

Table 39. Statistical results of local model comparison between the OBS and SIM waves at La Capte beach in 2009.

Cases	No. of mesh elements	Bathymetry	Wave	Wind	R ²	RMSE	SI
E1	9055				0.552831	0.059384	0.324989
E2	9826				0.555757	0.059189	0.323922
E3	10806				0.557898	0.059047	0.323145
E4	11844				0.557783	0.059054	0.323183
E5	12286				0.570414	0.058205	0.318537
E6	13244				0.557667	0.059062	0.323227
E7	14608	Litto3D for offshore zone and EOL for near-shore zone	Wave output of Regional model	Hyères station	0.569017	0.058299	0.319051
E8	14686				0.559313	0.058952	0.322625
E9	16195				0.573168	0.058018	0.317514
E10	18831				0.571036	0.058163	0.318307
E11	22960				0.620637	0.054697	0.299339
E12	25410				0.583528	0.057309	0.313634
E13	42610				0.619244	0.054797	0.299886
E14	60304				0.619396	0.054786	0.299826
E15	75145				0.619535	0.054776	0.299771

5.4. Model calibration

After determining the best meshes for both regional and local scales, the calibration procedure is conducted in order to obtain the best-fit hydrodynamic parameter set. Consequently, the regional model was run for the time period of one month from 31st October to 30th November 2000, whilst the local model was run for the period of one month from 12th March to 12th April 2009. The numerical results were also compared with field measurements at that time.

5.4.1. Regional area-Grand Var

Both the HD and SW models were run for the entire regional domain of Giens tombolo, including Giens gulf and Hyères bay, to arrive at boundary conditions to be used for the simulation for the site of interest on the eastern Giens tombolo for the period of November 2000.

5.4.1.1. HD model

a. Model setup

The purpose of this model run was to obtain sea level boundary conditions near the site of interest. The parameters controlling this model are given in Table 40.

Table 40. Parameters for the regional MIKE 21 HD model.

Parameter	Conditions
Bathymetry file	Grand Var Illi_v3.mesh
Grid numbers	6596 nodes and 12053 elements
Simulation period	31 st October to 30 th November 2000
No. of time steps	8640
Time step interval	300 seconds
Bed resistance	Manning's number of M= 10, 20, 24, 28, 32, 40, 45, 50, 55
Wind forcing	Wind data of Hyères station from 1979 to 2015
Eddy viscosity	0.65
Eastern boundary	Sea level at MEDIT-2185 point interpolated from Toulon station
Western boundary	Sea level at MEDIT-2021 point interpolated from Toulon station
Southern boundary	Sea level at Buoy 08301 interpolated from Toulon station

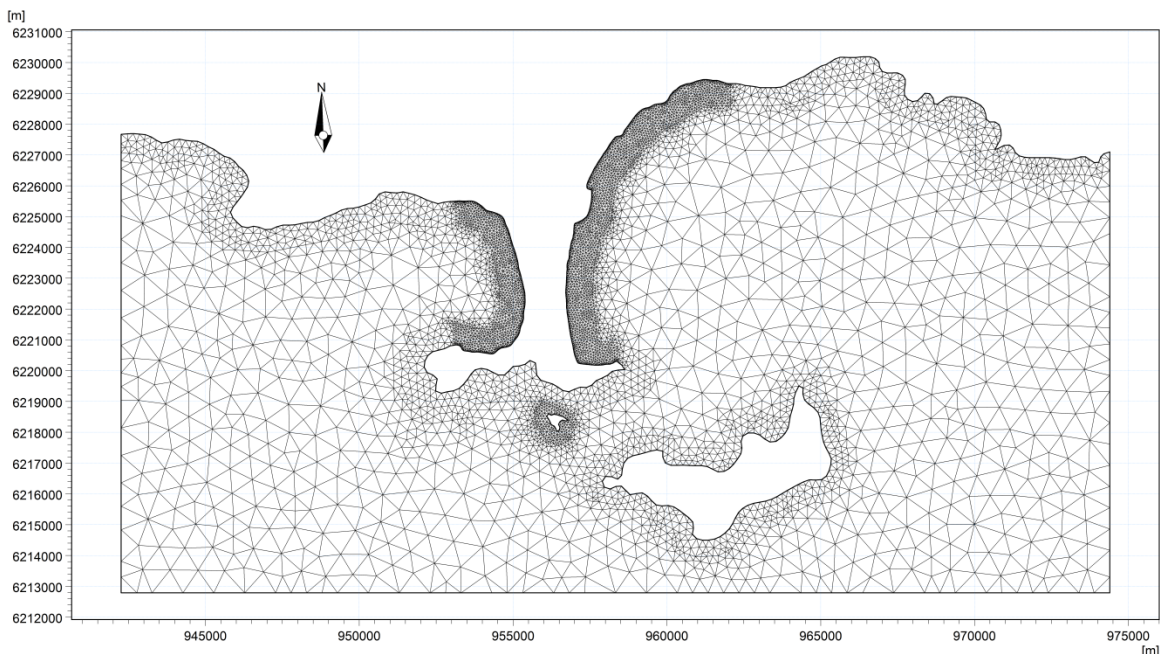


Figure 111. The computational mesh of the regional scale for calibration.

The computational mesh consisting 6,596 nodes and 12,053 elements determined in Part 4.3.2.1 was used in this model. The smaller grid cell length is about 30 m in the eastern and western coast of Giens tombolo (Figure 111). The time step of 300 seconds was selected considering the large extent of the area as a smaller time step increases the computational time by a large amount (Kulkarni, 2013). In the open-sea boundaries, the sea levels were applied as varying in time and along lines to obtain more realistic offshore conditions. A soft start of 900 seconds was used to linearly arrive at the first time step to avoid sudden changes.

The calibration focused primarily on adjustment of the bed resistance, whereas the eddy viscosity coefficient (Smagorinsky formulation) were kept at default values for these runs considering the effect of these variables will be negligible over such a large domain. The bed resistance of the hydrodynamic model is expressed as Manning's number, n or its reciprocal, M . Manning's number n is one of the most important calibration parameters affecting the current speed as well as water level. An increasing Manning's number leads to a decrease of current speed and an increase of water level, whilst a decreasing Manning's number results in higher current speed and lower water level. Uniform values of M ranging from 10 to 55 were considered.

b. Results

The model results were compared with the data available from Oceanoservice at the Almanarre beach (Figure 112 and Table 41). It is clearly seen that the simulated current speed in the case of $M = 20$ shows the best fit to the observed current speed (Figure 113). The goodness of fit statistics has R-square of 0.537 and RMSE of 0.0137 m/s. Hence, $M=20$ is used for official runs of the regional scale.

Table 41. Calibration of current speed for regional scale (from 9th to 11st, November, 2000).

Case	R ²	RMSE (m/s)	SI
OBS vs. Mn=10	0.362694772	0.016057343	0.475843612
OBS vs. Mn=20	0.537230919	0.013683024	0.405483018
OBS vs. Mn=24	0.52997564	0.013789868	0.408649231
OBS vs. Mn=28	0.50078851	0.014211575	0.421146106
OBS vs. Mn=32	0.471221166	0.014626384	0.433438549
OBS vs. Mn=40	0.415139044	0.015382476	0.455844603
OBS vs. Mn=45	0.374404639	0.01590914	0.471451761
OBS vs. Mn=50	0.333863089	0.016416542	0.486488134
OBS vs. Mn=55	0.297041742	0.01686416	0.49975284

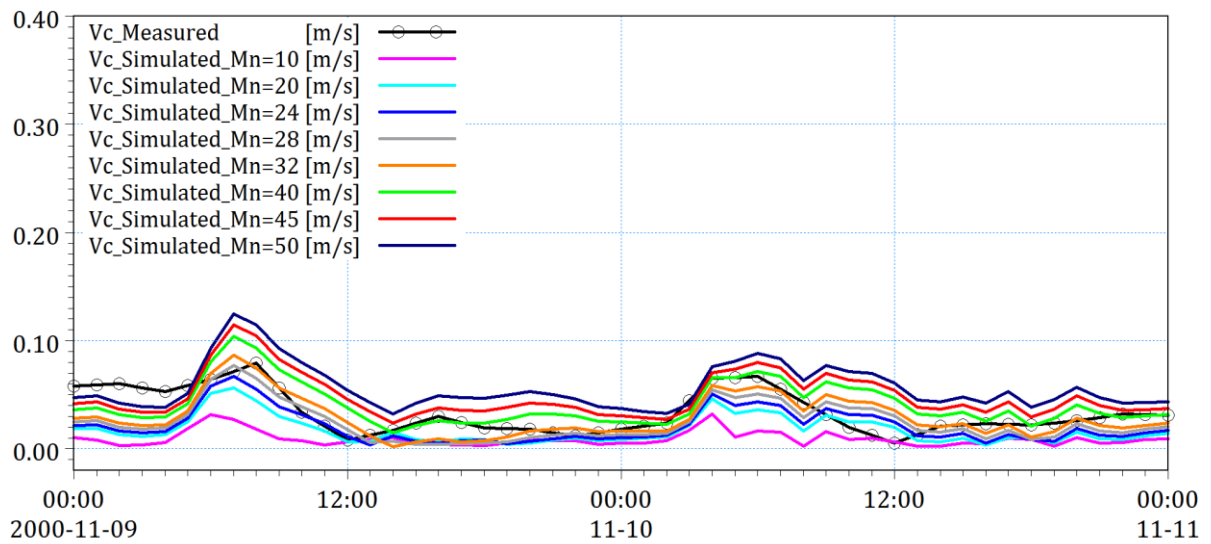


Figure 112. Calibration of current speed at Almanarre beach.

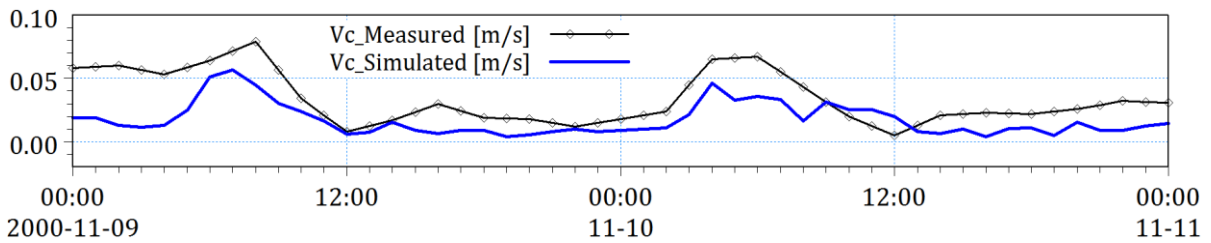


Figure 113. Comparison between the OBS and SIM current speed with Mn = 20 at Almanarre beach in November 2000.

5.4.1.2. SW model

a. Model setup

In the SW module, the fully spectral formulation was used with time formulation being instationary formulation. Like the hydrodynamic model, the time step of 300 seconds was chosen. The wave breaking and white capping were also included in the runs to improve accuracy. The wind data at 10 m height recorded at Hyères station was utilized for the entire domain. Diffraction and ice coverage were not considered in these simulations. At the southern boundary, the wave parameters measured by Buoy 08301 were applied as varying in time along the line, whereas the wave data at the western and eastern boundaries were interpolated from those of Buoy 08301.

The major parameter that is used for calibration is Nikuradse's roughness length, k_s . It greatly influences on the wave height. The larger the roughness length is, the lower the wave height is. Uniform values of k_s , ranging from 0.02 m to 0.08 m were taken into account. A detail of parameters used for regional SW model is listed in Table 42.

Table 42. Parameters for the regional MIKE 21 SW model.

Parameter	Conditions
Bathymetry file	Grand Var Illi_v3.mesh
Grid numbers	6596 nodes and 12053 elements
Simulation period	31 st October to 30 th November 2000
No. of time steps	8640
Time step interval	300 seconds
Basic equation	Fully spectral formulation Instationary formulation
Water Level Conditions	Sea level measured at Toulon gauge station
Wind forcing	Wind data of Hyères station from 1979 to 2015
Bottom Friction	kn = 0.02; 0.03; 0.04; 0.05; 0.0656; 0.07; 0.08
Eastern boundary	Wave data of MEDIT-2185 point interpolated from Buoy 08301
Western boundary	Wave data of MEDIT-2021 point interpolated from Buoy 08301
Southern boundary	Wave data of Buoy 08301

b. Results

Comparisons of measured and simulated wave height for the ranges of roughness length are shown in Figure 114 and Table 43. It can be seen that uniform roughness length value of 0.04 m gives the best result fit to the measured one (Figure 115). The goodness of fit statistics has R-square of 0.9118 and RMSE of 0.091 m. Accordingly, this value is applied for all official simulation of the regional area.

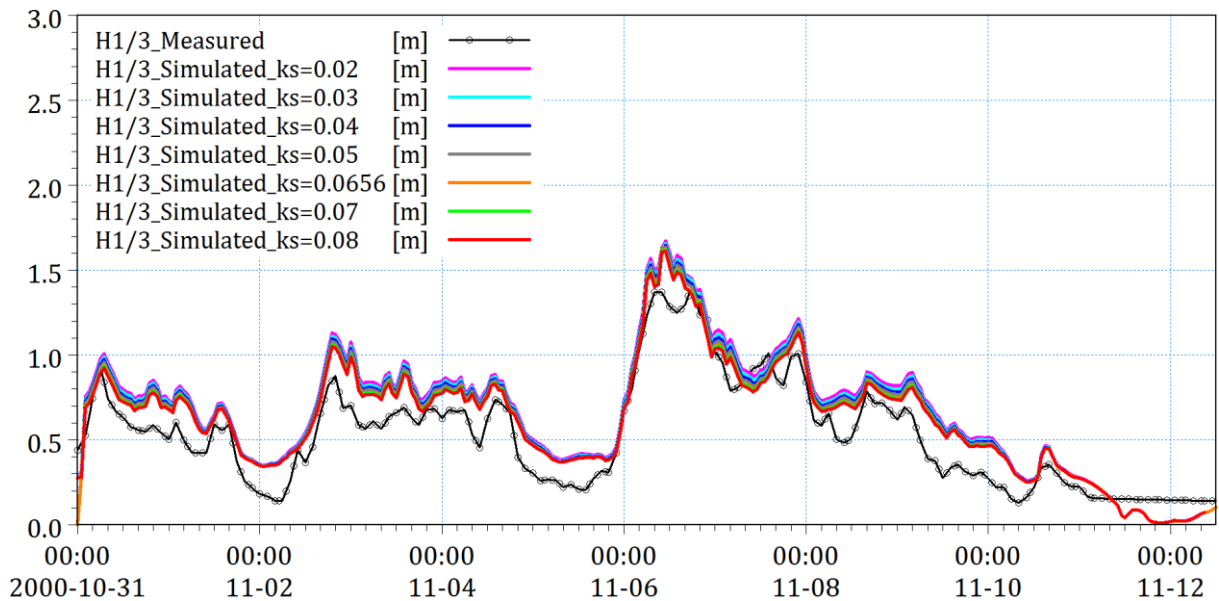


Figure 114. Calibration of wave height at Almanarre beach.

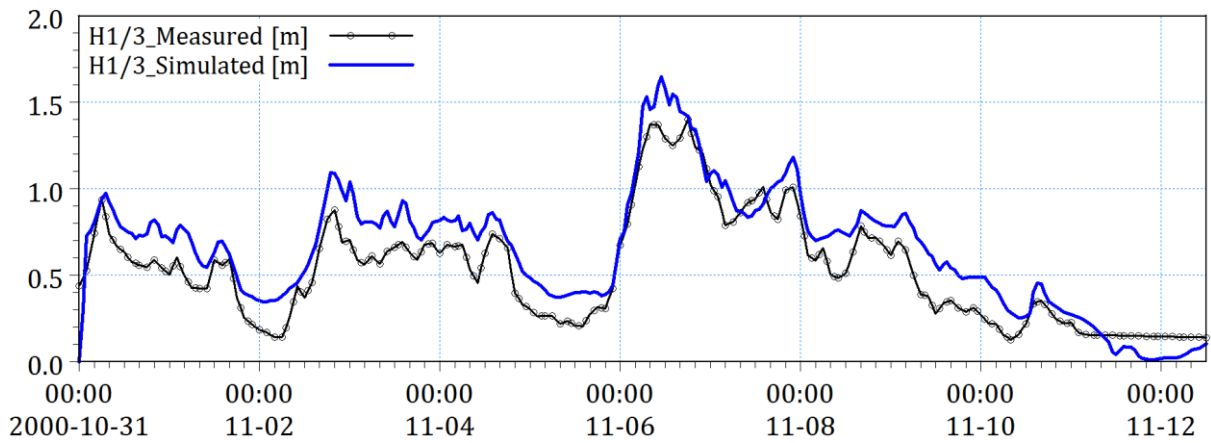


Figure 115. Comparison between the OBS and SIM wave height with $k_s = 0.04$ at Almanarre beach in November 2000.

Table 43. Calibration of wave height for regional scale (from 31st October to 12nd November, 2000).

Case	R ²	RMSE	SI
OBS vs. SIM of k=0.02	0.910648053	0.091706101	0.167530327
OBS vs. SIM of k=0.03	0.911556975	0.091238474	0.166676058
OBS vs. SIM of k=0.04	0.911816999	0.091104254	0.166430862
OBS vs. SIM of k=0.05	0.911618699	0.091206631	0.166617886
OBS vs. SIM of k=0.0656	0.910676775	0.091691361	0.167503399
OBS vs. SIM of k=0.07	0.910437985	0.091813839	0.167727145
OBS vs. SIM of k=0.08	0.909510784	0.092287872	0.168593116

5.4.1.3. Validation

A meaningful evaluation of the model quality must be performed with independent datasets, which have not been used for calibration. Therefore, the data of measurement campaign which was carried out by Meulé (2010) in March and April 2009 were hired here. The calibrated hydrodynamic and wave models of regional scale were validated through the wave height and the current speed. All the model parameters were kept same as the calibrated models.

The validation results of the wave model computed wave height was exhibited in Figure 116, while the hydrodynamic model computed current speed was validated in Figure 117. Moreover, the statistical errors of comparison between the simulation data and observation data were listed in Table 44. Overall, it can be concluded that the wave model produce reasonably good results for wave height ($R^2=0.795>0.6$) and reasonable results for current speed ($R^2 = 0.515< 0.6$) after proper calibration of key parameters and coefficients.

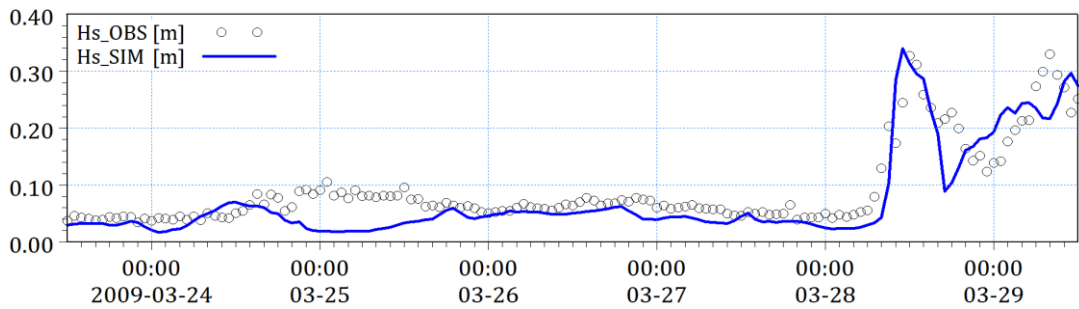


Figure 116. Comparison between the OBS and SIM wave height with $k_s = 0.04$ at La Capte beach in March 2009.

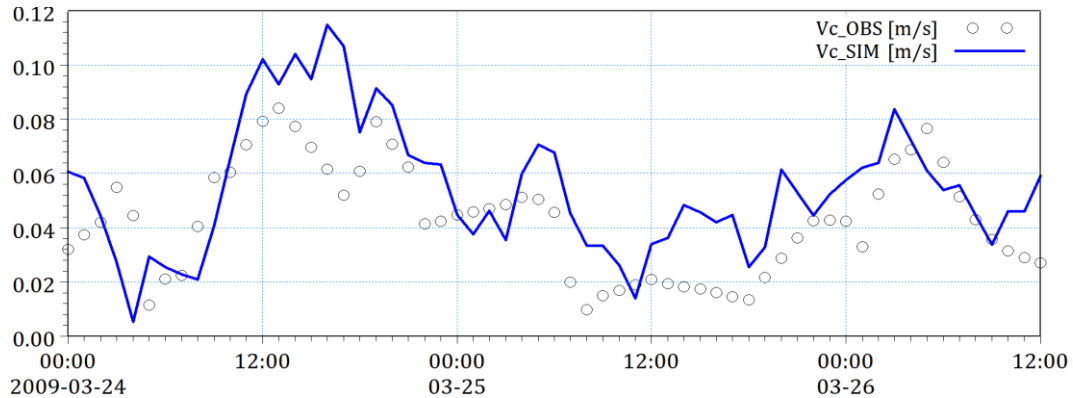


Figure 117. Comparison between the OBS and SIM current speed with $Mn = 20$ at La Capte beach in March 2009.

Table 44. Validation of wave height and current speed for regional scale (from 24th to 29th March, 2009).

Case	R ²	RMSE	SI
Hs_OBS vs. Hs_SIM	0.794842623	0.032019545	0.349177152
Vc_OBS vs. Vc_SIM	0.515047869	0.014183511	0.332314398

The validation results of both these two models of SW and HD were then used as boundary conditions in order to calibrate for the local scale.

5.4.2. Local area-The eastern Giens tombolo

The model was run for attempting a calibration against the data available from Meulé (2010). The area studied is on the eastern coast of Giens tombolo covering a distance of approximately 11 km from Salins beach to La Badine beach. MIKE 21/3 Coupled FM was used for the calibration runs of the local scale.

5.4.2.1. Model setup

The local model had a refined grid near the area of interest with increasing resolution towards the coast. It was nested directly within the regional model and was driven by water level and waves at 4 points on the offshore boundaries, taken from the regional model. The local model mesh is shown in Figure 118 and had 22,960 elements. The smallest grid cell area is approximately 9 m² inside the Gapeau river, while the largest one is about 12,000 m² in the offshore zone.

The HD, SW and ST were coupled dynamically. In the SW simulation, the directionally decoupled parametric and quasi-stationary formulation was applied considering the small area as recommended in the MIKE 21/3 manual; whilst the wave and current model type was selected in the ST model. A time step of 60 seconds was set up for the refined mesh in all modules. To avoid blow-up error, the water level and wave parameters varying in time extracted from the validation model of regional scale were assigned to the southern, southeastern, and eastern open-sea boundaries as input conditions; whereas the flow discharge of Gapeau river recorded at Sainte Eulalie station was utilized as fluvial upstream boundary. The wind data of Hyères station was still used for all simulations. For the morphological model, a condition of zero sediment flux gradient was applied at all the boundaries.

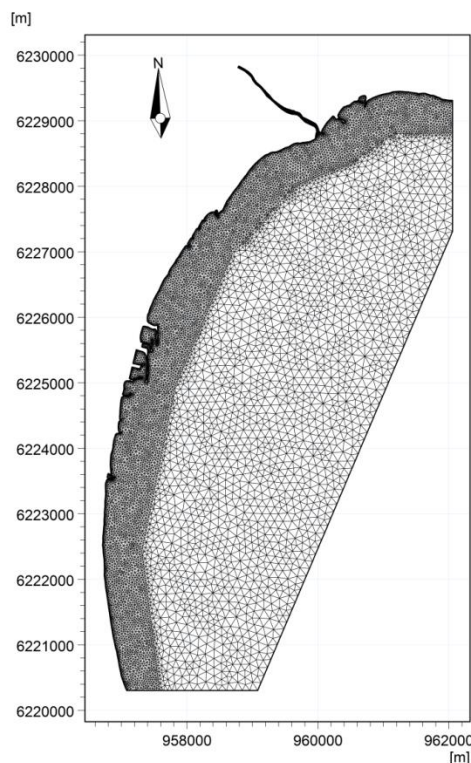


Figure 118. The computational mesh of the local scale for calibration.

The main calibration factors were chosen as Manning's number and Nikuradse's roughness height, namely M and k_s , respectively. They are functions of the median grain size, D_{50} (Figure 33). The presence of Posidonia seagrass was also taken into account in determining the values of Manning's number and Nikuradse's roughness height in some areas. The variations in Manning's number were used to calibrate the current field in the hydrodynamic model, whereas the variations in the roughness length play as the governing factor for calibrating the wave parameters in the SW model. Regarding the ST model, the distribution of the median grain size D_{50} was utilized to calibrate the bed level change. The known data for sediment properties acquired by Courtaud (2000) shows a varying range for the median grain diameter from 0.2 mm to 50 mm (Figure 33). Figure 34 shows the changes of roughness height values in Hyères bay, while the

distribution of Manning's number in the study area is illustrated in Figure 35. It is easily observed that the magnitude of Manning's number M is inversely proportional to the water depth and the roughness height k_s .

The above-mentioned parameters were tested systematically in order to determine the most appropriate model setup. The best setup was taken as the one that produced the highest average BSS, R-squared and lowest average RMSE. A summary of the parameters used for calibration of local model is described in Table 45.

Table 45. Parameters for the local MIKE 21/3 Coupled FM model.

Parameter	Conditions
Bathymetry file	Eastern Tombolo coastline-E11_Litto3D vs EOL.mesh
Grid numbers	13620 nodes and 22960 elements
Simulation period	12 th March to 12 th April 2009 for wave and current calibration 1 st November 2007 to 1 st November 2008 for sediment calibration
No. of time steps	44640
Time step interval	60 seconds
Eddy viscosity	0.5
Bed Resistance	Hydrodynamic parameters of Hyères bay in nature_v81.dfsu
Water Level Conditions	Open-sea boundaries: Sea level extracted from the validation model of the regional scale River boundary: Flow discharge of Gapeau river at Sainte Eulalie station
Wave Basic equations	Directionally decoupled parametric formulation Quasi stationary formulation
Wind forcing	Wind data of Hyères station from 1979 to 2015
Bottom Friction	Hydrodynamic parameters of Hyères bay in nature_v81.dfsu
Wave Conditions	Open-sea boundaries: Wave parameters extracted from the validation model of the regional scale
Model type of ST	Wave and current
Sediment properties	Hydrodynamic parameters of Hyères bay in nature_v81.dfsu
Sediment boundary conditions	Zero sediment flux gradient

5.4.2.2. Results

The simulated wave and current results are compared with the data measured at La Capte beach from 12th March to 12th April 2009. The simulated wave heights at the SCAPT3 and SCAPT4 show good agreement with measured values (Figure 119 and Figure 120). The RMSE ranges between 0.0542 m and 0.0358 m with the difference SI

between 47.1% and 41.2% at SCAPT3 and SCAPT4 points, respectively (Table 46). Furthermore, the comparison of SIM and OBS current speed at SCAPT4 point is displayed in Figure 121. It is shown that the flow is properly simulated by the model. The statistical score for this comparison is $R^2 = 0.435$ (reasonable), $RMSE = 0.0164$ m/s, and $SI = 33.88\%$.

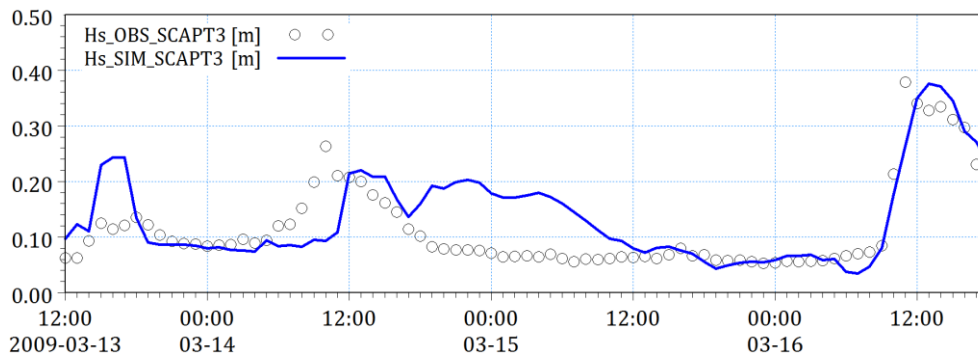


Figure 119. Comparison between the OBS and SIM wave heights of SCAPT3 station at La Capte beach in March 2009.

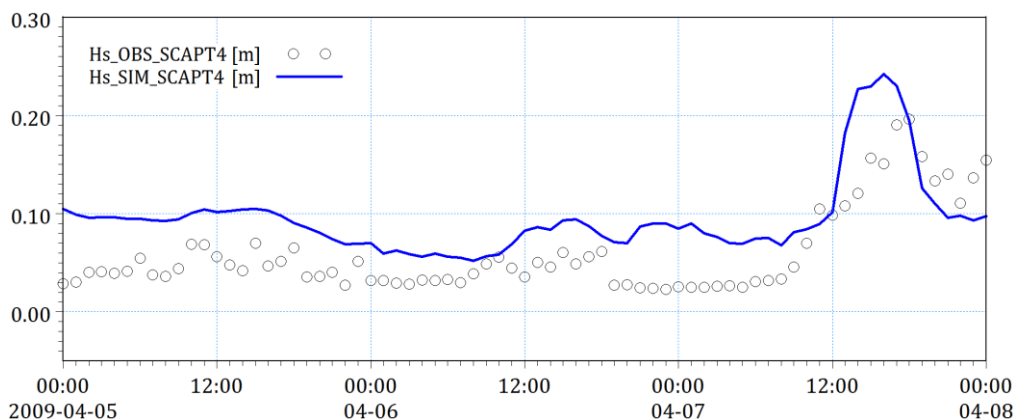


Figure 120. Comparison between the OBS and SIM wave heights of SCAPT4 station at La Capte beach in March 2009.

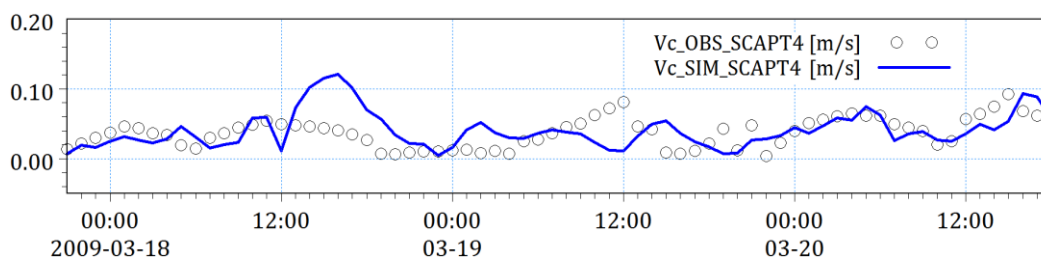


Figure 121. Comparison between the OBS and SIM current speeds of SCAPT4 station at La Capte beach in March 2009.

Table 46. Calibration of wave height and current speed for local scale (March, April, 2009).

<i>Case</i>	<i>R²</i>	<i>RMSE</i>	<i>SI</i>
Hs_OBS vs Hs_SIM_SCAPT3	0.536633512	0.054197698	0.470874876
Hs_OBS vs. Hs_SIM_SCAPT4	0.819809394	0.035766312	0.411921412
Vc_OBS vs. Vc_SIM	0.43511458	0.016442278	0.338806479

In addition to wave and current results, the morphological evolution obtained from the ST model is compared with the bathymetry which was measured by E.O.L (2010) in November 2008. Figure 122 show the difference between the measured and simulated beach profile at Aéroport beach. The result indicates that the model setup has resulted in BSS of 0.61, which is on good level according to Van-Rijn et al. (2003).

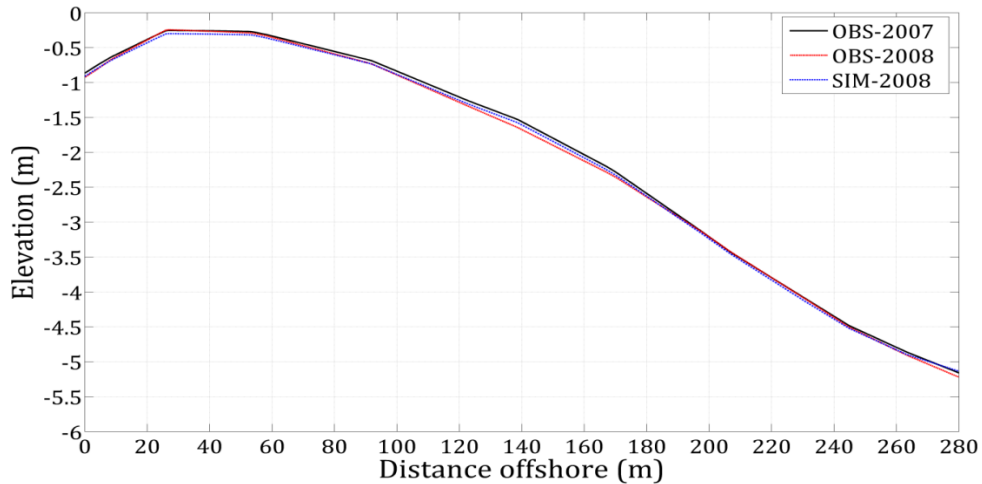


Figure 122. Comparison of OBS and SIM profile at Aéroport beach for the period from November 2007 to November 2008.

The input parameters of D_{50} , M , and k_s used for the best-fit configuration were then employed to run the official simulations for local scale.

5.5. Results of Regional area-Grand Var and discussion

The simulation results of the regional scale obtained from all the study scenarios taking into account wind variations, seasonal variations and extreme events are presented and discussed below.

5.5.1. Wind variations

5.5.1.1. Northeast wind

The current variation across the domain affected by the northeast wind is plotted in Figure 123. It is clearly seen that the strongest currents appear in the strait between Giens tombolo and Porquerolles island. In addition, the high current speed is also observed along the eastern Giens tombolo coast from Salins beach to the mouth of Roubaud river and near Pesquiers beach. The maximum longshore current speed of 0.25 m/s is found at the depth of 1.5 m near Gapeau river mouth. On the other hand, the weak currents occur in most of Giens gulf. The maximum current speed of 0.08 m/s is reported at a level of -3 m near Almanarre beach.

Figure 124 shows the wave height pattern in the study domain. The high waves with an average value of 0.9 m to 1.05 m approaching the coast from Roubaud river mouth to La Capte port. Along the eastern Giens tombolo, the maximum nearshore waves with the average height of 0.64 m is observed at the water depth of 1.5 m in front of Aygaude beach. Conversely, there are only small waves reaching the western tombolo because

Giens gulf is sheltered from the northeast winds. The highest wave with the height of 0.27 m is found at a level of -3 m close to Almanarre beach.

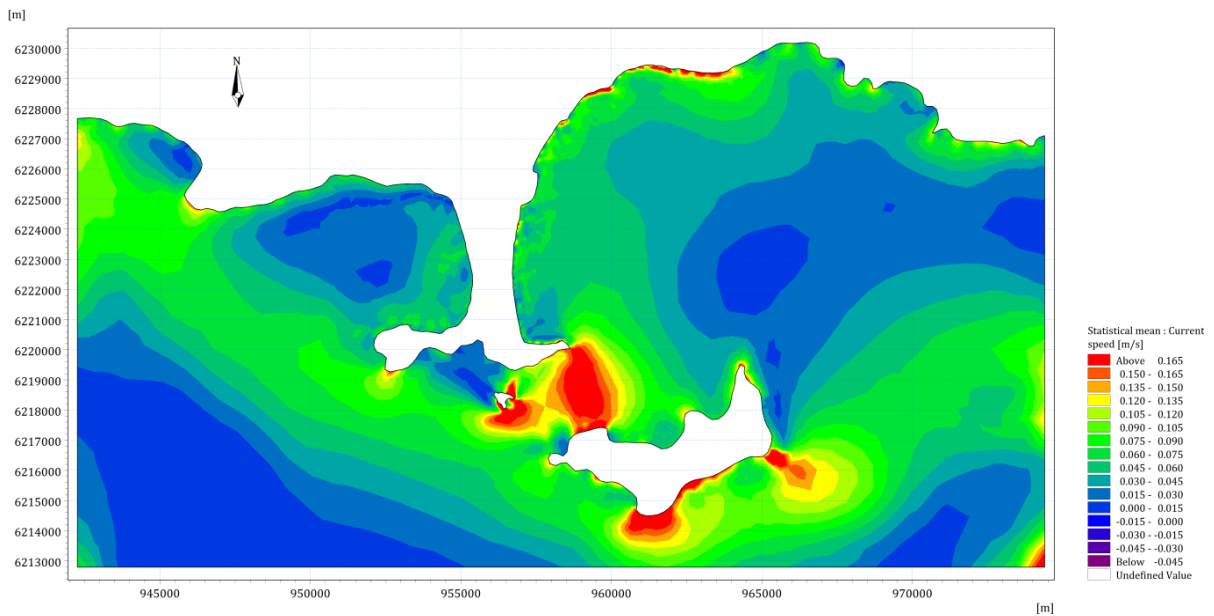


Figure 123. Current speed of the regional model under the impact of northeast wind.

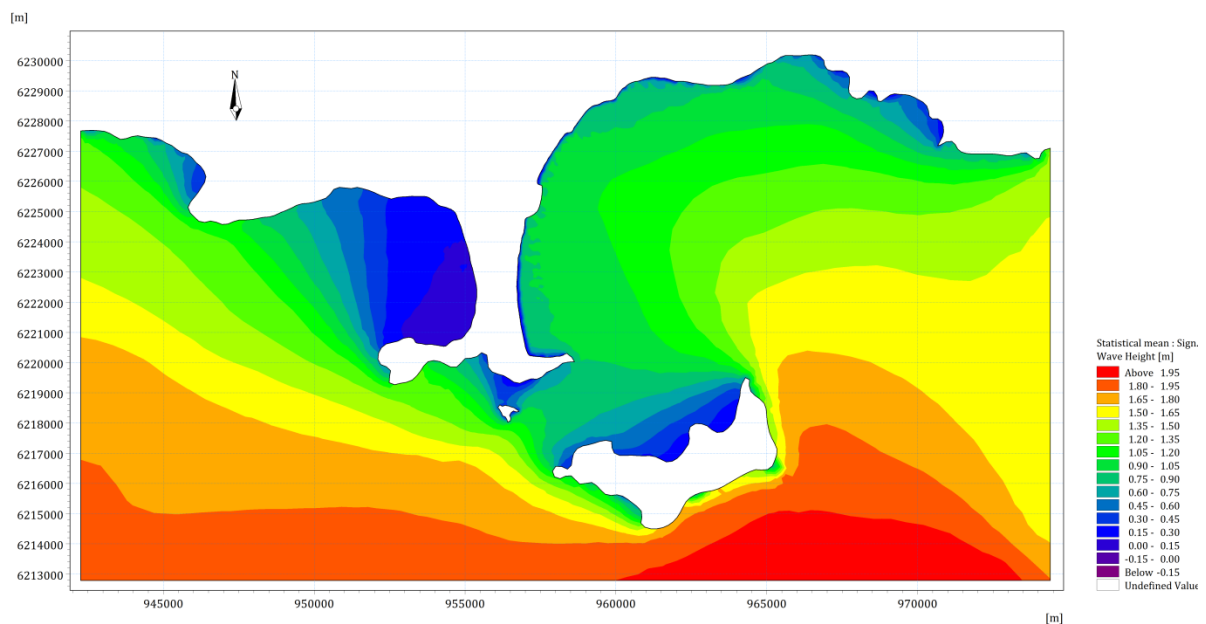


Figure 124. Significant wave height of the regional model under the impact of northeast wind.

5.5.1.2. East wind

Under the impact of the east wind, the strong currents occur around Porquerolles island and along the coast from Salins beach to Roubaud river mouth (Figure 125). The current speed in the order of 0.24 m/s is estimated at the depth of 1.5 m near Gapeau river mouth. In other words, the currents inside Giens gulf are generally much smaller than those in Hyères bay. Currents reach an average of 0.02 m/s at a level of -3 m near Almanarre beach with maximum values reaching 0.08 m/s.

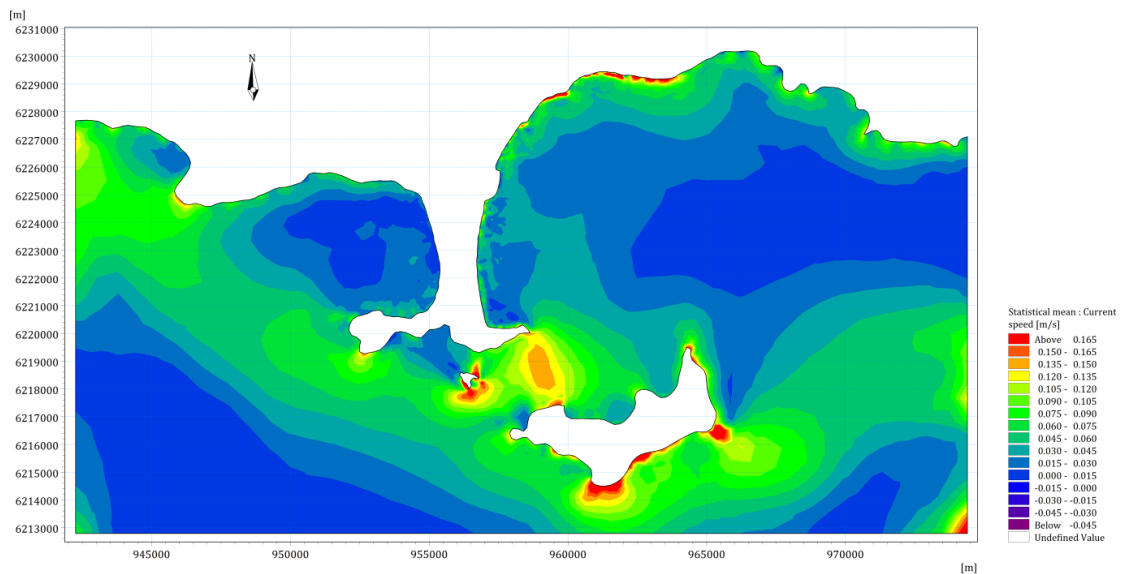


Figure 125. Current speed of the regional model under the impact of east wind.

Regarding the wave field, it is noticeable that the wave height is reduced when they enter the shallower depths of the bay (Figure 126). The wave data extracted at the depth of 1.5 m along the eastern Giens tombolo reveals that the highest nearshore waves approach the coast from Hyères port to Aygaude beach and reach the maximum values of 0.79 m near Aygaude beach. By contrast, the entire Giens gulf is sheltered from the east winds, so there are only small waves inside this domain.

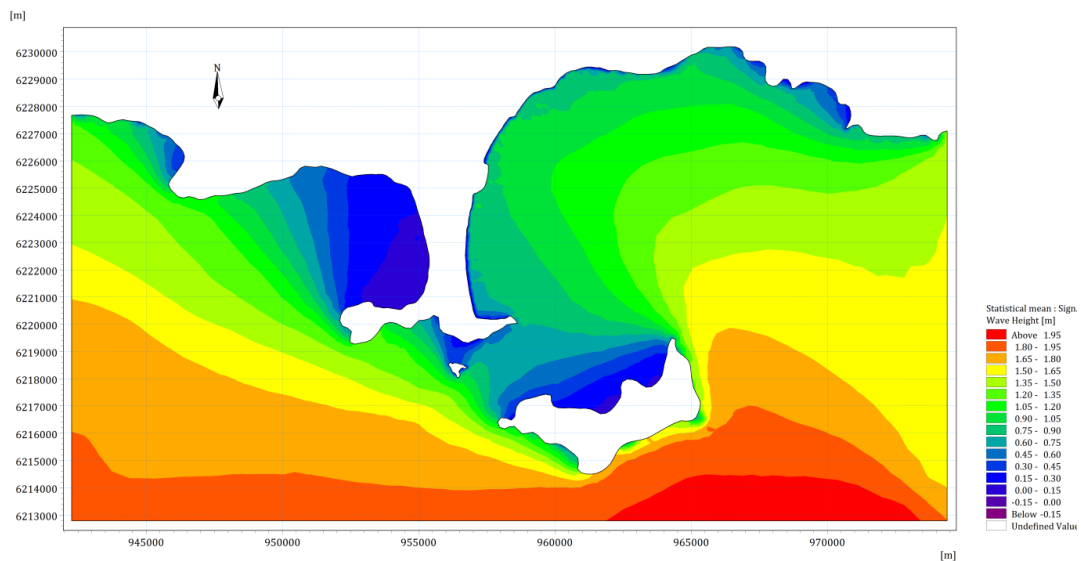


Figure 126. Significant wave height of the regional model under the impact of east wind.

5.5.1.3. Southeast wind

Figure 127 illustrates the current speed pattern due to the impact of the southeast winds in the regional scale. It is obviously seen that the high currents appear around islands as well as along the coast from Salins beach to Aygaude beach. Once again, the maximum nearshore current speed of 0.24 m/s is observed at the depth of 1.5 m near Gapeau river mouth. Like the east and northeast winds conditions, the western Giens tombolo is sheltered from the waves driven by the southeast winds.

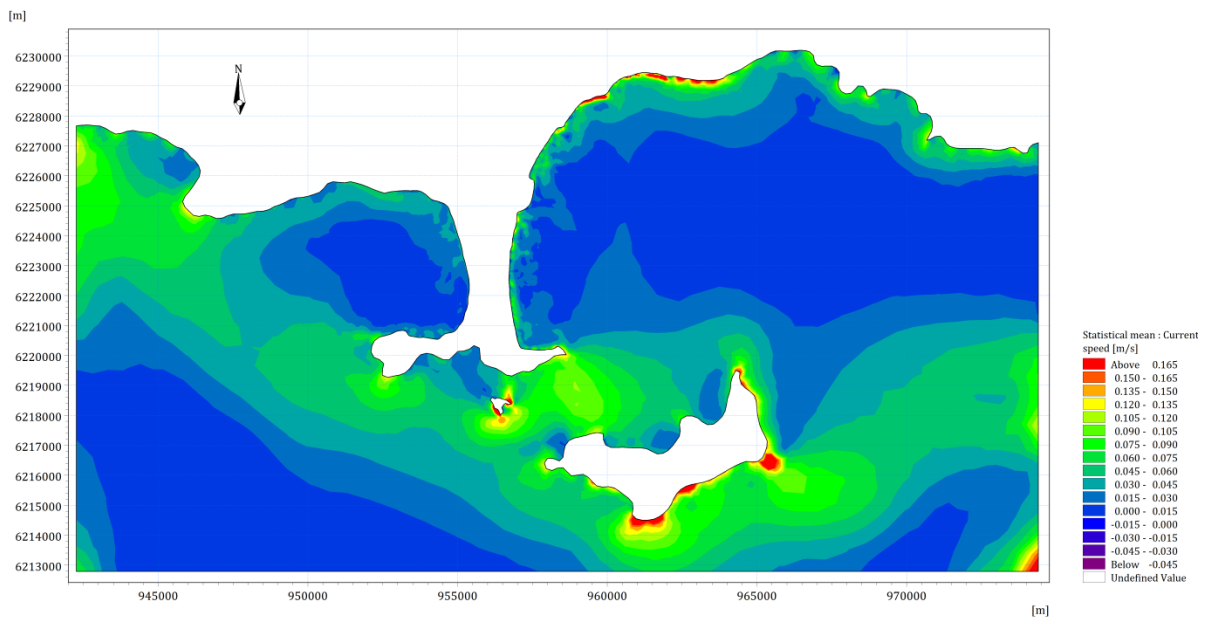


Figure 127. Current speed of the regional model under the impact of southeast wind.

The high waves only focus approaching the coast from Central Ceinturon beach to Aygaude beach, as shown in Figure 128. The nearshore wave height reaches the maximum values of 0.79 m at the depth of 1.5 m near Aygaude beach and varies at an average value of 0.65 m. Inversely, Giens gulf continuously maintain the calm condition under the impact of southeast winds.

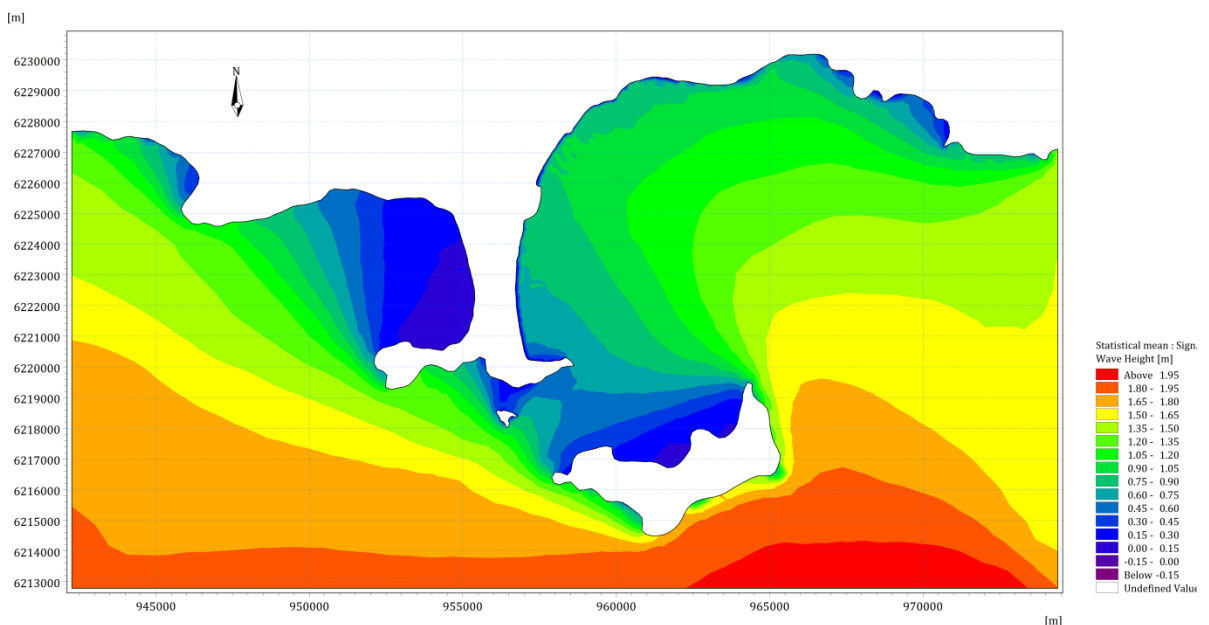


Figure 128. Significant wave height of the regional model under the impact of southeast wind.

5.5.2. Seasonal variations

5.5.2.1. Winter period

During the winter period simulation from 31st January to 1st March, 2007, the strong currents are commonly observed in Giens gulf and Gapeau river mouth (Figure 129).

Along the eastern Giens tombolo coast, the maximum current speed of 0.38 m/s is found at the water depth of 1.5 m near Gapeau mouth river, while the minimum current speed occurs in La Badine beach with the average value of 0.03 m/s. In the western part of Giens tombolo, the highest currents concentrate in the north and center of Almanarre beach. At Almanarre station at the water depth of 3.5 m, the maximum and average current speed is reported about 0.19 m/s and 0.05 m/s, respectively. With regard to current direction, the longshore current is mainly from north to south in Hyères bay due to the effect of northeastward wind. In the gulf of Giens, the dominant longshore directions on average are west to south and south to east, and then they create strong rip currents seaward through three troughs. All above-mentioned currents were found to be congruent to predictions of Blanc (1975), Jeudy De Grissac (1975), Courtaud (2000) and Capanni (2011).

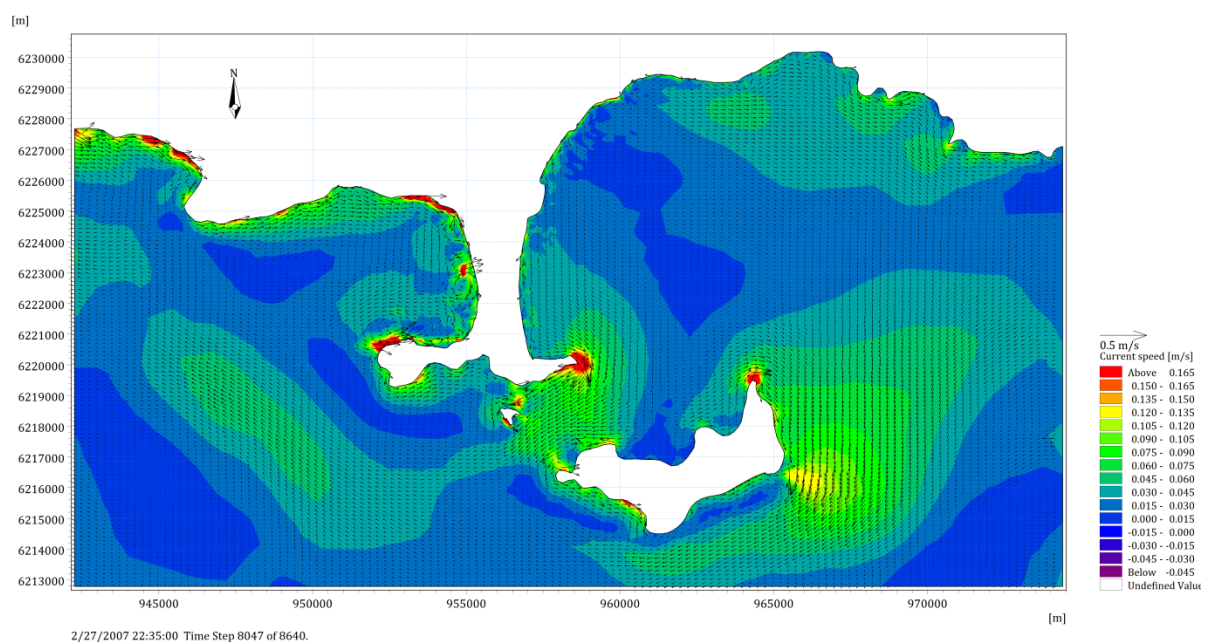


Figure 129. Current speed of the regional model in February 2007.

The wave pattern is mostly governed by the northwest and northeast wind regimes, but the northwest is dominant with highest frequency of 36.75% in the winter period (Table 16). As a result, the western Giens tombolo is affected by higher waves than the eastern part (Figure 130). In this period, the waves are mainly northwestern and the offshore wave height can reach up to 5.2 m. In the nearshore zone, the wave height decreases sharply due to the effect of bottom topography. At the water depth of 3.5 m near Almanarre beach, the wave height reaches the average value of 0.56 m and the maximum value of 1.6 m with an average peak period of 5 seconds. Along the eastern Giens tombolo, the high nearshore waves are observed near Aygaude beach whilst the small nearshore waves appear in Badine beach sheltered by Cape of Esterel. The maximum and average wave heights at a level of -1.1 m near Aygaude beach are in the order of 1.1 m and 0.31 m, respectively.

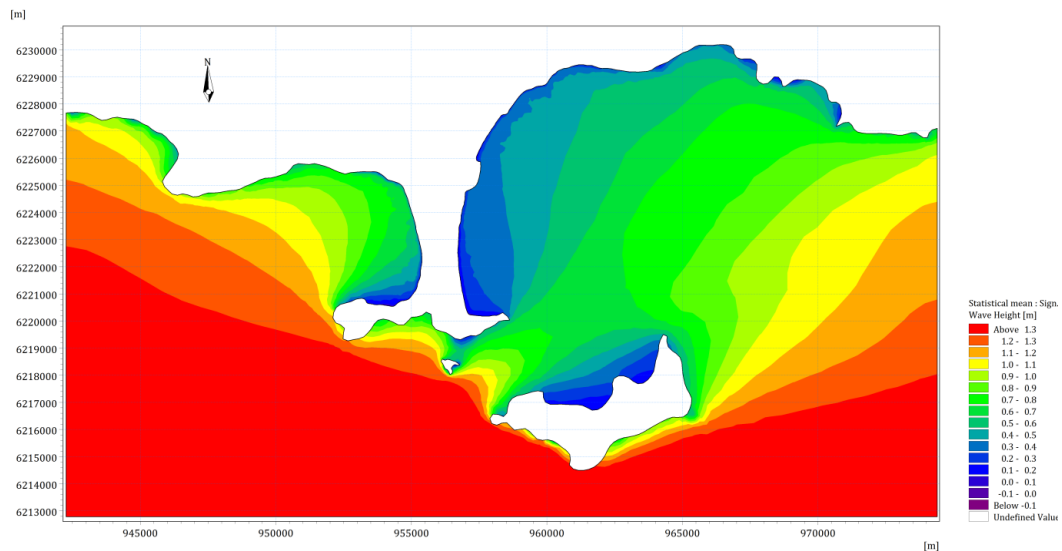


Figure 130. Significant wave height of the regional model in February 2007.

5.5.2.2. Summer period

In the summer period, the southwest and southeast winds are two prevailing directions affecting the wave and current fields in the study area. The current variation across the domain is as shown in Figure 131. In Hyères bay, the dominant longshore current follows the south-north direction due to the impact of southeast winds. It reaches the highest speed of 0.26 m/s and the average speed of 0.04 m/s at the water depth of 1.5 m near Gapeau mouth river. The low currents with the average speed of 0.024 m/s is observed at the water depth of 1.5 m in the south of Ceinturon beach. Meanwhile, the longshore current maintains two predominant directions like the winter period, but with lower speeds. At a level of -3 m near Almanarre beach, the maximum and average current speed is recorded in the order of 0.17 m/s and 0.04 m/s, respectively.

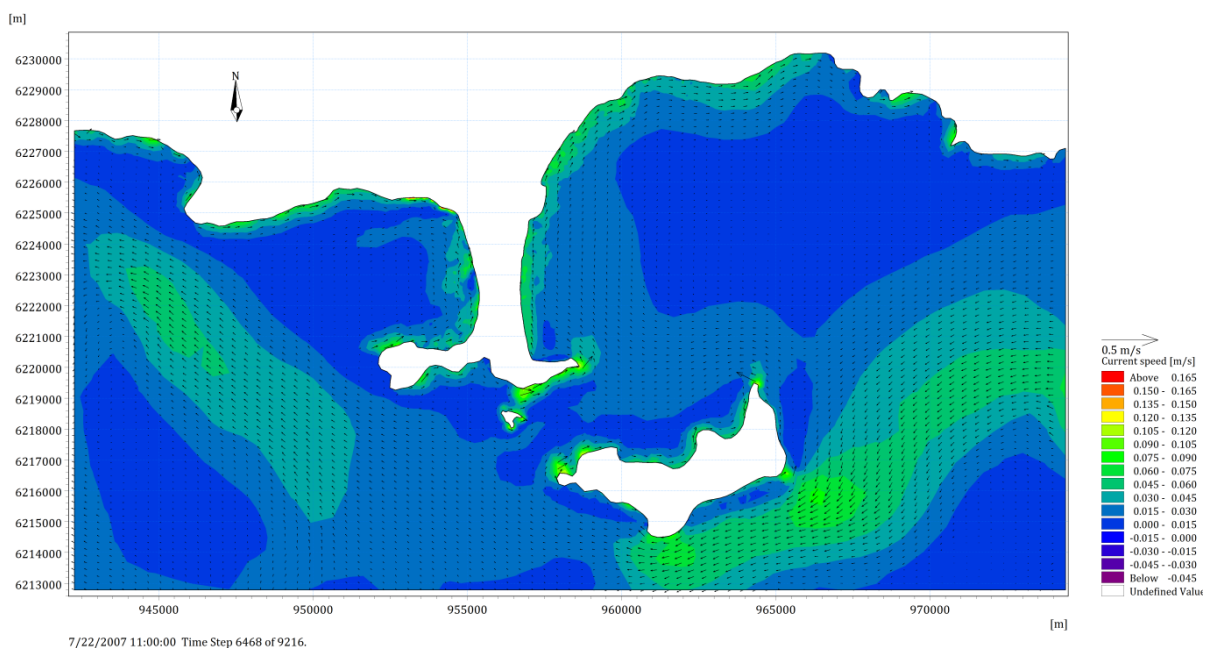


Figure 131. Current speed of the regional model in July 2007.

Figure 132 sketches the wave height contours developing across the study domain. It can be clearly seen that the wave regime is mostly affected by the southwest winds with a frequency of 20.89 % in the summer time. The highest offshore wave height is reported in the order of 4.15 m. Obviously, most of Giens gulf is exposed to the high southwest waves, whereas the Hyères bay is sheltered from them. The nearshore wave heights reaches to the maximum value of 1.55 m and the average value of 0.47 m at the water depth of 3.5 m in the centre of Almanarre beach. By contrast, the nearshore highest waves of 0.71 m is found at the water depth of 1.5 m near Gapeau mouth river.

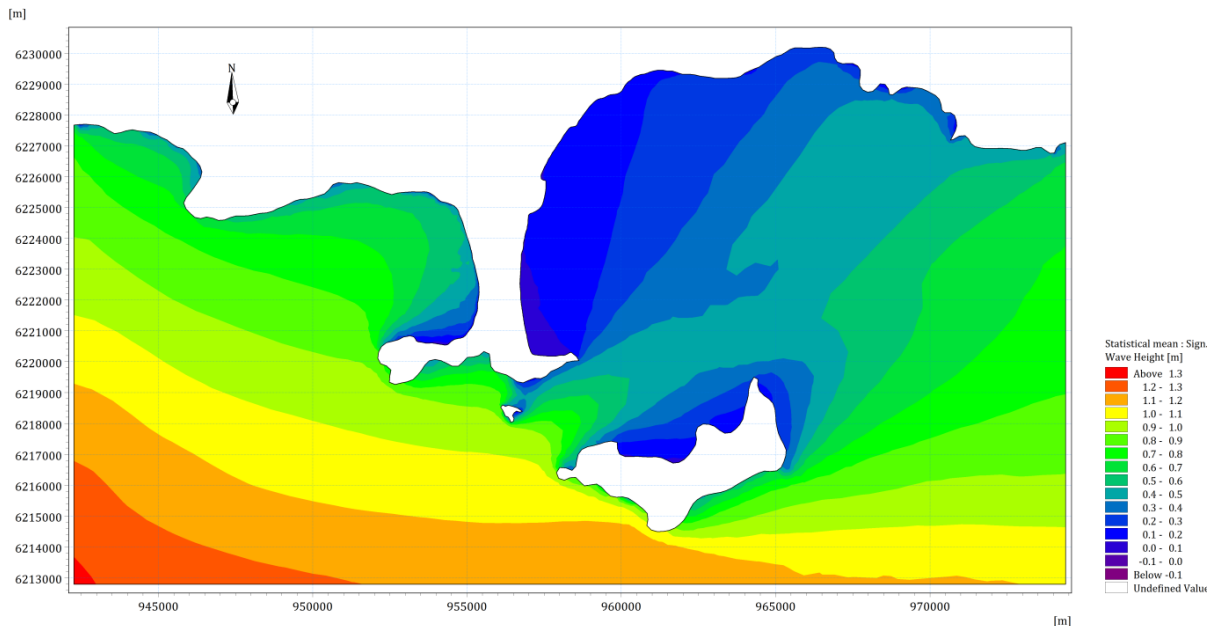


Figure 132. Significant wave height of the regional model in July 2007.

5.5.3. Extreme events

The hydrodynamic and wave simulation results of the regional domain which were taken into account the impact of four different storm scales comprising decadal, tri-decadal, semi-centennial and centennial storms are presented and discussed below. Because the shoreline of the eastern Giens tombolo extending over 10 km consisting of many beaches, each beach is directly exposed to one wave direction. Therefore, in each storm scale, two different wind directions induced two different wave directions, but with the same values of wind speed and wave height were modeled severally in order to elucidate the influence of each direction on each specific area.

5.5.3.1. Decadal storm

Figure 133 presents the current variation across the regional domain under the impact of the decadal storm. It can be clearly seen that the southeastern wind induces the stronger nearshore currents than the eastern wind, but generates the lower offshore current. The highest offshore current speed of 3.43 m/s is report at the western boundary of the domain affected by the eastern wind (Figure 133(a)). The strong nearshore currents normally occur along the coast from Salins beach to the mouth of

Roubaud river as well as around the islands. The nearshore currents reach the maximum value of 0.45 m/s at the water depth of 1.95 m near the mouth of Gapeau river in both of two wind scenarios. Nevertheless, the low nearshore currents are found at two different zones between two wind scenarios. In the eastern wind regime, the low nearshore currents occur near Bona beach with the average value of 0.08 m/s, whereas they are observed near Aéroport beach with the average value of 0.04 m/s under the southeastern wind condition (Figure 133(b)). In the gulf of Giens, the maximum nearshore current speed of 0.17 m/s is recorded at Almanarre station which is located at the water depth of 3.95 m in all two wind regimes.

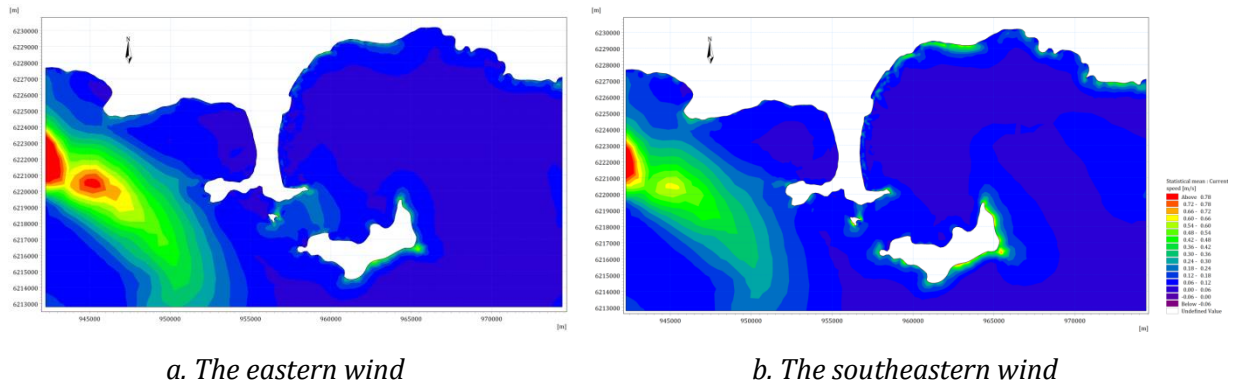


Figure 133. Current speed of the regional model under the decadal storm.

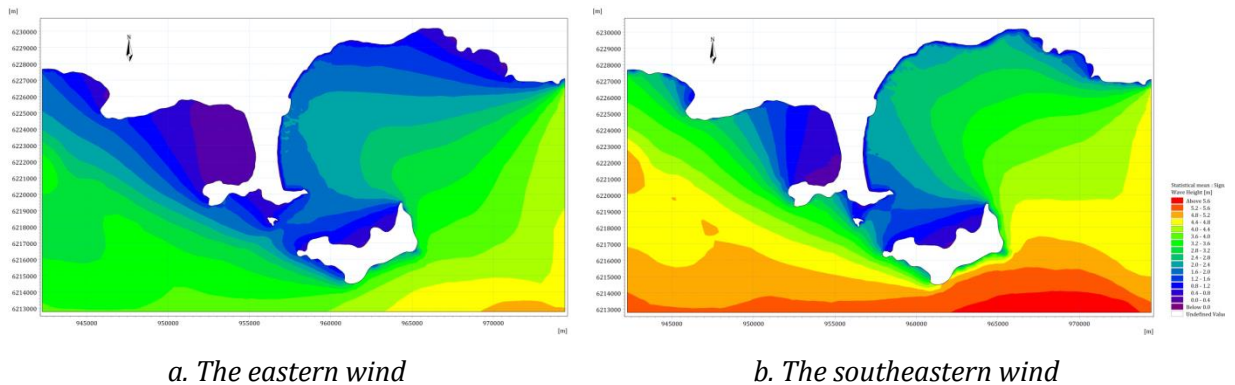


Figure 134. Significant wave height of the regional model under the decadal storm.

The wind-generated wave height contours developing across the regional domain are shown in Figure 134. It verifies that the southeastern wind regime induced the higher waves than the eastern wind. The offshore waves reach the maximum wave height of 7.9 m at the south boundary in the southeastern wind scenario (Figure 134(a)), while the maximum offshore wave height of 5.4 m is observed in the eastern regime (Figure 134(b)). The wave height reduces rapidly when they approach the shallow waters. In the eastern winds, the entire Giens gulf is sheltered, whereas only south part of Giens gulf maintains the calm condition under the impact of the southeastern winds. This means that the nearshore waves in Giens gulf in the eastern winds are lower than those in the southeastern regime. At the water depth of 3.95 m near Central Almanarre beach, the maximum wave height is in the order of 0.29 m under the eastern wind, while waves

reach the highest values of 0.77 m in the southeastern wind condition. In the Hyères bay, the area between Pesquiers beach and Hyères port can be influenced the most severely by the eastern waves, whereas the southeastern waves concentrate on attacking the shoreline between Ceinturon beach and Aygaude beach.

5.5.3.2. Tri-decadal storm

The stormy wind direction plays a significant role in the current fields, especially near shoreline. The current variation across the regional domain under the impact of the tri-decadal storm is depicted in Figure 135. It can be easily seen that the low nearshore currents occur in Giens gulf in both two-wind regimes. The maximum current speeds obtained at the water depth of 4.0 m near Almanarre beach under the impact of the east and southeast winds are in the order of 0.18 m/s and 0.2 m/s, respectively. Conversely, the strong nearshore currents generally take place from Salins beach to Hyères port as well as around the islands regardless the wind directions. However, the current speed in the east wind is little higher than that in the southeast wind. In the east wind condition, the strongest currents with the maximum speed of 0.51 m/s are found at the water depth of 2.0 m near Gapeau river mouth, whilst the nearshore currents reach the maximum value of 0.49 m/s under the impact of the southeast wind at the same location.

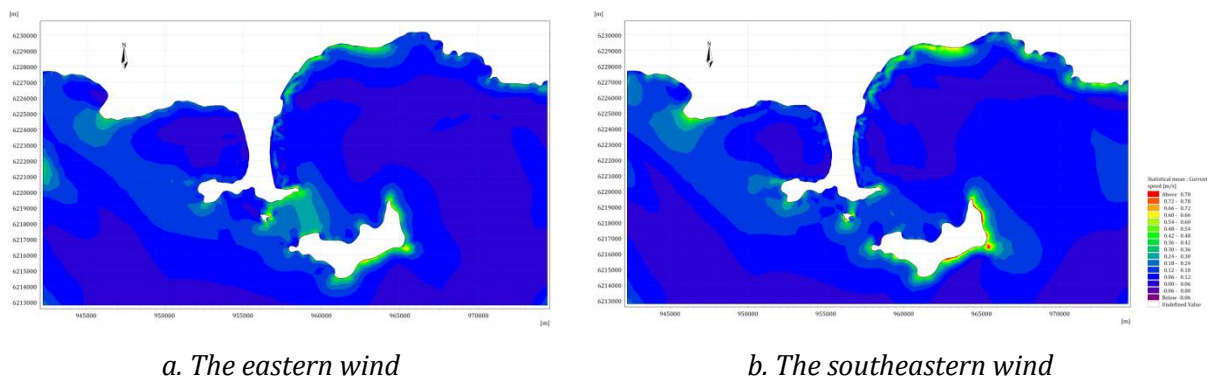


Figure 135. Current speed of the regional model under the tri-decadal storm.

The wave height pattern in the tri-decadal storm scenario is plotted in Figure 136. It is noticeable that the east winds do not cause the agitation in Giens gulf. Most of gulf is only affected by small waves with the average height of 0.4 m (Figure 136(a)). By contrast, the southeastern winds induces moderate waves approaching Almanarre beach in Giens gulf. The maximum wave height of 0.78 m is recorded at the water depth of 4.0 m near central Almanarre. In the Hyères bay, the eastern strong waves mostly attack the coast from Pesquiers to Hyères port and reach the maximum wave height of 1.5 m at the water depth of 2.0 m in front of Pesquiers beach. Only the area around Gapeau river mouth is influenced by the moderate waves with the average height of 0.8 m. When the southeastern waves enter the Hyères bay, they concentrate on reaching the coast between Hyères port and Gapeau river mouth (Figure 136(b)). The maximum

wave height of 1.5 m is also reported at the water depth of 2.0 m near the breakwater of Hyères port, while the smaller waves occur near Badine beach.

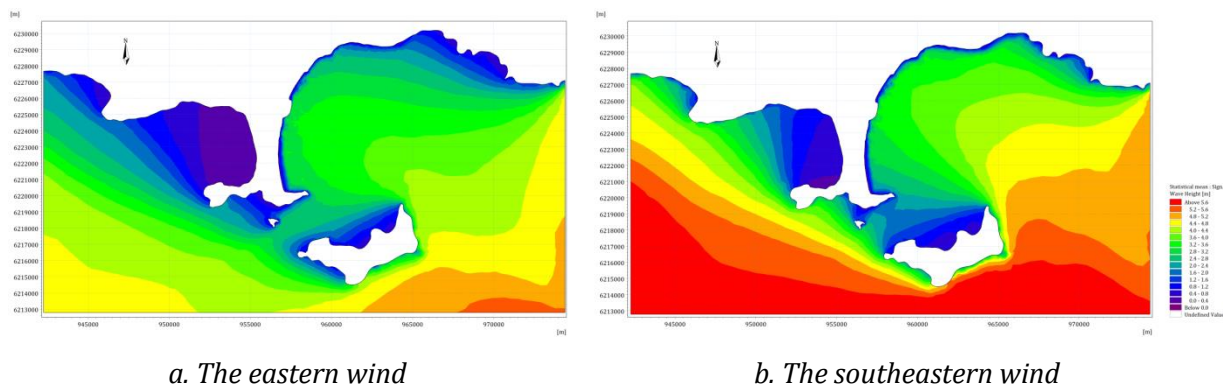


Figure 136. Significant wave height of the regional model under the tri-decadal storm.

5.5.3.3. Semi-Centennial storm

When the level of storm is intensified, the current speed is also increased significantly. Figure 137 shows the current speed pattern due to the impact of the semi-centennial storm. It is noted that the highest currents appear along Salins beach and the east coast of Porquerolles island in both of two wind conditions. Moreover, the currents inside the gulf of Giens are commonly much smaller than those in the Hyères bay. The nearshore currents reach the maximum value of 0.21 m/s and 0.26 m/s at the water depth of 4.15 m near Central Almanarre beach in the eastern wind and southeastern wind regimes, respectively. Along the eastern Giens tombolo coast, from the mouth Gapeau river to Badine beach, the nearshore currents in the eastern winds are moderately stronger than those in the southeastern winds. The maximum nearshore currents of 0.63 m/s is observed right in the mouth of Gapeau river in the eastern regime, whereas these currents reaches the highest speed of 0.56 m/s at the same location in the southeastern regime. The main reason is that the strong currents tend to move close to the shoreline under the impact of the eastern winds, while they are quite far from the shoreline in the southeastern winds.

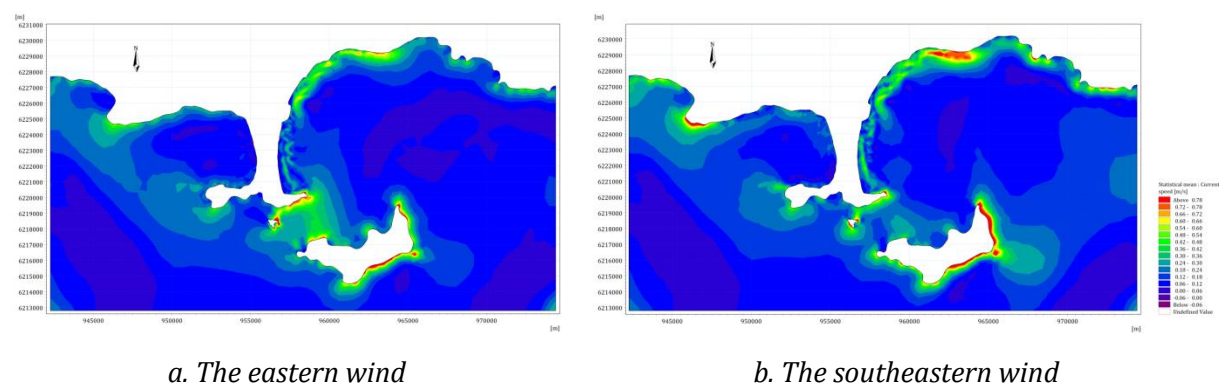


Figure 137. Current speed of the regional model under the semi-centennial storm.

For the semi-centennial storm scenario, the wave height pattern in the conditions of the eastern winds and southeastern winds are quite distinctive (Figure 138). In the

eastern wind regime, most of Giens gulf is still sheltered, but the eastern Giens tombolo coast in Hyères bay, from Hyères port to Badine beach, is exposed to the strong waves (Figure 138(a)). As a result, there are only the small waves with the average height of under 0.4 m near Almanarre beach, whereas the high nearshore waves vary around the average height of 1.41 m at the water depth of 2.15 m in Pesquiers beach. During the impact period of the southeastern winds, some moderate waves can approach the Almanarre beach in Giens gulf (Figure 138(b)). The maximum wave height of 0.96 m is recorded at the water depth of 4.15 m close to central Almanarre beach. Furthermore, the high waves mainly concentrate on reaching the coast from Pesquiers beach to Salins beach in Hyères bay. The highest waves with the maximum height of 1.7 m is still observed near Pesquiers beach.

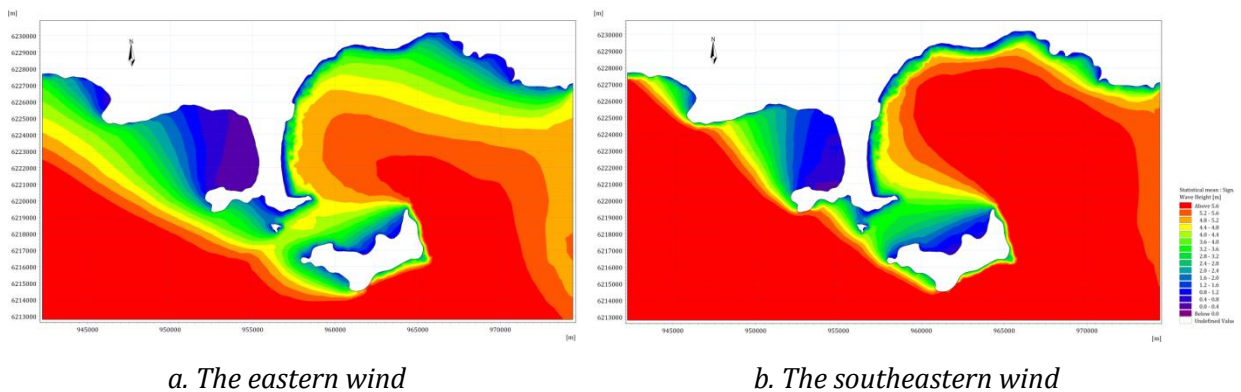
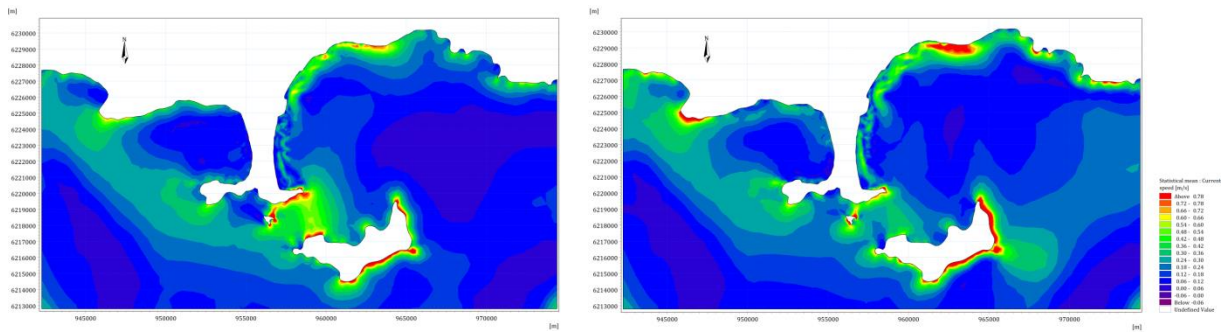


Figure 138. Significant wave height of the regional model under the semi-centennial storm.

5.5.3.4. Centennial storm

During the centennial storm along with the eastern wind regime, the strongest currents are found in the strait between Giens tombolo and Porquerolles island and around this island (Figure 139(a)). The analysis of the results indicates that the eastern winds blowing over Hyères bay cause the wind driven currents which flow along the eastern Giens tombolo from north to south and through the strait. The maximum current speed reaches up to 0.72 m/s at the water depth of 2.5 m right the mouth of Gapeau river. Meanwhile, the southeastern winds induce the strongest currents around Salins beach and Porquerolles island (Figure 139(b)). The maximum current speed of 0.66 m/s is observed at a level of -1.1 m near Gapeau river mouth. In both two wind regimes, the low currents usually occur at Badine beach with the average current speed of 0.08 m/s due to the blockage of currents by the cape of Esterel.

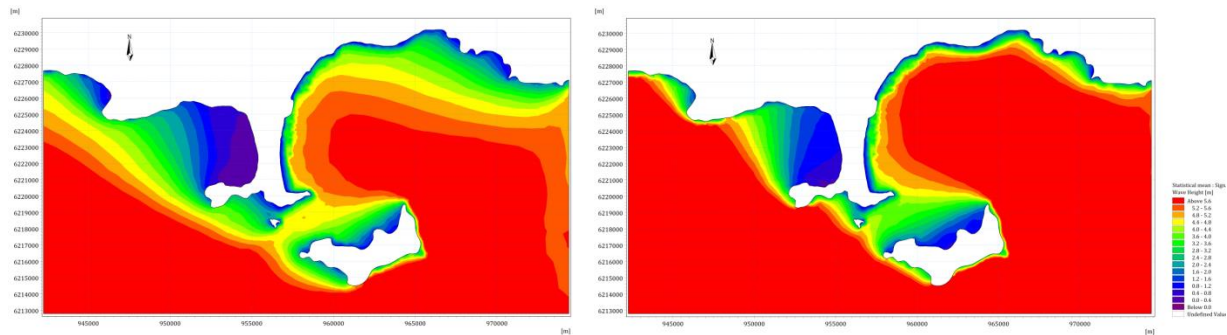


a. The eastern wind

b. The southeastern wind

Figure 139. Current speed of the regional model under the centennial storm.

The wave height contours developing across the regional domain under the impact of the centennial storm are illustrated in Figure 140. However, the different wind directions triggers the dissimilar agitation modes in Giens gulf and Hyères bay. Most of Giens gulf is continuously sheltered from the eastern winds. Therefore, only small waves with the average height of 0.4 m approach the western Giens tombolo coast (Figure 140(a)). Inversely, the southeastern winds cause the significant changes of wave mode in Giens gulf. The maximum wave height of 1.13 m is found at a level of -3 m in Almanarre beach. In Hyères bay, the high waves reach nearly the coast of the eastern Giens tombolo. The eastern waves mainly attack the coast from the mouth of Roubaud river to Badine beach, while southeastern waves mostly reach the area between Hyères port and Salins beach. The highest waves of over 1.82 m are recorded at the water depth of 2.5 m in front of Pesquiers beach under the impact of all wind conditions.



a. The eastern wind

b. The southeastern wind

Figure 140. Significant wave height of the regional model under the centennial storm.

5.6. Results of Local area-the eastern Giens tombolo and discussion

The results obtained from the official runs of the regional area were applied as boundary conditions for the local scale simulation. MIKE 21/3 Coupled FM was utilized for predicting the hydrodynamic conditions and the sediment transport patterns along the eastern Giens tombolo coast. The different wind directions, the changes of season and stormy conditions were considered, respectively. The computed results will be presented and analyzed below in order to determine which the main factors control the hydrodynamic and sediment transport conditions in the local area.

5.6.1. Effect of wind on hydrodynamics and sediment transport

Wind plays the key factor in coastal evolution in Hyères bay. It directly affects the sand transport in the emerged beach and indirectly generates waves. According to Jeudy De Grissac (1975), SOGREAH (1988a), Courtaud (2000), and Capanni (2011), the coastal evolution of the eastern Giens tombolo is affected by three main wind directions i.e. Northeast, East and Southeast. Hence, this work only focuses on simulating their effects on the change of hydrodynamics and sediment transport in the eastern Giens tombolo. The results of the simulations over the entire study area are illustrated in Figure 141, Figure 142, Figure 143, Figure 144, Figure 145, and Figure 146. The hydrodynamic and sediment transport parameters at the water depth of about 1.5 m near Gapeau, Aygaude, Ceinturon, Bona, Pesquiers, and La Capte beaches- subjected to severe erosion (E.O.L, 2010)- are also extracted and compared in Table 47.

Figure 141 describes the distribution of current speed field (V_c) triggered by different wind directions, viz. northeast, east and southeast winds, when taking into account the presence of *Posidonia*. It is clearly seen that the northeastern winds have the strongest impact on the current speed along the eastern tombolo, except the area around Bona beach. The highest nearshore currents are usually observed in both the Gapeau river mouth and Aygaude beach with the largest mean speed of over 0.257 m/s under the impact of northeastern winds (Table 47), while they only occur around the mouth of Gapeau river under the influence of other directions. In addition, the mean current speed of 0.128 m/s at the water depth of 1.5 m near Ceinturon beach generated by the northeastern winds is about 58% higher than that in the eastern and southeastern winds. At Bona beach, the eastern and southeastern winds cause the stronger longshore currents than the northeastern winds. The main reason comes from the presence of breakwaters of Hyères port. The longshore currents induced by the northeastern winds move along the coast from Gapeau river to Hyères port, then they have to change the direction and flow seaward after meeting with the breakwaters of Hyères port (Courtaud, 2000). As a result, these currents are decreased much more when reaching Bona beach right in the lee side of the structures. On the other hand, the currents generated by the eastern and southeastern easily approach this beach without any obstacles.

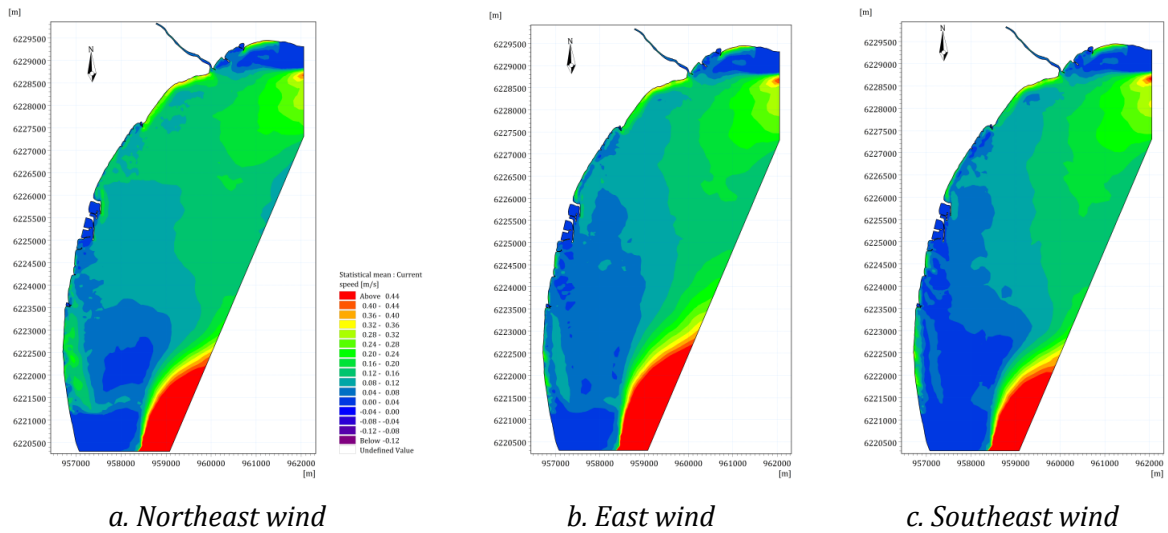


Figure 141. Current speed in the study area under the impact of variation of wind direction with Posidonia.

Because of low tidal range in Hyères bay, the wind-driven waves have the large influence on the coastal morphology along the eastern Giens tombolo (SOGREAH, 1988b). The change of wind direction can result in the strong modification of wave field. It is clearly seen that the northeastern winds trigger the high waves in the study area (Figure 142). The highest waves are found at Aygaude beach, Bona beach and La Capte beach corresponding to the mean wave heights (H_s) of 0.684 m, 0.681 m, and 0.683 m, respectively (Table 47). The wave height decreases gradually when they approach the shallow waters. In addition to generating the highest current speed and wave height, the northeast winds induce a raise of the components of radiation stresses. Cross-shore currents are a result of these changes in water level due to the normal radiation stresses (S_{xx} & S_{yy}) while longshore currents are a result of the forces due to the shear radiation stresses (S_{xy}) in the water column. The increase of radiation stresses means that the speed of the longshore and cross-shore currents is augmented by these winds.

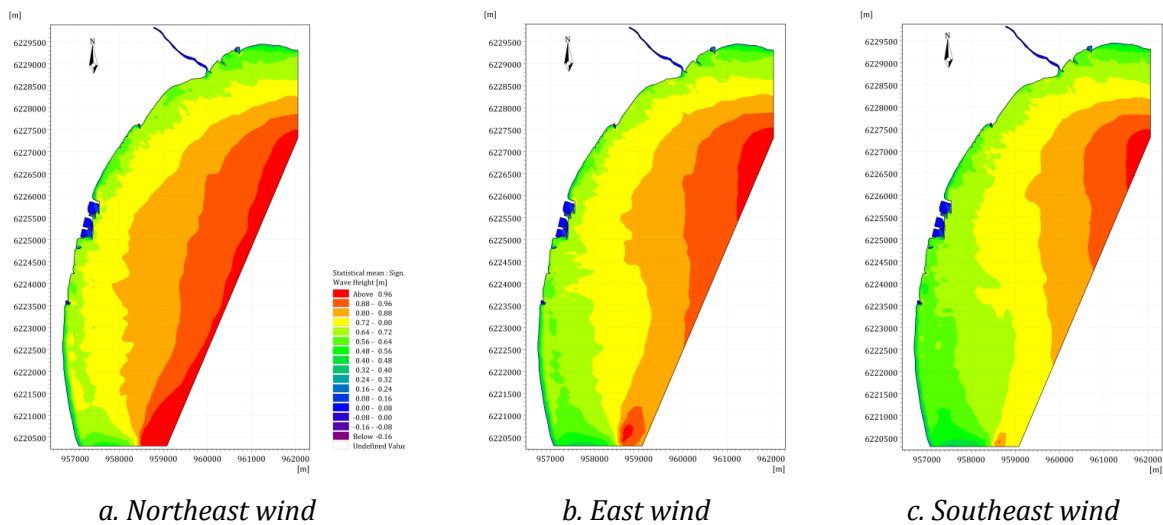


Figure 142. Significant wave height in the study area under the impact of variation of wind direction with Posidonia.

Because of current speed intensification, the total load of sediment transport (Q) (Figure 143) and the bed level change (Δz) (Figure 144) will be boosted by the northeast wind. These winds engender the high sediment rates not only along the coast from the Gapeau river mouth to Aygaude beach but also at La Capte beach and the upstream of Hyères port. A maximum total load of about $1.21 \times 10^{-4} \text{ m}^3/\text{s}/\text{m}$ occurs at the water depth of 1.5 m near Aygaude beach under the impact of northeast wind. Conversely, the southeastern and eastern wind directions cause the strong sediment transport at Bona beach with the largest rates of $7.64 \times 10^{-5} \text{ m}^3/\text{s}/\text{m}$ and $7.44 \times 10^{-5} \text{ m}^3/\text{s}/\text{m}$, respectively (Table 47).

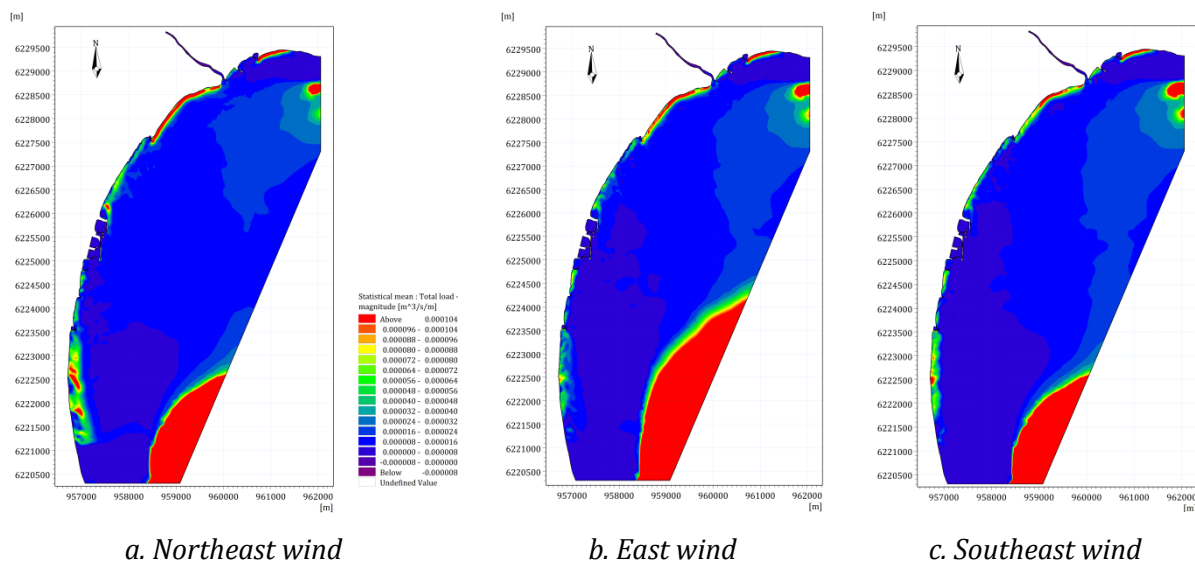
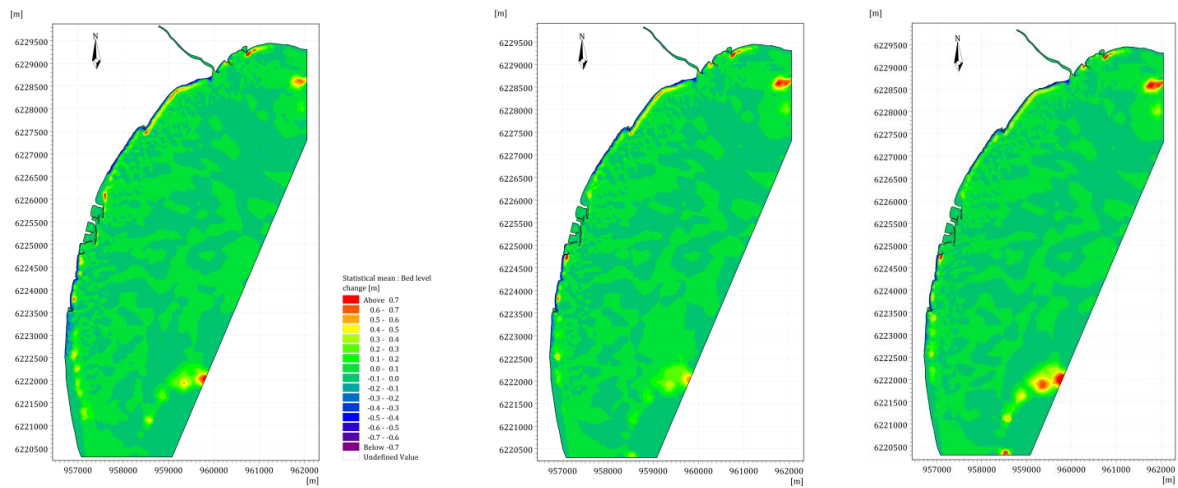


Figure 143. Sediment transport rates (total load) in the study area under the impact of variation of wind direction with Posidonia.

The sediment transport rate plays a decisive role in the bed level change. As a result, the strongest bed level changes are due to the northeast winds when taking into account the presence of Posidonia (Figure 144). These changes take place along the eastern Giens tombolo in which the areas such the south of Gapeau river mouth, Ceinturon beach, and Bona beach are suffered from severe erosion. The largest bed level change due erosion is found in the order of -0.23 m at Cabanes beach in the south of Gapeau river mouth under the impact of northeast wind. The bed level in offshore zones is quite stable with all wind directions. On the other hand, the accretion is observed in the upstream of Aygaude northern jetty, the upstream of the northern breakwater of Hyères port, the south of Bona groyne, the upstream of the northern jetty of La Capte port and the south of La Capte beach. The sediment accumulated in these areas is mainly due to the blockage of the longshore drift by the shore-normal structures. The largest accretion of $+0.18 \text{ m}$ is observed at the water depth of 1.5 m near the south of Pesquiers beach under the impact of the southeastern winds.



a. Northeast wind

b. East wind

c. Southeast wind

Figure 144. Bed level change in the study area under the impact of variation of wind direction with Posidonia.

In order to visualize the impact of the wind directions as well as Posidonia on the bed level, beach profile at the central Ceinturon beach and Bona beach are extracted and exhibited in Figure 145 and Figure 146, respectively. In all scenarios, the bed level changes commonly appear from the shoreline to 5 m of water depth. Moreover, the southeast winds cause the largest beach profile change. It may be due to the influence of highest waves generated by this wind. With the presence of Posidonia, the beach is simply eroded with the thickness of 0.4 m - 0.8 m near the coast and accumulated in a distance of 200 m seaward of shoreline.

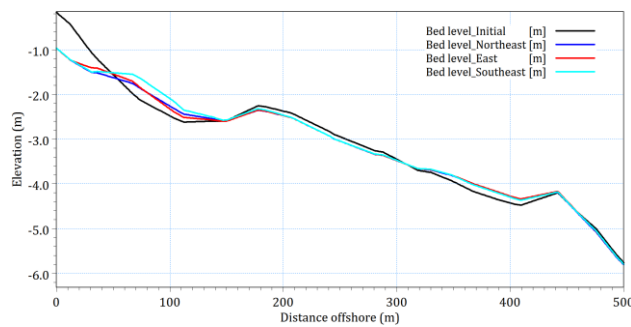


Figure 145. Beach profile evolution at Central Ceinturon beach under the impact of variation of wind direction with Posidonia.

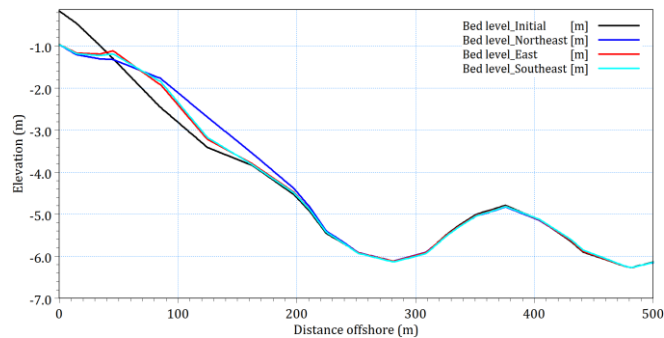


Figure 146. Beach profile evolution at Bona beach under the impact of variation of wind direction with Posidonia.

Table 47. Effect of wind direction and Posidonia on the hydrodynamics and sediment transport.

Beach	Wind direction	WL (m)	V _c (m/s)	H _s (m)	S _{xx} (m ³ /s ²)	S _{xy} (m ³ /s ²)	S _{yy} (m ³ /s ²)	Q (m ³ /s/m)	Δz (m)
Ceinturon	NorthEast (60°)	0.403	0.128	0.622	0.232	-0.064	0.158	5.05E-005	-0.134
	East (90°)	0.402	0.081	0.618	0.228	-0.064	0.155	3.12E-005	-0.03
	SouthEast (120°)	0.399	0.081	0.604	0.216	-0.061	0.147	3.88E-005	-0.043
Bona	NorthEast (60°)	0.402	0.105	0.681	0.336	-0.026	0.152	5.31E-005	-0.105
	East (90°)	0.399	0.165	0.648	0.305	-0.028	0.140	7.44E-005	-0.057
	SouthEast (120°)	0.396	0.172	0.630	0.288	-0.029	0.132	7.64E-005	-0.061
Pesquiers	NorthEast (60°)	0.403	0.124	0.614	0.272	-0.024	0.118	5.15E-005	-0.005
	East (90°)	0.400	0.064	0.582	0.248	-0.022	0.109	3.29E-005	0.111
	SouthEast (120°)	0.397	0.091	0.552	0.225	-0.022	0.099	4.02E-005	0.181
Gapeau	NorthEast (60°)	0.400	0.257	0.617	0.184	-0.081	0.213	3.62E-05	-0.228
	East (90°)	0.401	0.239	0.622	0.183	-0.082	0.209	2.78E-05	-0.228
	SouthEast (120°)	0.400	0.222	0.615	0.177	-0.081	0.205	2.29E-05	-0.226
Aygaude	NorthEast (60°)	0.399	0.259	0.684	0.274	-0.102	0.223	1.21E-04	-0.089
	East (90°)	0.398	0.224	0.700	0.283	-0.105	0.226	1.14E-04	-0.109
	SouthEast (120°)	0.397	0.178	0.694	0.276	-0.103	0.222	8.89E-05	-0.111
La Capte	NorthEast (60°)	0.402	0.087	0.683	0.335	0.001	0.149	4.73E-05	-0.172
	East (90°)	0.400	0.066	0.643	0.301	0.001	0.136	4.12E-05	0.005
	SouthEast (120°)	0.398	0.066	0.611	0.274	0.001	0.126	4.22E-05	0.107

5.6.2. Effect of seasonal changes on hydrodynamics and sediment transport

The climate in the study area is characterized by the seasonal variation. There are many extreme events, viz. storms, rough seas in the winter, whereas the calm sea state is almost maintained during the summer. Regarding the seasonal variation of wind, the southeast and east are the prevailing winds with a total frequency of over 20% in the summer, while the northeast winds are dominant with a frequency of about 10% in the winter (Table 16). The difference of wind climate between the winter and summer is illustrated by modeling the sea state in February and July 2007, respectively. The results are shown in Figure 147, Figure 148, Figure 149, Figure 150, Figure 151, Figure 152, and Table 48.

Table 48 reveals that the winter period influences on the coastal morphology in the coast of the eastern Giens tombolo more than the summer when taking into account the presence of *Posidonia*. The increase of the mean current speed along the coast during the winter is about 6%-46.27%, apart from La Capte area. The largest difference of mean current speed between the summer and winter is found at the water depth of 1.5 m near Aygaude beach while the smallest difference of 6% is reported at the same water depth in front of Pesquiers beach (Figure 147). At the La Capte beach, the nearshore currents in the winter and the summer are not different so much. The presence of jetties at La Capte port and two submerged geotube breakwaters interfere the longshore currents in both the winter and the summer and create a quite calm water area.

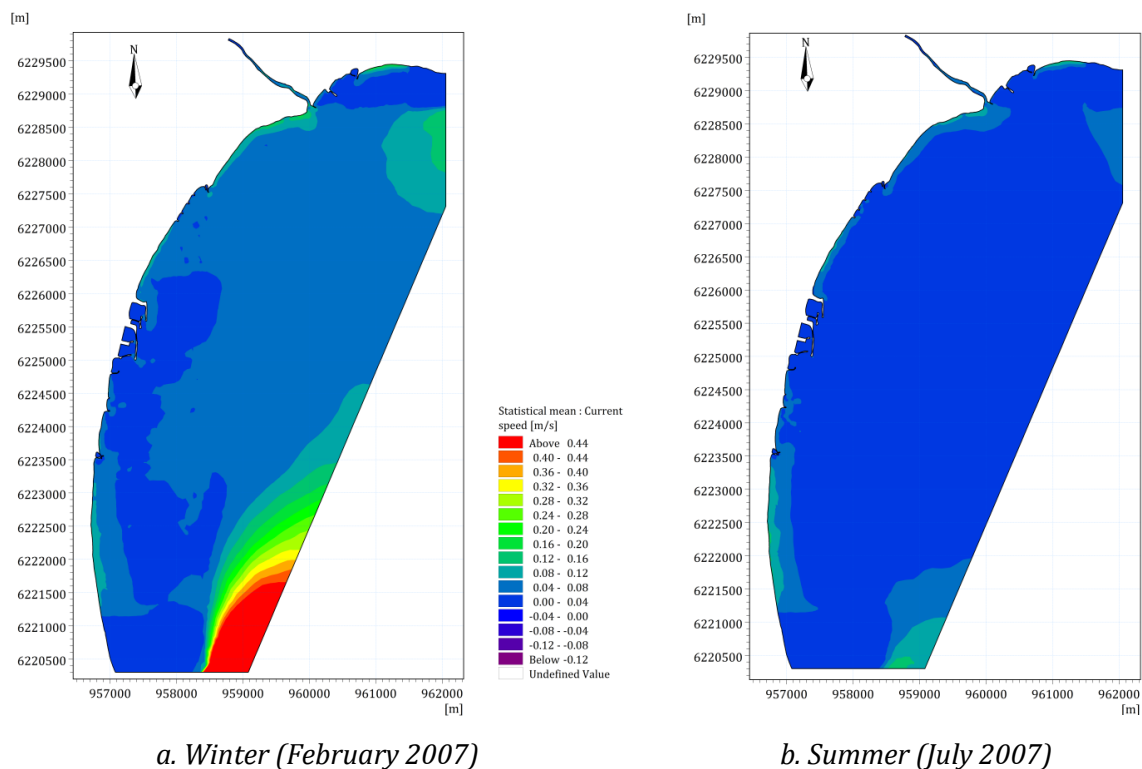


Figure 147. Current speed in the study area under the impact of seasonal variation with *Posidonia*.

Figure 148 shows the wave patterns in the summer and the winter. It is noticeable that the mean significant wave height in the winter is completely higher than that in the summer. The meteorological conditions in the winter induce an increase of the mean significant wave height by 68%-122%. The highest significant wave heights are observed at Gapeau and Aygaude beaches with the mean values of 0.378 m and 0.371 m, respectively; where the lowest mean wave height of about 0.262 m is found at the water depth of 1.5 m near Pesquiers beach (Figure 148). This difference of wave climate is due to the extreme events. The higher waves lead to larger radiation stresses in the winter. Particularly, the radiation stresses are augmented by 110%-410% comparing those in the summer. These radiation stresses involve in the wave set-up near shoreline as well as the formation of rip currents are the main factor causing the coastal erosion in this area. As a result, the sediment transport rates in the winter are about 180% and 800% higher than those in the summer. The largest sediment transport rates are observed from the mouth of Gapeau river to Aygaude beach (Figure 149). The main reason is that this area is right downstream and fed by the sediment from Gapeau river in the flood season (winter). At Aygaude beach, the sediment transport rate in the winter is boosted by 800% compared with the summer. On the other hand, only the low sediment transport rate is shown along La Capte beach in the summer (Figure 149(b)).

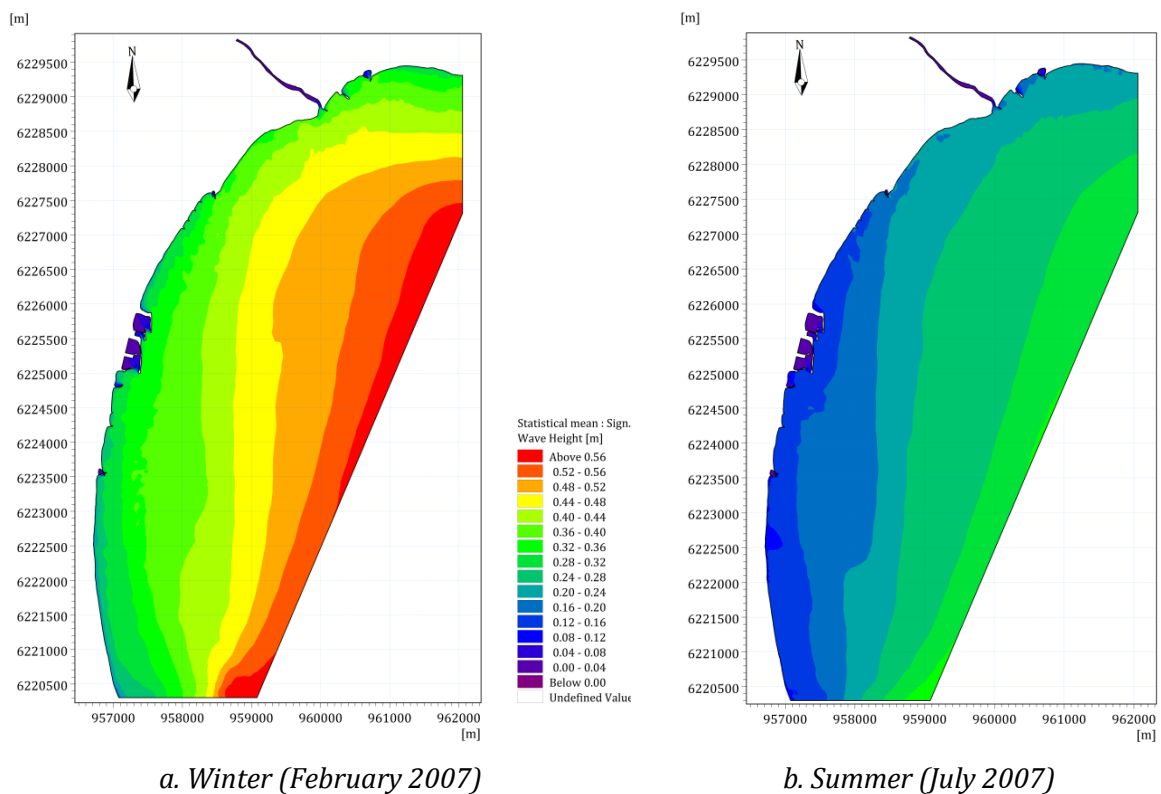


Figure 148. Significant wave height in the study area under the impact of seasonal variation with *Posidonia*.

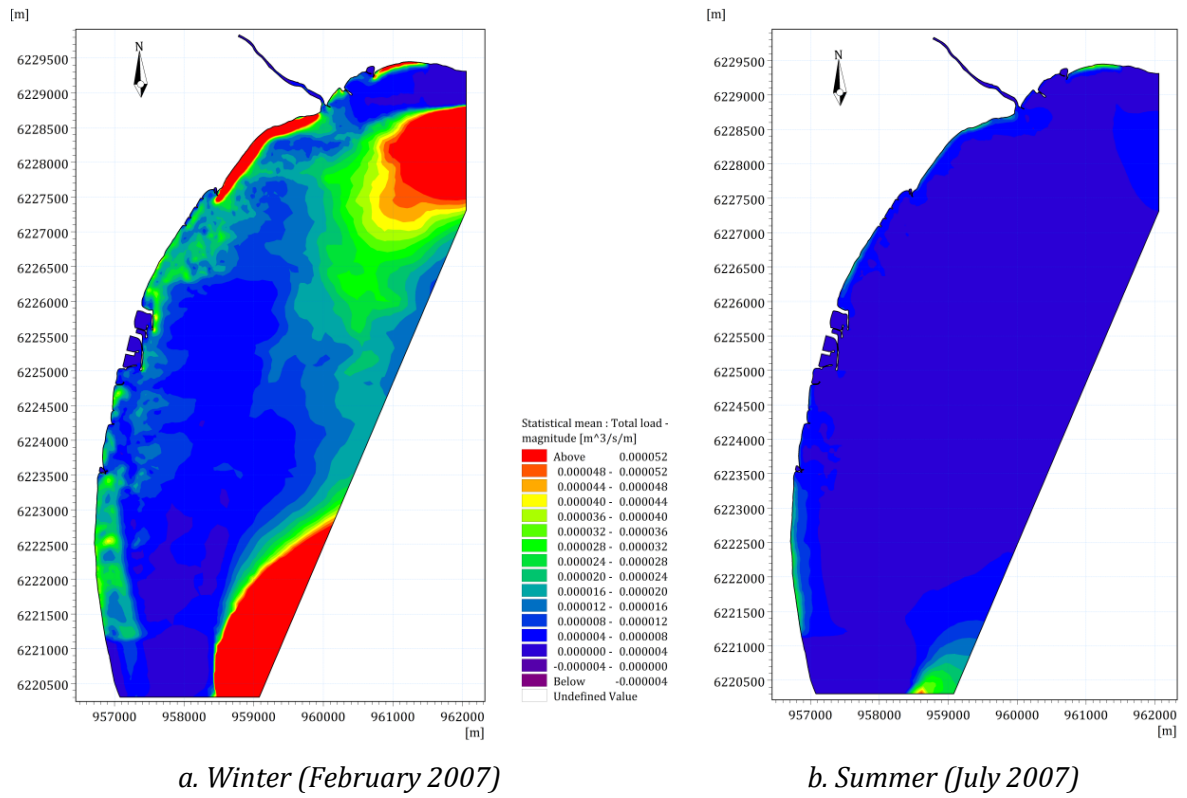


Figure 149. Sediment transport rates (total load) in the study area under the impact of seasonal variation with Posidonia.

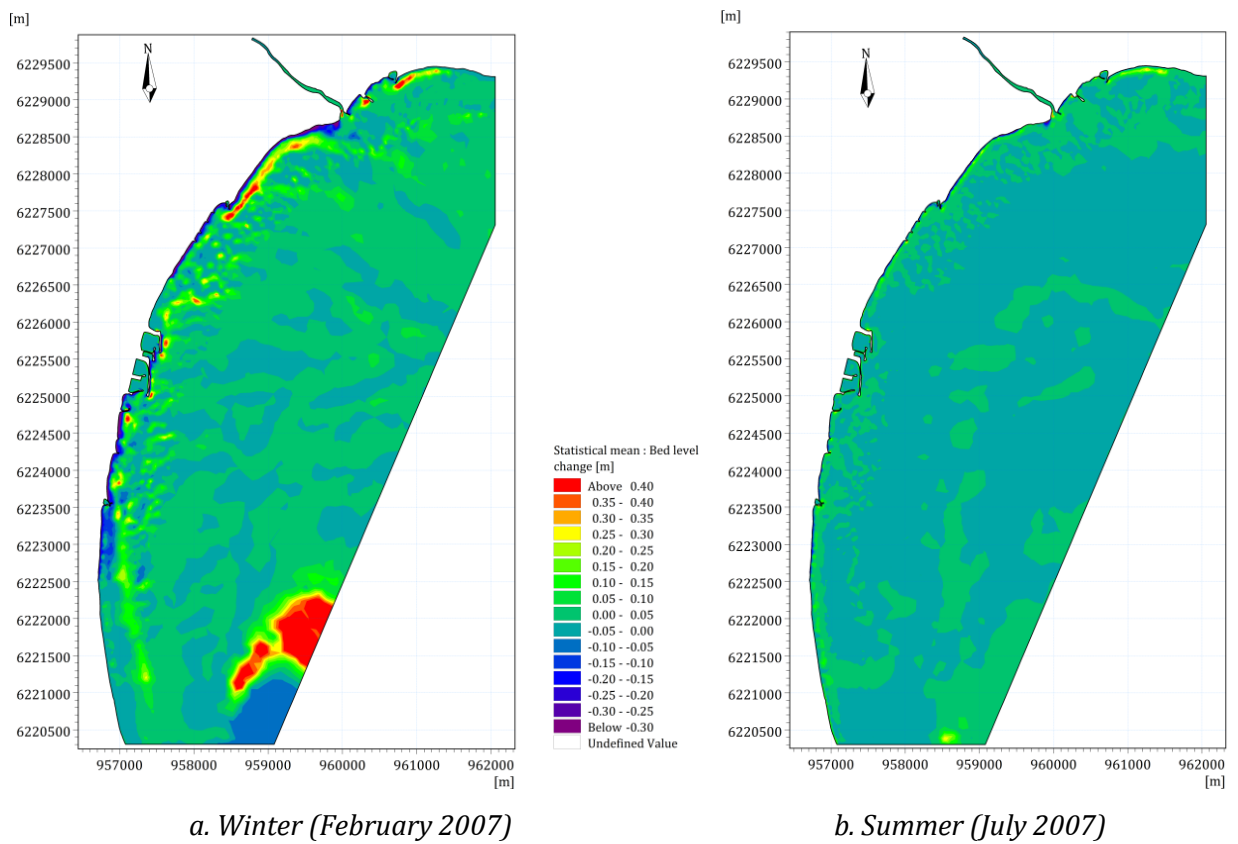


Figure 150. Bed level change in the study area under the impact of seasonal variation with Posidonia.

The complete difference of sediment transport rate between the summer and the winter also triggers the distinctive pattern of bed level change (Figure 150). It is clearly seen that sea bottom is quite stable in the summer; even almost bed level is risen. However, this positive trend totally changes when the winter comes. The erosion is observed along the eastern Giens tombolo in which Bona beach underwent the strongest erosion with the erosive bed change of -0.23 m at the water depth of 1.5 m (Table 48). Nevertheless, the accretion is still found in the upstream area of Roubaud jetty, Aéroport beach, and the upstream zone of La Capte jetty. These shore-normal structures interfere with the longshore currents along the eastern tombolo and promote the sediment to accumulate in the upstream realms.

Figure 151 and Figure 152 show the beach profile evolution of the central Ceinturon beach and Bona beach, respectively. It is clearly seen that beach profile is mostly changed from the shoreline to 300 m offshore. In all cases, the sediment is swashed near the shore and moved seaward. There is a light erosion occurring near the shore in the summer, whilst the moderate erosion with bed level change from -0.4 m to -1.0 m are observed in the winter. The Ceinturon and Bona beaches suffered the most severely erosion due to the impact of storms which commonly take place in the winter.

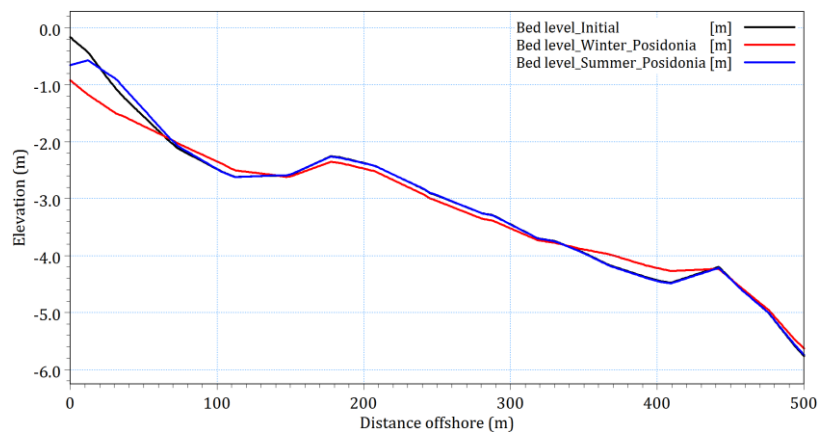


Figure 151. Beach profile evolution at Central Ceinturon beach under the impact of seasonal variation with Posidonia.

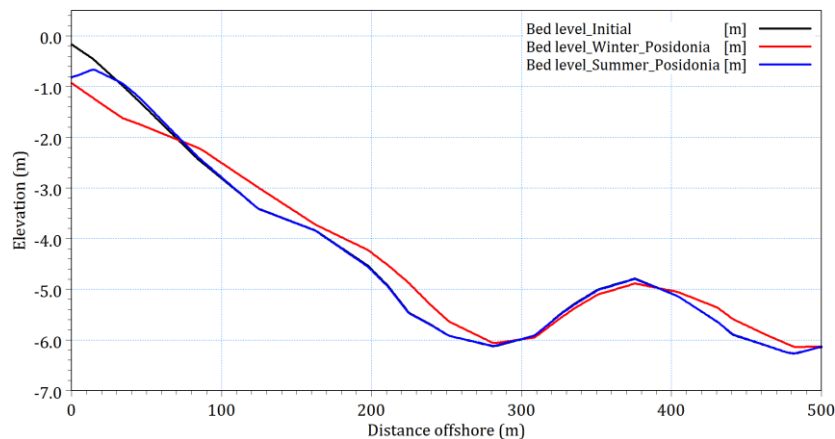


Figure 152. Beach profile evolution at Bona beach under the impact of seasonal variation with Posidonia.

Table 48. Effect of Posidonia and seasonal change on the hydrodynamics and sediment transport.

Beach	Wind direction	WL (m)	V _c (m/s)	H _s (m)	S _{xx} (m ³ /s ²)	S _{xy} (m ³ /s ²)	S _{yy} (m ³ /s ²)	Q (m ³ /s/m)	Δz (m)
Ceinturon	Winter (02-2007)	0.402	0.074	0.300	0.069	-0.021	0.049	2.38E-005	-0.116
	Summer (07-2007)	0.401	0.060	0.150	0.017	-0.006	0.014	8.46E-006	0.096
	Difference (%)	0.25	23.33	100.0	305.88	250.00	250.00	181.32	220.83
Bona	Winter (02-2007)	0.401	0.059	0.283	0.087	-0.010	0.040	3.09E-005	-0.226
	Summer (07-2007)	0.401	0.052	0.127	0.017	-0.003	0.009	7.96E-006	0.028
	Difference (%)	0.00	13.46	122.8	411.76	233.33	344.44	288.19	907.14
Pesquiers	Winter (02-2007)	0.401	0.053	0.262	0.072	-0.010	0.033	2.00E-005	-0.039
	Summer (07-2007)	0.401	0.050	0.123	0.015	-0.003	0.008	6.10E-006	0.047
	Difference (%)	0.00	6.00	113.0	380.00	233.33	312.50	227.87	182.98
Gapeau	Winter (02-2007)	0.401	0.128	0.378	0.070	-0.029	0.099	3.75E-05	-0.171
	Summer (07-2007)	0.401	0.091	0.225	0.020	-0.007	0.036	1.14E-05	0.019
	Difference (%)	0.11	40.34	68.04	246.83	313.37	177.68	230.21	-1021.8
Aygaude	Winter (02-2007)	0.401	0.099	0.371	0.090	-0.036	0.086	9.66E-05	-0.07
	Summer (07-2007)	0.401	0.068	0.207	0.024	-0.010	0.029	1.08E-05	0.14
	Difference (%)	0.05	46.27	79.21	277.23	258.57	199.45	796.97	-147.24
La Capte	Winter (02-2007)	0.401	0.044	0.273	0.079	-0.004	0.036	2.50E-05	-0.091
	Summer (07-2007)	0.401	0.045	0.123	0.016	-0.002	0.008	7.28E-06	0.044
	Difference (%)	-0.01	-2.27	121.4	400.09	117.88	365.71	243.77	-305.75

5.6.3. Effect of extreme events on hydrodynamics and sediment transport

In addition to the impact of seasonal variation and wind direction, the study area is also investigated under the impact of extreme events. The results of this investigation

are described in from Figure 153 to Figure 158. Furthermore, the results of hydrodynamics and sediment transport at the water depth of 1.5 m in front of Gapeau, Aygaude, Ceinturon, Bona, Pesquiers and La Capte beaches were listed in Table 49 to elucidate the effect of stormy scale. It is noticeable that the higher level of storm causes the larger and stronger impacts on wave and current fields as well as sediment transport. Particularly, the mean significant wave height increases from 0.93 m - 1.08 m in decadal storm condition to 1.29 m - 1.51 m in centennial storm condition. However, when the storm level increases, the current speed has a decrease trend (Table 49). The main reason maybe come the expansion of sea water volume when the sea level rises.

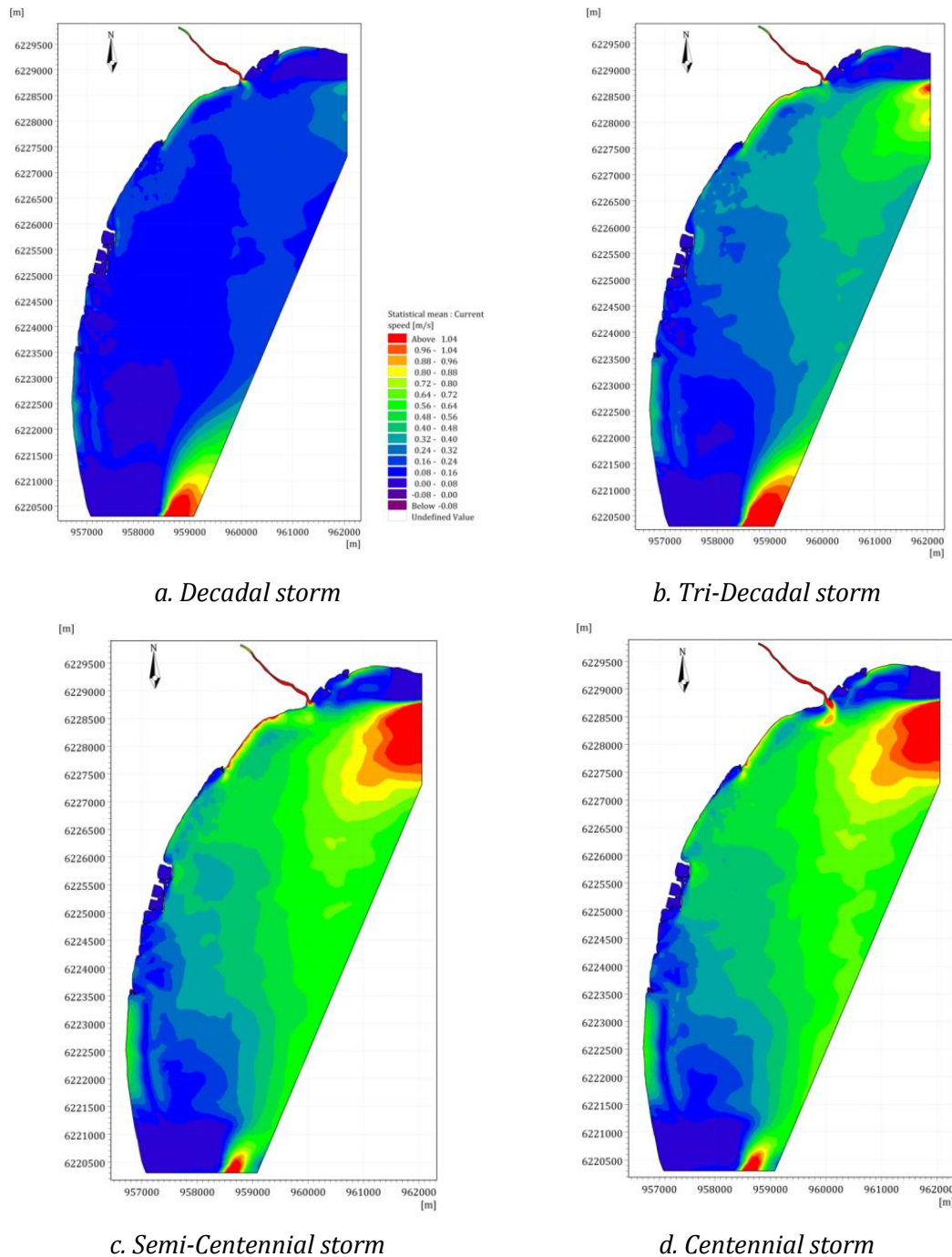


Figure 153. Current speed in the study area under the impact of variation of storm scale with Posidonia.

Figure 153 illustrates the current speed patterns in the study area under the different extreme events. The high nearshore currents commonly occur along the coast from the mouth of Gapeau river to Aygaude beach as well as along La Capte beach. The current speed is continuously intensified with the increase of storm level. The highest current speed is always observed in front of Aygaude beach regardless the storm scale (Table 49). On the other hand, the low currents are reported in the south of Hyères port, viz. Bona and Pesquiers beaches. The presence of northern breatwater at Hyères port causes the change of longshore current direction and thus the longshore current speed is decreased when they reach to Bona and Pesquiers beaches. Moreover, the lowest currents, even with current speed of zero value is also found in the south of Badine beach because the longshore currents from the north to the south is partly dissipated by bed friction and partly blocked by the cape of Esterel.

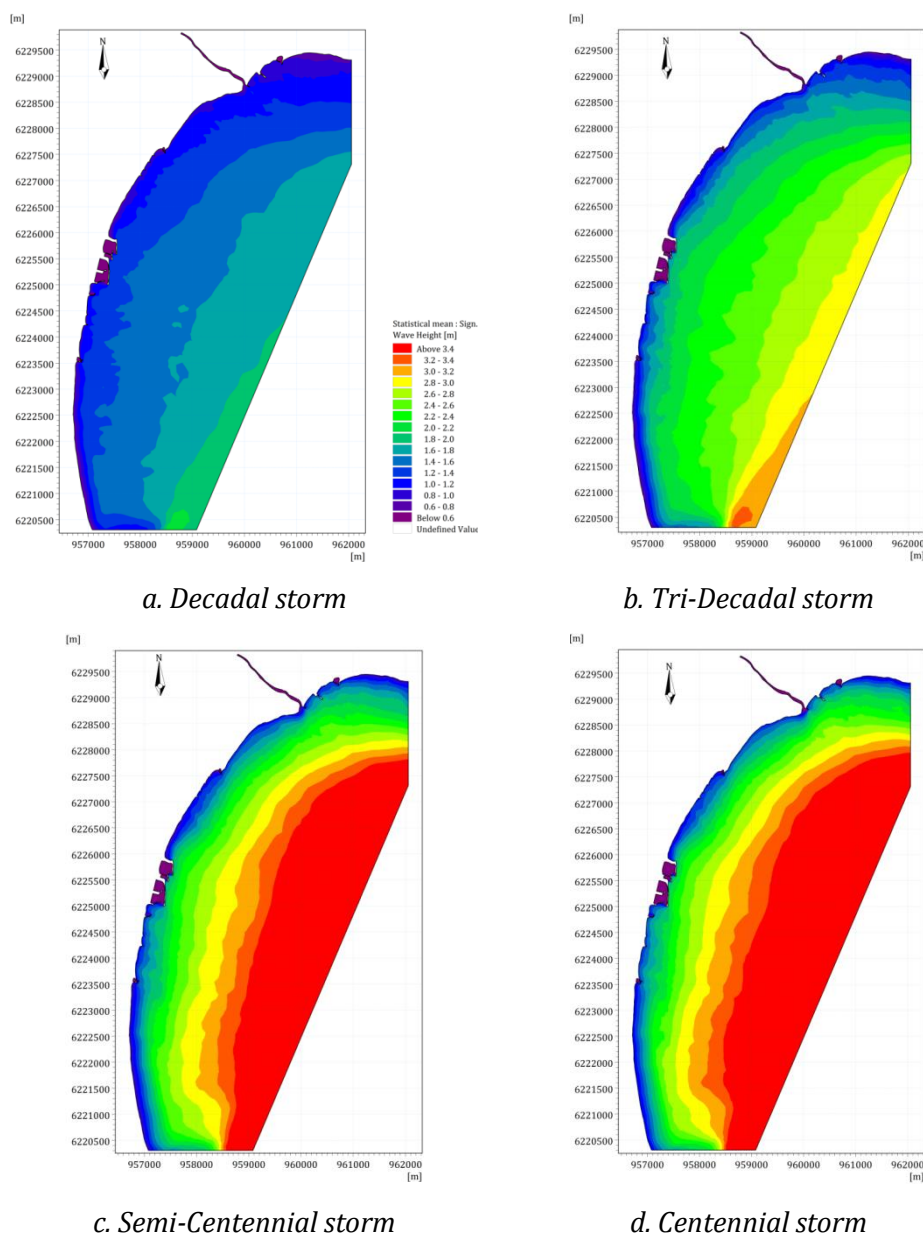


Figure 154. Significant wave height in the study area under the impact of variation of storm scale with Posidonia.

The intensification of storms induces an increase of significant wave heights (Figure 154). The high waves in the storms usually approach the coast along Aygaude and Bona beaches. The highest significant wave height is observed in front of Bona beach regardless the level of storms. Specifically, the mean significant wave height taking into account the presence of Posidonia increases from 1.0 m in decadal storm to 1.42 m in centennial storm at Aygaude beach, whereas this height increases from 1.08 m in decadal storm to 1.51 m in centennial storm at Bona beach (Table 49). The large radiation stresses are resulted in from the high waves. The largest radiation stresses always occur in Bona beach without taking into account the storm scale.

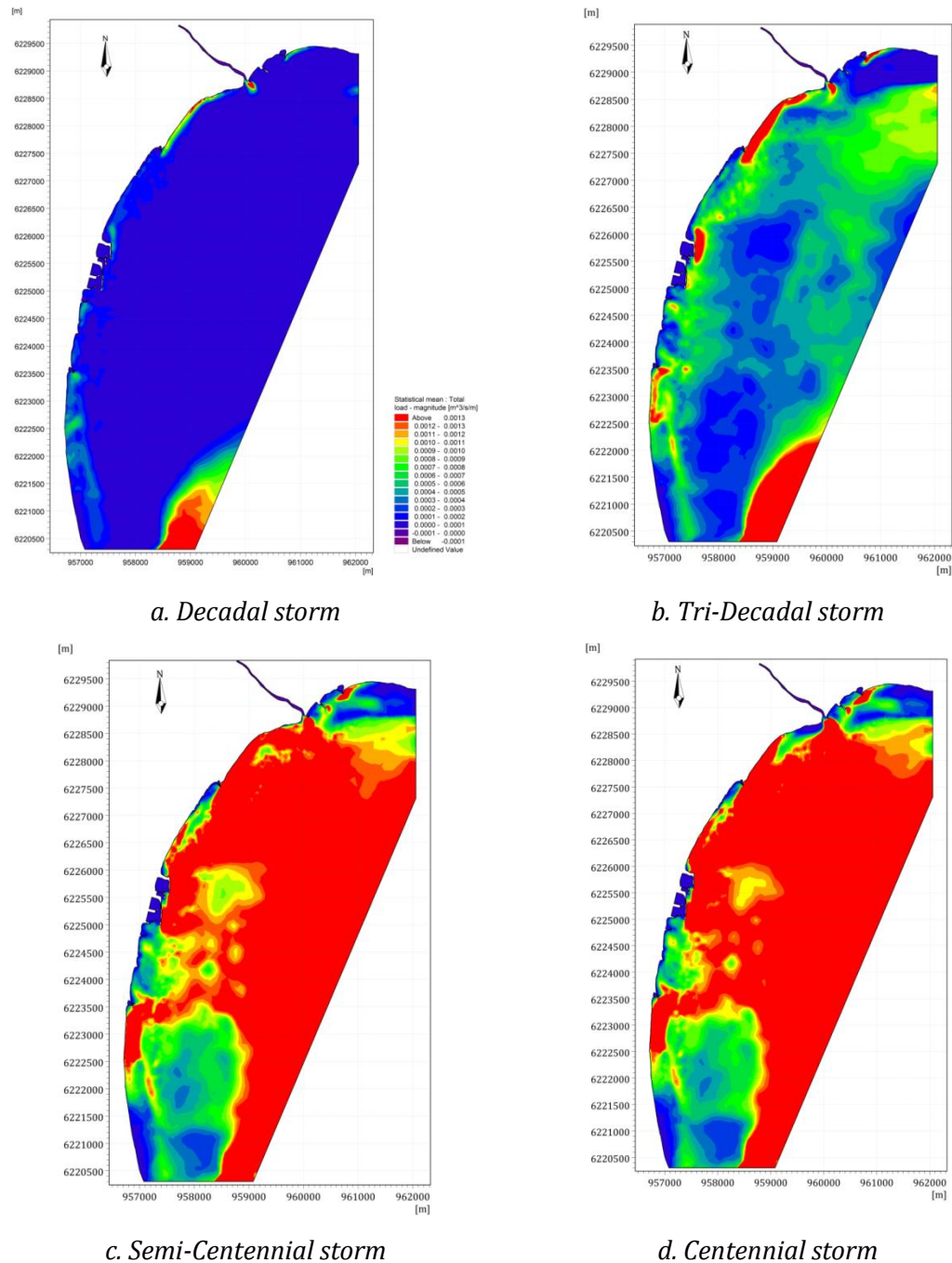


Figure 155. Sediment transport rates (total load) in the study area under the impact of variation of storm scale with Posidonia.

The extreme events greatly influence on the total sediment load pattern in the study area (Figure 155). In the decadal storm scenario, the sediment is mainly transported along the coast of the eastern tombolo, especially from the Gapeau river mouth to Aygaude beach. When the tri-decadal storm approaches the study area, the high sediment transport rates are observed not only in the mouth of Gapeau river, Aygaude beach, the south of Ceinturon beach, and La Capte, but also in offshore zones (Figure 155b). Under the impact of the semi-centennial and centennial storms, the sediment transport carried out with the high rates of over $1.2 \times 10^{-3} \text{ m}^3/\text{s}/\text{m}$ is found in most of the study area (Figure 155c,d).

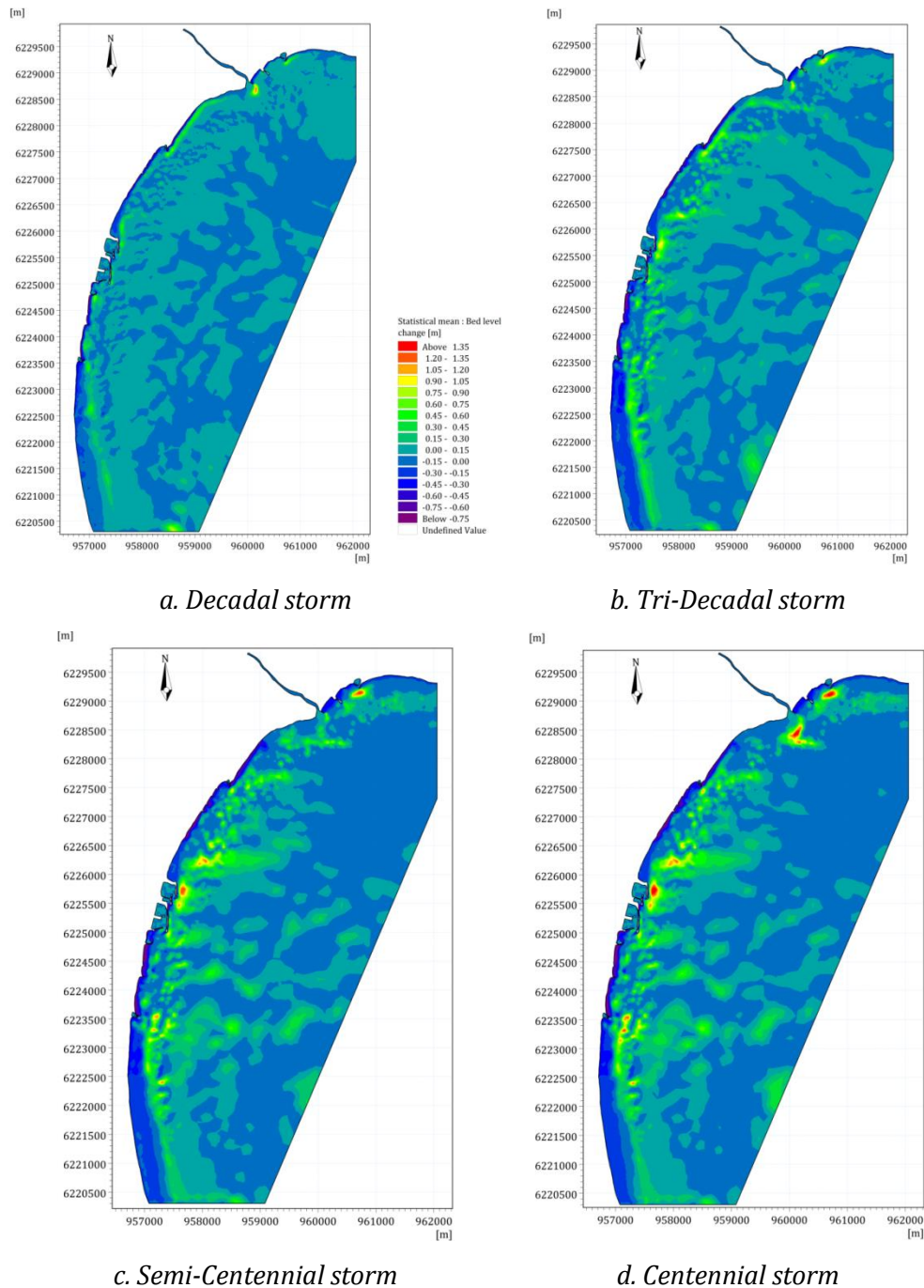


Figure 156. Bed level change in the study area under the impact of variation of storm scale with *Posidonia*.

The sediment transport rate due to the stormy conditions largely affects the bed level change in Hyères bay. In the scenarios of decadal and tri-decadal storms, a sandy bar is formed right in the south of jetty at Gapeau river mouth (Figure 156a,b). This bar develops and enlarges offshore in front of the mouth Gapeau river (Figure 156c,d). Under the impact of all storms, the most serious erosion is observed in Aygaude beach, Ceinturon beach and Bona beach, while accretion is found in the upstream of Hyères port, the south of Pesquiers beach, and the seaward side of two submerged geotube breakwaters in La Capte beach. An increase of the storm intensification provokes the augmentation of erosion level at Aygaude, Bona and Ceinturon beaches as well as the accretion expansion in the upstream side of shore-normal structures.

The impact of the storms triggers the change of beach profile. The post-storm beach evolution at the central Ceinturon and Bona are illustrated in Figure 157 and Figure 158, respectively. It is easily seen that the strong storm caused the large bed level change. With the presence of Posidonia, the beach profile is modified from the shoreline up to 5 m depth offshore. In the scenarios of all storms, the beach profile is changed upto 200 m seaward of the shoreline at the central Ceinturon beach (Figure 157), and 300 m seaward of the shoreline at Bona (Figure 158). The largest beach profile change is due to the impact of the centennial storm inducing the erosion of about 1.2 m close to the coast.

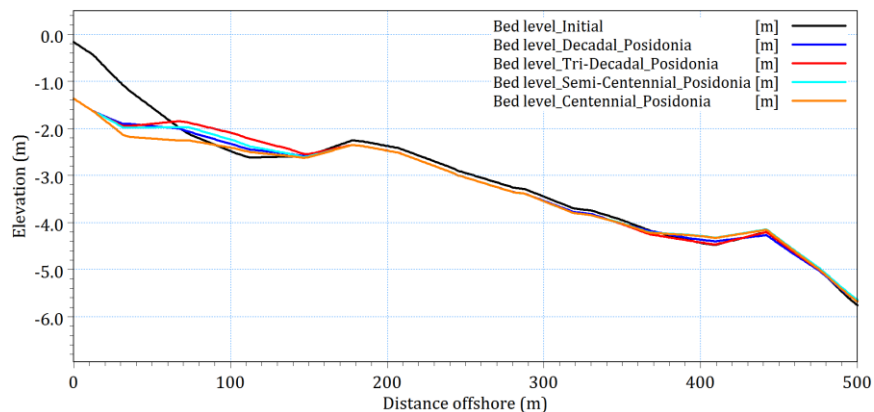


Figure 157. Beach profile evolution at Central Ceinturon beach under the impact of variation of storm scale with Posidonia.

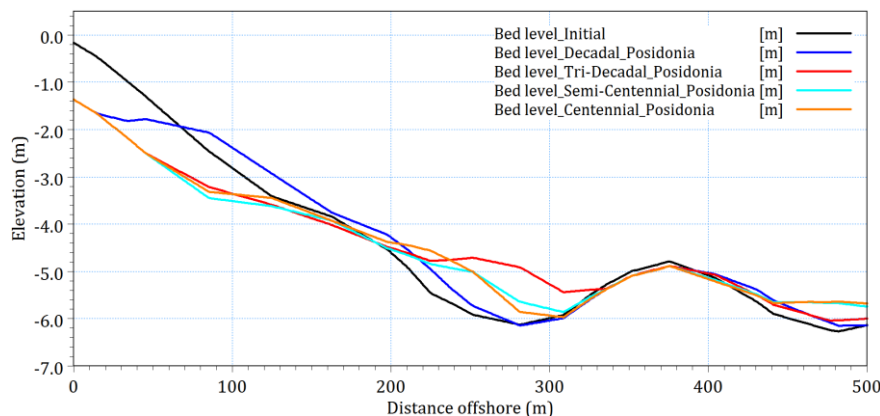


Figure 158. Beach profile evolution at Bona beach under the impact of variation of storm scale with Posidonia.

Table 49. Effect of Posidonia and storm scale on the hydrodynamics and sediment transport.

Beach	Storm	WL (m)	V _c (m/s)	H _s (m)	S _{xx} (m ³ /s ²)	S _{xy} (m ³ /s ²)	S _{yy} (m ³ /s ²)	Q (m ³ /s/m)	Δz (m)
Ceinturon	Decadal	0.954	0.204	0.930	0.424	-0.189	0.472	3.12E-05	-0.046
	Tri-Decadal	1.041	0.428	1.102	0.606	-0.274	0.673	4.86E-04	-0.047
	Semi-Centennial	1.252	0.588	1.209	0.705	-0.319	0.402	1.05E-03	-0.047
	Centennial	1.598	0.154	1.299	0.733	-0.320	0.894	5.43E-05	-0.046
Bona	Decadal	0.963	0.379	0.994	0.570	-0.203	0.424	1.06E-03	-0.091
	Tri-Decadal	1.063	0.637	1.194	0.785	-0.279	0.560	2.83E-03	-0.426
	Semi-Centennial	1.294	0.876	1.315	0.923	-0.326	0.634	3.16E-03	-0.519
	Centennial	1.673	0.751	1.418	1.064	-0.370	0.715	3.27E-03	-0.459
Pesquiers	Decadal	0.969	0.164	0.941	0.505	-0.131	0.322	2.05E-04	-0.195
	Tri-Decadal	1.074	0.276	1.027	0.566	-0.149	0.360	3.54E-04	-0.380
	Semi-Centennial	1.303	0.360	1.113	0.648	-0.157	0.380	6.97E-04	-0.559
	Centennial	1.687	0.371	1.254	0.806	-0.191	0.461	7.98E-04	-0.636
Gapeau	Decadal	0.965	0.242	1.079	0.803	-0.063	0.352	4.47E-04	-0.324
	Tri-Decadal	1.064	0.205	1.304	1.110	-0.070	0.462	5.68E-04	-0.702
	Semi-Centennial	1.290	0.062	1.393	1.234	-0.050	0.487	3.99E-04	-0.785
	Centennial	1.679	0.054	1.512	1.412	-0.069	0.563	4.63E-04	-0.786
Aygaude	Decadal	0.968	0.122	1.002	0.672	-0.070	0.300	2.77E-04	-0.147
	Tri-Decadal	1.070	0.174	1.157	0.848	-0.094	0.372	3.81E-04	-0.382
	Semi-Centennial	1.293	0.284	1.231	0.934	-0.091	0.402	5.65E-04	-0.429
	Centennial	1.684	0.291	1.364	1.111	-0.102	0.478	6.10E-04	-0.516
La Capte	Decadal	0.971	0.184	1.051	0.750	-0.016	0.343	4.20E-04	-0.236
	Tri-Decadal	1.078	0.333	1.072	0.777	-0.050	0.353	1.12E-03	-0.016
	Semi-Centennial	1.304	0.333	1.114	0.811	-0.035	0.382	1.22E-03	0.084
	Centennial	1.694	0.319	1.281	1.025	-0.037	0.489	1.40E-03	-0.008

5.6.4. Effect of Posidonia seagrass on hydrodynamics and sediment transport

5.6.4.1. Wave height

The wave height pattern completely changes when Posidonia disappears (Figure 159). Under the impact of eastern and northeastern winds, the waves with mean height of over 0.8 m mainly reach the coast from the mouth of Roubaud river to Hyères port (Ceinturon beach) and from the Bona beach to the La Capte port, whereas the southeastern winds only trigger the moderate agitation in front of Ceinturon beach. The significant wave height at the water depth of 1.5 m increases by 3.54%-6.05% at Bona beach and 17.58%-19.15% at Ceinturon beach if the area of Posidonia degrades totally (Table 50). As a result, the radiation stresses are also considerably boosted by 43.27%-55.14% at Ceinturon beach and 9.46%-49.96% at Bona beach.

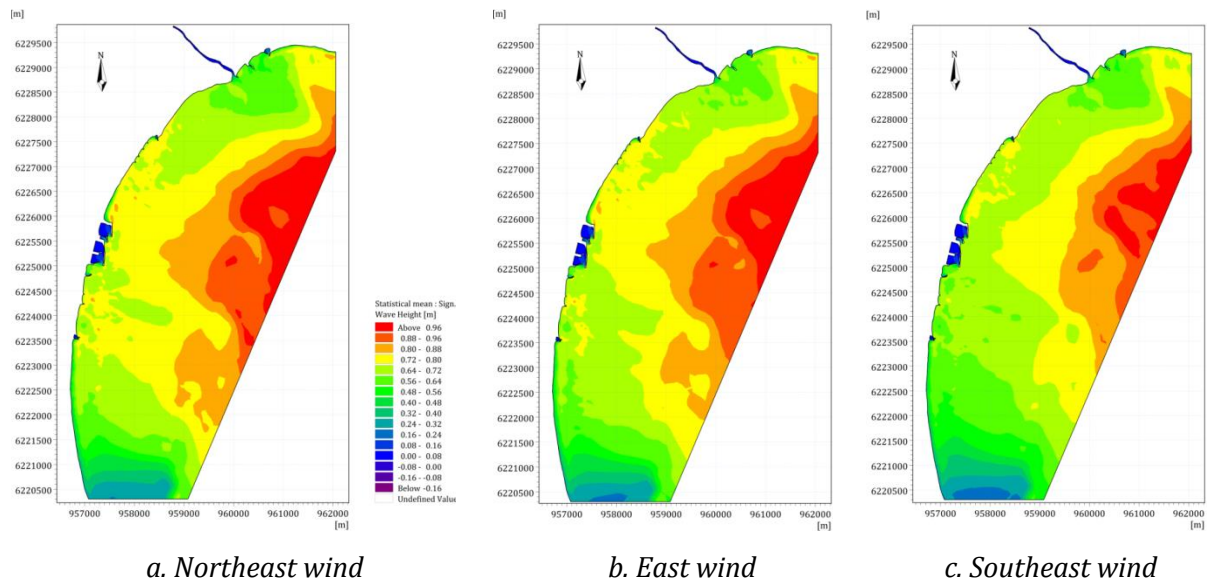


Figure 159. Significant wave height in the study area under the impact of variation of wind direction without Posidonia.

The regression of Posidonia makes the difference of wind climate between the winter and summer more distinct (Figure 160). Especially, the zone which high waves occur is displaced from offshore to nearshore right in the front of Ceinturon and Bona beaches regardless the seasonal variation. This results in a remarkable increase of wave height in the shallow water areas. The mean significant wave heights in both the winter and summer are intensified up to 29.53% and 45.60% at Ceinturon beach as well as 33.97% and 83.54% at Bona beach, respectively. Moreover, the values of the radiation stresses in both winter and summer are 65.33%-103.06% at Ceinturon beach and 51.50-260.97% at Bona beach larger than those in the cases of Posidonia presence (Table 50).

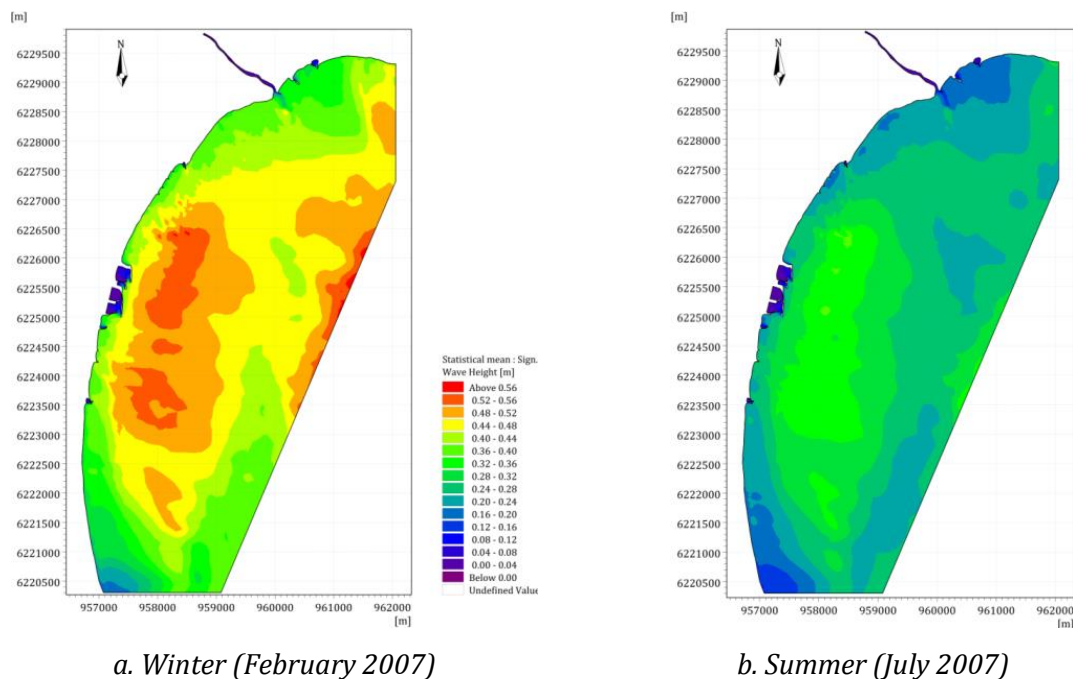
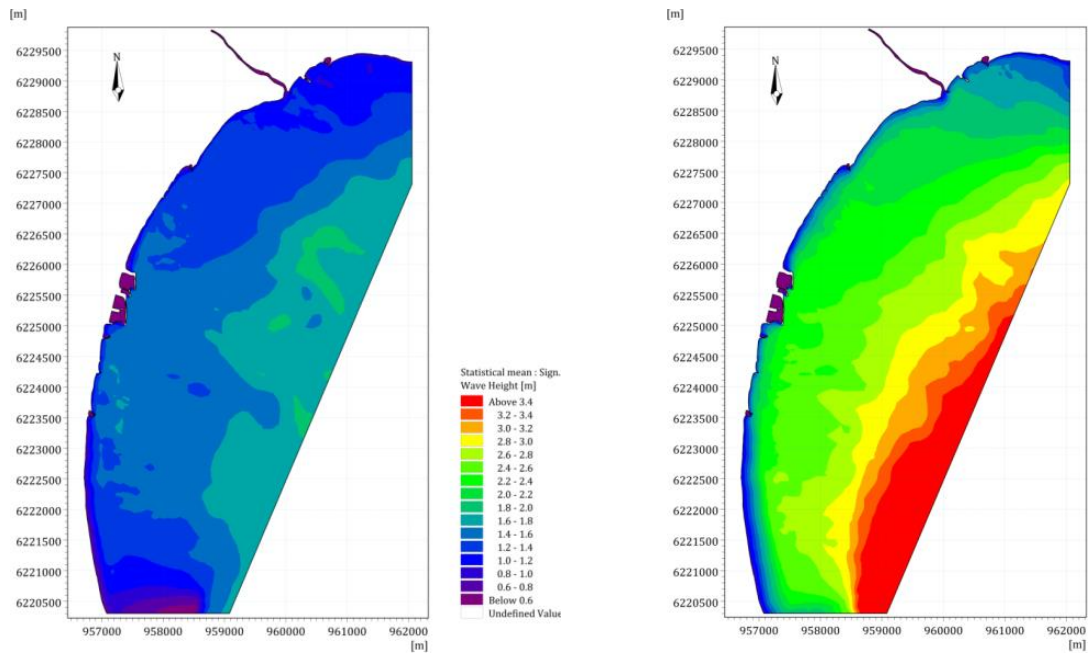
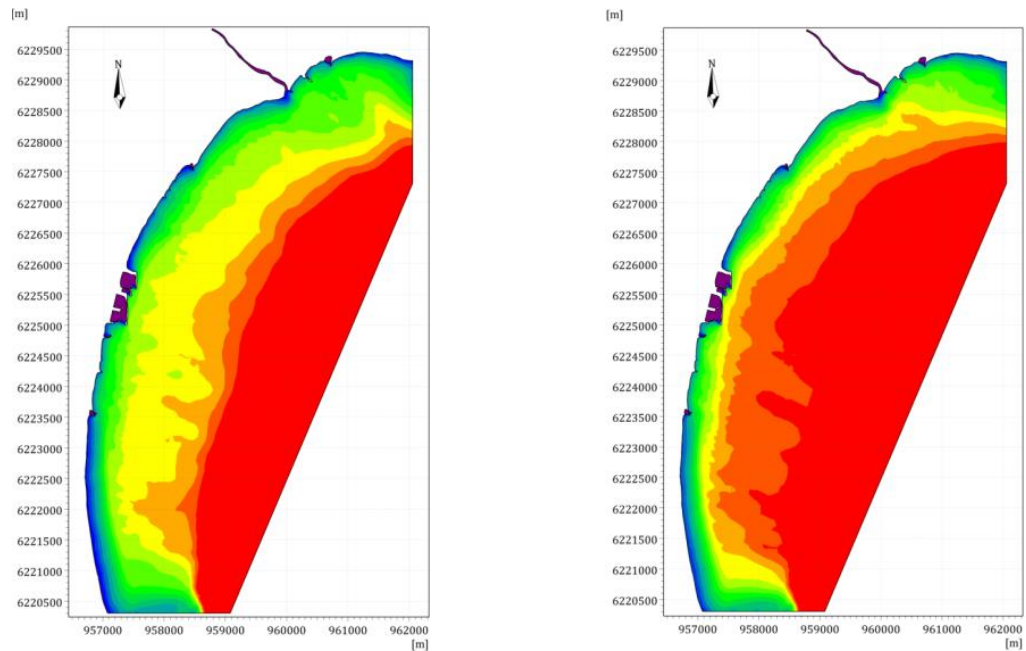


Figure 160. Significant wave height in the study area under the impact of seasonal variation without Posidonia.



a. Decadal storm

b. Tri-Decadal storm



c. Semi-Centennial storm

d. Centennial storm

Figure 161. Significant wave height in the study area under the impact of variation of storm scale without Posidonia.

The absence of Posidonia along with the impact of extreme events triggers the chaotic change of significant wave height pattern (Figure 161). The high waves mostly attack the coast from Pesquiers beach to the central Ceinturon beach. As a result, the nearshore significant wave height is boosted without Posidonia, viz. by 33.84%-47.86% at Ceinturon beach and by 18.01%-22.52% at Bona beach. The high wave heights induce the large radiation stresses in the cases of no Posidonia. Generally, the radiation stresses can be increased by 99.91%-202.17% at Ceinturon beach and 49.51%-249.14% at Bona beach (Table 50).

Table 50. Effect of Posidonia on wave field.

Scenario	Ceinturon				Bona				
	H _s (m)	S _{xx} (m ³ /s ²)	S _{xy} (m ³ /s ²)	S _{yy} (m ³ /s ²)	H _s (m)	S _{xx} (m ³ /s ²)	S _{xy} (m ³ /s ²)	S _{yy} (m ³ /s ²)	
Posidonia	NE	0.622	0.232	-0.064	0.158	0.682	0.337	-0.026	0.152
	E	0.618	0.228	-0.064	0.155	0.649	0.306	-0.028	0.140
	SE	0.604	0.216	-0.061	0.147	0.631	0.289	-0.029	0.132
	Winter	0.300	0.069	-0.021	0.049	0.283	0.087	-0.010	0.040
	Summer	0.150	0.017	-0.006	0.014	0.127	0.017	-0.003	0.009
	Decadal	0.941	0.505	-0.131	0.322	1.079	0.803	-0.063	0.352
	Tri-Decadal	1.027	0.566	-0.149	0.360	1.304	1.110	-0.070	0.462
	Semi-Centennial	1.113	0.648	-0.157	0.380	1.393	1.234	-0.050	0.487
	Centennial	1.254	0.806	-0.191	0.461	1.512	1.412	-0.069	0.563
No Posidonia	NE	0.738	0.335	-0.097	0.245	0.711	0.371	-0.039	0.18
	E	0.736	0.332	-0.096	0.237	0.688	0.35	-0.035	0.168
	SE	0.71	0.31	-0.09	0.22	0.653	0.316	-0.032	0.151
	Winter	0.388	0.117	-0.034	0.095	0.379	0.132	-0.022	0.071
	Summer	0.218	0.03	-0.01	0.029	0.233	0.052	-0.01	0.029
	Decadal	1.26	1.018	-0.262	0.679	1.273	1.2	-0.131	0.57
	Tri-Decadal	1.486	1.467	-0.386	0.982	1.598	2.004	-0.183	0.913
	Semi-Centennial	1.646	1.821	-0.453	1.148	1.684	2.244	-0.175	1.01
	Centennial	1.828	2.169	-0.505	1.354	1.833	2.517	-0.224	1.147
Difference (%)	NE	18.58	44.48	51.73	55.14	4.21	9.95	49.96	18.14
	E	19.15	45.81	50.33	52.76	6.05	14.43	24.27	19.92
	SE	17.58	43.27	47.81	49.31	3.54	9.46	10.90	14.02
	Winter	29.53	69.57	65.33	92.00	33.97	51.50	123.12	77.18
	Summer	45.60	72.37	68.47	103.06	83.54	211.82	260.97	239.22
	Decadal	33.84	101.66	99.91	110.80	18.01	49.51	108.21	61.83
	Tri-Decadal	44.75	158.98	158.27	172.92	22.52	80.56	162.92	97.69
	Semi-Centennial	47.86	180.96	187.72	202.17	20.91	81.90	249.14	107.21
	Centennial	45.80	169.27	164.18	193.63	21.25	78.22	223.85	103.88

5.6.4.2. Current speed

In the case of Posidonia absence and the variation of wind direction, the mean current speed at Ceinturon and Bona beaches are sharply increased by 99.7%-185.4% and 2.03-36.18%, respectively, when comparing with those in the case of Posidonia (Table 51). Regardless the wind direction, the high current speed over 0.40 m/s occurs in most of the study area, except the southern zone of Hyères bay due to its sheltered position (Figure 163). It is noticeable that the northeastern wind is still the predominant direction influencing the current field with the highest current speed of 0.255 m/s observed near Ceinturon beach.

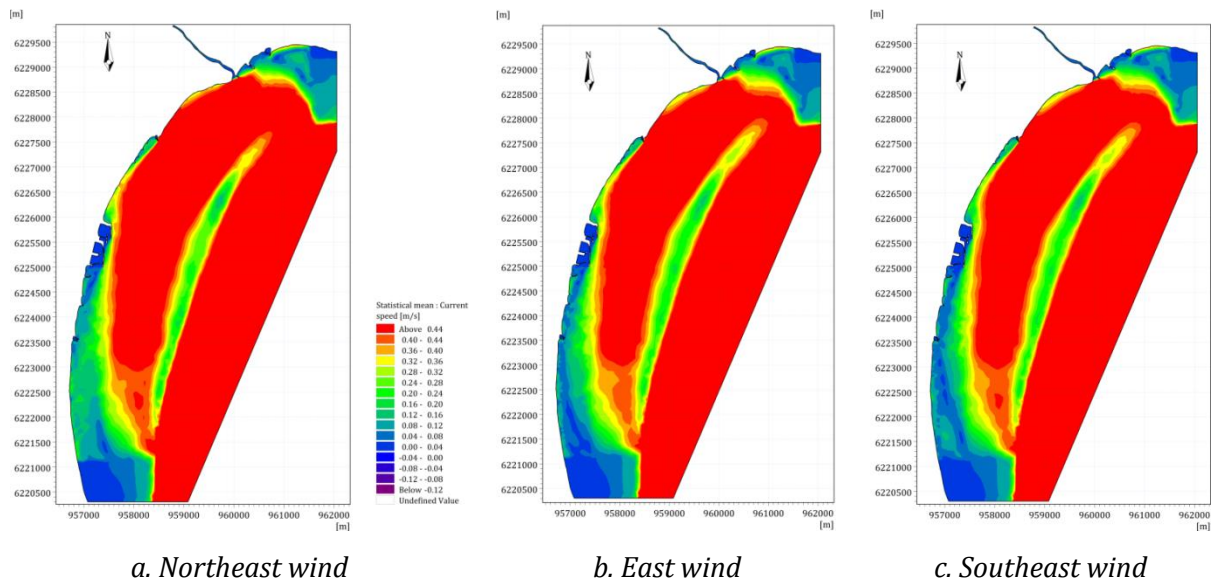


Figure 162. Current speed in the study area under the impact of variation of wind direction without Posidonia.

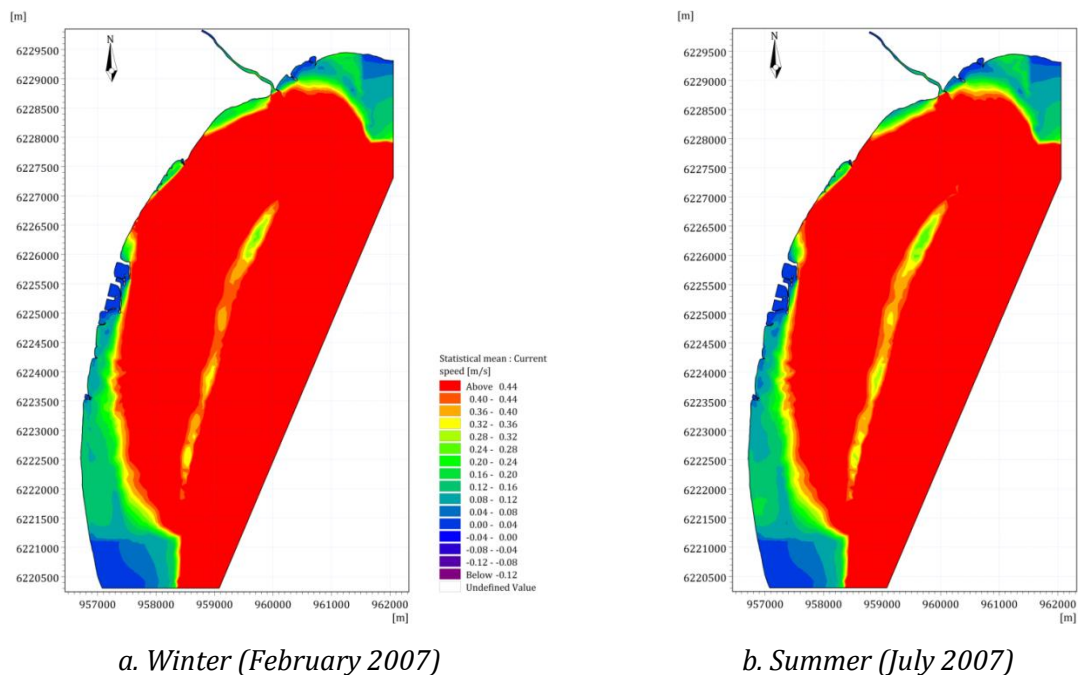


Figure 163. Current speed in the study area under the impact of seasonal variation without Posidonia.

Figure 163 reveals that when the Posidonia seagrass does not present in the study area, the seasonal difference showed through the current speed pattern is manifested more evidently. The mean current speed over 0.4 m/s is found along the coast from the Gapeau river mouth to Hyères port in both the summer and winter. Particularly, a distinct increase of 127.1%-138.2% in mean current speed is found in the front of Bona beach, while this speed at Ceinturon beach is boosted by 424%-555%, compared with the cases of Posidonia (Table 51).

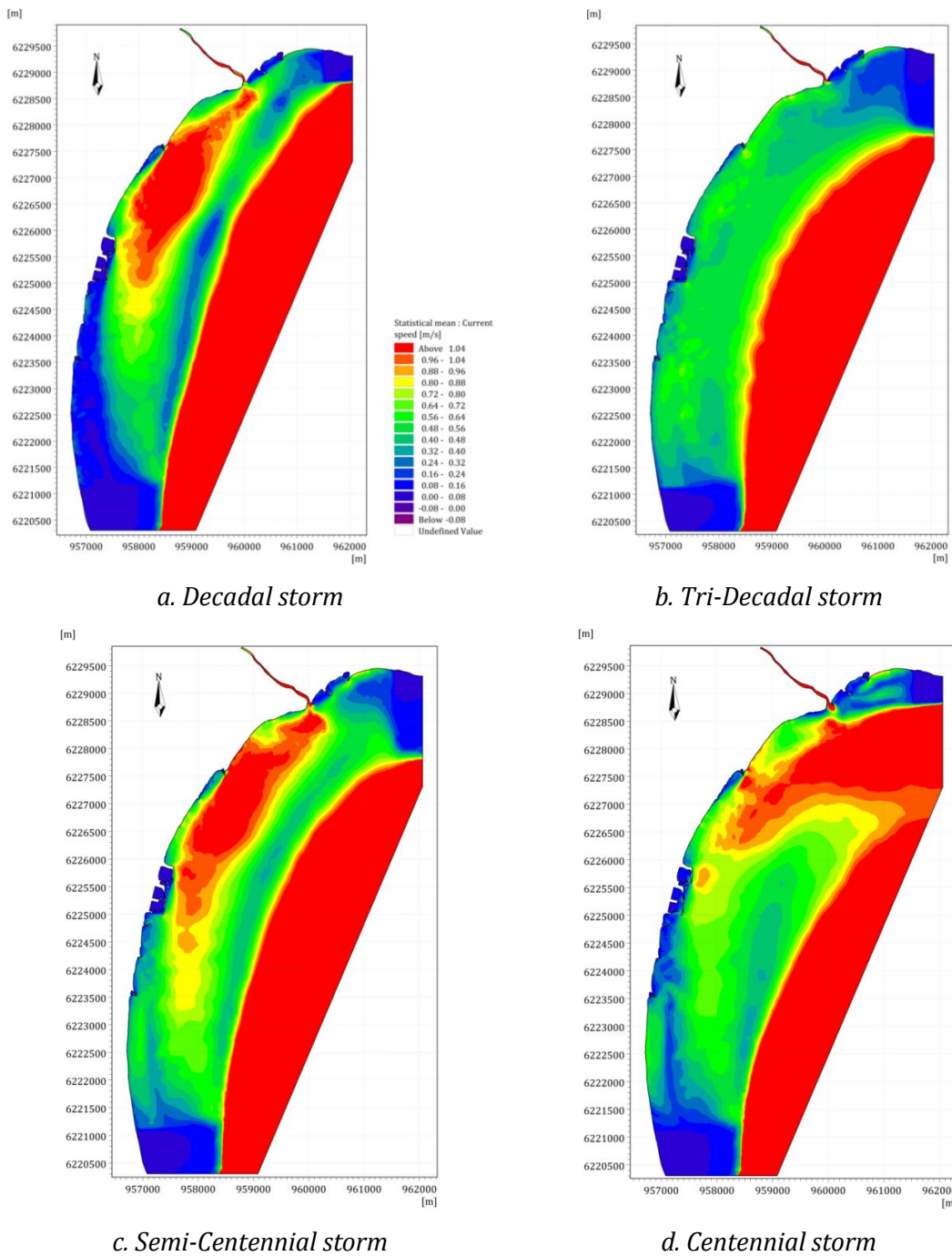


Figure 164. Current speed in the study area under the impact of variation of storm scale without Posidonia.

The impact of extreme events along with the absence of Posidonia causes high current speed (over 0.9 m/s) along the coast from Gapeau river mouth to Hyères port and offshore zone (Figure 164). When the storm reaches to tri-decadal level, the current speed is increased considerably more. The mean current speed may be added about 107.09% at Bona beach and 657.69% at Ceinturon beach when Posidonia is receded completely. With regard to the semi-centennial storm scenario, the mean current speed at Ceinturon beach is increased about 30%, while it is reduced to 230% at Bona beach, comparing with those in the tri-decadal storm conditions (Table 51). This difference of current speed pattern between Ceinturon and Bona beaches still occurs until the

Posidonia is reduced totally. The nearshore zone of high current speed is enlarged offshore. Under the influence of the centennial storm accompanied with the disappearance of Posidonia, the high current speed over 1 m/s spreads from nearshore to offshore areas. At the Ceinturon beach, the mean current speed reaches up to 0.46 m/s which is about 24.65% higher than that is the case of Posidonia. Similarly, the mean current speed at Bona beach increases to 0.21 m/s corresponding to 285.8% higher than that in the case, which Posidonia occurs.

5.6.4.3. Sediment transport

Figure 165 depicts the sediment transport pattern under the impact of northeastern, eastern, and southeastern winds, which does not take into account Posidonia. It is noted that the sediment transport is completely changed after the Posidonia seagrass is absent. The high total load over $1.00 \times 10^{-4} \text{ m}^3/\text{s}/\text{m}$ is observed in most of the study area, regardless the wind direction. The magnitude of sediment transport rates at the water depth of 1.5 m near Ceinturon beach is significantly increased by 230.2%-376.9% when comparing with those in the cases of Posidonia presence (Table 51). In other words, only a slight increase of sediment rates is reported at Bona beach, even these rates were reduced in the combinations of southeastern winds and the disappearance of Posidonia.

The entire regression of Posidonia disarranged the sediment transport pattern in both the winter and summer (Figure 166). The total load of sediment measured at the water depth of 1.5 m in the front of beach in the summer and winter is much larger than 380% compared to the situation with Posidonia. By contrast, the sediment rates at Bona beach are modified a little when the Posidonia disappears, even reduced about 12.84% in the winter (Table 51). Under the influence of the winter climate and the absence of Posidonia, the high sediment transport rates are found not only in offshore areas but also along La Capte beach.

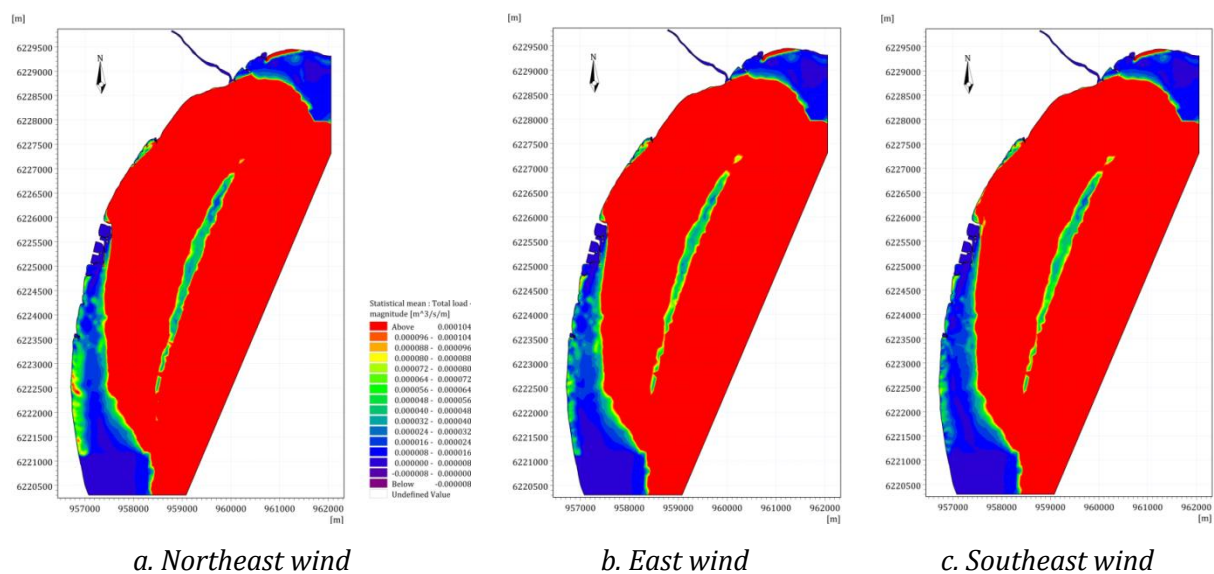


Figure 165. Sediment transport rates (total load) in the study area under the impact of variation of wind direction without Posidonia.

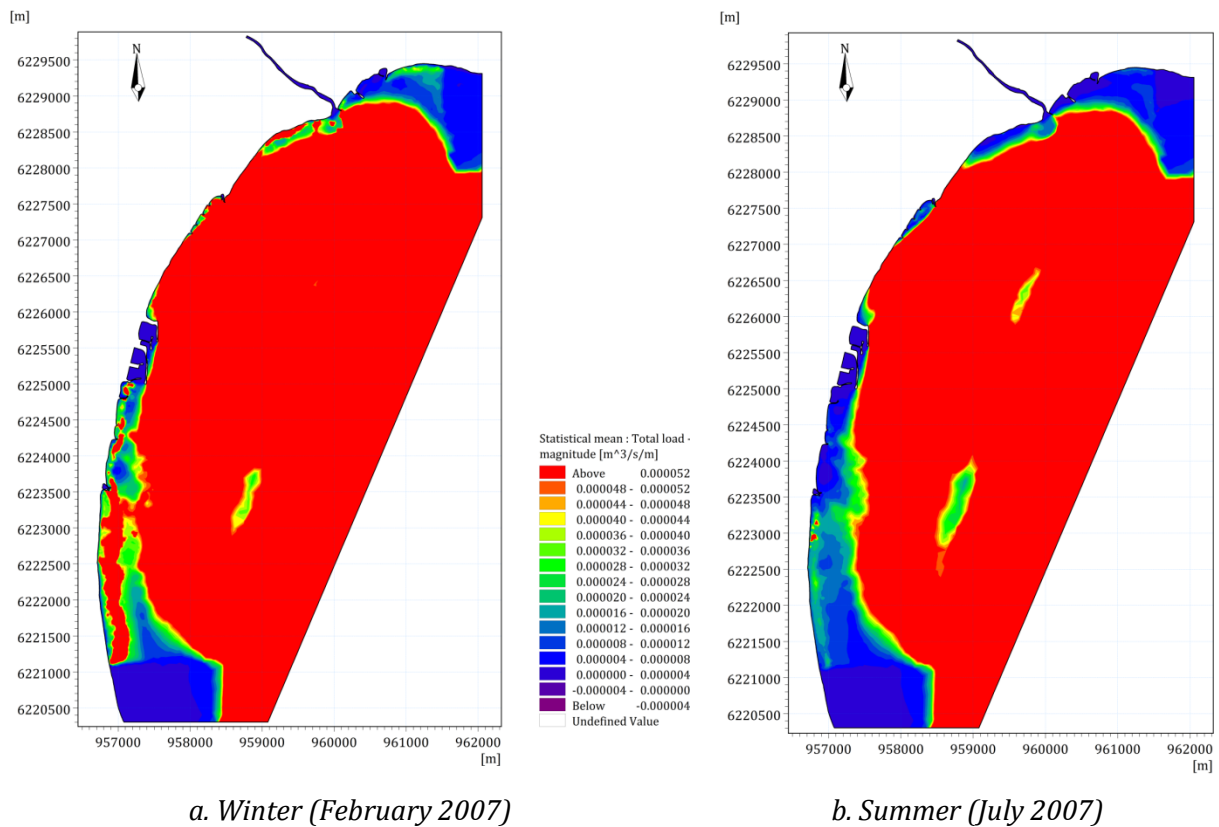
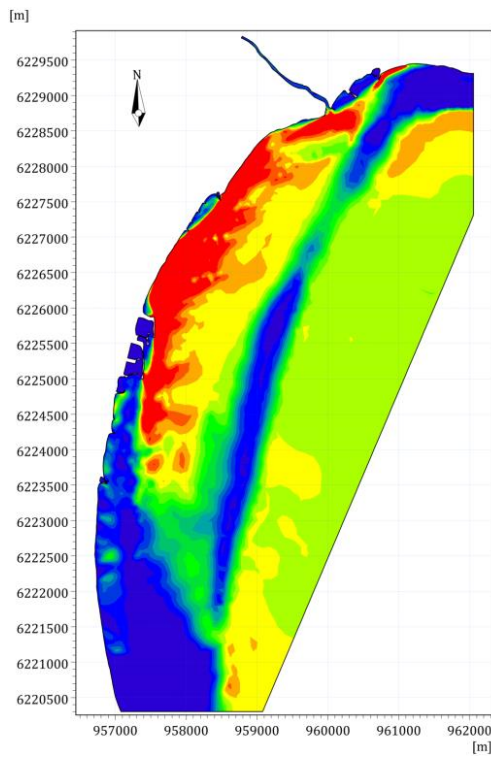
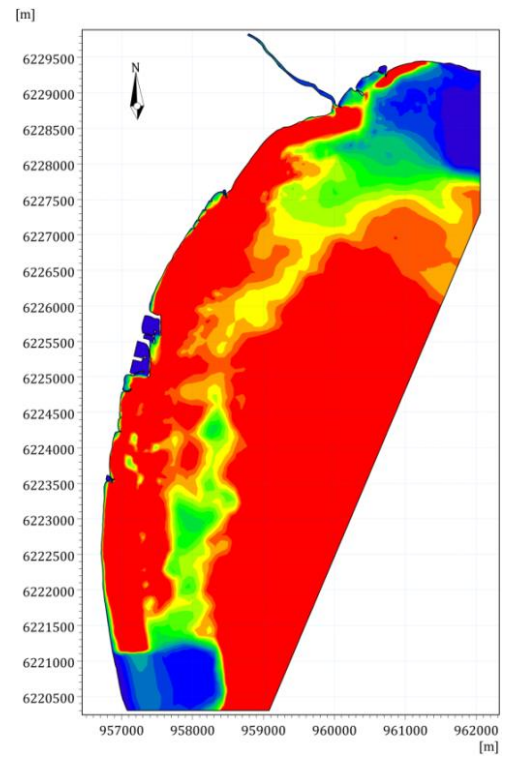


Figure 166. Sediment transport rates (total load) in the study area under the impact of seasonal variation without Posidonia.

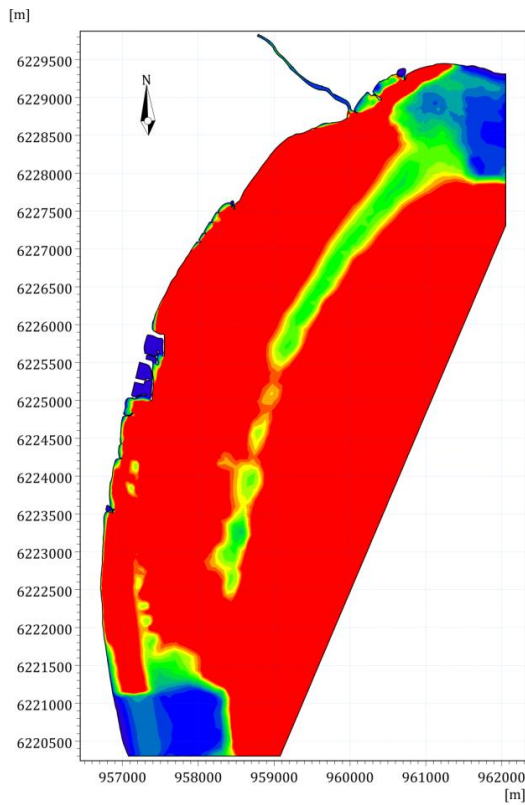
Under the combination of extreme events and the absence of Posidonia in Hyères bay, the total sediment load could be augmented sharply. The high sediment rates occur mainly from the mouth of Gapeau river to the seaward side of Hyères port in the decadal storm, but they present over the study area in the tri-decadal, semi-centennial and centennial storms (Figure 167). The absence of Posidonia along with the impact of storms can cause the evident increase of 87.61%-231.23% and 165.64%-657.69% at Bona and Ceinturon beaches, respectively (Table 51). It elucidates that the sediment transported by the longshore currents along the eastern Giens tombolo, is trapped mostly by Posidonia.



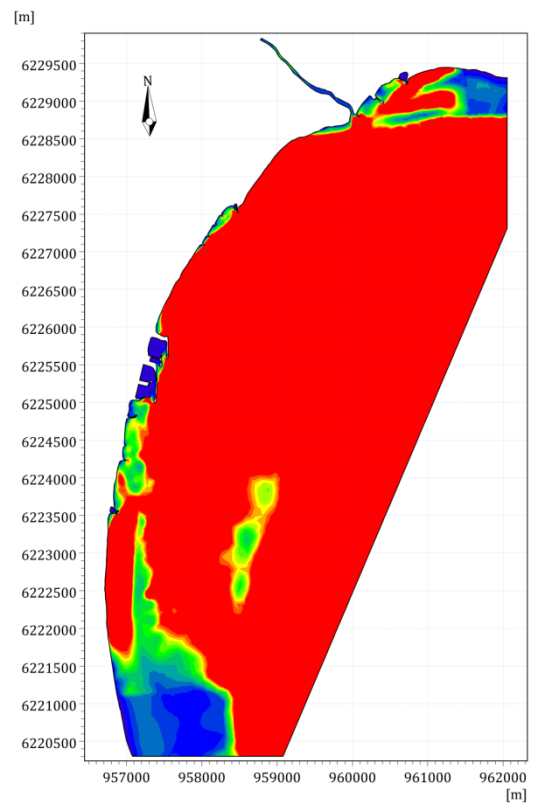
a. Decadal storm



b. Tri-Decadal storm



c. Semi-Centennial storm



d. Centennial storm

Figure 167. Sediment transport rates (total load) in the study area under the impact of variation of storm scale without Posidonia.

Table 51. Effect of Posidonia on hydrodynamics and sediment transport.

Scenario	Ceinturon				Bona				
	WL (m)	V _c (m/s)	Q (m ³ /s/m)	Δz (m)	WL (m)	V _c (m/s)	Q (m ³ /s/m)	Δz (m)	
Posidonia	NE	0.402	0.128	5.05E-05	-0.13	0.401	0.103	5.24E-05	-0.086
	E	0.402	0.081	3.12E-05	-0.03	0.399	0.163	7.35E-05	-0.032
	SE	0.400	0.081	3.88E-05	-0.04	0.396	0.171	7.57E-05	-0.037
	Winter	0.402	0.074	2.38E-05	-0.116	0.401	0.058	3.06E-05	-0.216
	Summer	0.401	0.060	8.46E-06	0.096	0.401	0.052	7.80E-06	0.027
	Decadal	0.969	0.164	2.05E-04	-0.195	0.965	0.242	4.47E-04	-0.324
	Tri-Decadal	1.074	0.276	3.54E-04	-0.380	1.064	0.205	5.68E-04	-0.702
	Semi-Centennial	1.303	0.360	6.97E-04	-0.559	1.290	0.062	3.99E-04	-0.785
	Centennial	1.687	0.371	7.98E-04	-0.636	1.679	0.054	4.63E-04	-0.786
No Posidonia	NE	0.454	0.255	1.79E-04	-0.53	0.453	0.14	6.07E-05	-0.13
	E	0.442	0.232	1.49E-04	-0.51	0.438	0.175	7.45E-05	-0.066
	SE	0.441	0.214	1.28E-04	-0.45	0.437	0.174	7.14E-05	-0.037
	Winter	0.535	0.39	1.15E-04	-0.467	0.521	0.139	2.67E-05	-0.185
	Summer	0.51	0.395	6.64E-05	-0.329	0.503	0.117	8.20E-06	0.011
	Decadal	1	0.466	1.55E-03	-0.658	0.984	0.335	9.25E-04	-0.413
	Tri-Decadal	1.212	0.366	1.45E-03	-0.566	1.21	0.325	1.63E-03	-0.542
	Semi-Centennial	1.356	0.496	2.10E-03	-0.772	1.354	0.284	1.32E-03	-0.53
	Centennial	1.803	0.462	2.12E-03	-0.76	1.822	0.208	8.68E-04	-0.402
Difference (%)	NE	12.81	99.7	254.2	293.8	12.84	36.18	15.91	50.94
	E	9.98	185.4	376.9	1615.2	9.77	7.37	1.42	106.91
	SE	10.33	163.0	230.2	961.2	10.36	2.03	-5.64	-0.78
	Winter	33.12	424.0	382.95	302.7	29.93	138.2	-12.84	-14.50
	Summer	27.12	555.0	685.09	-443.6	25.34	127.1	5.08	-59.84
	Decadal	3.18	184.5	657.69	237.8	1.93	38.29	107.09	27.35
	Tri-Decadal	12.87	32.50	309.21	48.95	13.67	58.58	187.14	-22.74
	Semi-Centennial	4.05	37.69	201.08	38.05	4.98	360.1	231.23	-32.49
	Centennial	6.85	24.65	165.64	19.46	8.51	285.8	87.61	-48.88

5.6.4.4. Bed level change

The pattern of bed level changes is totally modified after the Posidonia seagrass disappears, regardless the wind direction (Figure 168). The bed level change is observed in most of the study area. The most severe erosion presents in Aygaude, Ceinturon, Bona and the north of Pesquiers beaches. The increase of bed level erosion due to the absence of Posidonia varies from 50.94% to 106.91% at Bona beach and from 293.8%-1615.2% at Ceinturon beach (Table 51). Nevertheless, the accretion is also found in the upstream of Hyères breakwaters, Roubaud jetty, and right in the mouth of Gapeau river. The largest deposition areas are formed under the impact of the northeast winds.

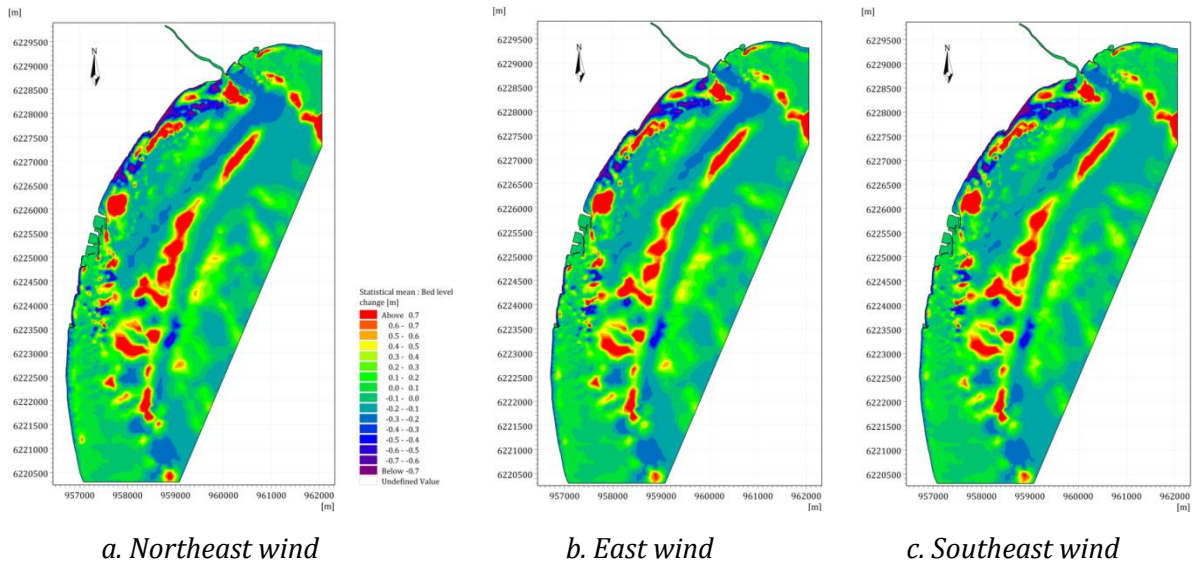


Figure 168. Bed level change in the study area under the impact of variation of wind direction without Posidonia.

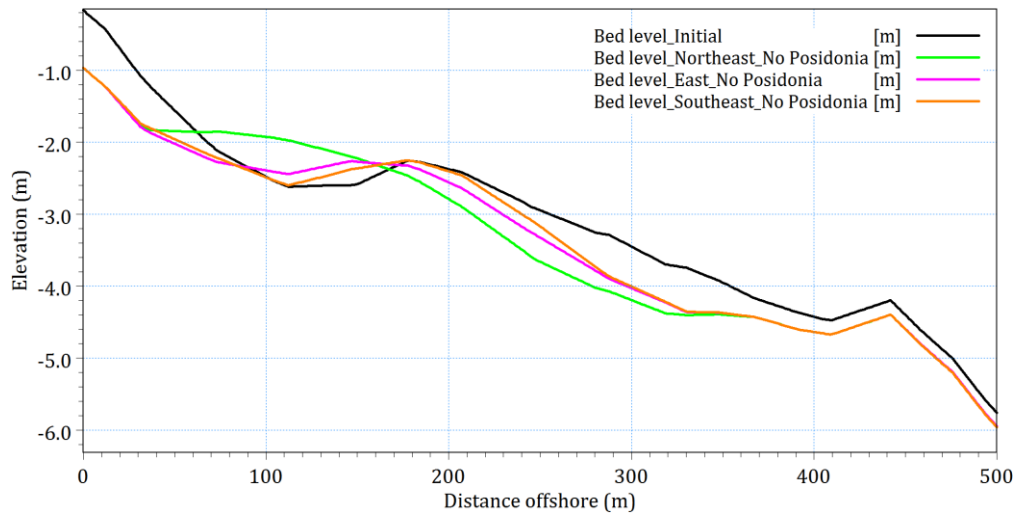


Figure 169. Beach profile evolution at Central Ceinturon beach under the impact of variation of wind direction without Posidonia.

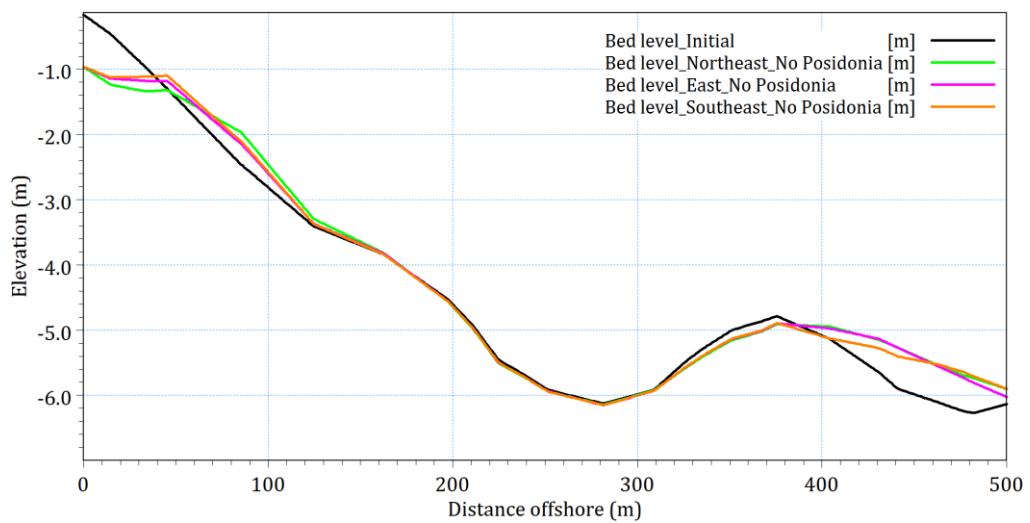


Figure 170. Beach profile evolution at Bona beach under the impact of variation of wind direction without Posidonia.

To interpret the change of bed level due to the variation of wind direction as well as the absence of Posidonia, the beach profiles at Ceinturon beach and Bona beach are plotted in Figure 169 and Figure 170. It is clearly seen that the northeast winds resulted in the largest beach profile change in both Bona and Ceinturon beaches. Furthermore, the erosion occurs not only in nearshore zone but also extend up to offshore at Ceinturon beach, whereas the accretion is observed and located 400 m seaward of the shoreline at Bona beach. If Posidonia is completely degraded, the beach profile at Ceinturon beach would be changed much more than that at Bona beach.

The disappearance of Posidonia generated the chaotic change of bed level in the study area in both the winter and the summer (Figure 171). The seriously eroded areas at Aygaude beach and Ceinturon beach are extended much more comparing with the cases of Posidonia, regardless the seasonal variation. The large sand bar occurs right in the mouth of Gapeau river in both two seasons. The bed level in offshore zones suffered from both erosion and accretion. Accretion is mainly found in the south of the study area and the seaward of Hyères port. This results in the presence of breakwaters that forces longshore currents to change the direction seaward and forms the nearshore sand bars. Table 51 also reveals that the erosion thickness at the water depth of 1.5 m at Bona beach is reduced to 14.5% in the winter and 59.84% in the summer when comparing with the case of Posidonia. The main reason maybe comes from the appearance of sand bars in the front of Bona and Pesquiers beaches which contributes to attenuate the wave heights before these waves reach the beaches and hence limits the coastal erosion.

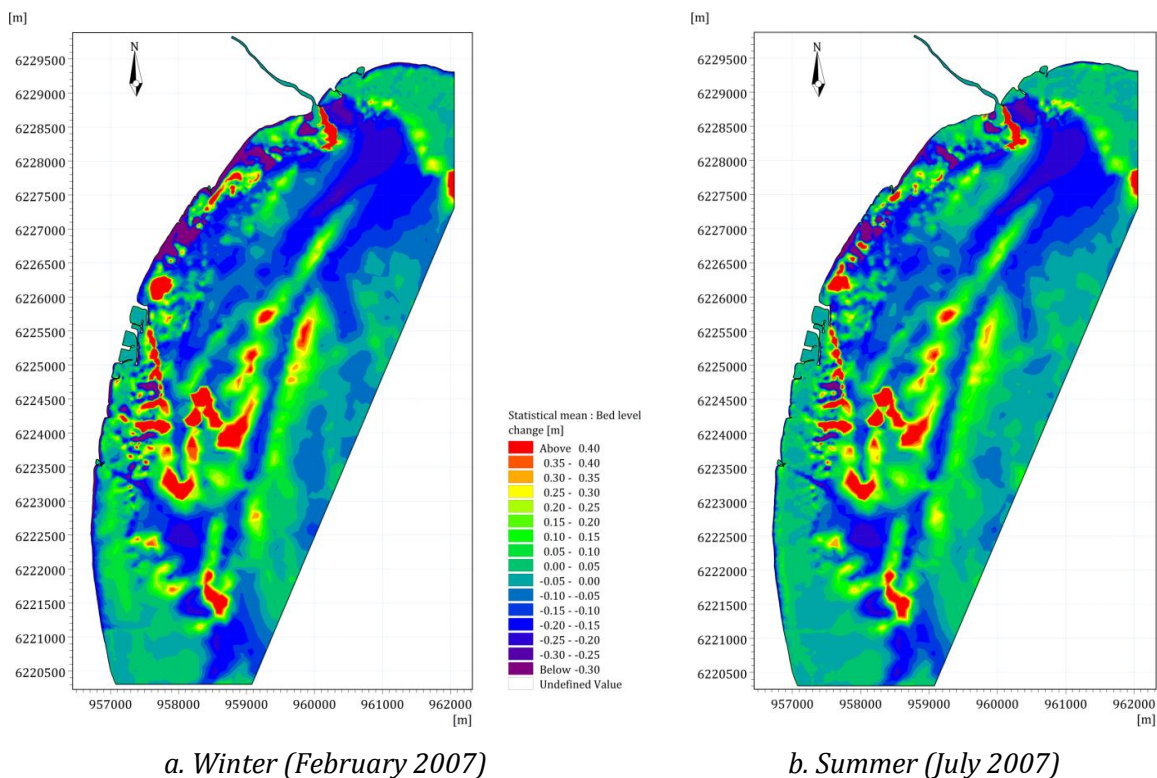


Figure 171. Bed level change in the study area under the impact of seasonal variation without Posidonia.

Figure 172 and Figure 173 show the beach profile evolution of the central Ceinturon beach and Bona beach when Posidonia totally disappears in the study area, respectively. It verifies that beach profile in the winter is mostly eroded more severely than that in the summer without distinction of places. At Ceinturon beach, the entire of beach profile is eroded severely from the shoreline to offshore. Meantime, the beach profile of Bona beach is mainly altered in offshore zone.

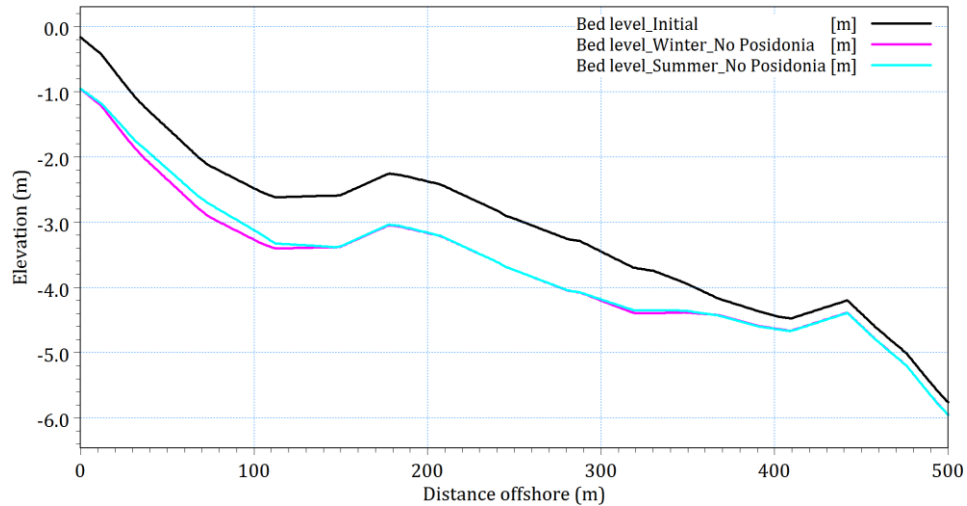


Figure 172. Beach profile evolution at Central Ceinturon beach under the impact of seasonal variation without Posidonia.

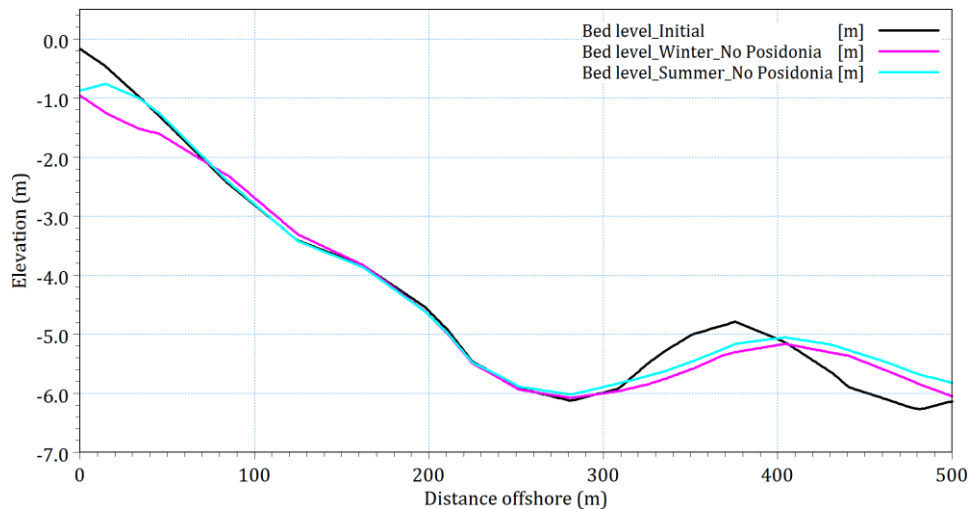
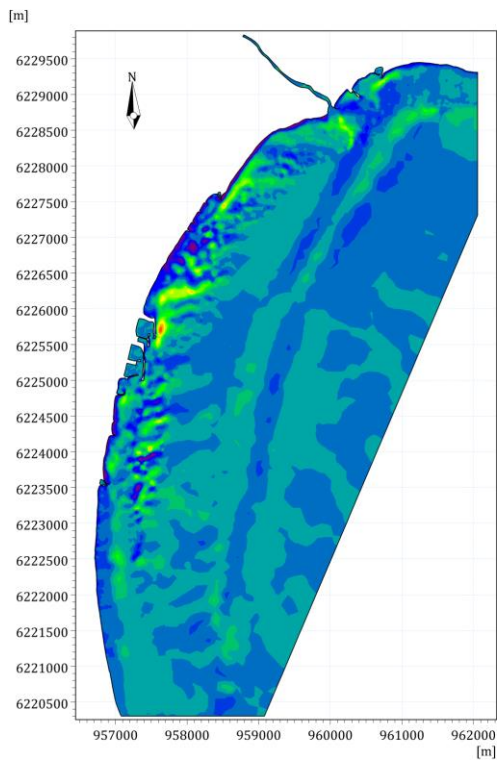
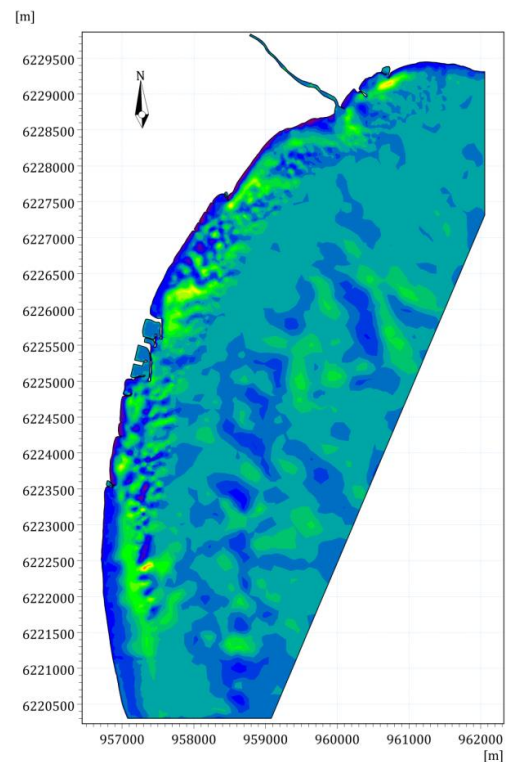


Figure 173. Beach profile evolution at Bona beach under the impact of seasonal variation without Posidonia.

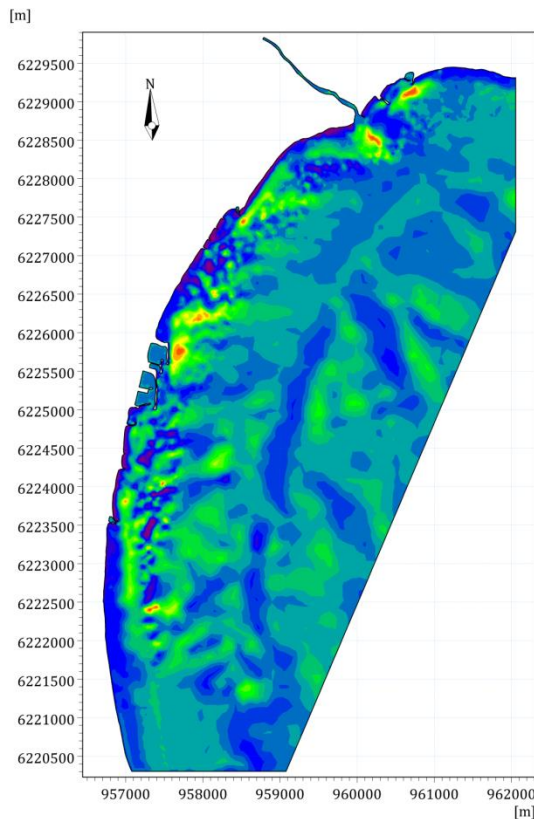
The extreme events combined with the disappearance of Posidonia boost the bed level change in the study area (Figure 174). The eroded areas at Ceinturon beach and the right south of Gapeau river mouth are enlarged, while the accreted areas at the mouth of Gapeau river, the upstream of Hyères port and the seaward side of Bona beaches are also developed in company with the increase of stormy level. As a result, the erosion thickness at the water depth of 1.5 m in the front of Ceinturon is increased by 19.46%-237.8%, compared with the case of Posidonia (Table 51). On the other hand, the erosion thickness at Bona beach is mostly decreased by 22.74%-48.88%.



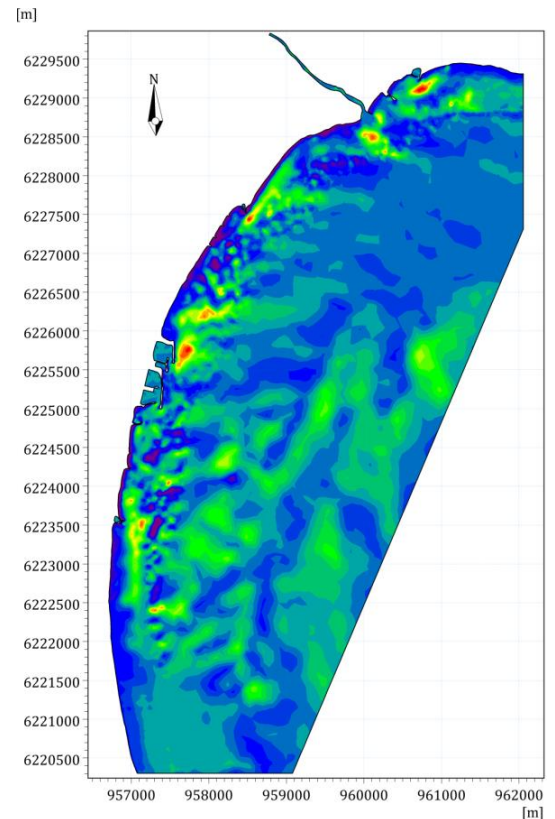
a. Decadal storm



b. Tri-Decadal storm



c. Semi-Centennial storm



d. Centennial storm

Figure 174. Bed level change in the study area under the impact of variation of storm scale without Posidonia.

The disappearance of Posidonia and the impact of the storms trigger the change of beach profile. Figure 175 and Figure 176 illustrate the post-storm beach evolution at Ceinturon beach and Bona beach when Posidonia is not taken into account, respectively. It is noticeable that the beach profiles at two beaches are changed not only in nearshore zones but also in offshore zones, especially in Bona beach. The largest beach profile change is due to the impact of the centennial storm. This storm may induce the erosion of about 2 m close to the shoreline.

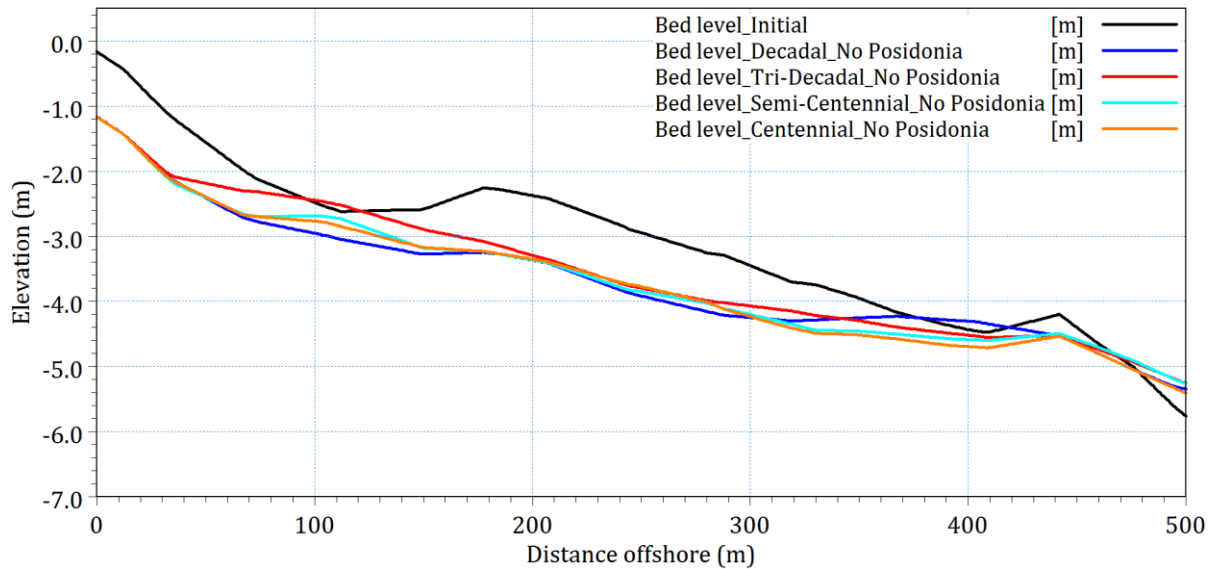


Figure 175. Beach profile evolution at Central Ceinturon beach under the impact of variation of storm scale without Posidonia.

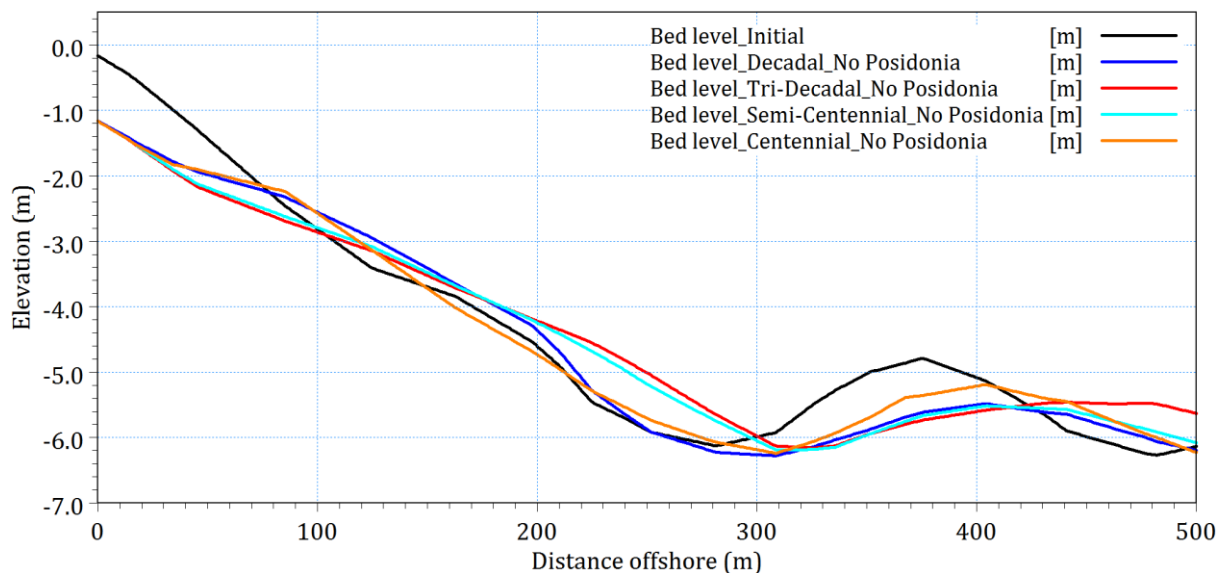


Figure 176. Beach profile evolution at Bona beach under the impact of variation of storm scale without Posidonia.

5.6.5. Effect of SLR on hydrodynamics and sediment transport

5.6.5.1. Effects of SLR on waves

With confidence that the numerical model was successfully reproducing the hydrodynamics and sediment dynamics under real conditions (mean sea level = +0.39 m from March to April, 2009 and from November 2007 to November 2008), mean sea level was then elevated +0.5, +1.3, 1.35, 1.5, and 1.85 m, respectively, to investigate the influence of SLR on waves along the eastern branch of Giens tombolo. Consequently, the five sets of forcing conditions, 5 different no SLR conditions (Table 32) and 5 different SLR scenarios (Table 33) result in 14 different model runs.

The coastal morphology of the eastern Giens tombolo is influenced by three main wind directions, viz. northeast, east and southeast. The change of wind direction accompanied with the SLR phenomenon can provoke the significant modification of wave field. It is clearly seen that the northeast winds cause the highest waves in the offshore zone of Bona beach (Figure 177), whereas the east winds play the most important role in generating the highest waves in the offshore zone of Ceinturon beach (Figure 178), regardless of SLR. However, the wave heights decrease gradually when they approach the shallow water areas and are dissipated by the bottom friction. In surf zones, the northeast winds generate the highest waves in both the Bona and Ceinturon beaches. The mean significant wave heights, H_s , found at the water depth of 1.5 m near Ceinturon and Bona beaches are about 0.682 m and 0.622 m, respectively (Table 52). In addition to generating the highest waves, the northeast winds also induce a raise of the components of radiation stress i.e. S_{xx} , S_{yy} and S_{xy} (Table 52). When the sea level rises, deeper water areas enable larger waves to reach and break closer to the shoreline, resulting in greater wave heights in nearshore zones. Indeed, the mean wave heights near Bona and Ceinturon beach are increased by 1.18%-2.86% and 1.34%-2.41%, respectively (Table 52). The eastern winds induced the largest increase of wave height up to 2.41% at Ceinturon beach, while the wave heights at Bona are augmented to the maximum value of 2.86% by northeastern winds, compared with the other wind directions. Moreover, Figure 177 also reveals that the location of maximum wave breaking moved landward, especially with southeast winds. As sea level increased, the propagation of larger waves over the shallow waters resulted in the higher radiation stresses. These stresses are boosted by 1%-5% at Ceinturon and Bona beaches when sea level rises about 11 cm, regardless of wind direction (Table 52).

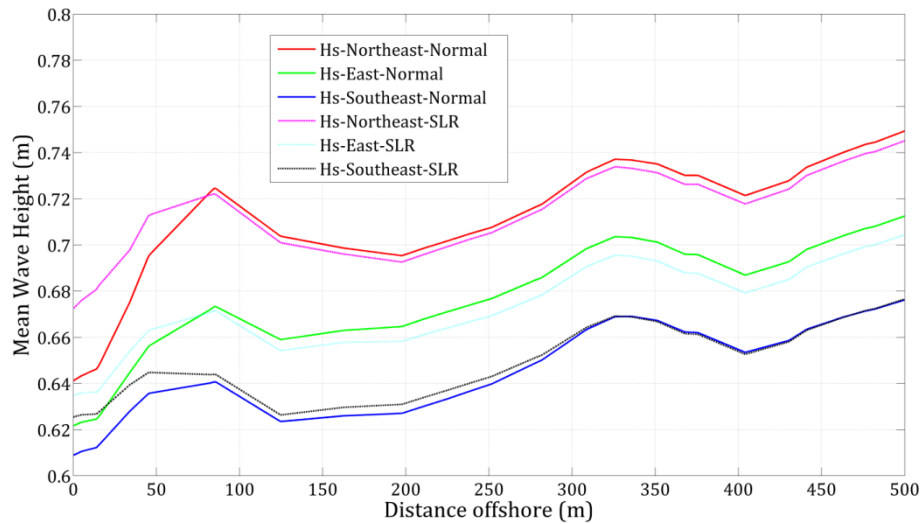


Figure 177. Modeled cross-shore variations in wave heights under the impact of SLR and variation of wind direction at Bona beach.

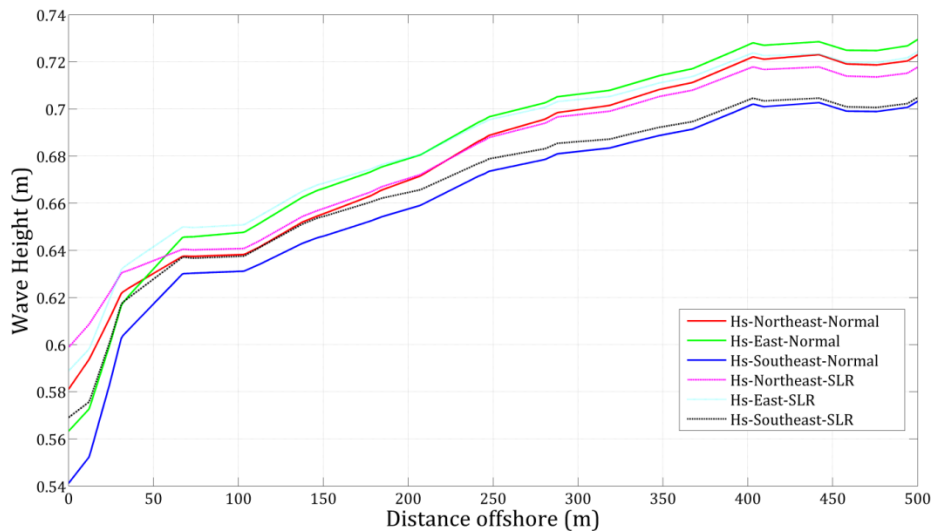


Figure 178. Modeled cross-shore variations in wave heights under the impact of SLR and variation of wind direction at Ceinturon beach.

There are many extreme events, viz. storms and rough seas occurring in the winter and attacking the Giens tombolo. They are one of the main factors causing the coastal erosion along the eastern branch of Giens tombolo (Capanni, 2011). A temporary increase of local sea level (storm surges) induced by the storms are accompanied by SLR due to climate change so that severe storm waves are able attack higher elevations of the beach and coastal erosion problem will become exacerbated in vulnerable coastal areas (Devoy, 2008). Therefore, the impact of extreme events, viz. decadal, tri-decadal, semi-centennial and centennial storms, needs to be also investigated in the study area. Figure 179 and Figure 180 depict the simulated cross-shore variations in wave heights at Bona and Ceinturon beaches under the influence of different storms as well as SLR. It is noticeable that the higher level of storm causes the larger and stronger impacts on wave fields, regardless of SLR. Particularly, the mean significant wave height without SLR increases from 0.94 m in decadal storm to 1.25 m in centennial storm at Ceinturon

beach, whereas this height increases from 1.08 m in decadal storm to 1.51 m in centennial storm at Bona beach. It also reveals that Bona beach is attacked by higher waves than Ceinturon beach in the same storm. Greater water depths due to storm surges in company with SLR would reduce bottom friction and increase water depth relative to the wave height, resulting in larger and more energetic waves that could reach the beaches (Vu et al., 2018). As a result, the nearshore significant wave height is intensified by 7.65%-11.23% at Ceinturon beach and by 8.41%-14.96% at Bona beach. When SLR occurs along with storms, an increase in wave heights would generate a corresponding raise of radiation stresses. The radiation stresses are boosted by 13.31%-24.07% at Ceinturon beach and by 2.64%-31.05% at Bona beach, compared with those cases without SLR. In the condition of centennial storm, the radiation stresses increased to the relative minima probably due to the sharply increase of water volume, as a result of the submergence of the shore.

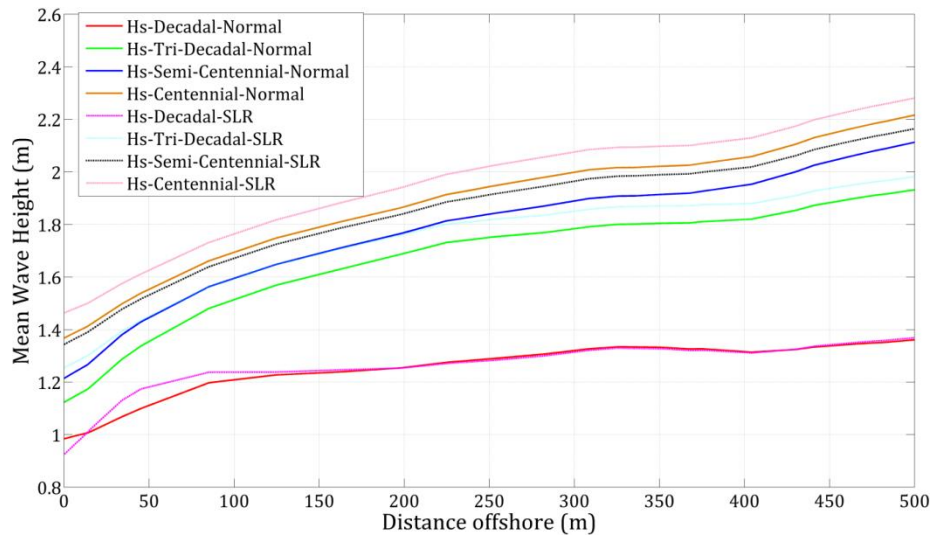


Figure 179. Modeled cross-shore variations in wave heights under the impact of SLR and variation of storm scale at Bona beach.

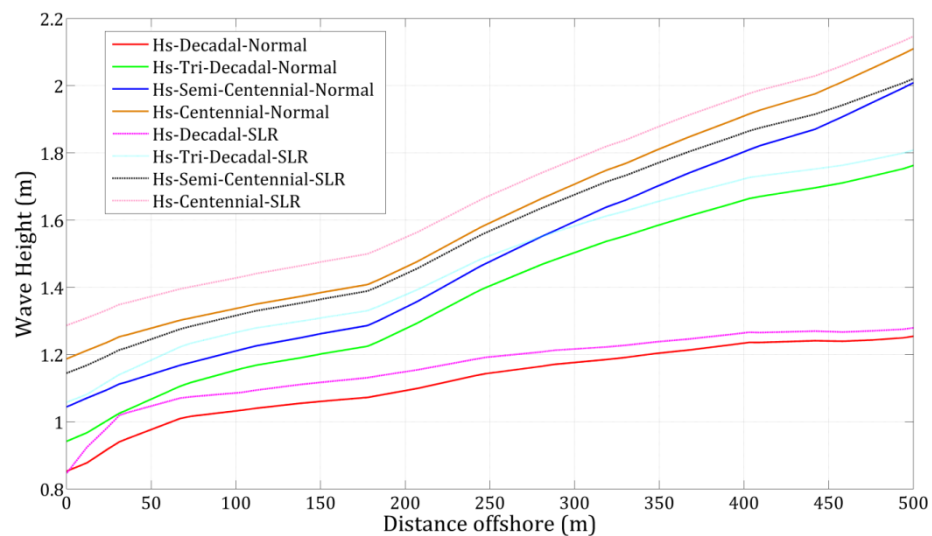


Figure 180. Modeled cross-shore variations in wave heights under the impact of SLR and variation of storm scale at Ceinturon beach.

Table 52. Effect of SLR on hydrodynamic fields and sediment transport.

Scenario		Ceinturon beach						Bona beach					
		H _s (m)	S _{xx} (m ³ /s ²)	S _{xy} (m ³ /s ²)	S _{yy} (m ³ /s ²)	V _c (m/s)	Q (m ³ /s/m)	H _s (m)	S _{xx} (m ³ /s ²)	S _{xy} (m ³ /s ²)	S _{yy} (m ³ /s ²)	V _c (m/s)	Q (m ³ /s/m)
Normal condition	NE	0.622	0.232	-0.064	0.158	0.128	5.05E-05	0.682	0.337	-0.026	0.152	0.103	5.24E-05
	E	0.618	0.228	-0.064	0.155	0.081	3.12E-05	0.649	0.306	-0.028	0.140	0.163	7.35E-05
	SE	0.604	0.216	-0.061	0.147	0.081	3.88E-05	0.631	0.289	-0.029	0.132	0.171	7.57E-05
	Decadal	0.941	0.505	-0.131	0.322	0.164	2.05E-04	1.079	0.803	-0.061	0.352	0.242	4.47E-04
	Tri-Decadal	1.027	0.566	-0.149	0.360	0.276	3.73E-04	1.304	1.110	-0.070	0.462	0.205	5.68E-04
	Semi-Centennial	1.113	0.648	-0.157	0.380	0.360	6.97E-04	1.393	1.234	-0.050	0.487	0.062	3.99E-04
	Centennial	1.254	0.806	-0.191	0.461	0.371	7.98E-04	1.512	1.412	-0.069	0.563	0.054	4.63E-04
SLR	NE	0.631	0.237	-0.065	0.161	0.130	4.93E-05	0.702	0.354	-0.026	0.159	0.081	4.47E-05
	E	0.633	0.237	-0.066	0.161	0.085	3.48E-05	0.656	0.311	-0.028	0.142	0.133	5.79E-05
	SE	0.618	0.227	-0.064	0.155	0.064	2.90E-05	0.641	0.296	-0.029	0.137	0.154	6.60E-05
	Decadal	1.020	0.596	-0.157	0.383	0.128	1.81E-04	1.141	0.923	-0.063	0.389	0.049	1.84E-04
	Tri-Decadal	1.142	0.703	-0.180	0.433	0.251	3.54E-04	1.404	1.264	-0.083	0.529	0.184	5.27E-04
	Semi-Centennial	1.215	0.766	-0.193	0.461	0.313	5.56E-04	1.487	1.374	-0.066	0.556	0.071	4.59E-04
	Centennial	1.350	0.920	-0.219	0.522	0.330	6.74E-04	1.584	1.531	-0.087	0.620	0.056	5.18E-04
Difference (%)	NE	1.34	2.11	1.88	2.06	2.09	-2.49	2.86	4.97	1.03	4.36	-24.0	-14.63
	E	2.41	4.22	3.38	3.53	4.35	11.35	1.18	1.83	-1.41	1.66	-18.4	-21.15
	SE	2.35	4.83	4.66	4.99	-21.0	-25.13	1.61	2.64	0.21	3.34	-9.87	-12.83
	Decadal	8.36	18.04	19.71	18.93	-22.0	-11.42	5.82	14.96	2.64	10.31	-79.8	-58.89
	Tri-Decadal	11.23	24.07	20.3	20.43	-9.16	-5.35	7.65	13.91	19.6	14.5	-10.4	-7.25
	Semi-Centennial	9.12	18.19	22.48	21.29	-13.3	-20.35	6.78	11.35	31.05	14.09	15.24	15.2
	Centennial	7.65	14.19	14.49	13.31	-10.9	-15.57	4.8	8.41	25.68	10.23	4.18	11.86

5.6.5.2. Effects of SLR on currents

Figure 181 and Figure 182 present the modeled cross-shore variations in current speed (V_c) at Bona and Ceinturon beaches, respectively, caused by different wind directions, viz. northeast, east and southeast winds, and by different sea levels. In the normal sea-level conditions without SLR, the northeast winds have the strongest impacts on the offshore current speed along the eastern Giens tombolo. Nevertheless, in the surf zone, the influence of winds on the beaches is altered by the position of these beaches and the bathymetry of seabed. Particularly, the highest mean current speed of 0.128 m/s at the water depth of 1.5 m at Ceinturon beach generated by the northeastern winds is higher than other winds about 58%. Conversely, the eastern and southeastern winds induce the stronger currents than the northeastern winds about 58%-66% (Table 52). The main reason of this difference maybe comes from the presence of breakwaters of Hyères port. The longshore currents induced by the northeastern winds move along the coast from Salins beach to Hyères port, then they have to change the direction and flow seaward after meeting with the breakwaters of Hyères port (Courtaud, 2000). As a result, the speed of these currents are reduced much more when reaching Bona beach right in the lee side of the structures, whereas the currents generated by the eastern and southeastern winds easily approach this beach without any obstacles. The highest current speed induced by the southeastern winds and the largest waves generated by the northeastern winds at Bona beach also reveal that the nearshore currents are mainly governed by the wind and the wave only plays a secondary role in the development of these currents. When sea level rises, the offshore currents (from 150 m seaward of the shoreline to offshore) are stronger than those in the cases of normal sea-level conditions. On the other hand, in the surf zone, the nearshore currents in the normal sea-level conditions are higher than those taking into account the impacts of SLR. For instance, the current speed at the water depth of 1.5 m near Bona beach is reduced by 9.87%-24% when sea level rises. At Ceinturon, the current speed induced by the southeastern winds is decreased to 21% by SLR. This reduction in the current speed would be results in the local water volume expansion, the extensive submergence of low-lying areas as well as the enlargement of river estuaries. Both the SLR and the normal sea-level conditions, it is easily seen that the current speed is suddenly decreased from 100 m seaward of the shoreline to 300 m seaward of the shoreline at Bona beach and from 50 m seaward of the shoreline to 150 m seaward of the shoreline at Ceinturon beach before sharply increasing close to the shoreline, regardless of wind direction. The swift reduction in the current speed at these positions would be caused by the presence of sand bars and troughs (Figure 145 and Figure 190). The incoming waves break when they pass over the sand bars. Subsequently, the presence of troughs causes the decrease of wave-induced radiation stresses, as a result of increased water depth. When the breaking waves approach the shore accompanied with the decreased water

depth, the radiation stresses are intensified again. This results in the sharply increase of current speed close to the shore.

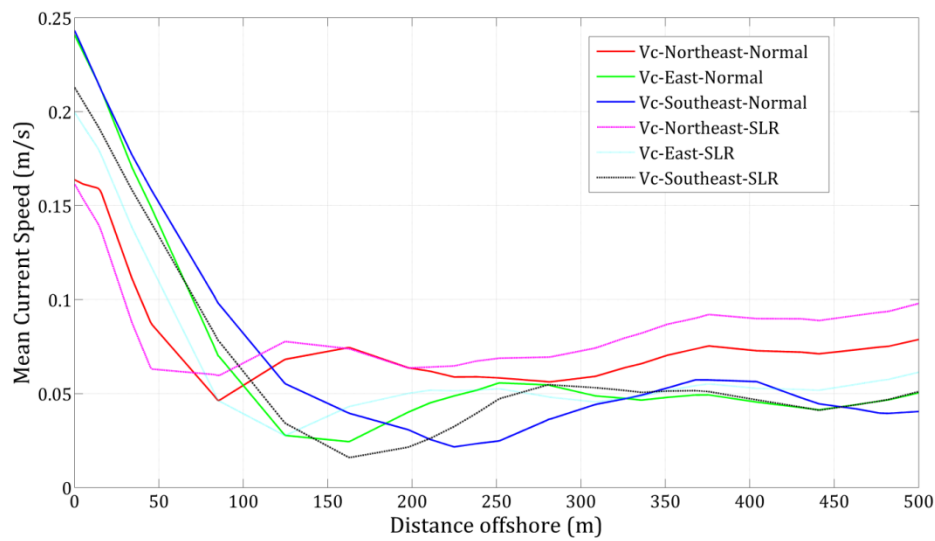


Figure 181. Modeled cross-shore variations in current speed under the impact of SLR and variation of wind direction at Bona beach.

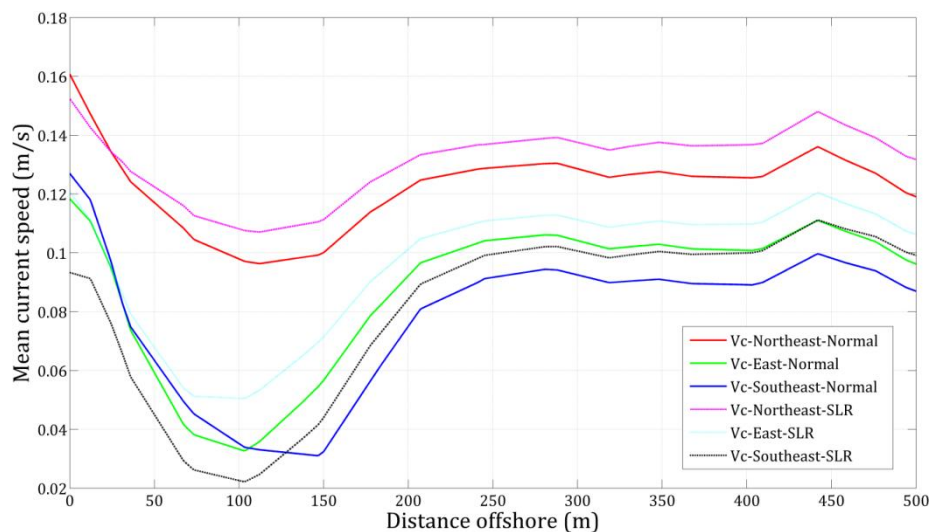


Figure 182. Modeled cross-shore variations in current speed under the impact of SLR and variation of wind direction at Ceinturon beach.

The impacts of decadal storm, tri-decadal storm, semi-centennial storm and centennial storm, along with SLR on the modeled cross-shore variations in current speed at Bona and Ceinturon beaches are illustrated in Figure 183 and Figure 184, respectively. It is noted that the higher level of storm causes the larger current speed at Ceinturon beach, but results in the smaller current speed at Bona beach in the cases without SLR. Specifically, the current speed of 0.128 m/s at the water depth of 1.5 m near Ceinturon beach in the decadal storm condition is increased up to 0.33 m/s in the centennial storm condition. On the other hand, at the same water depth in Bona beach, the current speed is decreased from 0.242 m/s in the decadal storm to 0.054m/s in the centennial storm (Table 52). In offshore zone of both Bona and Ceinturon beaches, from 150 m seaward of the shoreline, the higher level of storm generates the stronger

current, regardless of SLR. At Ceinturon beach, although the current speed is reduced generally, the strong storms still induce the high nearshore current speeds (Figure 184). However, this comment is completely changeable for the nearshore currents at Bona beach, from the shoreline to 150 m seaward of the shoreline (Figure 183). All currents induced by the storms are boosted in the speed when they flow near shore. The decadal and tri-decadal storms generated the highest current speeds close to the shoreline. As SLR, most of current speeds influenced by the storms are decreased by 9.16%-22% at Ceinturon beach and by 10.4%-79.8% at Bona beach. Apart from the cases of the semi-centennial and the centennial storms, the current speed at the water depth of 1.5 m near Bona beach is increased to 15.24% and 4.18%, respectively (Table 52).

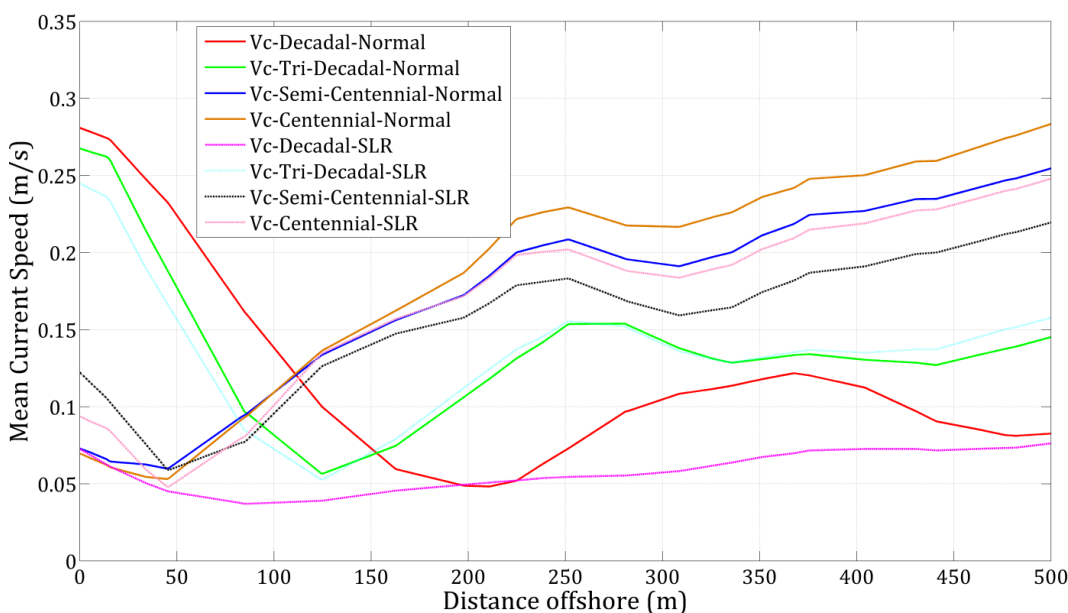


Figure 183. Modeled cross-shore variations in current speed under the impact of SLR and variation of storm scale at Bona beach.

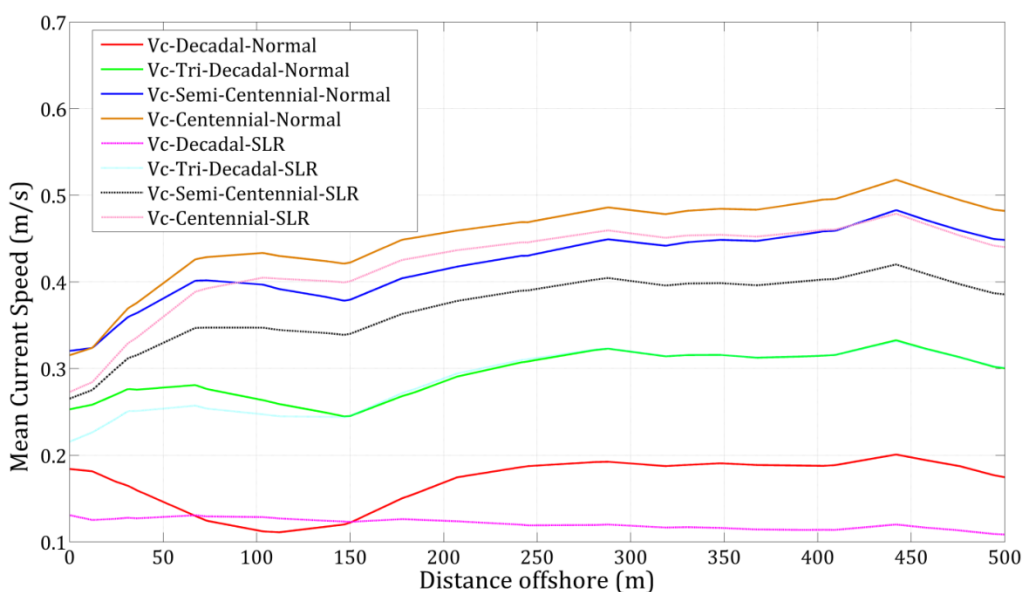


Figure 184. Modeled cross-shore variations in current speed under the impact of SLR and variation of storm scale at Ceinturon beach.

5.6.5.3. Effects of SLR on sediment dynamics

Similar to the study of hydrodynamics, the effect of SLR on sediment transport rates (Q) was investigated by elevating the mean sea level (+0.5, +1.3, 1.35, 1.5, and 1.85 m). Figure 185 and Figure 186 plot the modeled cross-shore variations in the sediment transport rates under the impacts of northeast, east, and southeast winds as well as SLR. It reveals that the higher wave-induced radiation stresses and current speeds (Figure 181 and Figure 182) close to shore resulted in a narrow band of sediment transport concentrations along the shoreline. From 150 m seaward of the shoreline to offshore, the northeast winds always have the strongest impact on the sediment transport rates, regardless of SLR. They induced the highest sediment transport rates at the cross-shores of both Bona and Ceinturon beaches. The northeast winds continuously dominated the sediment transport from the shoreline to 150 m seaward of the shoreline at Ceinturon beach. The highest total load of over $5 \times 10^{-5} \text{ m}^3/\text{s}/\text{m}$ induced by these winds is also reported near shore. By contrast, the southeast winds induced the highest sediment transport rate of about $9 \times 10^{-5} \text{ m}^3/\text{s}/\text{m}$ occurring close to the shoreline of Bona beach. In addition, the northeast winds generated the lower total load, compared with the other wind directions. This pattern of the sediment transport rates mostly depends on the current speed distribution (Figure 181). As SLR, the sediment transport rates are decreased from the shoreline to 150 m seaward of the shoreline, but intensified from 150 m seaward of the shoreline to offshore in both Bona and Ceinturon beaches, regardless of wind direction. Particularly, at the water depth of 1.5 m, the total load is decreased by 12.83%-21.15% in Bona beach and by 2.49%-25.13% in Ceinturon beach probably due to the reduction in nearshore current speed when taking into account the SLR phenomenon.

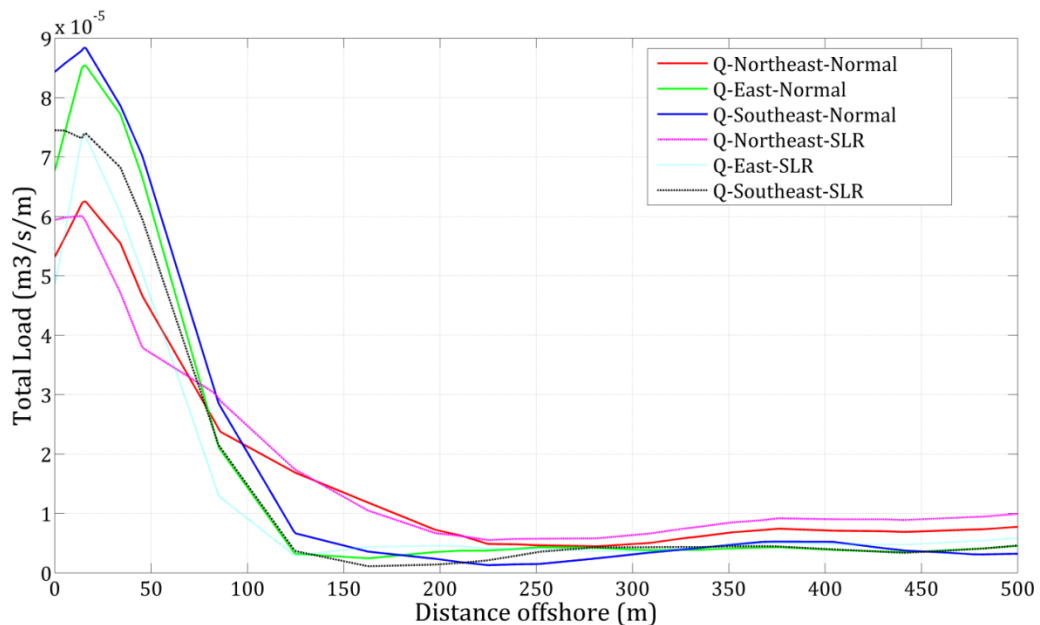


Figure 185. Modeled cross-shore variations in sediment transport rates under the impact of SLR and variation of wind direction at Bona beach.

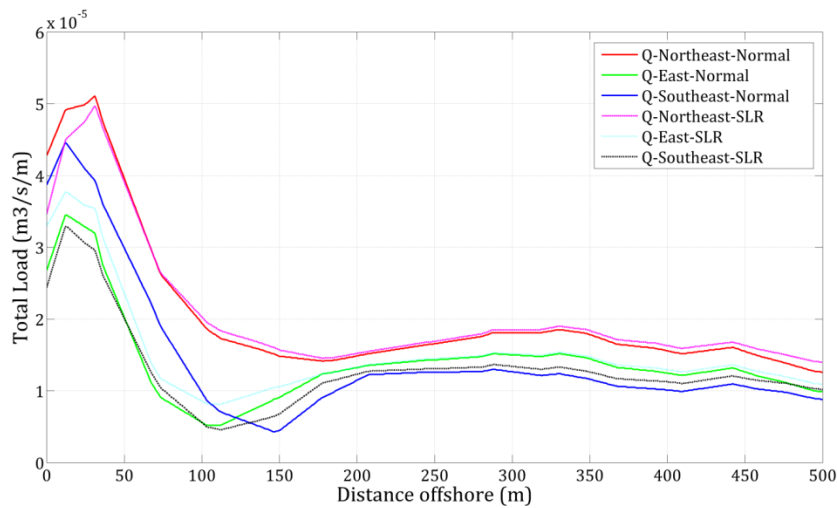


Figure 186. Modeled cross-shore variations in sediment transport rates under the impact of SLR and variation of wind direction at Ceinturon beach.

The storms greatly affect the sediment transport along the eastern Giens tombolo. As the sea level rises in tandem with the occurrence of greater and more frequent storms, more wave energy propagated to the shoreline, resulting in a greater energy transfer, higher radiation stresses, and higher sediment transport rates. The high sediment transport rates occur from 100 m seaward of the shoreline to 250 m seaward of the shoreline at Bona beach, whereas the high rates are normally observed from 50 m to 150 m seaward of the shoreline of Ceinturon beach, regardless of SLR. The maximum sediment transport rate of over $1.1 \times 10^{-3} \text{ m}^3/\text{s}/\text{m}$ was induced by the centennial storm at both two beaches. The current speed plays a decisive role in the sediment transport along the eastern Giens tombolo. Indeed, when sea level rises, the decrease of current speed results in the reduction in the total load at Ceinturon beach. The total load is dropped off by 5.35%-20.35% if SLR is taken into account (Table 52). On the other hand, the sediment transport rate is decreased in the decadal and tri-decadal storm conditions, but increased by 11.86%-15.2% under the impact of semi-centennial and centennial storms accompanied with SLR.

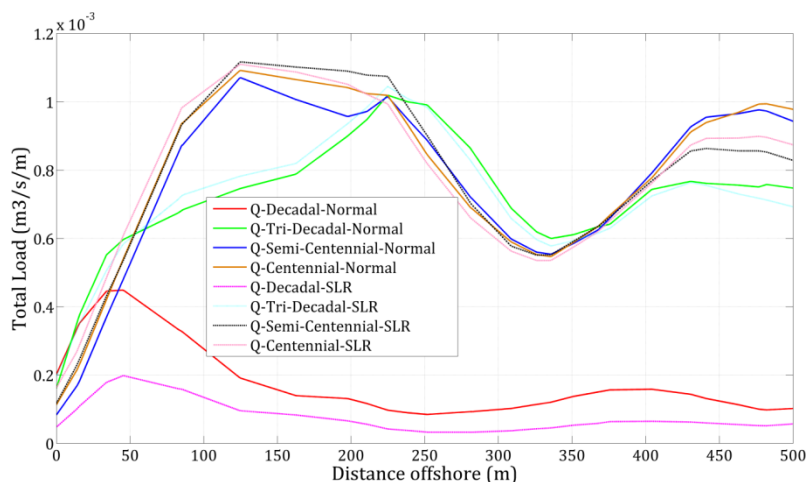


Figure 187. Modeled cross-shore variations in sediment transport rates under the impact of SLR and variation of storm scale at Bona beach.

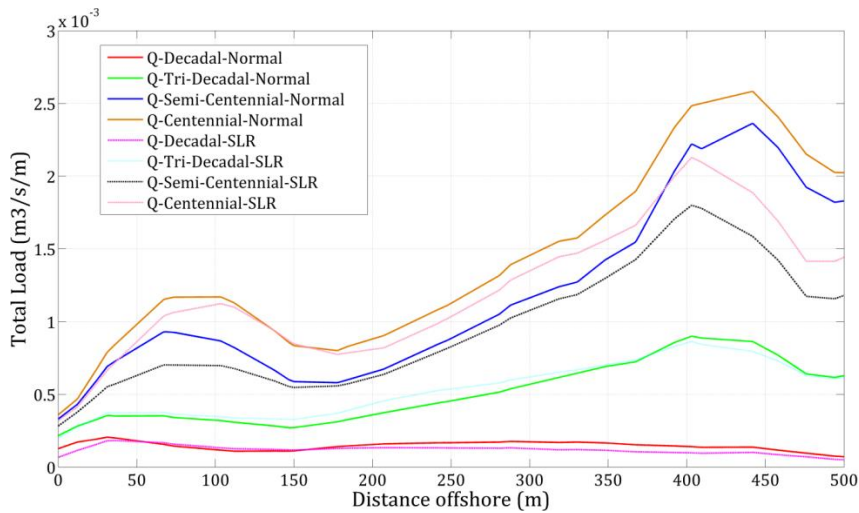


Figure 188. Modeled cross-shore variations in sediment transport rates under the impact of SLR and variation of storm scale at Ceinturon beach.

As a result of SLR, the river mouth and estuaries will tend to enlarge and the speed of fluvial currents will be also reduced by further intrusion of sea currents into inland, hence the sediment is deposited right in the river mouth and estuaries (Komar, 1998). This leads to the shortage of sediment in downstream zones. An accelerated SLR with this low rate of sediment supply is likely to trigger erosion on shorelines. In order to visualize the impact of the wind directions as well as SLR on the bed level change, the beach profiles at Ceinturon beach and Bona beach are extracted and exhibited in Figure 145 and Figure 190. It is clearly seen that the bed level changes commonly occur from the shoreline to a level of -2.5 m at Ceinturon beach and to a level of -5.0 m at Bona beach, regardless of wind direction and SLR. Additionally, the largest beach profile change at both Ceinturon and Bona beaches is triggered by the northeast winds. When sea level rises, the nearshore beach profile is eroded deeper than the normal sea-level cases. It may be due to the impact of the higher waves and higher radiation stresses generating the stronger cross-shore currents, which extract sediment and put into suspension by the waves and carried offshore.

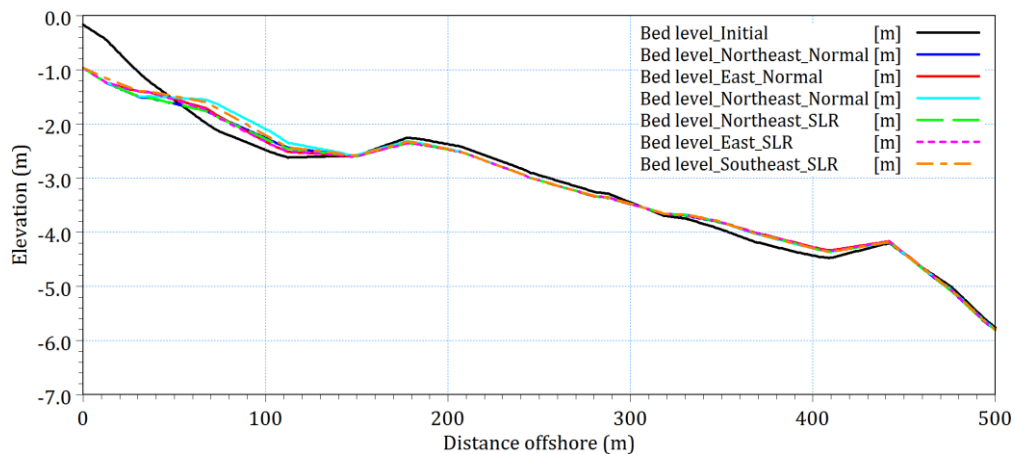


Figure 189. Beach profile evolution at the central Ceinturon beach under the impact of SLR and variation of wind direction.

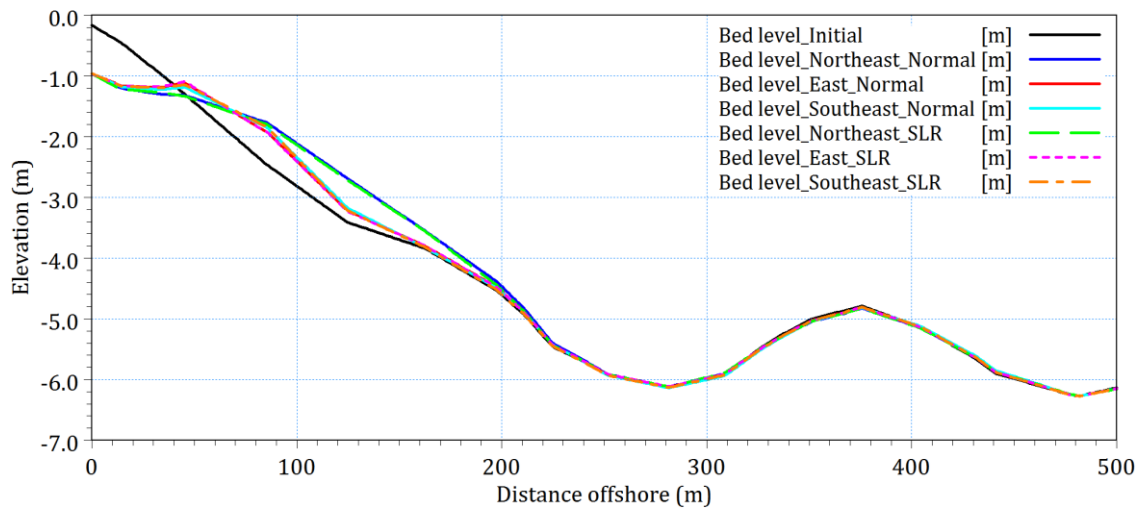


Figure 190. Beach profile evolution at Bona beach under the impact of SLR and variation of wind direction.

The storms along with SLR exacerbate the coastal erosion problem at Bona and Ceinturon beaches. At Ceinturon beach, the beach profile changes only concentrate from the shoreline to 150 m seaward of the shoreline (Figure 157), while these changes extend up to 330 m seaward of the Bona shoreline (Figure 192), regardless of SLR. The storms induce the high waves, which extract sediment near shoreline and carry them offshore. The presence of SLR provokes the coastal erosion more severely than that in the No SLR scenarios, especially in nearshore zones in both two beaches. It is noticeable that the higher level of storm causes the more serious erosion. Additionally, the erosive mode at Bona beach is more severe than that at Ceinturon beach. The eroded area extends from the shoreline to 4.5 m depth offshore at Bona beach. The main reasons may be that its location is exposed to the storm waves and so the higher waves can easily reach to this beach. At the same water depth of 1.5 m, the wave heights observed at Bona beach are larger than those at Ceinturon about 14.67%-26.97% without SLR and about 11.86%-22.94% with SLR.

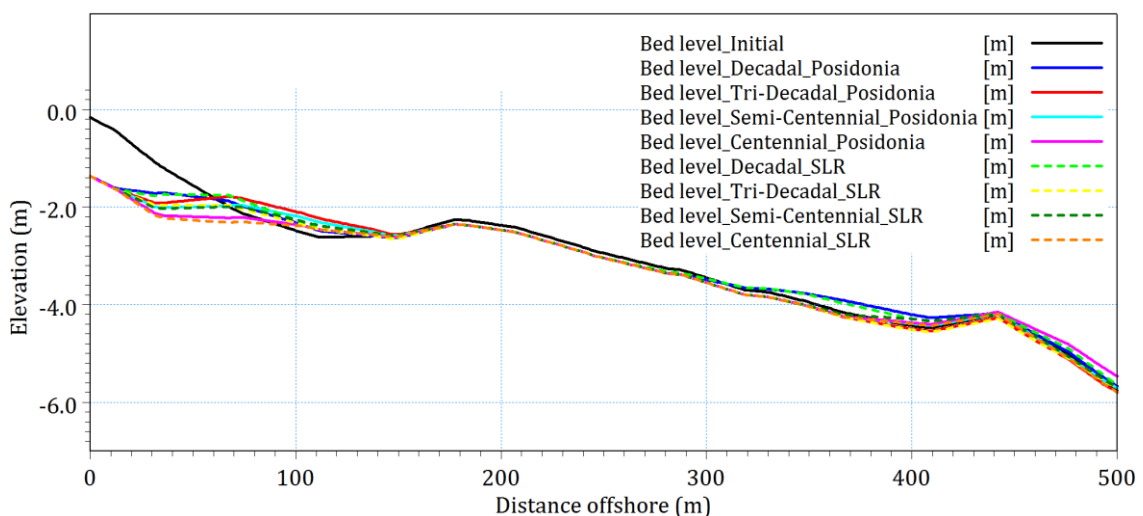


Figure 191. Beach profile evolution at the central Ceinturon beach under the impact of SLR and variation of storm scale.

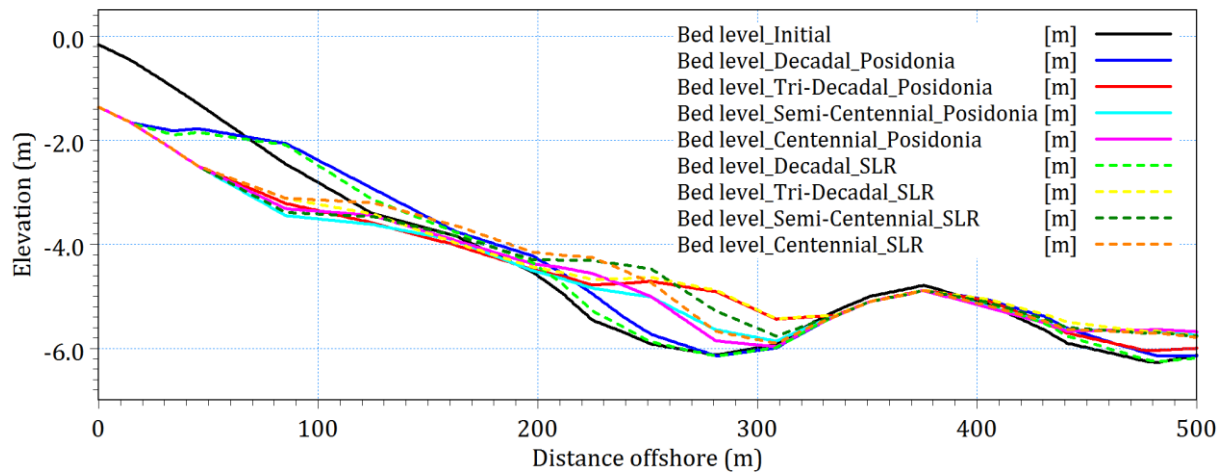


Figure 192. Beach profile evolution at Bona beach under the impact of SLR and variation of storm scale.

5.6.6. Effect of beach nourishment on hydrodynamics and sediment transport

5.6.6.1. Determining the design parameters of beach nourishment

a. Design wave data

There are no nearshore wave stations in the study area. Thus, in order to provide nearshore wave data for beach nourishment works in Bona and Ceinturon beaches, the wave and hydrodynamic numerical simulations of the regional scale were carried out during the period of 35 years from 1981 to 2015. The nearshore wave data at the water depth of 10 m in front of Ceinturon and Bona beaches were extracted and summarized in Table 53 and Table 54. It is clearly seen that the southeastern waves are dominant and has the largest impact on the beach evolution of both Bona and Ceinturon beaches. Moreover, more half of wave numbers approaching these two beaches is less than 0.3 m.

Table 53. Average percentage frequency of occurrence of significant wave height-direction offshore Ceinturon beach.

Direction	Significant wave height (m)								Total (%)
	0.1	0.3	0.6	0.9	1.2	1.5	1.8	2.0	
N	0.35	0.59	0.05	0	0	0	0	0	0.99
NE	0.76	1.67	0.75	0.02	0	0	0	0	3.21
E	0.42	0.39	0.18	0.02	0	0	0	0	1.01
SEE	0.9	3.7	7.08	3.01	0.96	0.18	0.01	0	15.84
SE	5.36	17.59	15.39	6.02	1.96	0.23	0.07	0.004	46.62
S	4.92	5.84	1.1	0.02	0	0	0	0	11.88
SW	3.55	4.93	0.27	0	0	0	0	0	8.75
W	2	4.98	0.05	0	0	0	0	0	7.02
NW	1.71	2.93	0.02	0	0	0	0	0	4.67
Total (%)	19.97	42.64	24.89	9.10	2.91	0.41	0.08	0.004	100.00

Table 54. Average percentage frequency of occurrence of significant wave height-direction offshore Bona beach.

Direction	Significant wave height (m)								Total (%)
	0.1	0.3	0.6	0.9	1.2	1.5	1.8	2.0	
N	1.26	1.43	0.214	0	0	0	0	0	2.90
NE	2.46	2.62	0.97	0.02	0	0	0	0	6.08
E	1.13	1.26	0.96	0.20	0.04	0.004	0	0	3.59
SEE	1.96	9.21	15.00	7.28	2.74	0.61	0.08	0.01	36.87
SE	5.43	10.83	4.16	0.68	0.06	0.004	0.01	0	21.18
S	4.27	3.48	0.37	0.004	0	0	0	0	8.12
SW	4.10	2.96	0.06	0	0	0	0	0	7.12
W	3.08	3.86	0.02	0	0	0	0	0	6.96
NW	2.96	4.21	0.02	0	0	0	0	0	7.19
Total (%)	26.63	39.86	21.76	8.19	2.84	0.61	0.09	0.01	100.00

b. Determining the median grain size (D_{50}) of fill material

Ideally, the grain size of the fill material should be the same size or larger than the native beach sand, and with an overfill factor within the range of 1.00 to 1.05. Fills with coarser material provide improved resistance to storm-induced erosion. In addition, a lesser volume of coarser fill will be required to create a beach of a given width, compared to the volume of native beach sand that would be needed. Material that has a smaller diameter than the native sand can remain in equilibrium only at slopes flatter than the existing beach, i.e. the beach nourishment would be expanded offshore. Thus, the volume of material required will be much greater and consequently, more costly. The grain size of nourished sediment is recommended by as U.S.A.C.E (2012):

If native material $D_{50}^N \geq 0.2mm \rightarrow$ fill material $D_{50}^F = \pm 0.02mm + D_{50}^N$.

If native material $D_{50}^N = 0.15mm$ to $0.2mm \rightarrow$ fill material $D_{50}^F > D_{50}^N \pm 0.01mm$.

If native material $D_{50}^N < 0.15mm \rightarrow$ fill material at least $D_{50}^F > D_{50}^N$.

In the study area, use of material finer than the native material should be avoided. Because use of finer sand will produce a gentler beach adjacent to an existing groin or jetty that is intended to block the longshore movement of sand and cause the deficit of sediment downstream. Furthermore, use of finer sand also increases the cross-shore length of nourished beach and sand can cover in the large area of Posidonia seagrass. Consequently, the grain size of sand is selected as shown in Table 55.

Table 55. Sediment characteristics of receiving beach.

Beach	D_{50}^N (mm)	D_{50}^F (mm)	A_N	A_F
Ceinturon	0.25	0.27	0.115	0.119
Bona	0.43	0.45	0.1498	0.153

c. Designing the shape of berm

The berm acts as a protective buffer between upland structures and the water and waves. Thus, the beach berm in front of the dune must be of sufficient width to withstand the erosion associated with the types of storms. The elevation of the constructed berm is usually set at the same elevation as the natural berm, or slightly higher. According to the measurement data of LITTO3D and E.O.L (2010), the elevation of natural berm at Ceinturon and Bona beaches vary from +0.3 m to +1.0 m (CM). In the present work, the design berm elevation can be specified about +1.0 m (CM). Hence, the height of berm, B_b , measured from the mean sea level of $H_{50\%} = +0.39$ m to the berm crest elevation as: $B_b = 1.0 - 0.39 = 0.61$ m.

If the berm in front of the dune is too narrow, the dune can quickly erode, even for relatively frequent storms, and the benefits of the higher dune elevations will be lost. Hence, selection of the design berm width depending on the purpose of the project and is often constrained by factors such as project economics, environmental issues, or local sponsor preferences. Based on the in-situ conditions of the beaches, it is found that the natural berm width ranges from 3 m to 15 m.

The berm slope is most appropriately estimated from profiles that represent a nearby, healthy beach. Alternatively, the slope can be estimated as Table 56.

Table 56. The values of berm slopes according to the grain size (U.S.A.C.E, 2012).

D_{50} (mm)	Upper slope	Lower slope
< 0.2	1:20 – 1:15	1:35 – 1:20
0.2-0.5	1:15 – 1:10	1:20 – 1:15
>0.5	1:10 – 1:7.5	1:15 – 1:10

Based the sediment data and the natural slope of the beaches, the author proposes the berm slope of 1:15 for beach nourishment work.

d. Design cross-section profile shape

Dean (1991) defines three basic types of nourished profiles including intersecting, nonintersecting, and submerged profiles. Figure 193 presents an intersecting profile, where the profile after nourishment intersects the native profile at a depth shallower than the depth of closure; a nonintersecting profile, where the nourished profile does not meet the native profile before closure depth; and a submerged profile, where after equilibrium there is no dry beach. A submerged profile is a special case of a nonintersecting profile, which occurs when insufficient volume is placed to fully developed the underwater equilibrium profile. Dean (1991) proposes the relationship of median grain size, berm width and the depth of closure which can determine the shape of design beach profile as follows:

$$W \left(\frac{A_N}{D_c} \right)^{3/2} + \left(\frac{A_N}{A_F} \right)^{3/2} < 1, \text{ Intersecting profile} \quad (5-5)$$

$$W \left(\frac{A_N}{D_c} \right)^{3/2} + \left(\frac{A_N}{A_F} \right)^{3/2} > 1, \text{ Non-intersecting profile}$$

Where

W is the design berm width;

A_N and A_F are the A parameters for native and fill sands, respectively (Table 55).

According to Equation (5-5), fill sand that is finer than the native material will always produce a nonintersecting profile, whereas fill sand that coarser than native sand may form either an intersecting or a nonintersecting profile.

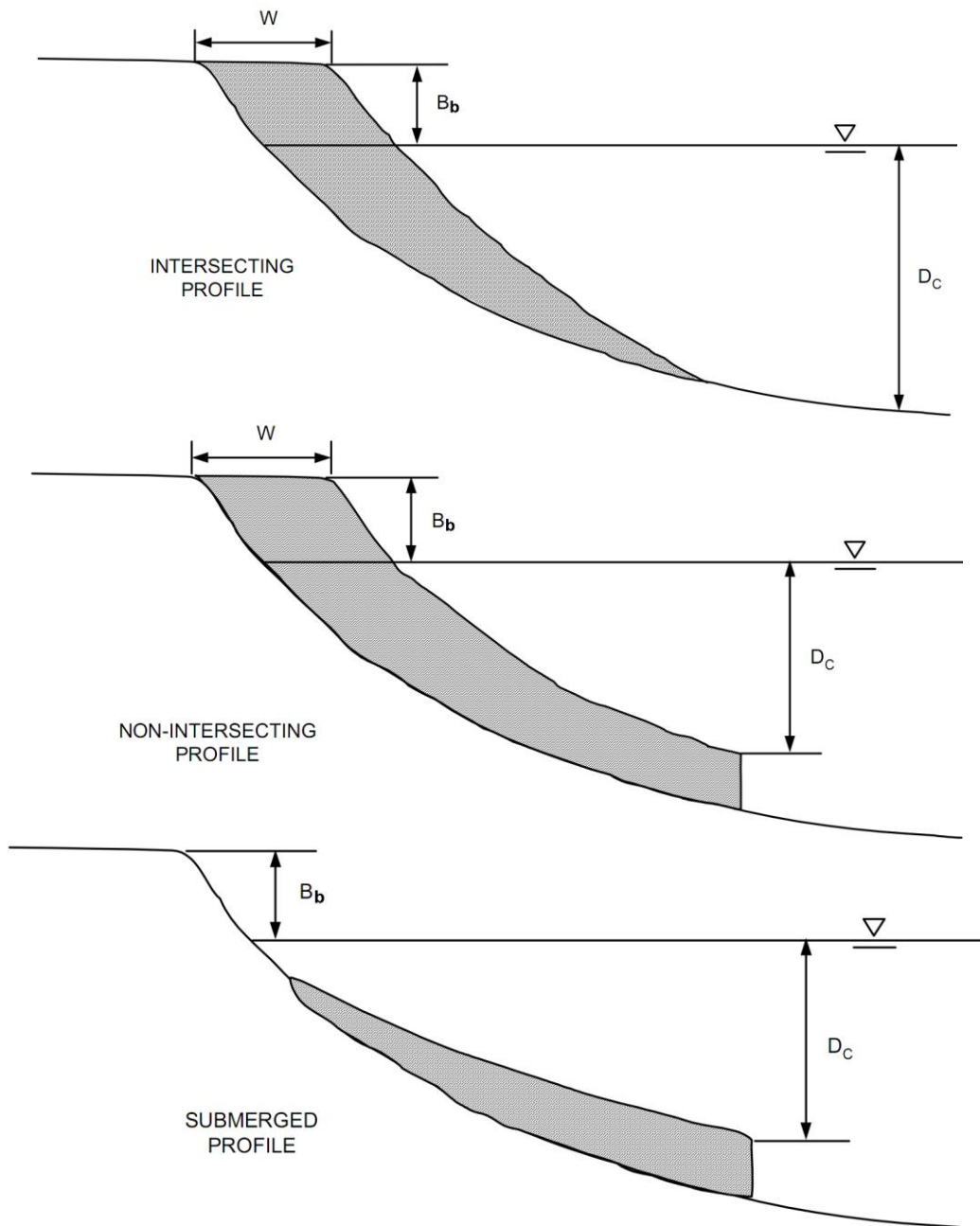


Figure 193. Three basic types of nourishment profiles (Dean, 1991).

In the study area, the fill material resource is limited, so the submerged profile is used to design beach nourishment. After defining the type of beach profile, the design slope of nourished beach need be estimated. The design slope is one of the important characteristics in reducing wave energy on the beach and creates a recreational area for touristic activities. The optimal slopes are primarily a function of the grain size characteristics of the fill and the wave and tide conditions that occur at the site during placement operations. It can be estimated as an average slope computed from the design profile in the elevation range from MLW to a depth below MSL which is approximately equal the typical storm wave height (U.S.A.C.E, 2012). The results of the design slope selection are described in Table 57.

Based on the depth of closure, the equilibrium beach profiles and the actual bathymetry, some representative shapes of beach profile in Ceinturon and Bona are suggested as shown in the following figures.

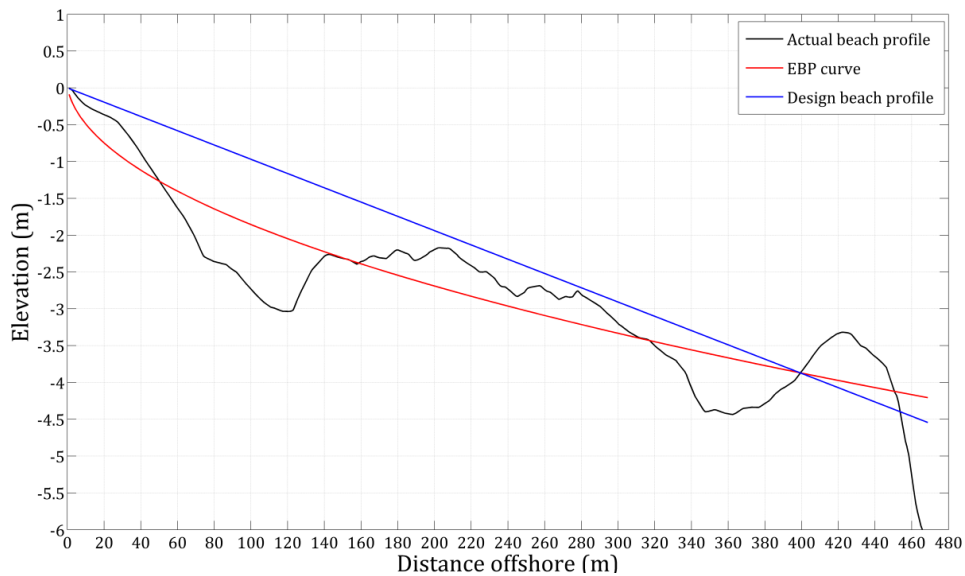


Figure 194. The typical design profile of Ceinturon beach.

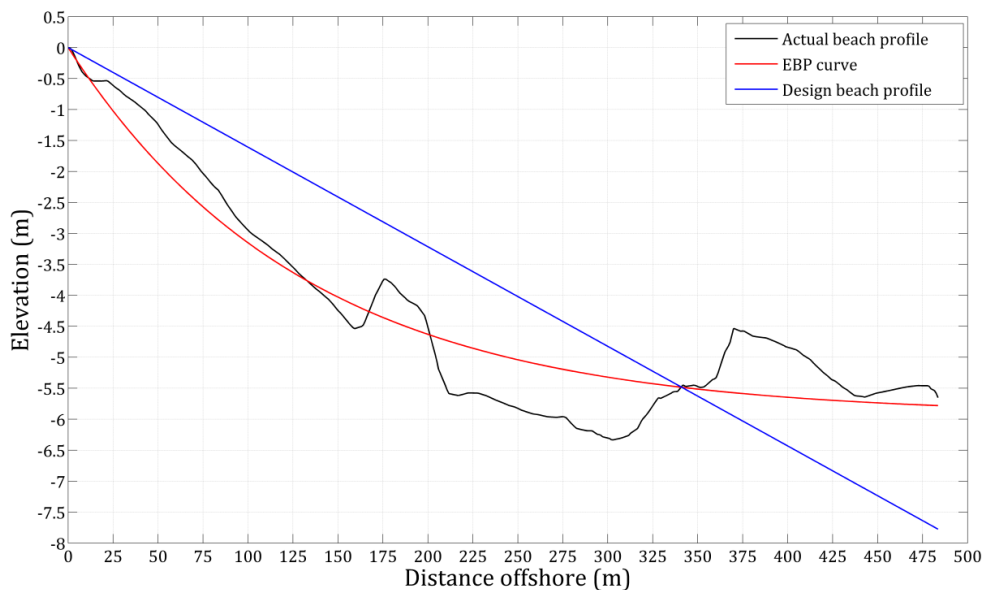


Figure 195. The typical design profile of Bona beach.

e. *Estimating the fill volume of sand*

For fill material different from the native beach sand, cross-sectional volume requirements should be estimated with consideration given to the differences in profile slope given by equilibrium profile concepts.

* Dean's EBP function

For intersecting profiles, the volume per unit length of beach required to advance the beach a distance W after equilibration can be estimated by:

$$V = W \cdot B_b + \frac{\frac{3}{5} \cdot W^{5/3} \cdot A_N \cdot A_F}{(A_F^{3/2} - A_N^{3/2})^{2/3}} \quad (5-6)$$

For a nonintersecting profile, the volume of sand per unit length of shoreline that must be placed before there is any dry beach after equilibrium is estimated as

$$V = \frac{3}{5} \left(\frac{D_c}{A_F} \right)^{5/2} (A_N - A_F) \quad (5-7)$$

For a nonintersecting profile with a dry beach after equilibrium (i.e., volume placed is equal to or exceeds that in Equation (5-7)), the volume of sand per unit length of shoreline required to produce a berm width W may be estimated as:

$$V = W B_b + \frac{3}{5} \left(\frac{D_c}{A_F} \right)^{5/2} \left(A_N \left[1 + W \left(\frac{A_F}{D_c} \right)^{3/2} \right]^{5/3} - A_F \right) \quad (5-8)$$

* Other EBP functions

$$V = \int_0^{x_c} h(x) \cdot dx - \frac{1}{2} (D_c + B_b) \cdot (x_{CB} - W) \quad (5-9)$$

Where x_{CB} is the cross-shore distance from the shoreline to the offshore end point of beach nourishment and $h(x)$ is the EBP function which was determined as in Part 4.3.

* Results of fill sand volume

The fill sand volume is estimated for each beach with different sediment characteristics and the different in-situ conditions. The results are given in Table 57.

Table 57. Summary of the results of the fill sand volume.

Name	$h(x)$	x_{CB} (m)	i	D_{50}^F (mm)	D_c (m)	W (m)	B_b (m)	V (m ³ /m)	V_t (m ³)
Ceinturon	Vellinga's EBP	400	1:100	0.27	5.35	10.0	0.61	236.13	190,834.9
Bona	Bodge's EBP	350	1:65	0.45	5.35	10.0	0.61	364.36	362,624.9
Total								553,459.8	

From Table 57, it can be concluded that the median grain diameter of fill sediment has the significant impact on the shape of design beach profile. An increase of the fill

grain size induces a corresponding increase of design slope. In other words, use of fine sand will produce a beach with gentle slopes, whereas use of coarse material will result in a beach with steep slopes. Moreover, when the grain size increases, the width of beach nourishment will decrease correspondingly.

f. Evaluating project longevity

The longevity of a beach nourishment project is primarily determined by the degree to which the placed sand volume addresses any preproject profile volume deficit, and the rate at which fill material is transported out of the project domain in the alongshore direction, i.e., lateral spreading losses (U.S.A.C.E, 2012). If these losses are approximately equal to the 50% of the initial placed beach-fill volume, periodic renourishment will be required to maintain the desired beach cross section. The time at which 50 percent of the beach-fill material remains within the placement area is called the half-life of a beach nourishment project. The rate of sand loss is mainly depended on the length of the nourishment project (U.S.A.C.E, 2012).

The influence of length is best illustrated by considering the simplest case of initially rectangular beach fill constructed on a long straight beach with no background (Figure 196). The beach fill exists from $-l_{1/2} < x < +l_{1/2}$ and extends Y distance seaward from the original beach. The change of distance between the original and new beach is defined as follows:

$$y = \frac{Y}{2} \left\{ \operatorname{erf} \left[\left(\frac{l_{1/2}}{2\sqrt{\varepsilon t}} \right) \left(1 - \frac{x}{l_{1/2}} \right) \right] + \operatorname{erf} \left[\left(\frac{l_{1/2}}{2\sqrt{\varepsilon t}} \right) \left(1 + \frac{x}{l_{1/2}} \right) \right] \right\} \quad (5-10)$$

Where:

$\operatorname{erf}()$ is the error function defined as

$$\operatorname{erf}() = \frac{2}{\sqrt{\pi}} \int_0^0 e^{-z^2} dz \quad (5-11)$$

ε (m^2/s) is the shoreline diffusivity parameter:

$$\varepsilon = \frac{K \cdot H_b^2 \cdot C_{gb}}{8} \left(\frac{\rho}{\rho_s - \rho} \right) \left(\frac{1}{1 - n} \right) \left(\frac{1}{B_b + D_C} \right) \quad (5-12)$$

Where:

B_b is beach berm height above still-water level, $B_b = 0.61$ m;

D_C is depth of appreciable sand transport as measured from still-water level, $D_C = 5.35$ m, as determined in Part 2.3.3.1 in Chapter 2;

ρ is density of water, with salt water, $\rho = 1,025$ kg/m³;

ρ_s is density of the sediment, $\rho_s = 2,650$ kg/m³;

n is in-place sediment porosity, $n \approx 0.4$;

C_{gb} is the wave group speed at the breaker line;

$$C_{gb} = \sqrt{gd_b} = \sqrt{g \frac{H_b}{\kappa}} \quad (5-13)$$

κ is the breaker index H_b/d_b , $\kappa=0.78$;

K is an empirical proportionality coefficient, $K = 0.77$ or determined as a function of grain size:

$$K = 1.4e^{(-2.5D_{50})} \quad (5-14)$$

where

D_{50} is the median grain size of the beach sediment in millimeters;

H_b is wave height at breaking.

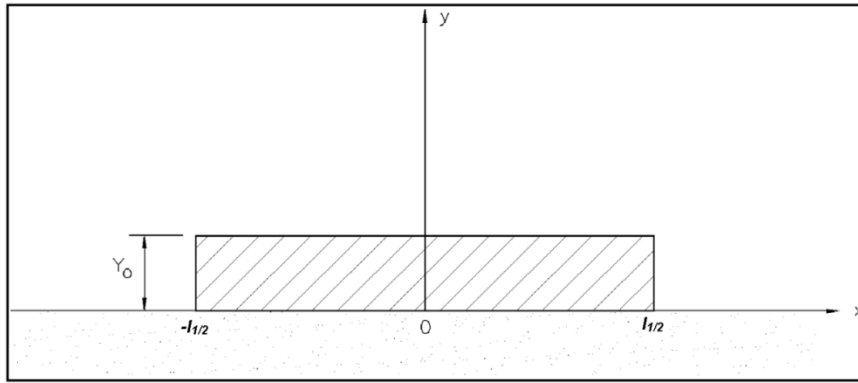


Figure 196. Rectangular beach fill ($t=0$).

In the equation (5-10), the important parameter is

$$\frac{l_{1/2}}{2\sqrt{\varepsilon t}} \quad (5-15)$$

Where $l_{1/2}$ is one-half the length of the rectangular project, $l_{1/2} = 404$ m for Ceinturon beach and $l_{1/2} = 553$ m for Bona beach, ε is the shoreline diffusivity parameter defined in equation (5-12), and t is time.

Here it is seen that if the quantity in Equation (5-15) is the same for two different projects their planform evolution would be the same. However, if two projects were exposed to the same wave climate but had different alongshore lengths, then the project with the greatest length would be predicted to last longer.

The proportion $p(t)$ of fill left within the project boundaries at a given time after project initiation to give:

$$p(t) = \frac{1}{\sqrt{\pi}} \left(\frac{\sqrt{\varepsilon t}}{l_{1/2}} \right) \left\{ \exp \left(- \left(\frac{l_{1/2}}{\sqrt{\varepsilon t}} \right)^2 \right) - 1 \right\} + \operatorname{erf} \left(\frac{l_{1/2}}{\sqrt{\varepsilon t}} \right) \quad (5-16)$$

In fact, according to Equation (5-16) the longevity of a project varies as the square of its length. If more than 50 percent of the placed beach-fill volume remains within the placement area ($0.5 < p(t) < 1.0$), Equation (5-16) can be approximated using the following relationship (with an accuracy of ± 15 percent).

$$p(t) = 1 - \frac{\sqrt{\varepsilon t}}{l_{1/2}\sqrt{\pi}} \quad (5-17)$$

If only 50 percent of the beach-fill material remains within the placement area, the half-life of the specified beach fill, $t_{50\%}$, can be defined as:

$$t_{50\%} = \frac{l_{1/2}^2\pi}{4\varepsilon} \quad (\text{second}) \quad (5-18)$$

The results of life estimation of beach nourishment project, corresponding to the height and frequency of waves, which could induce the morphological evolution of Ceinturon and Bona beaches, are summarized in Table 58 and Table 59. In addition, the relationship between the significant wave height and half-life of beach nourishment is illustrated in Figure 197 and Figure 198.

Table 58. A summary of results of beach nourishment longevity corresponding to wave height and frequency in Ceinturon beach.

No.	H_b (m)	N	NE	E	SEE	SE	S	Total (%)	ε (m ² /s)	$t_{50\%}$ (year)
1	0.3	0.95	2.43	0.81	4.60	22.95	10.76	42.5	0.00275	1.48
2	0.6	0.05	0.75	0.18	7.08	15.4	1.10	24.55	0.01554	0.26
3	0.9	0	0.02	0.02	3.01	6.02	0.02	9.09	0.04283	0.09
4	1.2	0	0	0	0.96	1.96	0	2.92	0.08792	0.05
5	1.5	0	0	0	0.18	0.23	0	0.41	0.15360	0.03
6	1.8	0	0	0	0.01	0.07	0	0.08	0.24229	0.02
7	2.0	0	0	0	0	0.004	0	0.004	0.31530	0.01
Total								79.55%		1.94

Table 59. A summary of results of beach nourishment longevity corresponding to wave height and frequency in Bona beach.

No.	H_b (m)	N	NE	E	SEE	SE	S	Total (%)	ε (m ² /s)	$t_{50\%}$ (year)
1	0.3	2.68	5.08	2.39	11.17	16.26	7.75	45.33	0.001752	4.35
2	0.6	0.21	0.97	0.96	15.00	4.16	0.37	21.67	0.009910	0.77
3	0.9	0	0.02	0.20	7.28	0.68	0.004	8.18	0.027310	0.28
4	1.2	0	0	0.04	2.74	0.06	0	2.84	0.056062	0.14
5	1.5	0	0	0.004	0.61	0.004	0	0.62	0.097937	0.08
6	1.8	0	0	0	0.08	0.01	0	0.09	0.154489	0.05
7	2.0	0	0	0	0.01	0	0	0.010	0.201044	0.04
Total								78.74%		5.70

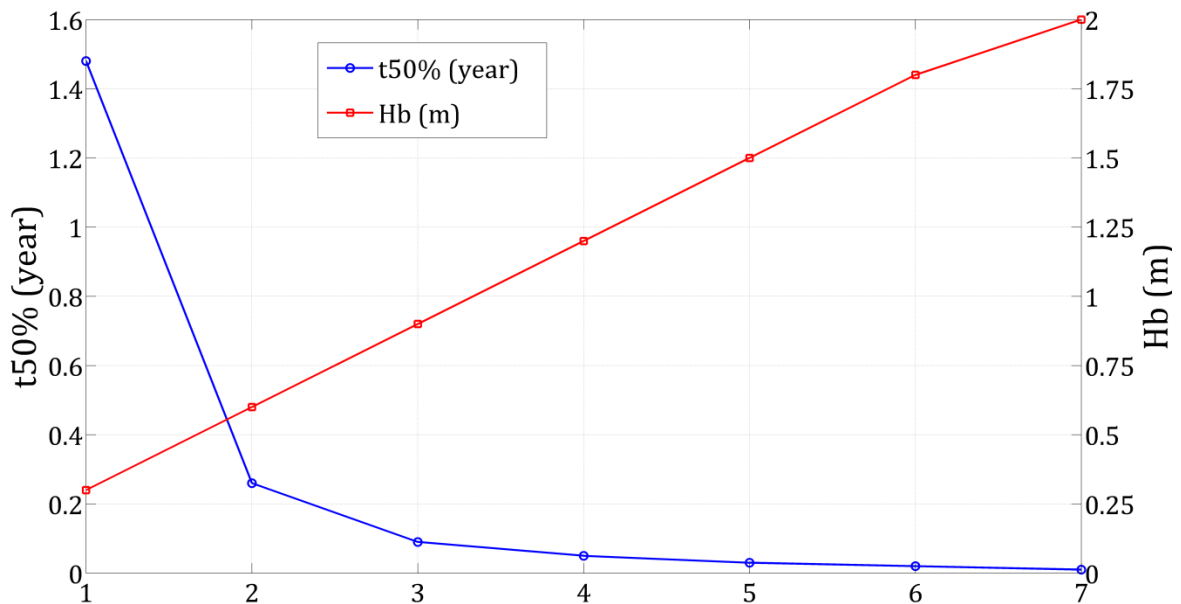


Figure 197. The relationship between the wave height and the half-life of beach nourishment in Ceinturon.

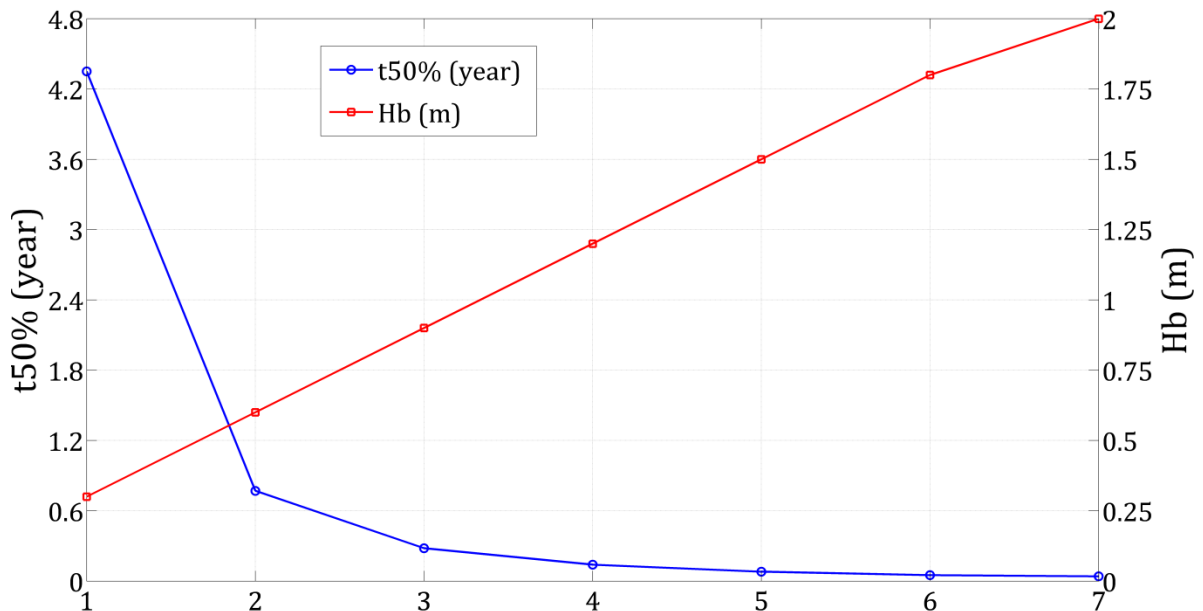


Figure 198. The relationship between the wave height and the half-life of beach nourishment in Bona.

In summary, the nourished sand volume will be lost about 50% of total (Table 57) by the wave impacts after 1.94 years and 5.7 years for the central Ceinturon and Bona beaches, respectively. This means that Ceinturon and Bona beaches need be renourished after about 1.94 years and 5.7 years since the completion of beach nourishment project. The higher the waves are the shorter the longevity of beach nourishment is. The frequencies of occurrence of waves mainly affecting the morphological evolution of Ceinturon and Bona beaches are almost the same and occupy about 79.55% and 78.74% of total duration, respectively. However, the half-life of beach nourishment in these two beaches is completely different. This implies that the length of beach nourishment plays a great role in the longevity of beach nourishment work.

5.6.6.2. Evaluating the effectiveness of beach nourishment in Ceinturon

In order to assess the influence of beach nourishment in Ceinturon, the simulated cross-shore variations in wave height, current speed and total load of sediment transport in the different scenarios are plotted and compared with those without beach nourishment. In addition, the hydrodynamic and sediment transport parameters at the water depth of about 1.5 m right located 32 m seaward of Ceinturon shoreline with and without beach nourishment are also extracted and listed in Table 60.

a. Modifications of wave field

In this work, three wind-driven wave directions including northeast, east and southeast, which predominantly affect the morphology of Ceinturon beach, are simulated to clarify the role of beach nourishment. It is easily seen that the east winds cause the highest waves, whereas the lowest waves are normally generated by the southeast winds regardless of beach nourishment (Figure 199). When the beach is nourished, the wave heights induced all directions are decreased from 6% to 7% (Table 60), comparing to those without beach nourishment. It is a result of bathymetry raises and wave energy dissipation due to wave breaking. The reduction in wave height results in a significant decrease of radiation stresses. Particularly, the shear radiation stresses (S_{xy}) resulting in the longshore currents are sharply reduced by 20%.

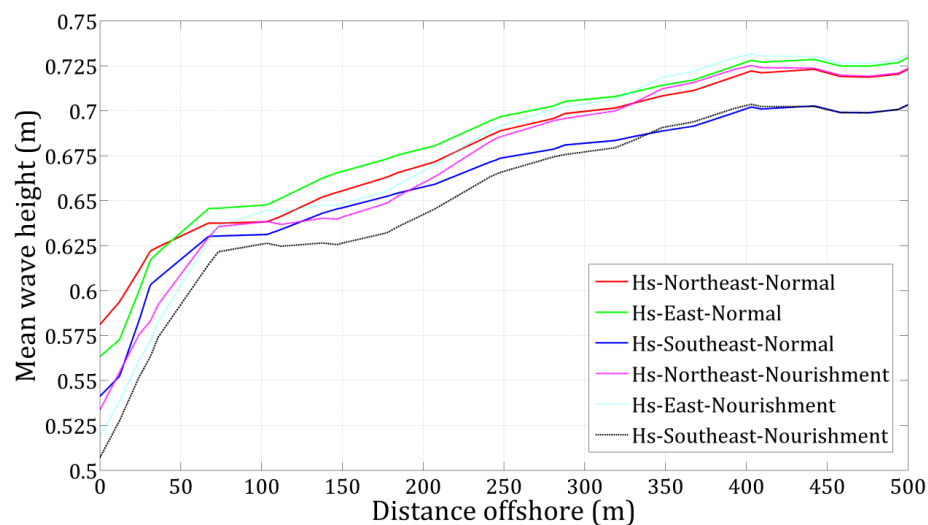


Figure 199. Modeled cross-shore variations in wave heights under the impact of beach nourishment and changes of wind direction at Ceinturon beach.

Figure 200 presents the modeled cross-shore variations in the wave heights due to the seasonal changes with and without beach nourishment. It is noticeable that the magnitude of significant wave height in the summer is less than about half of that in the winter, regardless of beach nourishment. As beach nourishment causes an increase of bathymetry, shallower water depths would increase bottom friction and decrease water depth relative to the wave height, resulting in the location of wave breaking moved seaward and the breaking wave height decreased. The nearshore wave height in the winter reduces by about 3%, comparing to that without beach nourishment. This leads

to a corresponding increase of the radiation stresses from 6.4% to 16.2% (Table 60). However, the wave height in the summer increases slightly by 3.41% due to beach nourishment in the surf zone from 120 m seaward of the shoreline to the shoreline (Figure 200). Along with the increase of wave height, the radiation stresses is also amplified by 5.5%-9.4%, compared with that without beach nourishment, except the shear radiation stress.

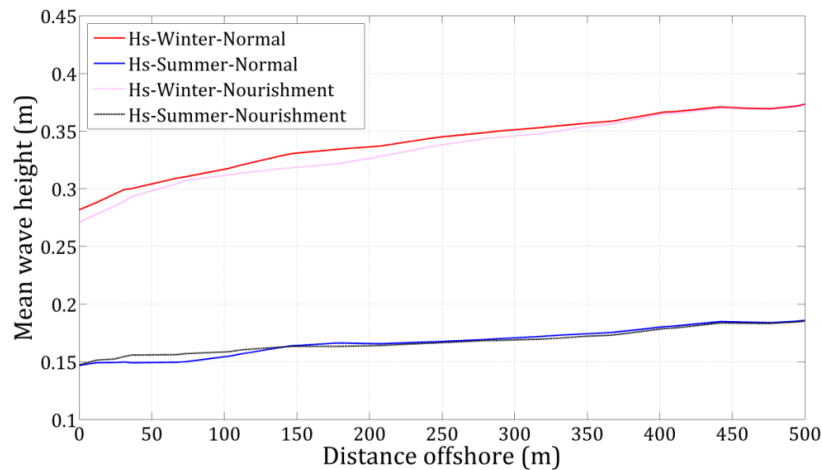


Figure 200. Modeled cross-shore variations in wave heights under the impact of beach nourishment and seasonal changes at Ceinturon beach.

In all the extreme cases, the magnitude of significant wave height reduces due to beach nourishment. The depth-limited nature of wave height in the nourished area is evident in the landward decrease in the wave height and energy dissipation due to wave breaking (Figure 201). The wave height is decreased by 12%-14% in all storm scenarios (Table 60). With regard to beach nourishment, the strong stormy level induces the high wave. As a result, the radiation stresses is also moderately declined by 15.5%-30%. It demonstrates that the impact of beach nourishment on the wave field in the extreme conditions is larger and more notable than that in the ordinary sea conditions, viz. annual and seasonal scenarios.

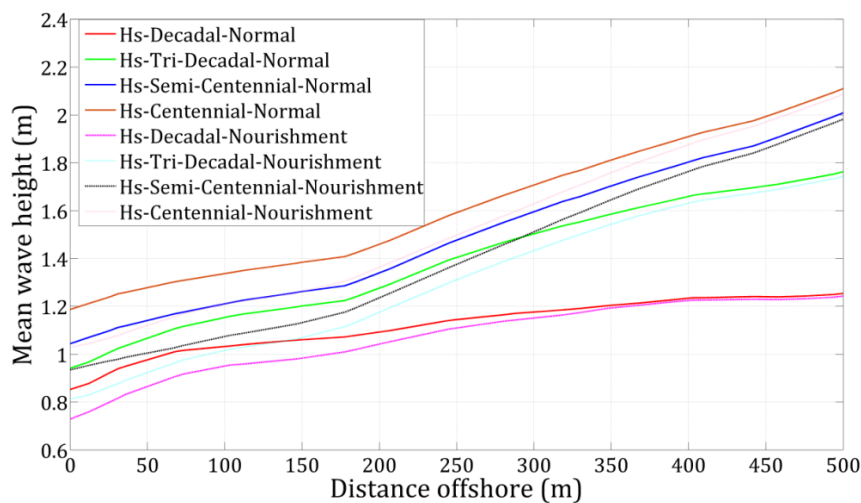


Figure 201. Modeled cross-shore variations in wave heights under the impact of beach nourishment and change of storm scale at Ceinturon beach.

b. Modifications of current and sediment transport

The near-shore currents are induced by the waves and winds. The variation in wind direction causes the change of current speed. Figure 202 shows the modification of current speed in the cross-shore due to northeast, east and southeast winds. It is clearly observed that the highest currents are attributed to the northeast winds (Figure 202), though the east winds trigger the highest waves (Figure 199). It proves that the near-shore currents in Ceinturon beach are mainly affected by the wind direction. When the replenishment project is carried out in Ceinturon beach, the current speed reduces in the surf zone. The largest reduction of 12.8% is caused by the southeast winds, whilst northeast winds trigger the minimum decrease of current speed (Table 60).

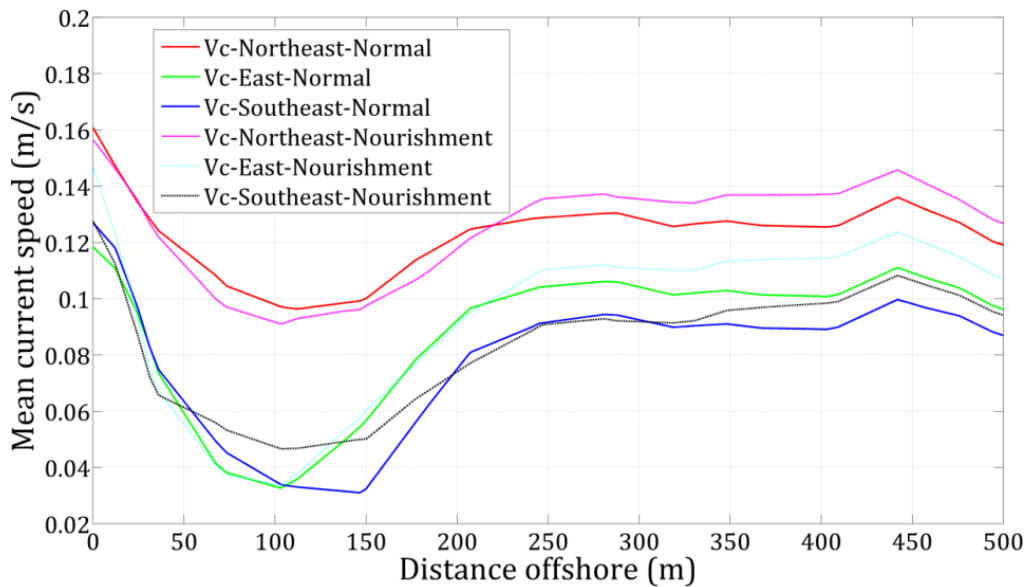


Figure 202. Modeled cross-shore variations in current speed under the impact of beach nourishment and changes of wind direction at Ceinturon beach.

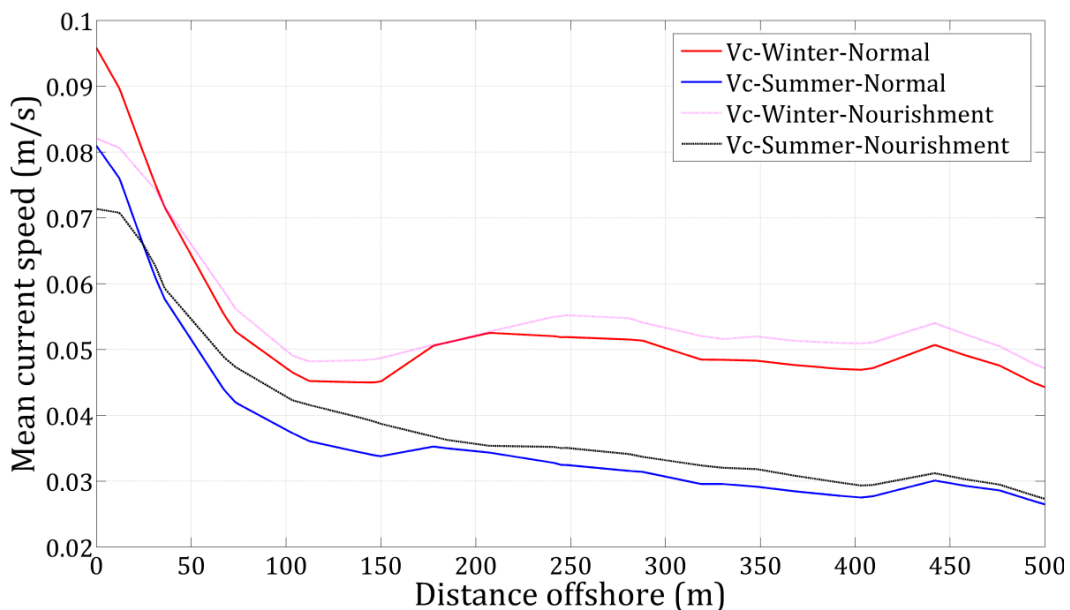


Figure 203. Modeled cross-shore variations in current speed under the impact of beach nourishment and seasonal changes at Ceinturon beach.

The modeled cross-shore variations in current speed due to the seasonal changes with and without beach nourishment are illustrated in Figure 203. It is easily seen that the current speed in the summer is less than that in the winter, regardless of beach nourishment. In both of the summer and winter, the current speed from 50 m seaward of the shoreline to offshore with beach nourishment is higher than that without beach nourishment. Conversely, near the shore inside 50 seaward of shoreline, the current speed is decreased, especially in the winter, if beach nourishment is implemented.

Contrary to the seasonal scenarios, the current speed in the stormy cases is almost reduced by beach nourishment. Figure 204 shows the cross-shore modifications of current speed caused by the different storms with and without beach nourishment. The maximum reduction of 52% is seen under the centennial storm, while the minimum reduction of 2.1% is found in the case of the tri-decadal storm (Table 60). These reductions would be mainly due to the decay of wave height and radiation stresses when the beach is replenished.

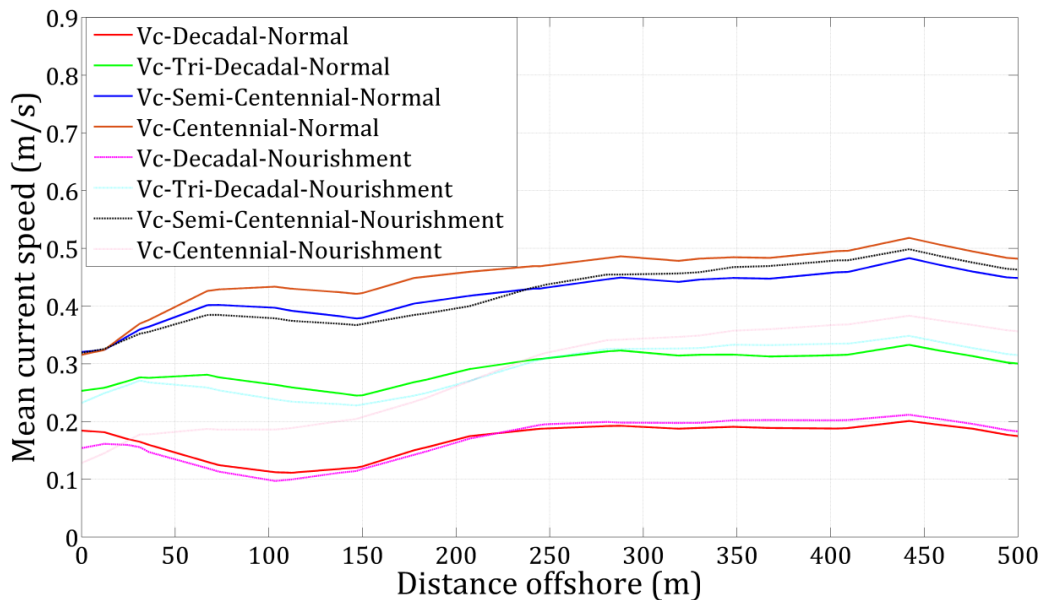


Figure 204. Modeled cross-shore variations in current speed under the impact of beach nourishment and changes of storm scale at Ceinturon beach.

A decrease in wave energy and circulation due to beach nourishment will also affect sediment dynamics across the beach. Smaller waves resulting from high friction bottom will generate decreased wave-induced stresses, which, in turn, would induce lower resuspension of sediment in the cross-shore. The modeled cross-shore variations in sediment transport rates due to the wind direction changes, the seasonal changes and the storm changes are depicted in Figure 205, Figure 206, and Figure 207, respectively. In most of the study cases, the total load of sediment transport is reduced by a decrease of wave height, apart from the summer. The maximum reduction of 17.5%-69% is observed in the stormy conditions, whereas the sediment transport rate is only decreased by 4%-16% due to wind direction changes (Table 60). The sediment

transport occurs severely in the distance between the shoreline and 150 m seaward of the shoreline due to the variations of wind direction (Figure 205). On the other hand, the highest sediment transport rates are observed at the distance between 350 m and 450 m seaward of shoreline under both of the seasonal changes and the extreme events, regardless of beach nourishment. In the winter, the sediment transport rate is decreased about 14% by beach nourishment. On the other hand, a slight increase of wave height and current speed in the summer due to beach nourishment brings out the corresponding raise of 10.4% in total load of sediment (Table 60).

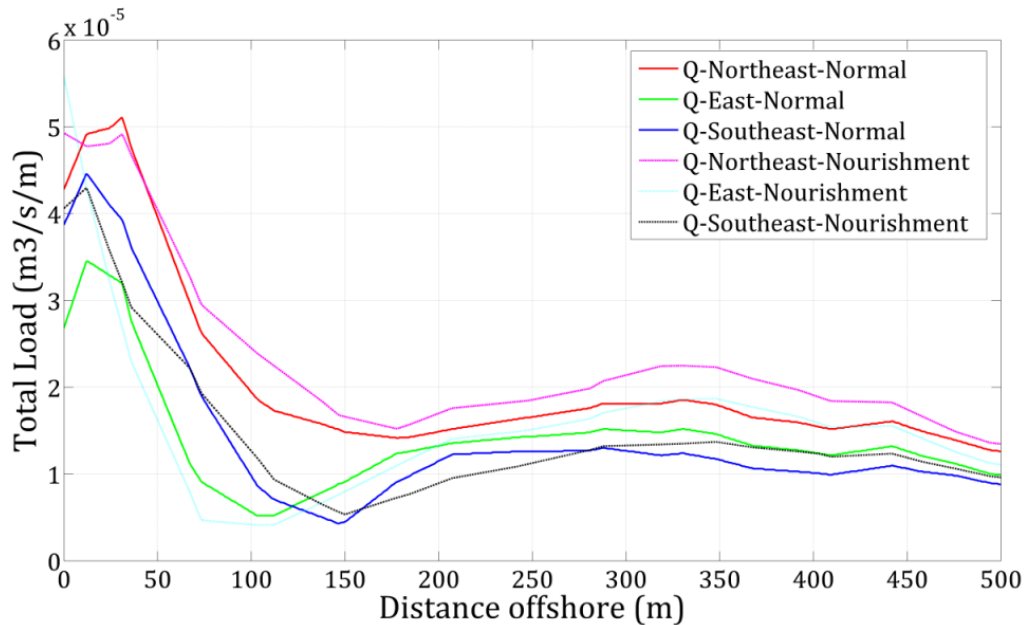


Figure 205. Modeled cross-shore variations in sediment transport rates under the impact of beach nourishment and changes of wind direction at Ceinturon beach.

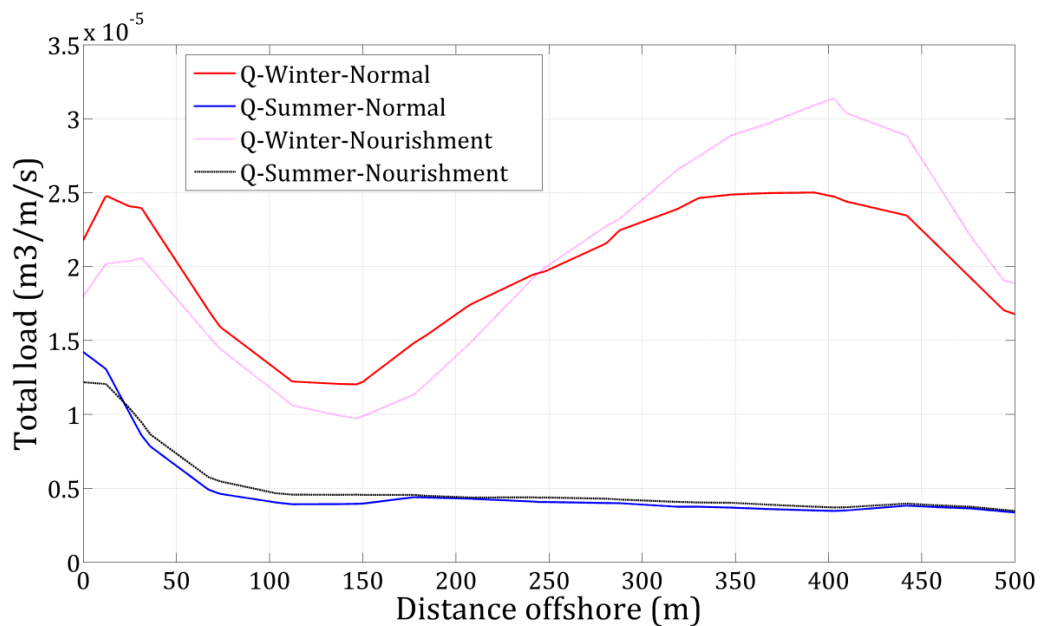


Figure 206. Modeled cross-shore variations in sediment transport rates under the impact of beach nourishment and seasonal changes at Ceinturon beach.

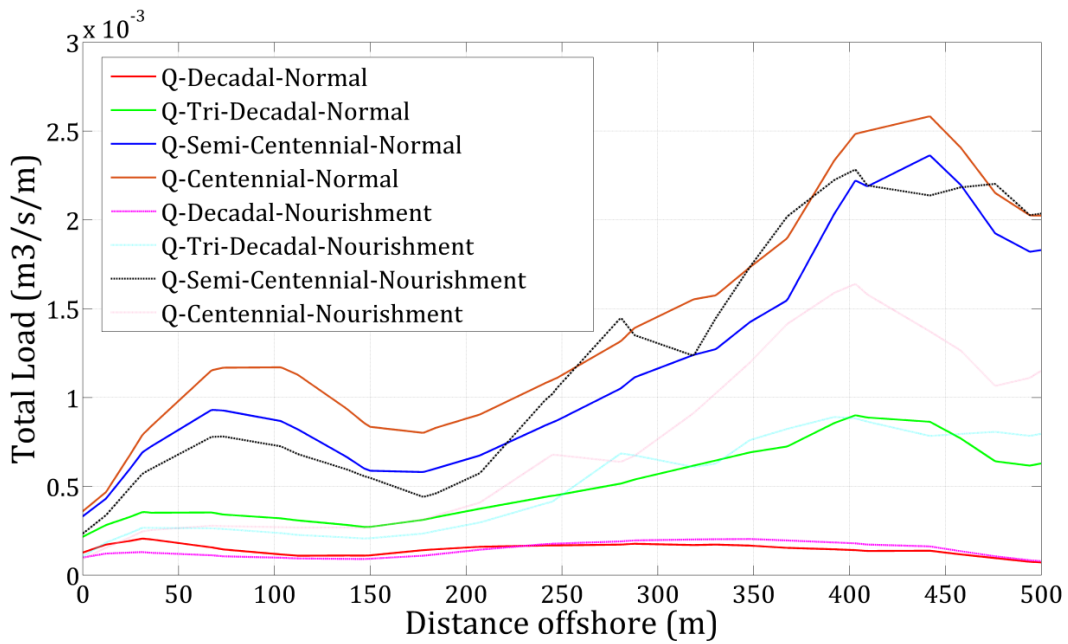


Figure 207. Modeled cross-shore variations in sediment transport rates under the impact of beach nourishment and changes of storm scale at Ceinturon beach.

c. Beach profile analysis

Although the current speed and total load of sediment transport decrease due to beach nourishment, erosion still occurs close to shore. Beach changes under the variations of wind direction with and without beach nourishment are shown in Figure 208. In all cases with and without beach nourishment, the most severe erosion is caused by the northeast winds. The maxima erosion area of $-26 \text{ m}^2/\text{m}$ is observed without beach nourishment, whereas the largest loss of $-31 \text{ m}^2/\text{m}$ is found with beach nourishment. Erosion mainly occurs in the distance between the shoreline and 75 m seaward of the shoreline.

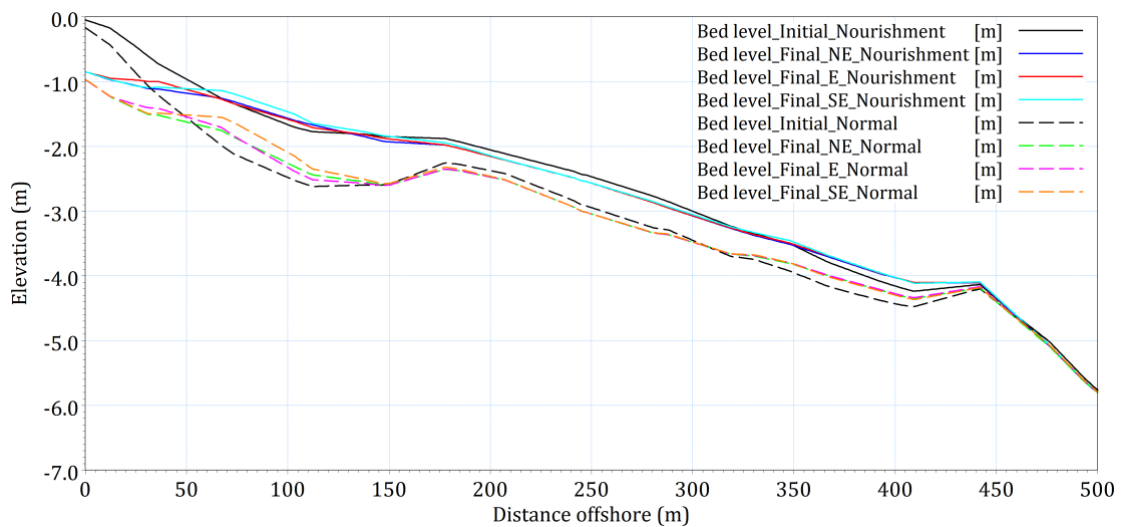


Figure 208. Beach profile evolution at the central Ceinturon beach under the impact of beach nourishment and changes of wind direction.

Figure 209 illustrates the beach profile evolution under the impact of the seasonal changes with and without beach nourishment. It is notably seen that the winter wave climate causes erosion larger than the summer, regardless of beach nourishment. In the summer, the beach profile almost does not change, except the vicinity of the shoreline. The erosion area still occurs in both with and without beach nourishment; however, the reduction amount of land loss with beach nourishment is much less than that without beach nourishment.

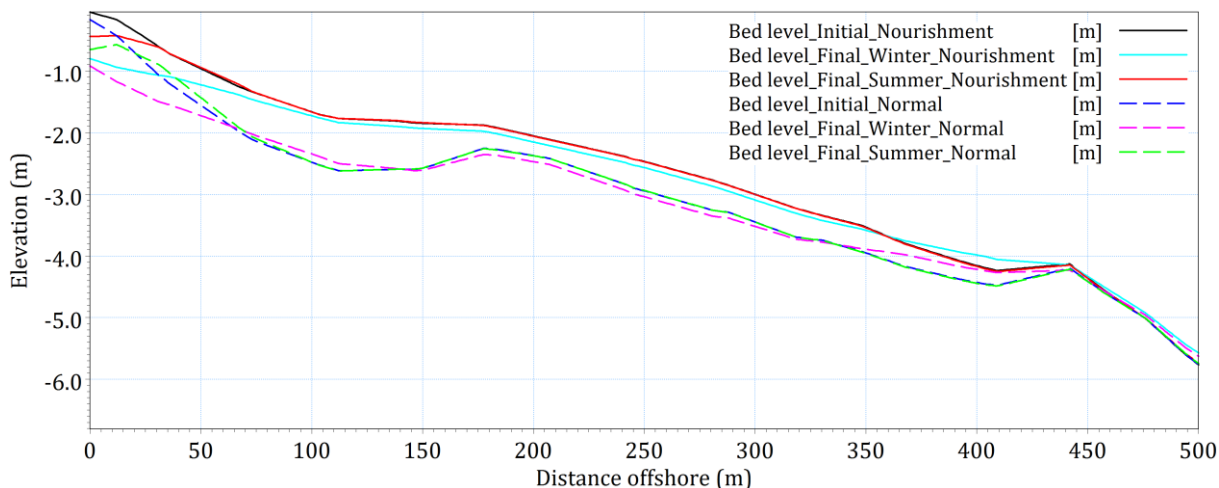


Figure 209. Beach profile evolution at Ceinturon beach under the impact of beach nourishment and seasonal changes.

The erosion area is enlarged much more when the storms approach the beach. Figure 210 demonstrates that the high storm level results in the large erosion area both with and without beach nourishment. The beach profile changes are mostly observed from the shoreline to 200 m seaward of the shoreline, regardless of storm scale and beach nourishment. The erosion area caused by the centennial storm with beach nourishment is almost the same as that without beach nourishment, viz. $-61 \text{ m}^2/\text{m}$ and $-67 \text{ m}^2/\text{m}$, respectively.

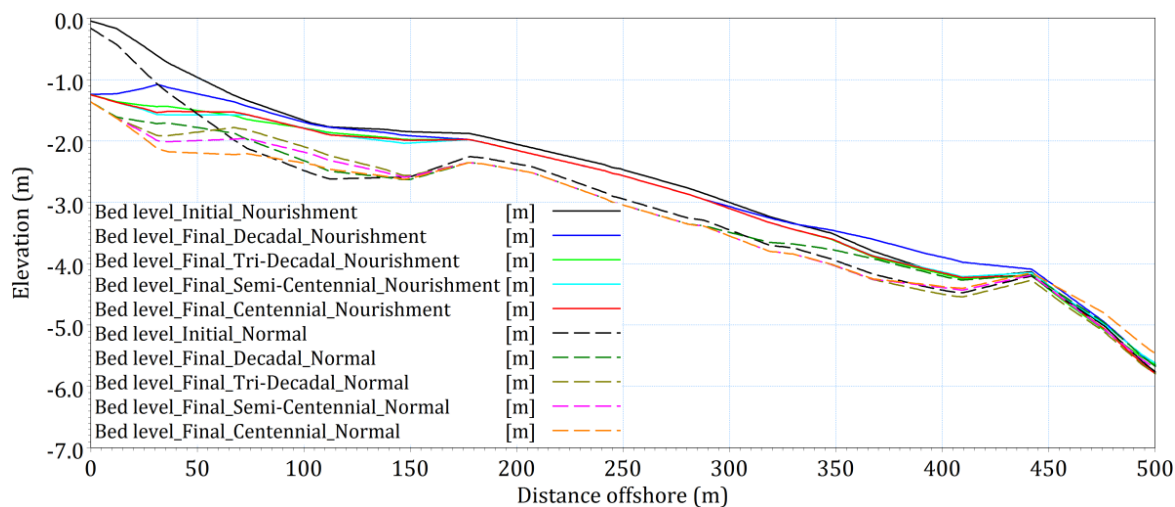


Figure 210. Beach profile evolution at the central Ceinturon beach under the impact of beach nourishment and changes of storm scale.

Table 60. Effect of beach nourishment on hydrodynamic field and sediment transport in Ceinturon.

Scenario		H_s (m)	S_{xx} (m^3/s^2)	S_{xy} (m^3/s^2)	S_{yy} (m^3/s^2)	V_c (m/s)	Q ($m^3/s/m$)
Normal	NE	0.622	0.232	-0.064	0.158	0.128	5.05E-05
	E	0.618	0.228	-0.064	0.155	0.081	3.12E-05
	SE	0.604	0.216	-0.061	0.147	0.081	3.88E-05
	Winter	0.300	0.069	-0.021	0.049	0.074	2.38E-05
	Summer	0.150	0.017	-0.006	0.014	0.060	8.46E-06
	Decadal	0.941	0.505	-0.131	0.322	0.164	2.05E-04
	Tri-Decadal	1.027	0.566	-0.149	0.360	0.276	3.54E-04
	Semi-Centennial	1.113	0.648	-0.157	0.380	0.360	6.97E-04
	Centennial	1.254	0.806	-0.191	0.461	0.371	7.98E-04
Nourishment	NE	0.584	0.201	-0.052	0.149	0.126	4.88E-05
	E	0.574	0.194	-0.051	0.139	0.073	2.62E-05
	SE	0.565	0.188	-0.049	0.134	0.071	3.16E-05
	Winter	0.290	0.060	-0.017	0.046	0.074	2.05E-05
	Summer	0.155	0.018	-0.006	0.016	0.062	9.33E-06
	Decadal	0.819	0.389	-0.099	0.269	0.154	1.29E-04
	Tri-Decadal	0.879	0.435	-0.105	0.281	0.270	2.66E-04
	Semi-Centennial	0.980	0.517	-0.113	0.312	0.353	5.76E-04
	Centennial	1.080	0.626	-0.145	0.390	0.178	2.47E-04
Difference (%)	NE	6.09	13.18	18.48	5.90	1.38	3.47
	E	7.12	14.78	19.90	10.23	9.67	16.14
	SE	6.44	12.93	19.54	9.34	12.78	18.57
	Winter	3.19	12.55	16.21	6.40	0.79	14.03
	Summer	-3.41	-5.51	0.66	-9.41	-2.93	-10.35
	Decadal	12.98	23.02	24.61	16.57	5.97	37.11
	Tri-Decadal	14.35	23.22	29.69	21.80	2.11	24.87
	Semi-Centennial	11.95	20.30	28.29	17.98	2.12	17.45
	Centennial	13.86	22.26	23.90	15.51	52.08	69.04

5.6.6.3. Evaluating the effectiveness of beach nourishment in Bona

Similar to Ceinturon beach, the numerical simulation is also carried out to evaluate the influence of beach nourishment on the hydrodynamic fields and sediment transport along Bona beach during the different forcing conditions. This is evidenced by the cross-shore variations in the wave height, current speed and sediment transport rate. These variations are quantified by comparing between the hydrodynamic parameters extracted at the water depth of 1.5 m in front of Bona beach, corresponding to 38 m seaward of the shoreline, as summarized in Table 61.

a. Modifications of wave field

The effect of beach nourishment is investigated by comparing the wave heights driven by the different wind directions with and without beach nourishment (Figure 211). In general, beach nourishment reduces the wave heights from 3% to 7% (Table 61). It is noted that the northeast winds have the strongest impact on the wave field in Bona beach in both of with and without beach nourishment. The decrease of wave height results in a reduction of radiation stresses in which the component of the shear radiation stresses (S_{xy}) inducing the longshore currents are rapidly receded by 36%-64%.

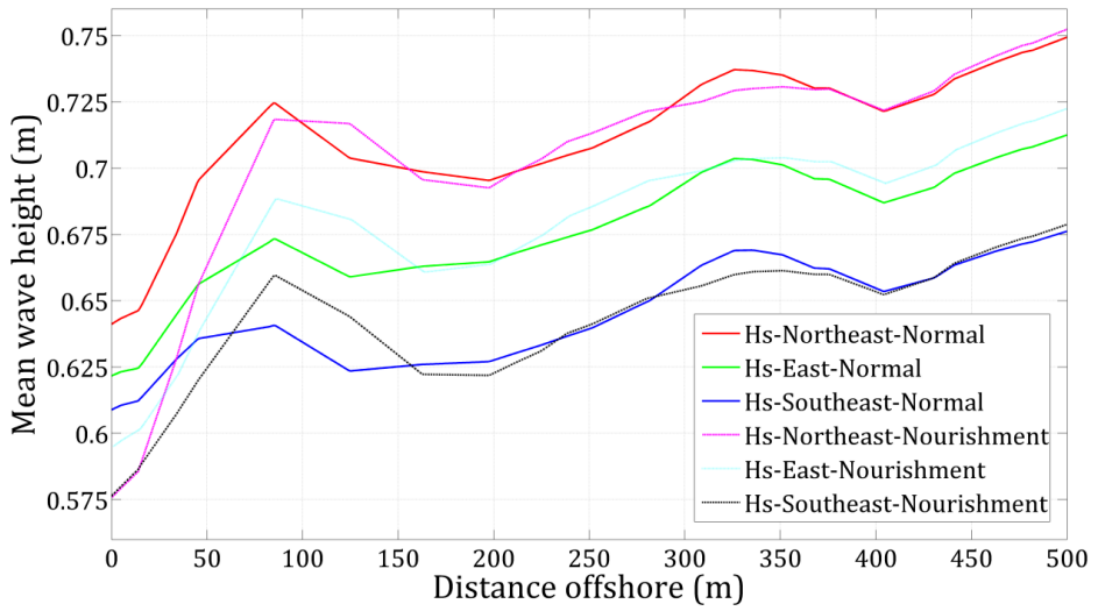


Figure 211. Modeled cross-shore variations in wave heights under the impact of beach nourishment and changes of wind direction at Bona beach.

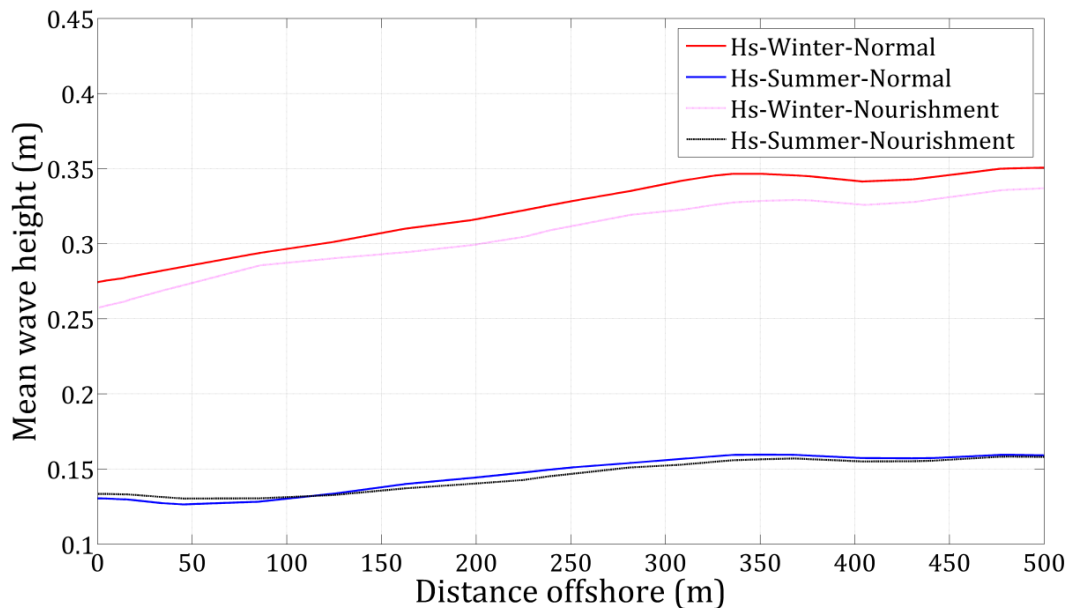


Figure 212. Modeled cross-shore variations in wave heights under the impact of beach nourishment and seasonal changes at Bona beach.

Figure 212 shows the modeled cross-shore variations in wave heights in summer and winter with and without beach nourishment. Similar to Ceinturon beach, beach nourishment induces a distinct reduction of 13.9% in wave height in the winter, but a moderate increase of 8.8% in nearshore wave height in the summer (Table 61). As a result, the radiation stresses decreases in the winter and increases proportionally in the summer. Again, the largest reduction is found in the shear radiation stress, viz. about 41% due to the winter climate and 13.4% due to the summer climate.

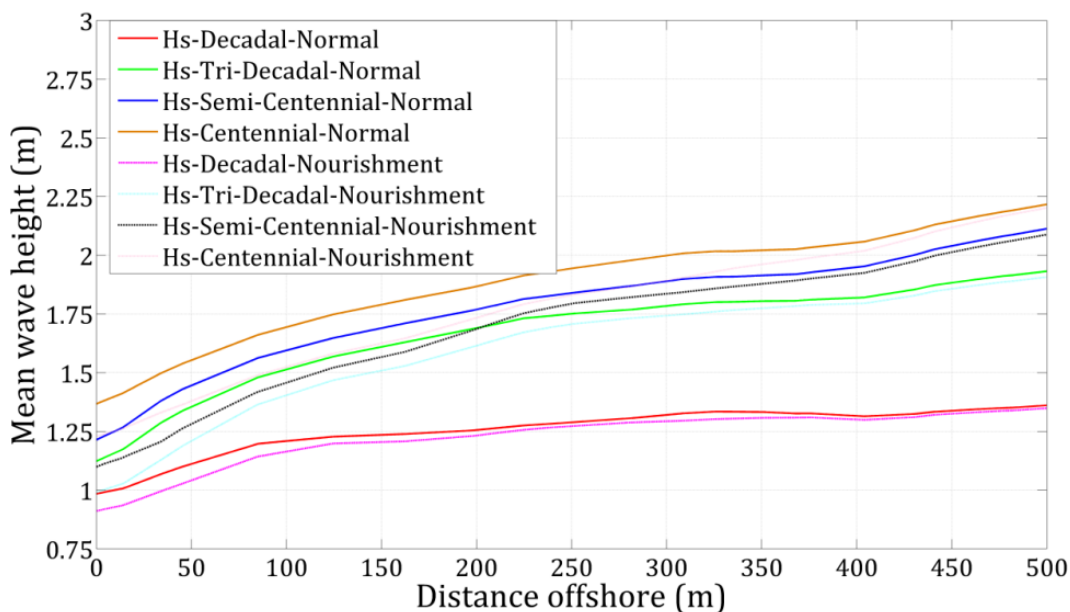


Figure 213. Modeled cross-shore variations in wave heights under the impact of beach nourishment and changes of storm scale at Bona beach.

The effect of beach nourishment on the wave field becomes more evidently under the storms. The comparison of wave heights under the different storms with and without beach nourishment is presented in Figure 213. It verifies that the strong stormy level causes the high wave height in Bona beach. Moreover, the wave heights under all storms will be significantly decreased if the Bona beach is replenished. The moderate reduction ranges from 7% to 12.4% (Table 61). Accordingly, the radiation stresses are also reduced by nourishment at the water depth of 1.5 m, corresponding to 38 m seaward of the shoreline, regardless of the storm levels and beach nourishment. The large reduction of 4% -71% in the radiation stresses is recorded in Table 61.

b. Modifications of current and sediment transport

Figure 214 shows the cross-shore variations in current speed of Bona beach with and without beach nourishment under the impact of wind direction changes. As can be seen in the figure, the current speed induced by the northeast winds is larger than that in other directions between 200 m and 500 m seaward of the shoreline. However, the current speed induced by the east and southeast winds reaches the highest values in the distance between the shoreline and 200 m seaward of the shoreline. Also in this zone, the current speed is reduced due to beach nourishment, regardless of wind directions. A

moderate reduction of 8%-19% is recorded at the water depth of 1.5 m, corresponding to 38 m seaward of the shoreline (Table 61).

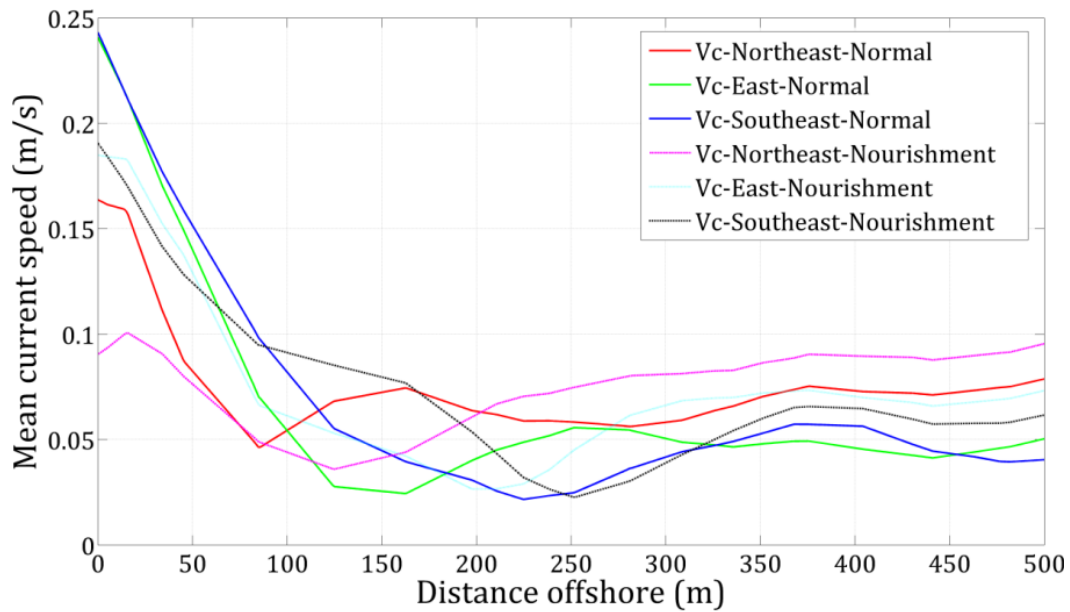


Figure 214. Modeled cross-shore variations in current speed under the impact of beach nourishment and changes of wind direction at Bona beach.

Figure 215 shows the cross-shore modifications of current speed due to the seasonal changes with and without beach nourishment. It is noticeable that beach nourishment triggers a paradox in current speed in the seasonal variation, viz. reducing the current speed down to about 6.5% in the winter, but increasing it upto 6.3% in the summer (Table 61). This would be explained by the fact that the raise of normal radiation stress components of S_{xx} and S_{yy} directly leads to the intensification of current speed in the summer with beach nourishment. In general, the current speed in the winter is larger than that in the summer, regardless of beach nourishment.

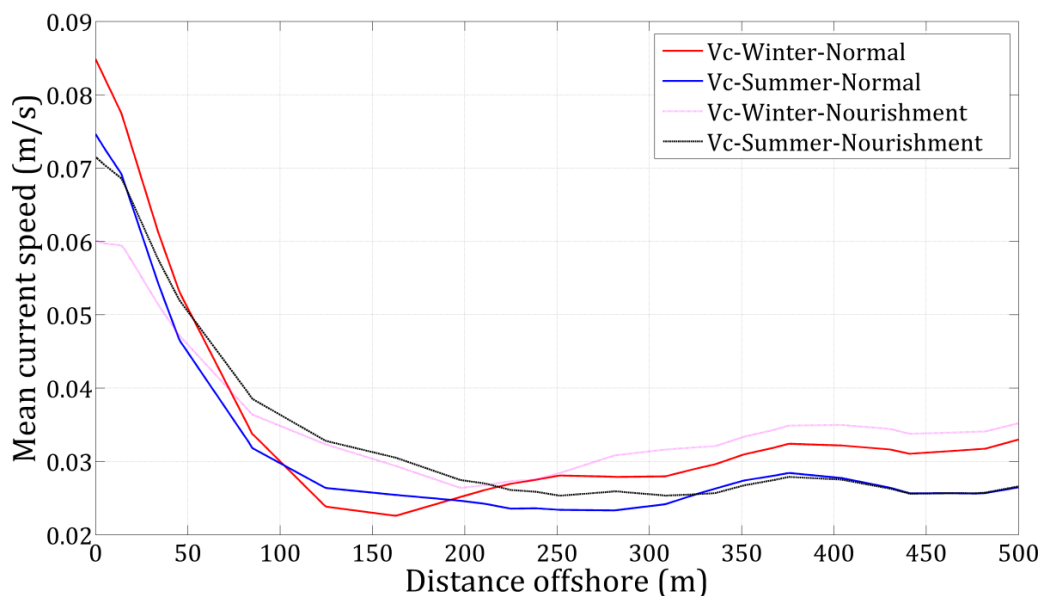


Figure 215. Modeled cross-shore variations in current speed under the impact of beach nourishment and seasonal changes at Bona beach.

Figure 216 illustrates the comparison of current speed under the different stormy scenarios with and without beach nourishment. The magnitude of current speed completely depends on the stormy level beyond 200 m seaward of the shoreline, i.e. the strong storm causes the high current speed. This trend will change behind the surf zone. The current speed driven by the decadal and tri-decadal storms is more than that in semi-centennial and centennial storms in the distance from the shoreline to 150 m seaward of the shoreline. When the beach nourishment is carried out, the current speed at the water depth of 1.5 m under the decadal and tri-decadal storms is decreased by 21% and 61%, respectively. While the current speed under the semi-centennial and centennial storms are boosted to 94% and 382%, respectively (Table 61).

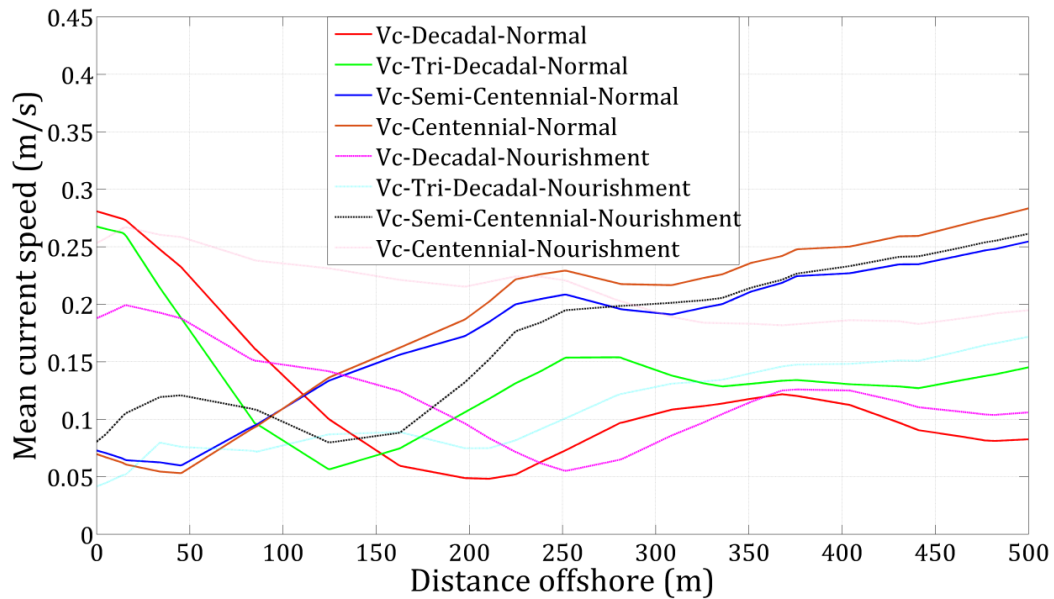


Figure 216. Modeled cross-shore variations in current speed under the impact of beach nourishment and changes of storm scale at Bona beach.

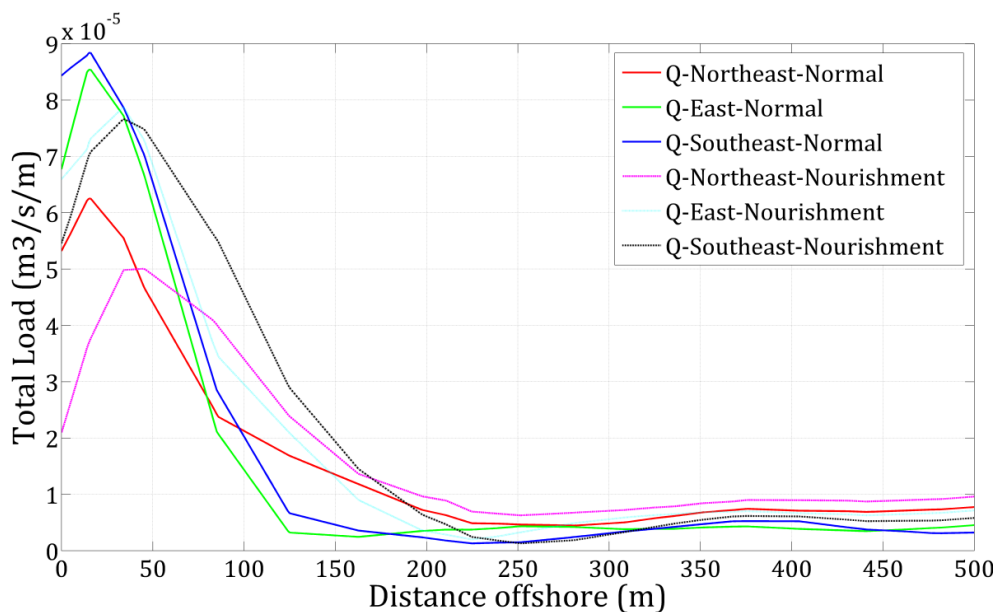


Figure 217. Modeled cross-shore variations in sediment transport rates under the impact of beach nourishment and changes of wind direction at Bona beach.

The changes of wave height and current speed greatly affect the sediment transport in Bona beach. Figure 217 illustrates the modeled cross-shore variations in sediment transport rates due to the changes of wind direction with and without beach nourishment. This comparison highlights the strongest influence of the southeast winds on sediment transport rate, regardless of beach nourishment. On the contrary, the northeast winds only result in the lowest rate of total load in both of with and without beach nourishment. This would be explained by the fact that the presence of Hyères port in the updrift side of Bona beach interfere with the longshore drift induced by the northeast winds and so reduces the total load from these winds. When Bona beach is nourished, most of sediment transport rates are decreased.

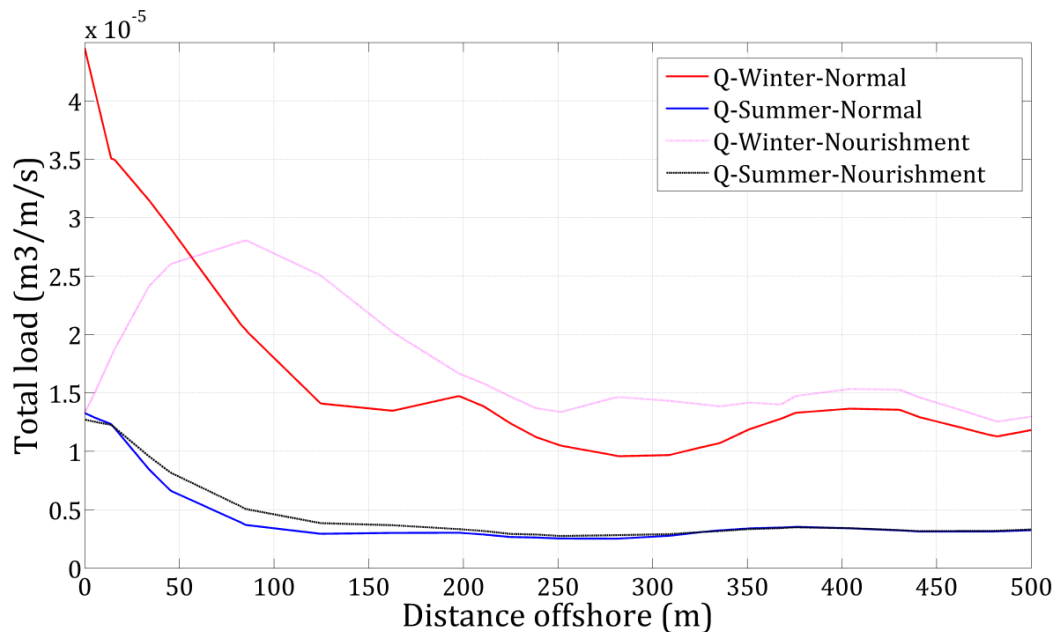


Figure 218. Modeled cross-shore variations in sediment transport rates under the impact of beach nourishment and seasonal changes at Bona beach.

The effect of beach nourishment on the sediment transport rate becomes clearer when taking into account the seasonal changes (Figure 218). As a result of changes in current speed, the total load of sediment transport decreases significantly due to beach nourishment in the winter, while it increases in the summer. Particularly, the reduced percentage of sediment transport rate is around 19.6% under the winter condition and a raise of 17.8% is reported under the summer condition (Table 61).

Figure 219 compares the sediment transport rates under the stormy conditions with and without beach nourishment. It is easily seen that the high total load is generated by the strong storms, regardless of beach nourishment. If Bona beach is nourished, most of sediment rates will be decreased significantly, except that under the centennial storm. At the water depth of 1.5 m, the total load reduces about from 10% to 40%. By contrast, the sediment transport rate increases up to 37% under the centennial storm (Table 61).

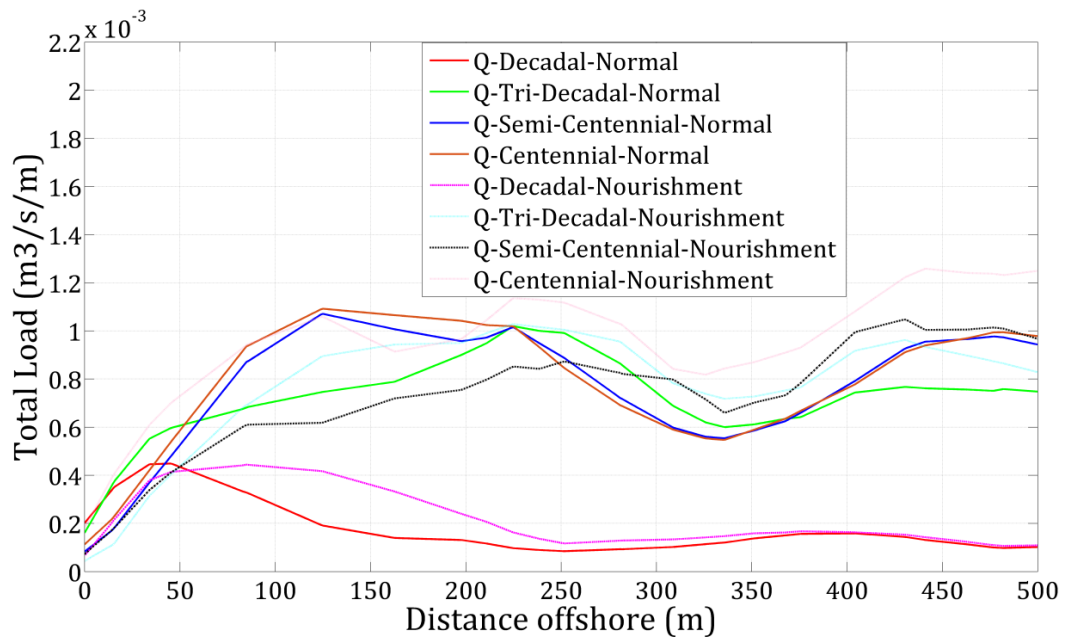


Figure 219. Modeled cross-shore variations in sediment transport rates under the impact of beach nourishment and changes of storm scale at Bona beach.

c. Beach profile analysis

The beach profile evolution is mostly decided by the sediment transport rate. The changes in bathymetry due to beach nourishment along with the impact of wind direction changes results in the significant modifications of beach profile. Figure 220 illustrates the comparison of beach profile changes under the different wind directions with and without beach nourishment. From the above-mentioned comments, even though the wave height and current speed are decreased by nourishment, erosion is still observed in near shore of Bona beach. The most severe erosion is induced by the impact of northeast winds, regardless of beach nourishment. Even, the erosive area with beach nourishment trends to increase larger than that without beach nourishment, viz. -35 m²/m and 27 m²/m.

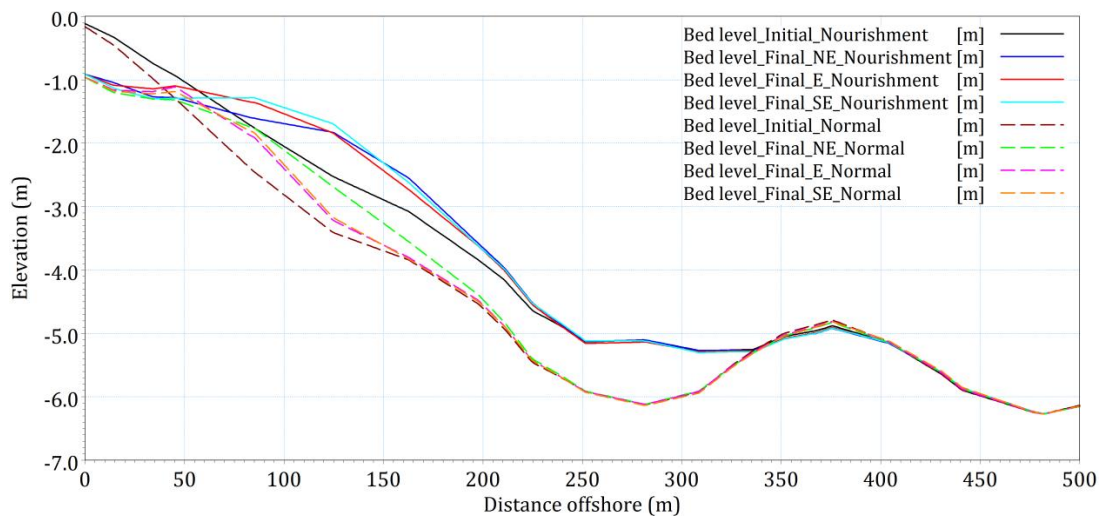


Figure 220. Beach profile evolution at Bona beach under the impact of beach nourishment and changes of wind direction.

Contrary to the different wind direction conditions, the beach nourishment plays a considerable role in limiting erosion under the seasonal changes. Figure 221 shows the changes of Bona beach profile under the winter and summer conditions with and without beach nourishment. It is noted that the winter climate causes the highest erosion rate, regardless of beach nourishment. Although the beach areas are still subjected to erode, the reduction amount of beach area with beach nourishment is much less than that without beach nourishment. Specifically, the erosion area under the winter is decreased by 42% comparing to that without beach nourishment.

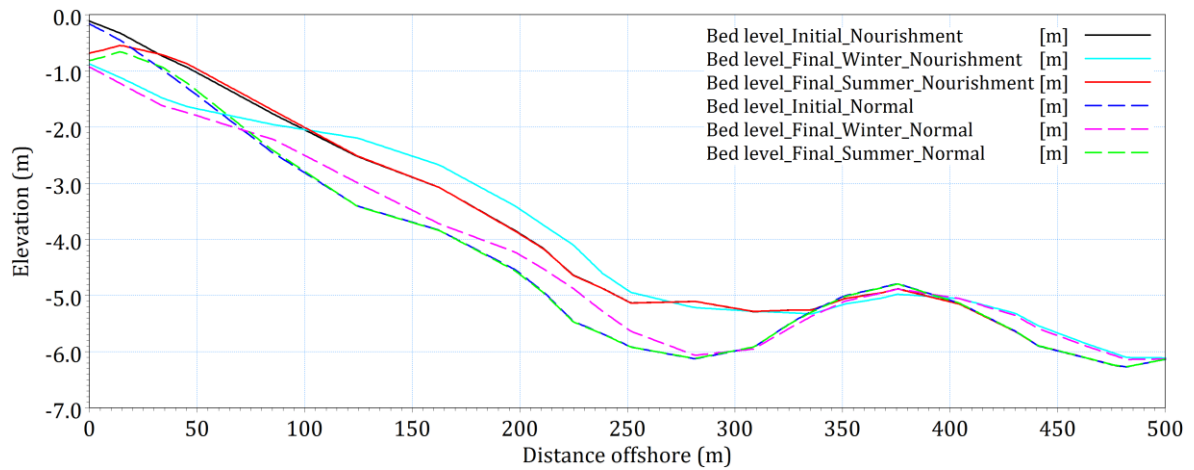


Figure 221. Beach profile evolution at Bona beach under the impact of beach nourishment and seasonal changes.

Figure 222 compares the beach profile changes in the different stormy scenarios with and without beach nourishment. Once again, it verifies that the centennial storm results in the severe erosion in Bona beach, regardless of beach nourishment. The erosion area is not reduced, but increased when the beach is nourished. Particularly, the beach loss is estimated about $-120 \text{ m}^2/\text{m}$ without beach nourishment after the centennial storm, whereas this area reaches $-150 \text{ m}^2/\text{m}$ with beach nourishment.

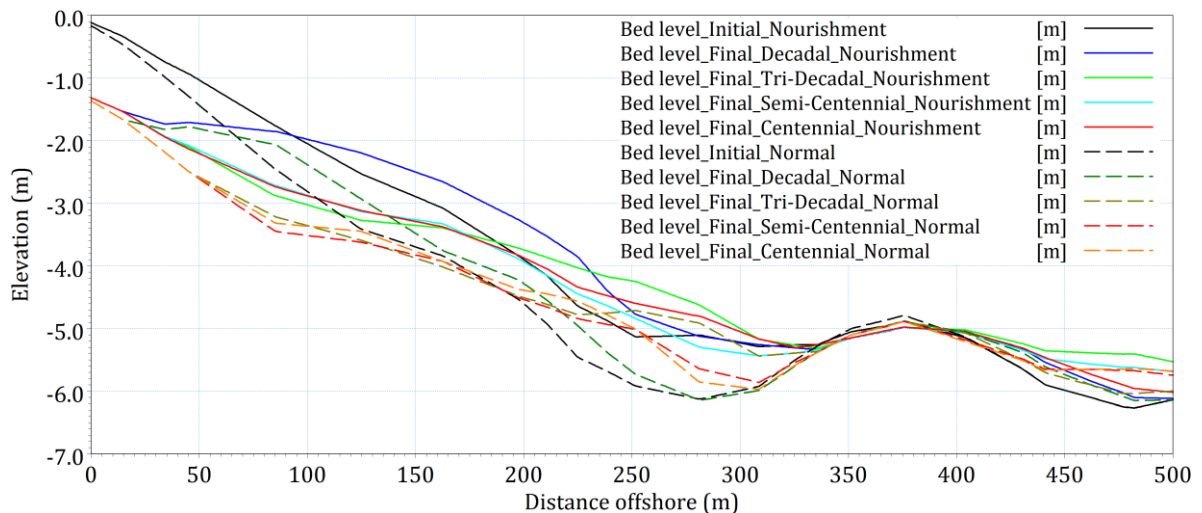


Figure 222. Beach profile evolution at Bona beach under the impact of beach nourishment and changes of storm scale.

Table 61. Effect of beach nourishment on hydrodynamic field and sediment transport in Bona.

Scenario		H_s (m)	S_{xx} (m ³ /s ²)	S_{xy} (m ³ /s ²)	S_{yy} (m ³ /s ²)	V_c (m/s)	Q (m ³ /s/m)
Normal	NE	0.682	0.337	-0.026	0.152	0.103	5.24E-05
	E	0.649	0.306	-0.028	0.140	0.163	7.35E-05
	SE	0.631	0.289	-0.029	0.132	0.171	7.57E-05
	Winter	0.283	0.087	-0.010	0.040	0.058	3.06E-05
	Summer	0.127	0.017	-0.003	0.009	0.052	7.80E-06
	Decadal	1.079	0.803	-0.063	0.352	0.242	4.47E-04
	Tri-Decadal	1.304	1.110	-0.070	0.462	0.205	5.68E-04
	Semi-Centennial	1.393	1.234	-0.050	0.487	0.062	3.99E-04
	Centennial	1.512	1.412	-0.069	0.563	0.054	4.63E-04
Nourishment	NE	0.636	0.287	-0.010	0.141	0.088	4.99E-05
	E	0.627	0.276	-0.012	0.141	0.148	7.72E-05
	SE	0.611	0.261	-0.018	0.134	0.138	7.62E-05
	Winter	0.270	0.077	-0.006	0.037	0.050	2.46E-05
	Summer	0.131	0.018	-0.002	0.009	0.056	9.19E-06
	Decadal	1.003	0.690	-0.029	0.325	0.191	3.88E-04
	Tri-Decadal	1.144	0.886	-0.019	0.383	0.079	3.38E-04
	Semi-Centennial	1.221	0.994	-0.015	0.410	0.120	3.58E-04
	Centennial	1.339	1.122	-0.067	0.496	0.260	6.33E-04
Difference (%)	NE	6.86	14.92	63.45	7.16	14.57	4.76
	E	3.39	9.77	58.43	-0.93	8.90	-5.08
	SE	3.19	9.69	36.72	-1.34	19.06	-0.67
	Winter	4.59	11.72	40.86	6.53	13.90	19.55
	Summer	-3.25	-5.33	13.39	-6.33	-8.80	-3.25
	Decadal	6.99	13.98	54.62	7.68	21.02	13.06
	Tri-Decadal	12.30	20.15	73.14	17.07	61.61	40.44
	Semi-Centennial	12.35	19.40	70.95	15.89	-93.83	10.19
	Centennial	11.44	20.56	3.77	11.90	-382.0	-36.87

5.7. Conclusion

Numerical models have been successfully developed to understand the hydrodynamic characteristics and sediment transport in Hyères bay with the presence of *Posidonia oceanica* seagrass. The presence of *Posidonia* was modeled using the proper Manning's number and Nikuradse roughness height. The models were calibrated and verified with the wave and current data measured in La Capte beach by Meulé (2010). The bed level change near Ceinturon beach was also validated by comparing the simulation results with the field data, which was conducted in a survey by E.O.L (2010). All calibrations and

comparisons show good agreement between the observed and computed results. The validated model was then used to simulate all the study scenarios taking into account wind variations, seasonal variations and extreme events. The important findings can be summarized as follows:

- There are three main wind directions of northeast, east and southeast affecting the coastal evolution of the eastern Giens tombolo, but the northeastern winds have the largest impact on the wave fields and the sediment transport. They generate the strong currents and high waves along the eastern tombolo. The northeast wind driven waves and currents are more than those in other directions about 2%-10% and 7%-48%, respectively. This engenders the higher sediment transport rates about from 6% to 38%. As a result, the largest bed level changes are observed in the northeast wind condition. These changes take place along the eastern Giens tombolo in which the areas such the south of Gapeau river mouth, Ceinturon beach, and Bona beach are suffered from severe erosion.
- The hydrodynamic and sediment transport conditions in the study area greatly depend on the seasonal variation. The winter period influences on the coastal morphology in the coast of the eastern Giens tombolo much more than the summer. An increase of the mean current speed along the coast during the winter is about 6%-46.27%, while the mean significant wave height in the winter is also completely higher than that in the summer about 68%-122%, comparing to that in the summer. The higher waves lead to larger radiation stresses in the winter, viz. the radiation stresses are augmented by 110%-410% comparing to those in the summer. As a result, the sediment transport rates in the winter are about 180% and 800% higher than those in the summer. It is evidenced by the stable state in sea bottom in the summer; even almost bed level is raised, but starting erosion in the winter.
- The higher level of storm causes the larger and stronger impacts on wave and current fields as well as sediment transport. However, when the storm level increases, the current speed has a decrease trend may be due to the expansion of sea water volume when the sea level rises. Under the impact of all storms, the most serious erosion are observed in Aygaude beach, Ceinturon beach and Bona beach, while the accretion is found in the upstream of Hyères port, the south of Pesquiers beach, and the seaward side of two submerged geotube breakwaters in La Capte beach because of the blockage of the longshore sediment drift.
- The regression of Posidonia may leads to a considerable increase of current speed, significant wave height, sediment transport rate and intensifies severe erosion along the eastern tombolo, i.e. Bona and Ceinturon. The regression of Posidonia has a significant impact on the increase of hydrodynamic parameters and sediment transport in the winter when compared with that in the summer. Eventually, the

absence of *Posidonia* mostly boosts the current speed and the sedimentation rate in the normal sea conditions regarding the change of wind direction and seasonal variation, while predominantly inducing the outstanding raise of the significant wave height in the extreme events

- The SLR would cause the moderate negative changes in the wave field, currents and sediment transport in the study area in both of the normal sea conditions and the stormy sea conditions. When the sea level rises, deeper water areas enable larger waves to reach and break closer to the shoreline, resulting in greater wave heights in nearshore zones. Indeed, the mean wave heights are increased by 1.18%-2.86% in the annual conditions and 7.65%-14.96% in the storm conditions, compared with those cases without SLR. By contrast, the nearshore currents in the normal sea-level conditions are higher than those taking into account the impacts of SLR. The decrease of current speed results in the reduction in the total load along the beaches in the eastern tombolo. The presence of SLR provokes the coastal erosion more severely than that in the No SLR scenarios, especially in nearshore zones in both two beaches.
- Beach nourishment can be used as an environment-friendly solution to stabilize the shoreline in the short term or as additional but not as primary tool for protecting the coast in the long term. If beach nourishment is carried out in Ceinturon and Bona beaches, it reduces the wave heights by 6% in the normal conditions and around 12% in the stormy conditions. This method also plays a considerable in decreasing the current speed and total load of sediment transport, especially in the extreme events. Nevertheless, erosion and sand loss still occur in these two beaches, even with higher intensification than without beach nourishment in some cases. This is a reason why it needed to be implemented periodically.

The SLR due to global warming and the regression in *Posidonia* seagrass area caused by both natural and anthropogenic factors combining with the high frequency of the storms would exacerbate the erosion problem along the eastern Giens tombolo, i.e. Ceinturon and Bona beaches. Moreover, the beach nourishment alternative which has been conducted annually shows the low efficiency in limiting the beach erosion as well as stabilizing the shoreline. Another rational and effective solution for protecting the study area which does not interfere with the landscape and must minimize the negative impacts on the surrounding environment will be discussed in detail in the next chapter.

CHAPTER 6. PRELIMINARY STUDY OF COASTAL PROTECTION MEASURES

6.1. Introduction

Coastal erosion is the recession of the shoreline and the loss of land area due to action of natural processes such as wave climate, currents, tides, storm vents, SLR, or even due to anthropogenic interventions. In order to mitigate or prevent coastal erosion, various coastal structures have been developed to protect and stabilize the shoreline, as listed in Table 62. They can be broadly classified as soft (geotubes, beach nourishment, beach drain, etc.) and hard (seawalls, dikes, breakwaters, groyne, etc.) solutions, and also combination of both.

Many of the conventional coastal protection methods described in Table 62 can solve local erosion in some cases, but may also trigger some undesirable effects as well as disadvantages. Seawall, sea dike, bulkhead, and armor stone revetment can be effective in reducing erosion landward of the structure but may cause erosion in the front of the structure due to wave reflection and scouring, generating a steeper seabed profile (U.S.A.C.E, 2002). Seawalls were established along La Capte beach (2008) and Pesquiers beach, whilst armor stone revetments were constructed in the central Ceinturon beach, the south of Hyères port and Cabanes du Gapeau (1995) in order to stop the coastal erosion. Unfortunately, the central Ceinturon beach has been suffered the recession due to the attacks of waves and storms. The erosion at the toe of seawall is observed in Pesquiers beach. Moreover, groynes and jetties, shore-normal structures that interfere with longshore sediment transport, result in accretion on the updrift side of the structures. This leads to the deficit of sediment and erosion in the downstream drift, especially in La Capte beach, Central Ceinturon and the south of Hyères port (Capanni, 2011). One of the most commonly used for shoreline stabilization and protection is breakwater. It is primarily designed to mitigate erosion on an existing beach, prompt in sediment deposition to form a new beach, protect the beach and against storm damage, or help to prolong beach nourishment. Breakwaters can be categorized as emergent or submerged, shore-parallel or oblique, shore-attached or detached (Pilarczyk et al., 1996). However, although emergent breakwaters are effective at controlling erosion, they can induce several major issues like amenity and aesthetic considerations as well as degradation of water quality due to limited water circulation. In the study area, beach nourishment is executed annually to maintain the sandy beach in Ceinturon, La Capte and Bona. This method can be used as additional but not as primary tool for coast stabilization and needed to be implemented periodically (Kliucininkaite et al., 2011). Therefore, a novel solution, which not only protects and stabilizes the shoreline, but also allows the longshore current to flow past as well as does not blot out surrounding landscape, need be required.

Table 62. Alternative Solutions for coastal Erosion Protection (U.S.A.C.E, 2002).

Type of structure	Objective	Principal function
Sea dike	Prevent or alleviate flooding by the sea of low-lying land areas	Separation of shoreline from hinterland by a high impermeable structure
Seawall	Protect land and structures from flooding and overtopping	Reinforcement of some part of the beach profile
Revetment	Protect the shoreline against erosion	Reinforcement of some part of the beach profile
Bulkhead	Retain soil and prevent sliding of the land behind	Reinforcement of the soil bank
Groyne	Prevent beach erosion	Reduction of longshore transport of sediment
Detached breakwater	Prevent beach erosion	Reduction of wave heights in the lee of the structure and reduction of longshore transport of sediment
Reef breakwater	Prevent beach erosion	Reduction of wave heights at the shore
Submerged sill	Prevent beach erosion	Retard offshore movement of sediment
Beach drain	Prevent beach erosion	Accumulation of beach material on the drained portion of beach
Beach nourishment and dune construction	Prevent beach erosion and protect against flooding	Artificial infill of beach and dune material to be eroded by waves and currents in lieu of natural supply
Breakwater	Shelter harbor basins, harbor entrances, and water intakes against waves and currents	Dissipation of wave energy and/or reflection of wave energy back into the sea
Floating breakwater	Shelter harbor basins and mooring areas against short-period waves	Reduction of wave heights by reflection and attenuation
Jetty	Stabilize navigation channels at river mouths and tidal inlets	Confine streams and tidal flow. Protect against storm water and crosscurrents

6.2. Proposed some suitable structures for coastal protection

One of the best ways to protect a beach from natural and seasonal erosion processes is to emulate natural defense mechanisms (Arnouil, 2008). Previous works have indicated that offshore reefs provide natural shoreline stabilization by reducing the amount of wave energy due to a combination of frictional dissipation and wave breaking. SBWs (artificial reefs) can generate effects similar as that of natural offshore reefs. Properly designed SBWs reduce the hydraulic loading to a required level that keeps the dynamic equilibrium of the shoreline, viz. they allow milder waves to be transmitted and attenuate only larger waves (Pilarczyk, 2003). When larger waves approach these structures, they will break, losing energy as they pass over the crest of the structure. The decrease in wave energy can result in the reduction in wave-induced currents and enhance the sediment accumulation at the shoreline without disrupting existing coastal processes (Arnouil, 2008). The SBWs have been widely used in recent years. The most important one is that they can provide desired beach protection without destroying or reducing beach amenity or aesthetics (Ranasinghe et al., 2006). This aesthetic feature is essential for maintaining the tourist value of many beaches and it is key one of the considerations in choosing such structures for shoreline protection. Furthermore, these structures can provide water flow circulation (and thus avoid stagnant zones and enhance the water quality), diminish sediment trapping behind the structure, and minimize downdrift erosion by allowing currents to pass over their crest and between the reef and the shoreline. Even they serve as facility to generate surfing waves for improving tourism in certain locations and reduce the danger for swimmers (Kliucininkaite et al., 2011). Consequently, SBWs are proposed for the study cases in this work.

Nowadays, there are three most popular types of SBWs such as rubble mound, geotube and artificial block. Breakwater type selection mainly depends on availability, cost, and execution methods. The rational selection is very important for the success and longevity of the project. Rubble mound is the most often used to build breakwaters. It allows high-energy dissipation due to its slope and transmission through porous of mound. Moreover, this type is simpler maintenance and construction, suitable for irregular bottom, and low toe scour due to small wave reflection. When the structure is long and wide, using rubble mound leads to not only high costs but also settlement of foundation and the need of quarrying a great deal of rocky material, which clearly induces an environmental damage (Buccino et al., 2013). In addition, rubble mound breakwaters are potentially more dangerous to the coastal users such as swimmers and divers (Burcharth et al., 2007). In areas with excessive wave action, the concrete blocks can be used as the most appropriate choice. The blocks are also easy to install and can be constructed locally. Additionally, these blocks with specialized surface textures and many holes allow fauna and floras colonize rapidly. In case they are manufactured on

site, a construction yard, a concrete plant, and a nearby port are required on the coast. These auxiliary works contribute to high cost and high consumption of construction time. With recent advances in design and construction techniques, geotube has become a feasible option for low impact and sustainable coastal protection. This type of structure is relatively cheap, easy to place, suitable for weak soil and flexible to allow for settlements and with little harm to swimmers. Besides, it can be used for in-situ filling materials by hydraulic pumping, so it can be also implemented with faster construction than other technology (Shin et al., 2007). However, it is relatively impermeable and reflective (including toe scour), easily vulnerable to vandalism and cutting for mussel collection with knives, low resistance to the hydraulic loadings (waves and currents), and low durability in respect to UV-radiation (Allsop et al., 1998). Experience shows that their service life is rather limited and reduced unless geotubes are protected by the cover layer. For example, in Chachoengsao's shorelines, Thailand, the geotubes installed experienced 0.6 m settlement after five years and were damaged (Saengsupavanich, 2013). Furthermore, in the study area, at La Capte beach, two submerged geotube breakwaters were implemented in March 2008. The measurement data of E.O.L (2010) shows that the height of these breakwater is decreased obviously. The main reason may be that the loss of sand inside the tube because the geotube bag has been stretched by hydrodynamic factors or this bag can be torn by anchors or mechanical forces (Lacroix et al., 2015). Hence, incidence waves overtop the geotubes, wave energy cannot be dissipated effectively, and some areas are eroded (OCEANIDE, 2010). In order to meet the demands of shoreline protection and stabilization along with the reduction in construction cost and the increase in longevity, the combination between rubble mound and geotube is utilized in this work. Geotubes will be placed in the core of SBW while rubble mound plays as one cover layer.

6.3. Design of SBWs

The basic idea in the use of SBWs is to reduce the amount of wave energy reaching the shoreline by forcing the waves to break over the structure, and thus reduces the sediment transport capacity of waves. Subsequently, sediment moved by waves and longshore currents accumulates in the lee of structure and forms a salient or a tombolo. The formation of tombolo or salient and the efficiency of shoreline protection mainly depend on the size and offshore position as well as transmission characteristics (Pilarczyk, 2003).

There are at least 13 key design parameters controlling shoreline response to an offshore breakwater, as follows:

- Length of the breakwater, L_s , measured along the breakwater crest;
- Cross-shore distance of the breakwater relative to a characteristic initial shoreline (MSL shoreline), X ;

- Gap distance between adjacent breakwaters, G , measured as the gap distance between the breakwater crests;
- Height of breakwater from seabed, h_c , and the size of the breakwater.
- Breakwater crest width, B_c , and the breakwater bottom width, B_t .
- Beach slope and water depth at toe of breakwater, d , measured relative to MSL.
- Freeboard of breakwater, F , measured relative to MSL and the crest level.
- Transmission characteristics of the structure, K_t .
- Orientation angle of structure to the shoreline.
- Mean wave height, H_b .
- Mean wave period, T .
- Predominant wave direction, θ .
- Stable weight of armor unit, W .

Some of these design parameters for a SBW are sketched in Figure 223.

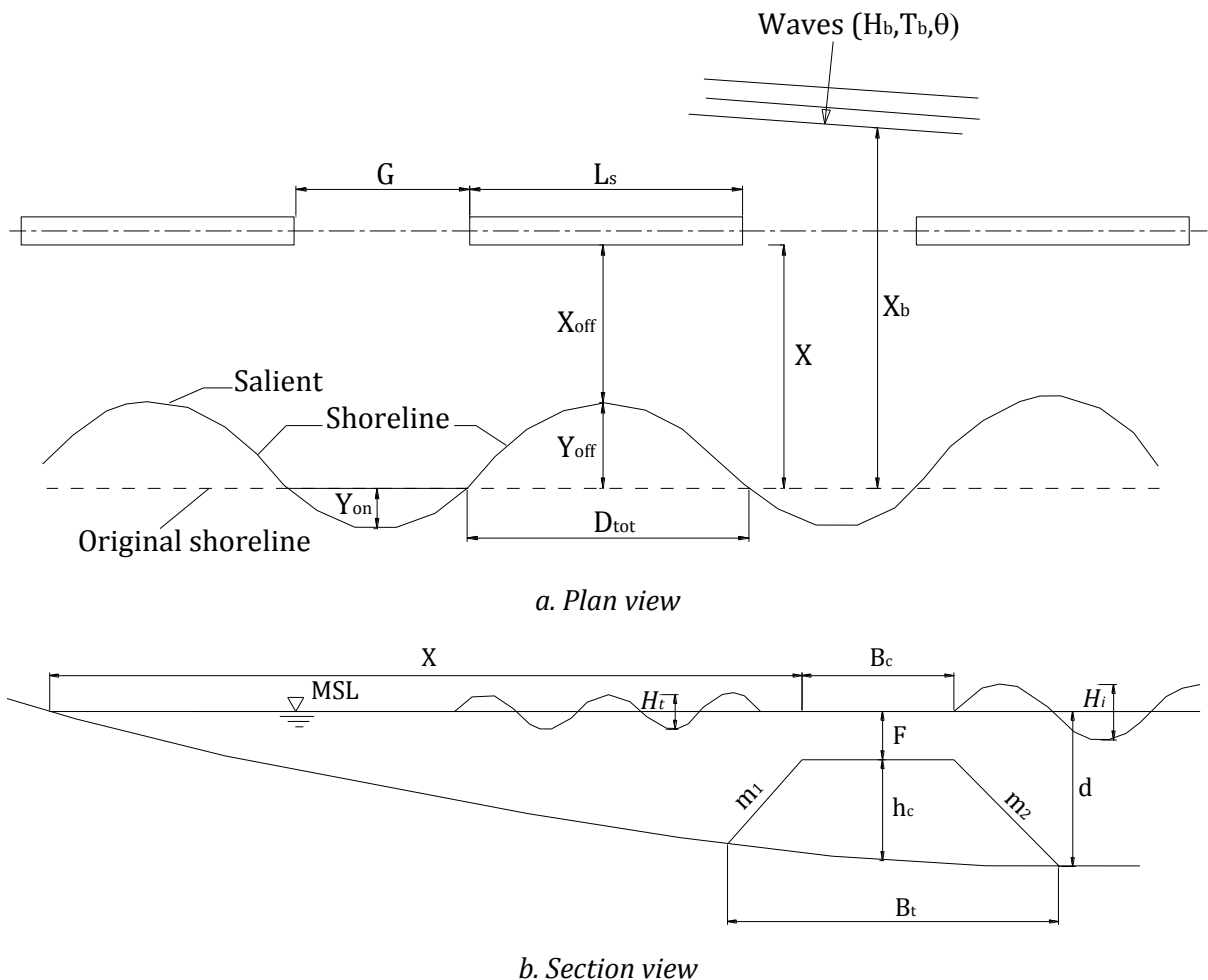


Figure 223. The main dimensions of SBW.

In addition to above-mentioned design parameters, other important ones, viz. settlement, sliding and overturning, which should be considered when designing SBWs, but are not covered in this work.

6.3.1. Considerations of SBW design parameters

6.3.1.1. Positioning of the SBWs

The position, which locates SBW, will be principally determined according to the wave and sediment transport conditions as well as the length of protected shoreline. The purpose of SBWs is to reduce the hydraulic loading to a required level that maintains the dynamic equilibrium of the shoreline by forcing wave breaking over the reef. To attain this goal, they are invariably placed inside the breaker line within the surf-zone and are attacked by breaking and broken waves. The surf zone can be limited seaward by the depth of which the local significant wave height starts breaking due to the shallow water depth (Dally, 2005). Accordingly, the location of breaking wave is very important because it will be considered as location of SBW position. Breaking depth, breaking index γ and breaking height can be obtained by trial and error process as follows:

- Guess water depth “ d ”.
- Calculate L_o , d/L_o , and $\tan(kd)$:

The wavelength in deep water:

$$L_o = \frac{g \cdot T_p^2}{2\pi} \approx 1.56T_p^2 \quad (6-1)$$

The wavelength in shallow water:

$$L = T_p \sqrt{g \cdot d} \quad (6-2)$$

$$\tanh(kd) = \tanh\left(\frac{2\pi \cdot d}{L}\right) \quad (6-3)$$

Where T_p is the peak period, $T_p = 7.43$ s (Table 32).

- Calculate the shoaling coefficient K_s

$$K_s = \frac{H}{H_o} = \sqrt{\frac{1}{2 \cdot n \cdot \tanh(kd)}} \quad (6-4)$$

Where H_o is the wave height in deep water, $H_o = 2.18$ m (Table 32),

$$n \text{ is energy flux parameter, } n = \frac{1}{2} + \frac{kd}{\sinh(2kd)}$$

$$\Rightarrow K_s = \sqrt{\frac{1}{2 \tanh(kd) \left[\frac{1}{2} + \frac{kd}{\sinh(2kd)} \right]}} \quad (6-5)$$

- Calculate the angle of refraction α

$$\alpha = \arcsin\left(\frac{L}{L_o} \sin \alpha_o\right) \quad (6-6)$$

Where α_o is the angle of incidence.

- Calculate the refraction coefficient K_r

$$K_r = \sqrt{\frac{\cos\alpha_0}{\cos\alpha}} \quad (6-7)$$

- Calculate the refraction wave height: $H = H_0 * K_s * K_r$
- Calculate the breaking wave height according to Weggel (1972):

$$H_b = \frac{C_1 h_b g T^2}{(g T^2 + h_b C_2)} \quad (6-8)$$

Where $C_1 = \frac{1.56}{1+e^{-19.5m}}$; $C_2 = 43.75(1 - e^{-19m})$; $T = 0.75T_p$; m is the bottom slope.

- Plot the graph showing the relationships between water depth d and wave height H and breaking wave height H_b in the same axis system. At the intersection of two lines, the breaking point is represented. In addition, breaking index γ can be computed by dividing breaking height by breaking depth. The results of calculation are presented from Table 63 to Table 65 and from Figure 224 to Figure 226.

Table 63. The calculation of breaking depth and breaking height for annual wave condition (1/1 year) in Ceinturon beach.

d	d/L₀	L	tanh(kd)	K_s	α	K_r	H(m)	H_b(m)
7	0.08	61.57	0.61	0.97	9.25	0.99	2.10	5.06
6.5	0.08	59.33	0.60	0.98	8.91	0.99	2.12	4.76
6	0.07	57.00	0.58	0.99	8.56	0.99	2.14	4.44
5.5	0.06	54.58	0.56	1.00	8.19	0.99	2.17	4.13
5	0.06	52.04	0.54	1.02	7.81	0.99	2.20	3.80
4.5	0.05	49.37	0.52	1.03	7.40	0.99	2.23	3.46
4	0.05	46.54	0.49	1.05	6.98	0.99	2.27	3.12
3.5	0.04	43.54	0.47	1.08	6.52	0.99	2.33	2.76
3	0.03	40.31	0.44	1.11	6.04	0.99	2.39	2.40
2.5	0.03	36.80	0.40	1.15	5.51	0.99	2.47	2.03
2	0.02	32.91	0.36	1.20	4.93	0.99	2.59	1.64

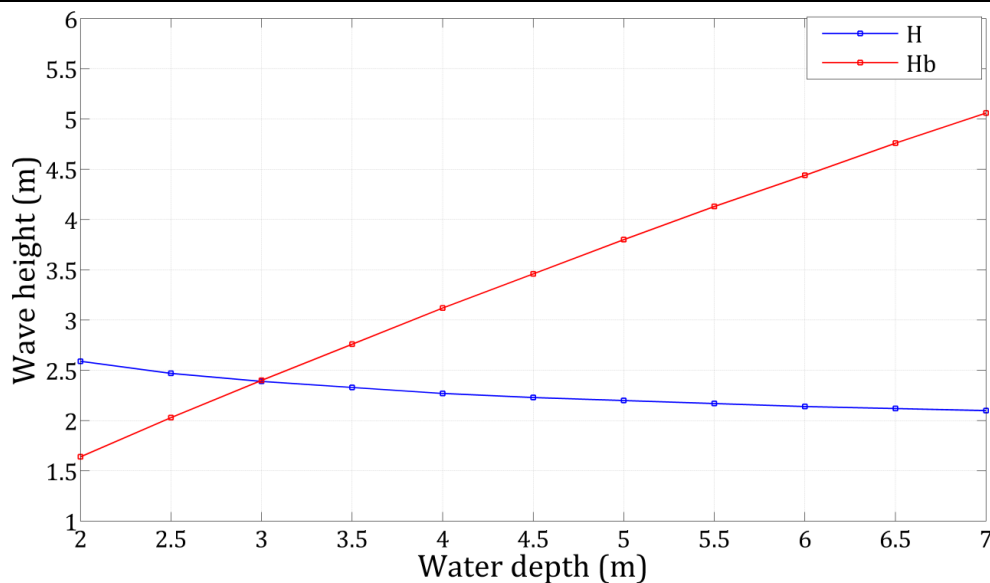


Figure 224. Relation between H_b and d_b of annual condition in Ceinturon beach.

Table 64. The calculation of breaking depth and breaking height for annual wave condition (1/1 year) in Bona beach.

d	d/L₀	L	tanh(kd)	K_s	α	K_r	H(m)	H_b(m)
7	0.08	61.57	0.61	0.97	27.33	0.93	1.97	4.94
6.5	0.08	59.33	0.60	0.98	26.26	0.92	1.98	4.67
6	0.07	57.00	0.58	0.99	25.16	0.92	1.99	4.39
5.5	0.06	54.58	0.56	1.00	24.02	0.92	2.00	4.09
5	0.06	52.04	0.54	1.02	22.83	0.91	2.02	3.79
4.5	0.05	49.37	0.52	1.03	21.60	0.91	2.04	3.48
4	0.05	46.54	0.49	1.05	20.31	0.90	2.07	3.15
3.5	0.04	43.54	0.47	1.08	18.95	0.90	2.11	2.81
3	0.03	40.31	0.44	1.11	17.49	0.90	2.16	2.46
2.5	0.03	36.80	0.40	1.15	15.93	0.89	2.23	2.09
2	0.02	32.91	0.36	1.20	14.21	0.89	2.32	1.71

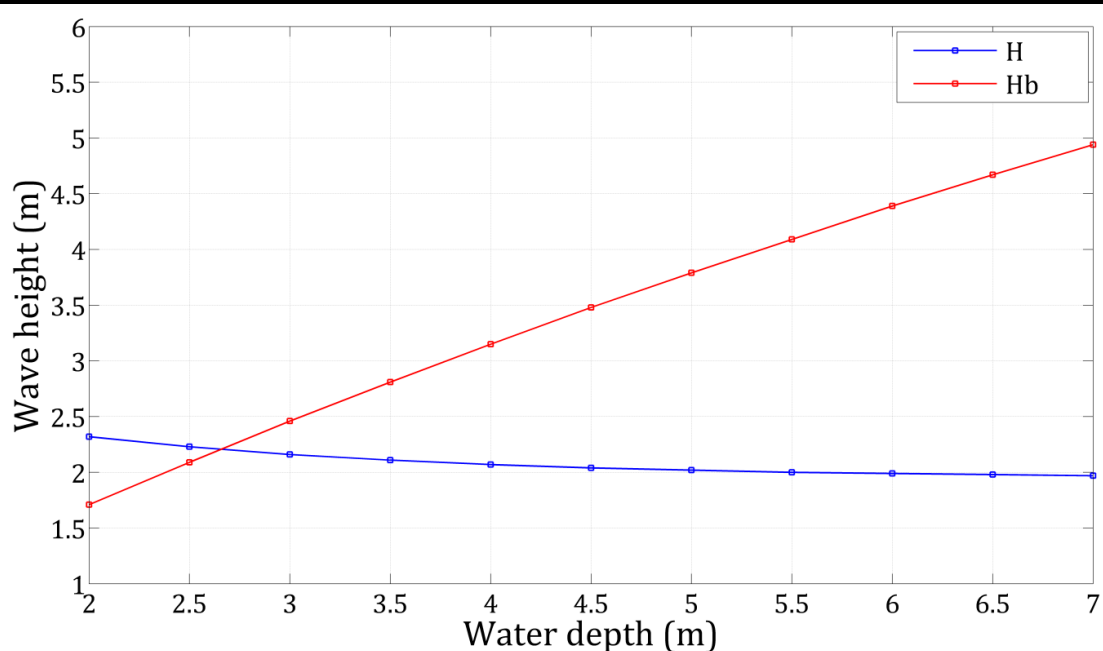


Figure 225. Relation between H_b and d_b of annual condition in Bona beach.

Table 65. The calculation of breaking depth and breaking height for annual wave condition (1/1 year) in Pesquiers beach.

d	d/L₀	L	tanh(kd)	K_s	α	K_r	H(m)	H_b(m)
7	0.08	61.57	0.61	0.97	26.09	0.94	1.98	4.97
6.5	0.08	59.33	0.60	0.98	25.07	0.93	1.99	4.69
6	0.07	57.00	0.58	0.99	24.03	0.93	2.01	4.40
5.5	0.06	54.58	0.56	1.00	22.94	0.93	2.02	4.10
5	0.06	52.04	0.54	1.02	21.82	0.92	2.04	3.79
4.5	0.05	49.37	0.52	1.03	20.65	0.92	2.07	3.47
4	0.05	46.54	0.49	1.05	19.42	0.91	2.10	3.14
3.5	0.04	43.54	0.47	1.08	18.12	0.91	2.14	2.79
3	0.03	40.31	0.44	1.11	16.73	0.91	2.19	2.44
2.5	0.03	36.80	0.40	1.15	15.24	0.90	2.26	2.07
2	0.02	32.91	0.36	1.20	13.60	0.90	2.35	1.68

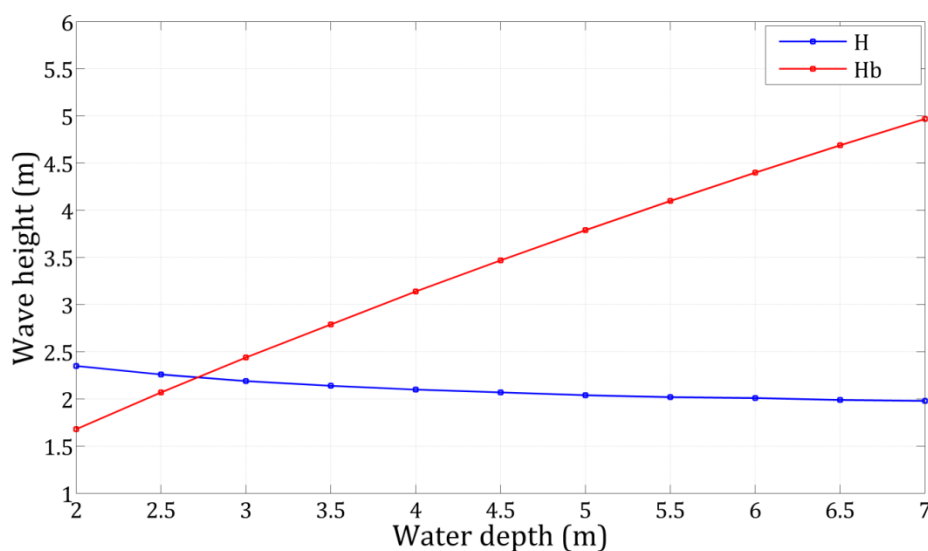


Figure 226. Relation between H_b and d_b of annual condition in Pesquiers beach.

Summary of breaking conditions, from above calculation, it can be concluded in Table 66.

Table 66. Summary of breaking conditions.

Beach	Annual wave condition			Centennial wave condition		
	H_b (m)	d_b (m)	γ	H_b (m)	d_b (m)	γ
Ceinturon	2.39	3.00	0.797	8.04	10.29	0.781
Bona	2.21	2.66	0.831	7.57	9.49	0.798
Pesquiers	2.23	2.72	0.820	7.63	9.63	0.792

On the other hands, the seabed in the study area includes Posidonia meadows at very close distances from the coast. Posidonia meadows are considered among the most important marine ecosystems, for biodiversity, ecological and economic reasons. The role of Posidonia meadows in marine coastal environments is often correctly compared to that of the forest in terrestrial environments. However, Posidonia meadows has considerably regressed by mainly human activities (Boudouresque et al., 2012). In order to prevent the disappearance, it is protected by the decree of 19 July 1988 on marine protected plant species by the Bern Convention on the conservation of European Wildlife and Natural Habitats in Europe ratified by France in 1990 and confirmed by the decree of 7 in July 1999 the Ministry of Foreign Affairs. Therefore, it must be considered in any project of construction that may have a direct or indirect impact on this species (OCEANIDE, 2010). To avoid to impact on Posidonia, the SBWs should be placed right inside the upper limit of Posidonia (Figure 32) in order to ensure the minimum distance of 10 m between the nearest living Posidonia and the structures which is recommended by Boudouresque et al. (2012). Based on the breaker depth (Table 66) as well as the position of Posidonia, it is proposed to place the breakwater at the water depth of 2.5 m in both of Ceinturon beach and Bona beach (Figure 230).

After determining the offshore position of SBWs, orientation angle of the structure to the shoreline need be estimated properly. Like the design dimensional parameters, this angle also plays an important role in success or failure of one SBW project. If SBWs are placed in the wrong direction, it even cause negative impacts, such as the project of a SBW (known as the PEP reef) in West Palm Beach, Florida (Dean et al., 1997), or another project of a SBW to hold a beach fill in Dalaware Bay (Weggel et al., 1987). The breakwater's orientation mostly depends on incident wave angle and orientation of the pre-project shoreline. If incident wave energy is predominantly oblique to the shoreline, orientation of the breakwater should be parallel to incoming wave crests in order to protect a greater length of shoreline and reduce toe scour at the breakwater ends (U.S.A.C.E, 1993). In the study area, the southeast waves, which are dominant, approach the shorelines of Ceinturon and Bona beaches almost perpendicularly. Hence, the SBWs are situated parallel to the shorelines.

6.3.1.2. Relationship between the dimensional parameters of the SBWs

The reduction in wave energy due to SBWs slows the littoral drift, produces sediment deposition and a salient or tombolo feature in the sheltered area behind the breakwater. However, the tombolo will block normal, longshore sediment behind structure, while salient allows some longshore sediment transport maybe continue to move through the project area to downdrift beaches. The relationship between the length of each segment, L_s , the distance from the shoreline to the breakwater X , and the gap between two segments G establish conditions salient or tombolos which will naturally form behind the breakwater. In this work, the authors will apply some experiential formulae for defining L_s , X , and G , which prompt in forming salient because it permits the longshore current pass between the SBWs and the shoreline, and diminish the shortage of sediment downstream. In addition to L_s , X , and G , the height and width of SBWs are also other important parameters deciding the wave dissipation capacity of SBWs.

a. Prediction of shoreline response

One of the first authors who recommended criterion to assure salient development is Dally et al. (1986). They suggested that salient would form if:

$$\frac{L_s}{X} = 0.67 \text{ to } 1.5 \quad (6-9)$$

Following Black et al. (2001), salient form in the lee side of submerged offshore breakwater when:

$$\frac{L_s}{X} < 2 \quad (6-10)$$

Coastal Engineering Manual (USACE, 2002) presents wide range of ratios of breakwater length with distance offshore (L_s/X) to forecast salient as follows:

$$\frac{L_s}{X} = 0.4 \text{ to } 1.5 \quad (6-11)$$

Most of above-mentioned geometrical criteria do not include the transmission characteristic. To take into account the effect of submergence (transmission) Pilarczyk (2003) proposes, at least as a first approximation, adding the factor $(1-K_t)$ to the existing rules. Then the rules for low-crested breakwaters can be modified to:

- Salient:

$$L_s < \frac{X}{(1 - K_t)} \quad (6-12)$$

- For salients where there are multiple breakwaters:

$$G > \frac{0.5L_s^2(1 - K_t)}{X} \quad (6-13)$$

- The gap width is usually $L \leq G \leq 0.8L_s$, where L is the wavelength at the structure defined as: $L = T_p.(g.d)^{0.5}$; T_p is wave period and d is local depth at the breakwater.

Seiji M. et al. (1987) introduces the following gap erosion relationships, where gap erosion is defined as the retreat of shoreline to the lee of the gap from the initial (pre-project) shoreline position:

- no erosion opposite gap: $\frac{G}{X} < 0.8$
- possible erosion opposite gap: $0.8 \leq \frac{G}{X} \leq 1.3$
- certain erosion opposite gap: $\frac{G}{X} \geq 1.3$

These relationships were evaluated with prototype data. The lower boundary for no erosion ($G/X < 0.8$) was a good predictor of either accretion or very little erosion. Gap erosion occurred for ratios of G/X greater than 0.8.

In this work, the offshore distance of the SBWs, $X = 80$ m has already calculated from the previous step. The L_s and G will be determined using formula as below:

$$\frac{L_s}{X} = 0.4 \text{ to } 1.5$$

$\Rightarrow L_s = (0.4 \text{ to } 1.5) * 80 = (32 \text{ to } 120)$ m. Choosing $L_s = 110$ m for Ceinturon and Pesquiers beaches; $L_s = 120$ m for Bona beach.

$$\frac{G}{X} < 0.8$$

$\Rightarrow G < 0.8 * 80 = 64$ m. Choosing $G = 60$ m.

It is proposed to protect the central Ceinturon beach in the distance of 800 m along the shoreline and the Bona beach in the distance of 1100 m along the shoreline. Hence, the numbers of the SBWs are five segments and seven segments at Ceinturon and Bona beaches, respectively.

When the gap erosion occurs, Silvester et al. (1997) proposed a method for determining the equilibrium shoreline planform in the lee of a single detached nearshore breakwater, based on the parabolic bay shape method. The key parameters are illustrated in Figure 227.

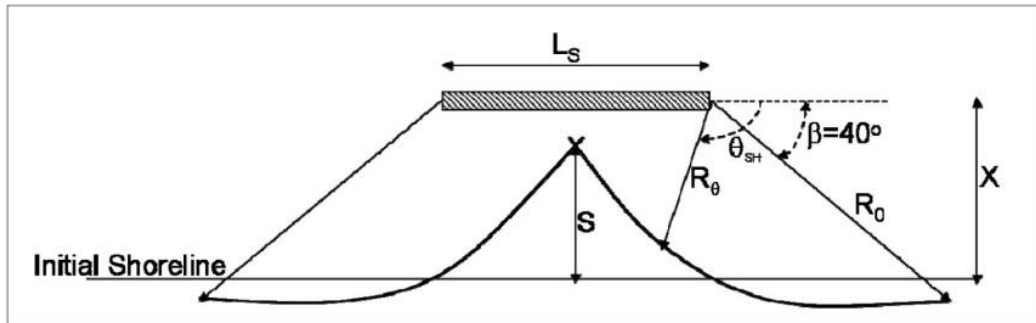


Figure 227. Key beach and breakwater parameters in the Silvester et al. (1997) method.

The maximum erosion at gap width can be estimated by assuming the effect of adjacent breakwaters are independent of each other.

$$x_{max} = L_s \left(0.1737 + \frac{1.683}{L_s/X} \right) \sin 40^\circ - X \quad (6-14)$$

$$\Rightarrow x_{max} = 110 \left(0.1737 + \frac{80 * 1.683}{110} \right) \sin 40^\circ - 80 = 18.8m$$

Therefore, a minimum beach fill of 20 m width in the gap between the segments should be provided.

b. Prediction of transmission characteristics

The height of SBW, h_c , or breakwater crest elevation is another design characteristic to be considered. If this height is too small compared with the water depth, the interaction of breakwater with approaching waves will be minimal, thus leading to ineffective wave attenuation (Armono et al., 2003). Accordingly, ideally, the crest level of a SBW should be as close as possible to the MLLW level without becoming exposed when considering only physical efficiency of the submerged structure. A shallow submerged crest will maximize its effectiveness at dissipating wave energy during higher tides with small waves as well as during high wave storm events (Hearin, 2009). Harris (1996) indicated that the ratio between the height of breakwater and the water depth, namely relative structure height, should be 60-80% for optimum effectiveness, whereas Armono et al. (2003) mentioned that the effect of breakwater length is noticeable when the breakwater height is more than 70% of water depth. The Hyères bay has small tide fluctuations (<0.3m) and is only affected by seasonal storm surges (SOGREAH, 1988b); hence the probability for long-term or frequent emersion is very low. According to all recommendations in previous studies and taking into account local specific conditions, the crest level of approximately 0.4 m below MSL is chosen for all scenarios. It means that the maximum wave height of 0.8 m could be transmitted through the breakwater crest.

When the SBWs are applied for coastal protection, the service lifetime of these structures will be as long as protection is required, provided that they are functioning satisfactorily. A 50 years lifetime or more is common for coastal structures (Burcharth et al., 2007). In this study, the design life of 50 years is proposed to use. This implies that extreme wave condition of the centennial storm (1/100 year) has to be considered as a design wave condition. For the design water depth of 2.5 m, the extreme deep-water wave height of 7.64 m will be broken with the breaking indexes of 0.781 and 0.798 at Ceinturon and Bona beaches, respectively. In this condition, the breaking depths are 10.29 m and 9.49 m, corresponding to the breaking heights of 8.04 m and 7.57 m at Ceinturon and Bona beaches, respectively (Table 66). In addition, wavelength can be determined as below:

$$L_{om} = 1.56 * 9.23^2 = 132.9 \text{ m}$$

$$L_{op} = 1.56 * 12^2 = 224.83 \text{ m}$$

Breakwaters crest width also plays a significant role in wave energy dissipation of a SBW. Stauble et al. (2003) indicated that narrow-crested breakwaters, such as the P.E.P reefs, have shown to have limited their effectiveness in wave attenuation and a steeper landward facing slope experienced scour on the landward base. In addition, in tidal environments and when frequent storm surges occur, they become less effective if the narrow-crested structures are used (Pilarczyk, 2003). This is also the reason why broad-crested SBW became popular. Nevertheless, broad-crested structures are much more expensive than narrow-crested ones and their use should be supported by proper cost-benefit studies. The development of alternative materials and construction technology, e.g. the use of sand-filled geotubes as a core of such structures, can effectively reduce the cost.

Structure such as breakwaters with low crest levels construction will transmit wave energy into the leeside of the breakwater. The transmission performance of low-crested breakwaters is dependent on the structure geometry, principally the crest freeboard, crest height, crest width, water depth, permeability, and on the wave conditions, mainly the wave height and period. The relationship between crest width and transmission coefficient is proposed by Tanaka (1976).

The design wave height is almost 2.0 m at both Ceinturon and Bona beaches, so the value of H_t/H_o is 0.4. The value of R/H_o is -0.2, so from the graph of Tanaka (1976), we find $B_c/L_o = 0.075$ (Figure 228). Finally, the crest width of the SBWs is found as $B_c = 9.97$ m for $L_{om} = 132.9$ m and $B_c = 16.86$ m for $L_{om} = 224.83$ m. In order to determine the rational crest width, a sensitive analysis with two values of the crest width of 10 m and 20 m should be carried out by using the numerical simulation. The results will be presented in the next part of this chapter.

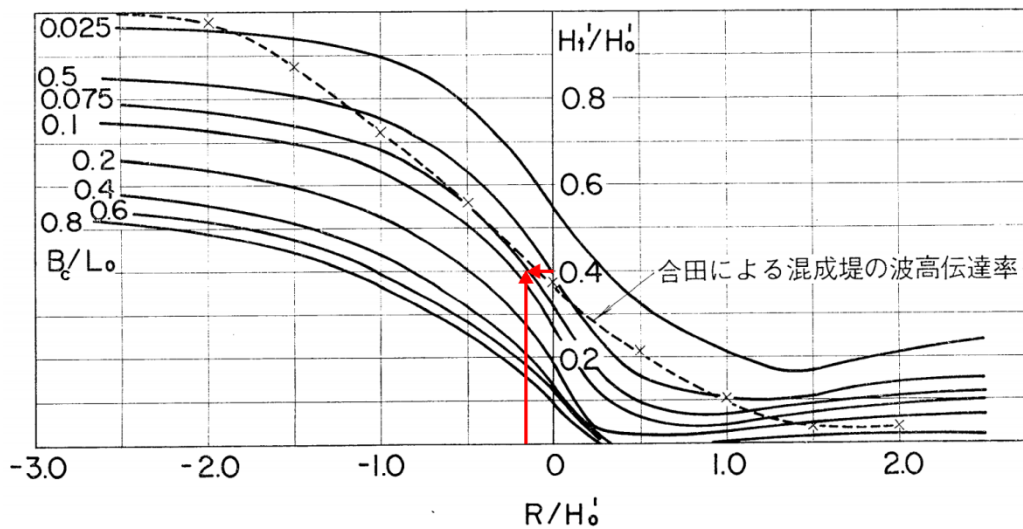


Figure 228. Wave transmission design curves (Tanaka, 1976).

6.3.2. Stability of SBW

The primary purpose of SBW is to attenuate the approaching waves, thus it has to be designed to resist the breaking wave forces, wave-induced currents and scour that occur in the surf zone. The submerged rubble mound breakwater consists of selected units of either quarry stones or artificial concrete blocks, which can receive the impacts of wave and current. As a result, the global stability of breakwater principally depends on the stability of each armor unit, specifically on the seaward slope of structure. The weight of individual unit plays a decisive role in its stability. Of course, the heavier the weight of armor unit is, the more stable it becomes. Nevertheless, this leads to high cost of construction as well as may exceed the bearing capacity of seabed resulting in the settlement of breakwater foundation. Therefore, it is necessary to define the minimum weight of armor units, but still ensure the ability to withstand wave and current-driven forces.

There are several empirical formulae which are available for the estimation of the minimum stable weight of the armor unit for the breakwater, but the most widely used is Hudson formula (U.S.A.C.E, 1984).

$$W_r = \frac{w_r H^3}{N_s^3 (S_r - 1)^3} \quad (6-15)$$

Where

W_r is the weight of the individual armor unit;

w_r is the unit weight of the armor unit, $w_r = 2650 \text{ kg/m}^3$;

H is the design wave height at the structure site in meters;

S_r is the specific gravity of the armor unit, $S_r = w_r / w_w$;

w_w is the unit weight of water, fresh water = 1000 kg/m^3 and seawater = 1025 kg/m^3 ;

N_s is the stability number, determined by using the graph (Figure 229) which is proposed by Gadre et al. (1992).

Based on the stable weight of armor, which is computed by equation (6-15), the nominal rubble unit diameter of the median size is estimated as follow:

$$D_{n50} = \left(\frac{W_r}{W_r} \right)^{1/3} \quad (6-16)$$

The average thickness of armor stone layer t_a of the structure on each side can be determined from the following formulas:

$$t_a = nk_{\Delta}D_{n50} \quad (6-17)$$

Where n is the number of quarry stone or concrete armor units in thickness, comprising the cover layer, $n = 2$, and k_{Δ} is the layer coefficient, with quarrystone, $k_{\Delta} = 1$ (U.S.A.C.E, 1984).

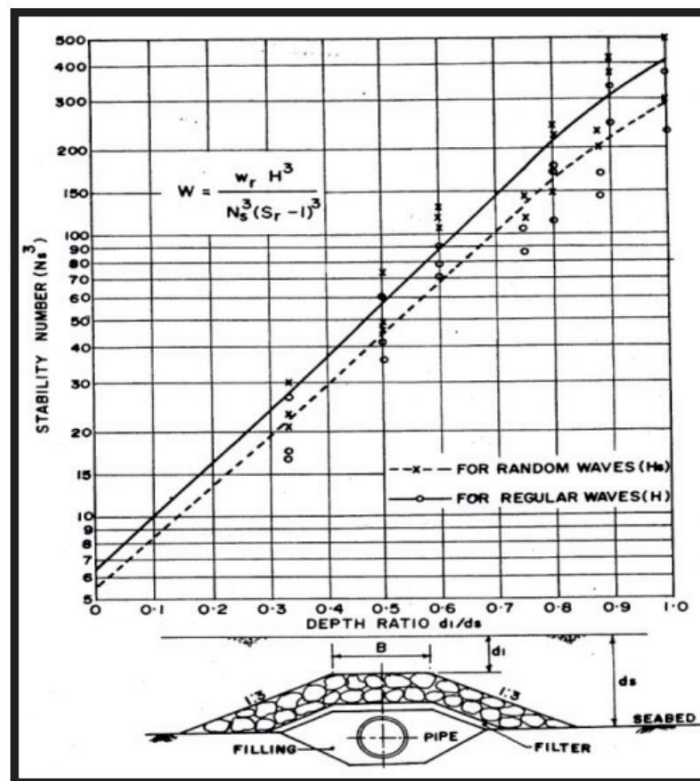


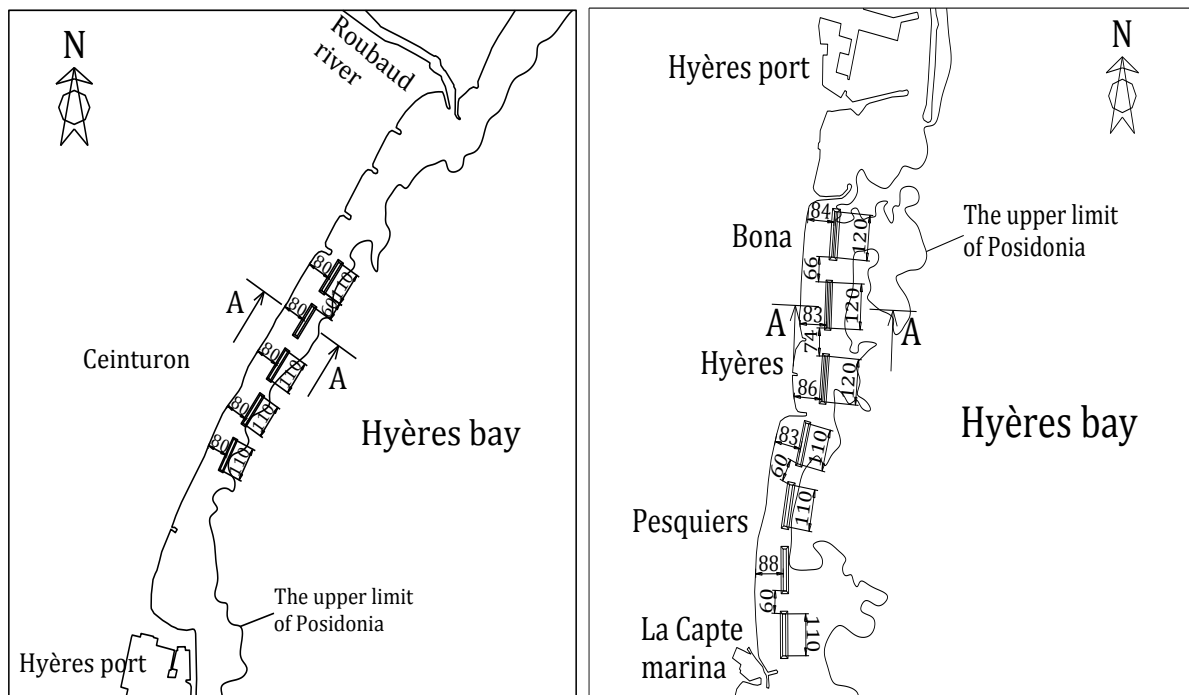
Figure 229. Design curve of stability number (N_s) and depth ratio for the submerged reefs (Gadre et al., 1992).

The stability of the armour layer in depth limited situation is verified by the maximum wave height at the structure site (located 80 m seaward of the shorelines) in the centennial storm condition (1/100 year), extracted from the numerical simulation. Summarized design parameters of armour layer are presented in Table 67.

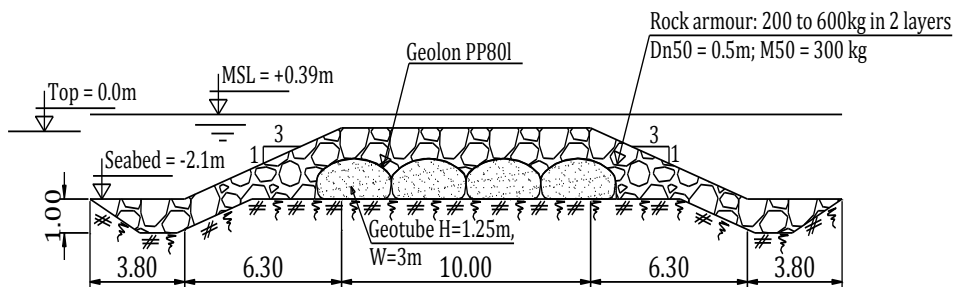
Table 67. Parameters of designed armour layer.

Beach	H (m)	N_s^3	W_r (kg)	D_{n50} (m)	t_a (m)
Ceinturon	1.68	11	285.2	0.48	0.95
Bona	1.99	10	520.2	0.58	1.16
Pesquiers	1.82	9.5	420.8	0.54	1.08

Final parameters of designed SBWs in front of Ceinturon and Bona beaches are presented in Figure 230 and shortly summarized design is described in Table 68.



a. Plan view



b. Cross-section view of A-A

Figure 230. The arrangement of the SBWs for Ceinturon and Bona beaches.

Table 68. Parameters of designed SBWs.

Beach	Ceinturon	Bona	Pesquiers
Distance from shoreline, X (m)	~80	83~86	80~88
Orientation to the coast	Parallel	Parallel	Parallel
Constructional material	Geotubes and quarrystone	Geotubes and quarrystone	Geotubes and quarrystone
Length of breakwater, L_s (m)	110	120	110
Crest width of breakwater, B_c (m)	10-20	10-20	10-20
Gap between two breakwaters, G (m)	60	66~74	60
Crest elevation of breakwater	+0.0 (CM)	+0.0 (CM)	+0.0 (CM)
Median diameter of rock, D_{50} (m)	0.5	0.6	0.55

6.4. Sensitivity analysis of design parameters

6.4.1. Salient predictions for the Ceinturon and Bona beaches

The artificial SBWs play as the natural reef in protection coastal. They dissipate the wave energy and reduce the current speed, so salient is formatted in the lee side of the structure as desired and favorable. The salient formation can be achieved and predicted by employing right constructional design methodology and parameters. The main indicator, which allows predicting the size of the salient is the ratio between distance offshore and breakwater length. The following empirical relationships were developed by Black et al. (2001), as shown in Figure 223(a).

The distance from the tip of the salient and the breakwater, X_{off} , is given by:

$$\frac{X_{off}}{L_s} = 0.498 \left(\frac{L_s}{X} \right)^{-1.268}$$
$$X_{off} = X - Y_{off} \quad (6-18)$$
$$Y_{off}/D_{tot} = 0.125 \pm 0.02$$

6.4.1.1. Ceinturon beach

The predicted salient size and length for the Ceinturon beach is presented in Figure 231 and Figure 232, respectively. They indicate that the maximal salient would form if the SBW would be constructed 600 m away from the shoreline. In this position, the amplitude of salient can reach up to 130 m seaward of the shoreline and the length of salient can develop to over 1000 m. However, the presence of Posidonia which is protected by the national law, limits the construction position of the SBWs. Therefore, the offshore distance of 80 m from the shoreline was chosen. This distance would promote the form of salient with the maximum amplitude of 43 m, corresponding to the length of 347 m. Consequently, the gap between the tip of the salient and the SBWs is still retained around 40 m which could allow not only the longshore sediment drift to bypass and move to the downstream area, but also the underwater recreational activities. This is very important in attracting tourist and economic development.

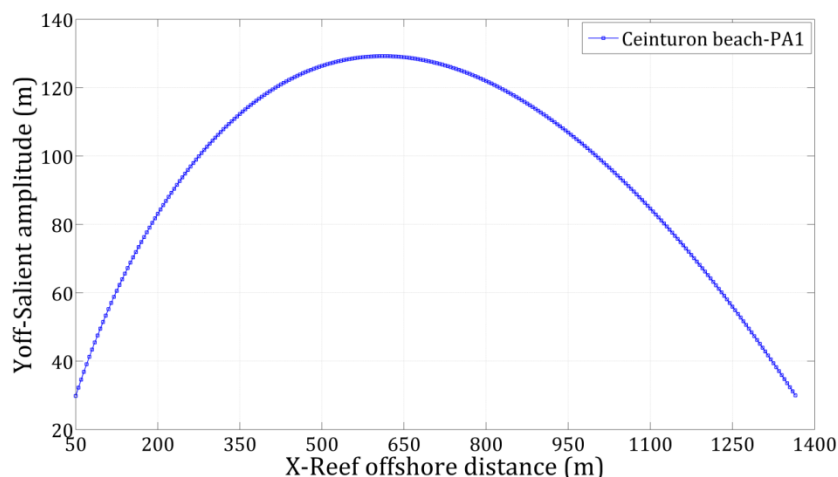


Figure 231. Prediction of salient amplitude in Ceinturon beach.

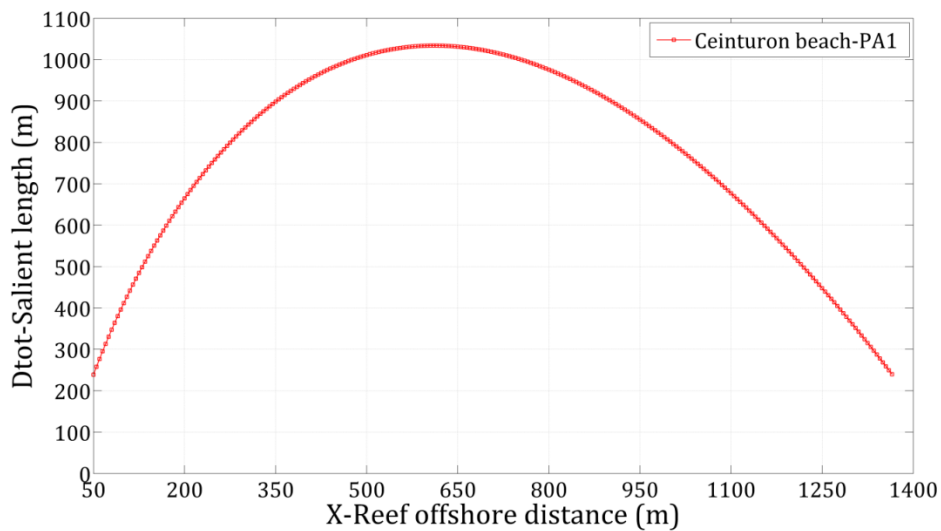


Figure 232. Prediction of salient length in Ceinturon beach.

6.4.1.2. Bona beach

The Bona beach research location can be described as having bed slope of more rapid gradient, with some sand bars and higher erosion rates than in Ceinturon beach. The predicted salient amplitude and width are plotted in Figure 233 and Figure 234, which reveal that the maximal salient would form if the SBWs would be placed 725 m seaward of the shoreline. This position maybe generates the maximum salient amplitude of 153 m, corresponding to the salient width of about 1220 m. Nevertheless, it should be avoided to interfere with Posidonia, it was desirable to install the SBWs as close to the coast as possible. Combining with the breaking wave condition, the SBWs were designed approximately over 80m away from the shoreline. Such distance reduces the probability that the structure could block the lonshore sediment flow and form a tombolo or tombolos. Also with the offshore distance of 80 m, the maximum salient amplitude can reach up to 45 m, corresponding to the salient width of 360 m. This condition ensures the bypassing of longshore sediment as well as allows the underwater recreational activies taking place comfortably on the beach.

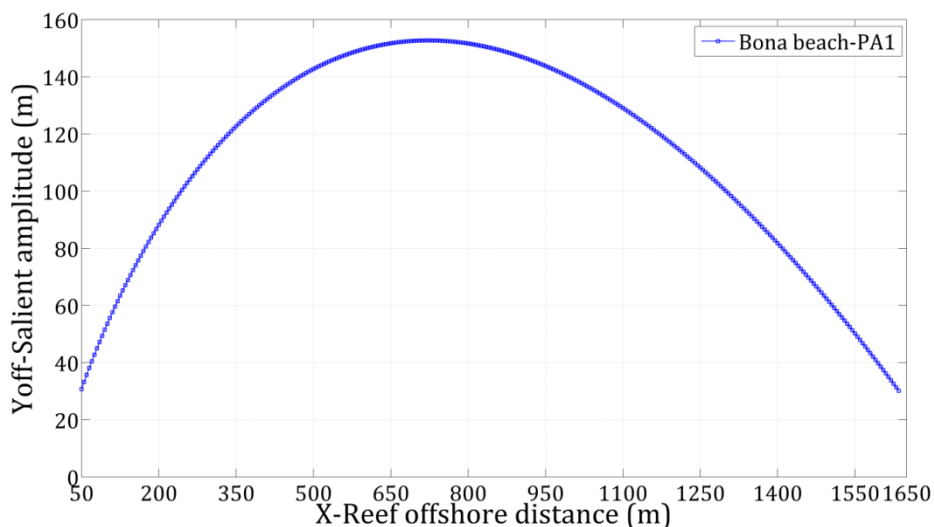


Figure 233. Prediction of salient amplitude in Bona beach.

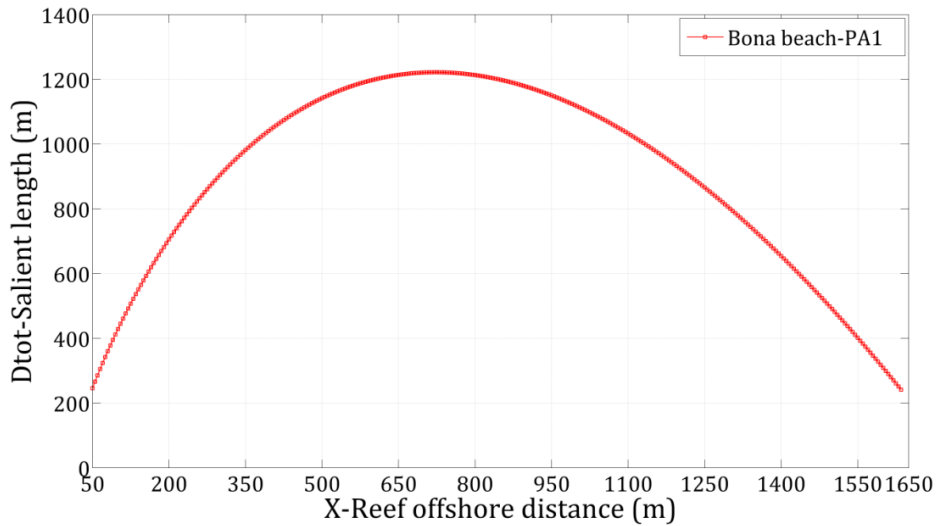


Figure 234. Prediction of salient length in Bona beach.

6.4.2. Determination of rational crest width

As above-mentioned, the SBWs are primarily designed to dissipate and allow the amount of wave energy that is transmitted past the structure. It is noted that higher submergence level of the low-crested breakwater, the less the wave impacts with the structure, which could result in the lower waver attenuation (Kliucininkaite et al., 2011). The parameter used to evaluate the effectiveness of a SBW alternative in terms of wave attenuation is the transmission coefficient, K_t . It can be determined as below:

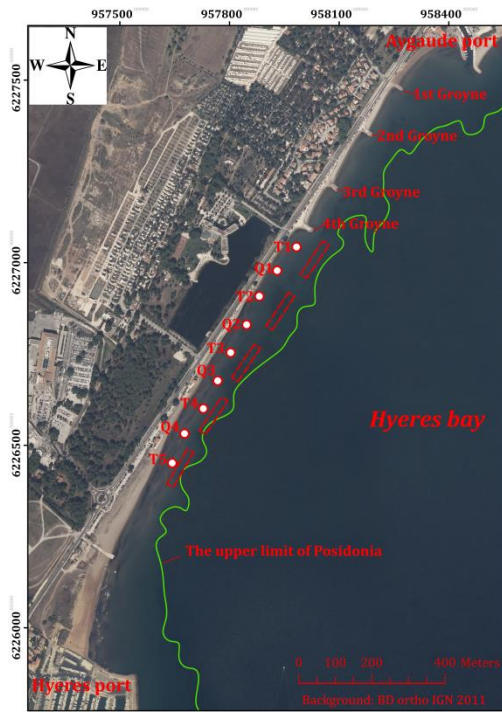
$$K_t = \frac{H_t}{H_i} \quad (6-19)$$

Where K_t is the wave transmission coefficient, H_t is the height of the transmitted wave on the landward side of the structure, and H_i is the height of the incident wave on the seaward side of the structure (U. S. A. C.E, 1984). The value of K_t ranges from 0 to 1. The greater the wave transmission coefficient is, the less the wave attenuation is.

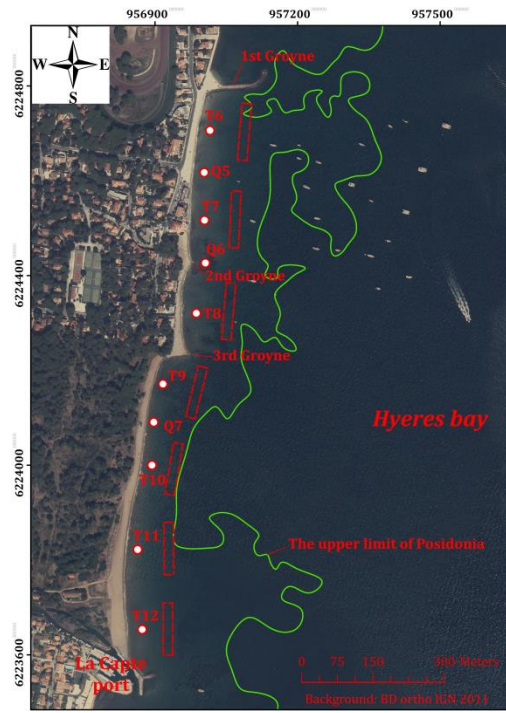
If the wave transmission coefficient is defined according to the equation of (6-19), its value can be significantly affected by the bathymetry of seabed, especially many troughs and sand bars occur in the study area. In order to limit the effects of seabed, Ahrens (1987) recommended an alternative method for determining the wave transmission coefficient which is the ratio between the transmitted wave height, H_t , and the wave height at the same location with no breakwater, H_c .

$$K_t = \frac{H_t}{H_c} \quad (6-20)$$

If using this formula, K_t should be somewhat conservative, i.e. higher than the traditional definition of the transmission coefficient (Ahrens, 1987). In this work, in order to enhance the safety degree, the equation proposed by Ahrens (1987) will be applied to assess the rational crest width of the SBWs.



a. Ceinturon beach



b. Bona beach

Figure 235. The location of observation points.

Table 69. Dissipation coefficient for SBWs in the winter scenario.

Point	H_s (m) (Nature)	H_s (m) (SBWs_B10m)	H_s (m) (SBWs_B20m)	K_{t10}	K_{t20}	%
T1	0.31	0.16	0.14	0.53	0.47	12.53
Q1	0.29	0.23	0.22	0.80	0.76	4.30
T2	0.28	0.16	0.13	0.55	0.48	13.56
Q2	0.29	0.23	0.22	0.80	0.76	5.52
T3	0.29	0.15	0.13	0.52	0.45	13.12
Q3	0.29	0.26	0.25	0.89	0.86	3.43
T4	0.29	0.15	0.13	0.50	0.44	13.30
Q4	0.27	0.25	0.24	0.92	0.86	6.08
T5	0.28	0.14	0.12	0.49	0.43	11.27
T6	0.28	0.14	0.13	0.51	0.45	12.30
Q5	0.28	0.22	0.21	0.78	0.74	4.87
T7	0.28	0.16	0.14	0.56	0.49	12.04
Q6	0.28	0.23	0.22	0.81	0.79	2.74
T8	0.28	0.16	0.15	0.56	0.52	7.22
T9	0.27	0.16	0.14	0.58	0.52	10.84
Q7	0.26	0.18	0.17	0.69	0.65	6.48
T10	0.27	0.14	0.12	0.52	0.45	13.41
T11	0.27	0.15	0.13	0.55	0.48	13.76
T12	0.29	0.16	0.14	0.54	0.48	12.39

Table 70. Dissipation coefficient for SBWs in the semi-centennial storm scenario.

Point	H_s (m) (Nature)	H_s (m) (SBWs_10m)	H_s (m) (SBWs_20m)	K_{t10}	K_{t20}	%
T1	1.10	0.70	0.65	0.64	0.59	7.31
Q1	1.11	0.86	0.82	0.77	0.74	4.27
T2	1.12	0.73	0.68	0.65	0.61	6.54
Q2	1.11	0.91	0.89	0.83	0.80	2.57
T3	1.03	0.68	0.63	0.66	0.61	6.49
Q3	1.05	0.94	0.92	0.90	0.88	1.92
T4	1.03	0.67	0.62	0.65	0.61	7.19
Q4	1.01	0.95	0.92	0.94	0.92	2.71
T5	1.06	0.66	0.60	0.62	0.57	7.92
T6	1.35	0.77	0.71	0.57	0.52	8.72
Q5	1.33	1.06	1.02	0.79	0.77	3.30
T7	1.31	0.79	0.74	0.61	0.57	6.59
Q6	1.29	1.06	1.07	0.82	0.83	-1.13
T8	1.25	0.76	0.72	0.61	0.58	5.11
T9	1.18	0.76	0.70	0.65	0.60	7.09
Q7	1.17	0.90	0.86	0.76	0.74	3.64
T10	1.16	0.71	0.66	0.61	0.56	8.11
T11	1.27	0.74	0.68	0.59	0.54	8.45
T12	1.23	0.77	0.72	0.63	0.58	7.05

In order to measure efficiency of structural alternatives for Ceinturon and Bona beaches, the DHI's MIKE 21 SW module was used to simulate two different scenarios including ordinary wave condition (the winter month of February, 2007) and strong wave condition (the semi-centennial storm) with and without SBWs. First of all, wave height is extracted at 19 points along Ceinturon and Bona beaches in which 12 of them are in the leeside of the structure (Point T1 to T12), and other seven in the gap between segments of SBWs (Point Q1 to Q7). The locations of these points are drawn in aerial pictures, as shown in Figure 235. The output results of extraction are presented in Table 69 and Table 70, respectively.

The results strongly confirm that both two SBWs alternatives of B=10m and B=20m are effective for the wave dissipation in the leeside of structures in Ceinturon and Bona beaches, even in the gap between SBWs. In the winter wave condition, the transmission coefficient continues to decrease as the wave height increase. When the semi-centennial storm induces storm surge and the water depth as well as wave height increase, the transmission coefficient continues to increase. For instances, the reduced percentages of wave height are about 42%-57% under ordinary wave condition and about 36%-48% under strong wave condition. In addition, the alternative of SBWs with the crest width of

20 m could dissipate wave energy more dominantly than that of 10 m. It is easily seen that the transmission coefficient in the case of 10 m width is larger than that in the case of 20 m width about 7.22%-13.76% under ordinary wave condition (Table 69) and about 5.11%-8.72% under stormy wave condition (Table 70). Consequently, the alternative of SBWs with the crest width of 20 m is utilized to protect the Ceinturon and Bona beaches from coastal erosion.

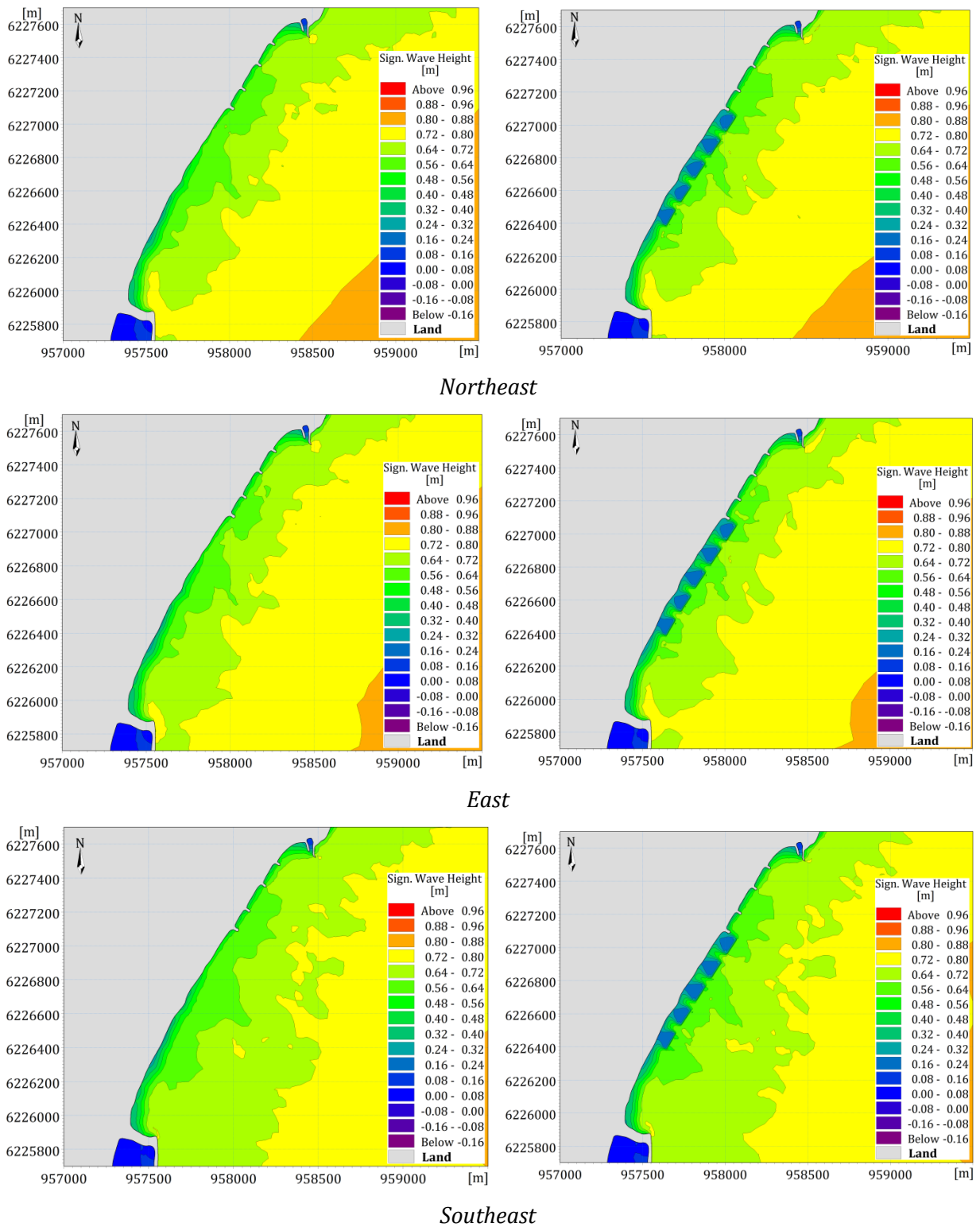
6.5. Results and discussion

In this part, total nine different scenarios including the wind variations, seasonal variations and storm changes were modeled with the presence of SBWs. The modeled significant wave height, current speed, sediment transport patterns and bed level change at Ceinturon and Bona beaches, where are being subjected to severe erosion (Capanni, 2011) are plotted. Moreover, the hydrodynamic and sediment transport parameters of 19 points at the water depth of about 1.2 m in both the leeside and gaps of SBWs along two these beaches are also extracted and compared to those without the SBWs in order to elucidate the impacts of SBWs on morphodynamics in these beaches. Finally, total 19 cross-shore beach profiles extracted along the shorelines will be used to visualize the bathymetry evolution of these two beaches under the different wave conditions.

6.5.1. Effects to wave fields

6.5.1.1. Ceinturon beach

In Hyères bay, three main wind directions of northeast, east and southeast play the decisive role in coastal morphology of the eastern Giens tombolo. Therefore, the installation of SBWs under the impact of these three winds was modeled in this work. The simulated results of wave height distribution due to the northeast, east and southeast winds are presented in Figure 236. This figure reveals that the northeast winds induce the highest waves with the approaching the shoreline of Ceinturon beach, whereas the southeast winds have the lowest impact on wave fields, regardless of SBWs. Without SBWs, the significant wave height at the water depth of 1.2 m along this beach is in the range of 0.55-0.61 m in the northeast winds and 0.51-0.6 m in the southeast winds (Table 71). When taking into account the presence of SBWs, the nearshore wave heights reduce significantly under all wind directions. The reduced percentages are from 61.69% to 71.16% at the water depth of 1.2 m in the leeside of SBWs and less than 26.16% in the gaps between SBWs. A significant decrease of wave height results in a corresponding reduction of radiation stresses. This reduction varies between 84.56% and 95.57% behind the structure, while it ranges below 46% in the gaps of SBWs (see in Appendix E.1). The largest reduced percentages are found in the shear radiation stresses in the rear of SBWs. On the other hand, the normal radiation stresses are decreased much more than the shear radiation stresses in the gaps between SBWs.



a. Without SBWs

b. With SBWs

Figure 236. Significant wave height distribution induced by annual winds in Ceinturon beach.

Figure 237 shows the wave fields of Ceinturon beach under summer and winter wave conditions with and without SBWs. The contours of significant wave height in the winter wave conditions are more parallel to the shoreline than that under summer wave conditions, and their directions are almost southeast. It is clearly seen that the average

significant wave height along the Ceinturon beach in winter is nearly two times larger than that in summer, regardless of with and without SBWs. Particularly, this height at the water depth of 1.2 m along the beach ranges from 0.27 m to 0.31 m in winter and from 0.14 m to 0.16 m in summer without SBWs, while it varies between 0.08 m and 0.09 m in summer and between 0.12 m and 0.14 m in winter in the leeside of SBWs (Table 71). It means that most of waves are dissipated when they are transmitted through the structure. The significant wave height at the water depth of 1.2 m in the leeside of SBWs is decreased by 52.08%-56.84% in winter and 42.22%-44.41% in summer. Even the wave height at the same water depth in the gaps between SBWs is also reduced about 3.42%-32.38% in both summer and winter. In other words, the transmission coefficient varies from 0.45 to 0.6 behind the SBWs and from 0.62 to 0.79 in the gaps of SBWs. It reduces more sharply behind SBWs in winter than that in summer because there are almost mild waves in summer and can easily pass through the structure without breaking or less wave energy dissipation.

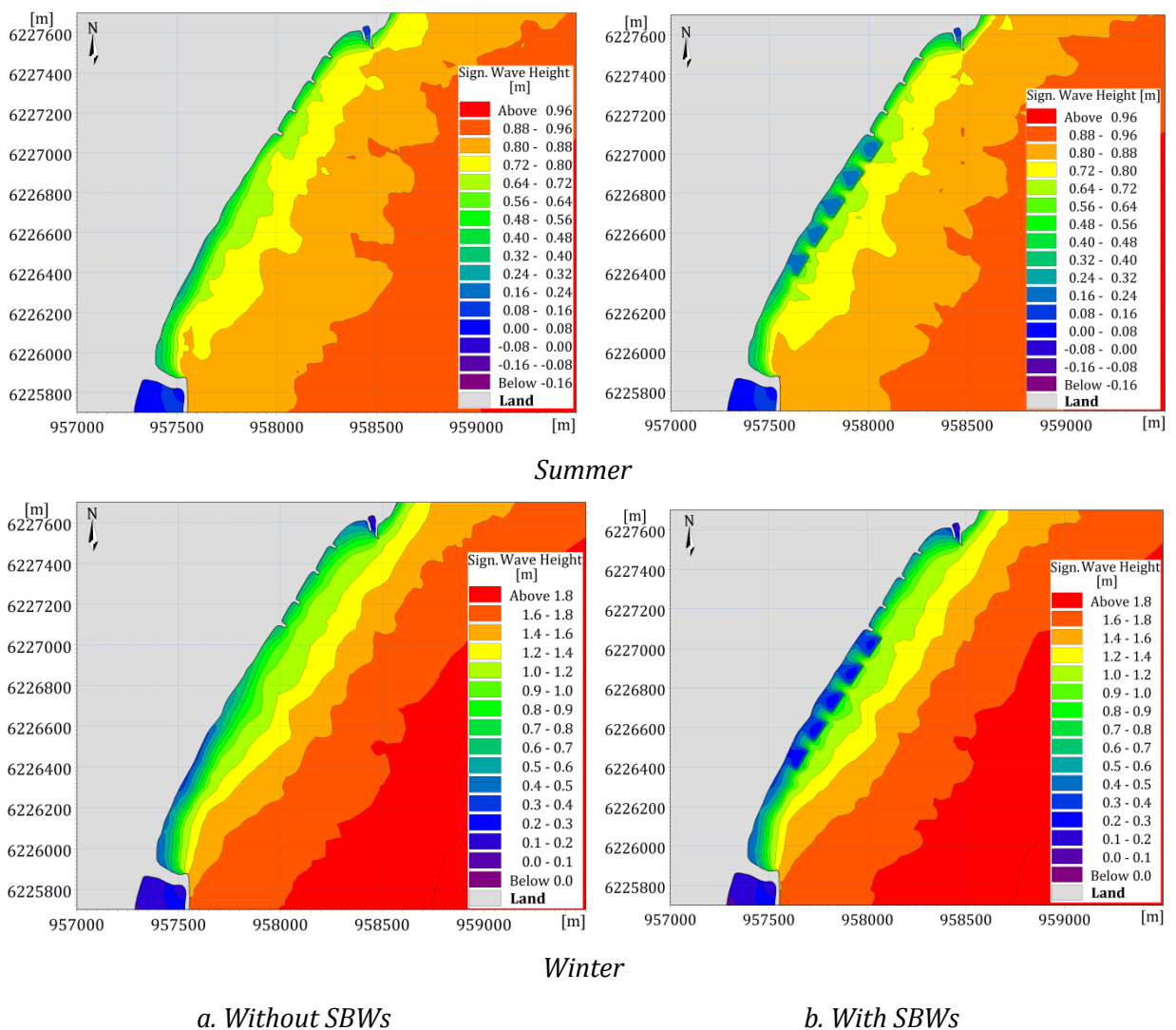
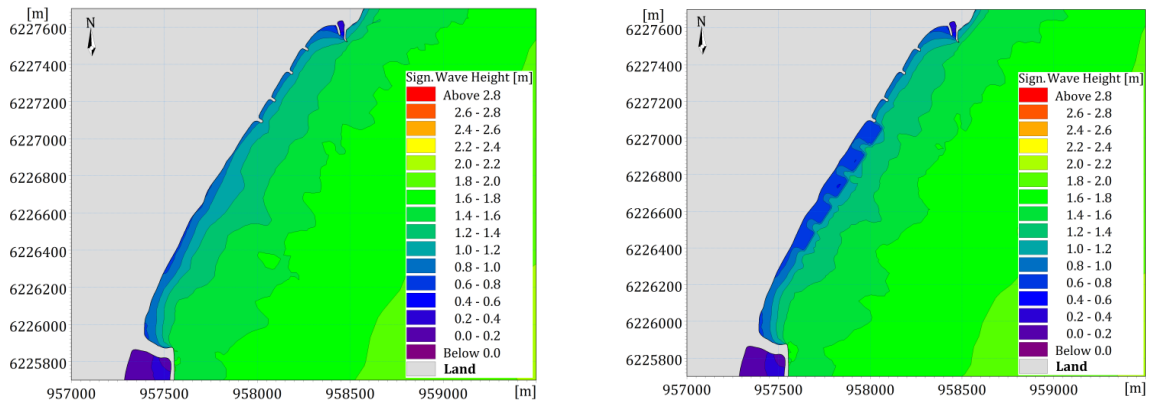


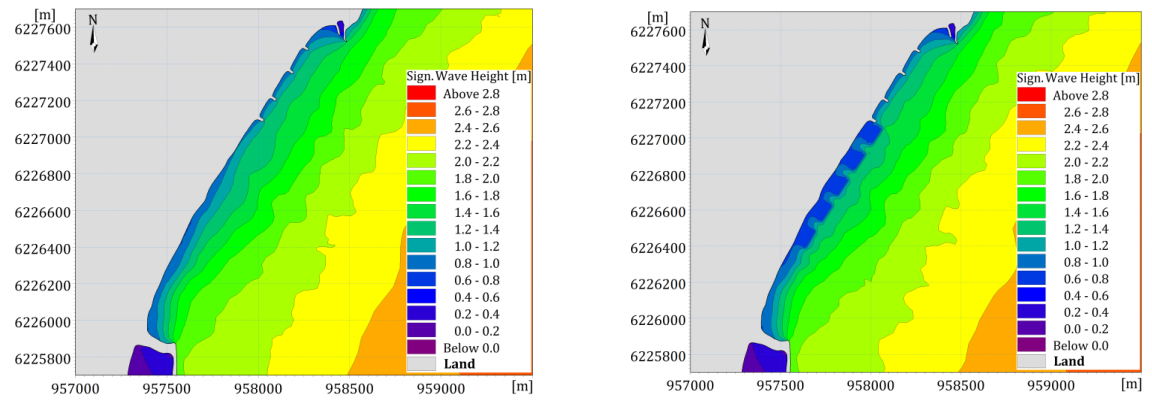
Figure 237. Significant wave height distribution induced by seasonal variation in Ceinturon beach.

Furthermore, a decrease in wave height results in the corresponding reduction of radiation stresses due to the presence of SBWs in both summer and winter. The largest reduction is normally observed in the shear radiation stress (S_{xy}) which mainly contributes to form longshore currents, whereas the normal radiation stresses (S_{xx} & S_{yy}) driven rip currents are decreased almost the same behind the SBWs. Conversely, the normal radiation stresses are decreased much more than the shear radiation stress in between the SBWs. The reduced percentage of the shear radiation stress at the water depth of 1.2 m in the leeside of SBWs is in the range of 80%-91.24%, whilst the value in the gaps of SBWs is lower than 40% (see in Appendix E.1).

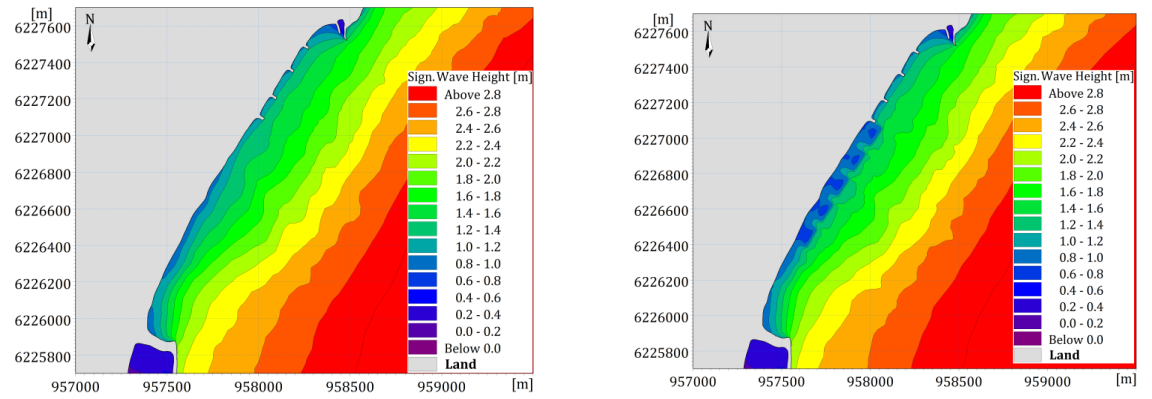
In addition to different wind directions and seasonal variation, the efficiency of SBWs in wave energy dissipation in Ceinturon beach is also investigated under various storms, viz. decadal, tri-decadal, semi-centennial and centennial storms. The modeled results are shown in Figure 238. It strongly demonstrates that the stronger storm induces the higher waves in this area. Particularly, the significant wave height at the water depth of 1.2 m along the Ceinturon beach falls in the range of 0.9-0.98 m under the decadal storm, 0.93-1.01 m under the tri-decadal storm, 1.0-1.12 m under the semi-centennial storm, and 1.17-1.27 m under the centennial storm (Table 72). The beach area which is commonly subjected to the highest waves is about from 500 m southward to the fourth groyne, regardless of the storm scale. This area has been also suffered severe coastal erosion. In order to dissipate wave energy and to combat coastal erosion, five SBWs are designed to install in the central part of Ceinturon beach. With the effect of the SBWs, the magnitudes of significant wave height in the nearshore area between the shoreline and the SBWs decrease considerably in all stormy wave conditions. Their transmission coefficient at the water depth of 1.2 m in the leeside of SBWs is the range of 0.48-0.54 in the decadal storm, 0.52-0.58 in the tri-decadal storm, 0.57-0.62 in the semi-centennial, and 0.63-0.67 in the centennial storm; whereas, it varies between 0.74 and 0.91 in the gaps of SBWs. It should be stressed that the wave energy dissipation efficiency of SBWs will reduce if the level of storm increases. This would be explained by the fact that the high level of storm results in the high storm surge increasing the water depth above the top crest of SBWs and allows the high waves to pass through the SBWs without breaking and approaching the beach. The reduction in wave height due to the presence of SBWs leads to decrease the radiation stresses. The reduced percentage of radiation stresses behind SBWs under stormy wave conditions is in the range of 47.27%-84.62%, while the value between them is lower than 42.41% (see in Appendix E.1).



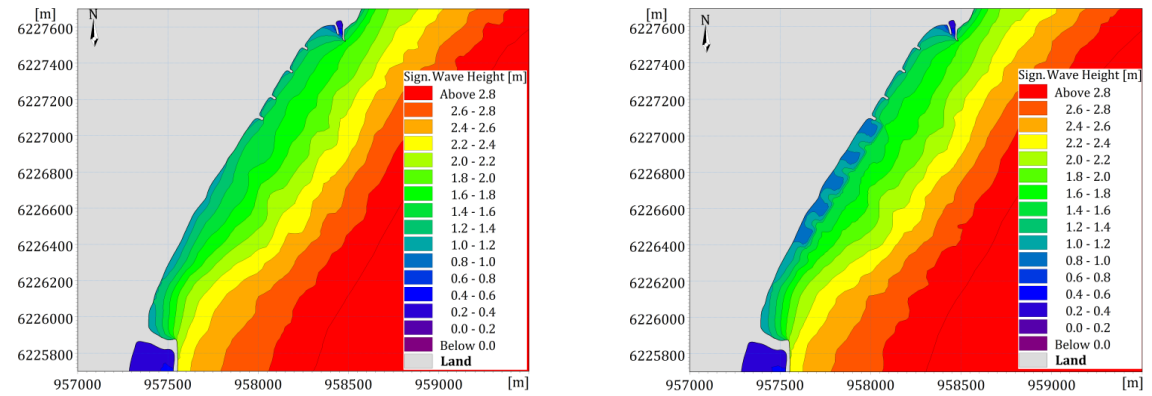
Decadal storm



Tri-Decadal storm



Semi-Centennial storm



Centennial storm

a. Without SBWs

b. With SBWs

Figure 238. Significant wave height distribution induced by storms in Ceinturon beach.

Table 71. Comparison of wave height at representative points under different winds and seasons.

Point	H_s (No SBWs) (m)			H_s (SBWs) (m)			K_t			H_s (No SBWs) (m)		H_s (SBWs) (m)		K_t	
	NE	E	SE	NE	E	SE	NE	E	SE	Winter	Summer	Winter	Summer	Winter	Summer
T1	0.60	0.61	0.60	0.23	0.23	0.22	0.38	0.38	0.36	0.31	0.16	0.14	0.09	0.47	0.56
T2	0.59	0.58	0.58	0.22	0.22	0.21	0.37	0.38	0.37	0.28	0.14	0.14	0.08	0.48	0.58
T3	0.57	0.56	0.54	0.20	0.19	0.18	0.36	0.34	0.34	0.29	0.15	0.13	0.09	0.45	0.57
T4	0.57	0.56	0.54	0.18	0.17	0.17	0.31	0.31	0.32	0.29	0.15	0.13	0.09	0.44	0.58
T5	0.57	0.56	0.54	0.16	0.16	0.16	0.29	0.29	0.30	0.28	0.14	0.12	0.08	0.43	0.58
T6	0.65	0.64	0.62	0.23	0.22	0.21	0.36	0.34	0.34	0.28	0.13	0.13	0.07	0.45	0.53
T7	0.67	0.65	0.62	0.28	0.26	0.24	0.41	0.40	0.39	0.28	0.14	0.14	0.07	0.49	0.55
T8	0.66	0.64	0.63	0.27	0.26	0.25	0.41	0.40	0.40	0.28	0.13	0.15	0.08	0.52	0.60
T9	0.65	0.63	0.61	0.27	0.26	0.25	0.42	0.42	0.42	0.27	0.14	0.14	0.08	0.52	0.58
T10	0.63	0.59	0.56	0.20	0.20	0.19	0.32	0.33	0.34	0.27	0.13	0.12	0.07	0.45	0.53
T11	0.63	0.59	0.56	0.23	0.23	0.22	0.36	0.40	0.40	0.27	0.13	0.13	0.07	0.48	0.55
T12	0.67	0.64	0.62	0.26	0.24	0.22	0.39	0.37	0.36	0.29	0.14	0.14	0.08	0.48	0.56
Q1	0.61	0.59	0.58	0.46	0.47	0.47	0.75	0.79	0.81	0.29	0.15	0.22	0.12	0.76	0.77
Q2	0.59	0.60	0.55	0.43	0.45	0.45	0.74	0.76	0.81	0.29	0.15	0.22	0.11	0.75	0.74
Q3	0.57	0.56	0.53	0.50	0.50	0.50	0.87	0.90	0.93	0.29	0.15	0.25	0.13	0.86	0.85
Q4	0.55	0.54	0.51	0.52	0.52	0.51	0.94	0.96	1.00	0.27	0.14	0.24	0.11	0.86	0.82
Q5	0.68	0.63	0.62	0.57	0.55	0.53	0.84	0.87	0.86	0.28	0.13	0.21	0.09	0.74	0.68
Q6	0.67	0.62	0.59	0.59	0.56	0.53	0.87	0.91	0.90	0.28	0.13	0.22	0.10	0.79	0.73
Q7	0.63	0.61	0.58	0.41	0.39	0.37	0.65	0.65	0.64	0.26	0.13	0.17	0.08	0.65	0.62

Note: NE-Northeast wind; E-East wind; SE-Southeast wind.

Table 72. Comparison of wave height at representative points under storms.

Point	H_s (No SBWs) (m)				H_s (SBWs) (m)				K_t			
	DS	TS	SS	CS	DS	TS	SS	CS	DS	TS	SS	CS
T1	0.98	1.00	1.09	1.25	0.53	0.56	0.65	0.82	0.54	0.56	0.59	0.65
T2	0.96	1.00	1.11	1.27	0.51	0.58	0.68	0.85	0.53	0.57	0.61	0.67
T3	0.90	0.93	1.03	1.19	0.48	0.54	0.64	0.80	0.53	0.58	0.62	0.67
T4	0.94	0.98	1.03	1.20	0.47	0.52	0.63	0.79	0.50	0.53	0.61	0.66
T5	0.93	0.96	1.05	1.21	0.44	0.49	0.60	0.76	0.48	0.52	0.57	0.63
T6	1.13	1.26	1.35	1.47	0.54	0.61	0.71	0.89	0.484	0.482	0.53	0.60
T7	1.08	1.21	1.30	1.44	0.58	0.64	0.74	0.91	0.54	0.53	0.57	0.64
T8	1.07	1.16	1.25	1.39	0.56	0.62	0.72	0.90	0.53	0.54	0.58	0.65
T9	1.01	1.09	1.17	1.33	0.56	0.61	0.71	0.88	0.55	0.55	0.60	0.66
T10	0.99	1.07	1.16	1.32	0.50	0.55	0.66	0.84	0.50	0.52	0.57	0.63
T11	1.04	1.19	1.26	1.40	0.53	0.59	0.68	0.85	0.51	0.50	0.54	0.61
T12	1.08	1.15	1.22	1.38	0.56	0.64	0.72	0.88	0.52	0.55	0.59	0.64
Q1	0.98	1.01	1.11	1.26	0.76	0.77	0.82	0.95	0.77	0.76	0.74	0.75
Q2	0.95	0.99	1.11	1.26	0.80	0.84	0.89	1.01	0.84	0.84	0.80	0.80
Q3	0.93	0.97	1.05	1.21	0.80	0.84	0.92	1.04	0.87	0.87	0.88	0.85
Q4	0.91	0.94	1.00	1.17	0.81	0.83	0.91	1.07	0.88	0.88	0.91	0.91
Q5	1.10	1.24	1.33	1.46	0.90	0.94	1.02	1.15	0.82	0.76	0.76	0.79
Q6	1.07	1.19	1.28	1.42	0.92	0.98	1.06	1.22	0.87	0.83	0.83	0.86
Q7	1.02	1.08	1.17	1.33	0.73	0.78	0.86	1.00	0.72	0.72	0.73	0.75

Note: DS-Decadal storm; TS-Tri-decadal storm; SS-Semi-Centennial storm; CS-Centennial storm.

More details about the values of radiation stresses as well as wave height of T1-T5 and Q1-4 are presented in Appendix E1.

6.5.1.2. Bona beach

Similar to Ceinturon beach, the effect of wind direction changes on wave fields along Bona beach with and without SBWs was detected in this work. The numerical results are shown in Figure 239. It is clearly seen that the northeast winds generate the highest waves reaching the Bona beach, while the southeast one has the lowest impact on wave height distribution in this area. In addition, the significant wave height at the water depth of 1.2 m in Bona beach is larger than that at the same water depth in Ceinturon beach around 10%, regardless of wind directions. Specifically, without SBWs, the significant wave height at the water depth of 1.2 m along Bona beach varies between 0.56m and 0.63 m in the southeast winds, between 0.59 m and 0.65 m in the east winds, and between 0.63 m and 0.68 m in the northeast winds (Table 71). The presence of SBWs modifies the wave fields in the water area between the shoreline and SBWs. The significant wave height decreases suddenly and appreciably. The reduced percentages of

wave height are the range from 57.92% to 67.86% in the leeside of SBWs and less than 36.4% in the gaps between SBWs, corresponding to its transmission coefficient of 0.32-0.42 behind the structure and lower than 0.64 in between SBWs. As wave height decreases due to the deployment of SBWs, the radiation stresses will be reduced adequately. A reduction of 16.58%-96.27% in radiation stresses is reported at the water depth of 1.2 m in the rear of SBWs. The reduction of lower than 61.46% of these stresses is even seen in the gaps of SBWs (see in Appendix E.2).

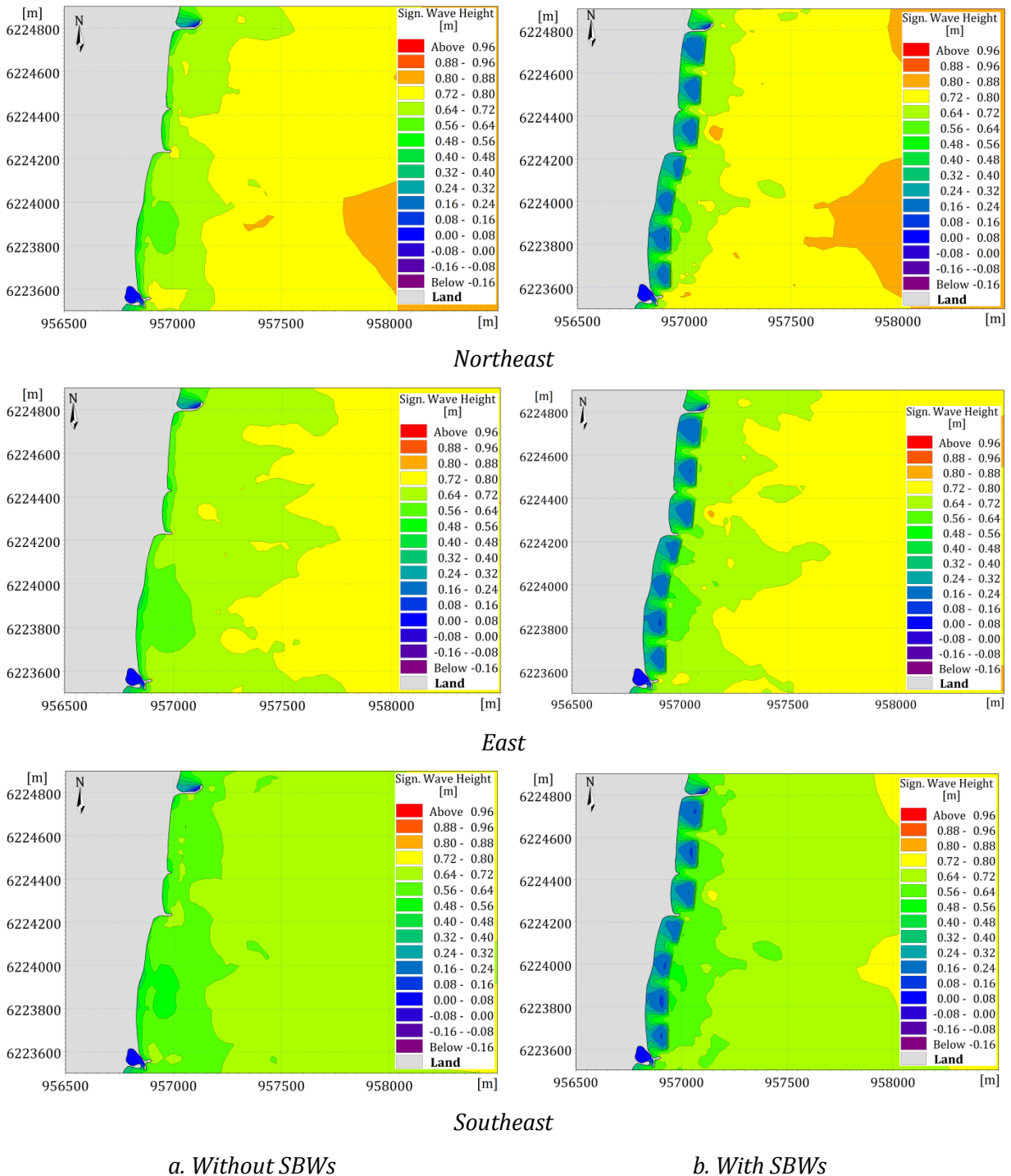


Figure 239. Significant wave height distribution induced by annual winds in Bona beach.

The difference of wave regime at Bona beach between summer and winter with and without SBWs is illustrated in Figure 240. In summer, mild waves with the average height of 0.13-0.14 m are usually observed at the water depth of 1.2 m along Bona beach. By contrast, the strong waves predominantly occur in this area with the average height of 0.26-0.29 m at the water depth of 1.2 m in winter (Table 71). It means that the wave height in winter is almost two times higher than that in summer due to the highly frequent presence of storms and rough seas. If the SBWs are placed in Bona beach, the nearshore wave fields are completely changed. Figure 240b gives rise to a significant reduction of wave heights as well as the apparition of wave height gradients in the leeside of the SBWs. The presence of SBWs causes a considerable reduction of significant wave height behind the structure from 40.46% to 47.43% in summer and from 47.73% to 55.06% in winter, comparing to that without SBWs. In addition, wave height at the water depth of 1.2 m in the gaps between SBWs is also decreased by 21.07%-37.67%. Similar to Ceinturon beach, the reduction percentage of wave height in winter is much more than that in summer. As a result, the radiation stresses are decreased by 54.32%-90.17% in the leeside of SBWs and by 23.6%-64.77% in the gaps of SBWs (see in Appendix E.2). The above-mentioned decreases prove that wave heights can be reduced by the wave reflections and wave dissipations with the SBWs.

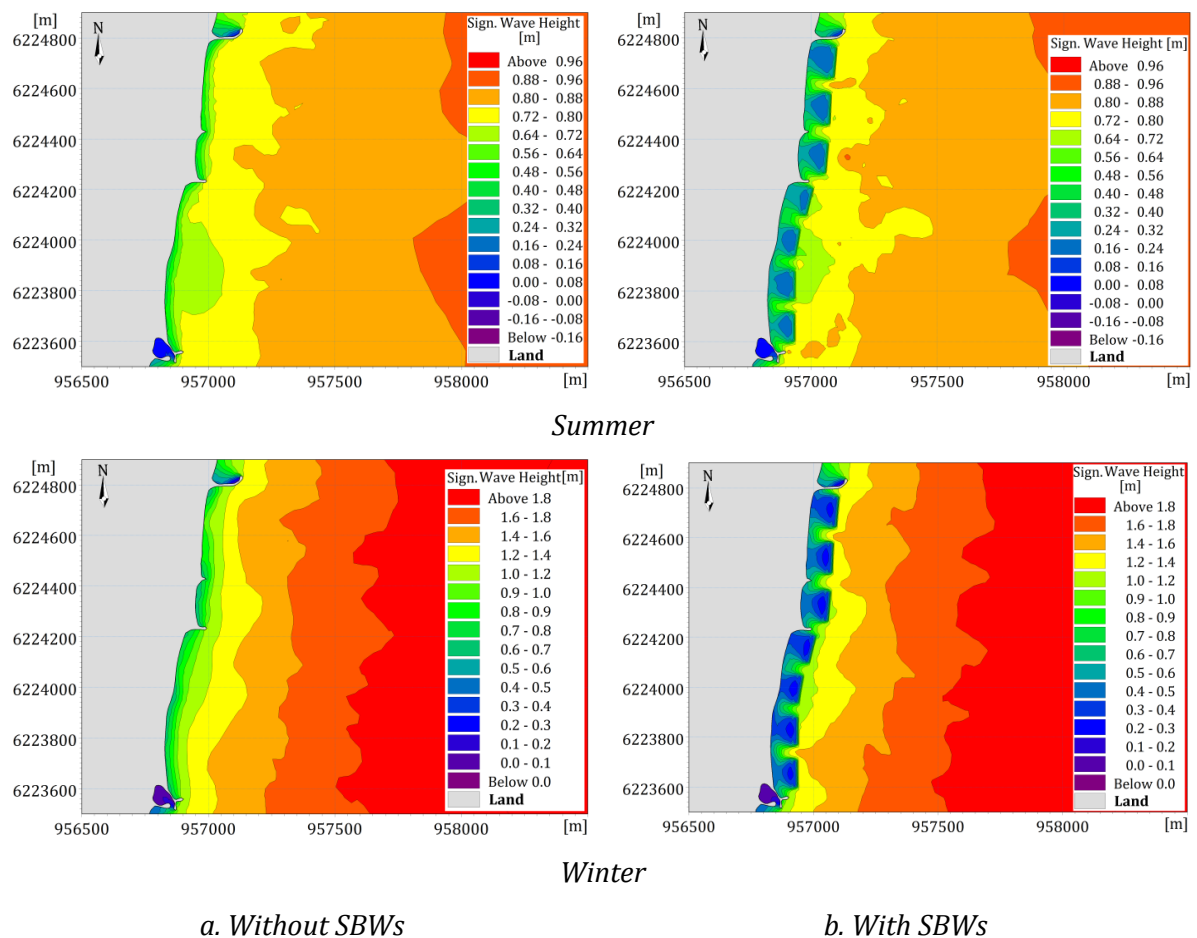
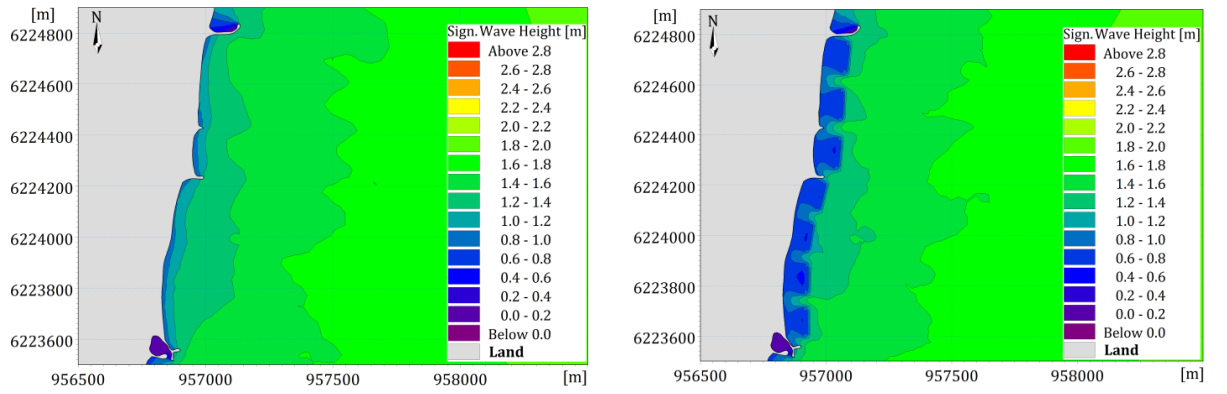
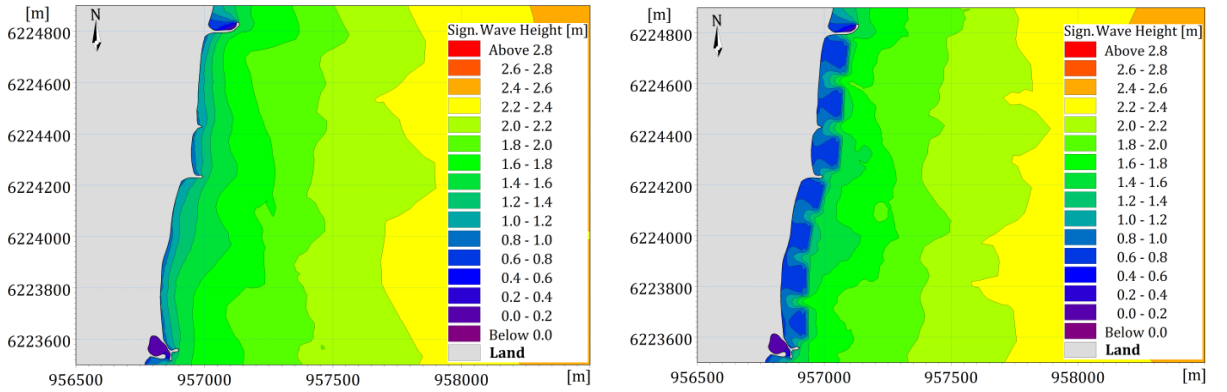


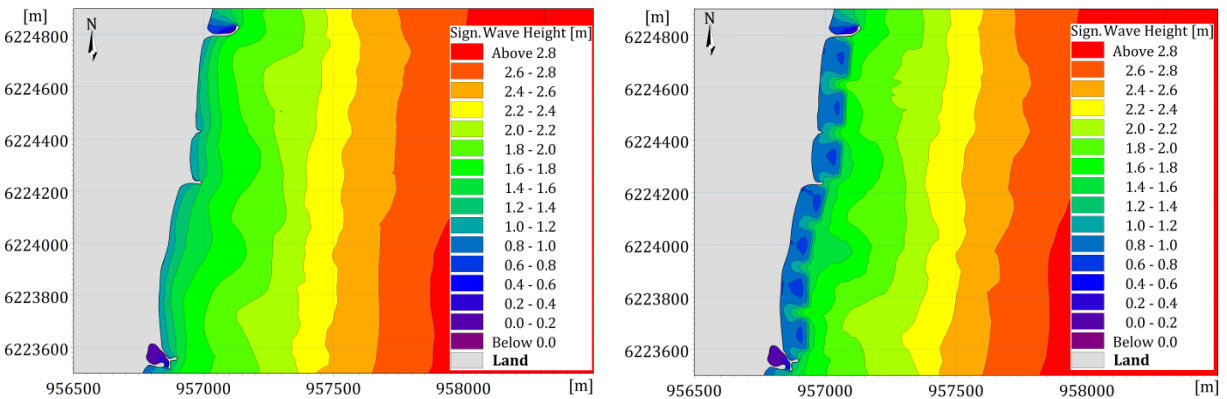
Figure 240. Significant wave height distribution induced by seasonal variation in Bona beach.



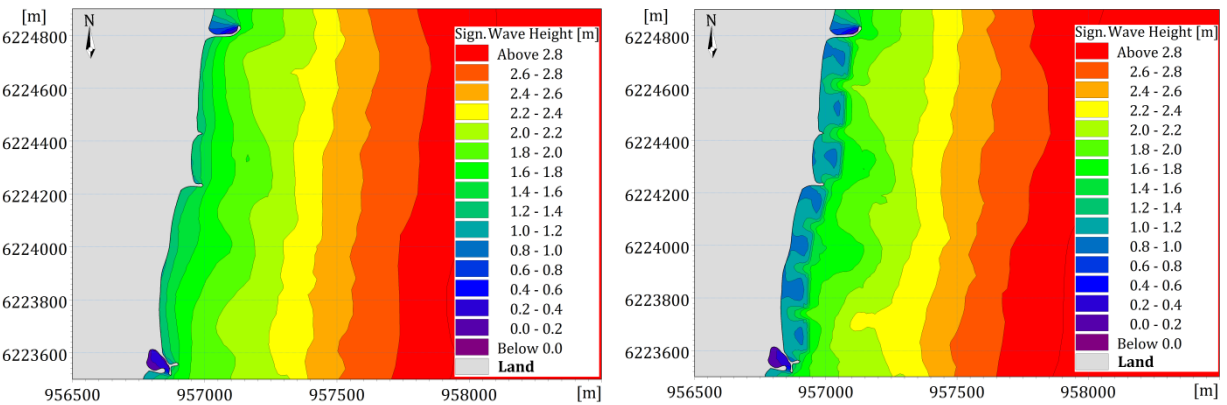
Decadal storm



Tri-Decadal storm



Semi-Centennial storm



Centennial storm

a. Without SBWs

b. With SBWs

Figure 241. Significant wave height distribution induced by storms in Bona beach.

The nearshore wave height distribution in Bona beach induced by the different storm levels with and without SBWs is illustrated in Figure 241. Comparison of the wave fields under the impact of the different stormy wave conditions in this figure indicates that an increase of storm level could cause considerable raise of wave height. For instance, the significant wave height at the water depth along this beach falls in the range of 1.0-1.13 m under the decadal storm, 1.07-1.26 m under the tri-decadal storm, 1.16-1.35 m under the semi-centennial storm, and 1.32-1.47 m under the centennial storm (Table 72). Moreover, it can be noticed that the northern beach (almost 600 m long) is subjected to greater wave heights and therefore it need be protected by SBWs. In all storm conditions, the SBWs work properly in reducing wave energy (Figure 241b). In particular, a quite calm region is generated between the shoreline and the SBWs, regardless of storm levels. The lowest transmission coefficient of 0.48 is observed in the decadal storm, whereas the largest one of 0.66 is found in the leeside of SBWs in the centennial storm. In addition, the significant wave height is moderately decreased in the gaps of SBWs. Its transmission coefficient there is larger than 0.72. It strongly proves that the high storm level would diminish the efficiency of SBWs in reducing wave energy. The presence of SBWs not only decreases wave height but also results in a reduction of radiation stresses. The reduced percentages of radiation stresses at the water depth of 1.2 m behind SBWs reach the maximum value of 84%, while the value between them is lower than 61.68% (see in Appendix E.2).

More details about the values of radiation stresses as well as wave height of T6-T12 and Q5-7 are presented in Appendix E.2.

6.5.2. Effects to current fields

6.5.2.1. Ceinturon beach

In the study area, the littoral current system is mainly driven by wind and waves, so wind direction changes could lead to the significant modification of nearshore current regime. Figure 242 shows the nearshore current fields of Ceinturon beach with and without SBWs under the impact of northeast, east and southeast winds. It can be noticed that the longshore current is well-defined, almost flows southward and mostly parallel to the shore, regardless of wind direction. In general, the nearshore current patterns of Ceinturon beach without SBWs are relatively quite simple (Figure 242a). Interaction of the main current system with the breakwater of Hyères port leads to formation of eddy circulation in the south of Ceinturon beach in both with and without SBWs. It is clearly seen that the northeast winds induce the highest current velocities along this beach. Particularly, the mean current speed at the water depth of 1.2 m along Ceinturon beach under the northeast winds varies between 0.1 m/s and 0.174 m/s, larger than that under other winds about 16.14%-51.9% (Table 73). However, the current fields become more complex with SBWs. Eddies at both heads of SBWs and rip-currents towards the gap between SBWs are formed by interaction of the main current system with the SBWs

(Figure 242b). In addition, a setup of water occurs, ponding in the leeside of SBWs in order to create the necessary head to reach equilibrium with the incoming transport (Kuang et al., 2014). This ponding of water behind the SBWs may result in the increase of longshore currents (Browder Albert et al., 1996). Especially, in the east and southeast winds, a northward longshore current is generated between the SBWs and the shoreline, which is good for water change as well as sediment transport.

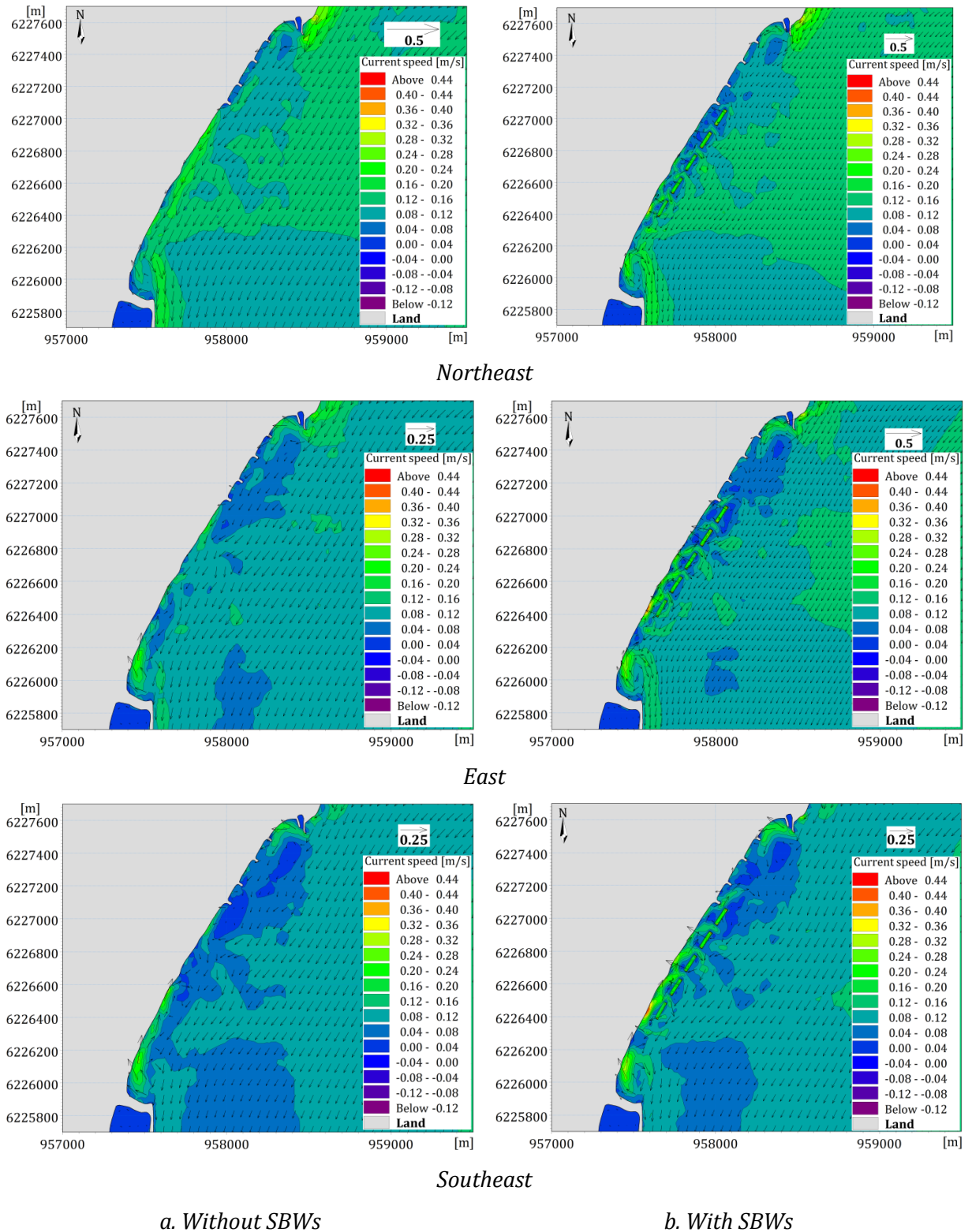
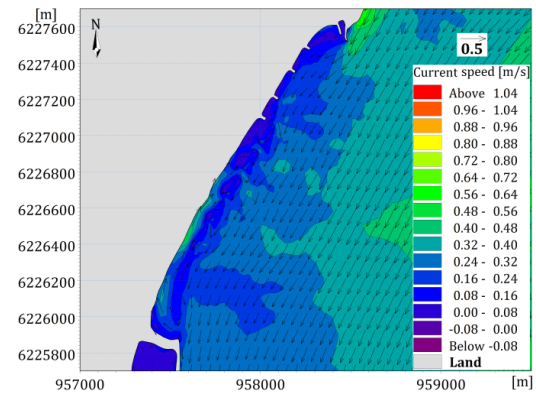
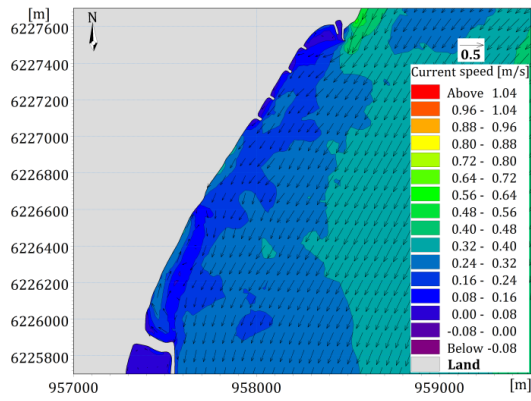
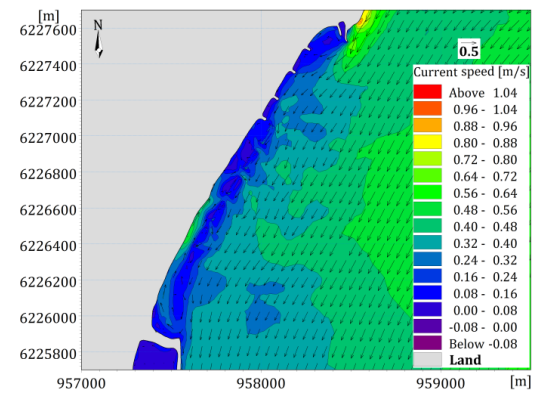
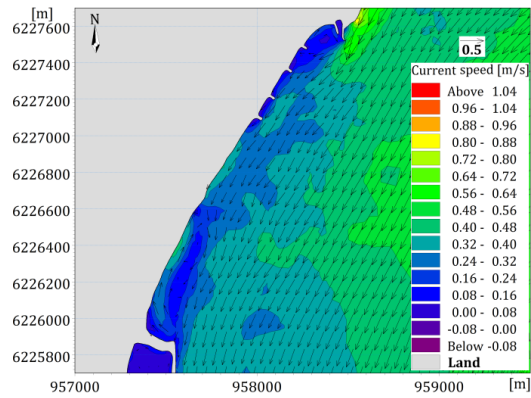


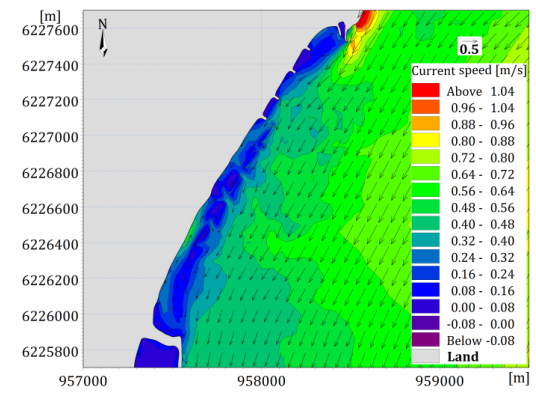
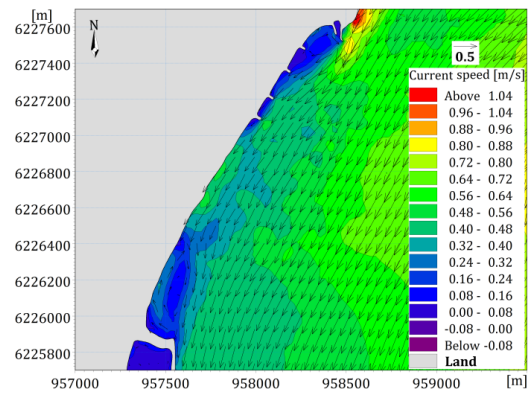
Figure 242. Current velocity distribution induced by annual winds in Ceinturon beach.



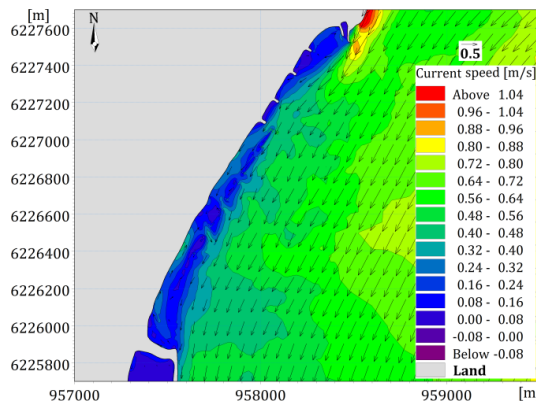
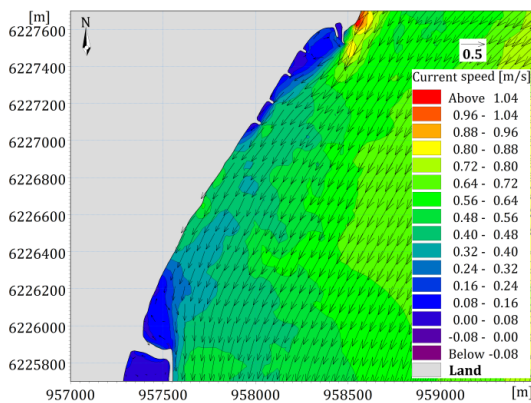
Decadal storm



Tri-Decadal storm



Semi-Centennial storm



Centennial storm

a. Without SBWs

b. With SBWs

Figure 244. Current velocity distribution induced by storms in Ceinturon beach.

The impact of the different storms with and without SBWs on the current fields along Ceinturon beach is elucidated and illustrated in Figure 244. It is noticeable that current intensities depend on the level of storm, i.e. the higher storm level causes the strong nearshore current in the study area, especially in the central zone. Specifically, the average current speed at the water depth of 1.2 m along the beach is in the range of 0.11-0.19 m/s under the decadal storm, 0.17-0.27 m/s under the tri-decadal storm, 0.19-0.38 m/s under the semi-centennial storm, and 0.21-0.41 m/s under the centennial storm (Table 74). The nearshore current system interacting with the jetties of Aygaude port and the emerged breakwater of Hyères port results in formation of eddy circulations in the north and south of Ceinturon beach, respectively, regardless of storm level (Figure 244a). The distribution size of these eddy circulations reduces significantly when the storm level increases. Nevertheless, the nearshore current pattern of Ceinturon beach becomes more complex due to the presence of SBWs. Vortexes induced by interaction of current system with jetties and emerged breakwater are still observed in the north and south of this beach. In addition, the SBWs also contribute to form small eddies at their roundheads as well as rip-currents towards the gaps between SBWs. In generally, the presence of SBWs generates a calm region with low currents behind the structure, except for the south area between the fifth SBW and the shoreline (Figure 244b). The average current speed at the water depth of 1.2 m in the leeside and the gaps of SBWs could be decreased to the maximum value of 88%, whereas its value between the fifth SBW and the shoreline increases by less than 70.52% (Table 74). An increase of current velocity in the vicinity of the fifth SBW could be explicated by the fact that the shortest distance between the shoreline and the fifth SBW accompanied by the intensification of southeast stormy winds and waves is attributed to boost the current velocity.

Table 73. Comparison of current speed at representative points under different winds and seasons.

Point	V_c (No SBWs) (m/s)			V_c (SBWs) (m/s)			Difference (%)			V_c (No SBWs) (m/s)		V_c (SBWs) (m/s)		Difference (%)	
	NE	E	SE	NE	E	SE	NE	E	SE	Winter	Summer	Winter	Summer	Winter	Summer
T1	0.098	0.067	0.048	0.044	0.053	0.076	55.55	20.99	-57.98	0.065	0.053	0.049	0.039	25.12	25.59
T2	0.170	0.113	0.142	0.049	0.089	0.151	70.95	20.88	-6.28	0.089	0.075	0.068	0.056	23.99	25.43
T3	0.155	0.075	0.097	0.079	0.104	0.139	49.00	-39.08	-43.07	0.085	0.071	0.068	0.054	19.82	24.42
T4	0.150	0.083	0.077	0.047	0.095	0.121	68.36	-14.62	-57.92	0.076	0.069	0.064	0.058	16.66	16.11
T5	0.133	0.081	0.098	0.051	0.069	0.077	61.49	14.79	21.18	0.075	0.068	0.044	0.036	40.89	47.04
T6	0.065	0.144	0.147	0.076	0.058	0.060	-15.79	59.73	59.23	0.044	0.047	0.046	0.035	-4.40	25.79
T7	0.108	0.169	0.182	0.099	0.107	0.108	8.29	36.45	40.25	0.066	0.059	0.063	0.051	4.10	13.92
T8	0.059	0.077	0.082	0.067	0.052	0.053	-13.58	31.93	34.70	0.045	0.040	0.049	0.040	-9.02	0.00
T9	0.103	0.084	0.043	0.099	0.080	0.067	3.82	5.27	-54.98	0.043	0.042	0.035	0.022	18.62	46.12
T10	0.147	0.073	0.060	0.099	0.052	0.038	32.59	28.11	37.33	0.050	0.063	0.045	0.046	11.36	26.31
T11	0.089	0.112	0.122	0.142	0.131	0.118	-60.65	-16.55	3.45	0.069	0.057	0.069	0.048	0.01	15.31
T12	0.066	0.093	0.099	0.087	0.071	0.065	-32.69	24.16	34.26	0.067	0.057	0.054	0.040	18.52	31.09
Q1	0.137	0.098	0.101	0.038	0.056	0.102	71.97	43.22	-1.24	0.082	0.068	0.058	0.053	29.50	21.45
Q2	0.174	0.100	0.107	0.034	0.083	0.143	80.54	16.80	-33.91	0.089	0.076	0.060	0.054	32.38	28.53
Q3	0.157	0.079	0.088	0.092	0.152	0.173	41.16	-93.05	-95.85	0.079	0.072	0.076	0.063	3.42	12.20
Q4	0.123	0.088	0.086	0.110	0.149	0.163	11.00	-69.63	-89.92	0.080	0.068	0.075	0.055	6.04	18.24
Q5	0.133	0.194	0.196	0.086	0.073	0.068	34.95	62.34	65.20	0.065	0.060	0.049	0.046	25.51	23.20
Q6	0.086	0.139	0.147	0.144	0.097	0.076	-68.23	30.66	48.43	0.059	0.060	0.062	0.061	-4.77	-1.10
Q7	0.134	0.091	0.060	0.117	0.071	0.052	12.75	22.43	12.15	0.050	0.051	0.041	0.037	17.06	27.14

Note: NE-Northeast wind; E-East wind; SE-Southeast wind.

Table 74. Comparison of current speed at representative points under storms.

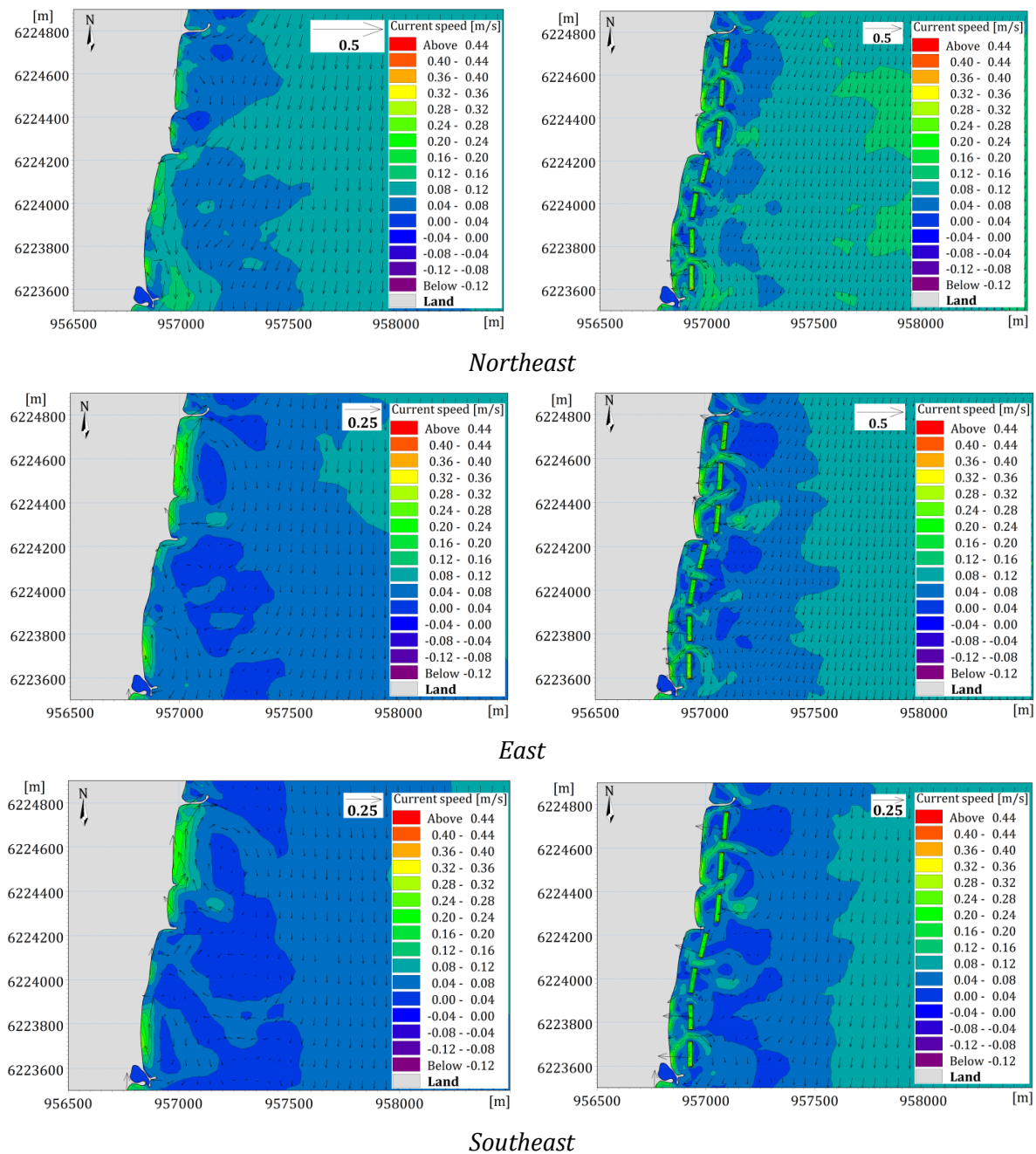
Point	V_c (No SBWs) (m/s)				V_c (SBWs) (m/s)				Difference (%)			
	DS	TS	SS	CS	DS	TS	SS	CS	DS	TS	SS	CS
T1	0.13	0.17	0.22	0.21	0.05	0.13	0.22	0.23	63.48	27.25	0.93	-6.74
T2	0.20	0.27	0.35	0.35	0.17	0.11	0.29	0.31	14.31	56.78	17.06	12.76
T3	0.17	0.26	0.38	0.40	0.21	0.14	0.17	0.24	-22.04	46.18	55.56	39.55
T4	0.11	0.17	0.36	0.42	0.19	0.21	0.06	0.15	-70.52	-22.93	81.93	64.78
T5	0.16	0.21	0.19	0.35	0.13	0.18	0.15	0.04	14.56	17.69	20.68	87.99
T6	0.23	0.25	0.24	0.24	0.08	0.08	0.09	0.12	63.59	66.13	62.56	50.07
T7	0.26	0.28	0.26	0.27	0.11	0.11	0.11	0.13	57.02	61.40	58.29	52.24
T8	0.16	0.17	0.17	0.15	0.07	0.08	0.08	0.10	54.11	55.28	50.53	32.53
T9	0.11	0.09	0.10	0.08	0.10	0.10	0.07	0.05	0.32	-10.59	27.43	33.60
T10	0.13	0.13	0.12	0.10	0.07	0.05	0.06	0.07	48.23	57.48	49.04	32.87
T11	0.24	0.14	0.12	0.10	0.10	0.12	0.11	0.11	57.01	14.11	11.77	-17.21
T12	0.20	0.10	0.10	0.11	0.09	0.08	0.07	0.08	55.71	14.64	28.23	27.01
Q1	0.17	0.23	0.29	0.29	0.08	0.12	0.26	0.27	55.14	49.53	10.54	5.16
Q2	0.19	0.27	0.37	0.39	0.18	0.06	0.24	0.27	6.71	79.08	35.66	29.03
Q3	0.14	0.22	0.37	0.40	0.23	0.17	0.16	0.24	-62.70	21.91	56.68	41.26
Q4	0.16	0.20	0.26	0.36	0.23	0.26	0.20	0.16	-36.95	-31.22	23.65	55.30
Q5	0.29	0.30	0.29	0.29	0.11	0.11	0.11	0.14	62.51	63.17	61.76	52.61
Q6	0.18	0.21	0.19	0.23	0.15	0.16	0.12	0.14	20.76	26.18	38.43	38.28
Q7	0.10	0.10	0.10	0.08	0.08	0.05	0.07	0.09	23.79	53.85	35.91	-10.31

Note: DS-Decadal storm; TS-Tri-decadal storm; SS-Semi-Centennial storm; CS-Centennial storm.

6.5.2.2. Bona beach

Figure 245 shows the current velocity distribution induced by the different wind directions with and without SBWs. In generally, the main longshore current directs from the north to south regardless of SBWs. It should be stressed that the southeast and east winds play the most dominant role in the current fields along Bona beach because they generate the highest current velocities, contrary to Ceinturon beach. Particularly, the average current speed at the water depth of 1.2 m along the beach falls in the range of 0.07-0.19 m/s and 0.04-0.2 m/s in the east and southeast winds, respectively, whereas it only varies from 0.05-0.15 m/s in other winds (Table 73). The complete difference of current patterns between Ceinturon and Bona beach could be explained by the fact that the longshore currents induced by the northeastern winds move along the coast from Salins beach to Hyères port, then they have to change the direction and flow seaward after meeting with the emerged breakwaters of Hyères port (Courtaud, 2000). As a result, the speed of these currents are reduced much more when reaching Bona beach right in the lee side of this port, whereas the currents generated by the east and southeast winds easily approach this beach without any obstacles. Moreover, interaction

of main current system with the groynes and breakwaters results in formation of two large eddy circulations in front of Bona beach (Figure 245a). If the SBWs are implemented along this beach, the nearshore current fields become more complicated. The presence of SBWs directly induces formation of eddies at their roundheads and rip-currents in the gaps between them. The average current speed of most of points at the water depth of 1.2 m is reduced by less than 65.2% under the southeast and east winds, whilst its value is increased by 13.58%-68.23% under the northeast winds. With the effect of SBWs, the current velocity behind the structure is even higher than that in front of the structure. It strongly confirm that SBWs do not interfere with the longshore sediment drift, but also ensure good water quality in their leeside.



a. Without SBWs b. With SBWs

Figure 245. Current velocity distribution induced by annual winds in Bona beach.

Comparison of the current fields induced by summer and winter wave conditions with and without SBWs is presented in Figure 246. Without SBWs, it is noted that the average current speed of Bona beach in winter is larger than that in summer. The average current speed at the water depth of 1.2 m varies between 0.04 m/s and 0.07 m/s in winter and between 0.04 m/s and 0.06 m/s in summer (Table 73). This difference may come from that the high waves usually occur and approach this area in winter, whereas there are most of mild waves in summer. As a result, these high waves cause an increase of current velocity. In addition, as can be seen in Table 73, the current speed in Ceinturon beach is much larger than that in Bona beach, regardless of seasonal variation. Particularly, its value in Ceinturon beach is about 20% and 30% higher than that in Bona beach in summer and winter, respectively. Many man-made shore-normal structures along Bona beach, especially the emerged breakwaters of Hyères port, limit the main southward longshore current and thus decrease the velocity of these currents. In both summer and winter, interaction of main current system with the long groyne and the jetty of La Capte port results in eddy circulations in the north and south of this beach, respectively (Figure 246a). The presence of SBWs modifies the nearshore current velocity distribution. They interact with the main current system and generate vortices at their roundheads as well as rip currents between them. These rip currents play an important role in water exchange between the leeside and the outside of SBWs, avoiding stagnant zones, which are not good for touristic beaches. The installation of SBWs basically decreases the current velocity in the water area behind them, even in the gaps between them. Table 73 reveals that the reduced percentage of average current speed in the leeside of SBWs in both summer and winter is less than 46.12%, while the value between them is lower than 27.14%.

In addition to the ordinary wave conditions (annual winds and different seasons), the effect of SBWs on the current fields of Bona beach was also investigated under the strong wave conditions, viz. decadal, tri-decadal, semi-centennial, centennial storms. Comparison of current velocity patterns triggered by the different storms with and without SBWs is shown in Figure 247. Without SBWs, the current velocity of Bona beach tends to increase in decadal and tri-decadal storms, and then decreases gradually in semi-centennial and centennial storms. The average current speed at the water depth of 1.2 m along this beach falls in the range of 0.11-0.29 m/s under the decadal storm, 0.1-0.3 m/s under the tri-decadal storm, 0.1-0.29 m/s under the semi-centennial storm, and 0.08-0.29 m/s under the centennial storm (Table 74). An eddy circulation is formed in the north of Bona beach, right in the downdrift of the long groyne in all storms (Figure 247a). Moreover, the northward longshore currents which flows around La Capte port and towards to the south of Bona beach, are intensified by the level of storm. This means that high level of storm results in the strong currents. Then these currents mix with the main southward longshore currents. However, the presence of SBWs completely

changes the nearshore currents along this beach. Interaction of main current system with these structures generates eddies at their roundheads and rip-currents in their gaps (Figure 247b). As they cause a significant reduction of wave height in all storms, the current velocity also decreases in both their leeside and gaps. The maximum reduced percentages are observed in the north of the beach, whereas the minimum values are found in the south part, regardless of storm level (Table 74). This would be explained by the fact that the emerged breakwaters of Hyères port, the groynes and SBWs in the north part interfere with the main longshore currents, while the current velocity in the south part could be boosted by the northward longshore currents from La Capte port.

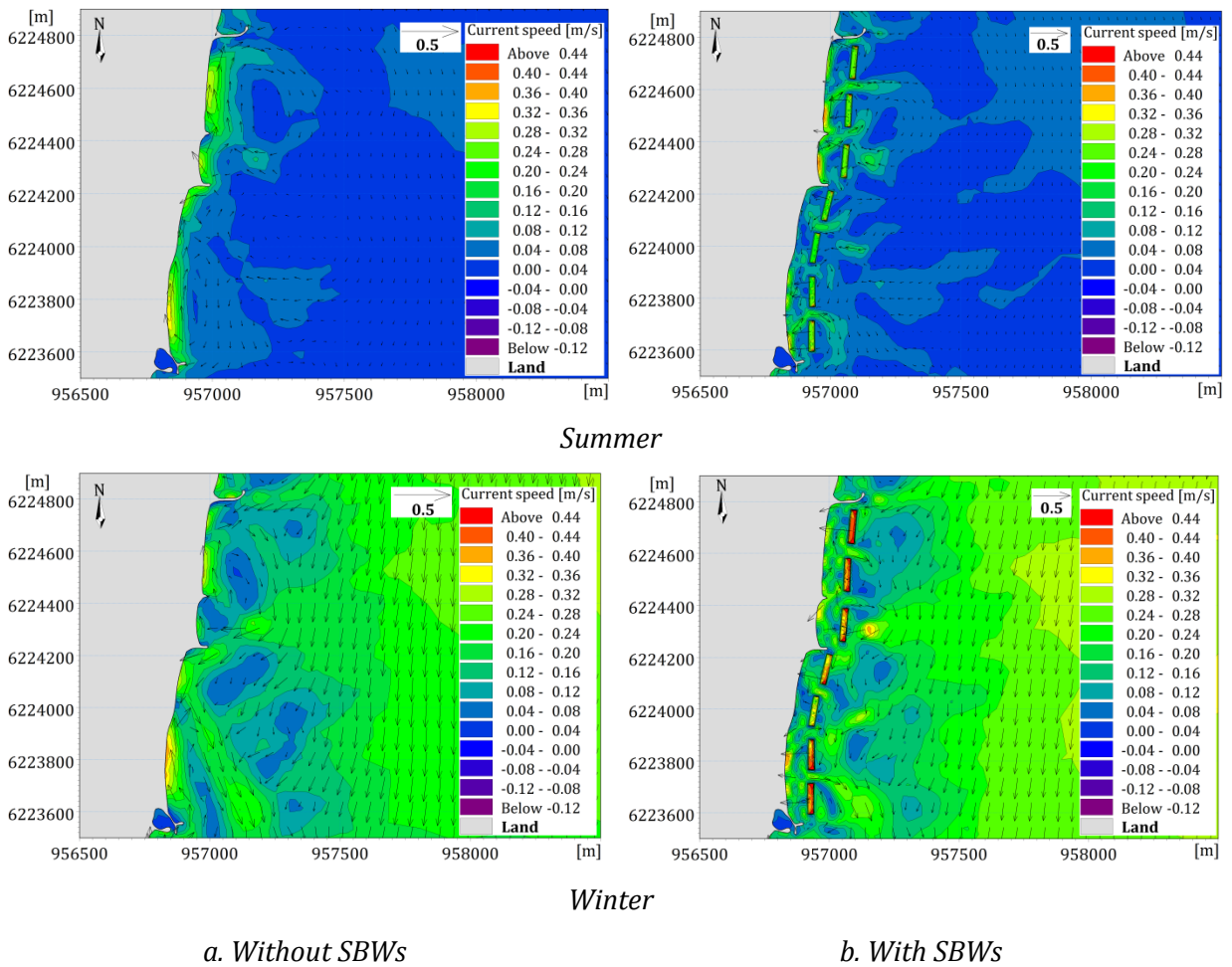
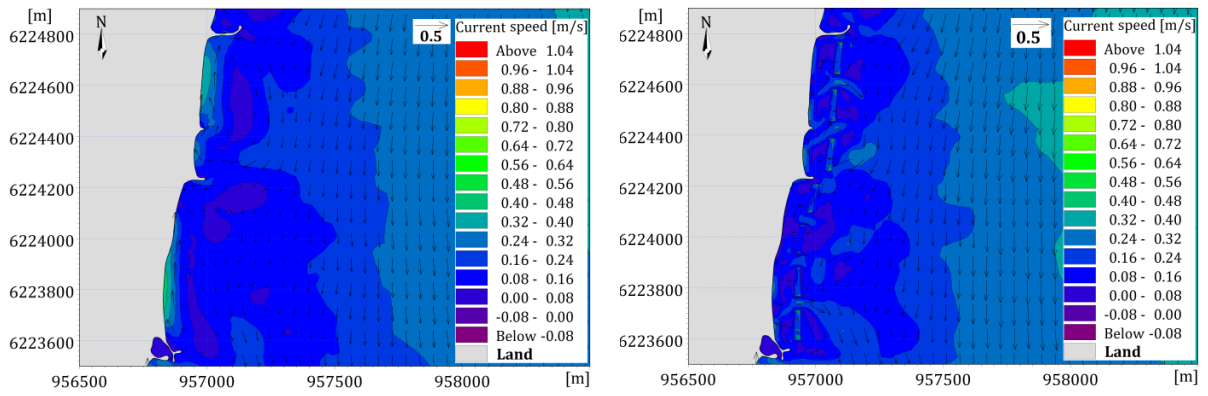
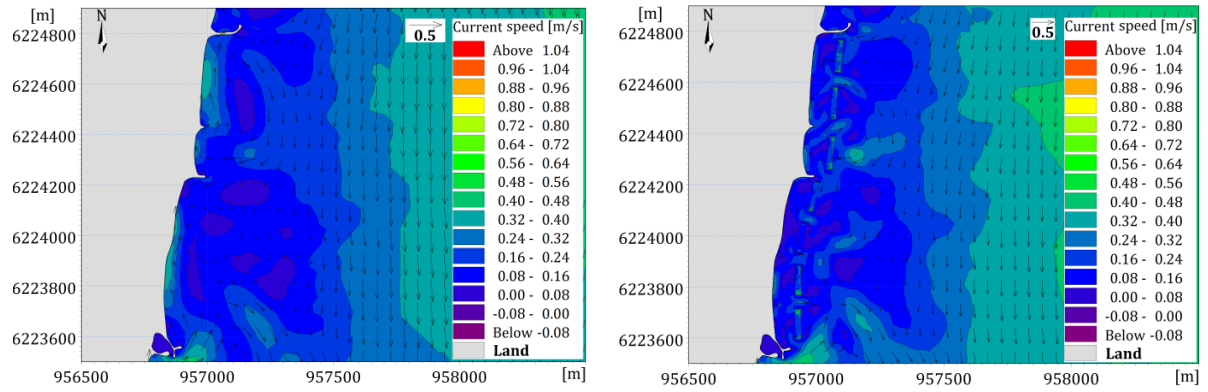


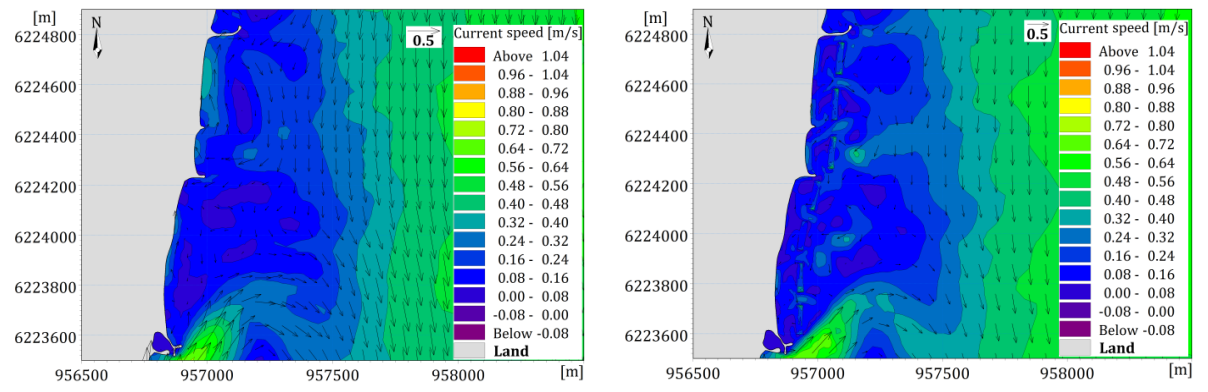
Figure 246. Current velocity distribution induced by seasonal variation in Bona beach.



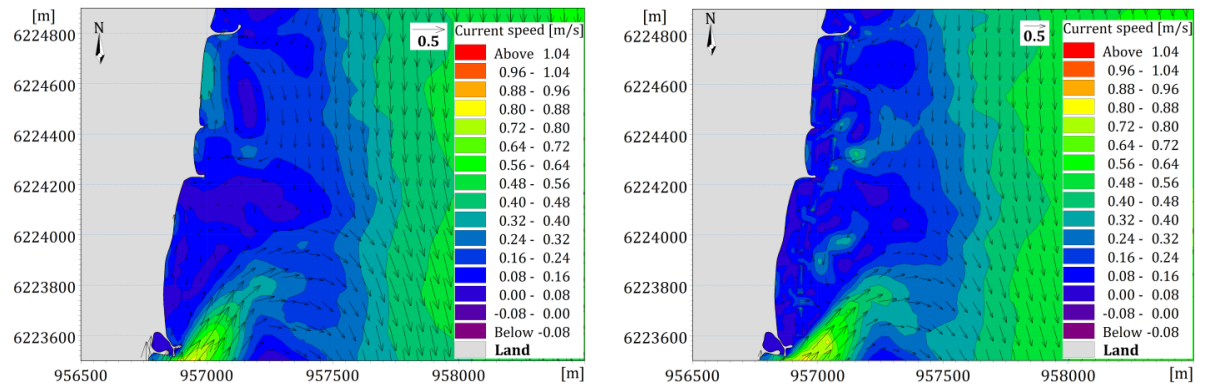
Decadal storm



Tri-Decadal storm



Semi-Centennial storm



Centennial storm

a. Without SBWs

b. With SBWs

Figure 247. Current velocity distribution induced by storms in Bona beach.

6.5.3. Effects to sediment transport

6.5.3.1. Ceinturon beach

Similar to the study of hydrodynamics, the impact of SBWs on sediment transport along Ceinturon beach was investigated by changing wind direction, season, and storm level. In the annual wind conditions, the largest sediment transport rates are driven by the northeast winds. The transport sediment rates in the northeast winds are about 16.1%-53.1% higher than that in other winds (Table 75). The reason of this phenomenon is that the high current speed induced by the northeast winds contributes to an increase of total load of sediment in this area. Nevertheless, the presence of SBWs completely modifies sediment transport along Ceinturon beach, especially in the water area between the shoreline and SBWs. With the effect of SBWs, the southeast winds become the dominant factor causing the largest sediment rates. The sediment transport rates induced by these winds are 1.71%-59.4% in the leeside of the structure and 24.4%-89%, comparing to that in east and northeast winds (Table 75). The main southward longshore currents blocked by the emerged breakwaters of Hyères port form the large eddy circulation in the south of Ceinturon beach and partly move northward. The impact of southeast winds along with the shelter of SBWs make these northward currents become stronger. However, the SBWs generally cause a sharp decrease of sediment transport rate. The maximum reduction of 89.34%-99.62% is observed under the northeast winds, whilst the minimum reduction of 50.24%-99.46% is found under the southeast winds (Table 75). Although total load is decreased, sediment is still transported along this beach behind the SBWs.

Considering the seasonal variation, the differences in current speed and significant wave height cause the total load of sediment in summer and winter. Naturally, the sediment transport rate in winter is much larger than that in summer about 50%-60% (Table 76). The presence of SBWs reduces the difference of sediment transport rate between winter and summer to 17.57%-48.9%. In addition, SBWs also trigger a large reduction in total load of sediment in both summer and winter. It is easily seen that the reduction of sediment rate in summer is lighter than that in winter. Particularly, sediment transport rate is decreased by 80%-99.3% in winter and 74.4%-95.6% in summer (Table 76). This reduction is resulted in a decrease of current speed and wave height due to the effect of SBWs.

Table 75. Comparison of sediment transport rate at representative points under different winds.

Point	<i>Q</i> (No SBWs) ($m^3/s/m$)			<i>Q</i> (SBWs) ($m^3/s/m$)			Difference (%)		
	NE	E	SE	NE	E	SE	NE	E	SE
T1	2.86E-05	1.80E-05	1.87E-05	3.05E-06	3.78E-06	4.55E-06	89.34	79.00	75.67
T2	5.84E-05	3.96E-05	5.94E-05	2.14E-06	4.16E-06	7.46E-06	96.34	89.49	87.44
T3	6.76E-05	3.17E-05	5.04E-05	5.76E-06	4.89E-06	5.86E-06	91.48	84.57	88.37
T4	7.56E-05	4.66E-05	3.63E-05	1.90E-06	3.74E-06	4.68E-06	97.49	91.97	87.11
T5	4.28E-05	2.70E-05	4.13E-05	1.63E-07	2.01E-07	2.21E-07	99.62	99.26	99.46
T6	2.95E-05	7.39E-05	7.28E-05	5.34E-06	3.10E-06	2.95E-06	81.90	95.81	95.95
T7	5.53E-05	7.70E-05	7.69E-05	8.46E-06	7.16E-06	6.13E-06	84.70	90.70	92.03
T8	1.37E-05	2.19E-05	2.44E-05	5.32E-06	2.48E-06	2.35E-06	61.17	88.68	90.37
T9	2.38E-05	2.04E-05	1.26E-05	2.90E-06	2.24E-06	1.71E-06	87.82	89.02	86.43
T10	3.92E-05	1.16E-05	1.40E-05	2.43E-06	1.29E-06	8.03E-07	93.80	88.88	94.26
T11	4.72E-05	5.15E-05	5.46E-05	4.54E-06	5.59E-06	4.68E-06	90.38	89.15	91.43
T12	1.66E-05	2.18E-05	2.31E-05	3.80E-06	2.13E-06	1.63E-06	77.11	90.23	92.94
Q1	4.97E-05	3.32E-05	4.17E-05	1.41E-06	2.88E-06	1.12E-05	97.16	91.33	73.14
Q2	7.43E-05	5.48E-05	5.15E-05	1.92E-06	8.71E-06	1.75E-05	97.42	84.11	66.02
Q3	7.39E-05	4.03E-05	4.18E-05	6.05E-06	1.50E-05	2.08E-05	91.81	62.78	50.24
Q4	5.19E-05	4.05E-05	4.22E-05	4.84E-06	6.08E-06	8.04E-06	90.67	84.99	80.95
Q5	6.64E-05	8.08E-05	8.22E-05	4.79E-06	3.44E-06	3.31E-06	92.79	95.74	95.97
Q6	2.00E-05	5.68E-05	6.16E-05	9.55E-06	5.98E-06	5.70E-06	52.25	89.47	90.75
Q7	3.93E-05	2.11E-05	2.67E-05	6.62E-06	3.34E-06	2.11E-06	83.16	84.17	92.10

In addition to wind direction and seasonal variation, the effect of SBWs on sediment transport along Ceinturon beach under the different storms is also detected in this work. It is noticeable that sediment transport rate is increased along with the storm level. This means that the strong storm causes the high total load of sediment, regardless of SBWs. Specifically, the sediment rate increases from 1.56×10^{-4} - 3.14×10^{-4} m³/s/m under the decadal storm up to 3.36×10^{-4} - 1.47×10^{-3} m³/s/m under the centennial storm without SBWs. With the impact of SBWs, the sediment rate falls in the range of 7.62×10^{-6} - 9.34×10^{-5} m³/s/m under the decadal storm and 1.02×10^{-5} - 1.54×10^{-4} m³/s/m under the centennial storm (Table 77). It also strongly demonstrates that the presence of SBWs results in a significant decrease in sediment transport rate in all storms. The reduced percentage of total load of sediment in the leeside of SBWs is in the range of 88.5%-98.9%, while its value in the gaps of SBWs varies between 63.9% and 93.6%.

Table 76. Comparison of sediment transport rate at representative points under seasonal changes.

Point	Q (No SBWs) (m ³ /s/m)		Q (SBWs) (m ³ /s/m)		Difference (%)	
	Winter	Summer	Winter	Summer	Winter	Summer
T1	1.55E-05	7.76E-06	2.22E-06	1.34E-06	85.68	82.73
T2	2.47E-05	1.16E-05	2.82E-06	1.86E-06	88.58	83.97
T3	2.58E-05	1.11E-05	2.95E-06	1.80E-06	88.57	83.78
T4	2.34E-05	9.83E-06	2.39E-06	1.97E-06	89.79	79.96
T5	2.04E-05	1.03E-05	1.50E-07	4.57E-07	99.26	95.56
T6	2.43E-05	8.42E-06	2.73E-06	1.15E-06	88.77	86.34
T7	2.62E-05	9.38E-06	3.99E-06	1.72E-06	84.77	81.66
T8	1.17E-05	5.71E-06	3.04E-06	1.27E-06	74.02	77.76
T9	1.07E-05	6.11E-06	8.73E-07	4.03E-07	91.84	93.40
T10	1.31E-05	7.78E-06	9.85E-07	8.68E-07	92.48	88.84
T11	2.50E-05	7.53E-06	2.06E-06	7.51E-07	91.76	90.03
T12	1.48E-05	7.01E-06	1.61E-06	6.01E-07	89.12	91.43
Q1	2.42E-05	1.07E-05	2.77E-06	1.89E-06	88.55	82.34
Q2	2.84E-05	1.15E-05	2.96E-06	1.87E-06	89.58	83.74
Q3	2.49E-05	1.06E-05	4.99E-06	2.55E-06	79.96	75.94
Q4	2.34E-05	1.05E-05	3.97E-06	2.69E-06	83.03	74.38
Q5	3.22E-05	9.99E-06	2.25E-06	1.65E-06	93.01	83.48
Q6	1.64E-05	8.45E-06	2.89E-06	2.04E-06	82.38	75.86
Q7	1.69E-05	7.04E-06	1.07E-06	7.03E-07	93.67	90.01

Table 77. Comparison of sediment transport rate at representative points under storms.

Point	Q (No SBWs) ($m^3/s/m$)				Q (SBWs) ($m^3/s/m$)				Difference (%)			
	DS	TS	SS	CS	DS	TS	SS	CS	DS	TS	SS	CS
T1	1.56E-04	1.85E-04	2.90E-04	3.36E-04	7.62E-06	9.47E-06	1.60E-05	3.00E-05	95.12	94.88	94.48	91.07
T2	2.62E-04	3.56E-04	6.53E-04	7.37E-04	1.61E-05	1.25E-05	4.34E-05	8.50E-05	93.85	96.49	93.35	88.47
T3	2.35E-04	3.63E-04	9.49E-04	1.23E-03	1.98E-05	1.89E-05	1.60E-05	4.48E-05	91.57	94.79	98.31	96.36
T4	3.14E-04	4.56E-04	9.57E-04	1.47E-03	1.70E-05	2.23E-05	1.02E-05	2.67E-05	94.59	95.11	98.93	98.18
T5	2.11E-04	3.79E-04	3.57E-04	8.32E-04	7.82E-06	1.21E-05	1.38E-05	1.45E-05	96.29	96.81	96.13	98.26
T6	4.77E-04	5.46E-04	5.85E-04	6.61E-04	1.07E-05	1.28E-05	1.66E-05	4.74E-05	97.76	97.66	97.16	92.83
T7	4.17E-04	4.57E-04	4.60E-04	5.23E-04	1.41E-05	1.58E-05	2.21E-05	4.19E-05	96.62	96.54	95.20	91.99
T8	1.55E-04	1.65E-04	1.84E-04	1.93E-04	5.72E-06	6.82E-06	8.27E-06	2.05E-05	96.31	95.87	95.51	89.38
T9	1.31E-04	1.43E-04	1.61E-04	1.91E-04	6.21E-06	6.55E-06	7.96E-06	2.04E-05	95.26	95.42	95.06	89.32
T10	2.03E-04	2.09E-04	2.24E-04	2.60E-04	2.58E-06	1.70E-06	2.31E-06	9.31E-06	98.73	99.19	98.97	96.42
T11	4.20E-04	3.15E-04	2.82E-04	2.75E-04	5.71E-06	7.52E-06	7.10E-06	1.60E-05	98.64	97.61	97.48	94.18
T12	1.80E-04	1.23E-04	1.27E-04	2.09E-04	6.13E-06	9.26E-06	6.99E-06	1.03E-05	96.59	92.47	94.50	95.07
Q1	2.23E-04	2.82E-04	4.33E-04	4.92E-04	1.84E-05	3.00E-05	6.62E-05	9.85E-05	91.75	89.36	84.71	79.98
Q2	2.93E-04	4.24E-04	9.18E-04	1.07E-03	6.12E-05	2.71E-05	9.05E-05	1.27E-04	79.11	93.61	90.14	88.13
Q3	2.84E-04	4.03E-04	9.81E-04	1.34E-03	7.04E-05	7.23E-05	1.07E-04	1.54E-04	75.21	82.06	89.09	88.51
Q4	2.59E-04	3.82E-04	5.48E-04	9.67E-04	9.34E-05	1.23E-04	1.05E-04	1.46E-04	63.94	67.80	80.84	84.90
Q5	5.33E-04	6.04E-04	6.36E-04	7.13E-04	1.48E-05	2.20E-05	4.02E-05	8.67E-05	97.22	96.36	93.68	87.84
Q6	2.82E-04	3.65E-04	3.63E-04	5.03E-04	2.69E-05	3.24E-05	5.73E-05	1.12E-04	90.46	91.12	84.21	77.73
Q7	1.89E-04	2.11E-04	2.29E-04	2.52E-04	9.64E-06	1.10E-05	1.93E-05	3.45E-05	94.90	94.79	91.57	86.31

Note: DS-Decadal storm; TS-Tri-decadal storm; SS-Semi-Centennial storm; CS-Centennial storm.

6.5.3.2. Bona beach

Contrary to Ceinturon beach, the southeast winds play the decisive role in sediment transport along Bona beach. The highest sediment transport rates are observed under these winds, whereas the lowest rates are normally induced by the northeast winds (Table 75). This would be explained by the fact that the higher southeast wind-induced current speeds results in a boost of sediment concentrations and transport along the shoreline. Meanwhile, the northeast wind-induced longshore currents are interfered by the breakwaters of Hyères port and so reduced their magnitude after reaching Bona beach. The implementation of seven SBWs entirely changes the pattern of sediment transport in this beach. With the effect of SBWs, the largest sediment rates occur under the northeast winds, while the minimum values are commonly generated in the southeast winds. For instance, the sediment transport rates induced by the northeast winds are about 15.4%-68.1% larger than that due to other winds. In general, the presence of SBWs results in a large decrease in total load of sediment in all annual wind conditions. The reduced percentage of sediment rates behind SBWs ranges from 61.2% to 96%, while its value varies between 52.3% and 96% between SBWs (Table 75).

Regarding the sediment transport under the impact of seasonal variation, the total load of sediment of 10 representative points, namely T6-12 and Q5-7, at the water depth of 1.2 m along Bona beach is extracted and listed in Table 76. As can be seen in this table, the sediment transport rate in winter is much larger than that in summer. Many storms and rough seas which usually occur in winter generate the high waves and strong currents. As a result, the sediment rate becomes larger, comparing to that in summer. In particular, the difference of total load between winter and summer falls in the range of 40.6%-70% behind SBWs and 48.5%-69% in the gaps of SBWs. Similar to Ceinturon beach, the presence of seven SBWs in Bona beach curtails this difference to 11.9%-63.5% in the leeward side of SBWs and 26.7%-34.3% in the gaps of SBWs. Moreover, the construction of SBWs also induces a remarkable reduction in the sediment transport rate in both winter and summer. Specifically, the reduced percentage of sediment rate falls in the range of 74%-93.4% behind the SBWs and 75.9%-93.7% between them (Table 76).

Akin to Ceinturon beach, the storm level would determine the magnitude of sediment transport rate in Bona beach. The sediment transport rate in decadal storm varies between 1.31×10^{-4} m³/s/m and 5.33×10^{-4} m³/s/m, while its value falls in the range of 1.91×10^{-4} - 7.13×10^{-4} m³/s/m under the centennial storm (Table 77). Although the presence of SBWs leads to a significant reduction in sediment transport rate in all storms, this rate still increases gradually corresponding to the level of storm, viz. from 2.58×10^{-6} - 2.69×10^{-5} m³/s/m in the decadal storm to 9.32×10^{-6} - 1.12×10^{-4} m³/s/m in the centennial storm. A sharp decline in wave height and current speed due to the effect of SBWs results in a considerable decrease of sediment transport, especially in the water

area between the shoreline and the SBWs. The maximum reduced percentage of sediment rate reaches to 99.2% in the leeside of SBWs and 97.2% in the gaps of SBWs (Table 77). In addition, the largest reduction is observed in the lowest storm level. In other words, the impact of SBWs on sediment transport will decrease if the level of storm increases. Particularly, the reduced percentage of the sediment transport rate is in the range of 91.1%-99.2% under the decadal storm, whereas its value varies from 77.7% to 96.4% under the centennial storm. The main reason of this phenomenon is that the high level of storm accompanied with the large storm surge increases the freeboard (the distance between the crest elevation and the water level), so easily allows high waves to approach the beach without breaking.

6.5.4. Effects to bathymetry evolution

In order to visualize the effect of SBWs on the morphological evolution of both Ceinturon and Bona beaches, comparison of bathymetry evolution with and without SBWs under the different wave conditions, viz. annual wind directions, winter, summer, various storms, is carried out. In addition, 19 representative beach profiles through SBW and the gap between SBWs along these beaches are extracted to illustrate the beach profile changes with and without SBWs. The location of 19 beach profiles can be found in Figure 248. From that, the role of SBWs in beach protection would be revealed clearly.

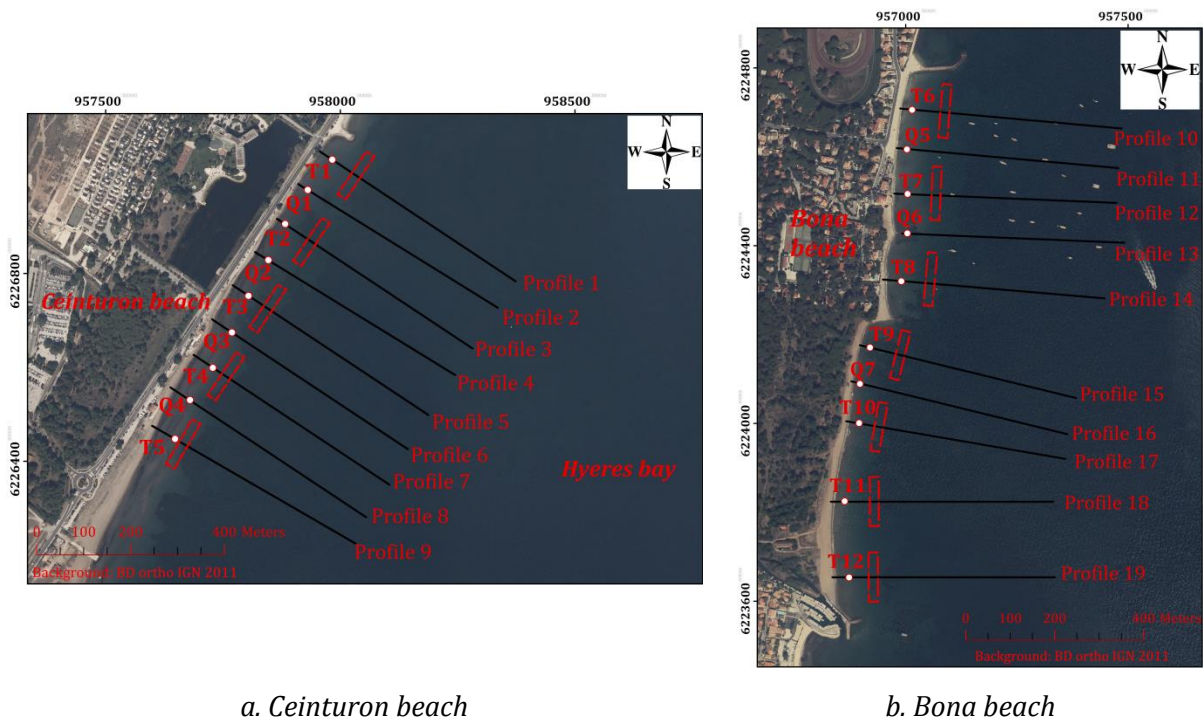
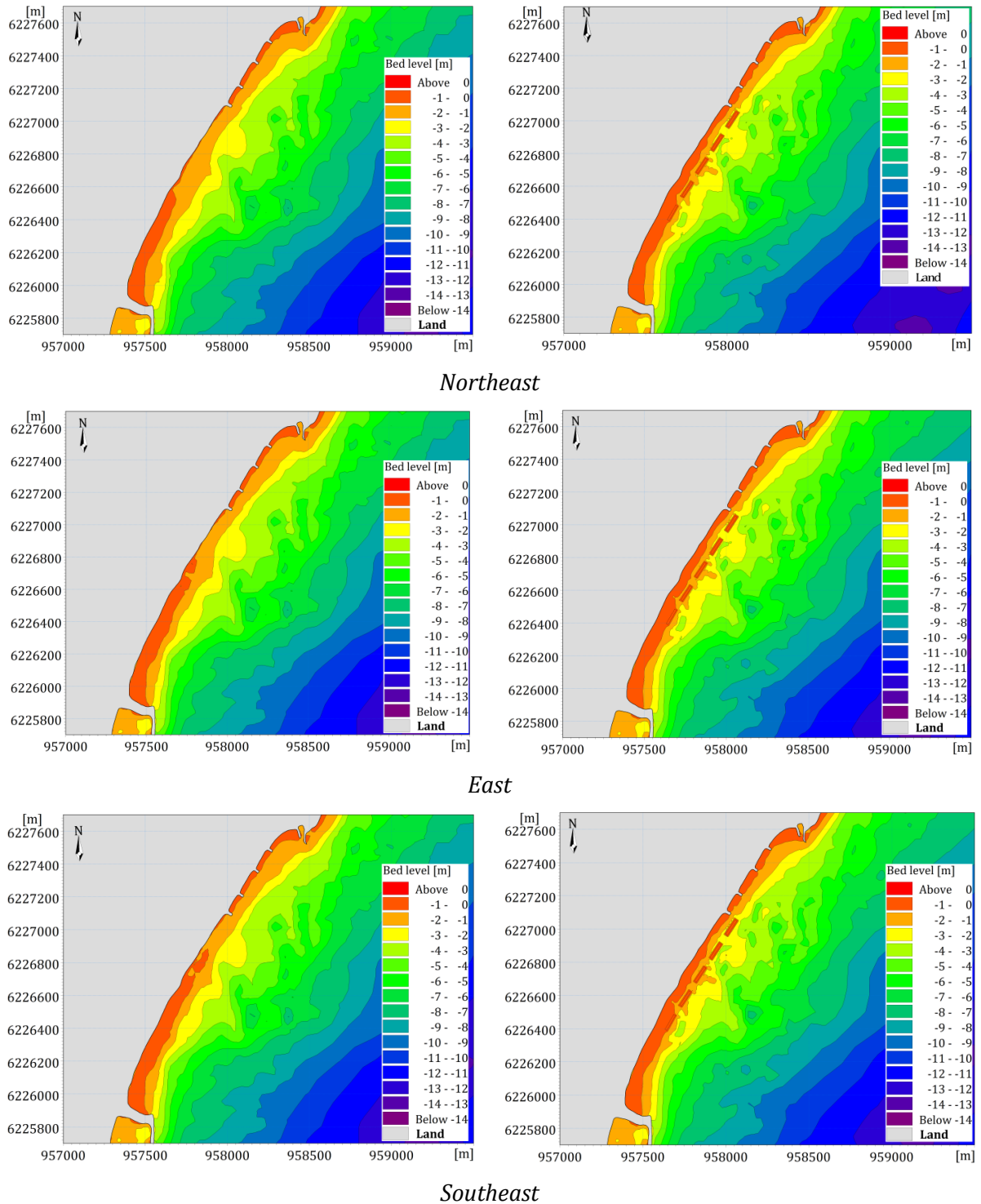


Figure 248. Location of cross-shore beach profiles.

6.5.4.1. Ceinturon beach

Figure 249 shows comparison of bathymetry with and without SBWs under the different annual wind directions. As can be seen in this figure, the greatest changes took place in the central part of Ceinturon beach. The largest erosive area is induced by the northeast winds, while the southeast winds trigger the smallest erosive area. The

isobath of -1.0 m almost vanishes under the northeast winds. The presence of SBWs dramatically modifies the bathymetry in the central part (Figure 249b). It is clearly seen that not only the isobath of -1.0 m is maintained in all wind directions, but also the depth in the sheltered area decreases where slight salient occur behind SBWs, especially in the leeside of the third to the fifth SBW. Although the SBWs result in the positive changes of the bathymetry, erosion still take places in the gaps between SBWs and can be explained by the action of seaward flow concentration, viz. rip-currents.



a. Without SBWs

b. With SBWs

Figure 249. Bed level change of Ceinturon beach induced by annual winds.

The cross-shore changes of profile 2 and 3 in the gaps and the leeside of SBWs under the effect of annual wind directions are plotted in Figure 250 and Figure 251, respectively. In addition, the other typical cross-shore profiles along Ceinturon beach can be found in Appendix E.1. As can be seen in these figures, the northeast winds cause more serious erosion than others in the case without SBWs. The statistical results of erosive area due to wind changes given in Table 78 indicate that erosive area induced by northeast winds is normally larger than that in other winds from 5% to 73%. The largest erosive area of $-38.65 \text{ m}^2/\text{m}$ is observed at the beach profile 7 in the northeast winds, while the smallest erosive area of $-3 \text{ m}^2/\text{m}$ is found at the beach profile 9 where moderate and high waves seldom occur. However, erosion state completely changes due to the presence of SBWs. It is clearly seen that erosive area of most beach profiles along Ceinturon beach sharply reduces, apart from two last profiles 8 and 9. The reduced percentage of erosive area falls in the range of 36.55%-79.2% behind the SBWs and 29.1%-75% between them (Table 78). Conversely, the erosive areas of the profile 8 and 9 increase by the maximum value of $-8.5 \text{ m}^2/\text{m}$ and $-2.8 \text{ m}^2/\text{m}$, respectively. This would be explained by the fact that an increase of current speed is due to the flow concentration of rip currents at the profile 8 and narrowing of the wetted area between the shoreline and SBW at the profile 9.

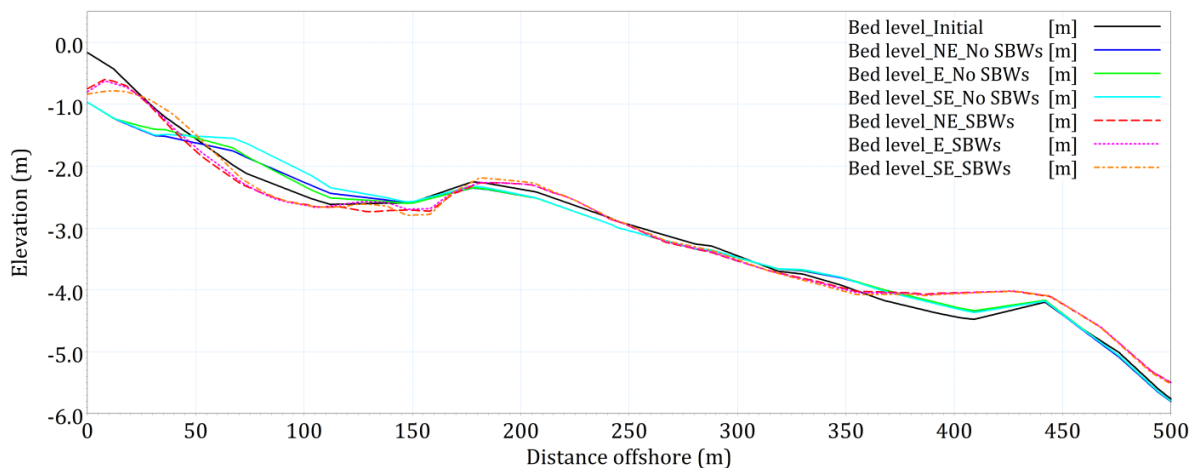


Figure 250. Cross-shore changes of beach profile 2 due to different wind directions.

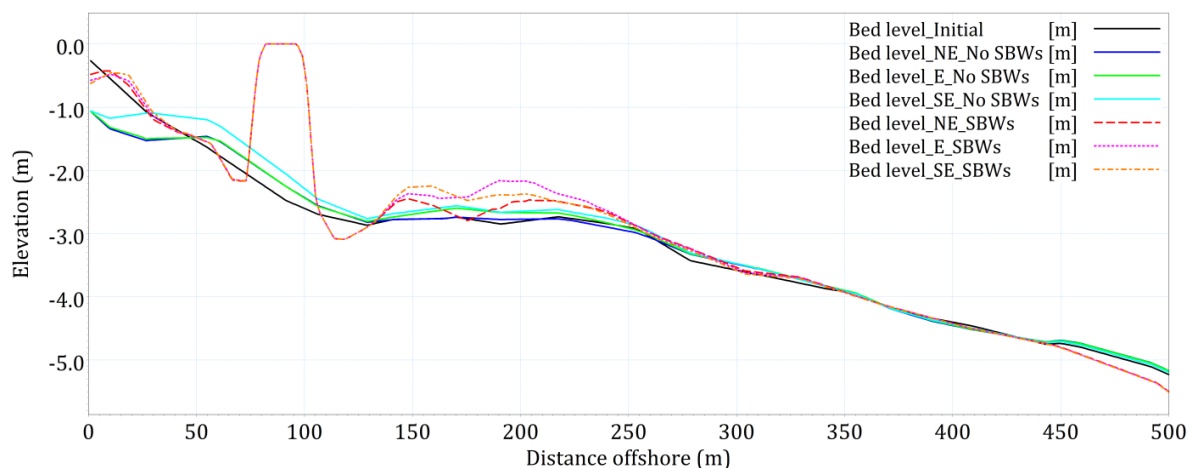


Figure 251. Cross-shore changes of beach profile 3 due to different wind directions.

In order to quantify the effect of SBWs on Ceinturon beach, 9 beach profiles were extracted along this beach. Figure 253 and Figure 254 present the cross-shore changes of beach profile 2 and 3 due to seasonal variation with and without SBWs in which are located in the gap and the leeside of SBWs, respectively. Without SBWs, all beach profiles are subjected to erosion, viz. moderate erosion in winter and slight erosion in summer. The maximum erosive area of $-32.81 \text{ m}^2/\text{m}$ is found at the beach profile 6 in winter, while the minimum values occur in profile 8 and 9 in both summer and winter (Table 78). All erosive areas usually take place from the shoreline to 70 m seaward of the shoreline. If five SBWs are installed in the central part of Ceinturon beach, the beach profile evolution is modified significantly. Erosive areas behind SBWs reduce dramatically in both summer and winter, except for the leeside of the fifth SBW. The reduced percentage of erosive area in the leeside of SBWs varies between 33.61% and 72.6%. Meanwhile, erosive areas in some gaps of SBWs increase due to rip currents. These erosive areas are mainly located from 50 m to 100 m seaward of the shoreline (see in Appendix E.1). Only small erosive areas are close to the shoreline.

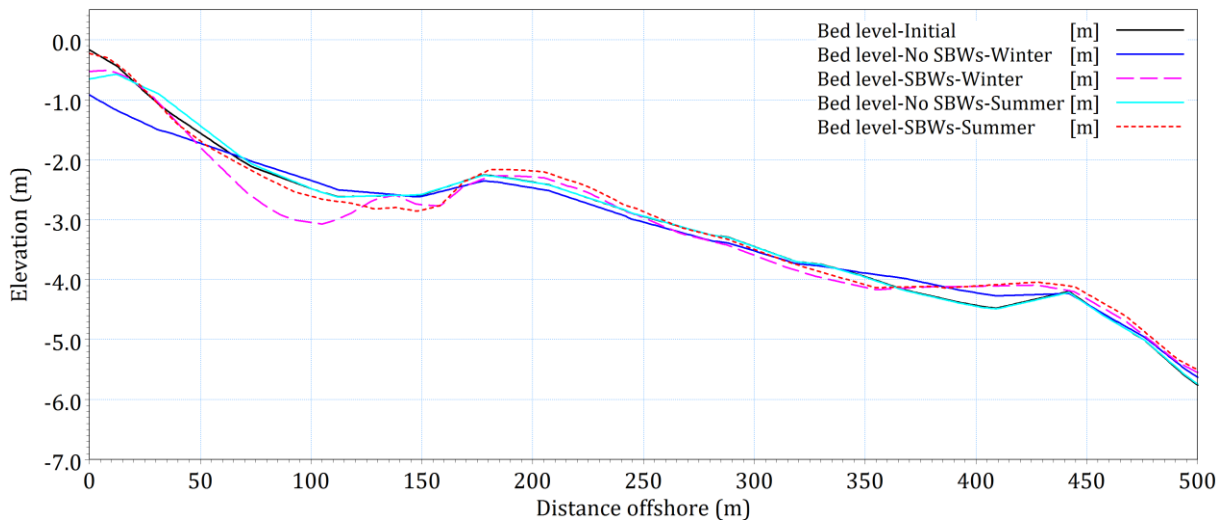


Figure 253. Cross-shore changes of beach profile 2 due to seasonal variation.

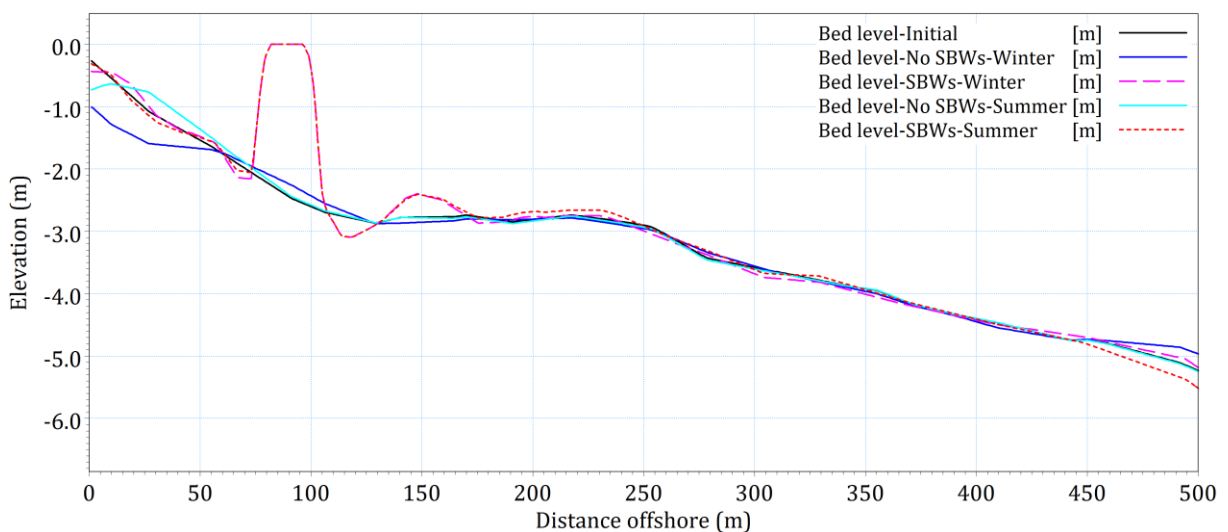
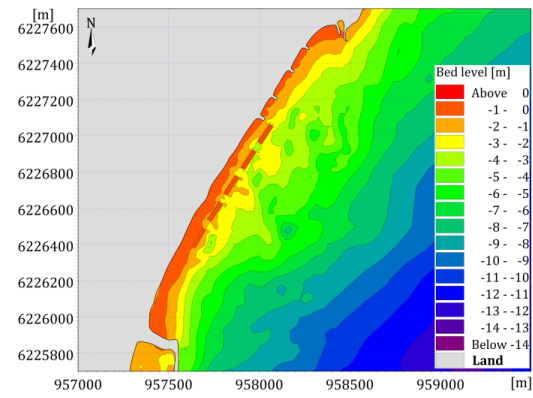
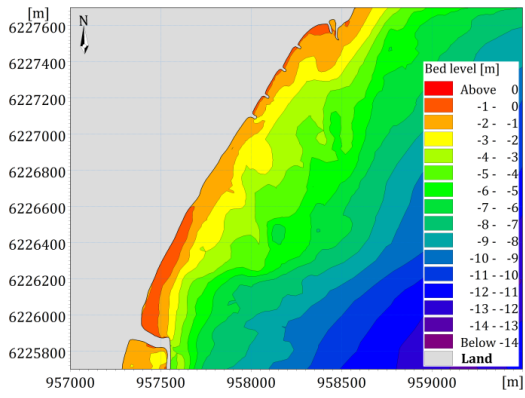


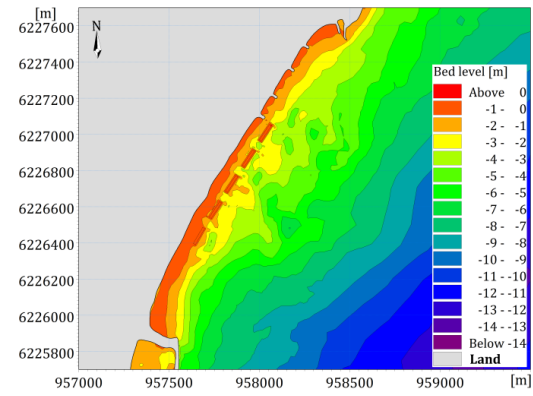
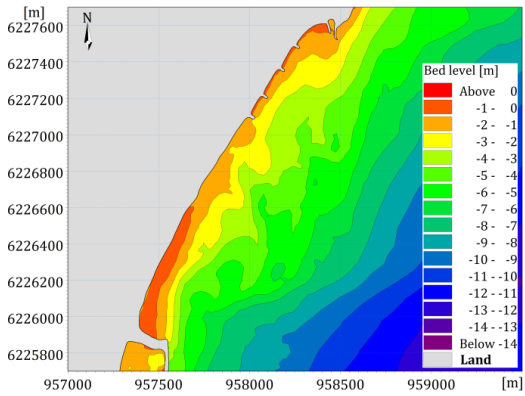
Figure 254. Cross-shore changes of beach profile 3 due to seasonal variation.

Under the impact of storms, the seabed around Ceinturon beach changes evidently, especially in the central part (Figure 255). It should be stressed that the storms cause severe erosion and the erosive area is enlarged along with the level of storm. Without SBWs, the isobath of -1.0 m in the central part disappears completely in all storms. In addition, the isobath of -2.0 m migrated landward. The seabed area of this isobath sharply reduces according to the increase of storm level. This means that the larger area is induced by the stronger storm. Even the isobath of -1.0 between the groynes in the north part also moves close to the shoreline. With the presence of SBWs, the erosion state of this beach basically alters according to the positive trend. Obviously, the erosive area decreases and one zone behind the SBWs are protected (Figure 254b). However, new erosive holes induced by strong rip currents occur in the gaps between SBWs, especially between the fourth and fifth SBW. In the semi-centennial and centennial storm conditions, the erosive area enlarges incessantly. Although the isobath of -1.0 m still exists after the centennial storm, the deep hole formed due to erosion run along the shoreline.

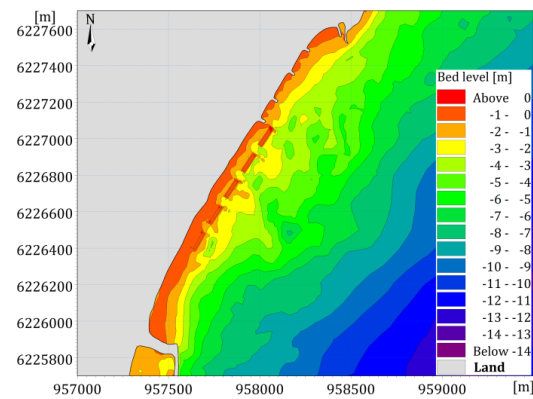
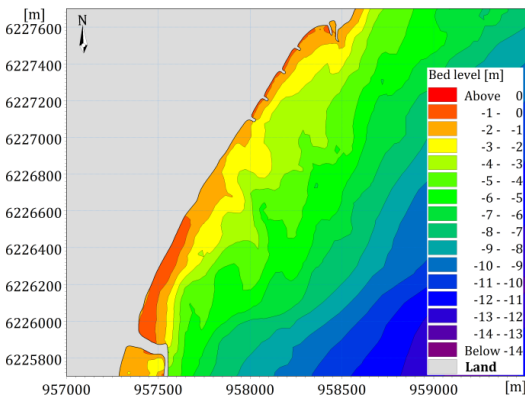
Similar to the scenarios of wind changes and seasonal variation, 9 beach profiles along the central Ceinturon beach are plotted to evaluate the effect of SBWs. The cross-shore changes of two representative beach profiles which are located in the gap and the leeside of SBWs are shown in Figure 256 and Figure 257, respectively. The evolution of other profiles can be found in Appendix E.1. In case of no SBWs, the largest erosive area is always generated by the semi-centennial and centennial storms. It occurs from the shoreline to 150 m seaward of the shoreline in most of beach profiles with maximum value of approximately 1.5 m at beach profile 3. If taking into account the presence of SBWs, the evolution trend of this beach modifies considerably. The erosive area behind the SBWs reduces swiftly. Particularly, the reduced percentage of erosive area ranges from 30% to 91% in the leeside of SBWs. The maximum reduction is observed in beach profile 3 and the minimum values are found in beach profile 9 (Table 78). Nevertheless, the erosion problem is exacerbated in some profiles located between SBWs. Also in these beach profiles, the role of SBWs in protecting the beach is greatly reduced under the impact of the semi-centennial and centennial storms.



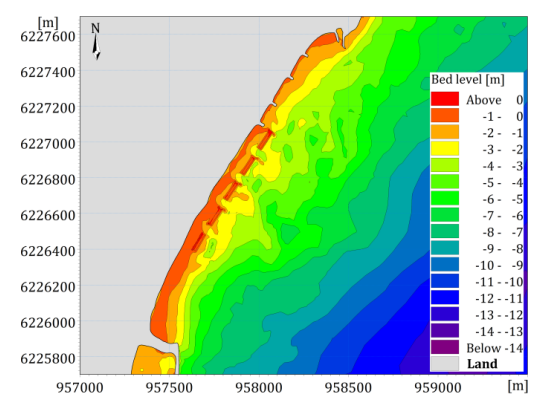
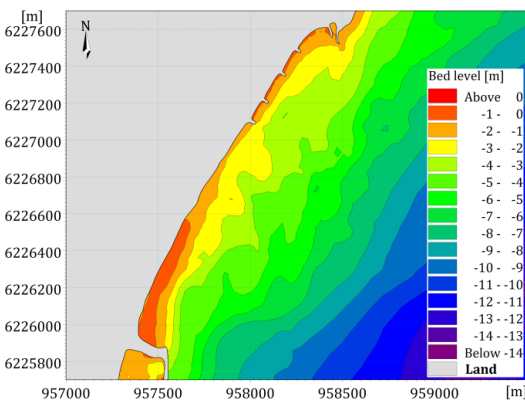
Decadal storm



Tri-Decadal storm



Semi-Centennial storm



Centennial storm

a. Without SBWs

b. With SBWs

Figure 255. Bed level change of Ceinturon beach induced by storms.

Table 78. Erosive area of beach profiles in Ceinturon beach with and without SBWs (m²).

Case	Profile	NE	E	SE	Winter	Summer	DS	TS	SS	CS
No SBWs	A-A	-29.82	-24.82	-24.15	-24.61	-4.93	-48.97	-48.67	-71.84	-94.87
	A'-A'	-29.72	-26.31	-26.70	-30.71	-4.77	-51.56	-50.45	-54.15	-66.00
	B-B	-21.68	-20.59	-11.08	-27.83	-4.51	-48.38	-66.66	-70.75	-84.38
	B'-B'	-28.17	-30.61	-17.21	-27.17	-4.45	-54.31	-59.67	-96.13	-112.8
	C-C	-35.83	-27.14	-27.97	-28.44	-6.90	-48.86	-52.93	-72.90	-97.66
	C'-C'	-36.91	-33.03	-21.21	-32.81	-6.64	-61.82	-86.17	-77.11	-104.0
	D-D	-38.65	-30.06	-15.12	-25.88	-6.70	-60.94	-77.48	-78.73	-96.88
	D'-D'	-4.69	-2.04	-1.27	-4.49	-1.20	-26.64	-34.65	-31.54	-35.31
E-E	-2.94	-2.02	-1.23	-2.19	-1.06	-20.46	-27.81	-23.50	-27.06	
SBWs	A-A	-15.63	-15.75	-14.18	-16.34	-2.63	-10.14	-10.58	-9.35	-11.15
	A'-A'	-15.00	-13.80	-13.61	-33.63	-2.91	-43.21	-48.60	-71.72	-89.51
	B-B	-5.30	-4.29	-4.31	-7.63	-2.78	-7.12	-6.20	-8.90	-16.34
	B'-B'	-10.04	-7.63	-12.21	-30.09	-0.73	-36.02	-63.70	-87.85	-106.7
	C-C	-13.52	-15.16	-15.13	-12.65	-3.90	-12.32	-11.24	-9.88	-15.64
	C'-C'	-17.73	-8.49	-11.28	-21.49	-1.63	-27.34	-35.04	-59.67	-72.73
	D-D	-14.42	-17.19	-17.76	-16.27	-3.94	-18.01	-17.02	-10.66	-15.28
	D'-D'	-13.18	-11.76	-7.32	-13.85	-3.39	-29.12	-30.50	-30.61	-30.39
E-E	-3.66	-3.86	-4.03	-10.61	-2.30	-14.15	-15.96	-15.38	-15.19	
%	A-A	47.59	36.55	41.28	33.61	46.77	79.29	78.26	86.99	88.25
	A'-A'	49.53	47.55	49.04	-9.51	39.12	16.19	3.66	-32.45	-35.64
	B-B	75.57	79.16	61.14	72.60	38.39	85.29	90.70	87.43	80.64
	B'-B'	64.36	75.08	29.06	-10.74	83.69	33.67	-6.75	8.61	5.40
	C-C	62.27	44.14	45.90	55.53	43.57	74.78	78.77	86.44	83.98
	C'-C'	51.98	74.29	46.83	34.50	75.43	55.78	59.33	22.61	30.08
	D-D	62.70	42.80	-17.47	37.14	41.22	70.44	78.04	86.45	84.23
	D'-D'	-181.2	-475.2	-478.0	-208.4	-181.68	-9.32	11.96	2.95	13.92
E-E	-24.78	-91.33	-228.1	-385.1	-117.24	30.84	42.61	34.55	43.87	

Note: DS-Decadal storm; TS-Tri-decadal storm; SS-Semi-Centennial storm; CS-Centennial storm.

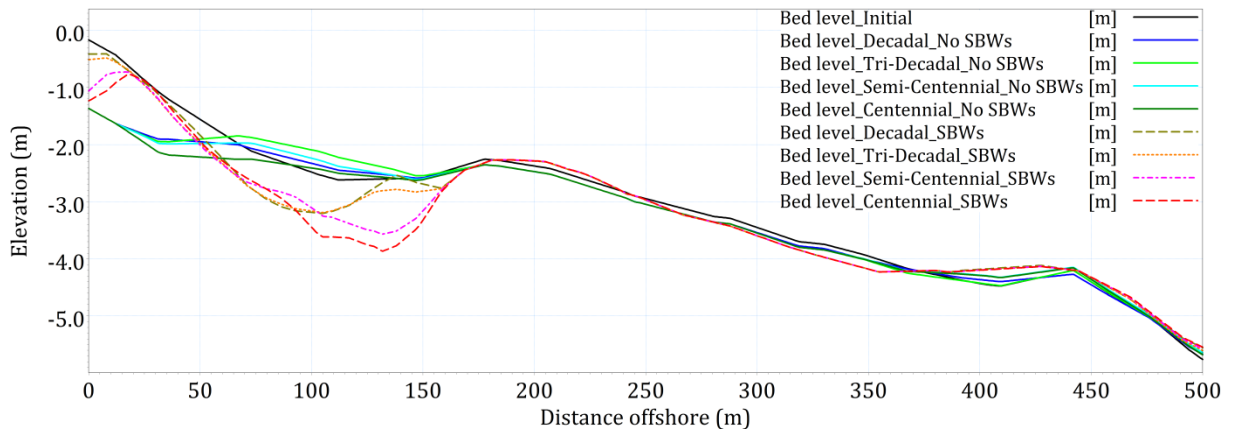


Figure 256. Cross-shore changes of beach profile 2 due to different storms.

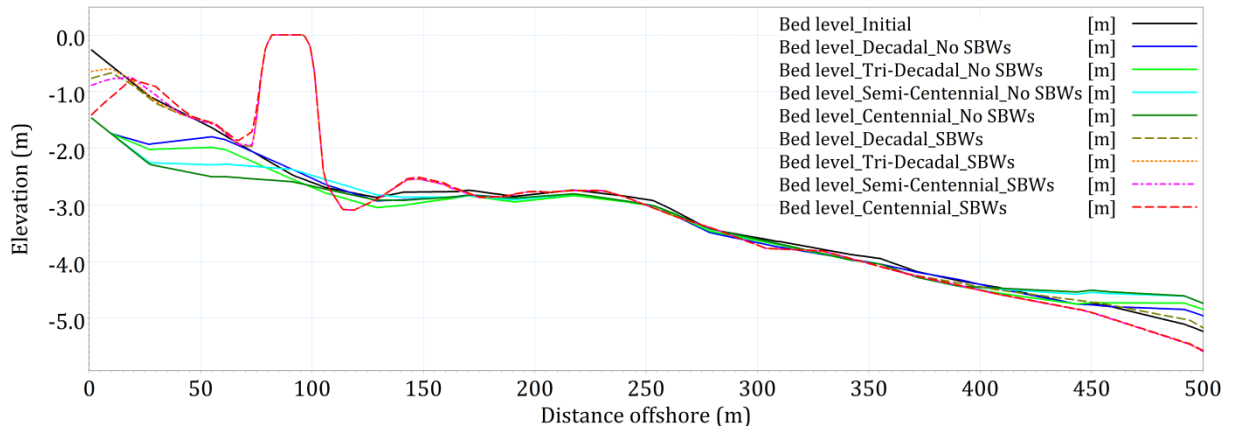
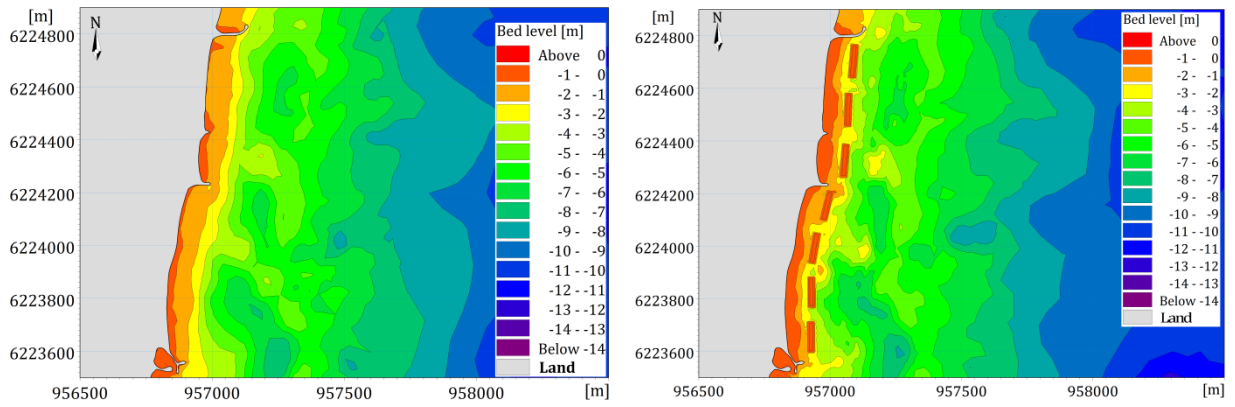


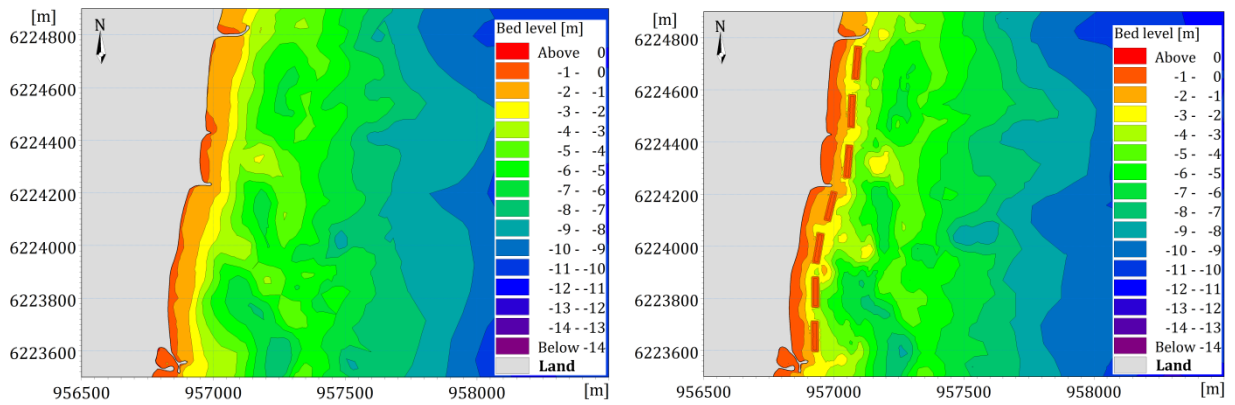
Figure 257. Cross-shore changes of beach profile 3 due to different storms.

6.5.4.2. Bona beach

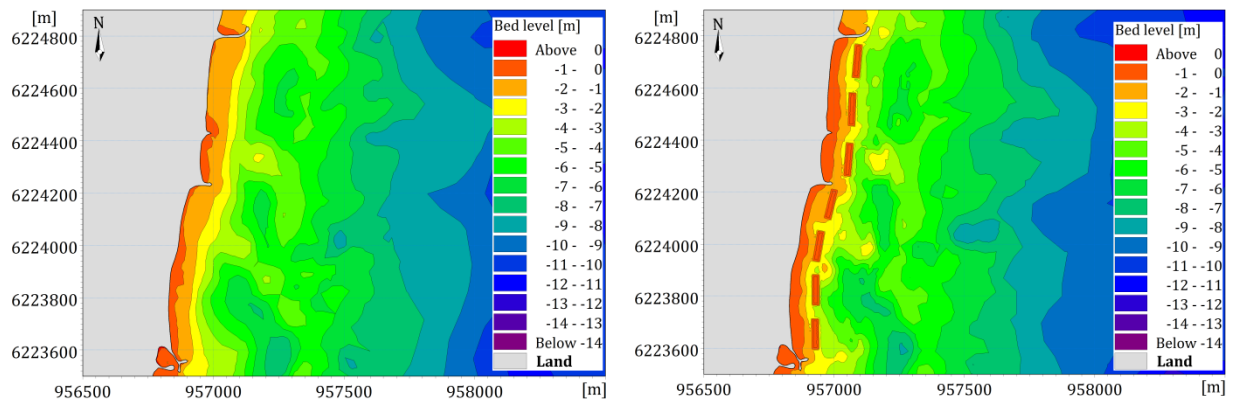
In this work, the effect of three main morphological winds including southeast, east and northeast on the seabed changes is modeled. The result proves that the north part of this beach from the first to second groyne would be eroded seriously landward in all annual wind conditions (Figure 258a). Moreover, moderate retreat of the shoreline is observed right in the downdrift of the third groyne. Without SBWs, the most severe erosion with the maximum value of 0.8 m is induced by the northeast winds. In case of the northeast winds, not only the isobath of -1.0 m move close to the shoreline but also the isobath of -2.0 m is migrated landward. This erosion situation of this beach suddenly alters when seven SBWs are implemented along the shoreline. Comparison of bathymetry with and without SBWs indicates that erosion is almost stopped in the leeside of SBWs. Even slight salient develops behind the structures (Figure 258b). Nevertheless, some new erosive areas take place in the gaps between the SBWs. This would be explained by the fact that the flow concentration due to rip currents in the gaps induces high current speed and pulls sediment offshore. As a result, the gaps would be deepened and forms rip embayment at the distance of 50 m and 100 m seaward of the shoreline.



Northeast



East



Southeast

a. Without SBWs

b. With SBWs

Figure 258. Bed level change of Bona beach induced by annual winds.

In order to exhibit the changes of bathymetry around Bona beach, 10 beach profiles were extracted. The typical cross-shore changes without and with the SBWs are shown in Figure 259 and Figure 260, respectively. It is noticeable that the erosive area induced by the northeast winds without SBWs is about 12.1%-79.2% larger than that in other winds (Table 79). The maximum erosive area of $-34.71 \text{ m}^2/\text{m}$ is observed at the beach profile 19 (see in Appendix E.2). Erosion usually occurs from the shoreline to 50 m seaward of the shoreline. Then the cross-shore currents take sediment to offshore area between 50 m and 200 m seaward of the shoreline. If taking into account the presence of SBWs, a moderate eroded state along the shoreline is halted instantly. The statics result

from Table 79 shows that the reduction in erosive area is found not only at the beach profiles behind the SBWs, but also at other profiles between SBWs. Particularly, the reduced percentage of erosive area varies from 28.12% to 83.44% in the leeside of SBWs and from 14.9% to 50.2% in the gaps of SBWs. It strongly demonstrates that erosion still takes place with SBWs; however, the loss amount of beach area due to erosion with SBWs is much less than that without SBWs.

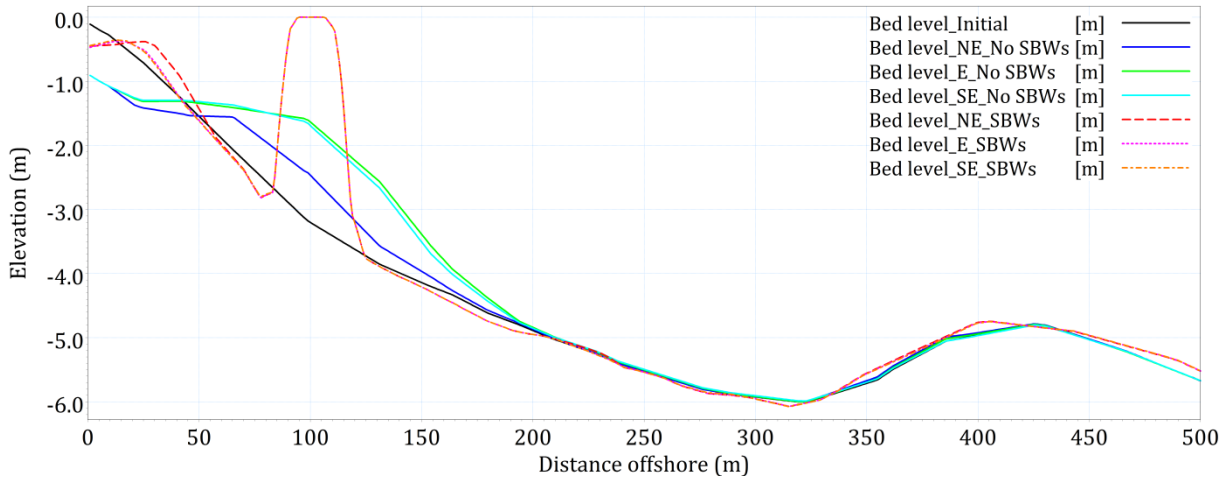


Figure 259. Cross-shore changes of beach profile 10 due to different wind directions.

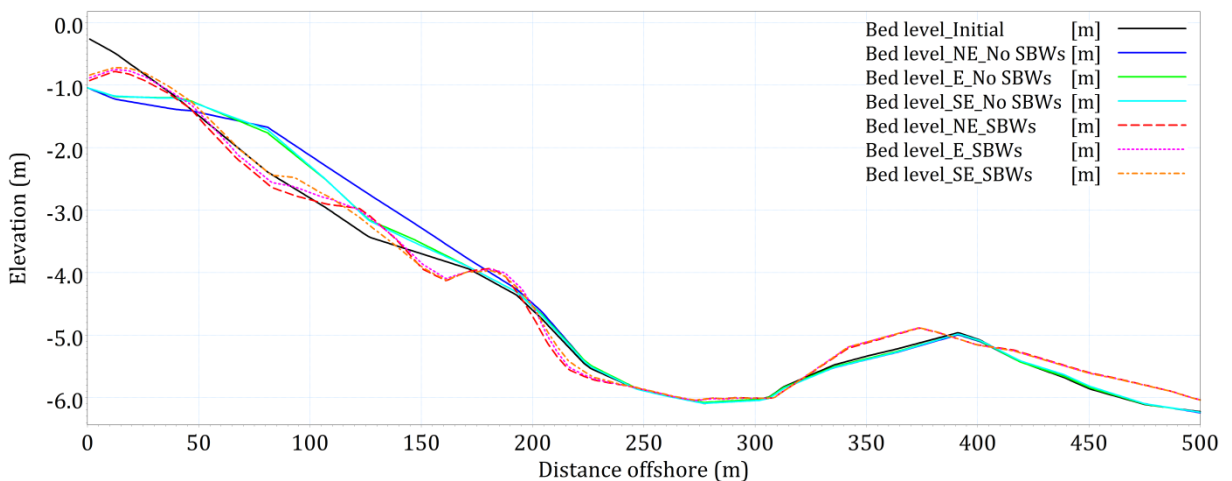


Figure 260. Cross-shore changes of beach profile 11 due to different wind directions.

Similar to Ceinturon beach, the bathymetry evolution in winter is very different from that in summer. A slightly eroded state near the shoreline is reported in summer, but severe erosion with the maximum value of 0.8 m is observed in winter (Figure 261a). The isobath of -1.0 m mostly disappears in the distance between the first and the second groyne and the beach area of this isobath also reduces by over 50% in the south part of Bona beach. By the support of seven SBWs, the beach bathymetry is nearly stable in summer. The isobath of -1.0 m even migrates seaward in the leeside of SBWs in both summer and winter (Figure 261b). However, a slight eroded state is found along the shoreline in winter. Some erosive areas occur in the gaps between SBWs due to rip currents; especially a significantly erosive hole is formed between the fifth and sixth SBWs in both summer and winter.

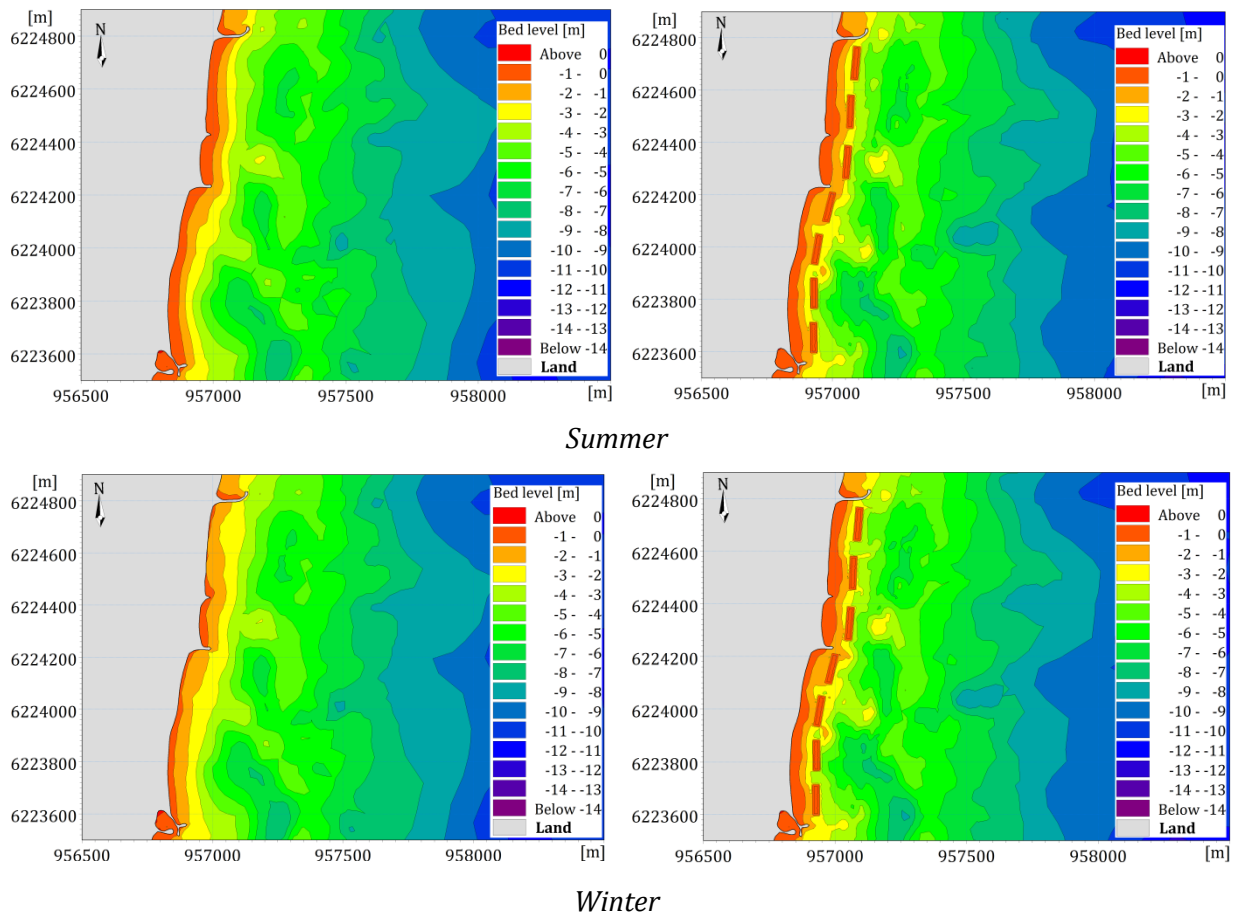


Figure 261. Bed level change of Bona beach induced by seasonal variation.

In addition to the plan view, the cross-sectional view is also shown through 10 cross-shore beach profiles along Bona beach. The typical cross-shore changes of beach profile behind as well as between the SBWs are depicted in Figure 262 and Figure 263, respectively. In the case of no SBWs, a slightly eroded state occurs along the shoreline in summer, with the maximum erosion value of about 0.5 m at the beach profile 12 (see in Appendix E.2). In winter, severe erosion is observed in most of beach profiles. The largest erosive area of over $-46 \text{ m}^2/\text{m}$ is found at the beach profile 12 again. However, the presence of SBWs converts from negative to positive trend of beach evolution. It is easily seen that all beach profiles keep stable after one summer month; even accretion occurs some places in the leeside of SBWs. The erosive area is also decreased significantly. The reduced percentage of erosive area in summer falls in the range of 40%-78.1% in the leeside of SBWs and 40.7%-80% in the gaps of SBWs (Table 79). For the winter wave scenario, only a slightly eroded state takes place near the shoreline behind SBWs with the maximum erosion value of 0.3 m. The reduced percentage of erosive area in the leeside of SBWs in winter ranges from 74.72% to 91.73% (Table 79). Nevertheless, new erosive areas appear in the gaps between SBWs and even erosion becomes more severe than that without SBWs at the same locations. The largest erosive area of $-50 \text{ m}^2/\text{m}$ is observed at the beach profile 11 (see in Appendix E.2).

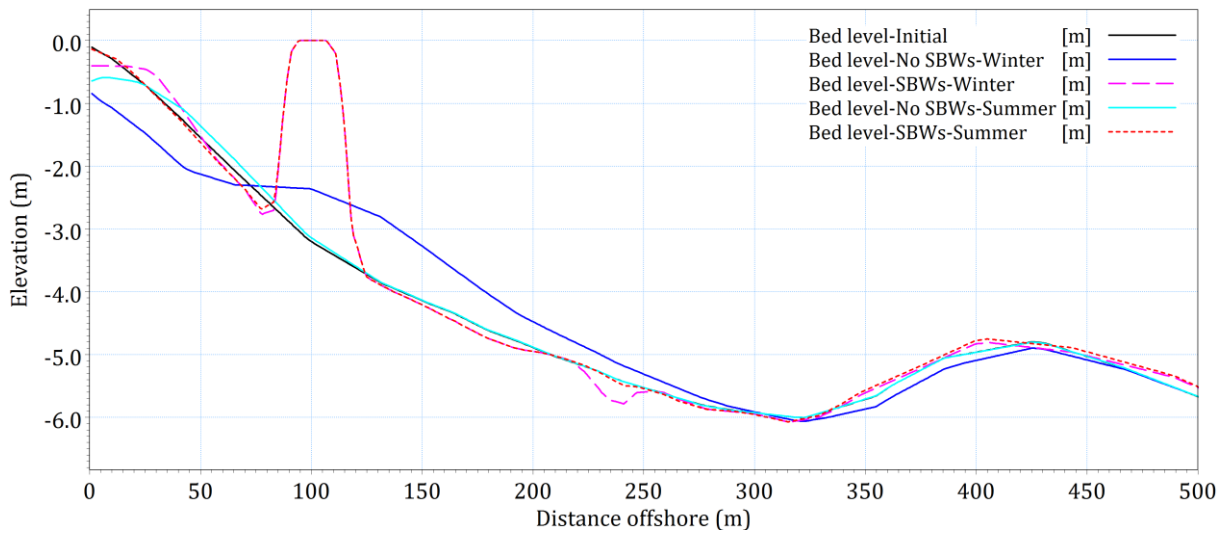


Figure 262. Cross-shore changes of beach profile 10 due to seasonal variation.

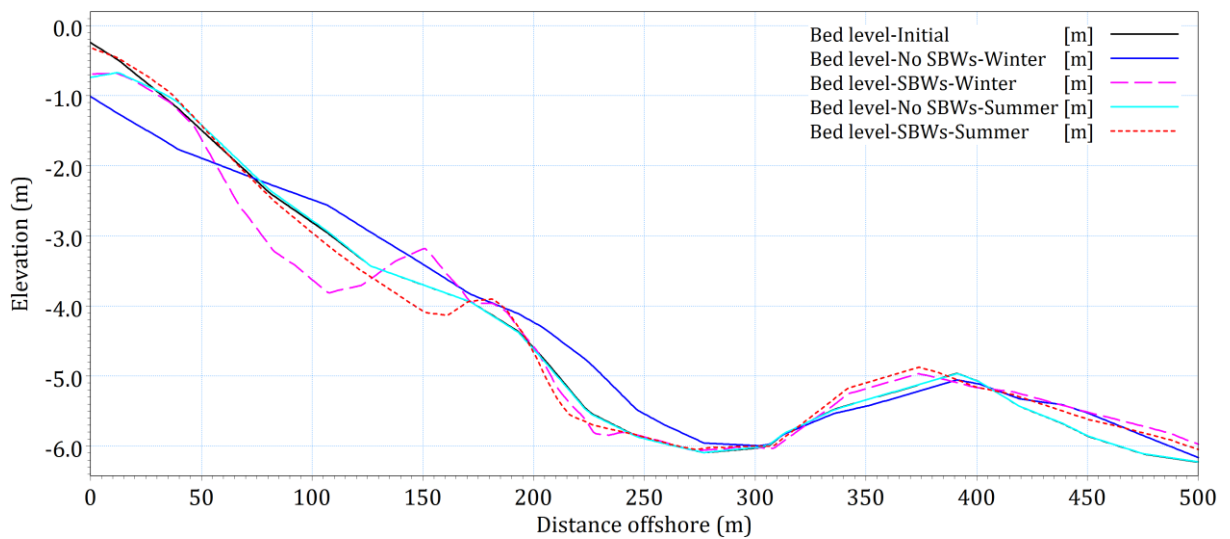
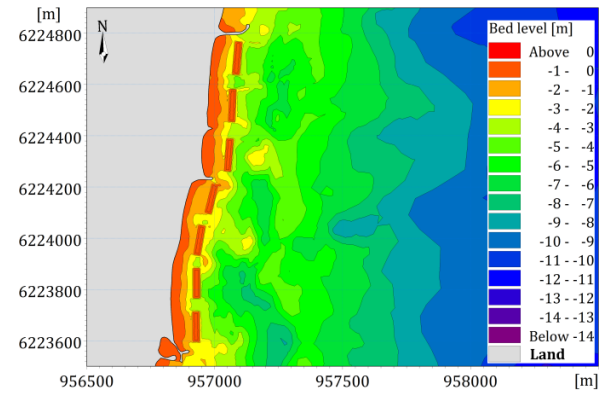
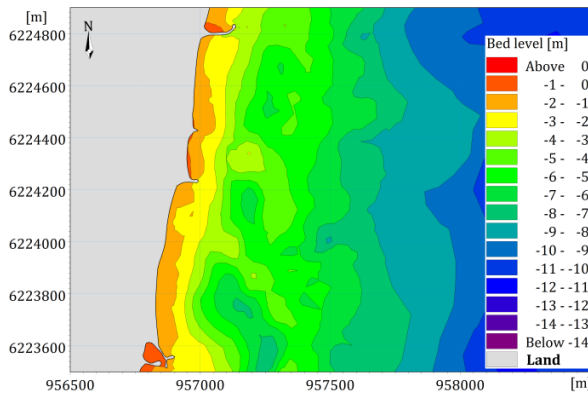
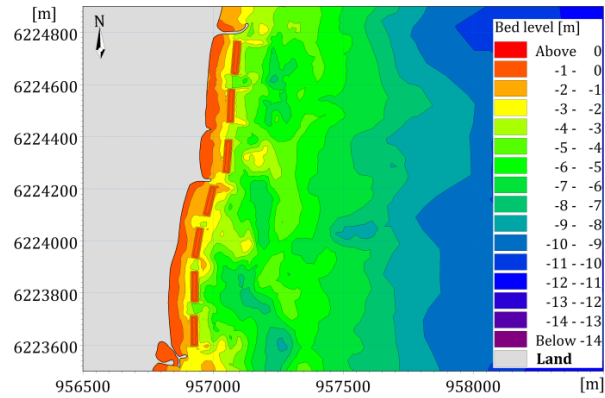
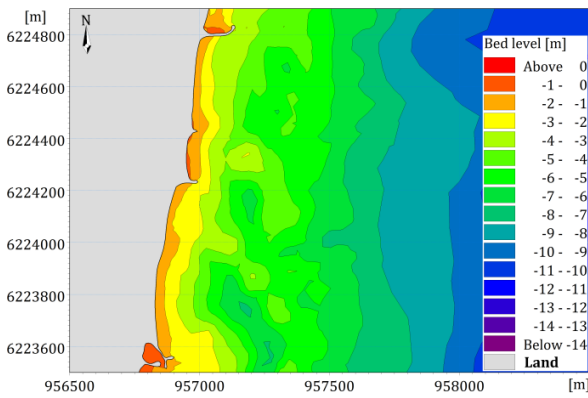


Figure 263. Cross-shore changes of beach profile 11 due to seasonal variation.

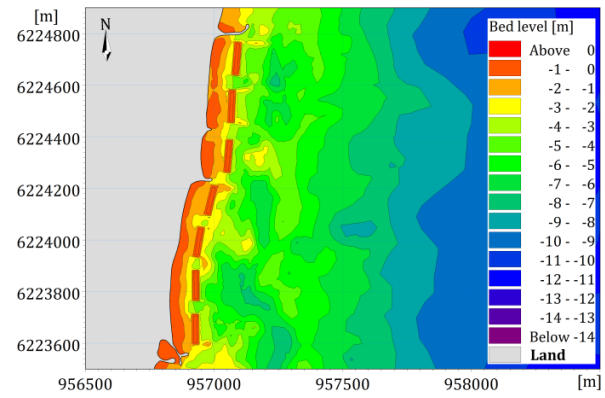
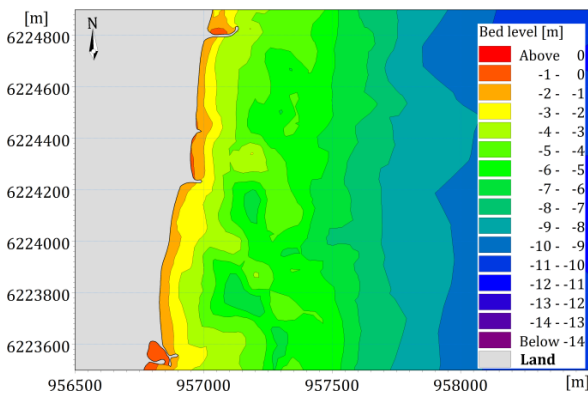
When the larger coastal storms attack Bona beach, increased wave height and current speed results in larger waves along the shoreline. These waves reach the higher part of beach and pull sand offshore. Figure 264 describes the seabed changes around Bona beach experiencing the different storms with and without SBWs. It is noted that this beach would be undergone very severe erosion under the impact of storms without SBWs. The more serious erosion is induced by the stronger storm. Of course, the largest erosive area is caused by the centennial storm. In all storms, not only the isobath of -1.0 m disappears completely, but also the isobaths of -2.0 m and -3.0 m decline sharply and migrate shoreward (Figure 264a). The presence of SBWs can protect Bona beach to a certain degree. Figure 264b indicates that the beach is protected effectively under the decadal and tri-decadal storms. However, rip embayments start occurring between the SBWs in the semi-centennial storm. These embayments interrupted the isobaths of -1.0 m and -2.0 m. In the centennial storm, severe erosion even takes place close the shoreline behind the SBWs, especially in the beach zone between the first groyne and the second groyne.



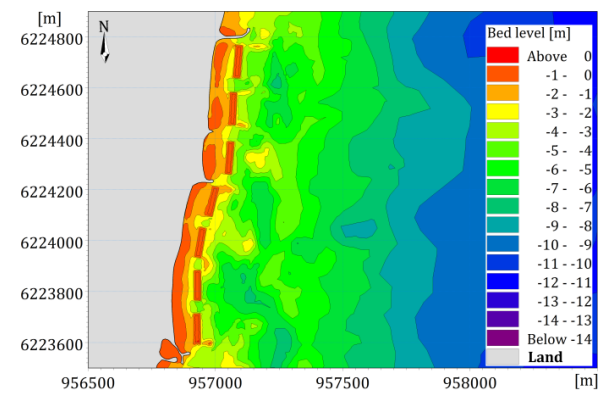
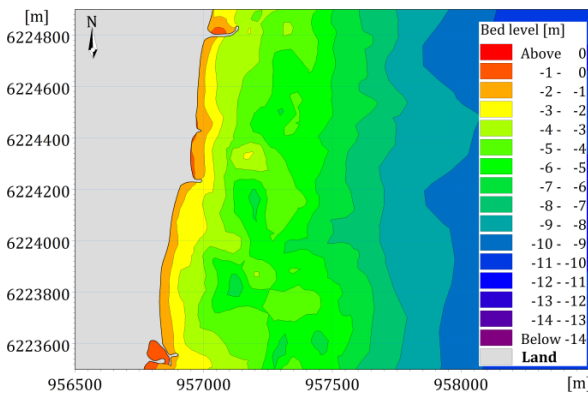
Decadal storm



Tri-Decadal storm



Semi-Centennial storm



Centennial storm

a. Without SBWs

b. With SBWs

Figure 264. Bed level change of Bona beach induced by storms.

In order to visualize the role of SBWs in protecting Bona beach from the storms, ten beach profiles are extracted and compared. Without the effect of SBWs, severe erosion takes place from the shoreline to about 200 m seaward of the shoreline along the beach in all storms. The maximum erosion value of 1.2 m is observed at the beach profiles 10, 11, and 12 under the centennial storm. The entire beach recedes seriously with the large land loss due to strong storms. If taking into account the presence of SBWs, the eroded area reduces dramatically in the leeside of these structures. The reduced percentage of eroded area is in the range of 75.1%-95.83% in the decadal storm, 51.37%-96.41% in the tri-decadal storm, 38.16%-95.32% in the semi-centennial storm, and 43.1%-90.89% in the centennial storm. This also means that the reduced percentage of eroded area is inversely proportional to the level of storm. It can be explained that the higher storm inducing the high storm surge leads to increase the water depth above the crest level of SBWs and allows larger waves to approach the shoreline. Nevertheless, the presence of SBWs exacerbate the erosion problem in the some places where are in the gaps between SBWs. It is clearly seen that the eroded area between SBWs increases by 12.47%-53.33% under the storms. In the case of the centennial storm, although total eroded area decreases, serious erosion takes place not only between the SBWs but also behind the SBWs in all beach profiles (see in Appendix E.2).

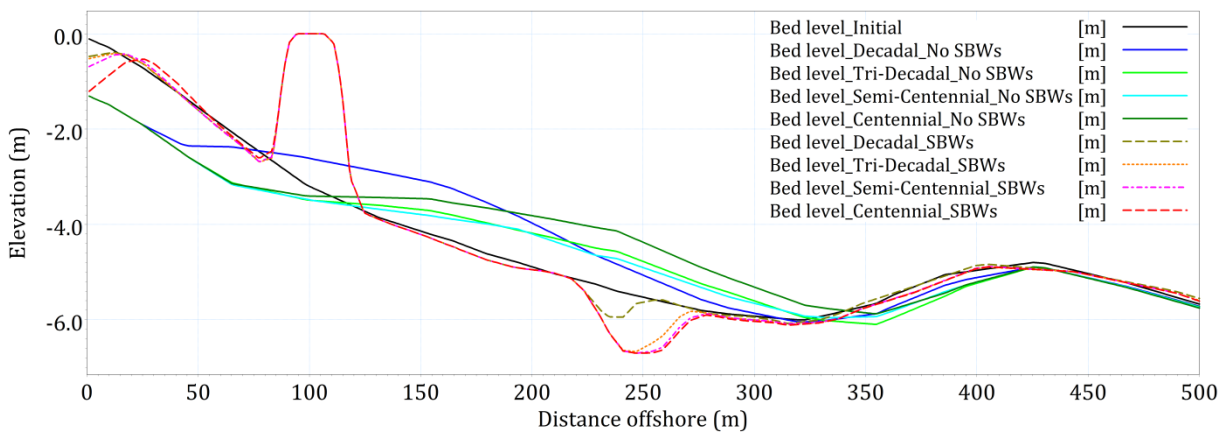


Figure 265. Cross-shore changes of beach profile 10 due to different storms.

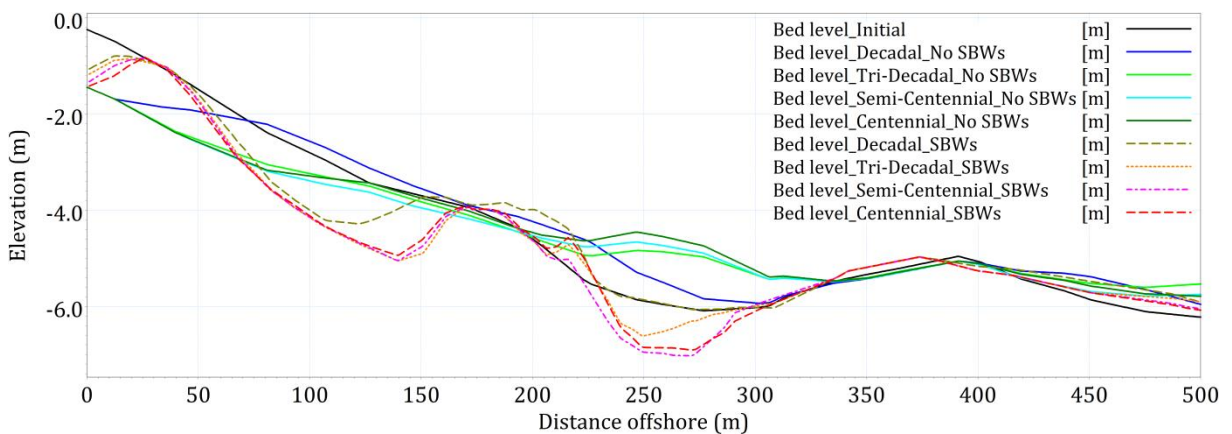


Figure 266. Cross-shore changes of beach profile 11 due to different storms.

Table 79. Erosive area of beach profiles in Bona beach with and without SBWs (m²).

Case	Profile	NE	E	SE	Winter	Summer	DS	TS	SS	CS
	F-F	-26.97	-22.54	-22.09	-42.94	-5.25	-64.42	-100.2	-101.4	-97.78
	F'-F'	-21.53	-17.47	-17.46	-36.06	-5.51	-49.57	-108.3	-124.7	-107.7
	G-G	-21.71	-24.59	-25.82	-46.20	-6.17	-61.01	-115.8	-122.8	-112.6
	G'-G'	-13.92	-6.56	-2.89	-14.84	-0.01	-32.34	-67.73	-67.59	-78.23
	H-H	-20.99	-18.46	-21.19	-30.41	-8.68	-58.15	-93.02	-94.29	-101.7
	I-I	-28.36	-20.61	-16.72	-31.56	-2.68	-52.13	-113.2	-119.6	-118.9
	I'-I'	-16.32	-12.98	-9.89	-20.63	-2.71	-48.36	-64.70	-78.74	-87.06
	J-J	-14.91	-16.27	-12.52	-27.41	-8.11	-36.31	-55.82	-69.44	-81.61
	K-K	-15.98	-13.52	-13.42	-19.25	-7.86	-43.31	-67.77	-77.66	-78.87
	L-L	-34.71	-27.15	-22.63	-46.93	-6.40	-53.84	-74.59	-89.60	-112.0
	F-F	-4.53	-4.67	-4.04	-3.55	-1.15	-2.69	-3.59	-4.75	-8.91
	F'-F'	-18.32	-12.25	-8.70	-49.99	-1.11	-73.74	-121.8	-121.7	-122.0
	G-G	-10.91	-9.81	-9.23	-10.92	-2.95	-7.89	-8.60	-10.17	-14.28
	G'-G'	-10.24	-6.95	-4.69	-29.12	-0.85	-49.59	-83.13	-88.61	-102.1
	H-H	-15.09	-8.13	-6.56	-7.55	-5.24	-5.05	-11.89	-13.65	-18.67
	I-I	-6.00	-5.46	-5.08	-6.51	-0.84	-9.91	-28.11	-32.17	-36.89
	I'-I'	-12.90	-7.74	-6.83	-24.63	-2.59	-31.55	-41.18	-44.71	-54.69
	J-J	-4.68	-2.85	-2.38	-6.06	-2.38	-9.06	-10.34	-10.60	-13.61
	K-K	-3.95	-3.31	-2.22	-2.07	-1.88	-2.44	-15.57	-24.37	-31.57
	L-L	-8.94	-8.21	-7.31	-11.86	-3.80	-12.77	-36.27	-55.42	-63.73
	F-F	83.19	79.27	81.72	91.73	78.09	95.83	96.41	95.32	90.89
	F'-F'	14.90	29.84	50.20	-38.65	79.86	-48.77	-12.47	2.41	-13.23
	G-G	49.72	60.10	64.25	76.36	52.22	87.07	92.57	91.72	87.31
	G'-G'	26.43	-5.81	-62.25	-96.19	-6241.04	-53.33	-22.74	-31.10	-30.44
	H-H	28.12	55.96	69.06	75.18	39.64	91.32	87.22	85.52	81.65
	I-I	78.84	73.51	69.62	79.38	68.74	80.99	75.17	73.10	68.97
	I'-I'	20.97	40.39	30.92	-19.42	4.48	34.76	36.35	43.21	37.18
	J-J	68.63	82.46	81.02	77.90	70.69	75.05	81.48	84.73	83.32
	K-K	75.27	75.49	83.44	89.26	76.09	94.37	77.03	68.62	59.97
	L-L	74.25	69.74	67.71	74.72	40.66	76.29	51.37	38.16	43.10

Note: DS-Decadal storm; TS-Tri-decadal storm; SS-Semi-Centennial storm; CS-Centennial storm.

6.5.5. Effects to shoreline change

6.5.5.1. Model calibration

The position of the initial shoreline (2007) and the cross-shore profiles are extracted from field surveys conducted by E.O.L (2010). A grid spacing of 10 m is considered for accurate representation of the shoreline and the location of structures. The known data for sediment properties were acquired by Courtaud (2000) and E.O.L (2010).

The shoreline evolution model for Ceinturon beach was run for eight cross section profiles, four of which located alternatively between four groynes and for in the downstream (Figure 267). Similar to Ceinturon beach, four cross-section profiles in Bona beach and four cross-section profiles in Pesquiers beach (Figure 268) were used in the numerical model. The variation of median grain diameter and other characteristic grain sizes along cross-shore profiles were assumed in accordance with available field data. For transformation of the offshore into the nearshore areas, wave parameters were extracted at water depth of approximately -9 m at different eight locations along Ceinturon beach (Figure 267) and eight positions along Bona and Pesquiers beaches (Figure 268).

In LITLINE, the active height of the profile is a main calibration parameter. In addition, the calibration can also be done by modifying the extension of the sediment transport tables (DHI, 2014a).

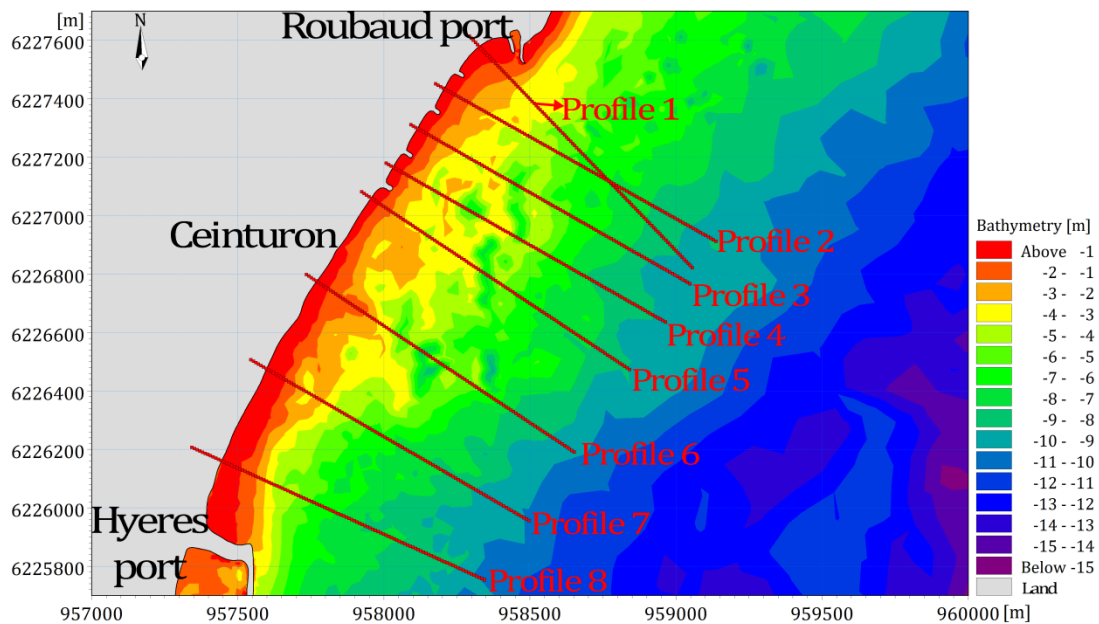


Figure 267. Bathymetry and cross section profiles along Ceinturon beach.

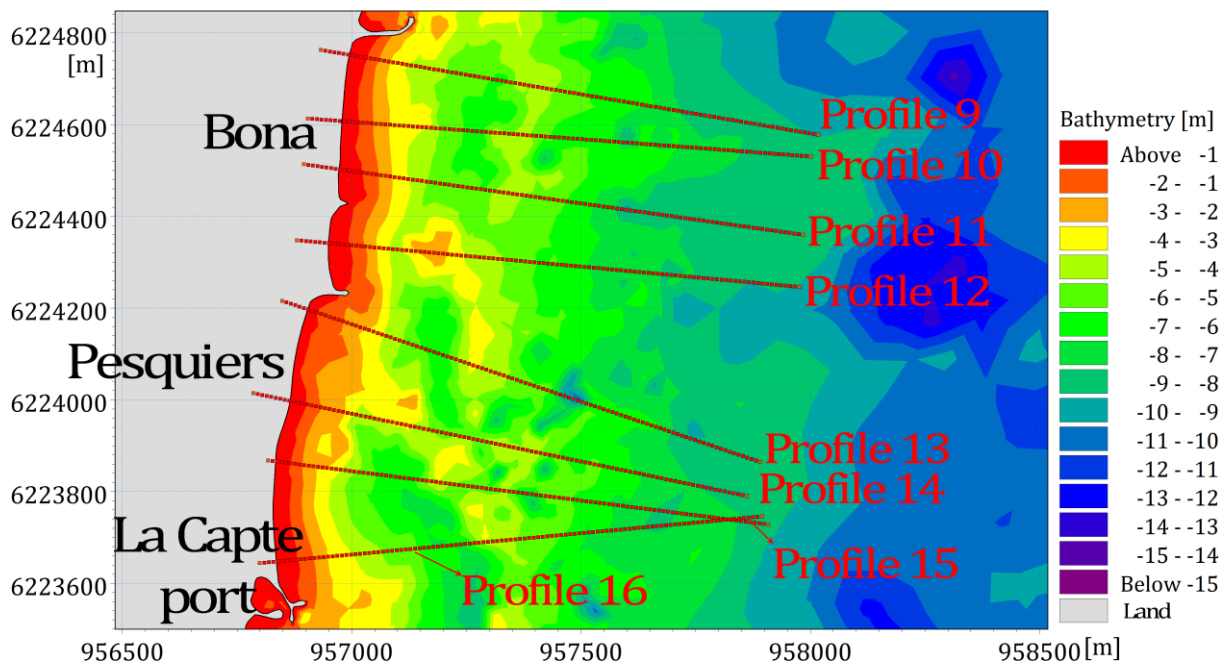


Figure 268. Bathymetry and cross section profiles along Bona beach.

The validation of the model result was done by comparing it with the actual shoreline data for the year 2008 extracted from the measurement data of E.O.L (2010). Figure 269 shows the difference between the measured and simulated shorelines of Ceinturon beach. The results agree closely with actual field data. The RMSE and the R-squared correlation coefficient (R^2) are about 1.234 m and 0.998, respectively, corresponding to SI of about 0.7% (Table 80). In addition to RMSE, R-squared and SI indexes, the prediction of shoreline evolution should be validated by the BSS. The model setup has resulted in BSS of 0.839 (Table 80), which is on excellent level according to Van-Rijn et al. (2003). On the other hand, Figure 270 presents comparison of the final predicted shoreline of Bona and Pesquiers beaches in 2008 with the measured shoreline in 2008. Although the RMSE of 2.1 m is quite larger, the BSS of 0.33 is reasonable and can be acceptable (Van-Rijn et al., 2003). Consequently, the good match between the field data and the simulated results demonstrates that the calibration parameter sets appropriately describe the shoreline evolution of Ceinturon, Bona, and Pesquiers beaches, so they can be employed to model the main study scenarios.

Table 80. Calibration of the shoreline (November 2007- November 2008).

<i>Beach</i>	<i>Case</i>	<i>R²</i>	<i>RMSE</i>	<i>SI</i>	<i>BSS</i>
Ceinturon	OBS_2008 vs. SIM_2008	0.998	1.23	0.007	0.839
Bona	OBS_2008 vs. SIM_2008	0.988	2.07	0.01	0.33

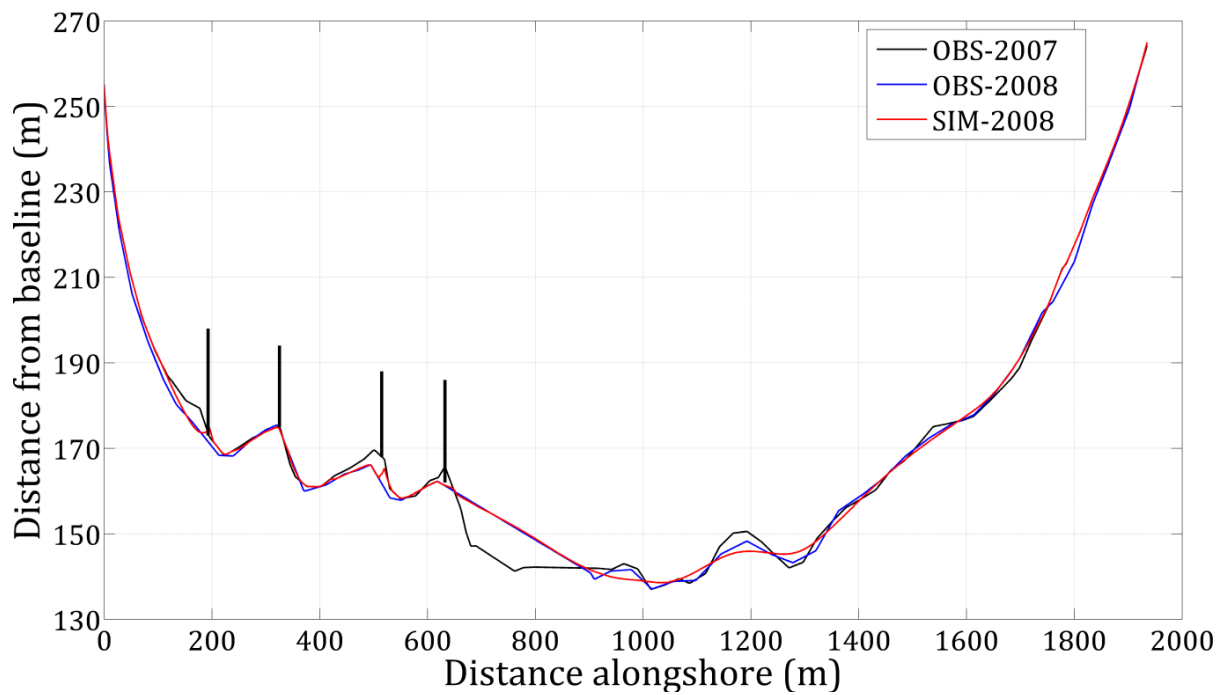


Figure 269. Comparison of OBS and SIM shorelines of Ceinturon beach for the period from November 2007 to November 2008.

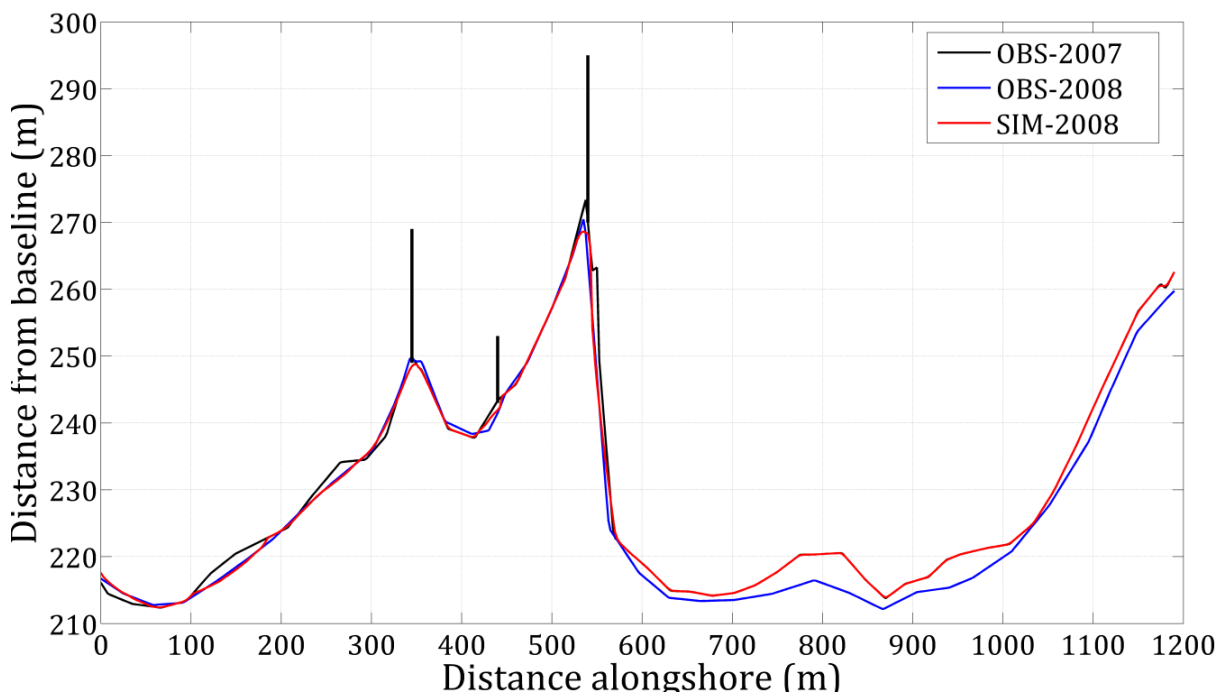


Figure 270. Comparison of OBS and SIM shorelines of Bona beach for the period from November 2007 to November 2008.

6.5.5.2. Ceinturon beach

The numerical simulations are carried out for the evolution of 2 km of shoreline between Aygaude port and Hyères port for the summer, winter, decadal storm, tri-decadal storm, semi-centennial storm and centennial storm scenarios. The initial shoreline used in the study is based on the field measurements conducted in 2007 using RTK-GPS (E.O.L, 2010). The results of shoreline change due to the wave climate events

are presented in Figure 271 to Figure 276. The x-axis is fixed parallel to the shoreline whilst the y-axis is taken perpendicular to the shoreline. Distance on x-axis refers to the southward distance measured from the origin fixed at the northernmost point on the reference baseline, and y-axis refers to the shoreline distance measured seaward from a reference baseline fixed on the landward-side. The curves represent the shoreline positions at the initial state (Black), the later state without SBWs (Red), and the later state with SBWs (Blue). Moreover, the accretion and erosion areas created by the initial shoreline and the shoreline after each wave event are summarized in Table 81.

a. Seasonal variation

Comparison of shoreline positions before and after one winter month is plotted in Figure 271. The change of shoreline positions reveals that considerable accretion is observed on the downdrift side of the first groyne and the fourth groyne with deposited areas of +110.6 m² and +186.4 m², respectively, and slight accretion is found on the downdrift side of the second groyne also. However, erosion occurs on the downdrift side of the third groyne and at the central Ceinturon beach (from Distance +800 m to Distance +1600 m in the x-axis) with retreat areas of -52 m² and -224 m², respectively. The shoreline migrated landward with a maximum of 1 m at the position of 970 m in the x-axis. In the southern part of this beach, the shoreline is quite stable. Totally, the wave climate of winter induces a lost area of -325 m² and an advance area of +486.3 m² for the entire Ceinturon beach (Table 81). The positions of the deposited and eroded areas demonstrate the northward longshore drift in the computational duration. This phenomenon would be caused by the southeast waves dominating in the winter. Hence, five SBWs are located 80 m seaward of the shoreline and below MSL about 0.4 m, from Distance +650 m to +1440 m, respectively, to limit the coastal erosion as well as stabilize the shoreline. The presence of SBWs results in the positive change of the shoreline. The salients are formed behind the SBWs, viz. from Distance +845 m to +935 m and from Distance +1180 m to 1250 m. The accretion area of these salients is estimated up to +378 m². The maximum offshore distance of salient is reported about 3.0 m from the initial shoreline, at Distance +910 m. In addition, a moderate erosion area of -155 m² is observed in the gap between segments of SBWs, especially from Distance +780 m to +845 m and from Distance +935 m to +990 m in the x-axis. The SBWs not only increase the accretion on the leeside but only contribute to decrease of the total erosion area along Ceinturon beach from -325 m² to -308 m² (about 5%) in the winter (Table 81).

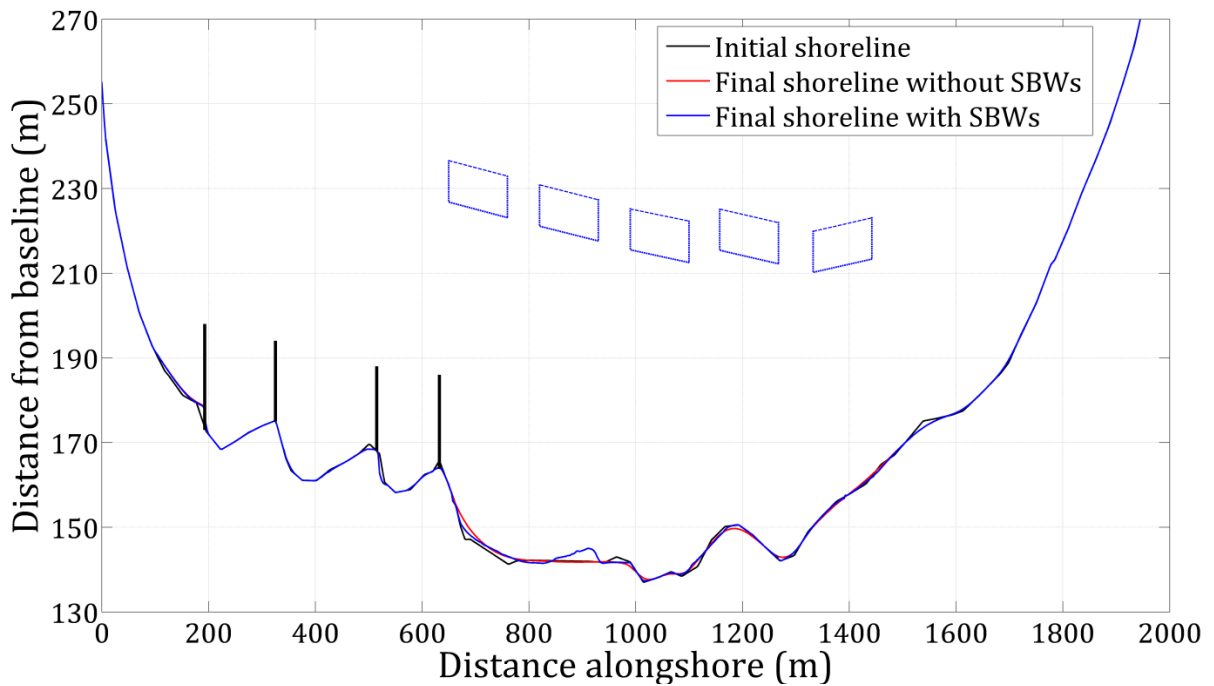


Figure 271. The Ceinturon shoreline changes before and after the construction of SBWs in the winter.

Contrary to the winter with high waves and storm surges, the wave climate in the summer is quite calm, but the erosion tendency is still dominant with the total retreat area of approximately -156 m^2 . Mostly the beach erosion is found on the updrift side of the groynes and the central Ceinturon beach, viz. from Distance $+700 \text{ m}$ to $+1000 \text{ m}$ in the x-axis (Figure 272). It is noticeable that moderate erosion occurs on the updrift side of the first groyne with a retreat area of about -69.4 m^2 . The main reason could be attributed to the deficit of sediment from Gapeau river in the dry season as well as impact of east waves which approach perpendicular to the shoreline of this zone. When the SBWs are placed in the Centre of Ceinturon beach, the evolution trend of the shoreline is changed completely. The accretion is observed in the leeside of the SBWs, viz. from Distance $+690 \text{ m}$ to $+765 \text{ m}$ and from Distance $+840 \text{ m}$ to $+940 \text{ m}$ in the x-axis. The maximum salient amplitude of 4.5 m is seen at the position of 905 m in the x-axis (Figure 272). The positive responses of the shoreline to presence of SBWs are shown by the total deposition area of $+384 \text{ m}^2$, comparing to $+125 \text{ m}^2$ without SBWs (about 208%). Although the accretion tendency dominates along the entire Ceinturon beach, the total erosion area is still increased upto 73.9%, viz. from -156 m^2 to -271 m^2 with the SBWs (Table 81). The severe erosion with the maximum retreat of 1.2 m occurs in the gap between the first and second SBWs, corresponding to the position of 765 m to 835 m in the x-axis. It maybe a result of the strong outgoing rip currents between the segments formed due to the moderate waves (Vu et al., 2017a). The moderate waves below 0.8 m with the high frequency dominating in the study area in the summer can be transmitted across the crests of the SBWs without breaking and reach the shoreline easily (Burcharth et al., 2007).

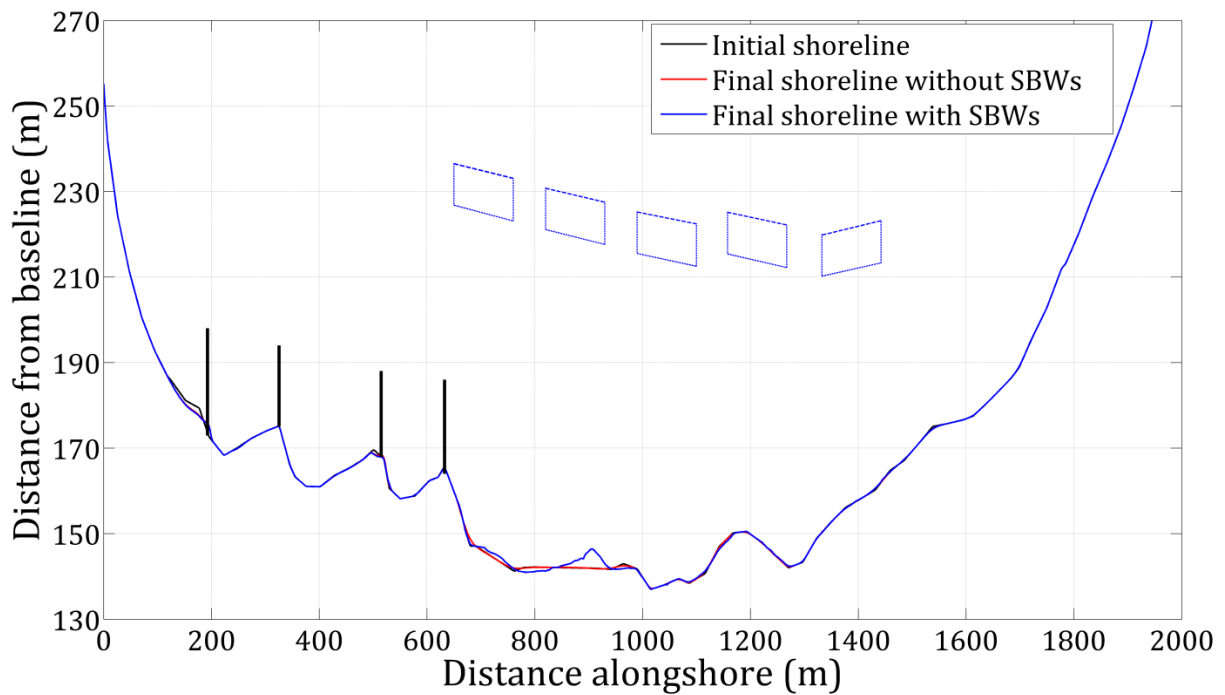


Figure 272. The Ceinturon shoreline changes before and after the construction of SBWs in the summer.

Table 81. The accretion and erosion area in Ceinturon beach for the different scenarios.

Scenario	No SBWs		SBWs		Difference	
	Accretion (m ²)	Erosion (m ²)	Accretion (m ²)	Erosion (m ²)	Accretion (%)	Erosion (%)
Winter	486.27	-324.99	535.56	-308.36	-10.14	5.12
Summer	124.90	-155.96	384.19	-271.20	-207.59	-73.90
Decadal storm	837.06	-445.07	685.35	-385.87	18.12	13.30
Tri-Decadal storm	1004.40	-525.90	915.76	-453.90	8.83	13.69
Semi-Centennial storm	1262.60	-605.09	1128.30	-534.07	10.64	11.74
Centennial storm	1344.50	-605.66	1214.10	-578.61	9.70	4.47

b. Storms

In order to examine the influence of extreme events on Ceinturon shoreline, different stormy scales, viz. decadal, tri-decadal, semi-centennial and centennial storms, are simulated in this work. The shoreline response due to storms is shown in Figure 273, Figure 274, Figure 275, and Figure 276. Furthermore, total deposition and erosion areas induced by these storms are also given in Table 81.

Under the impact of the decadal storm, the shoreline of Ceinturon beach is modified remarkably, especially in the central part and in the vicinity of groynes. Figure 273 illustrates the predicted shoreline changes of Ceinturon beach due to the decadal storm with and without the SBWs. Heavy accretion with the deposited area of +275.2 m² is observed on the updrift side of the first groyne, corresponding to Distance from +100 m to +200 m (Figure 273). The formation of this accretion area may be due to the blockage

of littoral sediment drift from Gapeau river. Slight accretion is also found on the updrift side of other groynes. In the central part of Ceinturon beach, i.e. from Distance +800 m to +1600 m, the shoreline migrated landward by about 0.2 m to 1.5 m with the decay area of approximately -231 m^2 . In addition, moderate erosion is reported at the groyne roots on the downdrift side, apart from the fourth groyne. On the downdrift side of the fourth groyne, viz. from Distance +650 m to +800 m, the shoreline is seaward with the deposition area of $+240.2 \text{ m}^2$. This accretion could be attributed to sediment eroded from the central and south part of Ceinturon beach and trapped by the fourth groyne (Vu et al., 2017a). The total accretion and erosion areas along the beach are estimated about $+837 \text{ m}^2$ and -445 m^2 (Table 81). This means that although there are some erosion areas, accretion is still predominant in the decadal storm scenario. With the effect of five SBWs, the shoreline of the central Ceinturon beach is not only kept as the initial shoreline, but also developed and much wider than that without the SBWs due to the presence of salients in the leeside of the SBWs (Figure 273). The predicted shoreline with the SBWs migrated seaward by a maximum of 2 m from the initial shoreline with the salient area of $+250 \text{ m}^2$. However, an erosion area of about -112 m^2 occurs in the gap between the segments, i.e. the position of 900 m to 930 m and the position of 1135 m to 1165 m in the x-axis. In this zone, the presence of the SBWs induces a reduction of 32% in the erosion area, viz. from -168 m^2 without the SBWs to -112 m^2 . The landward migration of predicted shoreline reached a maximum of 1.2 m at the position of 1160 m in the x-axis, comparing to the initial shoreline before the decadal storm. In general, both of the total erosive and accretive areas along Ceinturon beach are decreased down to 13.3% and 18.12%, respectively (Table 81).

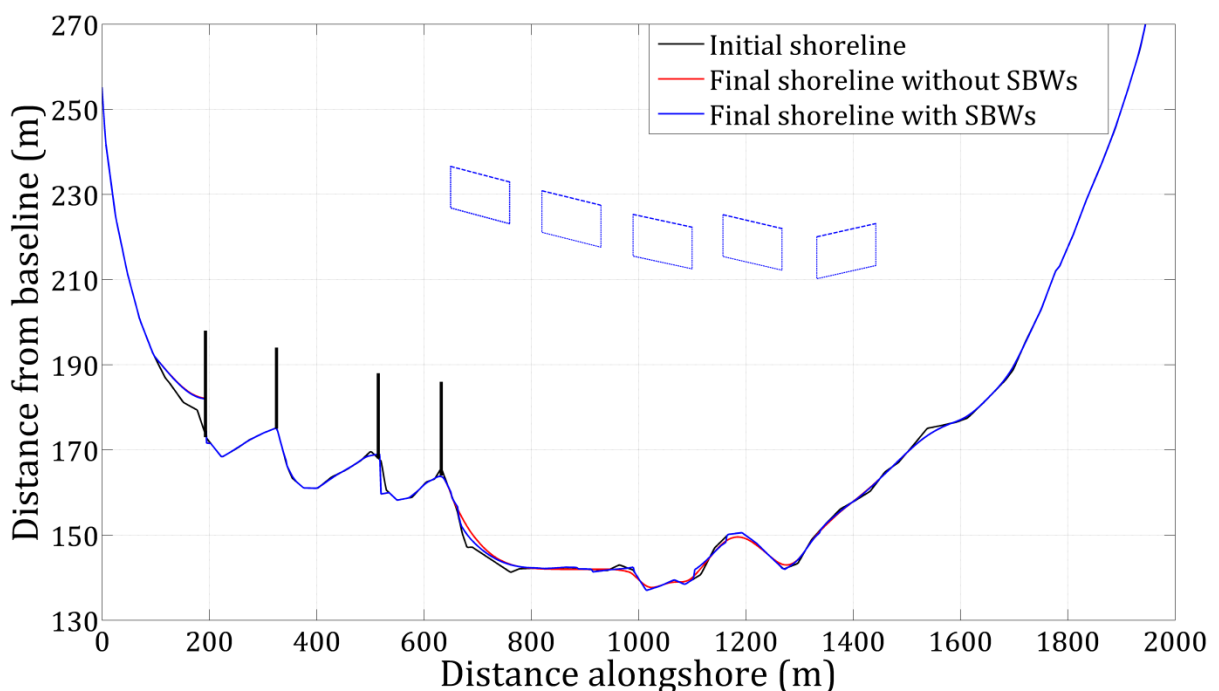


Figure 273. The Ceinturon shoreline changes before and after the construction of SBWs in the decadal storm.

Figure 274 shows the predicted shoreline changes of Ceinturon beach due to the tri-decadal storm with and without the SBWs. It is also evident that accretion and erosion are observed at the same positions as those in the decadal storm scenario without the SBWs, but the level is intensified. Heavy accretion is found on the updrift side of the first groyne and the downdrift side of the fourth groyne with the deposited areas of 360.5 m² and 307.7 m², respectively. On the other hand, erosion occurs on the downdrift sides of the first, second and third groynes. Especially, severe erosion area of about -280.6 m² is reported in the central part of Ceinturon beach, corresponding to the position of 800 m and 1600 m in the x-axis. The shoreline migrated landward by a maximum of 1.5 m at the positions of 965 m and 1190 m in the x-axis. To limit erosion, five SBWs are implemented in this area. In general, they induce the significant shoreline change by decreasing the recession area to 13.69% when compared with the case of no SBWs (Table 81). Notably, the progradation area still exists in the downdrift side of the fourth groyne, but slightly smaller than that without the SBWs. The maximum seaward advance of 3 m is seen at the position of 680 m in the x-axis. In addition, the salient is formed in the leeside of the first SBWs, viz. at the position of 830 m and 930 m in the x-axis. In detail, the erosion area in the central Ceinturon is reduced about 32% comparing to that without the SBWs. Slight erosion is observed in the gap between segments. It could be attributed to the incoming waves breaking over the SBWs, and then broken waves accumulate in shoreline and return towards offshore through the gap of the SBWs. The outflows will be manifested as concentrated in the gap and move seaward in the form of rip currents (Zyserman et al., 2002). The rip currents are seaward-directed jets that carry sediment offshore and cause erosion near shoreline.

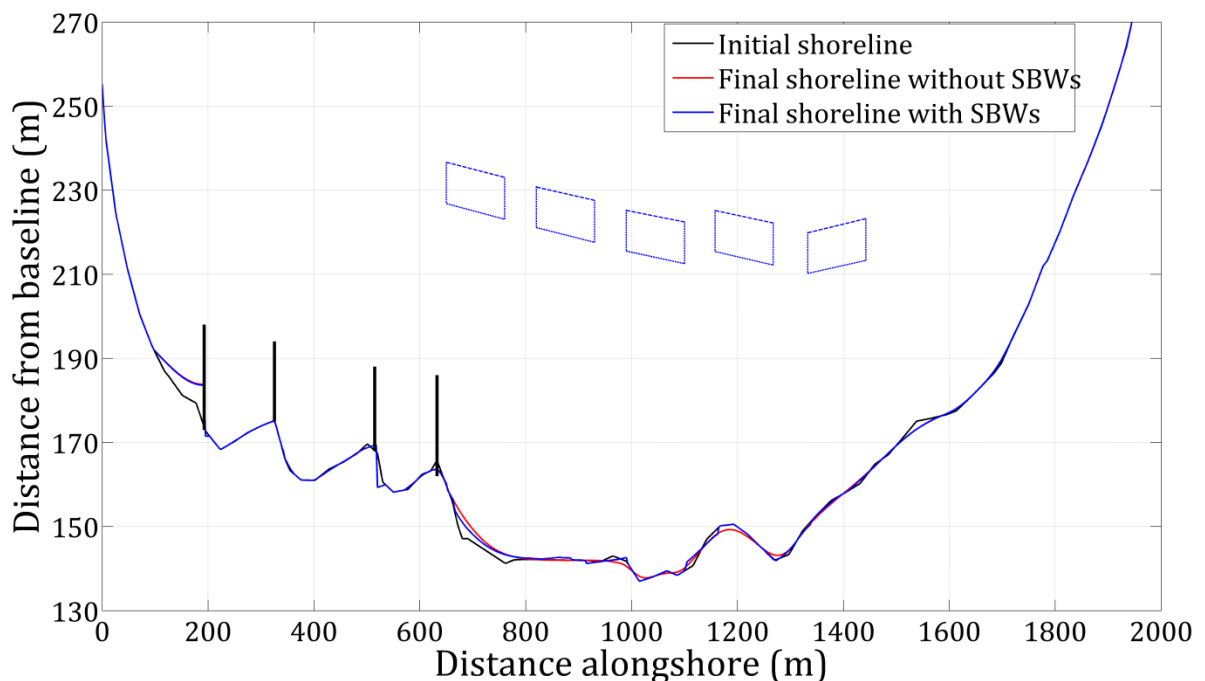


Figure 274. The Ceinturon shoreline changes before and after the construction of SBWs in the tri-decadal storm.

The higher waves cause the larger change of the shoreline. The semi-centennial storm approaches Ceinturon beach and modifies the response of the shoreline. The shoreline migrated seaward by a maximum of 12 m on the updrift side of the first groyne, corresponding to the position of 190 m in the x-axis (Figure 275). The total advance area in this zone is estimated about +459 m². In addition, considerable accretion is also observed on the downdrift side of the fourth groyne with the deposition area of +329.3 m², viz. at the positions of 660 m and 800 m in the x-axis. Moderate erosion is found on the downdrift sides of the first, second and third groynes. The main reason of this erosion could be attributed to the deficit of sediment due to two end groynes trapping the littoral sediment drift and the direct impact of high southeast waves in the semi-centennial storm. In the central region, severe erosion is noticed here and the landward migration of shoreline reached a maximum of 1.5 m. The presence of five SBWs not only stops the beach erosion and recovers the shoreline as the initial state before storm, but also prompts the formation of salient in the leeside of the first SBWs, viz. from the position of 650 m to 900 m in the x-axis (Figure 275). The maximum salient extent is about 2.5 m at the position of 750 m in the x-axis. For the entire Ceinturon beach, erosion areas still exists in both with and without the SBWs; however, the reduction amount of beach area with SBWs is much less than that without SBWs, approximately 11.74% (Table 81). In particular, in the vicinity of the central Ceinturon beach corresponding to the position of 650 m to 1450 m, the erosive area decreases from -279.4 m² to -202.1 m², approximately 28%.

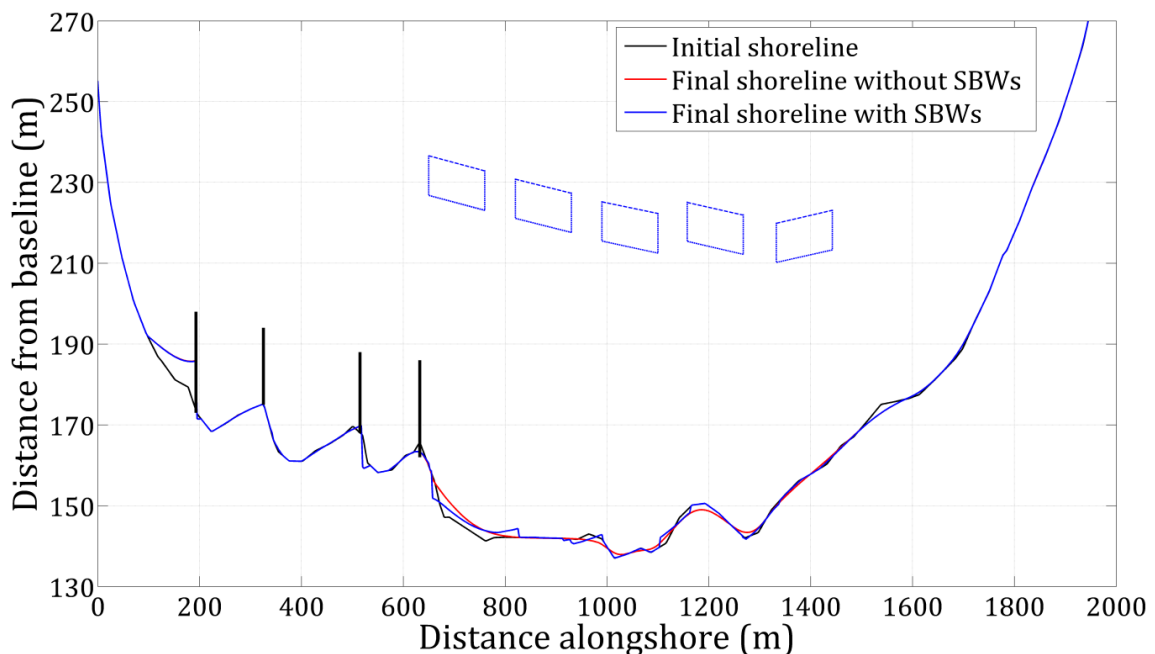


Figure 275. The Ceinturon shoreline changes before and after the construction of SBWs in the semi-centennial storm.

Under the impact of the centennial storm, the predicted shoreline change of Ceinturon beach with and without the SBWs is shown in Figure 276. Without the SBWs, the entire Ceinturon beach is eroded and accreted with the areas of -605.66 m² and

+1344.5 m², respectively (Table 81). The erosive area after the centennial storm is equivalent to that after the semi-centennial storm, but the accretion is increased by 6% comparing to the semi-centennial storm. Also similar to semi-centennial scenario, heavy accretion is still observed on the updrift side of the first groyne and the downdrift side of the fourth groyne. The total deposition area in the vicinity of the first groyne is estimated about +518 m² while the beach is widened with +351 m² in the fourth groyne. Conversely, erosion occurs on both sides of three middle groynes. This is a result of blockage of littoral sediment due to two end groynes as well as the impact of high waves. Most of the shoreline in the central part of Ceinturon beach, i.e. from the position of 800 m and 1600 m in the x-axis, is migrated landward by a maximum of 2 m at the position of 1200 m. When the SBWs are placed, the shape of the shoreline is changed completely. The accretion area on the downdrift side of the fourth groyne is receded and displaced southward, viz. from the position of 650 m and 800 m to the position of 675 m and 830 m in the x-axis (Figure 276). With the effect of the SBWs, the shoreline of the central Ceinturon beach is almost parallel to the initial shoreline before storm, especially for the position of 1165 m and 1245 m in the x-axis, it will be eroded without the SBWs, but it still remains a certain degree with the SBWs after storm. Generally speaking, the presence of SBWs reduces the erosive area along the entire Ceinturon beach to 4.5%, comparing to that without the SBWs. Furthermore, the total accretion area of this beach is also decreased by 9.7% (Table 81). These reductions are the lowest comparing to the other storms. It is a result of sharp SLR due to the centennial storm. The large crest clearance of the SBWs allows the higher waves to transmit and approach the shoreline, causing the moderate erosion than other cases.

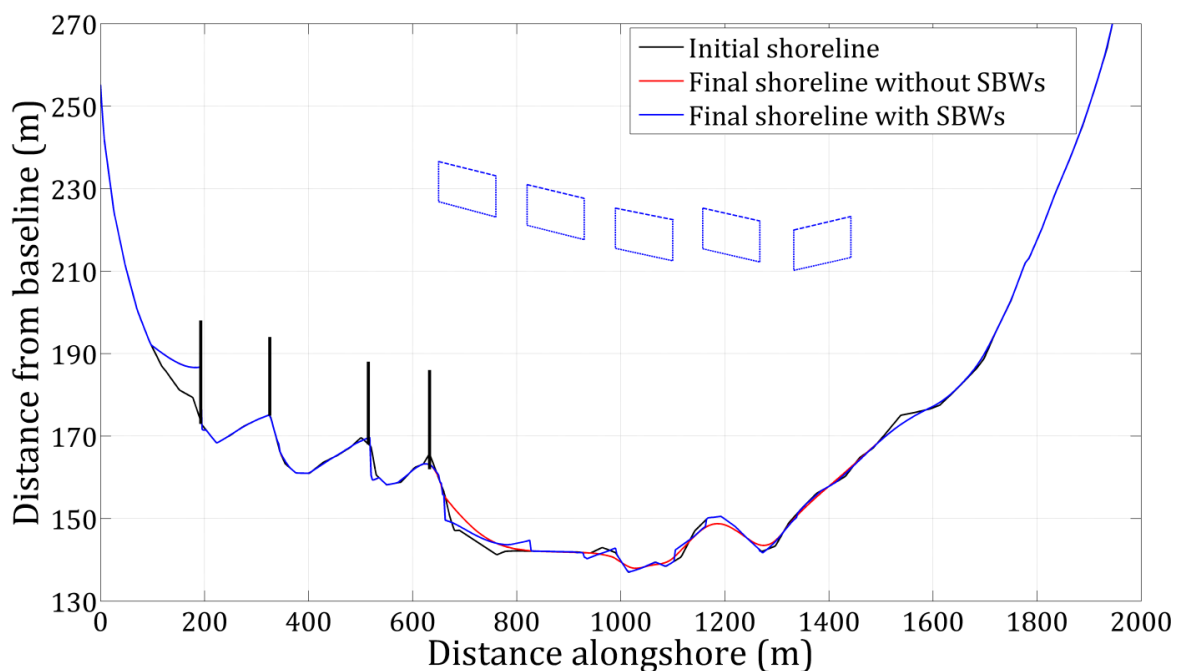


Figure 276. The Ceinturon shoreline changes before and after the construction of SBWs in the centennial storm.

6.5.5.3. Bona beach

Some previous studies (Capanni, 2011; Courtaud, 2000; Jeudy De Grissac, 1975; OCEANIDE, 2010; SOGREAH, 1988b) have been conducted on Bona beach in the southern area of Hyères port. All of them indicate that the implementation of transverse structures, i.e. jetties, breakwaters, and groynes, blocks the longshore sediment drift from east to west and from north to south, so results in accretion in the updrift vicinity of these structures and causes the sediment deficit in downstream which led to serious coastal erosion in Bona beach. Moreover, this beach is exposed directly to high southeast and east waves, which induce the rip currents transporting sediment offshore, especially in the winter with strong storms. In order to quantify the effects of wave climates as well as the influence of groynes, the numerical model of LITLINE is applied to simulate the response of Bona shoreline. The simulation results are presented in Figure 277 to Figure 282. The accretion and erosion areas for each scenario are also given in Table 82.

a. Seasonal variation

Figure 277 shows the predicted shoreline change of Bona beach with and without the SBW. If the SBWs were not installed, moderate erosion would be observed in the middle of Bona beach, corresponding to the position of 100 m and 280 m in the x-axis. The landward migration of shoreline reached a maximum retreat of 0.6 m with the total erosion area of about -56.8 m^2 . In addition, slight erosion is also observed in other places. However, slight accretion is found on the downdrift sides of the groynes. In generally, without the SBWs, the erosion trend is dominant with the total area loss of about -198 m^2 (Table 82). To reduce the retreat of the shoreline and prevent the coastal erosion, seven SBWs are implemented at the positions of 80 m seaward of the shoreline in the y-axis. The position of the erosion and accretion areas reveals that the longshore sediment drift is predominantly from south to north along the coastal area under analysis. It may be the result of the impact of the southeast waves, which is dominant in the winter with the high frequency of 21.3%. With the effect of the SBWs, the shoreline of Bona beach and Pesquiers beach is almost parallel to the initial shoreline just before the winter. Even, the salient are observed in the rear of the SBWs, viz. the position of 118 m and 132 m as well as the position of 550 m to 560 m in the x-axis. The maximum salient amplitude of 2.5 m occurs at the position of 555 m in the x-axis, right the downdrift side of the third groyne. Both of the accretion and erosion areas are decreased significantly to 11.55 m^2 and -117.7 m^2 , corresponding to 17.5% and 59.4%, respectively, comparing to those without the SBWs (Table 82). After the winter, the area losses still exist, but the reduction amount of beach area with the SBWs is much less than that without the SBWs. Hence, the SBWs play a very important role in protecting Bona and Pesquiers beaches to a certain degree.

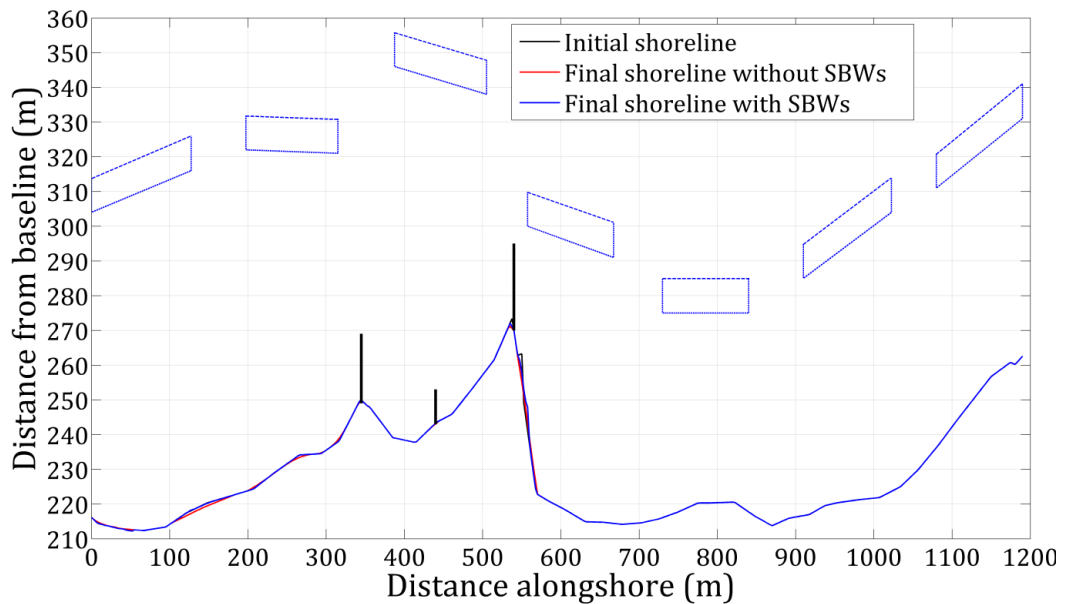


Figure 277. The Bona shoreline changes before and after the construction of SBWs in the winter.

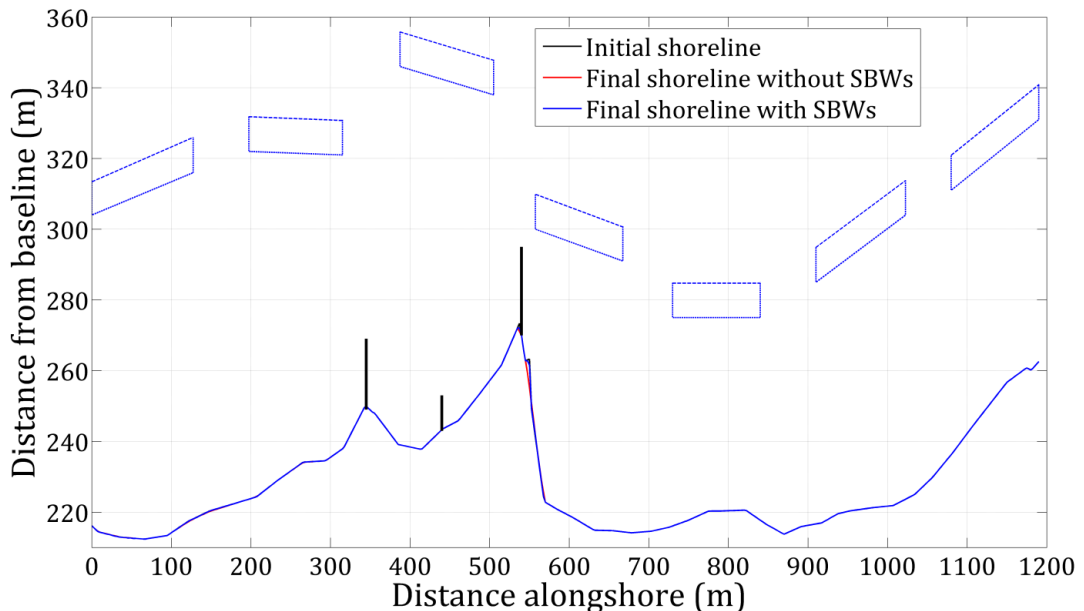


Figure 278. The Bona shoreline changes before and after the construction of SBWs in the summer.

The summer is also the dry season, so there is no sediment supplied by Gapeau and Roubaud rivers. As a result, slight accretion is observed in the downdrift side of the third groyne and the northern zone of Bona beach. Erosion is still found in the middle of Bona beach, viz. at the position of 100 m and 180 m in the x-axis. This area loss is caused by the direct impact of the moderate southeast waves which is dominant in the studied area in the summer. Without the presence of the SBWs, the total area loss is estimated approximately -134.3 m^2 (Table 82). When the SBWs are established, the shoreline is almost recovered as the initial shoreline before the summer. The small shoreline migration is landward in some places and seaward in other places. The total area loss is sharply reduced to 85.41%, corresponding to -114.7 m^2 , whereas the total advance area

is also decreased by about 73.2%, comparing to those without the SBWs (Table 82). Although, there are mostly moderate and low waves in the summer, the simulation results confirm that they are mostly broken and dissipate at the crest of the SBWs.

b. Storms

The predicted shoreline change of Bona and Pesquiers beaches with and without the SBWs due to the impact of the decadal storm is plotted in Figure 279. In the case of no SBWs, severe erosion occurs at the positions of from 100 m to 300 m and from 420 m to 450 m in the x-axis. The shoreline has migrated landward with a maximum retreat of 0.6 m at the position of 140 m in the x-axis. In addition, moderate erosion is noticed in the vicinity of the third groyne, corresponding to the position of 520 m and 555 m in the x-axis. On the other hand, considerable accretion is observed in the northern part of Bona beach and the downdrift side of the third groyne. These deposited areas coincide with the positions which are reported by Courtaud (2000), E.O.L (2010) and Capanni (2011). The presence of seven SBWs results in a minor impact on the modification of the shoreline. This is evidenced by the overlapping of the initial shoreline and the final simulated shoreline (Figure 279). Even, the small salients are formed in the leeside of the SBWs, viz. the position of 125 m and 135 m and the position of 550 m and 560 m in the x-axis. The maximum salient amplitude of 1.0 m is reported at the position of 555 m. However, the considerable change of the shoreline is only observed in the gap between the third and the fourth SBWs in the vicinity of the third groyne. This landward migration of the shoreline is caused by the rip currents which are formed by the broken waves. The effect of the SBWs reduces the erosion area from -220.5 m² down to -40 m², approximately 81.83% (Table 82). In other words, slight erosion is still found on the downdrift side of the third groyne and in the northern part of Bona beach.

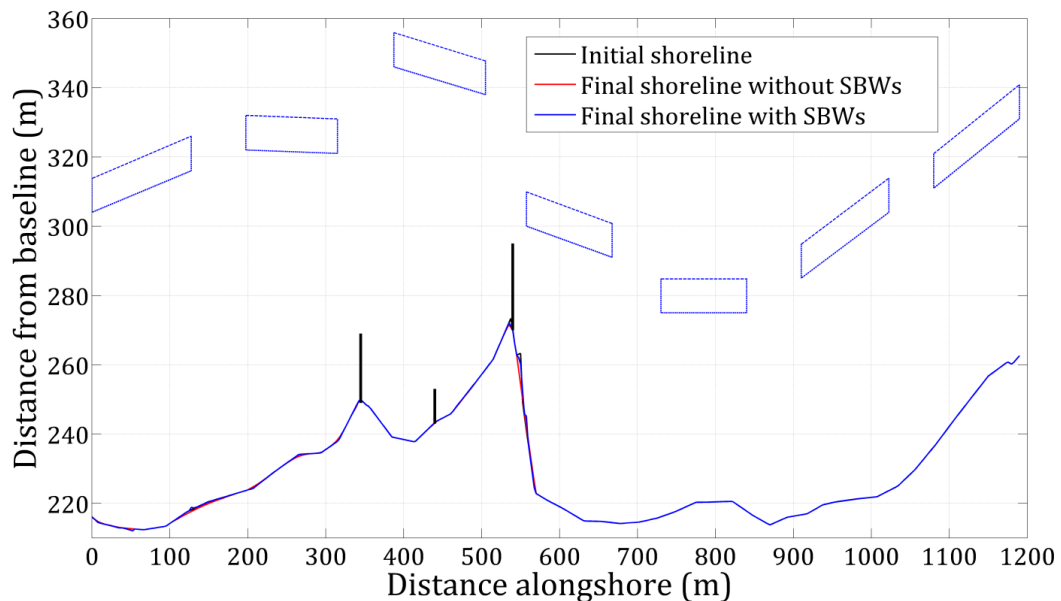


Figure 279. The Bona shoreline changes before and after the construction of SBWs in the decadal storm.

The response of the shoreline to the influence of the tri-decadal with and without the SBWs is shown in Figure 280. The result indicates that the high level of the storm causes the heavy erosion. It is proved by an increase of the erosion area of -249.21 m^2 which is larger than that in the decadal storm scenario (Table 82). The maximum loss is estimated about -77 m^2 at the position of 100 m and 300 m in the x-axis. The shoreline has been migrated landward by a maximum retreat of 1 m, corresponding to the position of 150 m in the x-axis. Slight erosion is also observed in other places. The groynes interfered with the littoral sediment drift from south to north and induced significant accretion with total area of $+71.6 \text{ m}^2$ on the downdrift side of the third groyne and in the northern Bona beach. The shoreline has been migrated seaward by a maximum advance of 1 m at the position of 565 m in the x-axis whilst the value of 0.5 m is observed at the position of 8 m in the x-axis. The effect of the SBWs is attributed to sharply decrease the area loss of about 83.83% (Table 82), from -249 m^2 without the SBWs to -40.3 m^2 with the SBWs. The position of the final predicted shoreline is almost recovered as the initial shoreline before the storm, especially the small salient occurs in the position of 100 m and 200 m in the x-axis where is suffering the severe landward migration due to the wave attacks. Slight accretion is seen on the downdrift side of the third groyne. In generally, after the tri-decadal storm, the beach areas both with and without SBW will reduce, but the reduction amount of beach area with the SBWs is much less than that without the SBWs. It demonstrates the role of the SBWs in limiting the coastal erosion and stabilizing the shoreline.

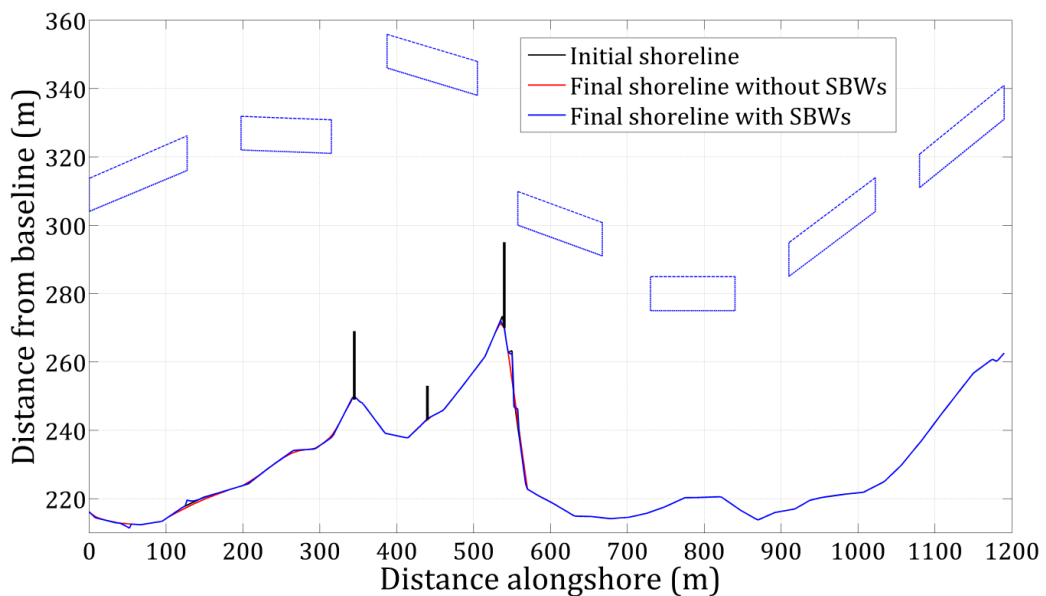


Figure 280. The Bona shoreline changes before and after the construction of SBWs in the tri-decadal storm.

Figure 281 illustrates the change of the shoreline along Bona and Pesquiers beaches in the semi-centennial storm with and without the SBWs. The high waves attacked the beach and caused severe erosion at the position of 100 m and 300 m in the x-axis. The highest territorial loss is estimated about -92 m^2 . The shoreline has been migrated

landward by a maximum retreat of 1.5 m at the location of 150 m in the x-axis. In addition, moderate erosion is also reported on the updrift sides of the second and third groynes. Totally, the area loss of about -290.71 m^2 is triggered by the semi-centennial storm without the SBWs (Table 82). There is some accretion areas of $+76.5 \text{ m}^2$ created after this storm, viz. on the downdrift side of the third groyne, the updrift side of the first groyne and at the position of 0 m to 50 m in the x-axis. With the construction of the SBWs, the area loss is reduced to 80%, in comparison without the SBWs (Table 82). The shoreline is not only stabilized but also slightly migrated seaward on the leeside of the SBWs. In addition, the remarkable salient still occurs on the downdrift side of the third groyne and the northern part of Bona beach, with the maximum amplitude of 4 m at the position of 553 m in the x-axis. It contributes to a significant increase of 18.9% in the accretion beach area, comparing to that without the SBWs. However, moderate erosion is observed till the tip of the third groyne where located in the gap between two segments, corresponding to the position of 535 m and 550 m in the x-axis.

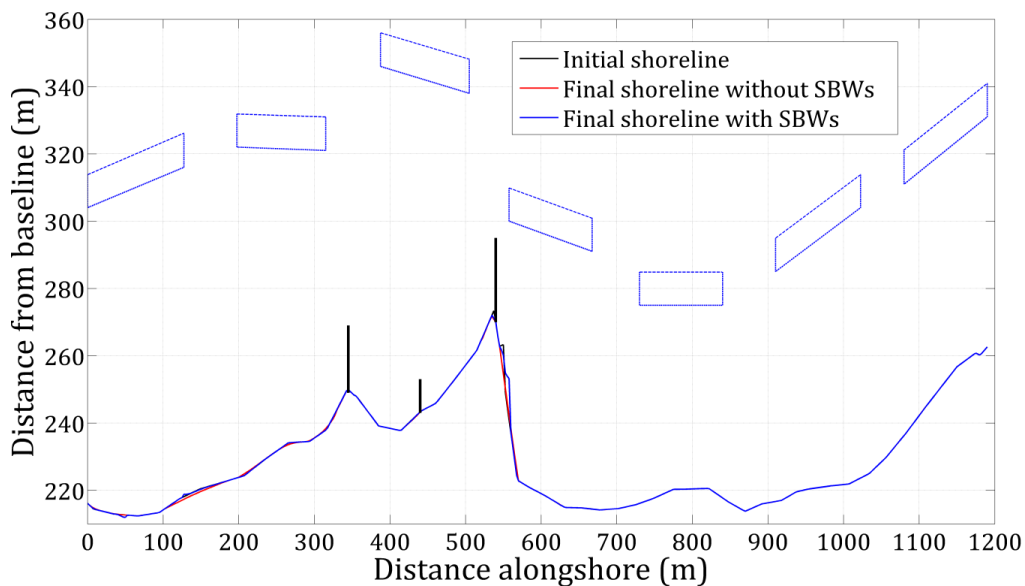


Figure 281. The Bona shoreline changes before and after the construction of SBWs in the semi-centennial storm.

Comparison of shoreline positions of Bona and Pesquiers beaches in the centennial storm scenario with and without the SBWs is presented in Figure 282. The moderate erosion predicted by the models is found in the middle of Bona beach, corresponding to the position of 100 m to 300 m in the x-axis. The maximum retreat after the centennial storm without the SBWs was recorded at the position of 150 m in the x-axis, corresponding to about 1.2 m. Moreover, slight erosion is observed on the updrift side of the second groyne, viz. at the position of 410 m and 450 m in the x-axis. This erosive area can be attributed to the blockage of littoral sediment drift due to the first groyne and the third groyne. The sediment is trapped and deposited on the updrift side of the first groyne and the downdrift side of the third groyne. Along the Bona and Pesquiers beaches, the total accretion area is about 63.3 m^2 , while the whole territorial loss is

estimated to -281.6 m^2 (Table 82). The results indicate that the decline trend is dominant without the SBWs. With the effect of the SBWs, the final predicted shoreline has changed insignificantly after the centennial storm, except the zone in the gap between the SBWs. The formation of rip currents causes erosion in this zone. The erosion area is reduced from -281.6 m^2 to -41.7 m^2 , corresponding to 85.2%. The salient is observed behind the fourth SBW, viz. the position of 552 m and 560 m in the x-axis.

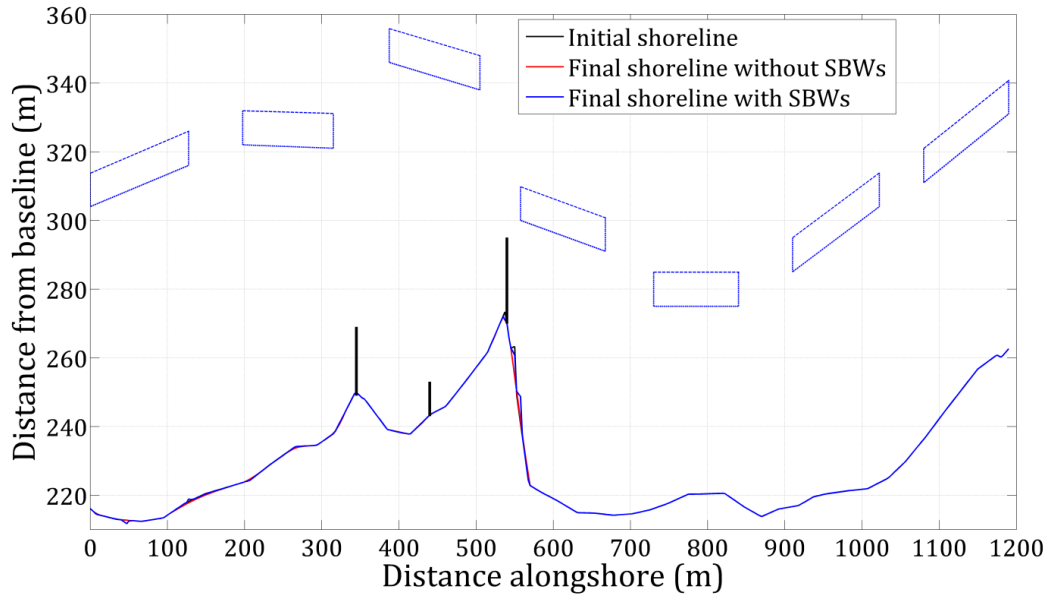


Figure 282. The Bona shoreline changes before and after the construction of SBWs in the centennial storm.

Table 82. The accretion and erosion area in Bona beach for the different scenarios.

Scenario	No SBWs		SBWs		Difference	
	Accretion (m^2)	Erosion (m^2)	Accretion (m^2)	Erosion (m^2)	Accretion (%)	Erosion (%)
Winter	66.03	-198.00	54.45	-80.31	17.54	59.44
Summer	18.30	-134.26	4.90	-19.58	73.20	85.41
Decadal storm	55.04	-220.53	35.40	-40.07	35.68	81.83
Tri-Decadal storm	71.58	-249.21	35.03	-40.29	51.07	83.83
Semi-Centennial storm	76.48	-290.71	90.90	-58.23	-18.87	79.97
Centennial storm	63.30	-281.56	41.01	-41.70	35.21	85.19

6.6. Conclusion

The SBW composed of geotube core and rubble cover layer is a popular method to protect beaches and reduce erosion of many beaches. In this chapter, a brief description of SBWs in Bona and Ceinturon beaches, Hyères Bay, is given. The effectiveness of SBWs to these beaches is investigated on current fields, wave fields, sediment transport and shoreline changes by using three modules of MIKE 21 including HD, SW and ST along with LITLINE module. Based on the discussion and analysis of numerical results, the following conclusions are drawn:

- When taking into account the presence of SBWs, the nearshore wave heights reduce suddenly and appreciably in both Bona and Ceinturon beaches under all wave conditions. This reduction in wave height is observed not only in the leeside of SBWs, but also in the gaps between them. It is mainly due to the wave reflections and wave dissipations with the SBWs. The wave energy dissipation efficiency of SBWs will reduce if the input wave condition is intensified, i.e the transmission coefficient is the lowest value in the annual wind conditions and reaches the largest value in the stormy conditions. A significant decrease of wave height results in a corresponding reduction of radiation stresses.
- The current fields in both Ceinturon and Bona become more complex with the presence of SBWs. Eddies at both heads of SBWs and rip currents towards the gap between SBWs are formed by interaction of the main current system with the SBWs. In generally, the presence of SBWs causes a decrease of mean current speed in the water area between the shoreline and SBWs, except for some places where current speed is increased due to the flow concentration of rip currents or narrowing of the wetted area between the shoreline and SBW.
- Although the SBWs generally cause a sharp decrease of total load, sediment is still transported along this beach behind the SBWs. In Ceinturon beach, the maximum reduction is observed under the northeast winds, whilst the minimum reduction is found under the southeast winds. Conservely, in Bona beach, the largest reduction occurs in the southeast winds, and the smallest reduction in the northeast winds. The presence of SBWs also curtails the difference of sediment transport rate between summer and winter in both the leeside and the gaps of SBWs. In addition, the impact of SBWs on sediment transport will decrease if the level of storm increases.
- The SBWs not only protect the sheltered area behind them but also promote to develop slight salient along the central Ceinturon beach and Bona. Although the SBWs result in the positive changes of the bathymetry, erosion still takes place in the gaps between SBWs and can be explained by the action of seaward flow concentration, viz. rip currents. Moreover, the role of SBWs in protecting the beach is greatly reduced under the impact of the semi-centennial and centennial storms.

Finally, erosion is still observed with the presence of SBWs; however, the loss amount of beach area due to erosion with SBWs is much less than that without SBWs. Accordingly, the SBWs play a very important in protecting Bona and Ceinturon beaches to a certain degree, but they are not enough. Other engineering measures, e.g. beach nourishment, may be considered to apply regularly for the gaps between SBWs in order to maintain the entire beach in the long term.

CHAPTER 7. CONCLUSIONS AND FUTURE WORK

7.1. Conclusions

In this work, numerical models have been developed successfully to simulate the hydrodynamic characteristics and sediment transport in the eastern Giens tombolo with and without SBWs. The different characteristics of seabed, viz. Posidonia, rock, sand, pebble, were modeled using the proper Manning's number and Nikuradse roughness height. The models were calibrated and verified with the wave and current data, which were measured at Almanarre beach in 2000 and at La Capte beach in 2009. The bed level change along Ceinturon and Bona beaches was also validated by comparing the simulation results with the field data, which was conducted in a survey of 2008 by E.O.L. All calibrations and comparisons show good agreement between the observed and computed results. The validated model was used to evaluate the effect of different wave scenarios as well as the presence of SBWs on the hydrodynamic characteristics and sediment transport in Hyères bay. Based on the findings during the study, a number of conclusions can be drawn as follows:

- All observed beach profiles along the eastern Giens tombolo can be described by a single function, but each EBP approximation can be only suitable for simulating the evolution of one specific beach profile. The logarithmic functions of Sierra et al. (1994) and Lee (1994) can be suitable for predicting the beach evolution with the upward concave shape of beach profile, while the exponential function of Bodge (1992) is the best choice for complex beach profile shapes. When the beach profile becomes more downward concave, Bodge (1992)'s function also prefers representing the beach profile to others. For the beach, which has the steep slope near the shoreline and the gentle offshore, Vellinga (1987)'s EBP is the most rational option. On the contrary, the exponential function of Komar et al. (1994) appropriates for the gentle beach. The equilibrium beach profiles are governed by three main factors of wave climate, sediment size and beach profile shape. Nonetheless, the role of these three factors is quite different in each profile. It depends on the position of the beach as well as the obstacles around the beach such as groynes, ports, etc. The EBPs could be applied for estimating the sand volume of beach nourishment.
- The shoreline along the eastern Giens tombolo from 1973 to 2015 underwent alternating trends of erosion and accretion. Both natural processes and anthropogenic interventions modify the configuration of shoreline and control the erosion and accretion of the coastal zones. The protection structures such as revetments or groynes, which were implemented in some areas, solely result in localized beach accretion; even they cause severe erosion at several downstream places. Moreover, the jetties constructed in the river mouths and ports, e.g. Gapeau,

Roubaud, and La Capte, have interfered in longshore sediment transport and accumulated the sediment around their upstream areas. This is the main reason provoking the shortage of sediment downstream. On the other hand, the estimation of shoreline changes during period from 2015 to 2050 also reveals that Cabanes beach, Pesquiers beach, Ceinturon beach and La Capte beach are the most vulnerable areas to the severe erosion. Especially, the road of DR 42 running parallel to Ceinturon beach may be disappeared in 2050 due to coastal erosion.

- Among three main winds, the northeastern winds has the strongest impact on the wave, current fields and sediment transport along the eastern tombolo, except the area around Bona beach. At Bona beach, the eastern and southeastern winds cause the stronger longshore currents than the northeastern winds and can be attributed to the presence of breakwaters of Hyères port. The northeast winds also trigger the most serious erosion in the south of Gapeau river, the central Ceinturon, Bona beaches. When taking into account the seasonal variation, the winter influences on the coastal morphology in the coast of the eastern Giens tombolo more than the summer. The current speed and wave height along the eastern part in winter is about 50% larger than that in summer. As a result, sea bottom is quite stable in the summer; even almost bed level is rised, whereas the erosion is observed along the eastern Giens tombolo in which Bona beach underwent the strongest erosion. For stormy scenarios, the higher level of storm causes the larger and stronger impacts on wave and current fields as well as sediment transport. When the storm level increases, the current speed has a decrease trend and can be explained by the expansion of seawater volume due to storm surge. In all scenarios, the main longshore current generally directs from north to south.
- The disappearance of Posidonia in Hyères bay may cause a considerable increase of current speed, significant wave height and sediment transport rate. In annual wind conditions, the northeast winds generate the highest waves and the current speed in Ceinturon beach, but the southeast winds drive the highest current speed and also play the most important role in promoting the sediment transport along Bona beach when Posidonia recedes entirely. The regression of Posidonia has a significant impact on the increase of hydrodynamic parameters and sediment transport in the winter when compared with that in the summer. Eventually, the absence of Posidonia mostly boosts the current speed and the sedimentation rate in the normal sea conditions regarding the change of wind direction and seasonal variation, while predominantly inducing the outstanding raise of the significant wave height in the extreme events.
- SLR may leads to increase the wave height, but decrease the current speed and sediment transport rate in the surf zone. When sea level rises, an increase of the wave heights in the stormy conditions is much larger than those in the annual

conditions. The northeast winds have the strongest impact on wave fields in both the Bona and Ceinturon beaches. In the stormy conditions, the nearshore significant wave height can be intensified, whereas the decrease of current speed is observed if sea level rises. The reduction in the current speed mainly leads to a corresponding decay of sediment transport rate, regardless of wave conditions. Although the total load and the mean current speed reduce when sea level raises, the rate of beach erosion is higher than that without SLR. This would be explained by the fact that deeper water areas due rising sea levels allow larger waves to reach and break closer to the shoreline, resulting in more wave energy to act further up the beach profile and take sediment offshore.

- Beach nourishment conducted in the Ceintral Ceinturon beach induces a decrease of wave height, current speed, and sediment transport rate in both the ordinary and strong wave conditions. The significant decrease of sediment transport rate is mainly attributed to the deceleration of the longshore currents due to beach nourishment. Although the wave height, current speed and total load reduce when beach nourishment is carried out in the central Ceinturon beach, erosion still occurs in all study scenarios. The most severe erosion is caused by the northeast winds, the winter climate and the storms. Sand loss from beach would be largely due to the cross-shore sediment transport. In summary, beach nourishment plays a certain role in reduction of wave height, current speed and total load of sediment transport, but it could not an effective and long-term solution for protecting the central Ceinturon beach from coastal erosion.
- If SBWs are placed in Bona and Ceinturon beaches, the nearshore wave heights, current speed and sediment transport reduce suddenly and appreciably under all wave conditions. This reduction is observed not only in the leeside of SBWs, but also in the gaps between them. Eddies at both heads of SBWs and rip currents towards the gap between SBWs are formed by interaction of the main current system with the SBWs. Sediment transport is still observed along this beach behind the SBWs. Erosion still takes place in gaps between SBWs; but the total loss amount of beach area due to erosion with SBWs is much less than that without SBWs. Under the highest storms, SBWs are believed to be less efficient at reducing wave energy, but they remain effective at reducing current speed and sediment transport locally. The presence of SBWs also counteracts the retreat of the shoreline and contributes to the stabilization of beaches. Accordingly, the SBWs play a very important in protecting Bona and Ceinturon beaches to a certain degree, but they are not enough. Other engineering measures, e.g. beach nourishment, may be considered to apply regularly for the gaps between SBWs in order to maintain the entire beach in the long term.

7.2. Future work

The novel research discussed and presented in this thesis has given rise to a number of potential future studies that can be recommended in order to improve the numerical modelling approach. These developments will support to validate as well as enhance the reliability of the model. Hence, coastal designers and managers can easily apply for protecting the Giens tombolo.

- Although the 2D numerical simulations is carried out for hydrodynamics and sediment transport and one line model is used to investigate the shoreline evolution, the 3D models should be considered to perform in future. With the 3D models, the effects of both SBWs and beach nourishment can be detected simultaneously. In addition, interaction of the bed level changes along with the shoreline evolution will be illustrated more details. From there, a complete view of beach evolution can be uncovered and supports coastal managers to decide the selection of beach protection measure.
- The local and general stability of SBW should be proposed to further studies. Despite the minimum weight of armour units of cover layer is estimated to withstand wave and current-driven forces and the toe scour aprons are designed for SBWs, settlement, sliding and overturning stability should be carried out. They need be checked around the roundheads of SBWs where current speed is intensified by flow concentration due to rip currents. These rip currents also cause erosion in the gaps between SBWs, and then instability can occur, especially in the winter and stormy wave climate. In addition, the impact of SLR on the wave attenuation efficiency of SBWs should be investigated by using numerical simulation.
- The analysis of morphological evolution of the eastern Giens tombolo is constrained by the limited available of field observations including wave data, tidal currents and water levels. Although the fact that modeling tools can transfer and interpolate data nonlinearly from surrounding sites to the study area, the accuracy of the transformation is still debated. Of course, the data shortage and discontinuity limits to some degree the model results and the analysis. Therefore, field observations regarding current, water level and wave should be carried out around Bona and Ceinturon beach.
- A combination of SBWs and beach nourishment is recommended for protecting Ceinturn and Bona beaches based on the theoretical analysis and numerical results. However, it is necessary to implement the physical model testing for further investigation.

APPENDICES

Appendix A - Data sources of bathymetry

A.1. EMODnet database

EMODnet bathymetry is provided by European Marine Observation and Data Network. It has a resolution of $1/8 * 1/8$ arc minutes. This data cover most of the European sea: the Greater North Sea, the English Channel and Celtic Seas, Western Mediterranean, the Ionian Sea and the Central Mediterranean Sea, Iberian Coast and Bay of Biscay, Adriatic Sea, Aegean-Levantine Sea, Madeira and Azores, Baltic Sea, Black Sea, Norwegian and Icelandic Seas, and Canary Islands. Moreover, EMODnet bathymetry uses the horizontal coordinate reference system of WGS84 and the vertical reference level of LAT.

This database is available to download on the website of EMODnet by clicking the Download products option and choosing the area. In this study, the area of C3 is downloaded. It includes the Adriatic Sea and the Central Mediterranean Sea. The EMODnet file is in the form of xyz. Afterwards, it has undergone the transformation associated with the projection in Lambert 93 through MIKE Datum Converter.

A.2. Litto3D database

Litto3D is a cooperative project between IGN and SHOM. The objective of this project is to produce a continuous reference digital elevation model of land-sea in France metropolitan and overseas territories by means of Lidar technology. The coastal strip is concerned:

- In sea, until the depth contour of 10 m and at most up to 6 miles offshore.
- On land, up to an altitude 10 m and at least 2 km inland.

Totally, the influence of the project represents about 45,000 km².

The Litto3D bathymetry is downloaded on the website of SHOM by clicking the Coastal altimetry option and choosing Litto3D-PACA 2015. After completing the download, the file of bathymetry is in the form of xyz. Furthermore, Litto3D bathymetry uses the horizontal coordinate reference system of RGF93 with the projection in Lambert 93 and the vertical reference level of MSL. In this study, the reference level of LAT is applied to all levels. Therefore, to ensure the unification of level, the data will be converted from the reference level of MSL to the vertical reference level of LAT by adding the datum shift of 0.253 m to each value of elevation (Figure A-1).

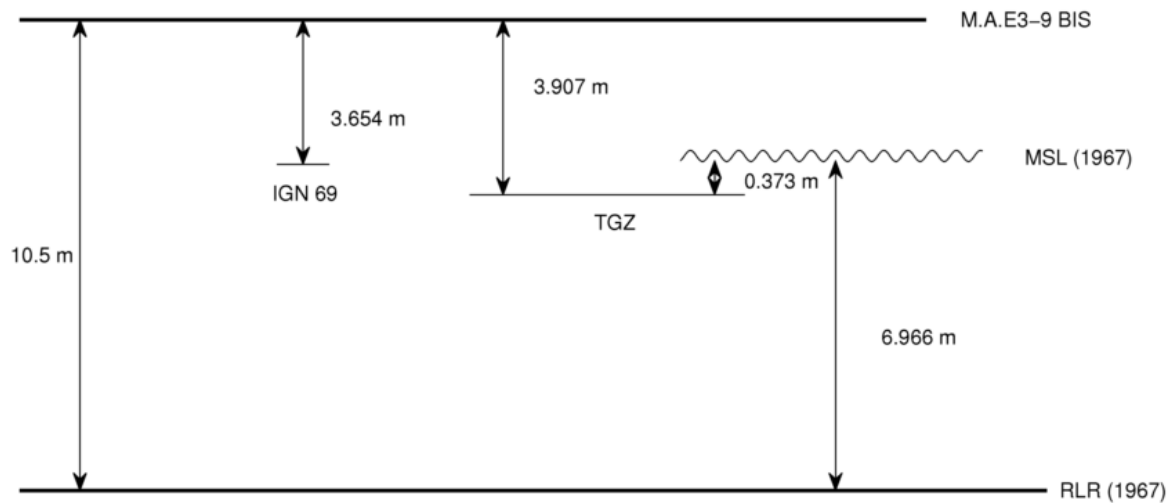


Figure A-1. Revised local reference diagram for Toulon.

(Source: Permanent service for Mean sea level)

A.3. EOL database

The available bathymetry data in formats of PDF, DBF and DWG is provided by E.O.L Association and the city of Hyères. Subsequently, these formats are converted to the form of xyz. The bathymetry data was come from the campaign of measurement carried out from 2000 to 2010 along two branches of Giens tombolo by means of D-GPS technology. The measured area extends from the shoreline to about 500 m offshore. EOL bathymetry uses the horizontal coordinate reference system of NTF with the projection in Lambert III (France Sud) and the vertical reference level of LAT. Once again, MIKE Datum Converter is used to transform from Lambert III projection into Lambert 93 projection.

Appendix B - Data treatment of water level

B.1. Observation data

The measured water level data of Port Ferreol and Toulon stations is downloaded in the text format. It is necessary to convert from the text format to the dfs0 format that can be used in MIKE model. To simulate the study area in long duration, the interpolation of water level data in Port Ferreol based on the data of Toulon should be carried out by means of MatLab curve fitting toolbox. This toolbox uses the nonlinear least squares formulation to fit a nonlinear model to the measured sea level data (MathWorks, 2015). Before interpolation, the relationship between water levels in Port Ferreol and that in Toulon in the period from 2012 to 2015 must be determined. The linear regression in the form $y=a*x+b$ is hired, where y corresponds to sea levels in Port Ferreol and x corresponds to sea levels in Toulon. In addition, the confidence level of 95%, the R-square, and the RMSE utilized to assess the accuracy and suitability of the function with the measured data. The result is shown in Figure B-1. The goodness of fit statistics has R-square of 0.8755 and RMSE of 0.0388. Consequently, this function can be used to determine the sea level data in Port Ferreol before 2012.

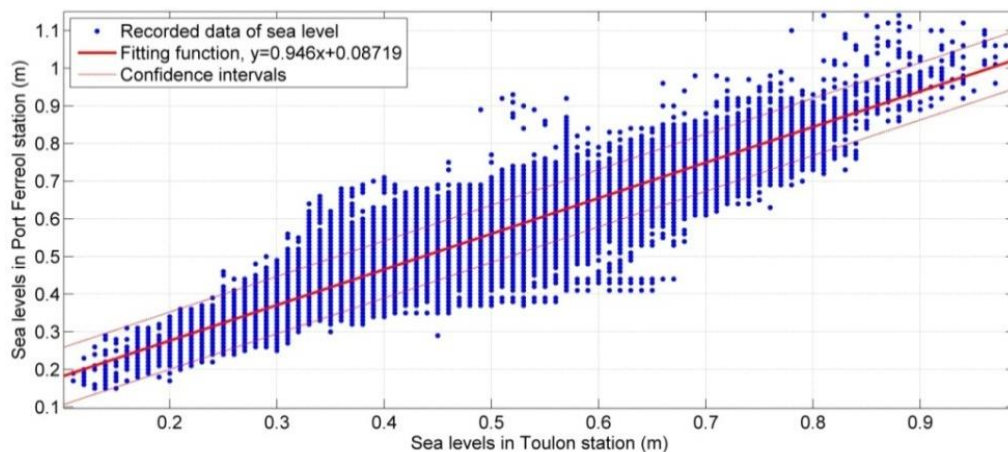


Figure B-1. Relationship between measured sea levels in Toulon and those in Port Ferreol.

B.2. Simulation data

The relationship between sea levels in Toulon and Port Ferreol and those in Medit points (Figure C-2) from the PREVIMER model in the period from 2010 to 2015 will be uncovered and shown in Figure B-2 and Figure B-3. The objective of determining these relationships is to support the interpolation the sea levels in Medit points and Buoy 08301 from the measured sea level data in Toulon and Port Ferreol in the next step. Once again, MatLab curve fitting toolbox is employed to detect the related functions through the linear regression in the form $y=a*x+b$. The coefficients with the confidence level of 95% and the statistical parameters such as R-square and RMSE are exhibited in Table B-1 and Table B-2. The goodness of fit statistics has R-square > 0.8755 and RMSE < 0.0388 . Correspondingly, the sea level conditions in the boundary points can be specified by means of these above-related functions.

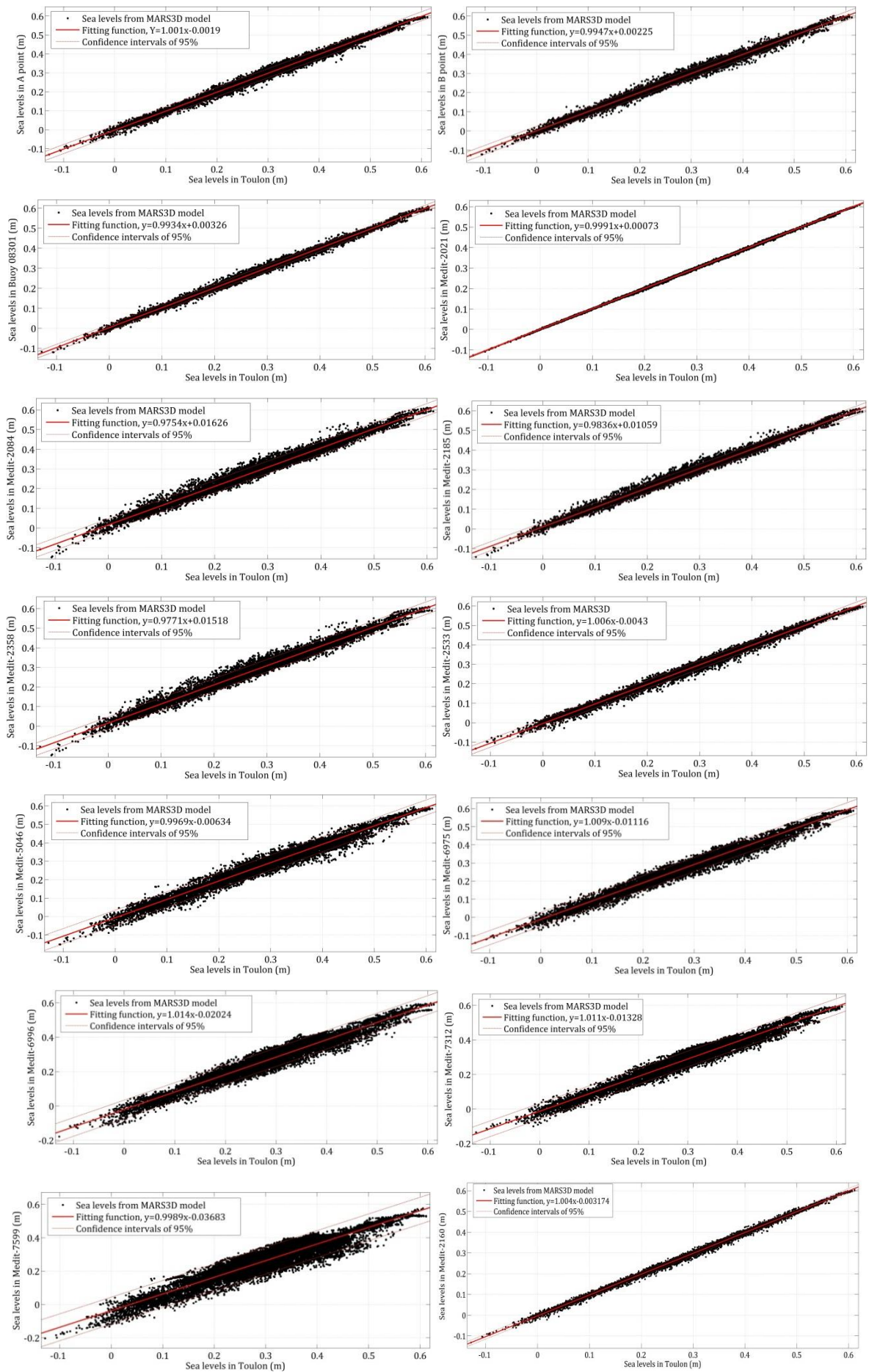


Figure B-2. Relationship between sea levels in Medit points and those in Toulon.

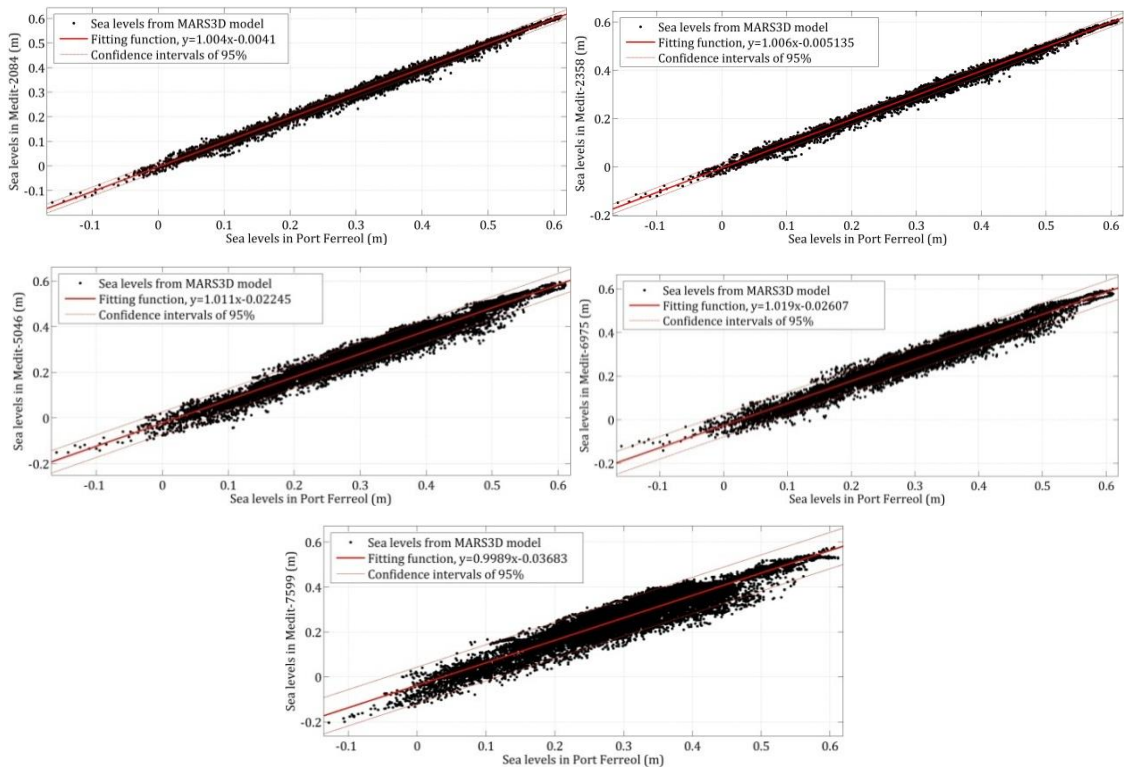


Figure B-3. Relationship between sea levels in Medit points and those in Port Ferreol.

Table B-1. Interpolation between sea levels in the boundary points and those in Toulon.

Station	Parameters		SSE	R-square	RMSE
	a	b			
Buoy 08301	0.9934	0.003257	1.128	0.9945	0.00815
Medit-2021	0.9991	0.000728	0.07073	0.9997	0.00204
Medit-2084	0.9754	0.01626	4.256	0.9788	0.01582
Medit-2185	0.9836	0.01059	2.279	0.9887	0.01158
Medit-2358	0.9771	0.01518	4.449	0.9779	0.01618
Medit-2533	1.006	-0.004302	1.911	0.9909	0.0106
Medit-5046	0.9969	-0.006339	7.47	0.9648	0.02096
Medit-6975	1.009	-0.01116	6.758	0.9688	0.01994
Medit-6996	1.014	-0.02024	12.98	0.9423	0.02763
Medit-7312	1.011	-0.01328	9.121	0.9585	0.02316
Medit-7599	0.9989	-0.0683	28.82	0.8771	0.04118

Table B-2. Interpolation between sea levels in the boundary points and those in Port Ferreol.

Station	Parameters		SSE	R-square	RMSE
	a	b			
Medit-2084	1.004	-0.004088	1.464	0.9927	0.009279
Medit-2358	1.006	-0.005135	1.739	0.9914	0.01011
Medit-5046	1.011	-0.02245	10.7	0.9496	0.02509
Medit-6975	1.019	-0.02607	11.9	0.9451	0.02646
Medit-7599	0.9989	-0.03683	28.82	0.8771	0.04118

Appendix C - Data sources of wave

C.1. Data collection

C.1.1. CANDHIS buoys

CANDHIS refers to both the coastal national network of in-situ measurement of wave and the website and the database archiving measures. They have been managed by CETMEF since 1972. CETMEF records the sea state parameters by using the directional and omnidirectional buoys. The information available on this website is the daily and hourly real-time data, the monthly graphs of wave heights, and statistical data (histograms and correlograms).

In the study area, the off-shore wave data is measured and recorded by the buoys 08301 and 08302 located approximately 1.8 km south of Porquerolles island (42°58,00'N and 6°12,29'E), at 90 m depth (Figure 12). The wave data of these two buoys was measured from May 1992 to May 2015 in which the wave data of Buoy 08301 is available from 14th May 1992 to 20th June 2012 and that of Buoy 08302 is available from 9th December 2013 to 11th May 2015. Afterward, this data is processed statistically by CETMEF.

C.1.2. Measurements in Almanarre in 2000

A wave recorder of OPHIURE III was installed on 29th October 2000 by Oceanoservice company. Its location is at the depth of 4 meters and about 100 m from the landmark of B09 (Figure 12). The wave data of this station is available from 30th October to 28th November 2000.

C.1.3. Measurements in La Capte in 2009

Near-shore wave data in La Capte beach was measured by Samuel Meulé with five submerged monitoring devices. These devices named from SCAPT1 to SCAPT5 were installed perpendicular to the coast on one line in order to understand the lateral dynamics (Figure C-1). The measurement was carried out from 12th March to 28th April 2009.

Five stations had the different measurement periods and were situated the different depths. Therefore, SCAPT2 station located at the depth of 3 meters, SCAPT3 located at the depth of 1.8 meters, and SCAPT5 (5-1 and 5-2) located in 1.6 meters deep all recorded wave data for the period from 12 to 17 March 2009. Nevertheless, both SCAPT1 station located at the depth of 7.5 meters and SCAPT4 station located at less than 1 meter deep monitored from 13 March to 22 April 2009 (Meulé, 2010).

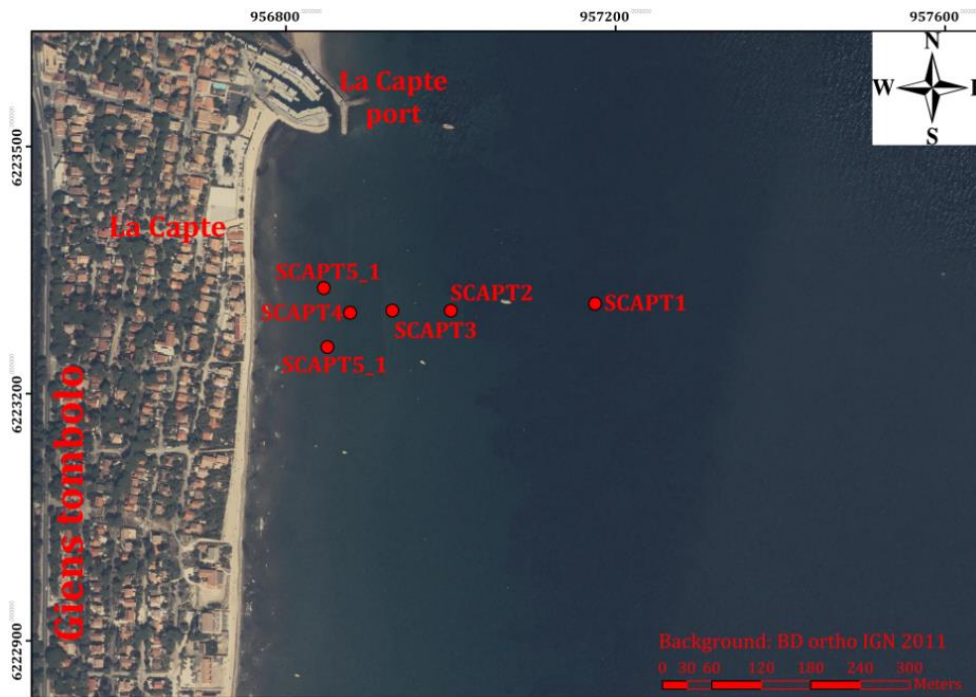


Figure C-1. Location of wave measuring stations in La Capte beach.

C.1.4. ANEMOC model

ANEMOC is one collaboration between CETMEF and EDF. The aim of this project is to establish a website and a database associated to broadcast the conditions of sea states obtained along the French coast. This database was built by using the wind reanalysis data from ERA-40 meteorological project of ECMWF. It is available for a period of 23 years and 8 months, from 01 January 1979 to 31 August 2002 for the surface of Atlantic, Manche channel, North Sea and 30 years from 01 January 1979 to 31 December 2008 for the Mediterranean surface.

The simulations were performed with the sea state modeling software of TOMAWAC, developed by EDF-LNHE with the support of CETMEF. TOMAWAC is a model called the third generation that solves the evolution in space and time of the spectro-angular density of wave action equation. A number of statistical analyses was performed by CETMEF and are available online on the website of Anemoc (<http://anemoc.cetmef.developpement-durable.gouv.fr/>). This includes the average climatology (histograms and correlograms on significant heights, periods and directions) and calculations of return periods associated with extreme events.

Regarding geographic distribution, time series of ANEMOC database have been reconstructed over 500 points in the North Sea, Manche Channel and Atlantic Ocean and 250 points in Mediterranean Sea. In this study, the offshore wave data of 11 ANEMOC points supported by CEREMA is utilized to simulate some cases, as show in Figure C-2. This data contains main parameters such as spectral significant wave height, average period, mean wave direction, directional standard deviation, energy average period and peak wave period.

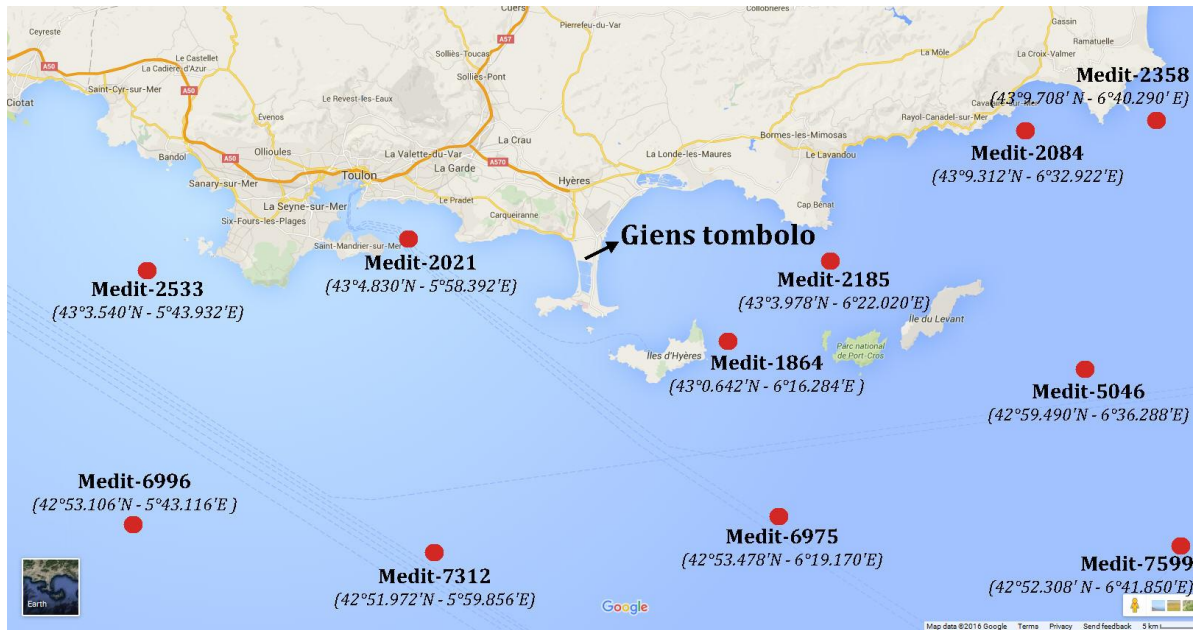


Figure C-2. Location of ANEMOC points in the study area (Background: Google map).

C.1.5. ECMWF models

ECMWF is an independent intergovernmental organisation supported by 34 states. This organisation was established in 1975 and now employs around 300 staff from more than 30 countries. It is based in Reading, UK. ECMWF periodically uses its forecast models and data assimilation systems to 'reanalyse' archived observations, creating global data sets describing the recent history of the atmosphere, land surface, and oceans. Reanalysis data are used for monitoring climate change, for research and education, and for commercial applications and can be downloaded on the website of ECMWF.

In this work, two main models of ERA-40 and ERA-Interim are used to extract the wave parameters for simulation. The primary objective of ERA-40 were to produce the use of a comprehensive set of global analyses describing the state of the atmosphere and land and ocean-wave conditions from during the 45 years from September 1957 to August 2002. ERA-40 had the resolution of 60 levels in the vertical and a reduced Gaussian grid with approximately uniform 125 km spacing for surface and other grid-point fields. On the other hand, ERA-Interim is a reanalysis of the global atmosphere covering the data-rich period since 1979, and continuing in real time. It was initiated in 2006 to provide a bridge between ECMWF's previous reanalysis, ERA-40, and the next generation extended reanalysis envisaged at ECMWF. This model had the resolution of 60 levels in the vertical and a reduced Gaussian grid with approximately uniform 79 km spacing for surface and other grid-point fields. The data assimilation and forecast suite of both ERA-Interim and ERA-40 produces four analyses per day, at 00, 06, 12 and 18 UTC. These two models have some main wave characteristics such as mean wave direction, mean wave period, and significant height of combined wind waves and swell. The data is downloaded in the format of NetCDF.

C.1.6. PREVIMER model

Previmer is the project coordinated by Ifremer, which receives support from financial, scientific, technical and industrial partners, and from data providers. It is co-financed by European Union and by key partners Météo-France and SHOM. PREVIMER provides for users with short-term observations and forecasts about the coastal environment (current, temperature, salinity, sea level, storm surge, waves, nutrients and plankton concentrations) along the French coastlines bordering the English Channel, the Atlantic Ocean, and the Mediterranean Sea. This data is calculated from the wind data provided by Météo-France and reanalyzed wind data from NOAA/NCEP, CFSR, and ECMWF.

In this study, some products of PREVIMER project with different scales are hired as follows: GLOBAL (with the spatial resolution of 0.5 degree), GLOBAL.05_NOC (with the spatial resolution of 0.5 degree), MEDNORD (with the spatial resolution of 2 minutes), WW3-MENOR-2MIN (with the spatial resolution of 2 minutes), and WW3-PROVENCE-200M (with the spatial resolution of 200 m). All these products provide sea states every 3 hours. Moreover, the data is downloaded in the format of NetCDF.

C.2. Data treatment

C.2.1. Determining the relationship between the wave direction and wind direction in Porquerolles Island

Wind is the origin of the wave generation, the wave motion suffered by the sea surface under the influence of wind. Moreover, wind is the key factor in the wave propagation in Gulf of Giens and Hyères bay, especially the northwest wind (Mistral) from the Rhone Valley. Hence, to complete the input data of wave for simulations, the author try to establish the relationship between the measured wave direction of Buoy 08302 and the observed wind direction of OGIMET as well as the simulated wind direction of ECMWF model in Porquerolles Island in the period from 2013 to 2015. The related functions is found by using MatLab curve fitting toolbox through the linear regression in the form $y=a*x+b$, where y is the wave direction of Buoy 08302 and x corresponds to the wind direction of OGIMET and ECMWF. The results are exhibited in Figure C-3 and Figure C-4. The goodness of fit statistics has R-square < 0.37 and RMSE > 45 . Correspondingly, the wave conditions in the boundary points cannot be specified by means of these above-related functions.

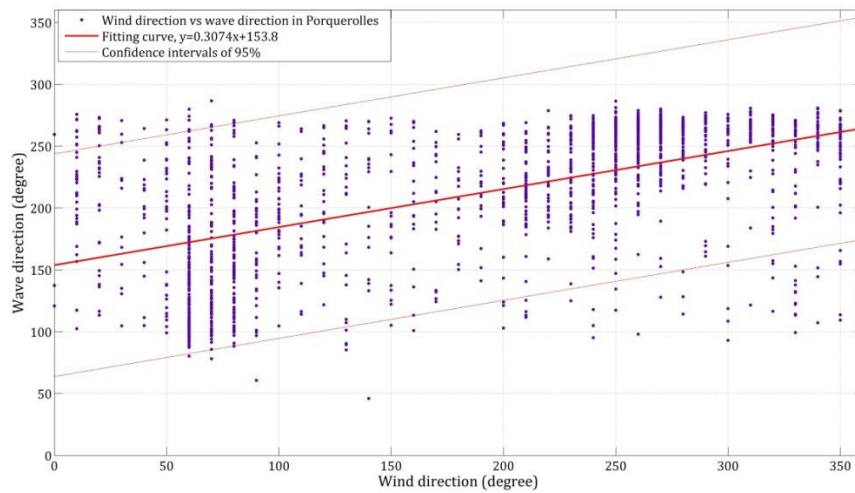


Figure C-3. Relationship between the wave direction of Buoy 08302 and the wind direction of OGIMET.

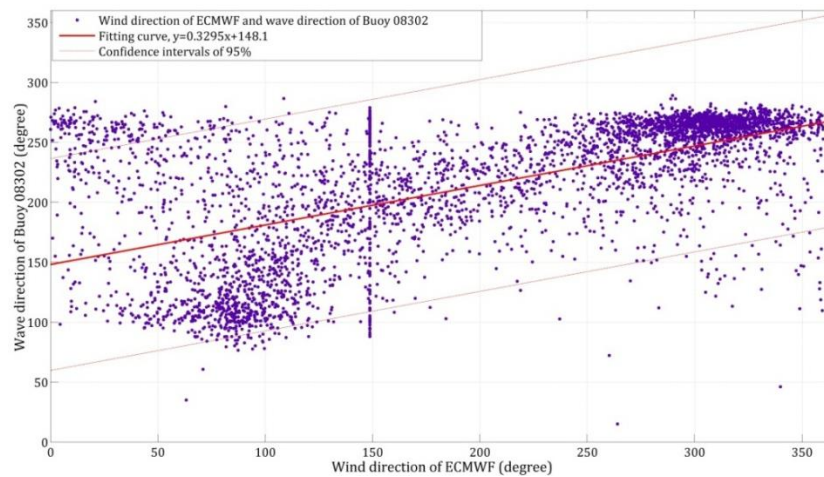


Figure C-4. Relationship between the wave direction of Buoy 08302 and the wind direction of ECMWF model.

C.2.2. Determining the relationship between the measured wave direction and the simulated wave direction in Porquerolles Island

Because the failure in investigating the relationship between the wind direction and the wave direction in Porquerolles Island, the author continues demonstrating the relationship between the measured wave parameters and those of models. The extracted wave parameters from GLOBAL, MEDNORD and WW3-MENOR-2MIN models will be compared with the measured wave parameters of Buoy 08302 by means of MatLab curve fitting toolbox. The linear regression in the form $y = a \cdot x + b$, where y is the wave parameters of Buoy 08302 and x is the wave parameters from GLOBAL, MEDNORD and WW3-MENOR-2MIN models, is utilized to fit the wave data. The results of these comparison are shown in Table C-1. The coefficients with the confidence intervals of 95% and statistical factors such as R-square and RMSE are presented from Figure C-5 to Figure C-10. It is easily seen that these above-found relationships can be believable enough to interpolate the wave parameters of Buoy 08302 as well as the other boundary points from the models of PREVIMER.

Table C-1. The statistical factors of the measured wave direction/directional standard deviation and the simulated wave direction/directional standard deviation.

Case	Parameter	Coefficients		R ²	RMSE
		a	b		
Buoy 08302 and GLOBAL_ECMWF	MWD	0.7639	56.18	0.7964	23.94
	DSD	0.551	16.65	0.2827	8.855
Buoy 08302 and MEDNORD	MWD	0.9117	28.7	0.8542	21.58
	DSD	0.5901	16.45	0.3854	8.308
Buoy 08302 and WW3-MENOR-2MIN	MWD	0.9021	27.86	0.8238	23.8
	DSD	0.5856	17.41	0.4379	7.963

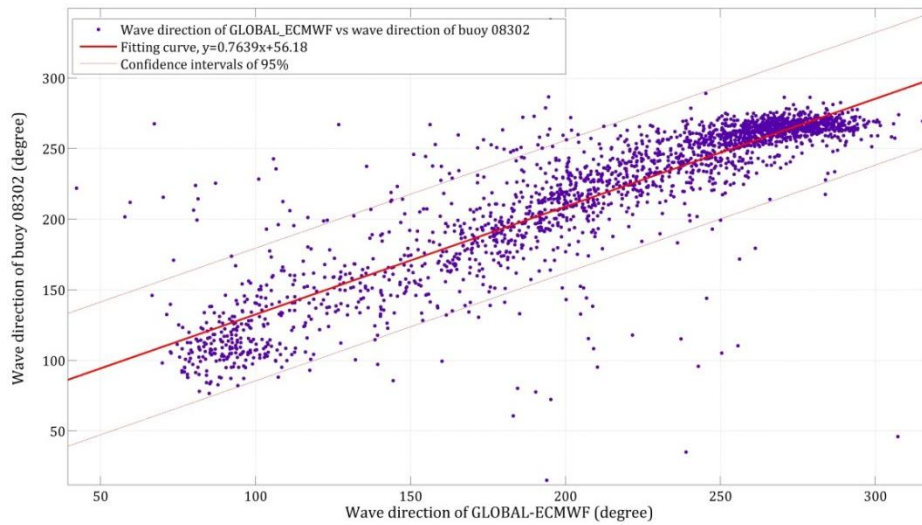


Figure C-5. Relationship between the wave direction of Buoy 08302 and that of GLOBAL_ECMWF model.

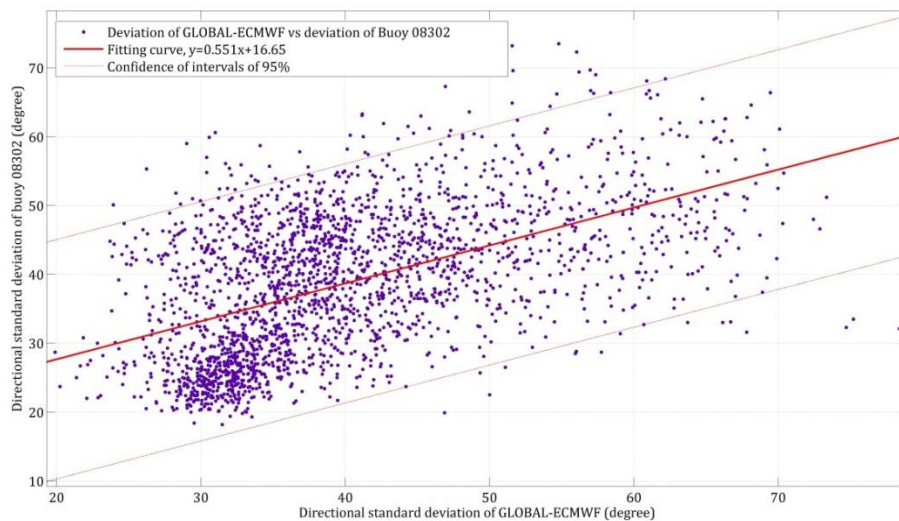


Figure C-6. Relationship between the directional standard deviation of Buoy 08302 and that of GLOBAL_ECMWF model.

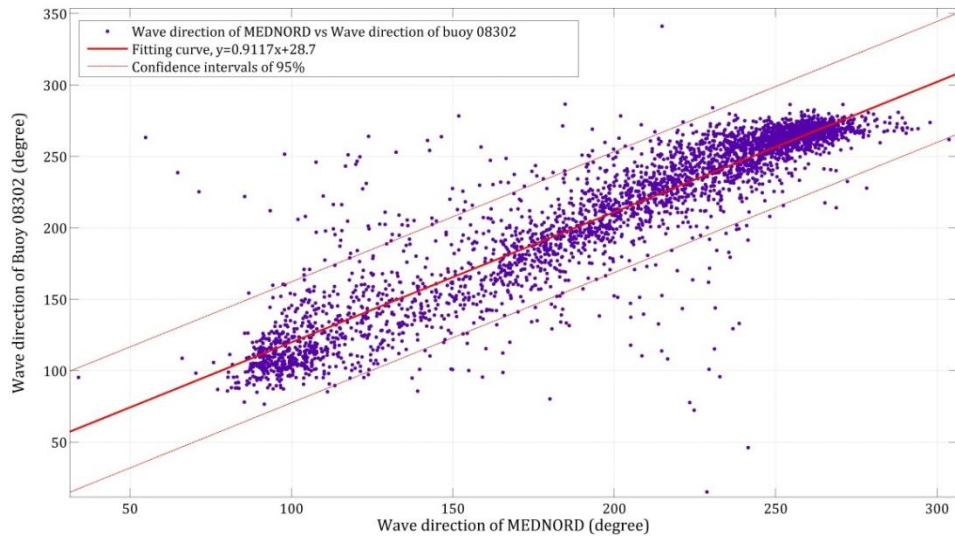


Figure C-7. Relationship between the wave direction of Buoy 08302 and that of MEDNORD model.

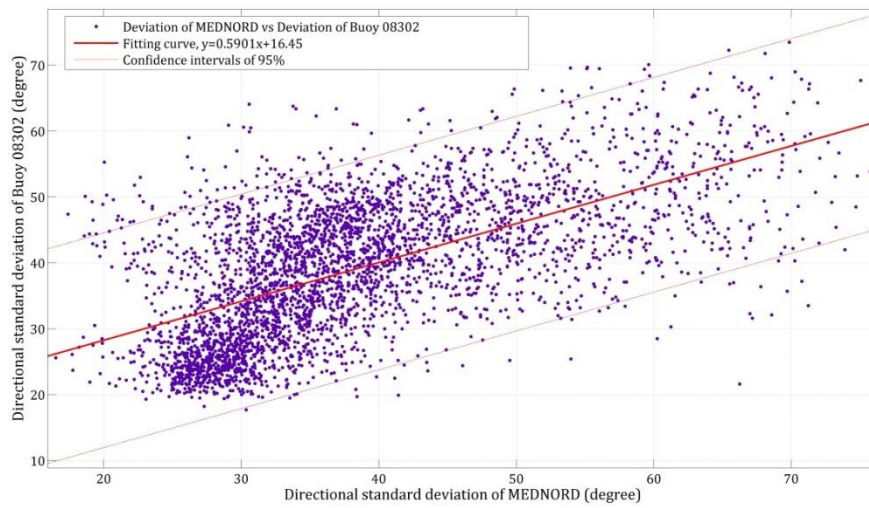


Figure C-8. Relationship between the directional standard deviation of Buoy 08302 and that of MEDNORD model.

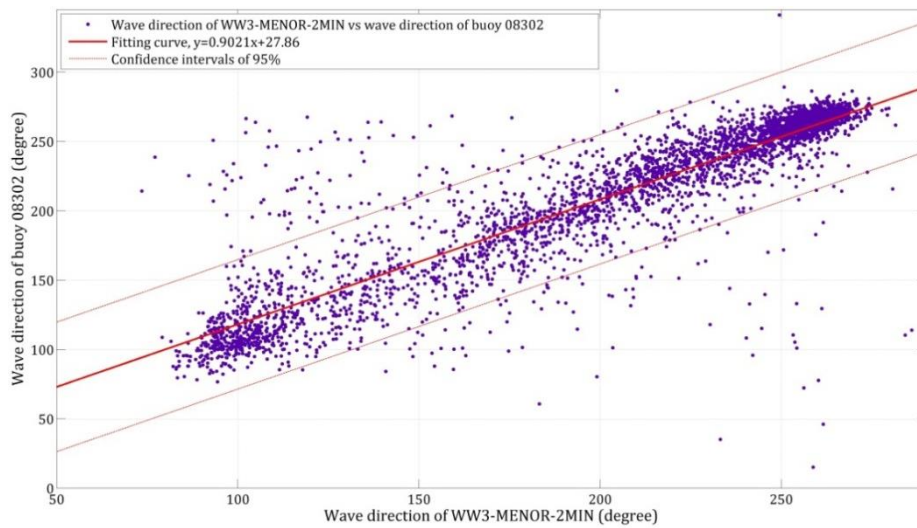


Figure C-9. Relationship between the wave direction of Buoy 08302 and that of WW3-MENOR-2MIN model.

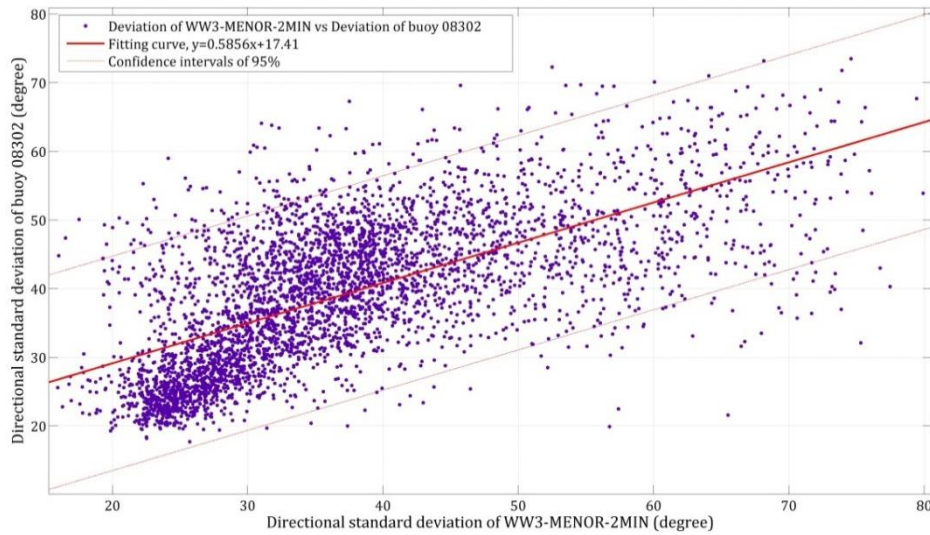


Figure C-10. Relationship between the directional standard deviation of Buoy 08302 and that of WW3-MENOR-2MIN model.

C.2.3. Determining the relationship between the measured mean wave period and the significant wave height in Porquerolles Island

The relationship between the mean wave period and the significant wave height of CANDHIS buoys near Porquerolles island is investigated by means of MatLab curve fitting toolbox. The linear regression in the form $y = a \cdot x + b$, where y is the mean wave period and x is the significant wave height, is utilized to fit the wave data. The result indicates that the mean wave period, T_z , has the strong agreement with the significant wave height, H_s . The statistical errors are R-squared = 0.58 and RMSE = 0.62. The result is shown in Figure C-11. With the above-found reliable relationship, the mean wave period can be interpolated from the significant wave height of 08301 and 08302 buoys.

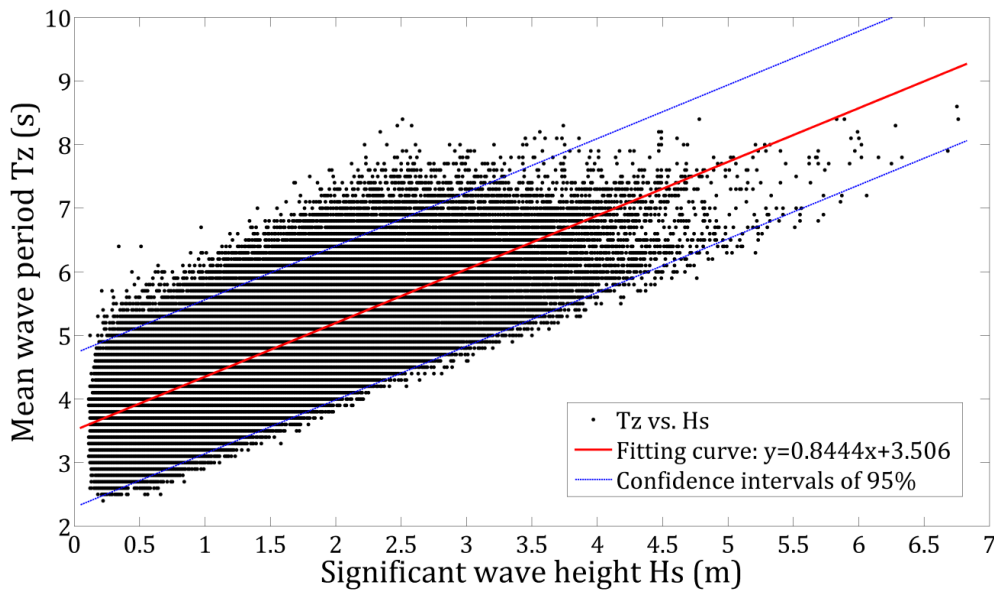


Figure C-11. Relationship between the mean wave period and the significant wave height of CANDHIS buoys.

C.2.4. Determining the relationship between the wave data of CANDHIS buoys and that of ANEMOC points extracted from numerical simulations

Only Buoy 08302 at Porquerolles island measures and records the wave parameters in real time. Hence, the wave data of other boundary points will be interpolated from that of Buoy 08302. To do that, the relationship between the wave data of these points and that of Buoy 08302 need be established by using the nonlinear least squares formulation in regression analysis. Nevertheless, there is no numerical model which can simulated the wave field in the study area in a long enough period. Moreover, these models have different degrees of accuracy at given time (Table C-1). As a result, the numerical models of GLOBAL-CFSR (1990-2003), GLOBAL-ECMWF (2011), MEDNORD (2004-2010), and WW3-MENOR-2MIN (2012-2015) are respectively utilized to extracted the wave data of the boundary points and detect the above-mentioned relationship. The results of this analysis are presented in the following tables.

Table C-2. The statistical factors of the wave parameters of Buoy 08302 and those of boundary points in GLOBAL-CFSR model.

Case	Parameter	Coefficients		R ²	RMSE
		a	b		
Buoy 08302 and Medit-2021	H _s	0.9678	0.008452	0.9786	0.0921
	T _p	0.9817	0.06669	0.9749	0.1322
	MWD	0.9782	13.12	0.928	19.7
	DSD	0.9827	0.07151	0.8448	4.224
Buoy 08302 and Medit-2084	H _s	1.002	-0.00092	0.9436	0.1576
	T _p	0.9983	-0.03049	0.9513	0.1898
	MWD	0.9943	-13.23	0.8824	26.24
	DSD	0.9824	1.456	0.7519	5.658
Buoy 08302 and Medit-2185	H _s	0.9886	-0.01427	0.9839	0.0814
	T _p	1.002	-0.04246	0.9856	0.1016
	MWD	1.004	-8.141	0.9569	15.4
	DSD	1.021	-0.4314	0.9091	3.239
Buoy 08302 and Medit-2358	H _s	1.005	0.005752	0.9331	0.1731
	T _p	0.9954	-0.01692	0.941	0.2095
	MWD	0.9887	-13.29	0.8645	28.28
	DSD	0.9654	2.166	0.7191	6.05
Buoy 08302 and Medit-2533	H _s	0.9144	0.06543	0.9144	0.192
	T _p	0.9519	0.1813	0.9312	0.2173
	MWD	0.8958	37.73	0.8406	28.19
	DSD	0.7518	8.671	0.6579	5.436

Table C-3. The statistical factors of the wave parameters of Buoy 08302 and those of boundary points in GLOBAL-CFSR model (continued).

Case	Parameter	Coefficients		R ²	RMSE
		a	b		
Buoy 08302 and Medit-5046	H _s	1.001	-0.00217	0.9452	0.1551
	T _p	0.9987	-0.03289	0.9528	0.1867
	MWD	0.9953	-13.22	0.8849	25.94
	DSD	0.9855	1.328	0.7569	5.6
Buoy 08302 and Medit-6975	H _s	1.058	0.006992	0.995	0.0483
	T _p	1.022	-0.03396	0.992	0.077
	MWD	1.023	-6.991	0.9866	8.62
	DSD	0.9942	0.521	0.9673	1.832
Buoy 08302 and Medit-6996	H _s	1.051	0.08643	0.8979	0.228
	T _p	0.9794	0.1596	0.9236	0.2367
	MWD	0.9279	32.3	0.84	29.26
	DSD	0.7365	9.456	0.6491	5.429
Buoy 08302 and Medit-7312	H _s	1.056	0.0343	0.9601	0.1385
	T _p	1.009	0.05406	0.9695	0.1504
	MWD	1.002	10.46	0.9215	21.13
	DSD	0.9375	1.975	0.8316	4.23
Buoy 08302 and Medit-7599	H _s	1.089	0.02178	0.9607	0.1417
	T _p	1.026	-0.02671	0.9485	0.2007
	MWD	1.021	-14.54	0.9148	22.52
	DSD	0.9569	2.405	0.7987	4.817

Table C-4. The statistical factors of the wave parameters of Buoy 08302 and those of boundary points in GLOBAL-ECMWF model.

Case	Parameter	Coefficients		R ²	RMSE
		a	b		
Buoy 08302 and Medit-2021	H _s	0.9703	0.0095	0.9774	0.08998
	T _p	0.996	0.004241	0.9596	0.1663
	MWD	0.9945	8.408	0.9533	16.34
	DSD	0.9616	1.112	0.8315	4.074
Buoy 08302 and Medit-2084	H _s	1.014	-0.01011	0.942	0.1533
	T _p	0.973	0.0716	0.9226	0.2293
	MWD	0.9808	-8.376	0.9124	22.55
	DSD	0.9973	0.6128	0.7429	5.522

Table C-5. The statistical factors of the wave parameters of Buoy 08302 and those of boundary points in GLOBAL-ECMWF model (continued).

Case	Parameter	Coefficients		R ²	RMSE
		a	b		
Buoy 08302 and Medit-2185	H _s	0.9918	-0.01582	0.9844	0.07615
	T _p	0.9941	-0.00069	0.9758	0.1273
	MWD	0.9923	-4.52	0.9706	12.81
	DSD	1.035	-1.028	0.9076	3.107
Buoy 08302 and Medit-2358	H _s	1.02	-0.00599	0.9307	0.1696
	T _p	0.9656	0.09785	0.9077	0.2504
	MWD	0.9769	-8.694	0.8969	24.58
	DSD	0.978	1.376	0.7074	5.918
Buoy 08302 and Medit-2533	H _s	0.9728	0.066	0.9118	0.1844
	T _p	0.9342	0.2236	0.8825	0.2773
	MWD	0.9386	26.15	0.874	26.45
	DSD	0.7523	9.474	0.6289	5.438
Buoy 08302 and Medit-5046	H _s	1.013	-0.01091	0.9438	0.1506
	T _p	0.9742	0.06699	0.9248	0.226
	MWD	0.9814	-8.313	0.9147	22.25
	DSD	1.001	0.4757	0.7484	5.461
Buoy 08302 and Medit-6975	H _s	1.051	0.007176	0.9945	0.04771
	T _p	1.013	-0.00352	0.9893	0.08567
	MWD	1.016	-5.233	0.9909	7.221
	DSD	1.006	-0.1368	0.9649	1.806
Buoy 08302 and Medit-6996	H _s	1.036	0.08971	0.8967	0.2143
	T _p	0.9539	0.217	0.8729	0.2961
	MWD	0.9722	19.98	0.8783	26.87
	DSD	0.7417	9.837	0.6221	5.441
Buoy 08302 and Medit-7312	H _s	1.045	0.038	0.9615	0.1274
	T _p	1.01	0.02419	0.9526	0.1833
	MWD	1.019	4.922	0.9472	17.86
	DSD	0.9254	2.494	0.8176	4.114
Buoy 08302 and Medit-7599	H _s	1.088	0.01248	0.9557	0.1427
	T _p	0.997	0.06523	0.9255	0.2301
	MWD	1.012	-11.1	0.9353	19.74
	DSD	0.9712	1.443	0.784	4.797

Table C-6. The statistical factors of the wave parameters of Buoy 08302 and those of boundary points in MEDNORD model.

Case	Parameter	Coefficients		R ²	RMSE
		a	b		
Buoy 08302 and Medit-2021	H _s	0.6676	0.04016	0.8784	0.1576
	T _p	0.7724	0.4474	0.6893	0.4515
	MWD	0.7019	70.02	0.8264	19.22
	DSD	0.4926	15.08	0.3531	7.681
Buoy 08302 and Medit-2084	H _s	0.6703	0.01179	0.6455	0.3152
	T _p	0.7424	0.4896	0.4924	0.6564
	MWD	0.6807	28.05	0.5058	40.2
	DSD	0.165	29.96	0.03	10.79
Buoy 08302 and Medit-2185	H _s	0.6934	-0.05832	0.8181	0.2074
	T _p	0.7737	0.2288	0.5898	0.5618
	MWD	0.9995	-24.14	0.6609	42.78
	DSD	0.3527	24.4	0.1	12.2
Buoy 08302 and Medit-2358	H _s	0.7789	0.01079	0.6841	0.3358
	T _p	0.784	0.4551	0.5845	0.5755
	MWD	0.733	18.58	0.5319	41.08
	DSD	0.271	27.61	0.06982	11.39
Buoy 08302 and Medit-2533	H _s	0.8826	0.07446	0.885	0.2018
	T _p	0.8374	0.47	0.8246	0.3363
	MWD	0.7554	64.89	0.7676	24.84
	DSD	0.5125	15.93	0.3895	7.392
Buoy 08302 and Medit-5046	H _s	1.091	-0.01213	0.9009	0.2296
	T _p	0.994	0.07139	0.8761	0.3255
	MWD	0.9933	-16.44	0.7636	33.02
	DSD	0.7551	11.36	0.4456	9.701
Buoy 08302 and Medit-6975	H _s	1.252	-0.00991	0.9791	0.1159
	T _p	1.1	-0.1012	0.9543	0.2096
	MWD	1.132	-27.35	0.9272	18.95
	DSD	1.093	-1.704	0.8966	4.275
Buoy 08302 and Medit-6996	H _s	1.273	0.04045	0.9074	0.2581
	T _p	0.9939	0.1859	0.8678	0.3378
	MWD	1.067	1.186	0.8153	30.34
	DSD	0.7841	9.292	0.6019	7.345

Table C-7. The statistical factors of the wave parameters of Buoy 08302 and those of boundary points in MEDNORD model (continued).

Case	Parameter	Coefficients		R ²	RMSE
		a	b		
Buoy 08302 and Medit-7312	H _s	1.289	0.008407	0.9513	0.185
	T _p	1.052	0.01982	0.9247	0.2612
	MWD	1.101	-10.49	0.903	21.56
	DSD	0.9534	2.948	0.8079	5.355
Buoy 08302 and Medit-7599	H _s	1.316	-0.01053	0.9385	0.2137
	T _p	1.093	-0.03639	0.8744	0.3607
	MWD	1.158	-38.3	0.8363	30.61
	DSD	0.9928	2.955	0.6907	7.653

Table C-8. The statistical factors of the wave parameters of Buoy 08302 and those of boundary points in WW3-MENOR-2MIN model.

Case	Parameter	Coefficients		R ²	RMSE
		a	b		
Buoy 08302 and Medit-2021	H _s	0.5694	0.05188	0.8716	0.1596
	T _p	0.6527	0.8435	0.6115	0.5152
	MWD	0.6233	83.71	0.8158	16.84
	DSD	0.3549	21.49	0.2551	7.226
Buoy 08302 and Medit-2084	H _s	0.5447	0.103	0.52	0.3822
	T _p	0.6289	0.9666	0.4228	0.7275
	MWD	0.6218	33.89	0.425	41.11
	DSD	-0.02673	44.09	0.001	9.061
Buoy 08302 and Medit-2185	H _s	0.5896	-0.0119	0.6845	0.2923
	T _p	0.656	0.5435	0.4699	0.6899
	MWD	0.9535	-23.86	0.5222	51.84
	DSD	0.08378	39.22	0.01	12.56
Buoy 08302 and Medit-2358	H _s	0.6461	0.1052	0.5599	0.4183
	T _p	0.6522	0.9308	0.4955	0.6516
	MWD	0.6911	20.53	0.4522	43.23
	DSD	0.09639	38.5	0.011	10.79
Buoy 08302 and Medit-2533	H _s	0.8327	0.05734	0.9058	0.1961
	T _p	0.7216	0.8061	0.7867	0.372
	MWD	0.736	66.5	0.7759	22.48
	DSD	0.3877	24.15	0.3671	6.065

Table C-9. The statistical factors of the wave parameters of Buoy 08302 and those of boundary points in WW3-MENOR-2MIN model (continued).

Case	Parameter	Coefficients		R ²	RMSE
		a	b		
Buoy 08302 and Medit-5046	H _s	0.9411	0.04753	0.8326	0.3082
	T _p	0.8679	0.3888	0.8219	0.4
	MWD	0.9736	-17.41	0.6907	37.04
	DSD	0.5546	21.56	0.3023	10.04
Buoy 08302 and Medit-6975	H _s	1.131	-0.00716	0.9798	0.1185
	T _p	1.015	0.008783	0.9716	0.1718
	MWD	1.132	-31.02	0.9116	20.04
	DSD	0.9891	3.392	0.8725	4.504
Buoy 08302 and Medit-6996	H _s	1.209	0.00941	0.9108	0.2762
	T _p	0.8858	0.4312	0.8672	0.3432
	MWD	1.087	-4.915	0.8335	27.63
	DSD	0.7486	12.39	0.6566	6.451
Buoy 08302 and Medit-7312	H _s	1.205	-0.01892	0.9634	0.1716
	T _p	0.9642	0.1625	0.9469	0.226
	MWD	1.112	-15.01	0.9286	17.54
	DSD	0.92	5.463	0.8686	4.263
Buoy 08302 and Medit-7599	H _s	1.195	0.002783	0.9207	0.2561
	T _p	1.009	0.08931	0.8927	0.3463
	MWD	1.16	-42.11	0.7882	34.16
	DSD	0.8605	9.476	0.618	8.06

Appendix D-MATLAB codes

D.1. Extraction and prediction of the shoreline

D.1.1. Extraction of the shoreline

```
DeltaK=9330.35;
DeltaV=11154.1;
K1=966014.1; %Pointe de l'Argentiere
V1=6230064.9;%Pointe de l'Argentiere
Gap_size=1;
im=imread('Landsat.png');
if (size(im,2)>1)
    im=rgb2gray(im);
end
DeltaX=size(im,2);
DeltaY=size(im,1);
Y1=1;
X1=DeltaX;
im1=edge(im, 'Canny');
imshow(im1);
[curve, curve_start, curve_end, curve_mode, cur_num, BW_edge]=extract_curve(im1, Gap_size);
lens=zeros(cur_num,1);
for i=1:cur_num
    lens(i)=size(curve{i},1);
end
[C,Ids]=sort(lens);
num=500;
image=zeros(size(im,1), size(im,2));
border_size=0;
for i=1:num
    id=Ids(cur_num-i+1);
    border_size=border_size+size(curve{id},1);
end
fid=fopen('Coastline_kinhdo_vido_Landsat8_2016_Eastern.txt','w');
borderKV=zeros(border_size,2);
iter=1;
%Estimation of longitude and latitude
for i=1:num
    id=Ids(cur_num-i+1);
    for j=1:size(curve{id},1)
        y=curve{id}(j,1);
        x=curve{id}(j,2);
        k=K1+(x-X1)*DeltaK/DeltaX;
        v=V1-(y-Y1)*DeltaV/DeltaY;
        borderKV(iter,1)=k; %Longitude
        borderKV(iter,2)=v; %Latitude
        fprintf(fid,'%f %f\n',k,v);
        iter=iter+1;
    end
end
fclose(fid);
%Display result
for i=1:num
    id=Ids(cur_num-i+1);
    curve{id}
    for j=1:size(curve{id},1)
        image(curve{id}(j,1), curve{id}(j,2))=255;
    end
end
figure, imshow(image);
```

D.1.2. Prediction of the shoreline

```
function predict_shoreline()
f=load('Input.txt');
x=f(:,1);
```

```

y=f(:,2);
n=length(x);
A=zeros(1,n);
B=A;
R=A;
R2=A;
fid=fopen('Predict_the_future_shoreline.txt','w');
fprintf(fid,'\t a\t\t \t b\t\t \t cor\t rsquared\n\n');
for i=1:5:n-4
    x1=x(i:i+4);
    y1=y(i:i+4);
    [a,b,r,r2]=linear_regression(x1,y1);
    A(i:i+4)=a;
    B(i:i+4)=b;
    R(i:i+4)=r;
    R2(i:i+4)=r2;
    fprintf(fid,'%9.6f\t%9.6f\t%9.6f\t%9.6f\n',a,b,r,r2);
end
fclose(fid);
end
% Calculation of statistical errors
function [a,b,r,r2]=linear_regression(x,y)
n=length(x);
a=(n*sum(x.*y)-sum(x)*sum(y))/(n*sum(x.^2)-(sum(x))^2);
b=mean(y)-a*mean(x);
r=(n*sum(x.*y)-sum(x)*sum(y))/(sqrt(n*sum(x.^2)-(sum(x))^2)*sqrt(n*sum(y.^2)-(sum(y))^2)); % Correlation coefficient
r2=r^2; %Determination coefficient
end

```

D.2. Wave statistics

```

close all
clear all
clc
filename = 'Dulieu'; % input filename without extension (only excel file)
a = xlsread([filename, '.xls'],1);
a = a(2:end,:);
[m,n]=size(a);
x=a(:,3);
y=a(:,4);
z=a(:,5);
rx=0:0.1:max(x);
ry=0:0.5:max(y);
rz=0:5:max(z);
nx =length(rx);
ny =length(ry);
nz =length(rz);
[zo,ido] =sort(z);
b = a(ido,:);
for j=1:m
    for i=1:nx
        if (i<nx && b(j,3)>=rx(i) && b(j,3)<rx(i+1))
            b(j,3) = rx(i);
        elseif (i==nx && b(j,3)>rx(i))
            b(j,3) = rx(i);
        end
    end
    for i=1:ny
        if (i<ny && b(j,4)>=ry(i) && b(j,4)<ry(i+1))
            b(j,4) = ry(i);
        elseif (i==ny && b(j,4)>ry(i))
            b(j,4) = ry(i);
        end
    end
    for i=1:nz
        if (i<nz && b(j,5)>=rz(i) && b(j,5)<rz(i+1))
            b(j,5) = rz(i);
        end
    end
end

```

```

        elseif (i==nz && b(j,5)>rz(i))
            b(j,5) = rz(i);
        end
    end
end
end
x=b(:,3);
y=b(:,4);
z=b(:,5);
zcount = zeros(nz,1);
ycount = zeros(ny,1);
xcount = zeros(nx,1);
Xcount = zeros(m,1);
Zcount = zeros(m,1);
for i=1:nz
    idz = ( z==rz(i));
    ys = y(idz);
    [yso,idso] = sort(ys);
    idb1 = sum(zcount) + 1;
    idb2 = idb1 + length(yso)-1;
    ibyo = idb1 + idso-1;
    if isempty(idso)==0
        b(idb1:idb2,:) = b(ibyo,:);
    end
    ycount = zeros(ny,1);
    for j=1:ny
        idy = (y == ry(j) & idz);
        xs = x(idy);
        [xso,idxso] = sort(xs);
        idb1x = sum(zcount) + sum(ycount) + 1;
        idb2x = idb1x + length(xso)-1;
        ibxo = idb1x + idxso-1;
        if isempty(idxso)==0
            b(idb1x:idb2x,:) = b(ibxo,:);
            w = tabulate(xso);
            [mw,nw] = size(w);
            for k=1:length(xso)
                for l=1:mw
                    if xso(k)==w(l)
                        Xcount(idb1x+k-1)= w(l,2);
                    end
                end
            end
        end
        ycount(j) = sum(idy);
    end
    zcount(i) = sum(idz);
    if isempty(idso)==0
        Zcount(idb1:idb2) = zcount(i);
    end
end
end
out = [b,Xcount];
fid=fopen(['out_',filename, '.txt'],'w');
fprintf(fid, 'Date \t Hour \t X \t Y \t Z \t # \t # \t frequency((X,Y,Z))\n');
for i =1:m
    fprintf(fid, '%9.2f \t %9.10f \t %9.2f \t %9.2f \t %9.2f \t %9.10f \t
%9.10f \t %9d \n', out(i,:));
end
fclose(fid);

```

Appendix E - Numerical results of SBWs

E.1. Ceinturon beach

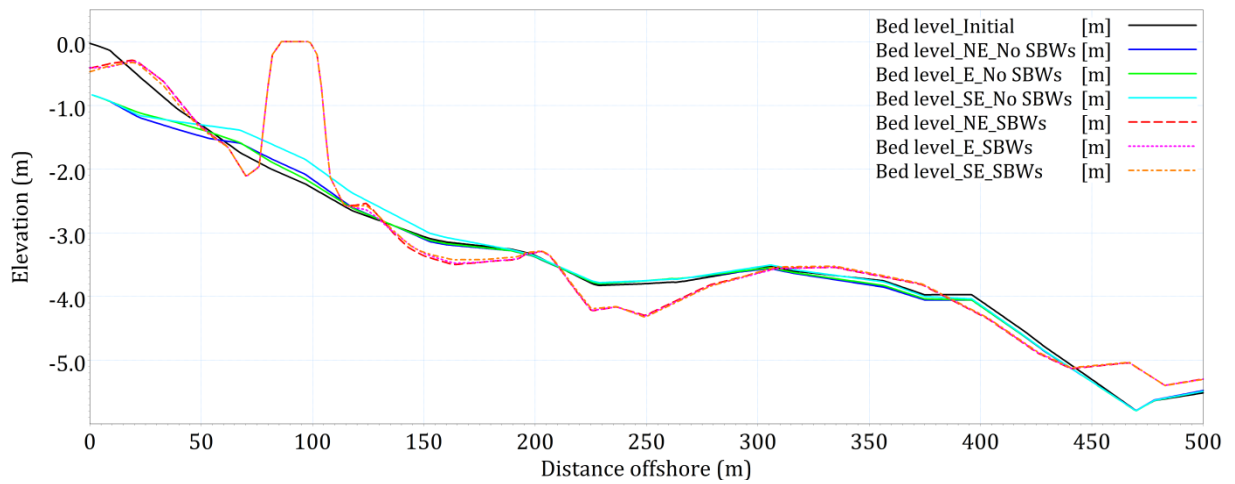


Figure E-1. Cross-shore changes of beach profile 1 due to different wind directions.

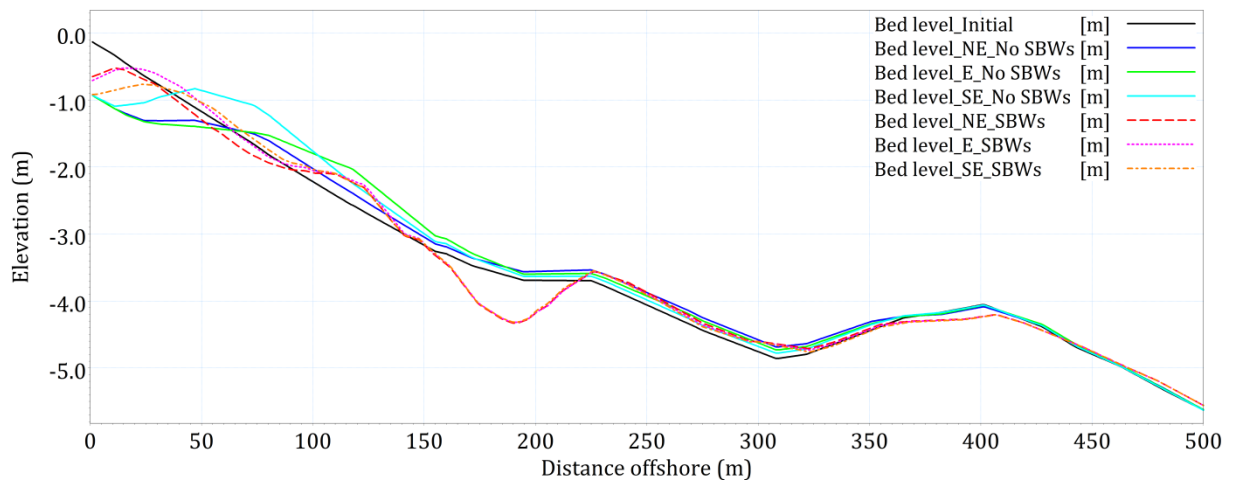


Figure E-2. Cross-shore changes of beach profile 4 due to different wind directions.

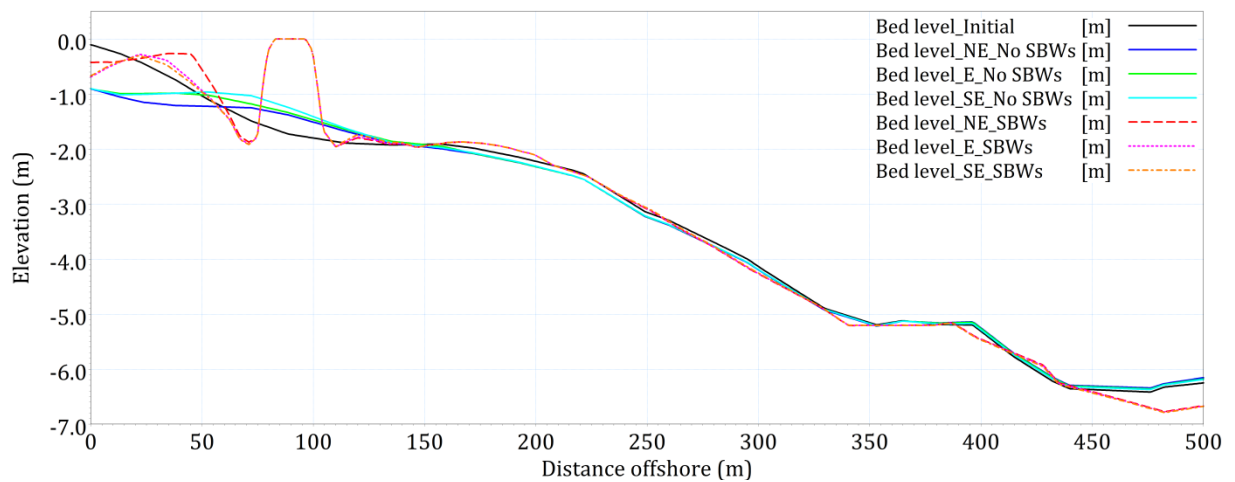


Figure E-3. Cross-shore changes of beach profile 5 due to different wind directions.

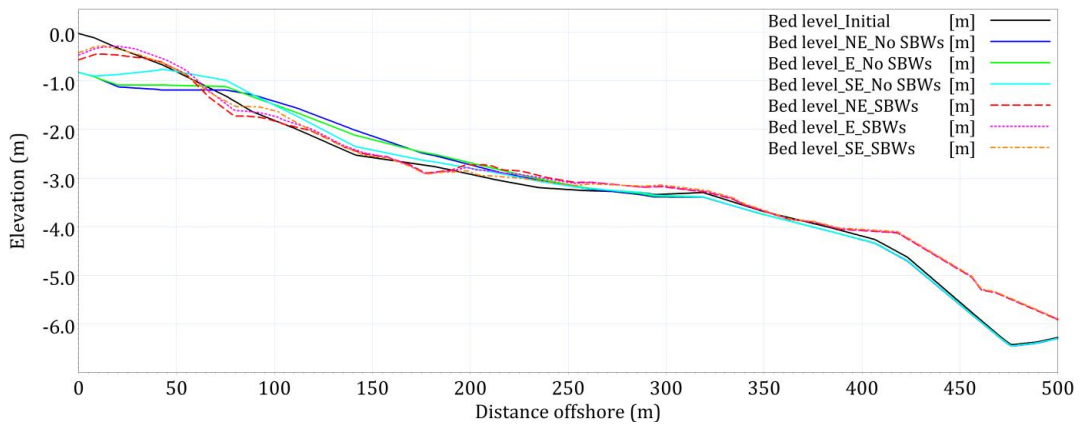


Figure E-4. Cross-shore changes of beach profile 6 due to different wind directions.

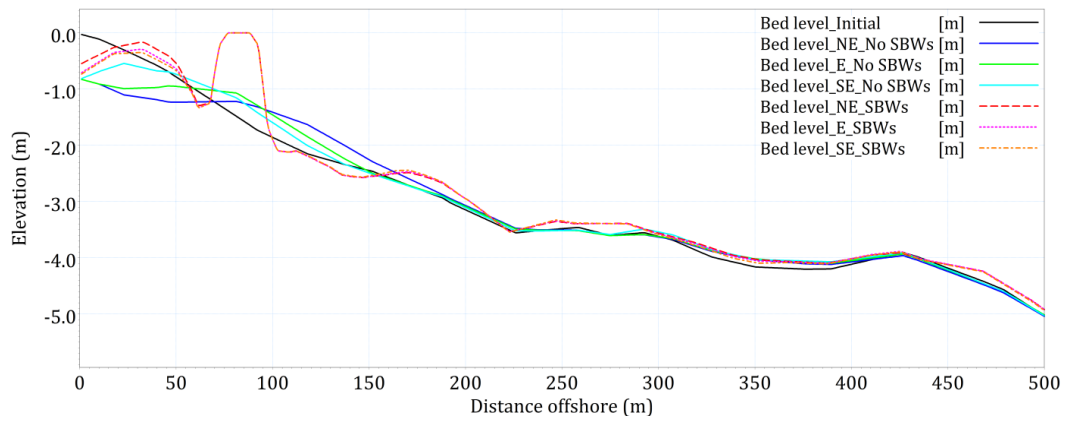


Figure E-5. Cross-shore changes of beach profile 7 due to different wind directions.

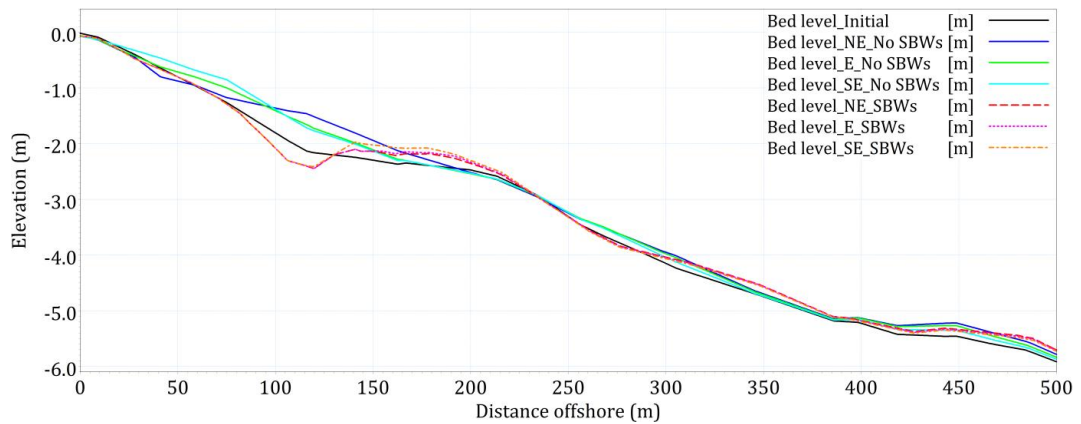


Figure E-6. Cross-shore changes of beach profile 8 due to different wind directions.

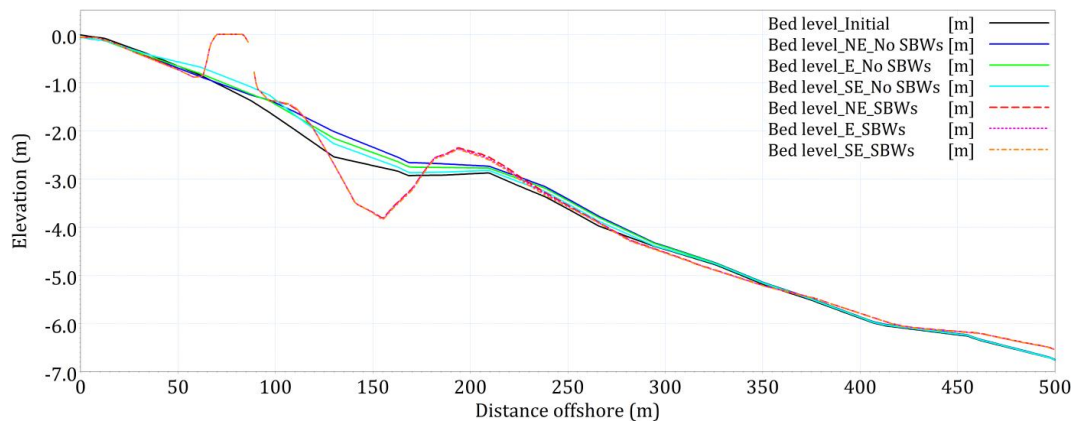


Figure E-7. Cross-shore changes of beach profile 9 due to different wind directions.

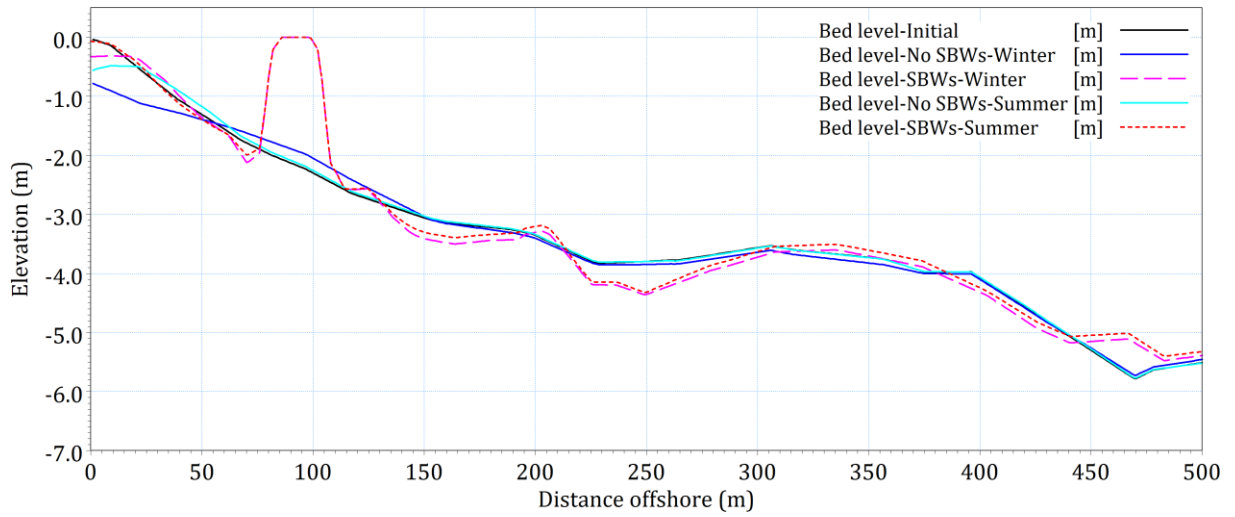


Figure E-8. Cross-shore changes of beach profile 1 due to seasonal variation.

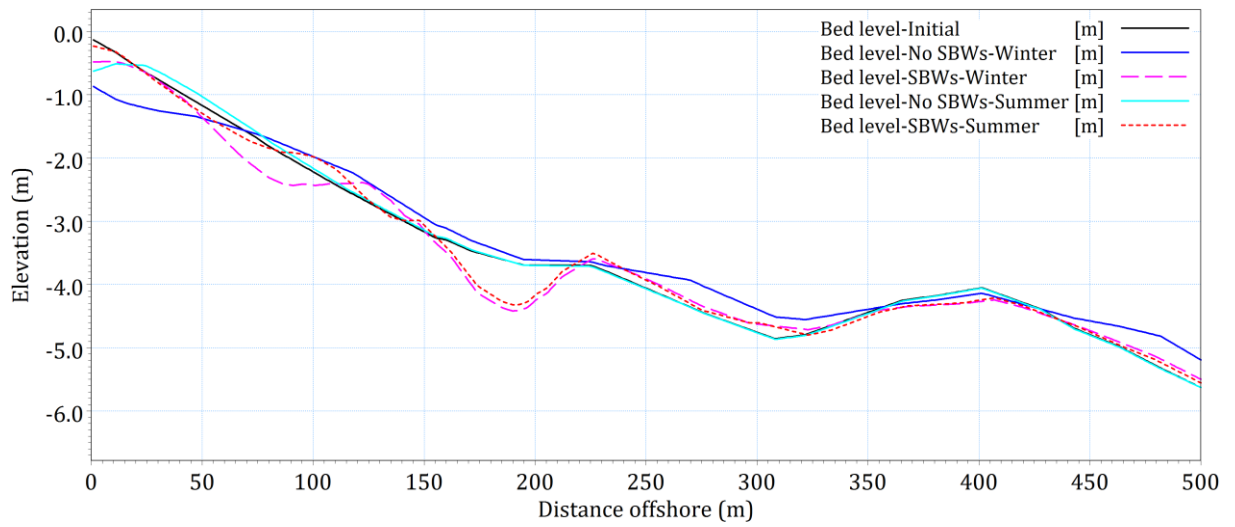


Figure E-9. Cross-shore changes of beach profile 4 due to seasonal variation.

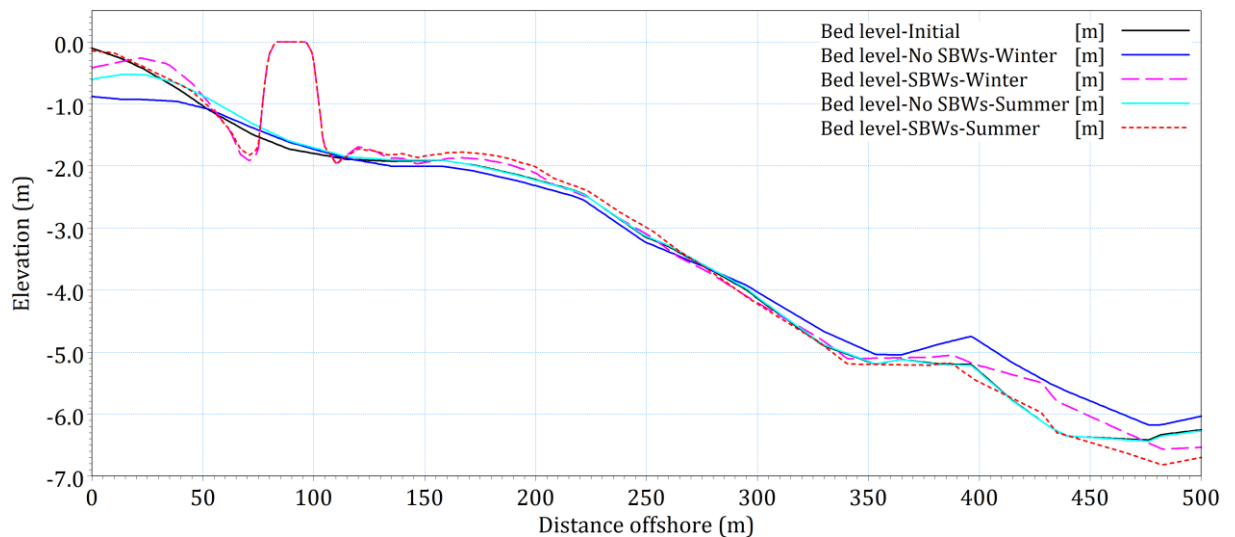


Figure E-10. Cross-shore changes of beach profile 5 due to seasonal variation.

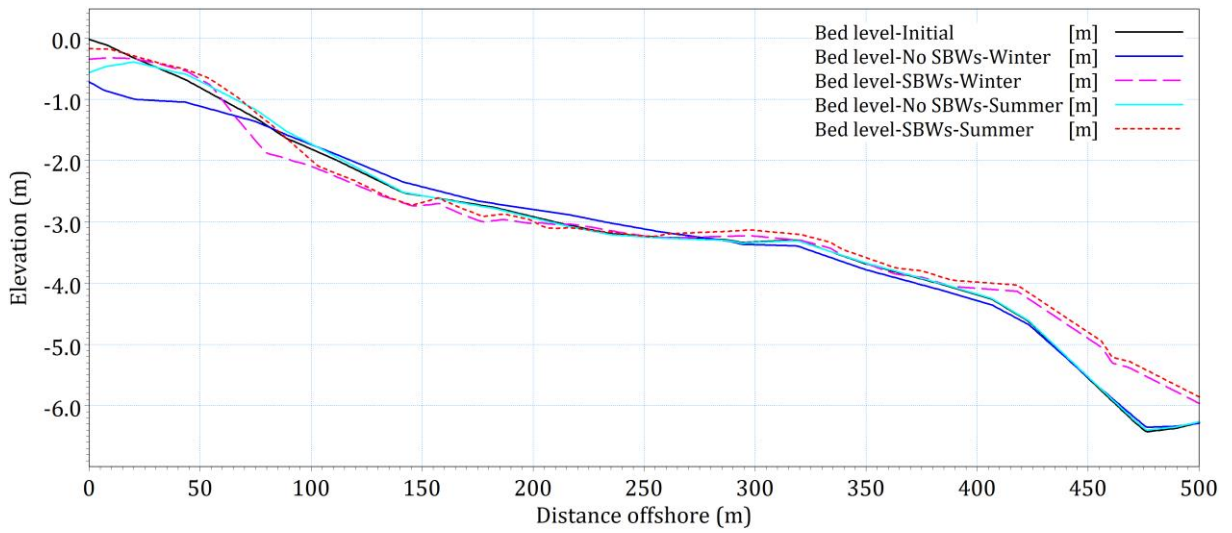


Figure E-11. Cross-shore changes of beach profile 6 due to seasonal variation.

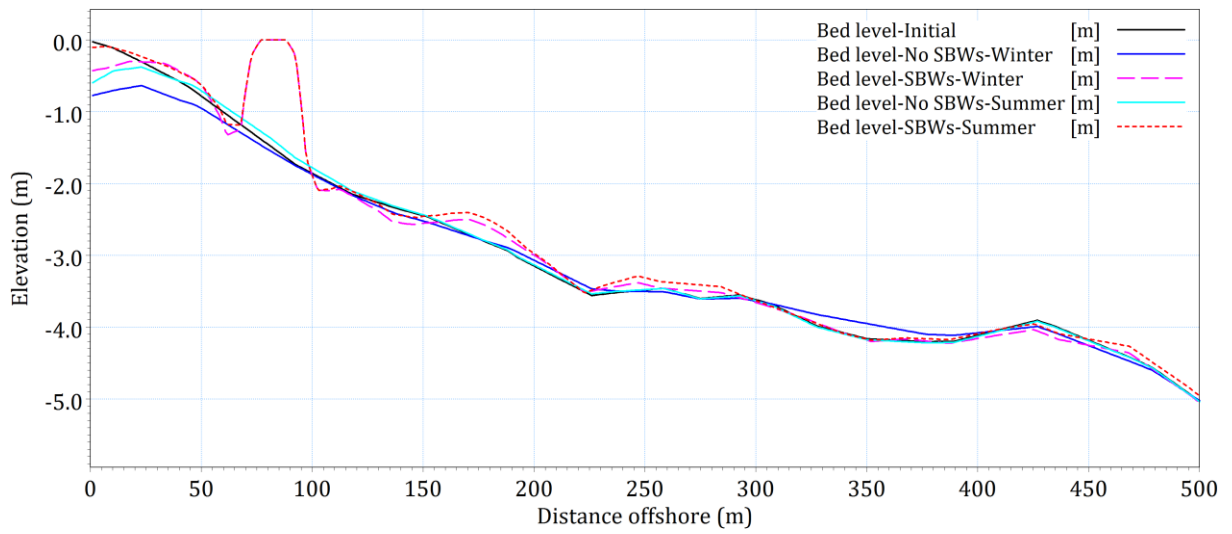


Figure E-12. Cross-shore changes of beach profile 7 due to seasonal variation.

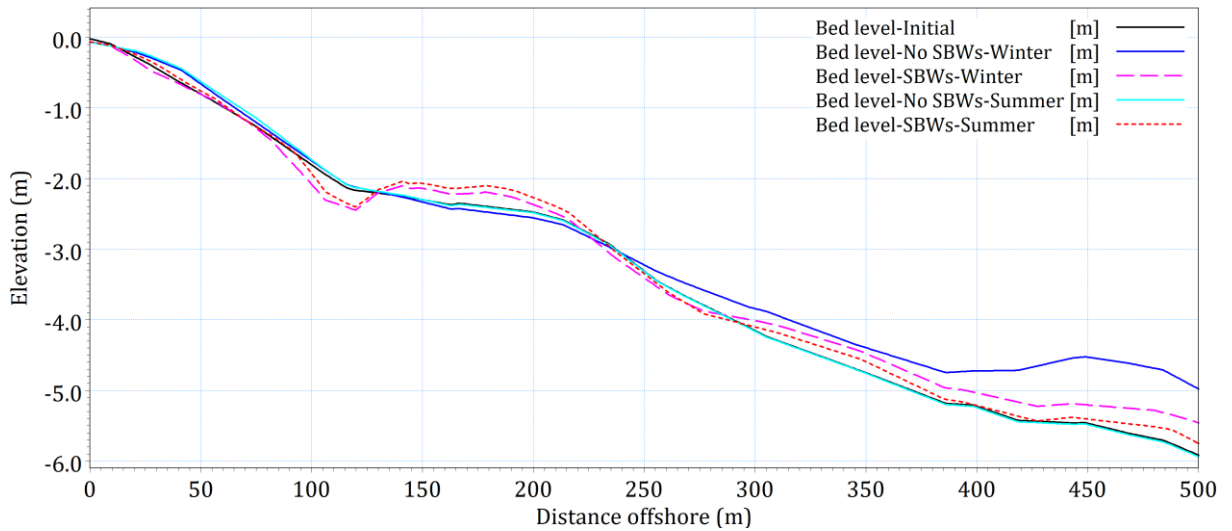


Figure E-13. Cross-shore changes of beach profile 8 due to seasonal variation.

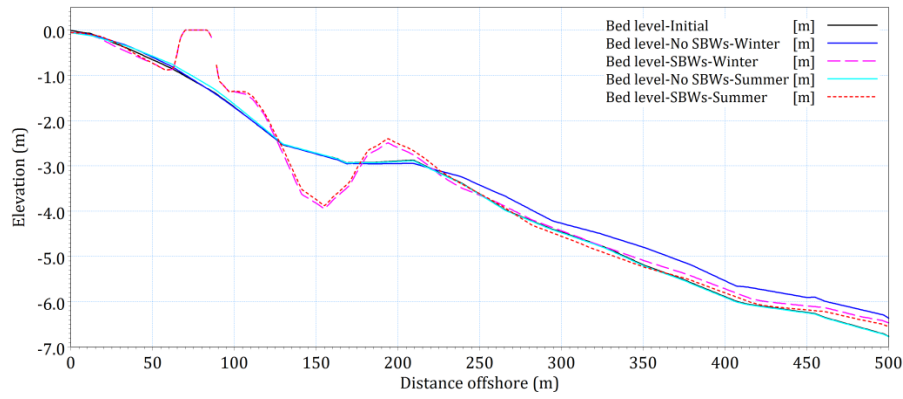


Figure E-14. Cross-shore changes of beach profile 9 due to seasonal variation.

Table E-1. Hydrodynamic parameters at T1 point.

Scenario		V_c (m/s)	H_s (m)	S_{xx} (m^3/s^2)	S_{xy} (m^3/s^2)	S_{yy} (m^3/s^2)	Q ($m^3/s/m$)
No SBWs	NE	0.098	0.605	0.219	-0.063	0.159	2.86E-05
	E	0.067	0.609	0.221	-0.064	0.159	1.80E-05
	SE	0.048	0.597	0.214	-0.062	0.153	1.87E-05
	Winter	0.065	0.305	0.068	-0.022	0.054	1.55E-05
	Summer	0.053	0.162	0.019	-0.007	0.018	7.76E-06
	Decadal	0.132	0.977	0.538	-0.152	0.370	1.56E-04
	Tri-Decadal	0.175	0.997	0.555	-0.149	0.354	1.85E-04
	Semi-Centennial	0.223	1.092	0.664	-0.171	0.396	2.90E-04
	Centennial	0.214	1.253	0.845	-0.219	0.506	3.36E-04
SBWs	NE	0.044	0.232	0.031	-0.005	0.024	3.05E-06
	E	0.053	0.230	0.029	-0.005	0.025	3.78E-06
	SE	0.076	0.216	0.025	-0.005	0.022	4.55E-06
	Winter	0.049	0.144	0.012	-0.003	0.011	2.22E-06
	Summer	0.039	0.090	0.004	-0.001	0.004	1.34E-06
	Decadal	0.048	0.530	0.149	-0.028	0.113	7.62E-06
	Tri-Decadal	0.127	0.558	0.164	-0.029	0.116	9.47E-06
	Semi-Centennial	0.221	0.649	0.219	-0.042	0.152	1.60E-05
	Centennial	0.228	0.821	0.346	-0.068	0.241	3.00E-05
Difference (%)	NE	55.55	61.69	85.67	92.45	84.90	89.33
	E	20.99	62.20	86.84	91.76	84.56	79.01
	SE	-57.98	63.81	88.46	91.89	85.72	75.65
	Winter	25.12	52.98	81.65	87.20	80.59	85.69
	Summer	25.59	44.41	78.01	80.98	77.04	82.68
	Decadal	63.48	45.74	72.35	81.61	69.56	95.11
	Tri-Decadal	27.25	44.04	70.44	80.27	67.23	94.88
	Semi-Centennial	0.93	40.55	67.01	75.71	61.50	94.49
	Centennial	-6.74	34.53	59.12	69.10	52.41	91.07

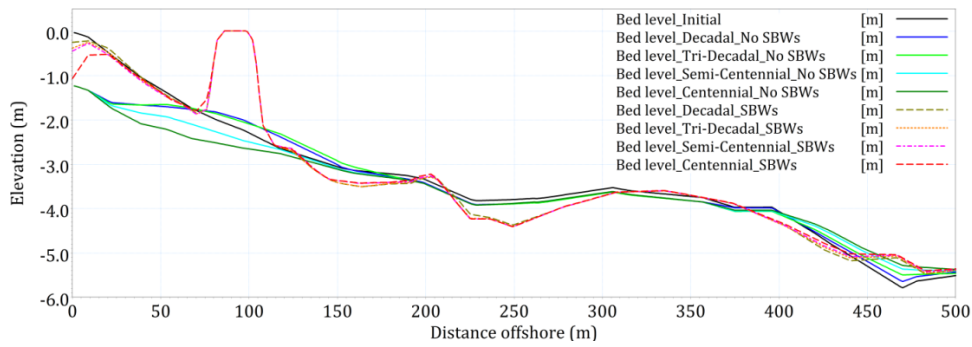


Figure E-15. Cross-shore changes of beach profile 1 due to different storms.

Table E-2. Hydrodynamic parameters at T2 point.

Scenario		V_c (m/s)	H_s (m)	S_{xx} (m^3/s^2)	S_{xy} (m^3/s^2)	S_{yy} (m^3/s^2)	Q ($m^3/s/m$)
No SBWs	NE	0.170	0.591	0.217	-0.056	0.139	5.84E-05
	E	0.113	0.583	0.209	-0.052	0.134	3.96E-05
	SE	0.142	0.579	0.204	-0.051	0.130	5.94E-05
	Winter	0.089	0.283	0.064	-0.018	0.043	2.47E-05
	Summer	0.075	0.141	0.017	-0.005	0.013	1.16E-05
	Decadal	0.197	0.961	0.519	-0.146	0.337	2.62E-04
	Tri-Decadal	0.266	1.000	0.539	-0.156	0.345	3.56E-04
	Semi-Centennial	0.351	1.113	0.638	-0.184	0.403	6.53E-04
	Centennial	0.353	1.269	0.814	-0.232	0.507	7.37E-04
SBWs	NE	0.049	0.218	0.029	-0.004	0.019	2.14E-06
	E	0.089	0.219	0.029	-0.004	0.018	4.16E-06
	SE	0.151	0.214	0.027	-0.004	0.018	7.46E-06
	Winter	0.068	0.136	0.012	-0.002	0.009	2.82E-06
	Summer	0.056	0.082	0.004	-0.001	0.003	1.86E-06
	Decadal	0.169	0.508	0.139	-0.027	0.096	1.61E-05
	Tri-Decadal	0.115	0.575	0.176	-0.032	0.118	1.25E-05
	Semi-Centennial	0.291	0.681	0.245	-0.047	0.165	4.34E-05
	Centennial	0.308	0.845	0.362	-0.074	0.256	8.50E-05
Difference (%)	NE	70.95	63.13	86.65	92.13	86.70	96.34
	E	20.88	62.39	86.37	91.91	86.27	89.50
	SE	-6.28	62.99	86.55	92.82	86.47	87.44
	Winter	23.99	52.08	81.02	86.30	80.11	88.62
	Summer	25.43	42.22	77.86	79.53	74.73	83.90
	Decadal	14.31	47.11	73.18	81.32	71.62	93.84
	Tri-Decadal	56.78	42.50	67.24	79.46	65.93	96.50
	Semi-Centennial	17.06	38.82	61.68	74.51	59.11	93.35
	Centennial	12.76	33.37	55.56	68.10	49.57	88.46

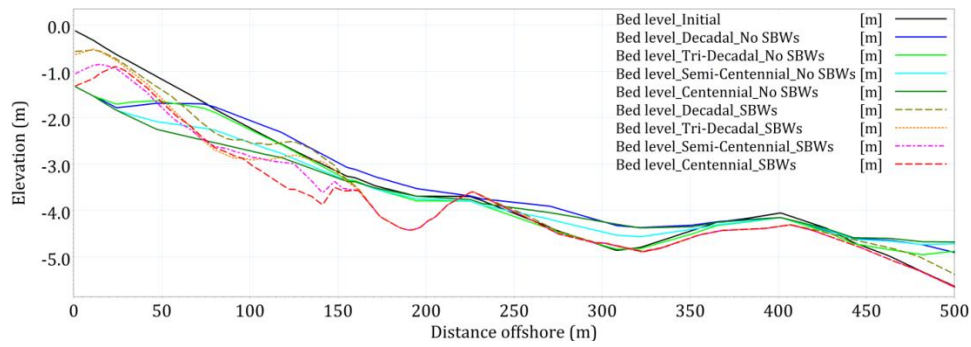


Figure E-16. Cross-shore changes of beach profile 4 due to different storms.

Table E-3. Hydrodynamic parameters at T3 point.

Scenario		V_c (m/s)	H_s (m)	S_{xx} (m^3/s^2)	S_{xy} (m^3/s^2)	S_{yy} (m^3/s^2)	Q ($m^3/s/m$)
No SBWs	NE	0.155	0.570	0.202	-0.045	0.128	6.76E-05
	E	0.075	0.561	0.197	-0.046	0.126	3.17E-05
	SE	0.097	0.537	0.181	-0.044	0.117	5.04E-05
	Winter	0.085	0.290	0.063	-0.017	0.044	2.58E-05
	Summer	0.071	0.152	0.018	-0.006	0.015	1.11E-05
	Decadal	0.171	0.902	0.476	-0.117	0.300	2.35E-04
	Tri-Decadal	0.260	0.931	0.496	-0.120	0.296	3.63E-04
	Semi-Centennial	0.383	1.031	0.594	-0.135	0.335	9.49E-04
	Centennial	0.405	1.195	0.768	-0.177	0.440	1.23E-03
SBWs	NE	0.079	0.205	0.024	-0.003	0.018	5.76E-06
	E	0.104	0.189	0.019	-0.003	0.015	4.89E-06
	SE	0.139	0.182	0.018	-0.003	0.013	5.86E-06
	Winter	0.068	0.132	0.010	-0.002	0.008	2.95E-06
	Summer	0.054	0.086	0.004	-0.001	0.003	1.80E-06
	Decadal	0.209	0.482	0.123	-0.021	0.089	1.98E-05
	Tri-Decadal	0.140	0.539	0.150	-0.025	0.106	1.89E-05
	Semi-Centennial	0.170	0.636	0.212	-0.033	0.142	1.60E-05
	Centennial	0.245	0.805	0.335	-0.058	0.232	4.48E-05
Difference (%)	NE	49.00	64.08	87.95	93.25	85.98	91.48
	E	-39.08	66.39	90.31	93.86	88.36	84.58
	SE	-43.07	66.05	90.24	94.19	88.53	88.38
	Winter	19.82	54.53	84.16	87.53	82.00	88.55
	Summer	24.42	43.29	78.61	81.00	76.20	83.74
	Decadal	-22.04	46.62	74.14	81.89	70.33	91.57
	Tri-Decadal	46.18	42.08	69.77	78.93	64.28	94.78
	Semi-Centennial	55.56	38.32	64.36	75.18	57.49	98.32
	Centennial	39.55	32.64	56.39	67.22	47.27	96.34

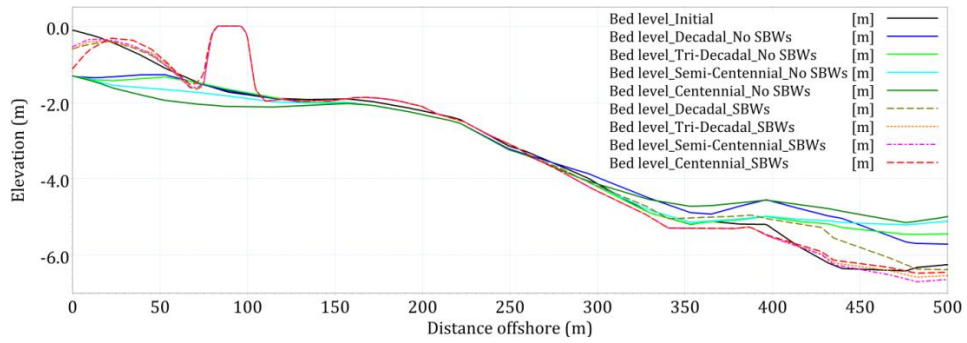


Figure E-17. Cross-shore changes of beach profile 5 due to different storms.

Table E-4. Hydrodynamic parameters at T4 point.

Scenario		V_c (m/s)	H_s (m)	S_{xx} (m^3/s^2)	S_{xy} (m^3/s^2)	S_{yy} (m^3/s^2)	Q ($m^3/s/m$)
No SBWs	NE	0.150	0.567	0.192	-0.050	0.133	7.56E-05
	E	0.083	0.556	0.187	-0.052	0.126	4.66E-05
	SE	0.077	0.538	0.179	-0.050	0.121	3.63E-05
	Winter	0.076	0.290	0.062	-0.019	0.046	2.34E-05
	Summer	0.069	0.151	0.018	-0.006	0.015	9.83E-06
	Decadal	0.114	0.937	0.482	-0.139	0.323	3.14E-04
	Tri-Decadal	0.175	0.976	0.501	-0.139	0.321	4.56E-04
	Semi-Centennial	0.358	1.029	0.566	-0.149	0.339	9.57E-04
	Centennial	0.415	1.196	0.742	-0.194	0.447	1.47E-03
SBWs	NE	0.047	0.177	0.017	-0.003	0.013	1.90E-06
	E	0.095	0.174	0.015	-0.003	0.012	3.74E-06
	SE	0.121	0.170	0.015	-0.003	0.012	4.68E-06
	Winter	0.064	0.127	0.009	-0.002	0.007	2.39E-06
	Summer	0.058	0.087	0.004	-0.001	0.004	1.97E-06
	Decadal	0.194	0.472	0.117	-0.024	0.088	1.70E-05
	Tri-Decadal	0.215	0.522	0.138	-0.029	0.102	2.23E-05
	Semi-Centennial	0.065	0.627	0.198	-0.040	0.143	1.02E-05
	Centennial	0.146	0.794	0.320	-0.066	0.230	2.67E-05
Difference (%)	NE	68.36	68.73	91.30	93.51	90.26	97.49
	E	-14.62	68.78	91.81	94.34	90.49	91.97
	SE	-57.92	68.34	91.86	94.42	90.51	87.11
	Winter	16.66	56.10	86.27	88.94	83.93	89.78
	Summer	16.11	42.46	78.06	81.69	75.39	79.97
	Decadal	-70.52	49.59	75.79	82.62	72.75	94.59
	Tri-Decadal	-22.93	46.57	72.45	79.18	68.07	95.11
	Semi-Centennial	81.93	39.07	64.98	73.22	57.70	98.93
	Centennial	64.78	33.57	56.96	65.72	48.50	98.18

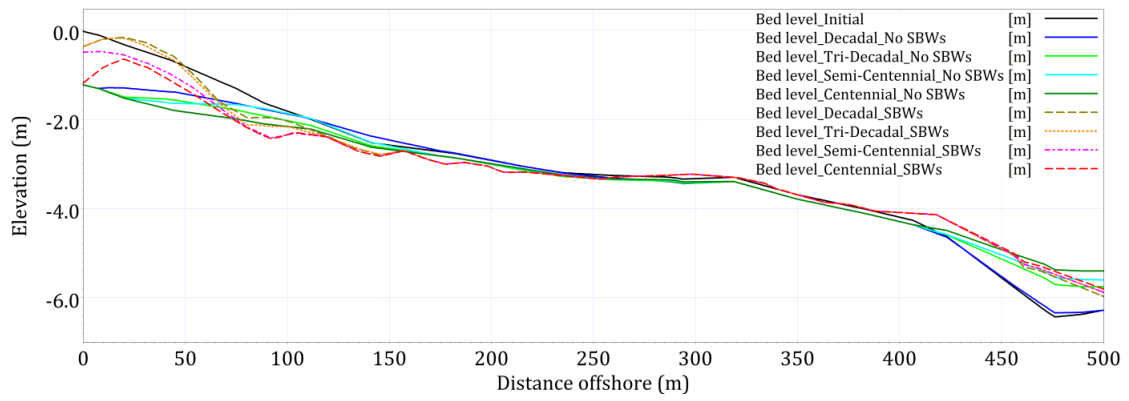


Figure E-18. Cross-shore changes of beach profile 6 due to different storms.

Table E-5. Hydrodynamic parameters at T5 point.

Scenario		V_c (m/s)	H_s (m)	S_{xx} (m^3/s^2)	S_{xy} (m^3/s^2)	S_{yy} (m^3/s^2)	Q ($m^3/s/m$)
No SBWs	NE	0.133	0.566	0.212	-0.056	0.126	4.28E-05
	E	0.081	0.558	0.208	-0.054	0.120	2.70E-05
	SE	0.098	0.537	0.195	-0.051	0.113	4.13E-05
	Winter	0.075	0.282	0.065	-0.019	0.042	2.04E-05
	Summer	0.068	0.142	0.017	-0.005	0.013	1.03E-05
	Decadal	0.158	0.931	0.524	-0.152	0.323	2.11E-04
	Tri-Decadal	0.214	0.958	0.533	-0.163	0.335	3.79E-04
	Semi-Centennial	0.191	1.055	0.622	-0.181	0.371	3.57E-04
	Centennial	0.353	1.206	0.804	-0.228	0.472	8.32E-04
SBWs	NE	0.051	0.163	0.013	-0.002	0.008	1.63E-07
	E	0.069	0.164	0.013	-0.002	0.008	2.01E-07
	SE	0.077	0.161	0.012	-0.002	0.008	2.21E-07
	Winter	0.044	0.122	0.007	-0.002	0.006	1.50E-07
	Summer	0.036	0.082	0.003	-0.001	0.003	4.57E-07
	Decadal	0.135	0.444	0.104	-0.023	0.069	7.82E-06
	Tri-Decadal	0.176	0.494	0.124	-0.030	0.084	1.21E-05
	Semi-Centennial	0.152	0.603	0.182	-0.047	0.125	1.38E-05
	Centennial	0.042	0.765	0.288	-0.075	0.200	1.45E-05
Difference (%)	NE	61.49	71.16	93.94	95.57	93.37	99.62
	E	14.79	70.67	93.84	95.46	93.15	99.26
	SE	21.18	69.94	93.58	95.38	92.86	99.47
	Winter	40.89	56.84	88.77	91.24	86.65	99.26
	Summer	47.04	42.24	81.59	84.96	77.42	95.57
	Decadal	14.56	52.36	80.23	84.62	78.68	96.29
	Tri-Decadal	17.69	48.45	76.77	81.56	74.99	96.80
	Semi-Centennial	20.68	42.79	70.72	74.11	66.21	96.14
	Centennial	87.99	36.58	64.20	66.97	57.61	98.26

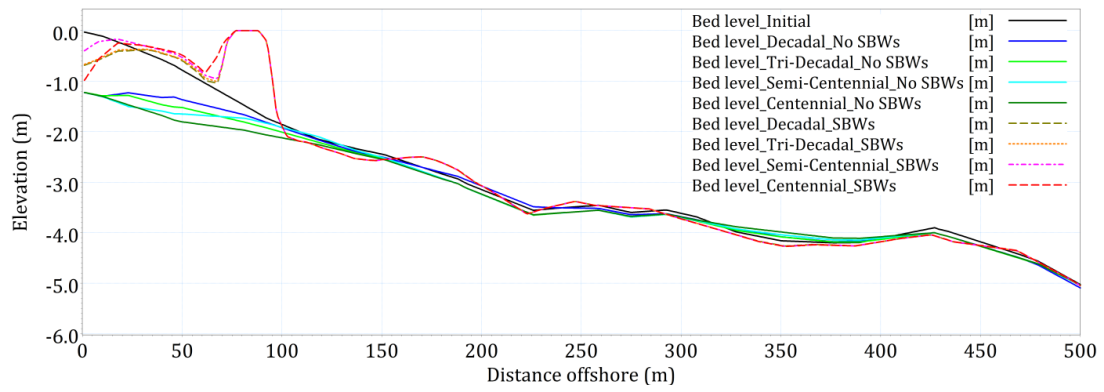


Figure E-19. Cross-shore changes of beach profile 7 due to different storms.

Table E-6. Hydrodynamic parameters at Q1 point.

Scenario		V_c (m/s)	H_s (m)	S_{xx} (m^3/s^2)	S_{xy} (m^3/s^2)	S_{yy} (m^3/s^2)	Q ($m^3/s/m$)
No SBWs	NE	0.137	0.608	0.224	-0.063	0.153	4.97E-05
	E	0.098	0.595	0.214	-0.061	0.147	3.32E-05
	SE	0.101	0.578	0.201	-0.057	0.139	4.17E-05
	Winter	0.082	0.294	0.067	-0.020	0.048	2.42E-05
	Summer	0.068	0.149	0.018	-0.006	0.014	1.07E-05
	Decadal	0.174	0.979	0.530	-0.153	0.360	2.23E-04
	Tri-Decadal	0.233	1.007	0.535	-0.157	0.360	2.82E-04
	Semi-Centennial	0.293	1.106	0.633	-0.177	0.408	4.33E-04
	Centennial	0.286	1.264	0.814	-0.226	0.517	4.92E-04
SBWs	NE	0.038	0.456	0.130	-0.046	0.089	1.41E-06
	E	0.056	0.470	0.136	-0.048	0.093	2.88E-06
	SE	0.102	0.468	0.134	-0.048	0.094	1.12E-05
	Winter	0.058	0.224	0.041	-0.015	0.028	2.77E-06
	Summer	0.053	0.116	0.011	-0.004	0.008	1.89E-06
	Decadal	0.078	0.759	0.338	-0.112	0.225	1.84E-05
	Tri-Decadal	0.118	0.765	0.331	-0.107	0.218	3.00E-05
	Semi-Centennial	0.262	0.817	0.375	-0.111	0.235	6.62E-05
	Centennial	0.271	0.953	0.497	-0.137	0.315	9.85E-05
Difference (%)	NE	71.97	25.07	42.25	26.92	41.65	97.16
	E	43.22	20.92	36.28	20.24	36.51	91.35
	SE	-1.24	18.89	33.24	15.41	32.36	73.20
	Winter	29.50	23.74	39.14	27.99	40.88	88.56
	Summer	21.45	22.64	39.10	35.90	44.38	82.41
	Decadal	55.14	22.50	36.32	26.66	37.33	91.76
	Tri-Decadal	49.53	24.03	38.10	31.82	39.48	89.39
	Semi-Centennial	10.54	26.15	40.86	37.53	42.41	84.72
	Centennial	5.16	24.63	38.98	39.46	39.04	79.98

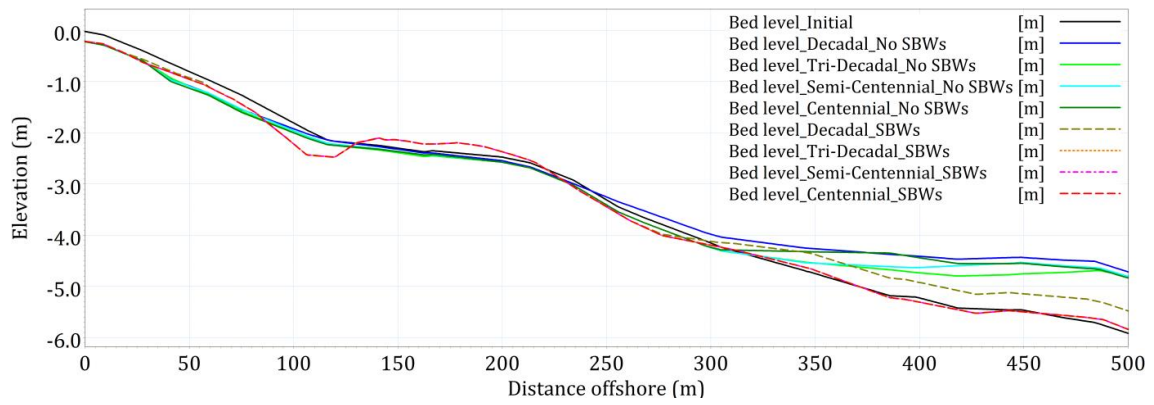


Figure E-20. Cross-shore changes of beach profile 8 due to different storms.

Table E-7. Hydrodynamic parameters at Q2 point.

Scenario		V_c (m/s)	H_s (m)	S_{xx} (m^3/s^2)	S_{xy} (m^3/s^2)	S_{yy} (m^3/s^2)	Q ($m^3/s/m$)
No SBWs	NE	0.174	0.588	0.219	-0.049	0.133	7.43E-05
	E	0.100	0.595	0.218	-0.048	0.133	5.48E-05
	SE	0.107	0.552	0.195	-0.044	0.124	5.15E-05
	Winter	0.089	0.291	0.066	-0.018	0.045	2.84E-05
	Summer	0.076	0.150	0.018	-0.006	0.015	1.15E-05
	Decadal	0.190	0.951	0.538	-0.135	0.323	2.93E-04
	Tri-Decadal	0.269	0.993	0.571	-0.148	0.329	4.24E-04
	Semi-Centennial	0.375	1.105	0.677	-0.174	0.378	9.18E-04
	Centennial	0.387	1.262	0.853	-0.218	0.479	1.07E-03
SBWs	NE	0.034	0.434	0.118	-0.040	0.081	1.92E-06
	E	0.083	0.454	0.132	-0.043	0.087	8.71E-06
	SE	0.143	0.445	0.124	-0.042	0.087	1.75E-05
	Winter	0.060	0.219	0.041	-0.014	0.028	2.96E-06
	Summer	0.054	0.112	0.010	-0.004	0.008	1.87E-06
	Decadal	0.177	0.799	0.383	-0.127	0.257	6.12E-05
	Tri-Decadal	0.056	0.839	0.414	-0.133	0.267	2.71E-05
	Semi-Centennial	0.241	0.886	0.450	-0.132	0.271	9.05E-05
	Centennial	0.275	1.011	0.571	-0.159	0.347	1.27E-04
Difference (%)	NE	80.54	26.16	45.81	18.65	39.11	97.41
	E	16.80	23.69	39.30	10.61	34.71	84.11
	SE	-33.91	19.31	36.05	4.77	29.69	66.12
	Winter	32.38	24.72	38.49	22.26	37.56	89.59
	Summer	28.53	25.70	45.38	39.41	47.64	83.77
	Decadal	6.71	15.93	28.84	6.19	20.44	79.11
	Tri-Decadal	79.08	15.53	27.56	10.40	18.96	93.61
	Semi-Centennial	35.66	19.82	33.57	23.73	28.37	90.14
	Centennial	29.03	19.85	33.00	26.91	27.58	88.18

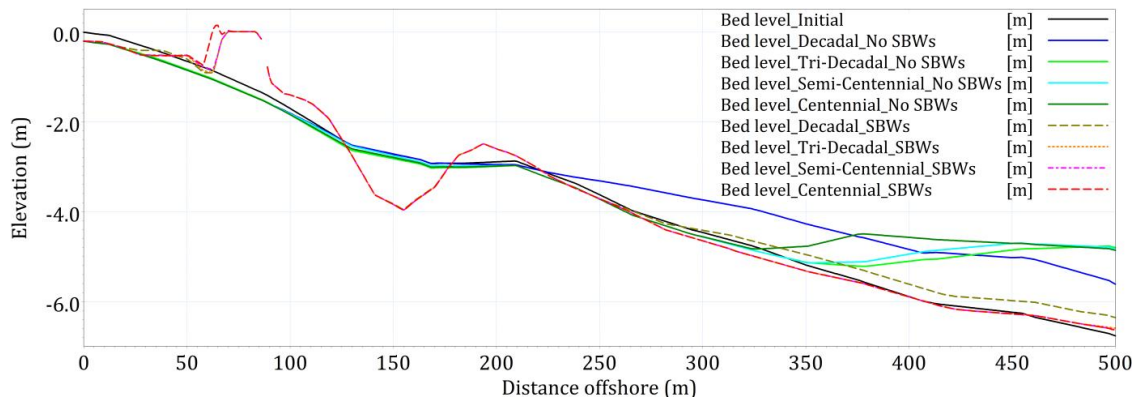


Figure E-21. Cross-shore changes of beach profile 9 due to different storms.

Table E-8. Hydrodynamic parameters at Q3 point.

Scenario		V_c (m/s)	H_s (m)	S_{xx} (m^3/s^2)	S_{xy} (m^3/s^2)	S_{yy} (m^3/s^2)	Q ($m^3/s/m$)
No SBWs	NE	0.157	0.573	0.203	-0.046	0.130	7.39E-05
	E	0.079	0.560	0.194	-0.047	0.121	4.03E-05
	SE	0.088	0.534	0.181	-0.043	0.113	4.18E-05
	Winter	0.079	0.287	0.062	-0.017	0.044	2.49E-05
	Summer	0.072	0.148	0.018	-0.005	0.014	1.06E-05
	Decadal	0.141	0.925	0.484	-0.126	0.309	2.84E-04
	Tri-Decadal	0.222	0.966	0.503	-0.134	0.314	4.03E-04
	Semi-Centennial	0.371	1.046	0.574	-0.151	0.351	9.81E-04
	Centennial	0.404	1.214	0.748	-0.196	0.457	1.34E-03
SBWs	NE	0.092	0.498	0.165	-0.045	0.101	6.05E-06
	E	0.152	0.502	0.162	-0.049	0.106	1.50E-05
	SE	0.173	0.496	0.154	-0.049	0.106	2.08E-05
	Winter	0.076	0.246	0.050	-0.015	0.033	4.99E-06
	Summer	0.063	0.125	0.014	-0.004	0.010	2.55E-06
	Decadal	0.229	0.802	0.388	-0.120	0.252	7.04E-05
	Tri-Decadal	0.174	0.836	0.407	-0.120	0.256	7.23E-05
	Semi-Centennial	0.161	0.916	0.468	-0.124	0.272	1.07E-04
	Centennial	0.237	1.037	0.585	-0.144	0.330	1.54E-04
Difference (%)	NE	41.16	13.15	18.82	2.89	22.09	91.82
	E	-93.05	10.36	16.45	-4.47	11.99	62.87
	SE	-95.85	7.17	15.05	-14.75	6.50	50.12
	Winter	3.42	14.18	19.02	9.28	23.78	79.93
	Summer	12.20	15.08	21.08	19.73	30.63	75.90
	Decadal	-62.70	13.34	19.84	4.98	18.36	75.20
	Tri-Decadal	21.91	13.39	19.00	10.33	18.22	82.08
	Semi-Centennial	56.68	12.40	18.56	17.88	22.47	89.06
	Centennial	41.26	14.58	21.74	26.69	27.94	88.54

Table E-9. Hydrodynamic parameters at Q4 point.

	Scenario	V _c (m/s)	H _s (m)	S _{xx} (m ³ /s ²)	S _{xy} (m ³ /s ²)	S _{yy} (m ³ /s ²)	Q (m ³ /s/m)
No SBWs	NE	0.123	0.552	0.197	-0.051	0.122	5.19E-05
	E	0.088	0.544	0.191	-0.052	0.119	4.05E-05
	SE	0.086	0.510	0.171	-0.047	0.108	4.22E-05
	Winter	0.080	0.273	0.059	-0.018	0.040	2.34E-05
	Summer	0.068	0.138	0.016	-0.005	0.012	1.05E-05
	Decadal	0.164	0.913	0.480	-0.141	0.312	2.59E-04
	Tri-Decadal	0.200	0.941	0.487	-0.144	0.318	3.82E-04
	Semi-Centennial	0.264	1.003	0.552	-0.156	0.342	5.48E-04
	Centennial	0.361	1.169	0.737	-0.202	0.450	9.67E-04
SBWs	NE	0.110	0.517	0.175	-0.049	0.104	4.84E-06
	E	0.149	0.522	0.176	-0.049	0.104	6.08E-06
	SE	0.163	0.512	0.169	-0.048	0.101	8.04E-06
	Winter	0.075	0.236	0.048	-0.014	0.030	3.97E-06
	Summer	0.055	0.113	0.012	-0.004	0.008	2.69E-06
	Decadal	0.225	0.807	0.387	-0.122	0.250	9.34E-05
	Tri-Decadal	0.262	0.830	0.388	-0.126	0.260	1.23E-04
	Semi-Centennial	0.202	0.915	0.449	-0.139	0.298	1.05E-04
	Centennial	0.162	1.065	0.595	-0.170	0.385	1.46E-04
Difference (%)	NE	11.00	6.28	11.05	3.73	14.59	90.68
	E	-69.63	4.08	7.64	5.40	12.86	84.98
	SE	-89.92	-0.43	1.22	-2.17	6.08	80.94
	Winter	6.04	13.80	18.69	17.76	24.83	83.03
	Summer	18.24	17.61	26.02	28.24	33.36	74.48
	Decadal	-36.95	11.55	19.30	13.59	19.83	63.88
	Tri-Decadal	-31.22	11.82	20.36	12.69	18.16	67.82
	Semi-Centennial	23.65	8.75	18.65	10.90	12.75	80.78
	Centennial	55.30	8.91	19.26	15.73	14.38	84.91

E.2. Bona beach

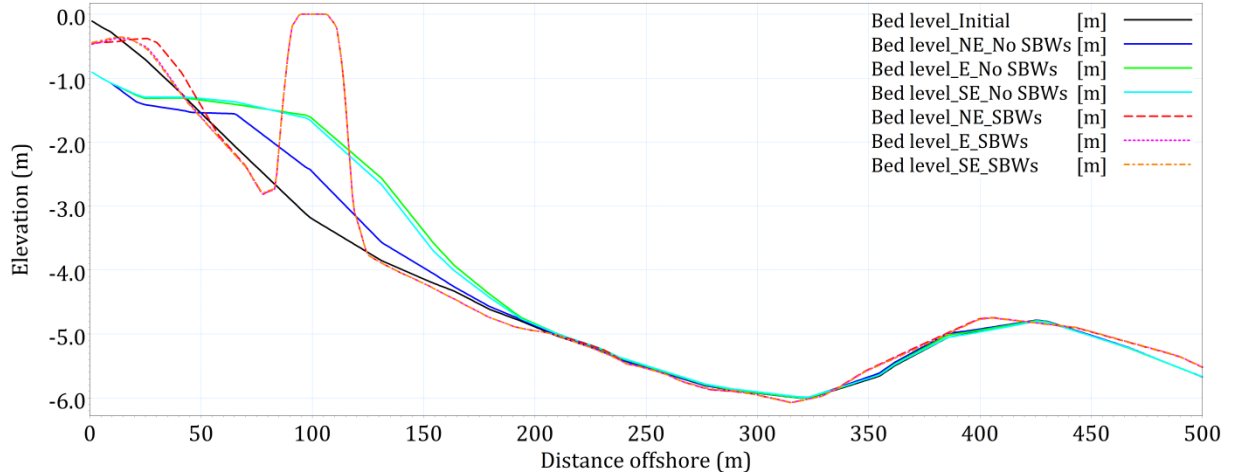


Figure E-22. Cross-shore changes of beach profile 10 due to different wind directions.

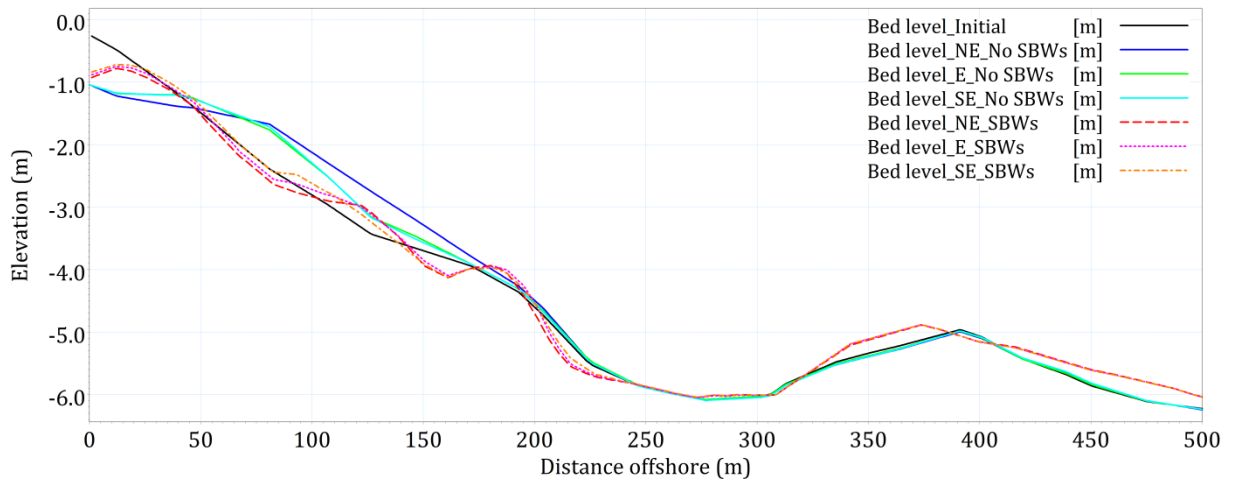


Figure E-23. Cross-shore changes of beach profile 11 due to different wind directions.

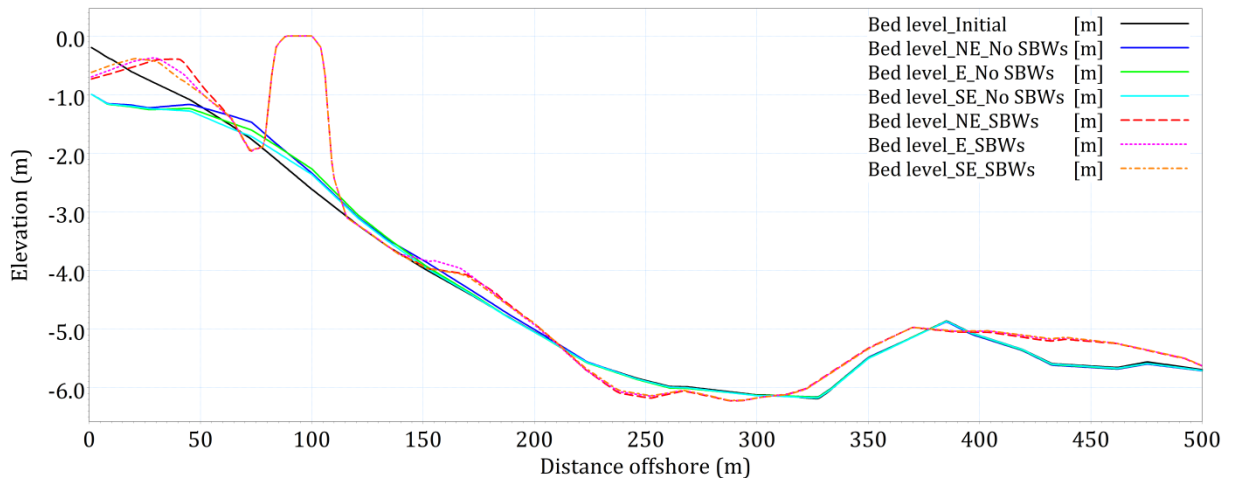


Figure E-24. Cross-shore changes of beach profile 12 due to different wind directions.

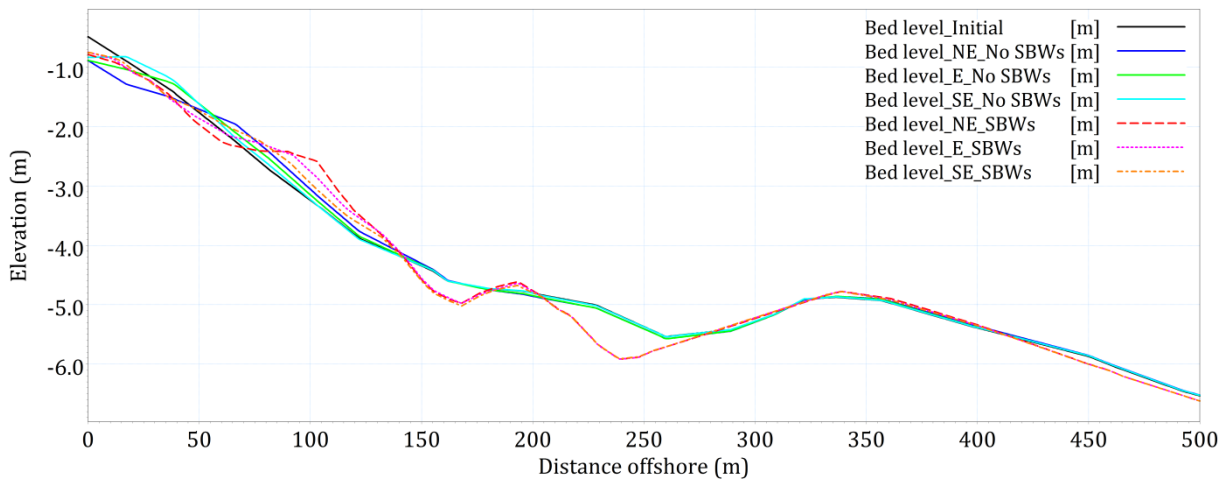


Figure E-25. Cross-shore changes of beach profile 13 due to different wind directions.

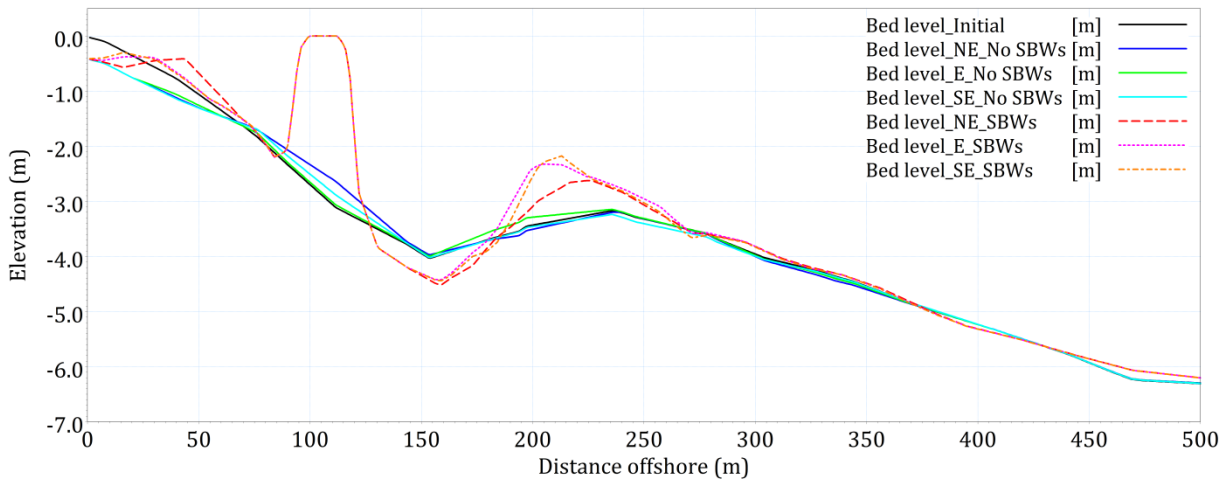


Figure E-26. Cross-shore changes of beach profile 14 due to different wind directions.

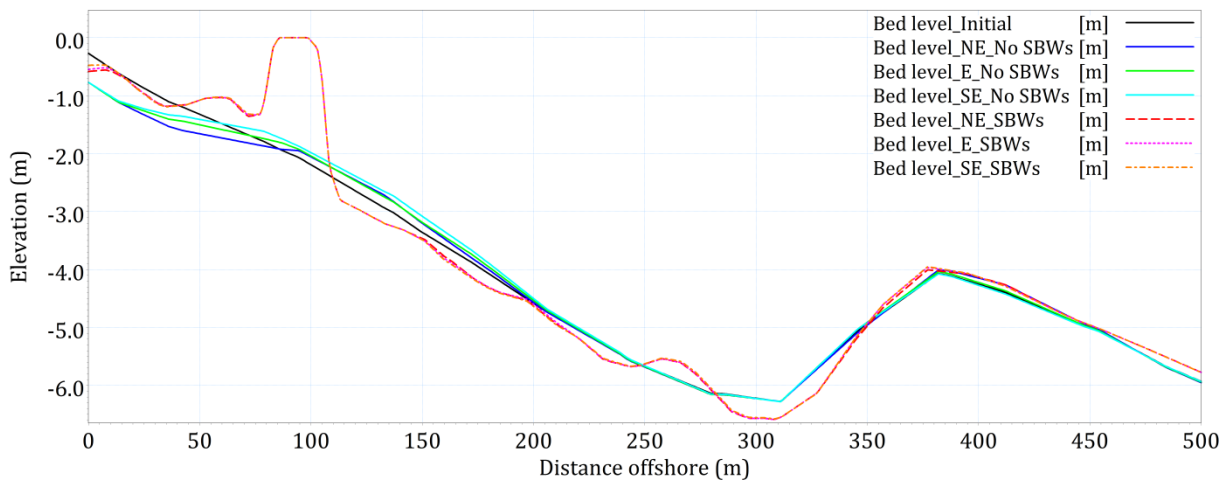


Figure E-27. Cross-shore changes of beach profile 15 due to different wind directions.

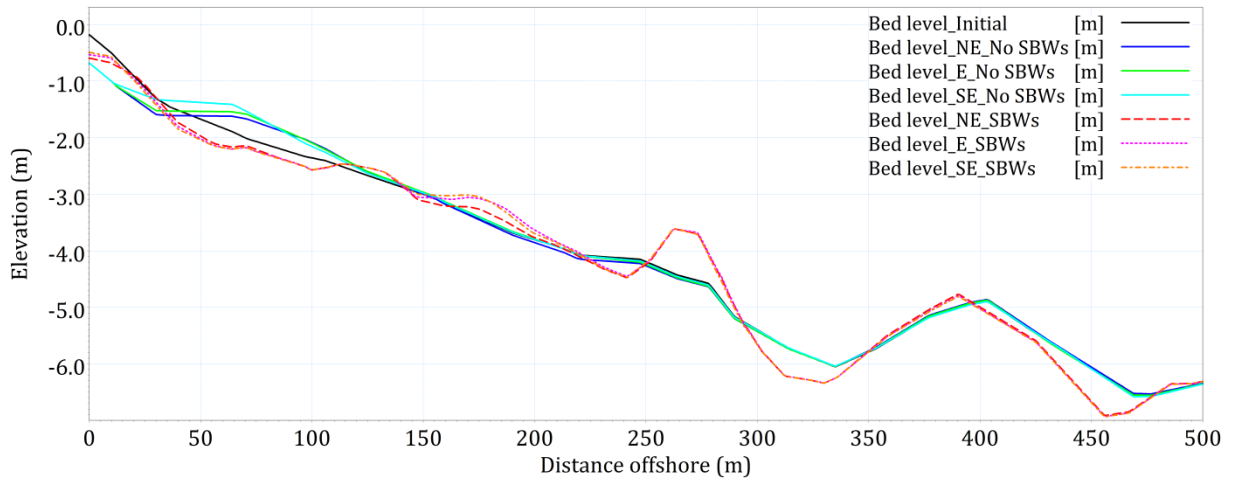


Figure E-28. Cross-shore changes of beach profile 16 due to different wind directions.

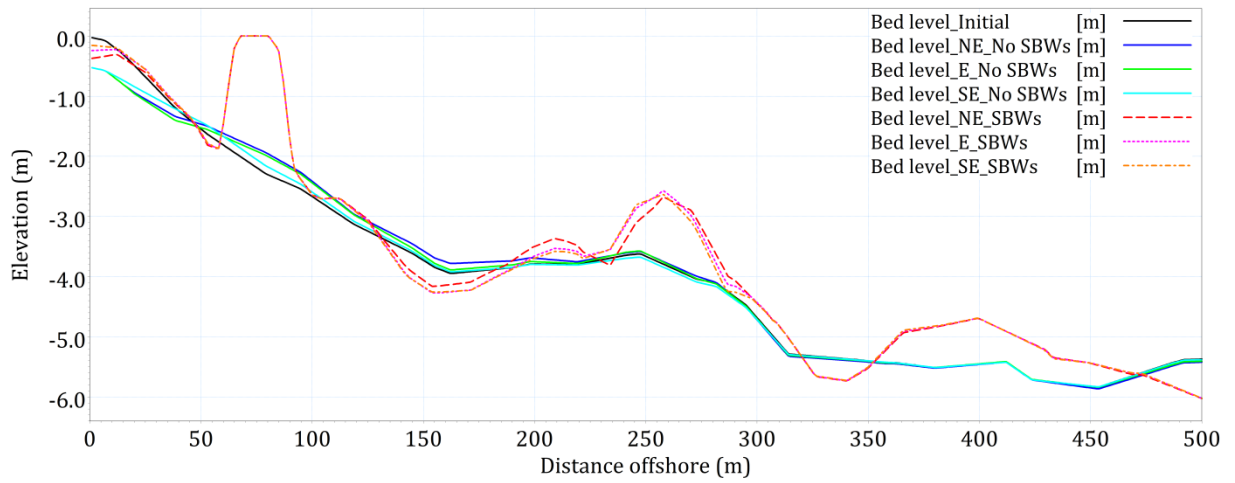


Figure E-29. Cross-shore changes of beach profile 17 due to different wind directions.

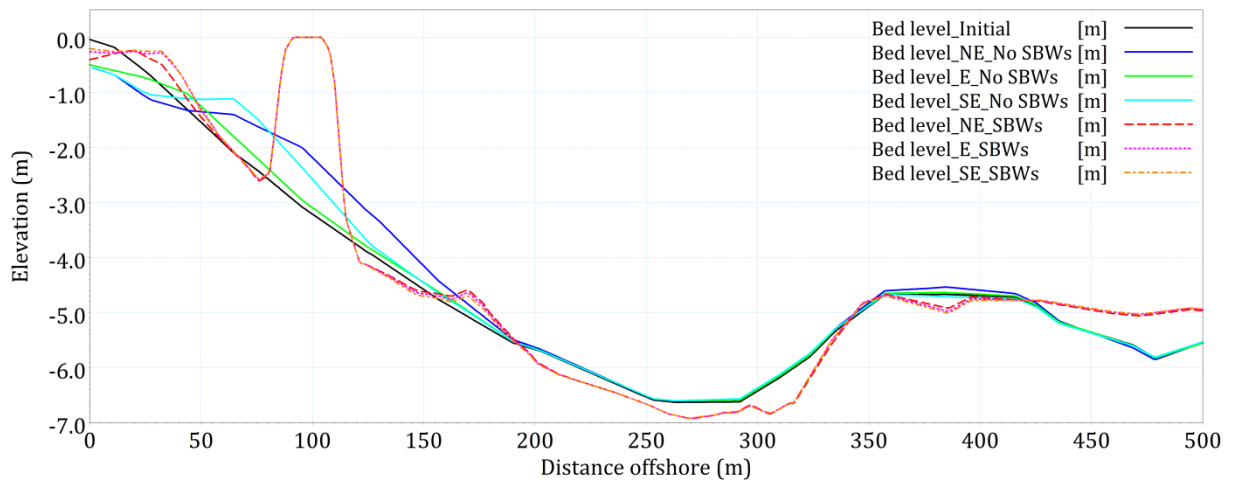


Figure E-30. Cross-shore changes of beach profile 18 due to different wind directions.

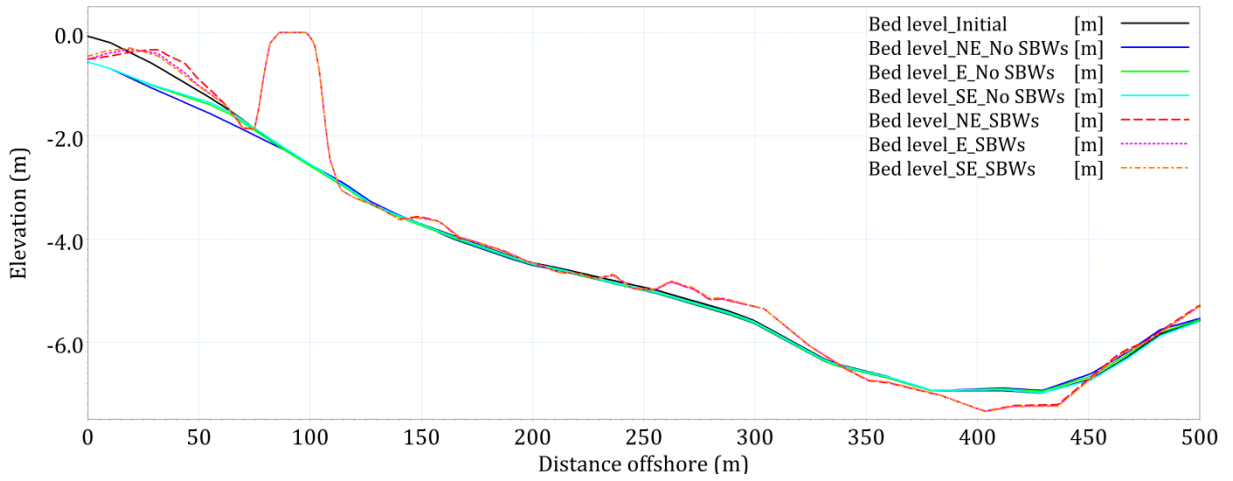


Figure E-31. Cross-shore changes of beach profile 19 due to different wind directions.

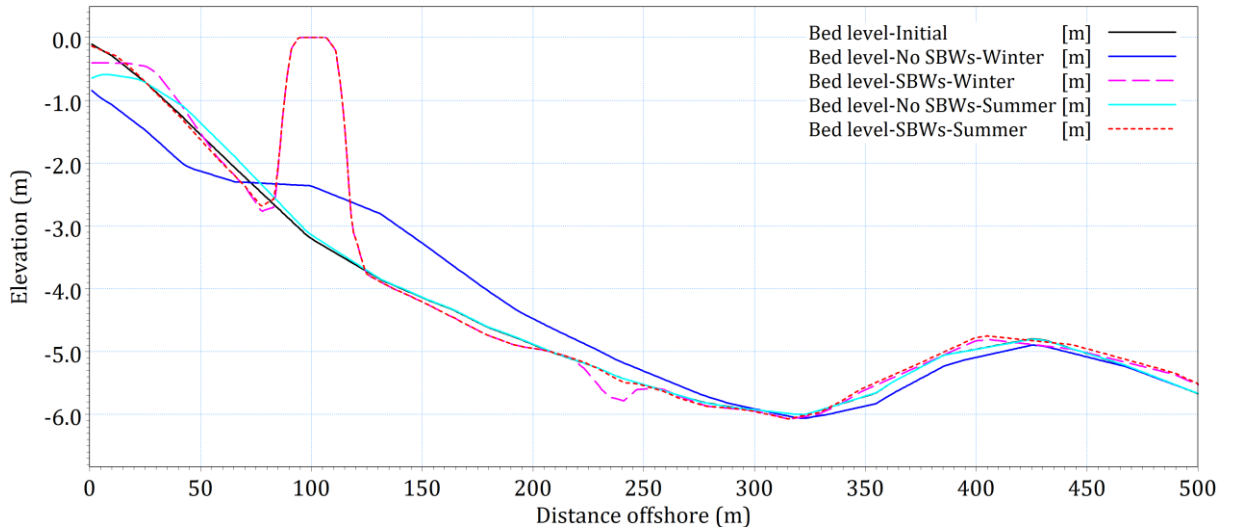


Figure E-32. Cross-shore changes of beach profile 10 due to seasonal variation.

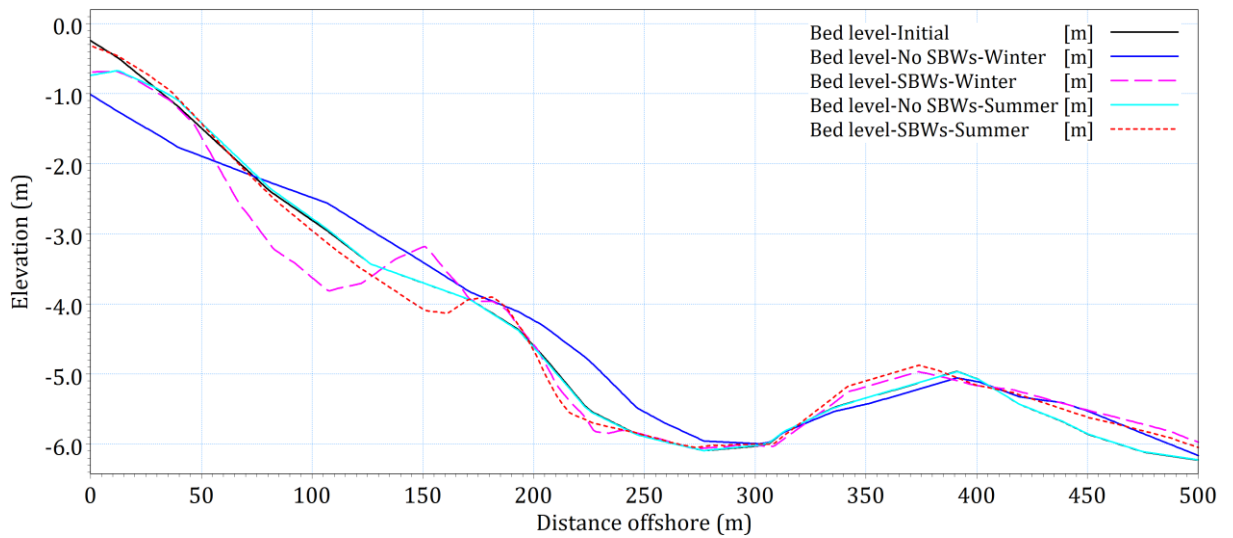


Figure E-33. Cross-shore changes of beach profile 11 due to seasonal variation.

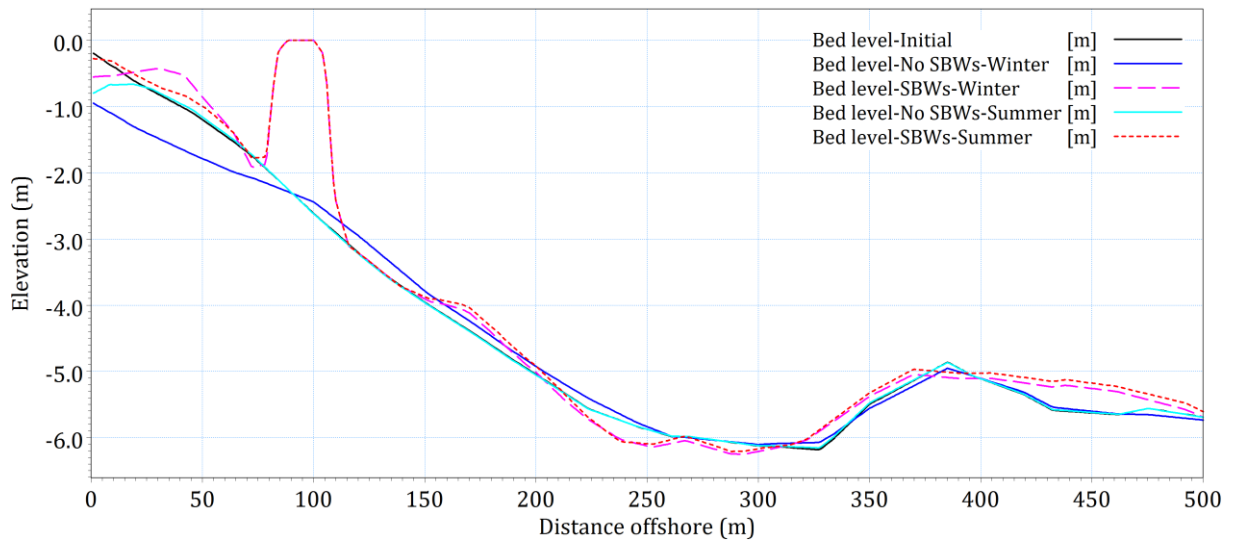


Figure E-34. Cross-shore changes of beach profile 12 due to seasonal variation.

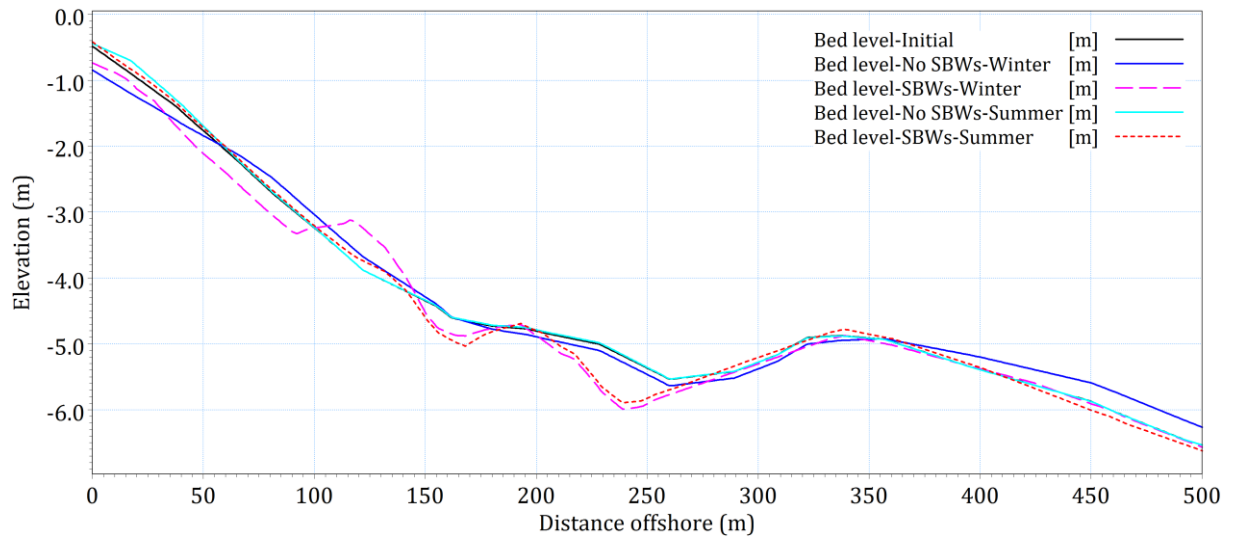


Figure E-35. Cross-shore changes of beach profile 13 due to seasonal variation.

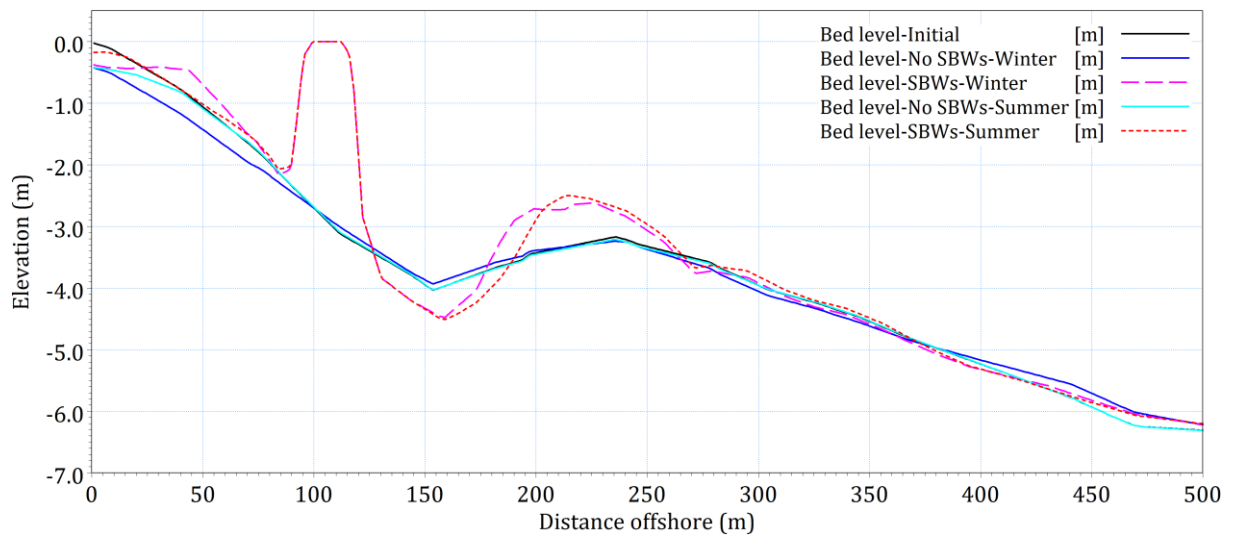


Figure E-36. Cross-shore changes of beach profile 14 due to seasonal variation.

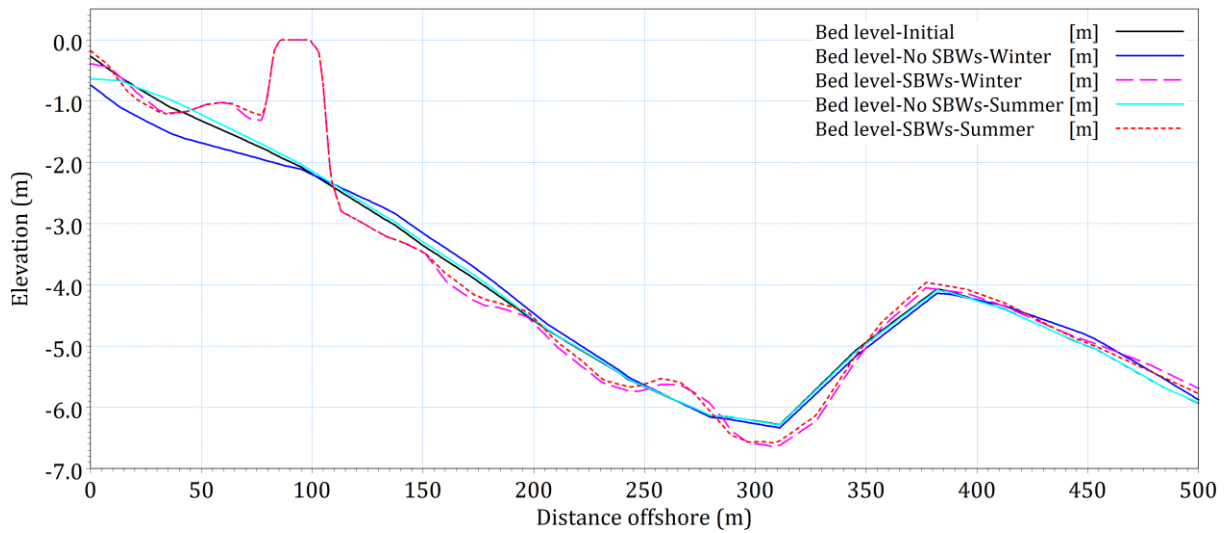


Figure E-37. Cross-shore changes of beach profile 15 due to seasonal variation.

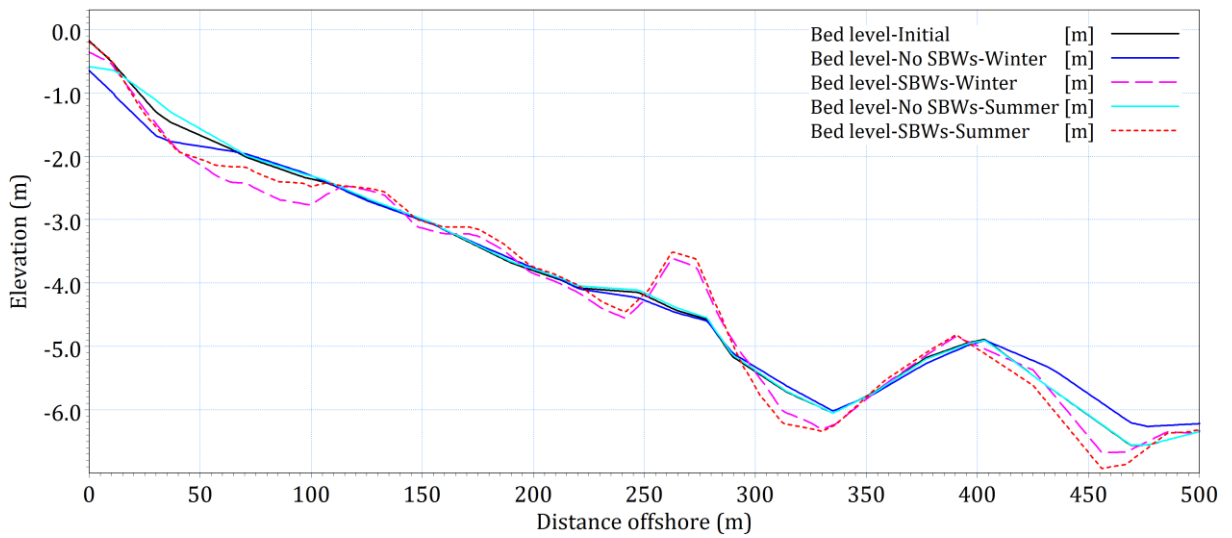


Figure E-38. Cross-shore changes of beach profile 16 due to seasonal variation.

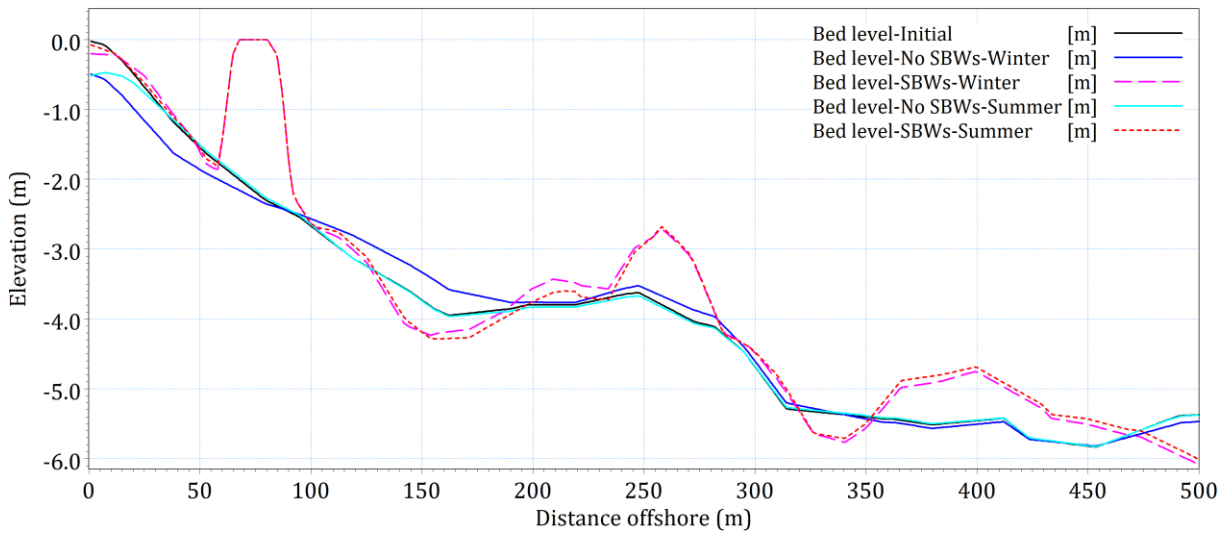


Figure E-39. Cross-shore changes of beach profile 17 due to seasonal variation.

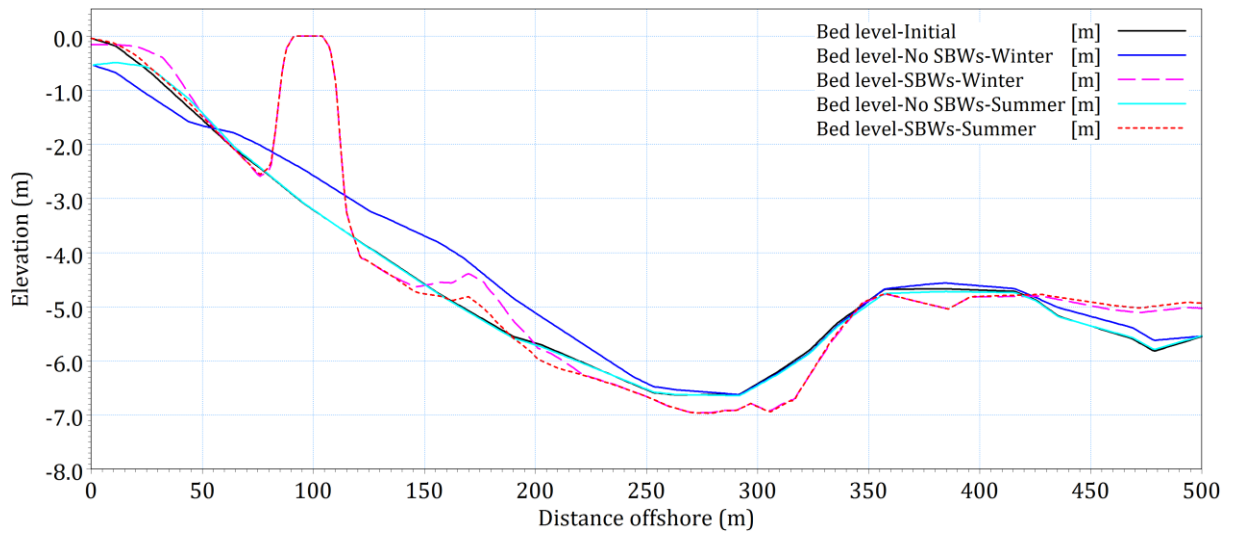


Figure E-40. Cross-shore changes of beach profile 18 due to seasonal variation.

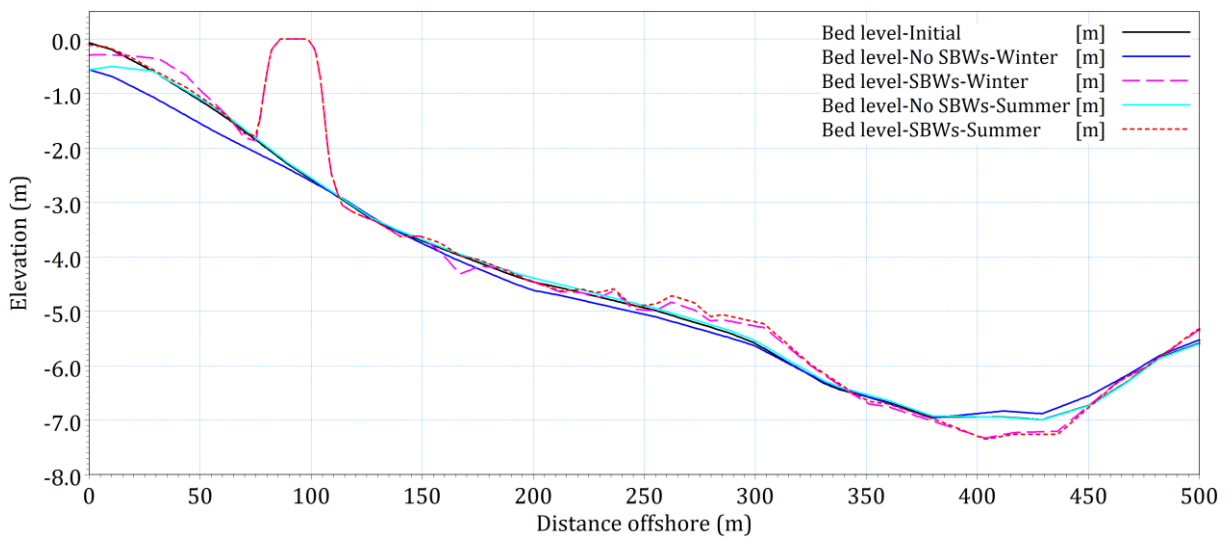


Figure E-41. Cross-shore changes of beach profile 19 due to seasonal variation.

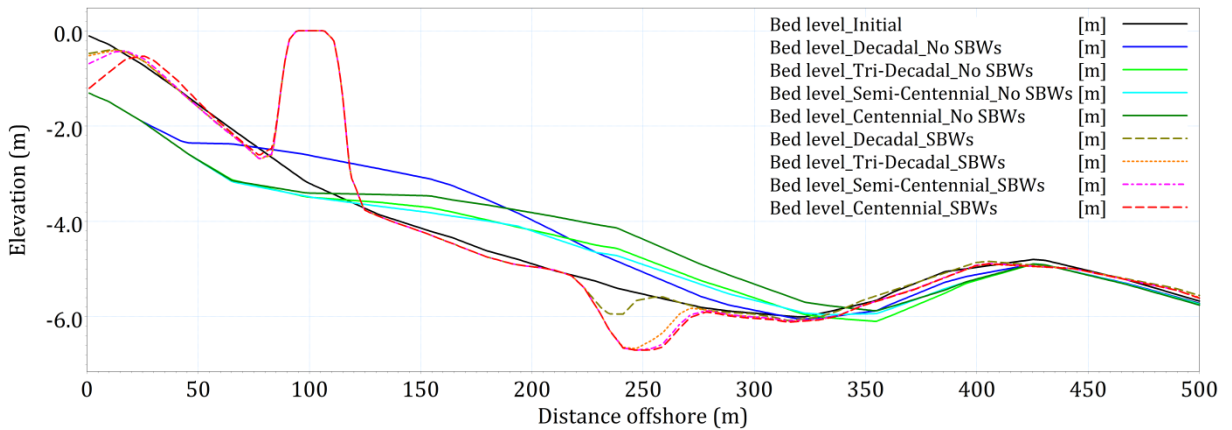


Figure E-42. Cross-shore changes of beach profile 10 due to different storms.

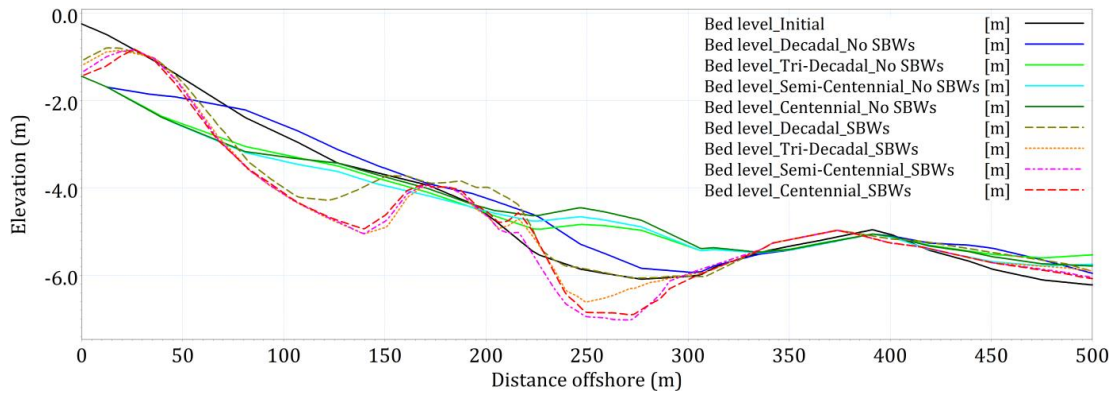


Figure E-43. Cross-shore changes of beach profile 11 due to different storms.

Table E-10. Hydrodynamic parameters at T6 point.

Scenario		V_c (m/s)	H_s (m)	S_{xx} (m^3/s^2)	S_{xy} (m^3/s^2)	S_{yy} (m^3/s^2)	Q ($m^3/s/m$)
No SBWs	NE	0.065	0.649	0.310	-0.038	0.142	2.95E-05
	E	0.144	0.643	0.294	-0.043	0.138	7.39E-05
	SE	0.147	0.616	0.270	-0.040	0.127	7.28E-05
	Winter	0.044	0.279	0.085	-0.014	0.040	2.43E-05
	Summer	0.047	0.126	0.017	-0.004	0.009	8.42E-06
	Decadal	0.228	1.125	0.870	-0.125	0.394	4.77E-04
	Tri-Decadal	0.250	1.262	1.061	-0.145	0.460	5.46E-04
	Semi-Centennial	0.244	1.345	1.168	-0.160	0.501	5.85E-04
	Centennial	0.243	1.474	1.353	-0.191	0.599	6.61E-04
SBWs	NE	0.076	0.234	0.035	-0.007	0.024	5.34E-06
	E	0.058	0.219	0.031	-0.006	0.020	3.10E-06
	SE	0.060	0.207	0.028	-0.005	0.018	2.95E-06
	Winter	0.046	0.126	0.013	-0.003	0.008	2.73E-06
	Summer	0.035	0.067	0.003	-0.001	0.002	1.15E-06
	Decadal	0.083	0.545	0.188	-0.032	0.112	1.07E-05
	Tri-Decadal	0.085	0.608	0.229	-0.037	0.133	1.28E-05
	Semi-Centennial	0.091	0.709	0.307	-0.045	0.173	1.66E-05
	Centennial	0.122	0.888	0.474	-0.066	0.268	4.74E-05
Difference (%)	NE	-15.79	63.86	88.65	81.79	83.23	81.91
	E	59.73	65.96	89.51	85.85	85.45	95.81
	SE	59.23	66.33	89.68	87.11	86.17	95.95
	Winter	-4.40	54.91	84.58	79.13	79.06	88.76
	Summer	25.79	46.99	79.68	80.38	77.81	86.36
	Decadal	63.59	51.61	78.34	74.03	71.63	97.76
	Tri-Decadal	66.13	51.82	78.39	74.65	71.18	97.65
	Semi-Centennial	62.56	47.32	73.72	71.61	65.46	97.17
	Centennial	50.07	39.76	64.93	65.33	55.23	92.84

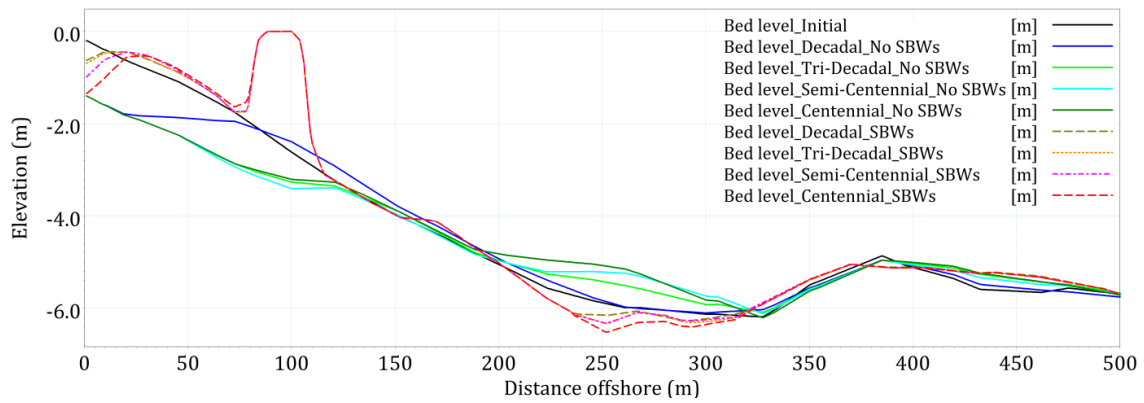


Figure E-44. Cross-shore changes of beach profile 12 due to different storms.

Table E-11. Hydrodynamic parameters at T7 point.

Scenario		V_c (m/s)	H_s (m)	S_{xx} (m^3/s^2)	S_{xy} (m^3/s^2)	S_{yy} (m^3/s^2)	Q ($m^3/s/m$)
No SBWs	NE	0.108	0.667	0.316	-0.024	0.152	5.53E-05
	E	0.169	0.649	0.303	-0.025	0.142	7.70E-05
	SE	0.182	0.622	0.280	-0.023	0.131	7.69E-05
	Winter	0.066	0.285	0.084	-0.008	0.040	2.62E-05
	Summer	0.059	0.137	0.019	-0.003	0.010	9.38E-06
	Decadal	0.264	1.083	0.811	-0.055	0.363	4.17E-04
	Tri-Decadal	0.279	1.214	0.983	-0.058	0.418	4.57E-04
	Semi-Centennial	0.262	1.303	1.097	-0.070	0.463	4.60E-04
	Centennial	0.267	1.438	1.290	-0.099	0.561	5.23E-04
SBWs	NE	0.099	0.276	0.044	-0.010	0.038	8.46E-06
	E	0.107	0.258	0.040	-0.009	0.032	7.16E-06
	SE	0.108	0.240	0.035	-0.007	0.027	6.13E-06
	Winter	0.063	0.141	0.015	-0.003	0.011	3.99E-06
	Summer	0.051	0.075	0.004	-0.001	0.003	1.72E-06
	Decadal	0.113	0.582	0.205	-0.028	0.140	1.41E-05
	Tri-Decadal	0.108	0.643	0.245	-0.029	0.163	1.58E-05
	Semi-Centennial	0.109	0.744	0.327	-0.034	0.209	2.21E-05
	Centennial	0.127	0.914	0.486	-0.045	0.303	4.19E-05
Difference (%)	NE	8.29	58.58	85.94	59.70	74.62	84.70
	E	36.45	60.30	86.85	64.36	77.56	90.70
	SE	40.25	61.38	87.48	68.92	79.54	92.03
	Winter	4.10	50.50	81.77	66.09	71.15	84.79
	Summer	13.92	45.17	77.72	72.24	72.21	81.66
	Decadal	57.02	46.31	74.75	49.39	61.52	96.62
	Tri-Decadal	61.40	47.07	75.03	50.09	60.87	96.55
	Semi-Centennial	58.29	42.91	70.23	51.10	54.97	95.19
	Centennial	52.24	36.47	62.32	55.00	46.02	91.98

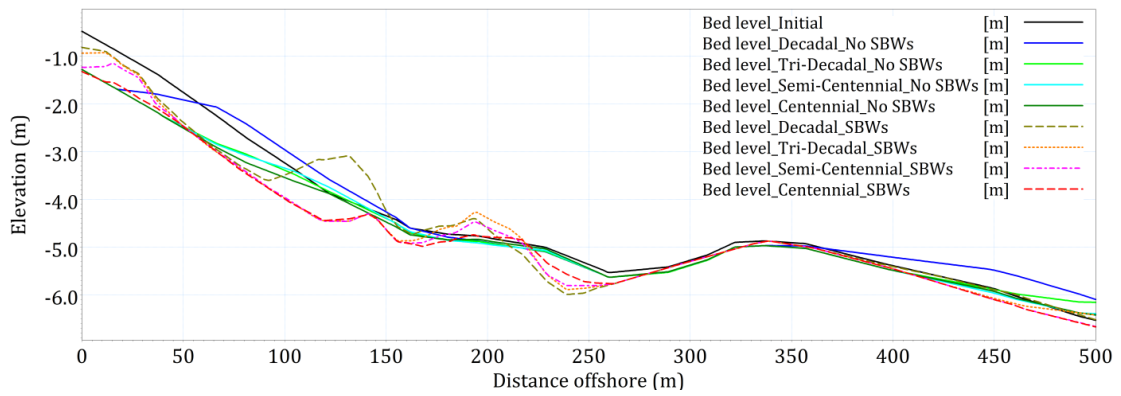


Figure E-45. Cross-shore changes of beach profile 13 due to different storms.

Table E-12. Hydrodynamic parameters at T8 point.

Scenario		V_c (m/s)	H_s (m)	S_{xx} (m^3/s^2)	S_{xy} (m^3/s^2)	S_{yy} (m^3/s^2)	Q ($m^3/s/m$)
No SBWs	NE	0.059	0.663	0.319	-0.027	0.149	1.37E-05
	E	0.077	0.638	0.296	-0.023	0.137	2.19E-05
	SE	0.082	0.625	0.283	-0.023	0.132	2.44E-05
	Winter	0.045	0.281	0.082	-0.008	0.039	1.17E-05
	Summer	0.040	0.135	0.018	-0.003	0.009	5.71E-06
	Decadal	0.159	1.066	0.783	-0.056	0.358	1.55E-04
	Tri-Decadal	0.171	1.155	0.894	-0.060	0.396	1.65E-04
	Semi-Centennial	0.167	1.245	1.002	-0.078	0.446	1.84E-04
	Centennial	0.150	1.392	1.212	-0.097	0.543	1.93E-04
SBWs	NE	0.067	0.271	0.041	-0.010	0.036	5.32E-06
	E	0.052	0.258	0.038	-0.009	0.032	2.48E-06
	SE	0.053	0.248	0.035	-0.008	0.029	2.35E-06
	Winter	0.049	0.147	0.016	-0.003	0.012	3.04E-06
	Summer	0.040	0.080	0.005	-0.001	0.003	1.27E-06
	Decadal	0.073	0.561	0.185	-0.028	0.128	5.72E-06
	Tri-Decadal	0.077	0.619	0.221	-0.033	0.150	6.82E-06
	Semi-Centennial	0.082	0.721	0.298	-0.041	0.193	8.27E-06
	Centennial	0.101	0.900	0.461	-0.057	0.289	2.05E-05
Difference (%)	NE	-13.58	59.21	87.06	64.85	75.72	61.22
	E	31.93	59.55	87.25	60.87	76.51	88.64
	SE	34.70	60.43	87.62	62.51	77.85	90.37
	Winter	-9.02	47.73	80.82	54.32	68.57	74.07
	Summer	0.00	40.46	74.50	59.63	64.43	77.75
	Decadal	54.11	47.39	76.45	50.23	64.22	96.31
	Tri-Decadal	55.28	46.42	75.26	45.82	62.20	95.86
	Semi-Centennial	50.53	42.07	70.28	47.16	56.65	95.50
	Centennial	32.53	35.39	61.96	40.62	46.77	89.37

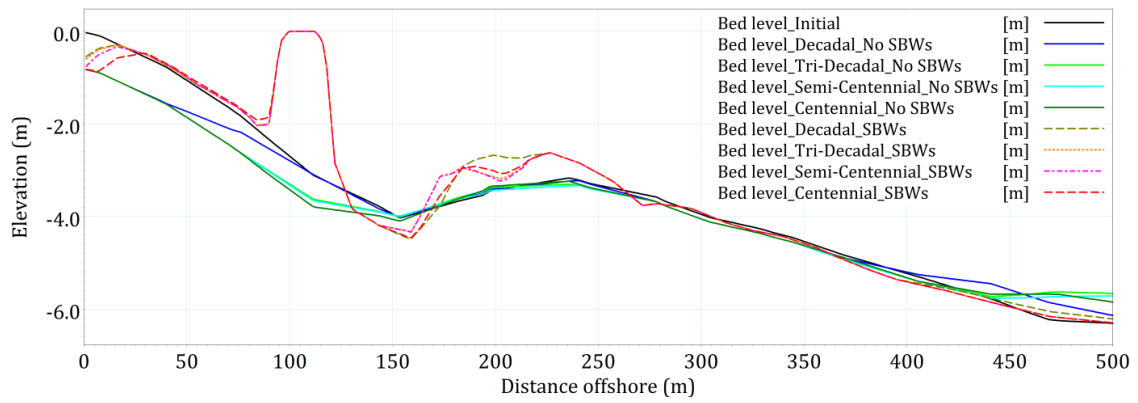


Figure E-46. Cross-shore changes of beach profile 14 due to different storms.

Table E-13. Hydrodynamic parameters at T9 point.

Scenario		V_c (m/s)	H_s (m)	S_{xx} (m^3/s^2)	S_{xy} (m^3/s^2)	S_{yy} (m^3/s^2)	Q ($m^3/s/m$)
No SBWs	NE	0.103	0.652	0.292	-0.039	0.150	2.38E-05
	E	0.084	0.629	0.270	-0.036	0.142	2.04E-05
	SE	0.043	0.607	0.250	-0.036	0.134	1.26E-05
	Winter	0.043	0.272	0.071	-0.012	0.038	1.07E-05
	Summer	0.042	0.136	0.016	-0.004	0.011	6.11E-06
	Decadal	0.105	1.014	0.667	-0.086	0.333	1.31E-04
	Tri-Decadal	0.091	1.095	0.767	-0.096	0.357	1.43E-04
	Semi-Centennial	0.103	1.173	0.861	-0.109	0.394	1.61E-04
	Centennial	0.082	1.335	1.068	-0.135	0.498	1.91E-04
SBWs	NE	0.099	0.271	0.036	-0.008	0.038	2.90E-06
	E	0.080	0.265	0.034	-0.008	0.036	2.24E-06
	SE	0.067	0.253	0.031	-0.008	0.033	1.71E-06
	Winter	0.035	0.142	0.012	-0.003	0.012	8.73E-07
	Summer	0.022	0.079	0.004	-0.001	0.004	4.03E-07
	Decadal	0.105	0.559	0.163	-0.029	0.130	6.21E-06
	Tri-Decadal	0.100	0.606	0.191	-0.031	0.142	6.55E-06
	Semi-Centennial	0.075	0.705	0.259	-0.040	0.179	7.96E-06
	Centennial	0.055	0.879	0.405	-0.061	0.266	2.04E-05
Difference (%)	NE	3.82	58.46	87.79	79.14	74.93	87.83
	E	5.27	57.92	87.55	77.53	74.58	89.00
	SE	-54.98	58.32	87.70	78.64	75.40	86.41
	Winter	18.62	47.83	82.77	75.66	69.02	91.86
	Summer	46.12	42.22	76.91	74.22	67.23	93.40
	Decadal	0.32	44.85	75.64	66.13	60.78	95.26
	Tri-Decadal	-10.59	44.66	75.11	67.93	60.18	95.43
	Semi-Centennial	27.43	39.86	69.92	63.14	54.45	95.06
	Centennial	33.60	34.14	62.04	54.75	46.64	89.31

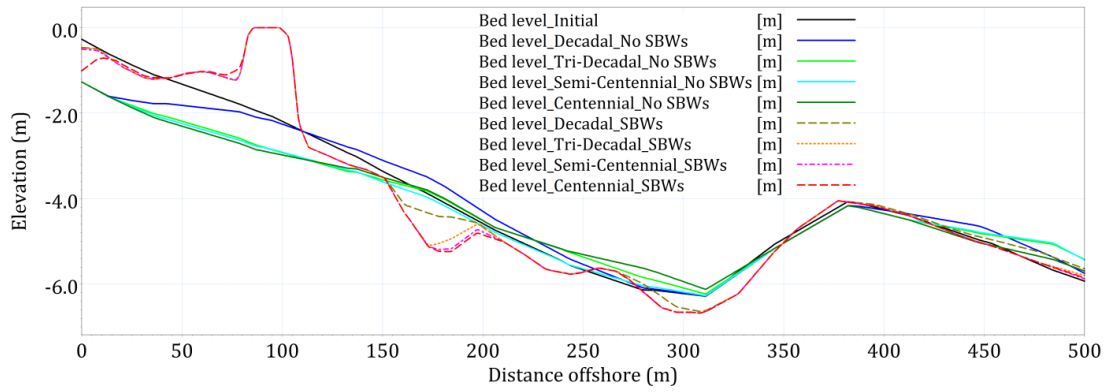


Figure E-47. Cross-shore changes of beach profile 15 due to different storms.

Table E-14. Hydrodynamic parameters at T10 point.

Scenario		V_c (m/s)	H_s (m)	S_{xx} (m^3/s^2)	S_{xy} (m^3/s^2)	S_{yy} (m^3/s^2)	Q ($m^3/s/m$)
No SBWs	NE	0.147	0.627	0.277	-0.026	0.132	3.92E-05
	E	0.073	0.595	0.250	-0.024	0.120	1.16E-05
	SE	0.060	0.560	0.225	-0.021	0.106	1.40E-05
	Winter	0.050	0.270	0.072	-0.009	0.036	1.31E-05
	Summer	0.063	0.134	0.017	-0.003	0.009	7.78E-06
	Decadal	0.130	0.994	0.642	-0.068	0.323	2.03E-04
	Tri-Decadal	0.127	1.067	0.722	-0.085	0.350	2.09E-04
	Semi-Centennial	0.117	1.158	0.819	-0.096	0.397	2.24E-04
	Centennial	0.103	1.324	1.024	-0.126	0.507	2.60E-04
SBWs	NE	0.099	0.202	0.024	-0.001	0.016	2.43E-06
	E	0.052	0.198	0.023	-0.001	0.016	1.29E-06
	SE	0.038	0.190	0.021	-0.001	0.015	8.03E-07
	Winter	0.045	0.121	0.010	-0.001	0.007	9.85E-07
	Summer	0.046	0.070	0.003	0.000	0.002	8.68E-07
	Decadal	0.068	0.497	0.143	-0.011	0.094	2.58E-06
	Tri-Decadal	0.054	0.553	0.172	-0.014	0.113	1.70E-06
	Semi-Centennial	0.060	0.658	0.239	-0.020	0.154	2.31E-06
	Centennial	0.069	0.835	0.382	-0.033	0.241	9.31E-06
Difference (%)	NE	32.59	67.86	91.46	96.27	87.57	93.80
	E	28.11	66.78	90.77	94.97	86.82	88.87
	SE	37.33	66.02	90.52	93.62	86.24	94.28
	Winter	11.36	55.06	85.72	90.17	81.20	92.48
	Summer	26.31	47.43	79.35	84.27	76.60	88.84
	Decadal	48.23	49.99	77.81	84.08	70.84	98.73
	Tri-Decadal	57.48	48.15	76.22	83.41	67.67	99.19
	Semi-Centennial	49.04	43.17	70.77	79.26	61.19	98.97
	Centennial	32.87	36.91	62.64	73.68	52.34	96.42

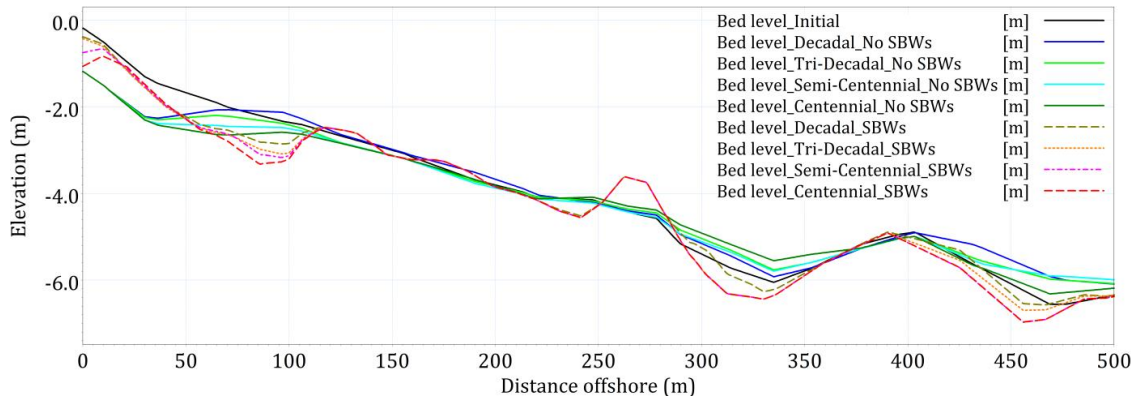


Figure E-48. Cross-shore changes of beach profile 16 due to different storms.

Table E-15. Hydrodynamic parameters at T11 point.

Scenario		V_c (m/s)	H_s (m)	S_{xx} (m^3/s^2)	S_{xy} (m^3/s^2)	S_{yy} (m^3/s^2)	Q ($m^3/s/m$)
No SBWs	NE	0.089	0.628	0.293	-0.012	0.125	4.72E-05
	E	0.112	0.586	0.257	-0.014	0.113	5.15E-05
	SE	0.122	0.555	0.234	-0.016	0.100	5.46E-05
	Winter	0.069	0.266	0.076	-0.007	0.033	2.50E-05
	Summer	0.057	0.126	0.017	-0.002	0.008	7.53E-06
	Decadal	0.240	1.041	0.758	-0.073	0.332	4.20E-04
	Tri-Decadal	0.142	1.186	0.954	-0.086	0.402	3.15E-04
	Semi-Centennial	0.123	1.260	1.017	-0.087	0.440	2.82E-04
	Centennial	0.096	1.403	1.207	-0.115	0.542	2.75E-04
SBWs	NE	0.142	0.225	0.034	0.000	0.020	4.54E-06
	E	0.131	0.233	0.037	-0.001	0.022	5.59E-06
	SE	0.118	0.222	0.033	-0.002	0.019	4.68E-06
	Winter	0.069	0.127	0.014	-0.001	0.008	2.06E-06
	Summer	0.048	0.069	0.004	0.000	0.002	7.51E-07
	Decadal	0.103	0.527	0.178	-0.021	0.102	5.71E-06
	Tri-Decadal	0.122	0.589	0.219	-0.027	0.123	7.52E-06
	Semi-Centennial	0.109	0.683	0.288	-0.033	0.158	7.10E-06
	Centennial	0.112	0.851	0.441	-0.048	0.239	1.60E-05
Difference (%)	NE	-60.65	64.14	88.47	95.98	84.31	90.38
	E	-16.55	60.25	85.78	89.70	80.93	89.15
	SE	3.45	60.04	85.83	89.22	80.55	91.42
	Winter	0.01	52.02	81.89	81.79	76.48	91.79
	Summer	15.31	45.40	77.53	81.35	74.08	90.04
	Decadal	57.01	49.37	76.49	70.87	69.32	98.64
	Tri-Decadal	14.11	50.36	77.03	68.71	69.51	97.61
	Semi-Centennial	11.77	45.84	71.72	61.66	64.16	97.49
	Centennial	-17.21	39.35	63.48	58.16	55.95	94.17

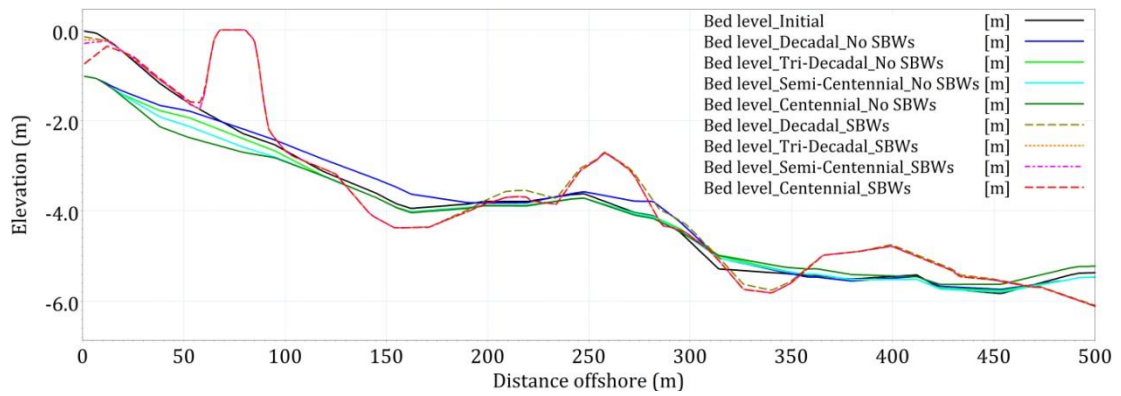


Figure E-49. Cross-shore changes of beach profile 17 due to different storms.

Table E-16. Hydrodynamic parameters at T12 point.

Scenario		V_c (m/s)	H_s (m)	S_{xx} (m^3/s^2)	S_{xy} (m^3/s^2)	S_{yy} (m^3/s^2)	Q ($m^3/s/m$)
No SBWs	NE	0.066	0.669	0.332	-0.007	0.147	1.66E-05
	E	0.093	0.644	0.308	-0.006	0.137	2.18E-05
	SE	0.099	0.620	0.286	-0.006	0.127	2.31E-05
	Winter	0.067	0.287	0.086	-0.004	0.038	1.48E-05
	Summer	0.057	0.137	0.019	-0.002	0.009	7.01E-06
	Decadal	0.195	1.078	0.827	-0.005	0.363	1.80E-04
	Tri-Decadal	0.099	1.150	0.898	0.026	0.400	1.23E-04
	Semi-Centennial	0.097	1.222	0.961	-0.001	0.446	1.27E-04
	Centennial	0.108	1.385	1.182	-0.029	0.558	2.09E-04
SBWs	NE	0.087	0.261	0.042	-0.006	0.031	3.80E-06
	E	0.071	0.237	0.035	-0.005	0.025	2.13E-06
	SE	0.065	0.220	0.030	-0.004	0.021	1.63E-06
	Winter	0.054	0.138	0.015	-0.001	0.010	1.61E-06
	Summer	0.040	0.076	0.004	-0.001	0.003	6.01E-07
	Decadal	0.086	0.562	0.195	-0.009	0.123	6.13E-06
	Tri-Decadal	0.084	0.636	0.243	-0.002	0.156	9.26E-06
	Semi-Centennial	0.070	0.718	0.302	-0.007	0.194	6.99E-06
	Centennial	0.079	0.881	0.447	-0.015	0.283	1.03E-05
Difference (%)	NE	-32.69	61.02	87.38	16.58	78.64	77.05
	E	24.16	63.17	88.67	21.33	81.83	90.22
	SE	34.26	64.47	89.42	33.37	83.63	92.96
	Winter	18.52	52.05	82.84	59.85	74.98	89.11
	Summer	31.09	44.44	77.80	66.33	71.61	91.42
	Decadal	55.71	47.89	76.38	-73.96	66.00	96.59
	Tri-Decadal	14.64	44.68	72.92	105.83	61.04	92.48
	Semi-Centennial	28.23	41.21	68.60	-450.59	56.49	94.47
	Centennial	27.01	36.39	62.14	47.30	49.33	95.08

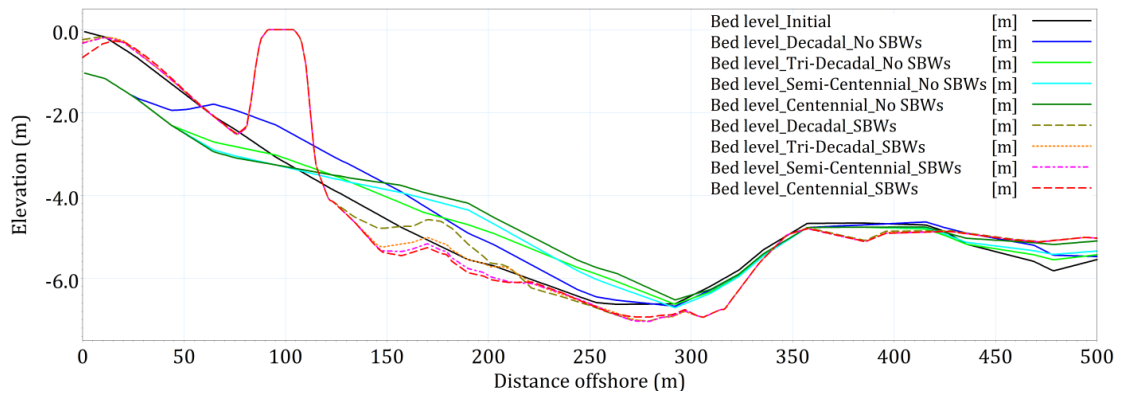


Figure E-50. Cross-shore changes of beach profile 18 due to different storms.

Table E-17. Hydrodynamic parameters at Q5 point.

Scenario		V_c (m/s)	H_s (m)	S_{xx} (m^3/s^2)	S_{xy} (m^3/s^2)	S_{yy} (m^3/s^2)	Q ($m^3/s/m$)
No SBWs	NE	0.133	0.677	0.334	-0.021	0.148	6.64E-05
	E	0.194	0.633	0.292	-0.026	0.133	8.08E-05
	SE	0.196	0.616	0.276	-0.027	0.127	8.22E-05
	Winter	0.065	0.279	0.085	-0.009	0.038	3.22E-05
	Summer	0.060	0.126	0.017	-0.003	0.008	9.99E-06
	Decadal	0.291	1.095	0.834	-0.081	0.370	5.33E-04
	Tri-Decadal	0.300	1.240	1.031	-0.098	0.437	6.04E-04
	Semi-Centennial	0.290	1.328	1.147	-0.111	0.482	6.36E-04
	Centennial	0.294	1.462	1.342	-0.144	0.581	7.13E-04
SBWs	NE	0.086	0.567	0.255	-0.016	0.098	4.79E-06
	E	0.073	0.551	0.242	-0.013	0.092	3.44E-06
	SE	0.068	0.528	0.224	-0.011	0.085	3.31E-06
	Winter	0.049	0.205	0.057	-0.004	0.022	2.25E-06
	Summer	0.046	0.085	0.010	-0.001	0.004	1.65E-06
	Decadal	0.109	0.896	0.624	-0.037	0.240	1.48E-05
	Tri-Decadal	0.110	0.942	0.672	-0.038	0.257	2.20E-05
	Semi-Centennial	0.111	1.015	0.755	-0.043	0.293	4.02E-05
	Centennial	0.139	1.152	0.929	-0.057	0.379	8.67E-05
Difference (%)	NE	34.95	16.21	23.47	25.38	33.83	92.78
	E	62.34	12.97	17.02	49.28	30.71	95.74
	SE	65.20	14.16	18.81	59.47	32.90	95.97
	Winter	25.51	26.28	32.73	58.69	43.31	93.00
	Summer	23.20	32.22	39.31	64.77	49.42	83.51
	Decadal	62.51	18.19	25.14	55.15	35.06	97.22
	Tri-Decadal	63.17	24.04	34.81	61.68	41.25	96.35
	Semi-Centennial	61.76	23.56	34.19	60.89	39.17	93.68
	Centennial	52.61	21.25	30.79	60.18	34.71	87.84

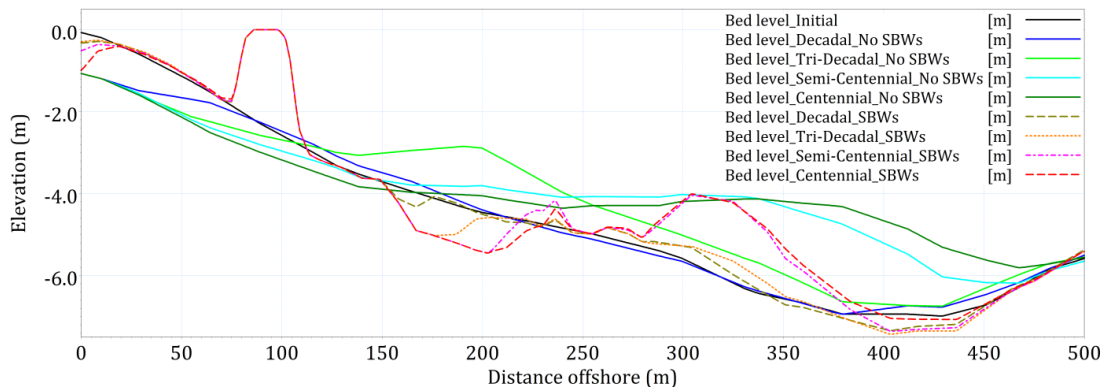


Figure E-51. Cross-shore changes of beach profile 19 due to different storms.

Table E-18. Hydrodynamic parameters at Q6 point.

Scenario		V_c (m/s)	H_s (m)	S_{xx} (m^3/s^2)	S_{xy} (m^3/s^2)	S_{yy} (m^3/s^2)	Q ($m^3/s/m$)
No SBWs	NE	0.086	0.674	0.326	-0.037	0.159	2.00E-05
	E	0.139	0.621	0.280	-0.035	0.138	5.68E-05
	SE	0.147	0.591	0.255	-0.033	0.125	6.16E-05
	Winter	0.059	0.279	0.079	-0.012	0.041	1.64E-05
	Summer	0.060	0.131	0.017	-0.004	0.010	8.45E-06
	Decadal	0.184	1.066	0.761	-0.103	0.382	2.82E-04
	Tri-Decadal	0.214	1.187	0.920	-0.112	0.436	3.65E-04
	Semi-Centennial	0.190	1.282	1.037	-0.123	0.488	3.63E-04
	Centennial	0.227	1.424	1.247	-0.151	0.585	5.03E-04
SBWs	NE	0.144	0.587	0.263	-0.027	0.112	9.55E-06
	E	0.097	0.564	0.243	-0.025	0.102	5.98E-06
	SE	0.076	0.534	0.218	-0.023	0.091	5.70E-06
	Winter	0.062	0.220	0.061	-0.007	0.026	2.89E-06
	Summer	0.061	0.096	0.011	-0.002	0.005	2.04E-06
	Decadal	0.146	0.923	0.636	-0.065	0.268	2.69E-05
	Tri-Decadal	0.158	0.980	0.702	-0.072	0.291	3.24E-05
	Semi-Centennial	0.117	1.064	0.793	-0.076	0.328	5.73E-05
	Centennial	0.140	1.217	0.966	-0.099	0.409	1.12E-04
Difference (%)	NE	-68.23	12.91	19.28	26.61	29.52	52.32
	E	30.66	9.16	13.03	29.02	25.82	89.47
	SE	48.43	9.57	14.21	30.36	27.05	90.75
	Winter	-4.77	21.07	23.60	38.63	36.50	82.37
	Summer	-1.10	27.06	32.85	48.51	46.03	75.81
	Decadal	20.76	13.35	16.41	36.89	29.63	90.46
	Tri-Decadal	26.18	17.47	23.69	36.04	33.18	91.13
	Semi-Centennial	38.43	17.05	23.52	38.00	32.84	84.24
	Centennial	38.28	14.49	22.54	34.24	30.14	77.79

Table E-19. Hydrodynamic parameters at Q7 point.

	Scenario	V _c (m/s)	H _s (m)	S _{xx} (m ³ /s ²)	S _{xy} (m ³ /s ²)	S _{yy} (m ³ /s ²)	Q (m ³ /s/m)
No SBWs	NE	0.134	0.628	0.275	-0.030	0.135	3.93E-05
	E	0.091	0.609	0.255	-0.031	0.128	2.11E-05
	SE	0.060	0.580	0.234	-0.028	0.117	2.67E-05
	Winter	0.050	0.263	0.069	-0.010	0.035	1.69E-05
	Summer	0.051	0.126	0.015	-0.003	0.009	7.04E-06
	Decadal	0.105	1.016	0.650	-0.071	0.323	1.89E-04
	Tri-Decadal	0.099	1.079	0.722	-0.075	0.342	2.11E-04
	Semi-Centennial	0.103	1.170	0.824	-0.085	0.384	2.29E-04
	Centennial	0.079	1.327	1.020	-0.112	0.489	2.52E-04
SBWs	NE	0.117	0.409	0.120	-0.022	0.055	6.62E-06
	E	0.071	0.393	0.110	-0.021	0.051	3.34E-06
	SE	0.052	0.369	0.097	-0.019	0.045	2.11E-06
	Winter	0.041	0.171	0.032	-0.006	0.015	1.07E-06
	Summer	0.037	0.078	0.006	-0.001	0.003	7.03E-07
	Decadal	0.080	0.728	0.358	-0.060	0.164	9.64E-06
	Tri-Decadal	0.046	0.782	0.400	-0.065	0.181	1.10E-05
	Semi-Centennial	0.066	0.859	0.467	-0.072	0.214	1.93E-05
	Centennial	0.087	0.995	0.603	-0.090	0.286	3.45E-05
Difference (%)	NE	12.75	34.85	56.32	26.20	59.37	83.17
	E	22.43	35.47	56.78	33.43	60.48	84.19
	SE	12.15	36.38	58.44	33.62	61.46	92.07
	Winter	17.06	35.03	53.40	39.93	57.30	93.67
	Summer	27.14	37.67	58.13	56.83	62.23	90.01
	Decadal	23.79	28.36	44.99	15.17	49.30	94.89
	Tri-Decadal	53.85	27.55	44.60	13.88	46.91	94.81
	Semi-Centennial	35.91	26.61	43.24	14.93	44.32	91.55
	Centennial	-10.31	25.01	40.84	19.70	41.41	86.31

BIBLIOGRAPHY

- Ahrens, J. P. (1987). *Characteristics of Reef Breakwaters*: United States. Army. Corps of Engineers, U. S. Army Engineer Waterways Experiment Station, Coastal Engineering Research Center.
- Alesheikh, A., Ghorbanali, A., & Nouri, N. (2007). *Coastline change detection using remote sensing*. International Journal of Environmental Science & Technology, 4(1), 61-66. doi: 10.1007/BF03325962
- Allsop, N. W. H., & Institution of Civil, E. (1998). *Coastlines, Structures and Breakwaters: Proceedings of the International Conference Organized by the Institution of Civil Engineers and Held in London, UK, on 19-20 March 1998*: Thomas Telford.
- Aragonés, L., Serra, J. C., Villacampa, Y., Saval, J. M., & Tinoco, H. (2015). *New methodology for describing the equilibrium beach profile applied to the Valencia's beaches*. Geomorphology.
- Armono, H. D., & Hall, K. R. (2003). *Wave transmission on submerged breakwaters made of hollow hemispherical shape artificial reefs*. Paper presented at the Canadian Coastal Conference, Kingston, Canada.
- Arnouil, D. S. (2008). *Shoreline Response for a Reef Ball Submerged Breakwater System Offshore of Grand Cayman Island*. (Master of Science in Ocean Engineering), Florida Institute of Technology.
- Astier, J. M. (1984). *Impact des aménagements littoraux de la rade de Toulon, liés aux techniques d'endigage, sur les herbiers à Posidonia oceanica*. Paper presented at the The International Workshop on Posidonia oceanica Beds.
- Basterretxea, G., Orfila, A., Jordi, A., Casas, B., Lynett, P., Liu, P. L. F., Duarte, C. M., Tintor, J., & xe. (2004). *Seasonal Dynamics of a Microtidal Pocket Beach with Posidonia Oceanica Seabeds (Mallorca, Spain)*. Journal of Coastal Research, 20(4), 1155-1164.
- Battjes, J. A., & Janssen, J. P. F. M. (1978). *Energy Loss and Set-Up Due to Breaking of Random Waves*. Coastal Engineering. doi: doi:10.1061/9780872621909.034
10.1061/9780872621909.034
- Ben Alaya, H. (1972). *Repartition et condition d'installation de Posidonia oceanica Delile et Cymodocea nodosa Ascherson dans le Golfe de Tunis*. Bull. Instit. Nation. Peche de Salammbou, 2, 331-416.
- Benassai, G. (2006). *Introduction to Coastal Dynamics and Shoreline Protection*: WIT Press.
- Bernabeu, A. M., Medina, R., & Vidal, C. (2003). *A morphological model of the beach profile integrating wave and tidal influences*. Marine Geology, 197(1-4), 95-116. doi: [http://dx.doi.org/10.1016/S0025-3227\(03\)00087-2](http://dx.doi.org/10.1016/S0025-3227(03)00087-2)
- Bird, E. (2005). *Coastline Changes*. In M. L. Schwartz (Ed.), *Encyclopedia of Coastal Science* (pp. 319-323). Dordrecht: Springer Netherlands.
- Birkemeier, W. A. (1985). *Field Data on Seaward Limit of Profile Change*. Journal of Waterway, Port, Coastal, and Ocean Engineering, 111(3), 598-602.
- Black, K. P., & Andrews, C. J. (2001). *Sandy Shoreline Response to Offshore Obstacles Part 1: Salient and Tombolo Geometry and Shape*. Journal of Coastal Research, 82-93.
- Blanc, J. J. (1958). *Recherches de sédimentologie littorale et sous-marine en Provence occidentale*: Masson et Cie.
- Blanc, J. J. (1960). *Etude sédimentologique de la presque l'île de Giens et de ses abords*.
- Blanc, J. J. (1971). *Mouvements de la mer et notes de sédimentologie littorale*: Travaux du Laboratoire de Géologie de Luminy.
- Blanc, J. J. (1973). *Recherches sédimentologiques sur la protection du littoral à la presque île de Giens (Var)*.
- Blanc, J. J. (1974). *Phénomènes d'érosions sous-marines à la Presqu'île de Giens (Var)*. CR Acad. Sci. Paris, 278, 1821-1823.

- Blanc, J. J. (1975). *Recherches de sédimentologie appliquée au littoral rocheux de la Provence. Aménagement et protection*. Marseille.
- Bodegom, M. (2004). *Beach Nourishment: an evaluation of equilibration design methods-Cancún Beach Rehabilitation Project*. (Msc thesis), Delft University of Technology.
- Bodge, K. R. (1992). *Representing Equilibrium Beach Profiles with an Exponential Expression*. *Journal of Coastal Research*, 8(1), 47-55.
- Boudouresque, C.-F., Bernard, G., Bonhomme, P., Charbonnel, E., Diviacco, G., Meinesz, A., Pergent, G., Pergent-Martini, C., Ruitton, S., & Tunesi, L. (2012). *Protection and conservation of Posidonia oceanica meadows: RAMOGE and RAC/SPA*.
- Boudouresque, C.-F., Bernard, G., Pergent, G., Shili, A., & Verlaque, M. (2009). *Regression of Mediterranean seagrasses caused by natural processes and anthropogenic disturbances and stress: a critical review*. *Botanica Marina*, 52, 395-418.
- Boudouresque, C.-F., & Grissac, A. J. d. (1983). *L'herbier à Posidonia oceanica en Méditerranée: les interactions entre la plante et le sédiment*. *Journal de Recherche Océanographique*, 8, 99-122.
- Bouma, T. J., De Vries, M. B., Low, E., Peralta, G., Táncoz, I. C., van de Koppel, J., & Herman, P. M. J. (2005a). *Trade-offs Related to Ecosystem Engineering: A Case Study on Stiffness of Emerging Macrophytes*. *Ecology*, 86(8), 2187-2199. doi: 10.1890/04-1588
- Bouma, T. J., Friedrichs, M., Klaassen, P., van Wesenbeeck, B. K., Brun, F. G., Temmerman, S., van Katwijk, M. M., Graf, G., & Herman, P. M. J. (2009). *Effects of shoot stiffness, shoot size and current velocity on scouring sediment from around seedlings and propagules*. *Marine Ecology Progress Series*, 388, 293-297.
- Bouma, T. J., Vries, M. B. D., Low, E., Kusters, L., Herman, P. M. J., Táncoz, I. C., Temmerman, S., Hesselink, A., Meire, P., & Regenmortel, S. v. (2005b). *Flow hydrodynamics on a mudflat and in salt marsh vegetation: identifying general relationships for habitat characterisations*. *Hydrobiologia*, 540(1-3), 259-274. doi: 10.1007/s10750-004-7149-0
- Brière, C., Abadie, S., Bretel, P., & Lang, P. (2007). *Assessment of TELEMAC system performances, a hydrodynamic case study of Anglet, France*. *Coastal Engineering*, 54(4), 345-356.
- Børker, I., Zyserman, J., Østergaard Madsen, E., Mangor, K., & Jensen, J. (2007). *Morphological Modelling: A Tool For Optimisation of Coastal Structures*. *Journal of Coastal Research*, 1148-1158. doi: 10.2112/04-0380.1
- Browder Albert, E., Dean Robert, G., & Chen, R. (1996). *Performance of a Submerged Breakwater for Shore Protection*. *Coastal Engineering*.
- Brunel, C. (2010). *Evolution séculaire de l'avant-côte de la Méditerranée française, impact de l'élévation du niveau de la mer et des tempêtes*. (DOCTEUR), UNIVERSITE AIX-MARSEILLE I.
- Brunel, C., & Sabatier, F. (2007). *Pocket Beach Vulnerability to Sea-level Rise*. *Journal of Coastal Research*(Special Issue 50).
- Brunel, C., & Sabatier, F. (2009). *Potential influence of sea-level rise in controlling shoreline position on the French Mediterranean Coast*. *Geomorphology*, 107(1-2), 47-57. doi: <https://doi.org/10.1016/j.geomorph.2007.05.024>
- Bruun, P. (1954). *Coast Erosion and the Development of Beach Profiles*: U.S. Beach Erosion Board.
- Buccino, M., Del Vita, I., & Calabrese, M. (2013). *Predicting wave transmission past Reef Ball™ submerged breakwaters*. *Journal of Coastal Research*, 171-176. doi: 10.2112/SI65-030.1
- Burcharth, H. F., Hawkins, S. J., Zanuttigh, B., & Lamberti, A. (2007). *Environmental Design Guidelines for Low Crested Coastal Structures*: Elsevier Science.
- Calafat, F. M., & Gomis, D. (2009). *Reconstruction of Mediterranean sea level fields for the period 1945-2000*. *Global and Planetary Change*, 66(3-4), 225-234. doi: <http://dx.doi.org/10.1016/j.gloplacha.2008.12.015>

- Canny, J. (1986). *A Computational Approach to Edge Detection*. IEEE Transactions on Pattern Analysis and Machine Intelligence, PAMI-8(6), 679-698. doi: 10.1109/TPAMI.1986.4767851
- Capanni, R. (2011). *Étude et gestion intégrée des transferts sédimentaires dans le système Gapeau/rade d'Hyères*. (Ph.D.), Aix Marseille 1.
- Cavallaro, L., Lo Re, C., Paratore, G., Viviano, A., & Foti, E. (2010). *Response of Posidonia Oceanica plants to wave motion in shallow-waters - Preliminary experimental results*. Coastal Engineering Proceedings; No 32 (2010): Proceedings of 32nd Conference on Coastal Engineering, Shanghai, China, 2010.
- Cazenave, A., Cabanes, C., Dominh, K., Gennero, M. C., & Provost, C. (2003). Present-Day Sea Level Change: Observations and Causes. In G. Beutler, M. R. Drinkwater, R. Rummel & R. Steiger (Eds.), *Earth Gravity Field from Space — From Sensors to Earth Sciences: Proceedings of an ISSI Workshop 11–15 March 2002, Bern, Switzerland* (pp. 131-144). Dordrecht: Springer Netherlands.
- CEREMA. (2014). *Details of the campaign 08301 and 08302-Porquerolles*.
- Chen, S.-N., Sanford, L. P., Koch, E. W., Shi, F., & North, E. W. (2007). *A nearshore model to investigate the effects of seagrass bed geometry on wave attenuation and suspended sediment transport*. Estuaries and Coasts, 30(2), 296-310.
- Colas, S. (2007). *Analyse statistique et cartographique de l'érosion marine* (Vol. 06): Institut Français de l'environnement.
- Council, N. R., Studies, D. E. L., Board, O. S., Resources, B. E. S., & Committee on Sea Level Rise in California, O. W. (2012). *Sea-Level Rise for the Coasts of California, Oregon, and Washington: Past, Present, and Future*: National Academies Press.
- Courtaud, J. (2000). *Dynamiques geomorphologiques et risques littoraux cas du tombolo de giens (Var, France méridionale)*. (Ph.D. dissertation), Université Aix-Marseille I.
- Dai, Z.-J., Du, J.-z., Li, C.-C., & Chen, Z.-S. (2007). *The configuration of equilibrium beach profile in South China*. Geomorphology, 86(3-4), 441-454. doi: <http://dx.doi.org/10.1016/j.geomorph.2006.09.016>
- Dally, W. R. (2005). Surf Zone Processes. In M. L. Schwartz (Ed.), *Encyclopedia of Coastal Science* (pp. 929-935). Dordrecht: Springer Netherlands.
- Dally, W. R., Pope, J., Station, U. S. A. E. W. E., & Coastal Engineering Research, C. (1986). *Detached Breakwaters for Shore Protection*: U.S. Army Engineer Waterways Experiment Station.
- Davis, R., & Fitzgerald, D. (2009). *Beaches and Coasts*: Wiley.
- Dean, R. G. (1977). *Equilibrium Beach Profiles: U.S. Atlantic and Gulf Coasts*: Center for Applied Coastal Research.
- Dean, R. G. (1987). *Coastal Sediment Processes: Toward Engineering Solutions*. American Society of Civil Engineers, Proceedings of Coastal Sediments '87, 24.
- Dean, R. G. (1991). *Equilibrium Beach Profiles: Characteristics and Applications*. Journal of Coastal Research, 7(1), 53-84.
- Dean, R. G., Chen, R., & Browder, A. E. (1997). *Full scale monitoring study of a submerged breakwater, Palm Beach, Florida, USA*. Coastal Engineering, 29(3), 291-315. doi: [http://dx.doi.org/10.1016/S0378-3839\(96\)00028-2](http://dx.doi.org/10.1016/S0378-3839(96)00028-2)
- Dean, R. G., & Dalrymple, R. A. (2004). *Coastal Processes with Engineering Applications*: Cambridge University Press.
- Deigaard, R., Fredsøe, J., & Hedegaard, I. B. (1986). *Suspended Sediment in the Surf Zone*. Journal of Waterway, Port, Coastal, and Ocean Engineering, 112(1), 115-128. doi: 10.1061/(ASCE)0733-950X(1986)112:1(115)
- Devoy, R. J. N. (2008). *Coastal Vulnerability and the Implications of Sea-Level Rise for Ireland*. Journal of Coastal Research, 24(2), 325-443.

- Dewidar, K. (2011). *Changes in the Shoreline Position Caused by Natural Processes for Coastline of Marsa Alam and Hamata, Red Sea, Egypt*. International Journal of Geosciences, 2, 523-529.
- DHI. (2014a). *Coastline evolution-LITLINE USER GUIDE*.
- DHI. (2014b). *MIKE 21 Spectral Wave Module Scientific Documentation*.
- DHI. (2014c). *MIKE 21 ST - Non-Cohesive Sediment Transport Module - User Guide*.
- DHI. (2014d). *MIKE 21/3 Coupled Model FM*.
- Dijkstra, J. T. (2009). *Measurements and modelling of the effects of seagrass meadows on flow and sediment transport in the Bay of l'Ecluse, Dinard, France*. Paper presented at the RCEM 2009, Delft University of Technology and Deltares, Delft, the Netherlands.
- Douglas, B. C., & Mark, C. (2000). *Long-Term Shoreline Position Prediction and Error Propagation*. Journal of Coastal Research, 16(1), 145-152.
- E.O.L. (2010). *Suivi de l'évolution des plages de la commune Hyères-les-palmiers*. Commune de Heres-Les-Palmiers.
- Eldeberky, Y., & Battjes, J. A. (1996). *Spectral modelling of wave breaking: Application to Boussinesq equations*. J. Geophys. Res., 101, 1253-1264.
- Engelund, F., & Fredsøe, J. (1976). *A sediment transport model for straight alluvial channels*. Nordic Hydrology, 7, 296-306.
- ERAMM. (2001). *Etude sur la protection de la partie Nord du tombolo Ouest de Giens* (Vol. phase I+II+III).
- Finkl, C. W., & Walker, H. J. (2005). Beach Nourishment. In M. L. Schwartz (Ed.), *Encyclopedia of Coastal Science* (pp. 147-160). Dordrecht: Springer Netherlands.
- Fletcher, C. H., Romine, B. M., Genz, A. S., Barbee, M. M., Dyer, M., Anderson, T. R., Lim, S. C., Vitousek, S., Bochicchio, C., & Richmond, B. M. (2012). *National assessment of shoreline change: Historical shoreline change in the Hawaiian Islands* (U. S. G. Survey Ed.). Reston, VA.
- Folkard, A. M. (2005). *Hydrodynamics of model Posidonia oceanica patches in shallow water*. Limnology and Oceanography, 50(5), 1592-1600. doi: 10.4319/lo.2005.50.5.1592
- Fonseca, M. S., & Cahalan, J. A. (1992). *A preliminary evaluation of wave attenuation by four species of seagrass*. Estuarine, Coastal and Shelf Science, 35(6), 565-576. doi: [http://dx.doi.org/10.1016/S0272-7714\(05\)80039-3](http://dx.doi.org/10.1016/S0272-7714(05)80039-3)
- Fonseca, M. S., & Koehl, M. A. R. (2006). *Flow in seagrass canopies: The influence of patch width*. Estuarine, Coastal and Shelf Science, 67(1-2), 1-9. doi: <http://doi.org/10.1016/j.ecss.2005.09.018>
- Fredsøe, J. (1984). *Turbulent Boundary Layer in Wave-current Motion*. Journal of Hydraulic Engineering, 110(8), 1103-1120. doi: 10.1061/(ASCE)0733-9429(1984)110:8(1103)
- Fredsøe, J., & Deigaard, R. (1992). *Mechanics of Coastal Sediment Transport*: World Scientific.
- Gacia, E., & Duarte, C. M. (2001). *Sediment Retention by a Mediterranean Posidonia oceanica Meadow: The Balance between Deposition and Resuspension*. Estuarine, Coastal and Shelf Science, 52(4), 505-514.
- Gacia, E., Granata, T. C., & Duarte, C. M. (1999). *An approach to measurement of particle flux and sediment retention within seagrass (Posidonia oceanica) meadows*. Aquatic Botany, 65(1-4), 255-268. doi: [http://dx.doi.org/10.1016/S0304-3770\(99\)00044-3](http://dx.doi.org/10.1016/S0304-3770(99)00044-3)
- Gadre, M. R., Poonawala, I. Z., & Kudale, M. D. (1992). *Stability of Rock Armour Protection for Submarine Pipelines*. Paper presented at the Eighth Congress of the Asia and Pacific Division of the International Association for Hydraulic Research (VIII APD -IAHR Congress), Pune, India.
- Galassi, G., & Spada, G. (2014). *Sea-level rise in the Mediterranean Sea by 2050: Roles of terrestrial ice melt, steric effects and glacial isostatic adjustment*. Global and Planetary Change, 123, Part A, 55-66. doi: <http://dx.doi.org/10.1016/j.gloplacha.2014.10.007>

- GEOMER. (1996). *Aménagement du littoral- Etude de faisabilité d'un port intérieur à l'embouchure du Gapeau: Etude courantologique et sédimentologique.*
- Ghisalberti, M., & Nepf, H. M. (2002). *Mixing layers and coherent structures in vegetated aquatic flow.* JOURNAL OF GEOPHYSICAL RESEARCH, 107, 1-11.
- Gómez-Pujol, L., Orfila, A., Álvarez-Ellacuría, A., Terrados, J., & Tintoré, J. (2013). *Posidonia oceanica beach-cast litter in Mediterranean beaches: a coastal videomonitoring study.* Journal of Coastal Research, 1768-1773. doi: 10.2112/SI65-299.1
- Gómez-Pujol, L., Orfila, A., Álvarez-Ellacuría, A., & Tintoré, J. (2011). *Controls on sediment dynamics and medium-term morphological change in a barred microtidal beach (Cala Millor, Mallorca, Western Mediterranean).* Geomorphology, 132(3-4), 87-98. doi: <http://dx.doi.org/10.1016/j.geomorph.2011.04.026>
- Gomis, D., Tsimplis, M., Marcos, M., L. Fenoglio-Marc, B. Pérez, F. Raicich, I. Vilibić, G. Wöppelmann, S. Monserrat, & Jordà, G. (2011). *Sea Level Rise and its Forcing in the Mediterranean Sea.* MedCLIVAR – Mediterranean CLimate VARiability.
- Grizzle, R. E., Short, F. T., Newell, C. R., Hoven, H., & Kindblom, L. (1996). *Hydrodynamically induced synchronous waving of seagrasses: 'monami' and its possible effects on larval mussel settlement.* Journal of Experimental Marine Biology and Ecology, 206(1), 165-177. doi: [http://dx.doi.org/10.1016/S0022-0981\(96\)02616-0](http://dx.doi.org/10.1016/S0022-0981(96)02616-0)
- Hallermeier, R. J. (1978). *Uses for a Calculated Limit Depth to Beach Erosion.* Paper presented at the 16th Conference on Coastal Engineering, Hamburg, Germany.
- Hallermeier, R. J. (1981a). *Fall Velocity of Beach Sands:* United States. Army. Corps of Engineers, Coastal Engineering Research Center.
- Hallermeier, R. J. (1981b). *A profile zonation for seasonal sand beaches from wave climate.* Coastal Engineering, 4, 253-277.
- Hamm, L., Capobianco, M., Dette, H. H., Lechuga, A., Spanhoff, R., & Stive, M. J. F. (2002). *A summary of European experience with shore nourishment.* Coastal Engineering, 47(2), 237-264. doi: [http://dx.doi.org/10.1016/S0378-3839\(02\)00127-8](http://dx.doi.org/10.1016/S0378-3839(02)00127-8)
- Hanson, H., Aarninkhof, S., Capobianco, M., Jim, x, nez, J. A., Larson, M., Nicholls, R. J., Plant, N. G., Southgate, H. N., Steetzel, H. J., Stive, M. J. F., & Vriend, H. J. d. (2003). *Modelling of Coastal Evolution on Yearly to Decadal Time Scales.* Journal of Coastal Research, 19(4), 790-811.
- Hapke, C. J., Himmelstoss, E. A., Kratzmann, M. G., List, J. H., & Thieler, E. R. (2011). *National Assessment of Shoreline Change: Historical Shoreline Change along the New England and Mid-Atlantic Coasts:* U.S. Geological Survey.
- Harris, L. E. (1996). *Wave attenuation by rigid and flexible-membrane submerged breakwaters.* (Doctoral dissertation), Florida Atlantic University.
- Hasselmann, K. (1962). *On the non-linear energy transfer in a gravity-wave spectrum Part 1. General theory.* Journal of Fluid Mechanics, 12(04), 481-500.
- Hasselmann, K. (1974). *On the spectral dissipation of ocean waves due to whitecapping.* Bound. Layer Meteor., 6, 107-127.
- Hasselmann, S., Hasselmann, K., Allender, J. H., & Barnett, T. P. (1985). *Computations and Parameterizations of the Nonlinear Energy Transfer in a Gravity-Wave Specturm. Part II: Parameterizations of the Nonlinear Energy Transfer for Application in Wave Models.* Journal of Physical Oceanography, 15.
- Hearin, J. (2009). *Preliminary Design of an Artificial Surfing Reef for Cocoa Beach, Florida.* Reef journal, 1, 212-234.
- Hendriks, I. E., Sintès, T., Bouma, T. J., & Duarte, C. M. (2008). *Experimental assessment and modeling evaluation of the effects of the seagrass Posidonia oceanica on flow and particle trapping.* Marine Ecology Progress Series, 356, 163-173.
- Holthuijsen, L. H. (2007). *Waves in Oceanic and Coastal Waters:* Cambridge University Press.
- Holthuijsen, L. H., Herman, A., & Booij, N. (2003). *Phase-decoupled refraction-diffraction for spectral wave models.* Coastal Engineering, 49, 291-305.

- Hsu, M., Kuo, A., Kuo, J., & Liu, W. (1999). *Procedure to Calibrate and Verify Numerical Models of Estuarine Hydrodynamics*. Journal of Hydraulic Engineering, 125(2), 166-182. doi: 10.1061/(ASCE)0733-9429(1999)125:2(166)
- HYDRO-M. (1993). *Etude d'impact sur l'environnement du projet de protection du tombolo ouest de la presqu'île de Giens*.
- IARE. (1996). *Le Tombolo Occidental de Giens - Synthèse des connaissances- Analyse globale et scénarios d'aménagement et de gestion*.
- Infantes, E., Orfila, A., Simarro, G., Terrados, J., Luhar, M., & Nepf, H. (2012). *Effect of a seagrass (Posidonia oceanica) meadow on wave propagation*. Marine Ecology Progress Series, 456, 63-72.
- Infantes, E., Terrados, J., Orfila, A., Cañellas, B., & Álvarez-Ellacuria, A. (2009). *Wave energy and the upper depth limit distribution of Posidonia oceanica*. Botanica Marina, 52(5), 419. doi: 10.1515/BOT.2009.050
- IPCC. (1996). *Climate changes: The science of climate change, summary for policymakers and technical summary of the working group I report* (N. Y. Cambridge University Press Ed.): Intergovernmental Panel on Climate Change.
- Janssen, P. A. E. M., Lionello, P., & L., Z. (1989). *On the interaction of wind and waves*. Phil. Trans. R. Soc. Lond., A 329, 289-301.
- Jayson-Quashigah, P.-N., Addo, K. A., & Kodzo, K. S. (2013). *Medium resolution satellite imagery as a tool for monitoring shoreline change. Case study of the Eastern coast of Ghana*. Journal of Coastal Research, 511-516. doi: 10.2112/SI65-087.1
- Jeudy De Grissac, A. (1975). *Sédimentologie dynamique des rades d'Hyères et de Giens (Var). Problèmes d'Aménagements*. (Ph.D. dissertation), Université d'Aix-Marseille II, Marseille.
- Jeudy de Grissac, A. (1984). *Effects des herbiers à Posidonia oceanica sur la dynamique marine et la sédimentologie littorale*. Paper presented at the International workshop on Posidonia oceanica Meadows, France.
- Jeudy de Grissac, A., & Blanc, J. J. (1989). *Reflexion sur la regression des herbiers a Posidonies (Departements du Var et des bouches di Rhone)*. Paper presented at the International workshop on Posidonia oceanica Meadows, France.
- Jeudy de Grissac, A., & Boudouresque, C. F. (1985). *Rôles des herbiers de phanérogames marines dans les mouvements des sédiments côtiers: les herbiers à Posidonia oceanica*. Paper presented at the Colloque franco-japonais Oceanographie, Marseille, France.
- Jonsson, I. G., & Carlsen, N. A. (1966). *Experimental and theoretical investigations in an oscillatory turbulent boundary layer*. Journal of Hydraulic Research, 14, 45-60.
- Jonsson, I. G., & Carlsen, N. A. (1976). *Experimental and theoretical investigations in an oscillatory turbulent boundary layer*. Journal of Hydraulic Research, 14(1), 45-60. doi: 10.1080/00221687609499687
- Kaiser, M. F. M., & Frihy, O. E. (2009). *Validity of the equilibrium beach profiles: Nile Delta Coastal Zone, Egypt*. Geomorphology, 107(1-2), 25-31. doi: <http://dx.doi.org/10.1016/j.geomorph.2006.09.025>
- Karcz, J., & Kacperski, L. (2012). *An effect of grid quality on the results of numerical simulations of the fluid flow field in an agitated vessel*. Paper presented at the 14th European Conference on Mixing, Warszawa.
- Karunarathna, H., Horrillo-Caraballo, J., Ranasinghe, R., Short, A., & Reeve, D. (2012). *An analysis of cross-shore profile evolution of a sand and a composite sand-gravel beaches*. Paper presented at the 33rd International Conference on Coastal Engineering, Santander, Spain.
- Kliucinikaite, L., & Ahrendt, K. (2011). *Modelling different artificial reefs in the coastline of Probstei*. RADOST journal, 5.
- Koch, E. W., Shafer, D. J., Smith, J. M. K., United States. Army. Corps of, E., Engineer, R., Development, C., Environmental, L., Coastal, Hydraulics, L., System-Wide Water

- Resources Research, P., & Submerged Aquatic Vegetation Restoration Research, P. (2006). *Waves in Seagrass Systems: Review and Technical Recommendations*: US Army Corps of Engineers, Engineer Research and Development Center, Environmental Laboratory, Coastal and Hydraulics Laboratory.
- Koftis, T., & Prinos, P. (2011). *Estimation of wave attenuation over Posidonia oceanica*. Paper presented at the 5th SCACR International Short Conference on Applied Coastal Research, RWTH Aachen University, Germany.
- Koftis, T., Prinos, P., & Stratigaki, V. (2013). *Wave damping over artificial Posidonia oceanica meadow: A large-scale experimental study*. Coastal Engineering, 73, 71-83. doi: <http://dx.doi.org/10.1016/j.coastaleng.2012.10.007>
- Komar, P. D. (1998). *Beach Processes and Sedimentation*: Prentice Hall.
- Komar, P. D., & McDougal, G. W. (1994). *The Analysis of Exponential Beach Profiles*. Journal of Coastal Research, 10(1), 59-69.
- Kombiadou, K., Ganthy, F., Verney, R., Plus, M., & Sottolichio, A. (2013). *Modelling the effects of Zostera noltei meadows on sediment dynamics: application to the Arcachon lagoon*. Ocean Dynamics, 64(10), 1499-1516. doi: 10.1007/s10236-014-0754-1
- Komen, G. J., Cavaleri, L., Donelan, M., Hasselmann, K., Hasselmann, S., & Janssen, P. A. E. M. (1996). *Dynamics and Modelling of Ocean Waves*: Cambridge University Press.
- Kouwen, N. (1969). *Flow Retardance in Vegetated Channels*. Journal of the Irrigation and Drainage Division, 95(2), 329-344.
- Kraus, N. C., Larson, M., & Wise, R. A. (1998). *Depth of Closure in Beach-fill Design-Coastal Engineering Technical Note CETN II-40*: U.S. Army Engineer Waterways Experiment Station.
- Kriebel, D. L., Kraus, N. C., & Larson, M. (1991). *Engineering methods for predicting beach profile response*. Paper presented at the Coastal Sediments (1991).
- Kuang, C., He, L., Gu, J., Pan, Y., Zhang, Y., Yang, Y., Qiu, R., & Zhang, J. (2014). *Effects of Submerged Breakwater on Hydrodynamics and Shoreline Change of the East Beach of Beidaihe, Bohai Bay, China*. Journal of Coastal Research, 30(3), 598-614.
- Kulkarni, R. (2013). *Numerical Modelling of Coastal Erosion using MIKE21*. (Master), Norwegian University of Science and Technology, Trondheim, Norway.
- Lacroix, Y., Vu, M. T., Than, V. V., & Nguyen, V. T. (2015). *Modeling the effect of geotextile submerged breakwater on hydrodynamics in La Capte beach*. Paper presented at the Vietnam-Japan Workshop on Estuaries, Coasts and Rivers, Hoi An, Vietnam.
- Larson, M., & Wise, R. A. (1998). *Simple models for equilibrium profiles under breaking and non-breaking waves*. Coastal Engineering. doi: <http://dx.doi.org/10.9753/icce.v26.%25p>
- Leatherman, S. P., Zhang, K., & Douglas, B. C. (2000). *Sea level rise shown to drive coastal erosion*. Eos, Transactions American Geophysical Union, 81(6), 55-57. doi: 10.1029/00E000034
- Lee, P. Z.-F. (1994). *The submarine equilibrium profile: a physical model*. Journal of Coastal Research, 10(1).
- Lefebvre, A., Thompson, C. E. L., & Amos, C. L. (2010). *Influence of Zostera marina canopies on unidirectional flow, hydraulic roughness and sediment movement*. Continental Shelf Research, 30(16), 1783-1794. doi: <http://doi.org/10.1016/j.csr.2010.08.006>
- Lillesand, T. M., Kiefer, R. W., & Chipman, J. W. (2008). *Remote sensing and image interpretation*: John Wiley & Sons.
- Liu, H., & Jezek, K. C. (2004). *Automated extraction of coastline from satellite imagery by integrating Canny edge detection and locally adaptive thresholding methods*. International Journal of Remote Sensing, 25(5), 937-958. doi: 10.1080/0143116031000139890
- Liu, W., Hsu, M., & Kuo, A. (2002). *Modelling of hydrodynamics and cohesive sediment transport in Tanshui River estuarine system, Taiwan*. Marine Pollution Bulletin, 44(10), 1076-1088. doi: [http://dx.doi.org/10.1016/S0025-326X\(02\)00160-1](http://dx.doi.org/10.1016/S0025-326X(02)00160-1)

- Liu, Z. (2014). *Hydrodynamic and Sediment Transport Numerical Modelling and Applications at Tairua Estuary, New Zealand* (Doctor of Philosophy), University of Waikato.
- Longuet-Higgins, M. S., & Stewart, R. W. (1964). *Radiation stresses in water waves; a physical discussion, with applications*. Deep Sea Research and Oceanographic Abstracts, 11(4), 529-562.
- Loos, E. A., & Niemann, K. O. (2002). *Shoreline feature extraction from remotely-sensed imagery*. Paper presented at the IEEE International Geoscience and Remote Sensing Symposium.
- López, F., & García, M. H. (2001). *Mean Flow and Turbulence Structure of Open-Channel Flow through Non-Emergent Vegetation*. Journal of Hydraulic Engineering, 127(5), 392-402. doi: 10.1061/(ASCE)0733-9429(2001)127:5(392)
- Manca, E. (2010). *Effects of Posidonia oceanica seagrass on nearshore waves and wave-induced flows*. (PhD thesis), University of Southampton.
- Marbà, N., & Duarte, C. M. (2010). *Mediterranean warming triggers seagrass (Posidonia oceanica) shoot mortality*. Global Change Biology, 16(8), 2366-2375. doi: 10.1111/j.1365-2486.2009.02130.x
- Mashriqui, H. S. (2003). *Hydrodynamic and Sediment Transport Modeling of Deltaic sediment processes*. (Doctor of Philosophy), Louisiana State University.
- MathWorks. (2015). *Curve Fitting Toolbox-User's Guide*
- Medina, J. R., Tintoré, J., & Duarte, C. M. (2001). *Las praderas de Posidonia oceanica y la regeneración de playas*. Revista de obras publicas.
- Meulé, S. (2010). *IMplantation d'Atténuateur de Houle en GEOTextile: Suivi scientifique de la plage de La Capte, Hyères, Var : Instrumentation, Modélisation*. Hyères.
- Michael, S. F., Dolan, R., & Elder, J. F. (1993). *A New Method for Predicting Shoreline Positions from Historical Data*. Journal of Coastal Research, 9(1), 147-171.
- Miche, R. (1944). *Mouvements ondulatoires de la mer en profondeur constante ou décroissante forme limite de la houle lors de son déferlement, application aux digues maritimes*. Paris.
- Nepf, H., & Ghisalberti, M. (2008). *Flow and transport in channels with submerged vegetation*. Acta Geophysica, 56(3), 753-777. doi: 10.2478/s11600-008-0017-y
- Nepf, H. M. (1999). *Drag, turbulence, and diffusion in flow through emergent vegetation*. Water Resources Research, 35(2), 479-489. doi: 10.1029/1998WR900069
- Nepf, H. M. (2000). *Flow structure in depth-limited, vegetated flow*. Journal of Geophysical Research-Oceans, Vol. 105, pp 28547-28557.
- Nepf, H. M., & Vivoni, E. R. (2000). *Flow structure in depth-limited, vegetated flow*. Journal of Geophysical Research: Oceans, 105(C12), 28547-28557. doi: 10.1029/2000JC900145
- Nguyen, L. D., Minh, N. T., Thy, P. T. M., Phung, H. P., & Huan, H. V. (2010). *Analysis of changes in the riverbanks of Mekong river-Vietnam by using multi-temporal remote sensing data*. Paper presented at the International Archives of the Photogrammetry, Remote Sensing and Spatial Information Science, Kyoto, Japan.
- Nguyen, V. T. (2012). *Morphological evolution and back siltation of navigation channel in Dinh An Estuary, Mekong River Delta: understanding, simulating and solving*. (Doctor of Philosophy), Hohai University.
- Nguyen, V. T., Zheng, J.-h., & Zhang, C. (2012). *Beach profiles characteristics along Giao Thuy and Hai Hau coasts, Vietnam: A field study*. China Ocean Engineering, 26(4), 699-712. doi: 10.1007/s13344-012-0052-y
- Nicholls, R. J., Wong, P. P., Burkett, V., Codignotto, J., Hay, J., McLean, R., Ragoonaden, S., & Woodroffe, C. D. (2007). *Climate Change 2007 - Impacts, Adaptation and Vulnerability: Working Group II Contribution to the Fourth Assessment Report of the IPCC*: Cambridge University Press.
- Nicholson, J., Broker, I., Roelvink, J. A., Price, D., Tanguy, J. M., & Moreno, L. (1997). *Intercomparison of coastal area morphodynamic models*. Coastal Engineering, 31(1-4), 97-123. doi: [http://dx.doi.org/10.1016/S0378-3839\(96\)00054-3](http://dx.doi.org/10.1016/S0378-3839(96)00054-3)

- Nielsen, P. (1979). *Some basic concepts of wave sediment transport*. Series paper 20-Institute of Hydrodynamic and Hydraulic Engineering, Technical University of Denmark.
- NRC. (1995). *Beach Nourishment and Protection*: National Academies Press. Washington, D.C.
- OCEANIDE. (2010). *Etude pour la protection de la plage du Ceinturon et du secteur Sud du port Saint-Pierre – Phase 1 : Synthèse des connaissances - Rapport*.
- Özkan-Haller, H. T., & Sarah, B. (2007). *Equilibrium Beach Profile Concept for Delaware Beaches*. Journal of Waterway, Port, Coastal, and Ocean Engineering, 133(2), 147-160. doi: 10.1061/(ASCE)0733-950X(2007)133:2(147)
- Paquier, A. E. (2009). *L'herbier de Posidonie à la Capte (Var, France) : Evaluation de sa rugosité et méthode de cartographie par courantomètre profileur acoustique*. (Master Mémoire de stage d'initiation à la Recherche).
- Paskoff, R. P. (2009). Effects of sea-level rise on coastal cities and residential areas. In A. Yotova (Ed.), *Climate Change, Human Systems and Policy* (Vol. 2, pp. 1-16): Eolss Publishers Co. Ltd.,
- Pasqualini, V., Pergent-Martini, C., Clabaut, P., & Pergent, G. (1998). *Mapping of Posidonia oceanica using Aerial Photographs and Side Scan Sonar: Application off the Island of Corsica (France)*. Estuarine, Coastal and Shelf Science, 47(3), 359-367. doi: <http://dx.doi.org/10.1006/ecss.1998.0361>
- Pender, D., & Karunaratna, H. (2013). *A statistical-process based approach for modelling beach profile variability*. Coastal Engineering, 81, 19-29.
- Pereira, C., Coelho, C., Ribeiro, A., Fortunato, A. B., Lopes, C. L., & Dias, J. M. (2013). *Numerical modelling of shoreline evolution in the Aveiro coast, Portugal – climate change scenarios*. Journal of Coastal Research, 2161-2166. doi: 10.2112/SI65-365.1
- Peterson, C. H., & Bishop, M. J. (2005). *Assessing the Environmental Impacts of Beach Nourishment*. BioScience, 55(10), 887-896. doi: 10.1641/0006-3568(2005)055[0887:ATEIOB]2.0.CO;2
- Peterson, C. H., Bishop, M. J., Johnson, G. A., D'Anna, L. M., & Manning, L. M. (2006). *Exploiting beach filling as an unaffordable experiment: Benthic intertidal impacts propagating upwards to shorebirds*. Journal of Experimental Marine Biology and Ecology, 338(2), 205-221. doi: <http://dx.doi.org/10.1016/j.jembe.2006.06.021>
- Pham, T. N., Larson, M., Hanson, H., & Le, X. H. (2011). *A numerical model of beach morphological evolution due to waves and currents in the vicinity of coastal structures*. Coastal Engineering, 58(9), 863-876. doi: <http://dx.doi.org/10.1016/j.coastaleng.2011.05.006>
- Pilarczyk, K. W. (2003). *Design of low-crested (submerged) structures: An overview*. 6th COPEDEC (Int. Conf. on Coastal and Port Engng. in Develop. Countries).
- Pilarczyk, K. W., Zeidler, R., & Zeidler, R. B. (1996). *Offshore Breakwaters and Shore Evolution Control*: A.A. Balkema.
- Pilkey, O. H., & Wheeler, K. D. (1996). *The Corps and the Shore*: Island Press.
- Rajasree, B. R., Deo, M. C., & Sheela Nair, L. (2016). *Effect of climate change on shoreline shifts at a straight and continuous coast*. Estuarine, Coastal and Shelf Science, 183, Part A, 221-234. doi: <http://doi.org/10.1016/j.ecss.2016.10.034>
- Ranasinghe, R. (2016). *Assessing climate change impacts on open sandy coasts: A review*. Earth-Science Reviews, 160, 320-332. doi: <https://doi.org/10.1016/j.earscirev.2016.07.011>
- Ranasinghe, R., & Turner, I. L. (2006). *Shoreline response to submerged structures: A review*. Coastal Engineering, 53(1), 65-79. doi: <http://dx.doi.org/10.1016/j.coastaleng.2005.08.003>
- Richard, L. (2010). *Analyse du comportement des houles suite a la mise en place de tubes en geotextiles, La Capte, Hyeres*. (Mémoire de stage d'initiation à la Recherche).
- Roelvink, D., Reniers, A., van Dongeren, A., van Thiel de Vries, J., McCall, R., & Lescinski, J. (2009). *Modelling storm impacts on beaches, dunes and barrier islands*. Coastal Engineering, 56(11-12), 1133-1152. doi: <http://dx.doi.org/10.1016/j.coastaleng.2009.08.006>

- Roelvink, J. A., Roelvink, D., & Reniers, A. (2012). *A Guide to Modeling Coastal Morphology*: World Scientific.
- Romańczyk, W., Boczar-Karakiewicz, B., & Bona, J. L. (2005). *Extended equilibrium beach profiles*. *Coastal Engineering*, 52(9), 727-744. doi: <http://dx.doi.org/10.1016/j.coastaleng.2005.05.002>
- Rongxing Li, J.-K. L. Y. F. (2001). *Spatial Modeling and Analysis for Shoreline Change Detection and Coastal Erosion Monitoring*. *Marine Geodesy*, 24(1), 1-12. doi: 10.1080/01490410121502
- Rubey, W. W. (1933). *Settling velocity of gravel, sand, and silt particles*. *American Journal of Science, Series 5* Vol. 25(148), 325-338.
- Ruessink, B. G., Walstra, D. J. R., & Southgate, H. N. (2003). *Calibration and verification of a parametric wave model on barred beaches*. *Coastal Engineering*, 48, 139-149.
- Ruiz, J. M., & Romero, J. (2003). *Effects of disturbances caused by coastal constructions on spatial structure, growth dynamics and photosynthesis of the seagrass Posidonia oceanica*. *Marine Pollution Bulletin*, 46(12), 1523-1533. doi: <http://dx.doi.org/10.1016/j.marpolbul.2003.08.021>
- Saengsupavanich, C. (2013). *Erosion protection options of a muddy coastline in Thailand: Stakeholders' shared responsibilities*. *Ocean & Coastal Management*, 83, 81-90. doi: <http://dx.doi.org/10.1016/j.ocecoaman.2013.02.002>
- Seiji M., Uda T., & S., T. (1987). *Statistical study on the effect and stability of detached breakwaters*. *Coastal Engineering in Japan*, 30, 131-141.
- Sheik, M., & Chandrasekar. (2011). *A shoreline change analysis along the coast between Kanyakumari and Tuticorin, India, using digital shoreline analysis system*. *Geo-spatial Information Science*, 14(4), 282-293. doi: 10.1007/s11806-011-0551-7
- Shields, I. A., Ott, W. P., & Van Uchelen, J. C. (1936). *Application of Similarity Principles and Turbulence Research to Bed-load Movement*: Soil Conservation Service Cooperative Laboratory, California Institute of Technology.
- Shin, E. C., & Oh, Y. I. (2007). *Coastal erosion prevention by geotextile tube technology*. *Geotextiles and Geomembranes*, 25(4-5), 264-277. doi: <http://dx.doi.org/10.1016/j.geotexmem.2007.02.003>
- Sierra, J., Presti, A., & Sánchez-Arcilla, A. (1994). *An Attempt to Model Longshore Sediment Transport on the Catalan Coast Coastal Engineering 1994* (pp. 2625-2638): American Society of Civil Engineers.
- Silvester, R., & Hsu, J. R. C. (1997). *Coastal Stabilization*: World Scientific.
- Simeone, S. (2008). *Posidonia oceanica banquette removal: sedimentological, geomorphological and ecological implications*. (PhD thesis), Università degli Studi della Tuscia.
- Sinnassamy, J. M., & Pergent-Martini, C. (1990). *Localisation et état de l'herbier de Posidonies sur le littoral P.A.C.A: Var. D.R.A.E. & G.I.S. Posidonie*.
- SOGREAH. (1988a). *Défense du littoral oriental du golfe de Giens* (Vol. tome 3).
- SOGREAH. (1988b). *Etudes sédimentologiques de la rade d Hyères. Littoral de port Pothuau à la Badine* (Vol. tome 4).
- SOGREAH. (1988c). *Etudes sédimentologiques de la rade d Hyères. Littoral de port Pothuau au Ruisseau du Pansard* (Vol. tome 5).
- Sorensen, R. M. (2006). *Basic Coastal Engineering*: Springer US.
- Soulsby, R. (1997). *Dynamics of Marine Sands: A Manual for Practical Applications*: Telford.
- Stauble, D. K., & Tabar, J. R. (2003). *The Use of Submerged Narrow-Crested Breakwaters for Shoreline Erosion Control*. *Journal of Coastal Research*, 19(3), 684-722.
- Sutherland, J., Peet, A. H., & Soulsby, R. L. (2004a). *Evaluating the performance of morphological models*. *Coastal Engineering*, 51(8-9), 917-939.

- Sutherland, J., Walstra, D. J. R., Chesher, T. J., van Rijn, L. C., & Southgate, H. N. (2004b). *Evaluation of coastal area modelling systems at an estuary mouth*. Coastal Engineering, 51(2), 119-142.
- Swart, D. H. (1976). *Predictive equations regarding coastal transports*. Proc 15th Conf Coastal Engng, 2, 1113-1132.
- Tanaka, N. (1976). *Effects of submerged rubble-mound breakwater on wave attenuation and shoreline stabilization*. Paper presented at the Proceedings 23rd Japanese Coastal Engineering Conference.
- Techet, A. (2005). *Design Principles for Ocean Vehicles*.
- Telesca, L., Belluscio, A., Criscoli, A., Ardizzone, G., Apostolaki, E. T., Frascchetti, S., Gristina, M., Knittweis, L., Martin, C. S., Pergent, G., Alagna, A., Badalamenti, F., Garofalo, G., Gerakaris, V., Louise Pace, M., Pergent-Martini, C., & Salomidi, M. (2015). *Seagrass meadows (Posidonia oceanica) distribution and trajectories of change*. Scientific Reports, 5, 12505. doi: 10.1038/srep12505
- Temmerman, S., Bouma, T. J., Govers, G., Wang, Z. B., De Vries, M. B., & Herman, P. M. J. (2005). *Impact of vegetation on flow routing and sedimentation patterns: Three-dimensional modeling for a tidal marsh*. Journal of Geophysical Research: Earth Surface, 110(F4), n/a-n/a. doi: 10.1029/2005JF000301
- Than, V. V. (2015). *Modélisation d'érosion côtière : application à la partie Ouest du tombolo de Giens*. (Ph.D. dissertation), Aix Marseille Université, Marseille.
- Thiruvengkatasamy, K., & Baby Girija, D. K. (2014). *Shoreline evolution due to construction of rubble mound jetties at Munambam inlet in Ernakulam-Trichur district of the state of Kerala in the Indian peninsula*. Ocean & Coastal Management, 102, Part A, 234-247. doi: <https://doi.org/10.1016/j.ocecoaman.2014.09.026>
- Toorman, E. A. (2002). *Modelling of turbulent flow with suspended cohesive sediment*. In C. W. Johan & K. Cees (Eds.), *Proceedings in Marine Science* (Vol. Volume 5, pp. 155-169): Elsevier.
- Tran, T. V., & Tran, T. B. (2009). *Application of remote sensing for shoreline change detection in Cuu Long Estuary*. VNU Journal of Earth and Environmental Sciences, 25.
- Tsimplis, M., Marcos, M., Somot, S., & Barnier, B. (2008). *Sea level forcing in the Mediterranean Sea between 1960 and 2000*. Global and Planetary Change, 63(4), 325-332. doi: <http://dx.doi.org/10.1016/j.gloplacha.2008.07.004>
- U. S. A. C.E, U. S. (1984). *Shore Protection Manual*: Department of the Army.
- U.S.A.C.E. (2012). *Coastal Engineering Manual Part V: Coastal Project Planning and Design* (EM 1110-2-1100): Books Express Publishing.
- U.S.A.C.E, U. S. (1984). *Shore Protection Manual*: Department of the Army.
- U.S.A.C.E, U. S. (1993). *Engineering Design Guidance for Detached Breakwaters as Shoreline Stabilization Structures*: U.S. Army Engineer Waterways Experiment Station.
- U.S.A.C.E, U. S. (2002). *Coastal Engineering Manual (CEM), Engineer Manual 1110-2-1100*. U.S. Army Corps of Engineers, Washington, D.C. (6 volumes).
- Vacchi, M., De Falco, G., Simeone, S., Montefalcone, M., Morri, C., Ferrari, M., & Bianchi, C. N. (2016). *Biogeomorphology of the Mediterranean Posidonia oceanica seagrass meadows*. Earth Surface Processes and Landforms, 42(1), 42-54. doi: 10.1002/esp.3932
- Van-Rijn, L. C., Walstra, D. J. R., Grasmeijer, B., Sutherland, J., Pan, S., & Sierra, J. P. (2003). *The predictability of cross-shore bed evolution of sandy beaches at the time scale of storms and seasons using process-based profile models*. Coastal Engineering, 47(3), 295-327. doi: 10.1016/S0378-3839(02)00120-5
- Van Rijn, L. C. (1993). *Principles of sediment transport in rivers, estuaries and coastal seas*: Aqua Publications.

- Van Rijn, L. C., Walstra, D. J. R., Grasmeijer, B., Sutherland, J., Pand, S., & Sierra, J. P. (2003). *The predictability of cross-shore bed evolution of sandy beaches at the time scale of storms and seasons using process-based Profile models*. Coastal Engineering, 47(3), 295–327.
- Vellinga, P. (1987). *Beach and dune erosion during storm surges*. Coastal Engineering, 6(4), 361-387. doi: [http://dx.doi.org/10.1016/0378-3839\(82\)90007-2](http://dx.doi.org/10.1016/0378-3839(82)90007-2)
- Vellinga, P., & Leatherman, S. P. (1989). *Sea level rise, consequences and policies*. Climatic Change, 15(1), 175-189. doi: 10.1007/BF00138851
- Vu, M. T., & Lacroix, Y. (2017a). *Investigation of shoreline changes in Ceinturon beach, Giens double tombolo, France*. Mediterranean Marine Science (In Review).
- Vu, M. T., & Lacroix, Y. (2018). *Investigating the effects of sea-level rise on morphodynamics in the western Giens tombolo, France*. Paper presented at the ICESE 2018, Barcelona, Spain.
- Vu, M. T., Lacroix, Y., & Nguyen, V. T. (2017b). *Empirical equilibrium beach profiles along the eastern tombolo of Giens*. Journal of marine Science and Application (Accepted).
- Vu, M. T., Lacroix, Y., & Nguyen, V. T. (2017c). *Investigating the impacts of the regression of Posidonia oceanica on hydrodynamics and sediment transport in Giens Gulf*. Ocean Engineering, 146, 70-86. doi: <https://doi.org/10.1016/j.oceaneng.2017.09.051>
- Vu, M. T., Lacroix, Y., Than, V. V., & Nguyen, V. T. (2017d). *Application of geospatial techniques for prediction of shoreline changes in Almanarre beach, France*. Indian Journal of Geo-Marine Science (Accepted).
- Weber, S. L. (1991). *Bottom friction for wind sea and swell in extreme depth-limited situations*. J. Phys. Oceanogr., 10, 1712-1733.
- Weggel, J. R. (1972). *Maximum breaker height for design*. Journal of the Waterways, Harbors and Coastal Engineering Division, 98(4), 529-548.
- Weggel, J. R., Douglass, S. L., Drexel University. Department of Civil, E., Physics, H., & Hydrology, L. (1987). *Performance of a Perched Beach at Slaughter Beach, Delaware*: Hydraulics & Hydrology Laboratory, Drexel University.
- Winarso, G., Janto, J., & Budhiman, S. (2001). *The potential application of remote sensing data for coastal study*. Paper presented at the 22nd Asian Conference on Remote Sensing, Singapore.
- Wu, J. (1980). *Wind-stress Coefficients over sea surface and near neutral conditions – A revisit*. Journal of Physical. Oceanography, 10, 727-740.
- Wu, J. (1994). *The sea surface is aerodynamically rough even under light winds*. Boundary layer Meteorology, 69, 149-158.
- Young, I. R. (1999). *Wind Generated Ocean Waves*: Elsevier Science.
- Zheng, J., & Dean, R. G. (1997). *Numerical models and intercomparisons of beach profile evolution*. Coastal Engineering, 30(3–4), 169-201. doi: [http://dx.doi.org/10.1016/S0378-3839\(96\)00040-3](http://dx.doi.org/10.1016/S0378-3839(96)00040-3)
- Zyserman, J. A., & Johnson, H. K. (2002). *Modelling morphological processes in the vicinity of shore-parallel breakwaters*. Coastal Engineering, 45(3–4), 261-284. doi: [http://dx.doi.org/10.1016/S0378-3839\(02\)00037-6](http://dx.doi.org/10.1016/S0378-3839(02)00037-6)